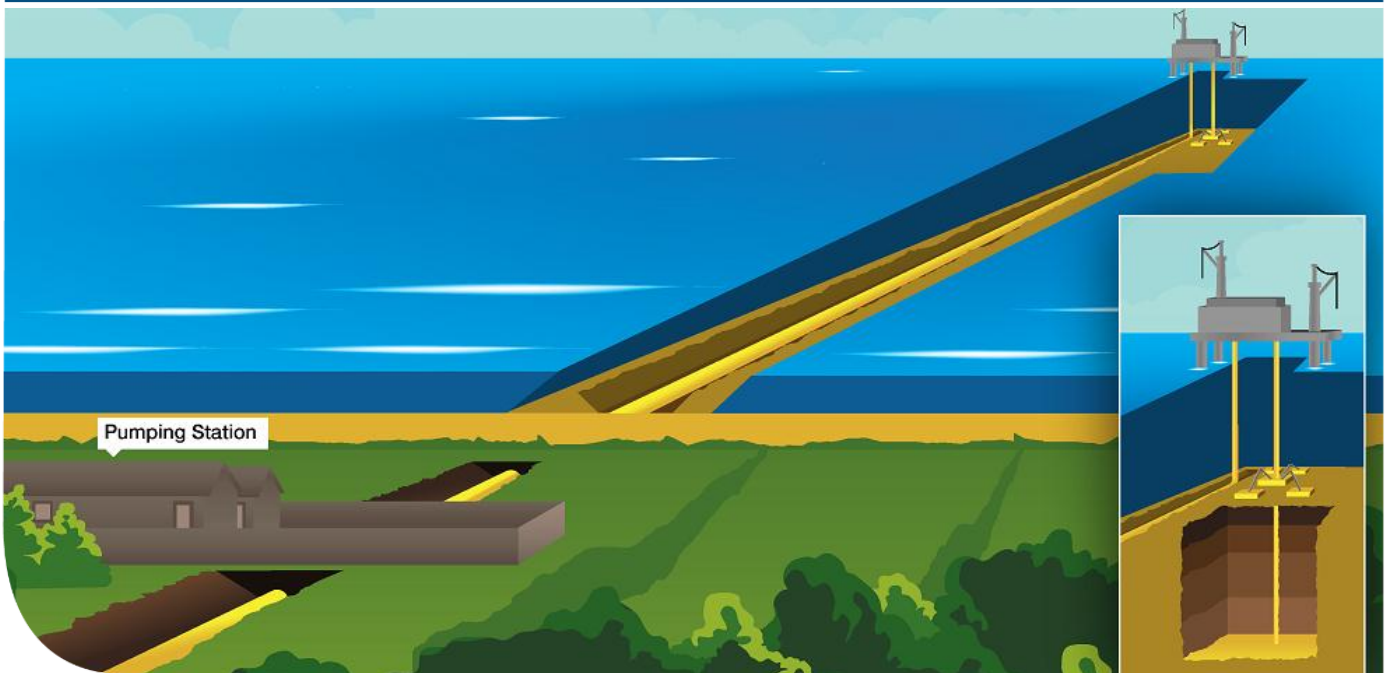




K40: Subsurface Geoscience and Production Chemistry Reports

Technical: Storage



IMPORTANT NOTICE

The information provided further to UK CCS Commercialisation Programme (the Competition) set out herein (the Information) has been prepared by Capture Power Limited and its sub-contractors (the Consortium) solely for the Department of Energy and Climate Change in connection with the Competition. The Information does not amount to advice on CCS technology or any CCS engineering, commercial, financial, regulatory, legal or other solutions on which any reliance should be placed. Accordingly, no member of the Consortium makes (and the UK Government does not make) any representation, warranty or undertaking, express or implied, as to the accuracy, adequacy or completeness of any of the Information and no reliance may be placed on the Information. In so far as permitted by law, no member of the Consortium or any company in the same group as any member of the Consortium or their respective officers, employees or agents accepts (and the UK Government does not accept) any responsibility or liability of any kind, whether for negligence or any other reason, for any damage or loss arising from any use of or any reliance placed on the Information or any subsequent communication of the Information. Each person to whom the Information is made available must make their own independent assessment of the Information after making such investigation and taking professional technical, engineering, commercial, regulatory, financial, legal or other advice, as they deem necessary.

Contents

Chapter	Title	Page
	Executive Summary	i
1	Introduction	1
2	Purpose	3
3	Overview	4
3.1	Project Overview	4
4	Integrated Geoscience Report	9
4.1	Summary	9
4.2	Geological and Structural Setting	9
4.2.1	Geological History	9
4.2.2	Endurance Storage Site	12
4.2.3	Endurance Storage Complex	15
4.2.4	Endurance Monitoring Area	15
4.3	Geological Characterisation of the Endurance Storage Site and Storage Complex	16
4.3.1	Geological and Structural Setting	16
4.4	Geological Horizon Mapping	17
4.4.1	Depth Conversion and Uncertainties	29
4.4.1.1	Gross Rock Volume Uncertainty Workflow	32
4.4.2	Structural Configuration and Faulting	40
4.5	Depositional Setting and Sedimentological Framework	44
4.5.1	Petrographic and Chemostratigraphic Input	46
4.5.1.1	Chemostratigraphic Input	46
4.5.1.2	Petrographic Input	49
4.5.2	Reservoir Quality and Correlation	49
4.6	Stratigraphic and Structural Framework	54
4.7	Primary and Secondary Seals	57
4.7.1	Characterisation	60
4.7.2	Core & Cuttings Analysis	64
4.8	Reservoir Facies Modelling	64
4.9	Reservoir Properties	71
4.9.1	Porosity	71
4.9.2	Permeability	72
4.9.3	Net to Gross	74
4.9.4	Temperature	74
4.9.5	Pressure	75
4.10	Volumetric Ranges and Uncertainties	76
4.10.1	Net Pore Volume Range	76
4.10.2	Net Pore Volumetric Uncertainty	78
4.10.3	Geological Models	79
4.10.4	Regional Structural Framework Model	80
4.10.5	Static (Geological) Model	80
4.10.6	Simulation Models	81
4.10.7	Geomechanical Models	82

4.11	Geochemistry _____	82
4.11.1	Laboratory Testing _____	83
4.11.1.1	Permeability as a function of throughput _____	83
4.11.1.2	Impact of CO ₂ exposure on rock mechanical properties _____	83
4.11.2	Geochemical modelling and simulation _____	84
4.11.3	Mineralogy and Fluid Chemistry _____	84
4.11.3.1	Geochemical Composition of Bunter Formation _____	85
4.11.3.2	Formation water composition _____	85
4.11.3.3	CO ₂ Composition _____	86
4.11.3.4	Thermodynamic data _____	87
4.11.3.5	Porosity-permeability relationship in dynamic simulation _____	88
4.11.3.6	Interaction among CO ₂ , formation water, reservoir and seal facies _____	88
4.11.3.7	Equilibrium batch 0D modelling (PHREEQC) _____	88
4.11.3.8	Kinetic batch 0D modelling (PHREEQC) _____	92
4.11.3.9	Summary of Kinetic batch 0D modelling (PHREEQC) _____	95
4.11.3.10	Fluid Flow and Geochemical Reaction Coupled Modelling (GEM) _____	95
4.11.4	Summary of Fluid Flow and Geochemical Reaction Coupled Modelling _____	99
4.11.4.1	CO ₂ Exposure in Analogous Reservoirs: Literature survey _____	99
4.12	Overview of plausible leakage pathways _____	101
4.12.1	Reservoir Leakage Through the Primary Seal and Secondary Seals _____	101
4.12.1.1	via Faults/Fractures _____	101
4.12.1.2	Diffuse Leakage _____	103
4.12.2	Well Failure _____	104
4.12.2.1	Injection Wells _____	104
4.12.2.2	Other Wells _____	105
4.12.3	Conclusions Regarding Leakage Paths _____	107
5	Petrophysical Workflows & Coefficients _____	108
5.1	Summary _____	108
5.2	Available Data _____	108
5.3	Petrophysical Evaluation _____	110
5.3.1	Clay Volume Determination _____	110
5.3.2	Porosity Determination _____	112
5.3.3	Permeability Prediction _____	115
5.3.4	Net Reservoir Determination _____	117
5.3.5	Water Saturation _____	118
5.3.6	Electrofacies _____	118
5.4	Results by Wells _____	121
5.4.1	Diagenesis _____	122
5.4.2	Primary Depositional Facies _____	122
5.4.3	Depth of Burial _____	122
5.5	Uncertainties and Sensitivities _____	123
5.5.1	NTG Sensitivity _____	123
5.5.2	Porosity Sensitivity _____	125
5.5.2.1	Cored Wells _____	125
5.5.2.2	Uncored Wells _____	126
5.6	Conclusions _____	127
6	Geomechanical Modelling _____	128
6.1	Summary _____	128

6.2	Introduction	128
6.3	Pre-Geomechanical Model (Pre-Gm)	129
6.4	Results of Geomechanical Tests from 42/25d-3	129
6.5	Test Process	130
6.6	Test Results	130
6.6.1	Rot Halite	130
6.6.2	Rot Clay	132
6.6.3	Bunter Sandstone	133
6.7	Geomechanical Model Build	134
6.7.1	Make Geomechanical Model	134
6.8	Distributed Sonic and Density	135
6.8.1.1	Fully Populated Velocity (VP_Log) and Density (Density_Merge) Properties	140
6.9	Geomechanical Property Calculations	142
6.9.1	Shear Velocity (Vs)	143
6.9.2	Linear Elastic Parameters	144
6.9.2.1	Shear Modulus (G)	144
6.9.2.2	Bulk Modulus (K)	144
6.9.2.3	Young's Modulus (E)	144
6.9.2.4	Poisson's Ratio	145
6.9.3	Non-linear Failure Parameters	145
6.9.3.1	Unconfined Compressive Strength (UCS)	145
6.9.3.2	Friction and Dilation Angles	146
6.9.3.3	Tensile Strength	146
6.9.4	Additional Geomechanical Parameters	146
6.9.4.1	Biot's Elastic Constant	146
6.9.4.2	Linear Thermal Expansion Coefficient (LTEC)	146
6.10	Conclusions	146
7	Geomechanical Simulation	148
7.1	Introduction	148
7.2	VISAGE Model Setup	148
7.2.1	Material Modelling	149
7.2.2	Populate Properties	149
7.2.3	Discontinuity Modelling	150
7.2.4	Define Pres/Temp/Sat Conditions	151
7.2.5	Define Boundary Conditions	155
7.2.6	Define Reservoir Geomechanics Simulation Case	157
7.2.7	Stress Charting and property generation	158
7.3	Simulation Cases and Results	159
7.4	Limit Cases	160
7.4.1	Rock Displacement	160
7.4.2	Yield Mode	161
7.5	Fault Yield Mode	164
7.6	Fault Elastic Shear and Normal Strains	165
7.6.1	Very Weak Faults, non-linear case	166
7.7	Reference Cases	167
7.8	Summary and Conclusion	169
8	Reservoir Engineering Field Report	171
8.1	Appraisal of Endurance structure with Well 42/25D-3	171

8.1.1	Core Analysis _____	173
8.1.1.1	Conventional Core Analysis _____	174
8.1.1.2	Special Core Analysis _____	183
8.1.2	Well Testing and Vertical Interference Test Results _____	197
8.1.2.1	Well Test Results _____	197
8.1.2.2	Vertical Interference Test (VIT) _____	198
8.2	SectionSectionExtent and Effective Hydraulic Communication of the Aquifer _____	198
8.3	Dynamic Simulation Models _____	199
8.3.1	Sub-regional simulation model _____	199
8.3.2	Upscaling for Reservoir Simulation _____	200
8.3.2.1	Simulation and Grid Design _____	200
8.3.2.2	Up-Scaled Parameters _____	202
8.3.3	Fluid Properties _____	204
8.3.4	Carbon Dioxide _____	205
8.3.4.1	Brine _____	205
8.3.5	Relative Permeability and Capillary Pressure functions _____	206
8.3.5.1	Measured Endurance Data _____	206
8.3.5.2	Capillary Pressure _____	207
8.3.5.3	Endurance Relative Permeability Analogues _____	209
8.3.6	Initialisation _____	211
8.3.7	Pressure Variation _____	212
8.3.7.1	Temperature Variation _____	212
8.3.8	Salinity Variation _____	212
8.3.9	Greater Bunter Size and Properties _____	213
8.3.10	The Outcrop _____	214
8.3.11	Simplified AOI Simulation Model _____	216
8.3.12	Simplified Injection Model _____	216
8.3.13	Wells _____	217
8.3.13.1	Well Locations and Trajectories _____	218
8.3.13.2	Perforation Interval _____	218
8.3.13.3	Well Switching _____	218
8.3.14	CO ₂ Storage Capacity and Reservoir Pressure Profiles _____	219
8.3.14.1	Endurance Maximum CO ₂ Storage Capacity _____	219
8.3.14.2	Pressure Increase in Endurance Due to White Rose CO ₂ Injection and Hydraulic Isolation _____	220
8.3.14.3	Dynamic Pressure Profiles Associated with White Rose CO ₂ Injection; Outcrop Open or Closed. _____	221
8.3.14.4	Aquifer Strength _____	224
8.3.15	Plume Development _____	226
8.3.15.1	Horizontal Permeability _____	226
8.3.15.2	Sub-Seismic Baffling _____	232
8.3.15.3	Impact of Relative Permeability data on Model Behaviour _____	235
8.3.15.4	Maximum Gas Relative Permeability _____	238
8.3.15.5	Drainage Critical Gas Saturation _____	238
8.3.15.6	Imbibition Critical Gas Saturation _____	239
8.3.15.7	Critical Water Saturation _____	239
8.3.15.8	Reservoir Location of White Rose CO ₂ _____	240
8.3.16	Injectivity _____	241
8.3.16.1	CO ₂ Injection Wells Injectivity _____	242
8.3.16.2	Skin Factor _____	245
8.3.17	Temperature Effects _____	246
8.4	Simulation of the Diffusion-Dissolution-Convection (DDC) process _____	248

8.4.1	DDC Process Overview and Simulation Model Set Up	248
8.4.2	DDC Simulation Results	250
8.5	Possible Influence and Effects on Regional Hydrocarbon Developments	251
8.6	Conclusions	252
9	Production Chemistry	255
9.1	Summary	255
9.2	Hydrate Inhibition Requirements	256
9.2.1	General Hydrate Management	257
9.2.1.1	General Operational Prevention	257
9.2.1.2	Removal of Free Water / Use of Nitrogen	257
9.2.1.3	Temperature	257
9.2.1.4	Pressure	258
9.2.1.5	Chemical Inhibition	258
9.2.1.6	Methanol	258
9.2.1.7	Glycols	259
9.2.1.8	Kinetic Inhibitors	261
9.2.2	Hydrate Modelling	262
9.2.2.1	Well Parameters	262
9.2.2.2	Static Shut in Well temperature and pressure Profiles	262
9.2.2.3	Hydrates in the Context of white rose ccs project	264
9.2.2.4	Hydrate Formation Curves	265
9.2.2.5	Input Data	265
9.2.2.6	CO ₂ 99% Composition #1 Fresh Water Case	265
9.2.2.7	CO ₂ 99% Mixture Composition #1 Formation Water Case	267
9.2.2.8	CO ₂ 99% Mixture Composition #1 Seawater Case	270
9.2.2.9	CO ₂ 96% Mixture Composition #2 Fresh Water Case	272
9.2.2.10	Summary of Hydrate Modelling	275
9.2.3	Recommended Hydrate Prevention Practice	276
9.2.3.1	Well Configuration	276
9.2.3.2	Shut in / Start Up	276
9.2.4	Operating / Treatment System Requirements	277
9.2.4.1	Monoethylene Glycol (MEG)	277
9.2.4.2	Low Dose Hydrate Inhibitors	277
9.2.4.3	Saline Brine	278
9.2.4.4	Nitrogen	278
9.3	Water Wash Specification	278
9.3.1	Water Wash Parameters	279
9.3.2	Water Wash Solution	282
9.3.2.1	Equipment Specification	282
9.3.2.2	Redundancy	282
9.3.2.3	Filtrations and Sea Water Source	282
9.3.2.4	Chemical Inhibitors	283
9.4	Conclusions	285
10	Overview Field Development	286
10.1	Storage Permit Application	286
10.2	Key Technological Aspects	286
10.2.1	Use of Dense Phase CO ₂ Pipeline:	287
10.2.2	Oversizing of the pipeline for future expansion:	287

10.2.3	Use of injection platform instead of a subsea installation: _____	287
10.2.4	CO ₂ storage volume _____	288
10.2.5	Storage mechanisms for CO ₂ _____	288
10.2.6	Geological modelling of the Storage Site and Storage Complex: _____	289
10.2.7	Multiple injection wells for maximum system availability _____	290
10.3	Additional Components of the Field Development Plan _____	290
10.3.1	Measurement, Monitoring and Verification Plan _____	290
10.3.2	Corrective Measures Plan _____	290
10.3.3	Storage Site and Storage Complex Risk Assessment _____	290
10.3.4	Project Environmental Statement _____	291
11	References	292
12	Glossary	295

Key Words

Key Word	Meaning or Explanation
Carbon	An element, but used as shorthand for its gaseous oxide, carbon dioxide CO ₂ .
Capture	Collection of CO ₂ from power station combustion process or other facilities and its process ready for transportation.
Endurance	The name given to the geological structure forming the storage reservoir and which is also applied to the platform that would service the wells.
Key knowledge	Information that may be useful if not vital to understanding how some enterprise may be successfully undertaken
Well	A structure which forms a conduit from surface to a storage reservoir (in the case of CCS). The structure is formed of concentric tubes or pipes (casings), decreasing in diameter from surface to the reservoir depth. The outermost tubes are known as casings and are inserted into drilled holes and cemented in place. The innermost pipe is known as the tubing and conveys the CO ₂ transported by pipeline from onshore and into the store.
Storage	The containment of CO ₂ in a store for an indefinite period of time. The store is composed of porous rock, with the pores initially containing saline water, but as CO ₂ injection commences the pores will contain CO ₂ and water. With respect to the White Rose project, the Storage Site comprises the BSF (Bunter Sandstone Formation) within the Endurance structure. The lithologies above and below Bunter sandstone are mainly shales and evaporites, hence they are all envisaged to have a good sealing quality. The areal dimensions of the Storage Site are taken from the most likely Top Bunter depth map which closes at 1460m TVDSS.
Reservoir	A unit or volume of rock which has both porosity and permeability and can store, produce or receive (by injection in the CCS case) fluids. In the context of CCS, the reservoir forms the main storage facility for CO ₂ injected into the store.
Subsurface	Pertaining to the rocks below the seabed, for an offshore development. Also, in the context of disciplines, can mean the activities of individuals, such as geologist, geophysicists and petrologists who perform technical work related to defining and analysing the rocks and fluids below the seabed.
Endurance	The proposed Storage site for this project was previous referred to as "5/42" as the geological formation partially underlies hydrocarbon licensing blocks 42/25 in the southern North Sea. The site has been renamed "Endurance"; this name is also used for the proposed platform.

Executive Summary

This report is one of a series of reports; these “key knowledge” reports are issued here as public information. These reports were generated as part of the Front End Engineering Design (FEED) Contract agreed with the Department of Energy and Climate Change (DECC) as part of the White Rose Project.

White Rose seeks to deliver a clean coal-fired power station using oxy-fuel technology, which would generate up to 448MWe (gross), integrated into a full-chain Carbon Capture and Storage (CCS) Project. CCS technology allows 90% of the carbon dioxide produced during combustion to be captured, processed and compressed before being transported to permanent storage in dense phase. The dense phase carbon dioxide would be kept under pressure while it is pumped through a buried onshore pipeline to the seashore and then through an offshore pipeline to be stored in a specially chosen rock formation under the seabed of the southern North Sea.

Delivery of the full-chain project is to be provided by National Grid Carbon Limited (NGCL), which is responsible for the Transport and Storage (T&S) network, and Capture Power Limited (CPL), which is responsible for the Oxy Power Plant (OPP) and the Gas Processing Unit (GPU).

The structure of interest (identified as Endurance, previously known as 5/42) is a four-way dip-closure straddling blocks 42/25 and 43/21 in the UK sector of the North Sea, some 60 miles east of Flamborough Head. This structure is a saline aquifer, approximately 22km long, 7km wide and over 200m thick. The crest of the reservoir is located at a depth of approximately 1020m below the sea bed. Reservoir datum (at 1300mTVDSS) pressure and temperature were determined as 140.0bar and 55.9°C, respectively. A layer of mudstone called the Rot Clay provides the primary cap rock or seal. This in turn is overlain by more than 90m of a salt layer known as the Rot Halite which is anticipated to provide additional seal capability.

This document provides a summary of the methodologies, results and conclusions of the geological, structural and sedimentological interpretation of the regional and sub-regional data that has been gathered for the Endurance structure, together with descriptions of the petrophysical workflows and coefficients that have been used to generate reservoir properties; the modelling workflow used to build the Geomechanical Model; an assessment of the potential chemical interactions along the subsurface CO₂ flow stream from the wells to near-well reservoir region; an overview of the Storage Complex and the offshore infrastructure required for the permanent storage; an analysis of the dynamic behaviour of the reservoir simulation models to assess the capacity, injectivity, hydrodynamics, containment and monitorability; and an assessment of the effect of dynamic pressure and temperature responses of the Endurance storage complex due to CO₂ injection.

Her Majesty's Government (HMG) Autumn Statement and Statement to Markets on 25 November 2015 regarding the Carbon Capture and Storage Competition confirmed that the £1 billion ring-fenced capital budget for the Carbon Capture and Storage Competition was no longer available. This meant that the Competition could not proceed on the basis previously set out. A notice of termination of the White Rose FEED Contract was issued to CPL on 23 December 2015 and the FEED Contract was terminated on 25 January 2016; a date which was earlier than the expected completion date. The Government, CPL and National Grid are committed to sharing the knowledge from UK CCS projects, and this Key Knowledge Deliverable represents the learning achieved up to the cancellation of the CCS Competition and termination of the FEED Contract and therefore does not necessarily represent the final and completed constructible project.

1 Introduction

National Grid Carbon Limited (NGCL) is a wholly owned subsidiary of the National Grid group of companies. Capture Power Limited (CPL) is a special purpose vehicle company, which has been formed by a consortium consisting of General Electric (GE), Drax and BOC, to pursue the White Rose (WR) carbon capture and storage (CCS) Project (the WR Project).

CPL have entered into an agreement, the Front End Engineering Design (FEED) Contract, with the UK Government's Department of Energy and Climate Change (DECC) pursuant to which it will carry out, among other things, the engineering, cost estimation and risk assessment required to specify the budget required to develop and operate the White Rose Assets. The contents of this K40 report draws on work, which was undertaken by National Grid in support of the Don Valley Power Project, which was partly funded under the European Union's European Energy Programme for Recovery (EEPR). The WR Assets comprise an end-to-end electricity generation and CCS system comprising, broadly: a coal fired power station utilising oxy-fuel technology, carbon dioxide capture, processing, compression and metering facilities; transportation pipeline and pressure boosting facilities; offshore carbon dioxide reception and processing facilities and injection wells into an offshore storage reservoir.

CPL and NGCL have entered into an agreement, the Key Sub-Contract, pursuant to which NGCL will perform a project, the WR Transport and Storage (T&S) FEED Project, which will meet that part of CPL's obligations under the FEED Contract which would be associated with the T&S Assets. The T&S Assets include, broadly: the transportation pipeline and pressure boosting facilities; offshore carbon dioxide reception and processing facilities and injection wells into an offshore storage reservoir.

A key component of the WR T&S FEED Project is the Key Knowledge Transfer process. A major portion of this is the compilation and distribution of a set of documents termed Key Knowledge Deliverables, of which this document is one.

This report:

- provides a summary of the methodologies, results and conclusions of the geological, structural and sedimentological interpretation of the regional and sub-regional data that has been gathered for the Endurance structure (previously known as 5/42);
- provides a description of the petrophysical workflows and coefficients that have been used to generate reservoir properties from which have subsequently been used to build the static reservoir model; the 'best case' results of the interpretation are presented in addition to a discussion of the uncertainty ranges;
- describes the modelling workflow used to build the Geomechanical Model (GM) of the Endurance Storage Complex using the Petrel Geomechanics software. Output from this modelling workflow will provide the necessary framework for assessing the geomechanical integrity of the Endurance Storage Complex during and at the cessation of White Rose CO₂ injection;
- documents an assessment of the potential chemical interactions along the subsurface CO₂ flow stream from the wells to near-well reservoir region that are likely to result in significant loss of operations performance/efficiency and the development of appropriate strategies to manage or mitigate these;
- provide an overview of the Storage Complex and the offshore infrastructure required for the permanent storage of White Rose CO₂.
- reports on the use analytical and full field simulation models to assess the capacity, injectivity, hydrodynamics, containment and monitorability of the Endurance structural closure for the safe and permanent storage of White Rose CO₂; and

- assesses the effect of dynamic pressure and temperature responses due to White Rose CO₂ injection on the stress, deformation, and failure properties and behaviours of the Endurance Storage Complex.

2 Purpose

The purpose of this report is to provide:

- an integrated report on geology/geophysics describing geophysical and geological modelling including description of static reservoir model build. This will include:
 - regional setting sedimentological setting and structural review;
 - an overview of the storage complex and site will be included with a review of any potential leakage paths; and
 - seismic interpretation report as a section in the main report;
- an overview report on petrophysics describing petrophysical model and results from petrophysical analysis of relevant wells;
- a detailed geomechanical analysis and building of coupled reservoir simulation model, production chemistry and on a conventional core analysis; Special Core Analysis (SCAL) will only be reported in so far as the input to the reservoir simulation model;
- a reservoir engineering field report covering all storage reservoirs within Endurance to include:
 - PVT report;
 - geoscience reports;
 - pore pressure prediction report;
 - evidence or otherwise of reservoir compartmentalisations/barriers to vertical flow; and
 - dynamic modelling output report (including any cross sections or fine scale sectional modelling) and full field simulation report; and
- comments on monitoring, which include:
 - Storage risk assessment report describing identified risks and mitigation measures through the project;
 - monitoring plan report describing potential technologies and proposed monitoring plan with frequency of monitoring exercises; and
 - remediation plan report describing potential mitigations for potential issues related to the safe storage of CO₂.

3 Overview

3.1 Project Overview

The White Rose CCS Project aims to provide an example of a clean coal-fired power station of up to 448MW gross output, built and operated as a commercial enterprise.

The project comprises a state-of-the-art coal-fired power plant that is equipped with full CCS technology. The plant would also have the potential to co-fire biomass; where part of the fossil fuel supplied to the plant would be replaced with a 'carbon lean', renewable alternative.

The project is intended to prove CCS technology at a commercial scale and demonstrate it as a competitive form of low-carbon power generation and as an important technology in tackling climate change. It would also play an important role in establishing a carbon dioxide (CO₂) transportation and storage network in the Yorkshire and Humber area. Figure 3.1 below gives a geographical overview of the proposed CO₂ transportation system.

Figure 3.1: Geographical Overview of the Transportation Facility

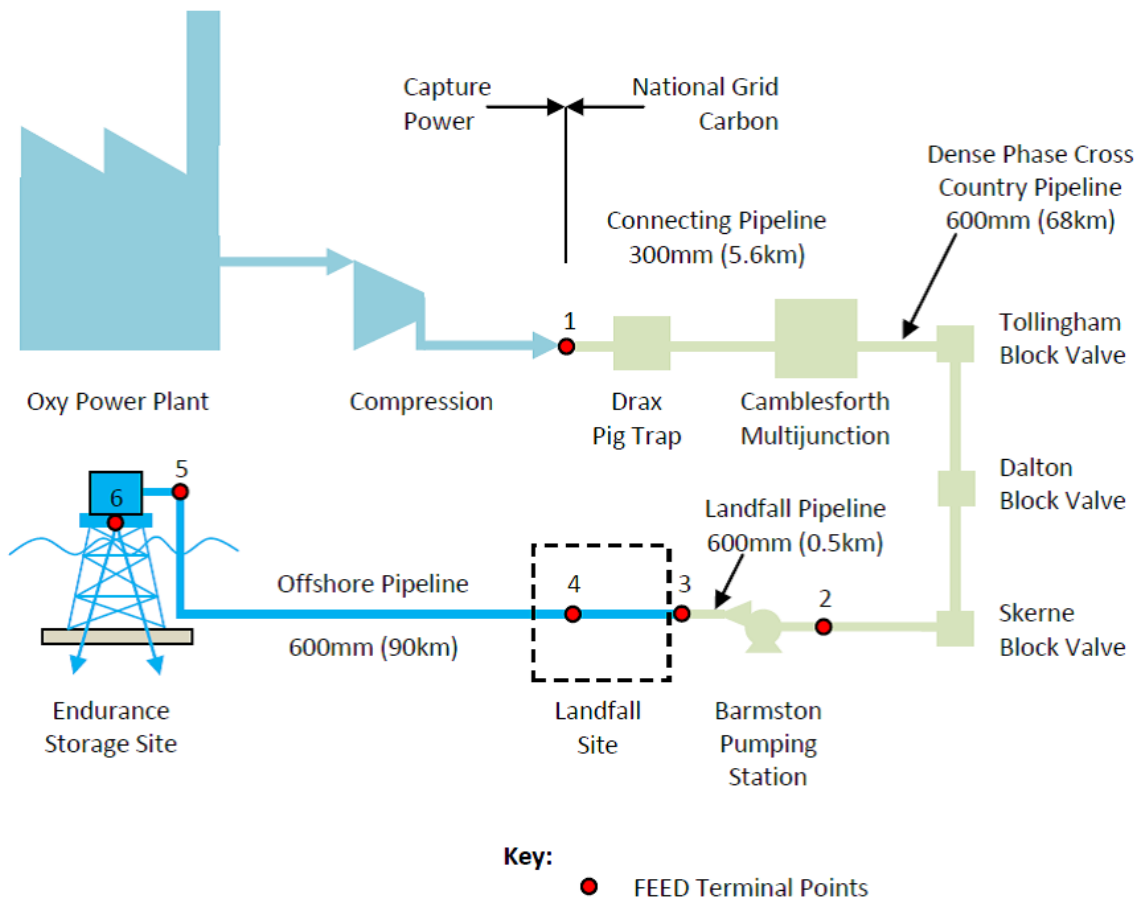


The standalone power plant would be located at the existing Drax Power Station site near Selby, North Yorkshire and generating electricity for export to the Electricity Transmission Network (the Grid) as well as capturing over two million tonnes of CO₂ per year, some 90% of all CO₂ emissions produced by the plant. The by-product CO₂ from the power plant would be compressed and transported via an export pipeline for injection into an offshore saline formation for permanent storage.

The power plant technology, which is known as oxy-fuel combustion, burns fuel in a modified combustion environment with the resulting combustion gases being high in CO₂ concentration. This allows the CO₂ produced to be captured without the need for additional chemical separation, before being compressed into dense phase and transported for storage within the Endurance structure.

The overall integrated control of the end-to-end CCS chain would have similarities to that of the National Grid natural gas pipeline network. Operation of the transport and storage system would be undertaken by NGCL. However, transportation of CO₂ presents differing concerns to those of natural gas; suitable specific operating procedures would be developed to cover all operational aspects including start-up, normal and abnormal operation, controlled and emergency shutdowns. These procedures would include a hierarchy of operation, responsibility, communication procedures and protocols. Figure 3.2 below provides a schematic diagram of the overall end-to-end chain for the White Rose CCS Project.

Figure 3.2: End To End Chain Overall Schematic Diagram



The Endurance structure is one of several structural closures of the Bunter Sandstone Formation found within the Triassic Southern North Sea (SNS) basin. It has been penetrated by three exploration and appraisal wells drilled between 1970 and 2013. Several other exploration and appraisal wells drilled with various objectives surround the structure as shown in Figure 3.3. This figure shows the Top Bunter depth structure map over Endurance Storage Site showing licence block boundaries (broken black line) as well as exploration and appraisal wells within the Area Of Interest (AOI). Note wells 42/25d-3, 42/25-1, and 43/21-1 are the only ones to have penetrated the Endurance structure.

The Endurance Storage Site comprises the Bunter Sandstone formation within the closure of the Endurance structure. The Bunter sandstone is a regionally extensive and laterally continuous formation that extends tens of kilometres in all directions. Across the structure the Bunter sandstone is approximately 275m thick and generally possesses high porosity and moderately high permeability. Although hydrocarbon gas bearing in other structures in the North Sea, it has been clearly demonstrated to have never been exposed to hydrocarbon gas at the Endurance location.

Although connected structures, particularly the Esmond Field is hydrocarbon gas filled, there are a number of Bunter structures that are much closer to the Endurance (5/42) structure that are not hydrocarbon charged (Esmond is about 40km north of Endurance). The generally accepted theory is that Bunter structures are only charged when there is a thinning or absence in the underlying Zechstein salt near to the structure in question so that hydrocarbons can migrate into them from the deeper formations. The Zechstein salt in Quadrants 42 and 43 are thick and continuous and hence the lack of charge.

The Storage Complex comprises the Storage Site, its Triassic underburden down to the base of the Zechstein Halite and the overburden up to the top Jurassic Lias. The Storage Complex has a number of proven secondary sealing formations including the Rot Halite immediately above the primary Rot Clay seal, the Dowsing Shales, the Muschelkalk Evaporites and the Keuper Anhydrite (The Haisborough Group). The Rot Clay is the caprock and primary seal for the Storage Site. The Rot Halite is the most important of the secondary seals and it is composed principally of pure sodium chloride and as such has important fracture healing properties as, under its ambient pressure and temperature condition, the salt behaves as a rheid (a non-molten solid that deforms by viscous flow). The Rot Halite is present as a thick (greater than 80m) and continuous layer over the Endurance Storage Site.

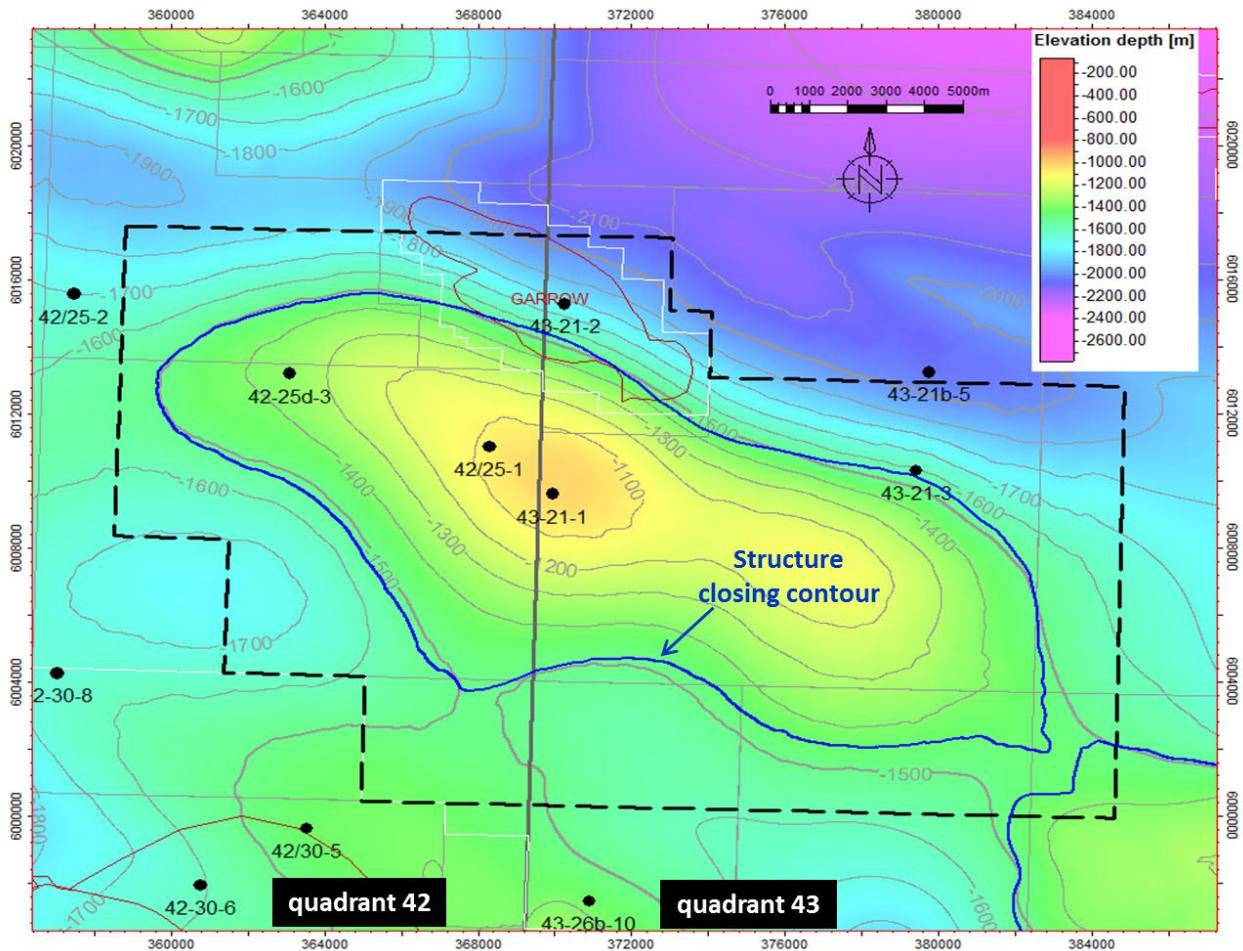
The characterisation of the Storage Site and Storage Complex is based on 2-D and 3-D seismic; more than 20 regional wells including the three wells that have been drilled into the Endurance Structure itself. Two of these wells, 43/25-1 and 42/21-1 drilled in 1970 and 1990 respectively, are unsuccessful hydrocarbon exploration wells. The third well, 42/23d-3, drilled in 2013 by Carbon Sentinel Limited (CSL) was specifically designed as a CCS appraisal well for the Endurance Storage Complex.

The White Rose CCS Project proposes the injection of up to 2.68MTPA of CO₂ for a period of 20 years. The total volume of up to 54MT of CO₂ will occupy less than 2% of the estimated total static capacity of the Endurance Storage Site.

During the injection of the 2.68MTPA of CO₂, under the Measurement, Monitoring and Verification (MMV) Plan, the conformance of the Storage Site in response to CO₂ injection is the most important aspect. If the operation of the Storage Site behaves as forecast and the dynamic capacity is confirmed, consideration may be given to increasing the quantity of CO₂ to be stored in the Endurance Structure. Expansion of the Storage Site is not considered as part of this application.

After injection ceases, the Storage Site and Storage Complex will be monitored for a number of years after which the platform and wells will be decommissioned before responsibility for the Storage Complex will be transferred to the Competent Authority.

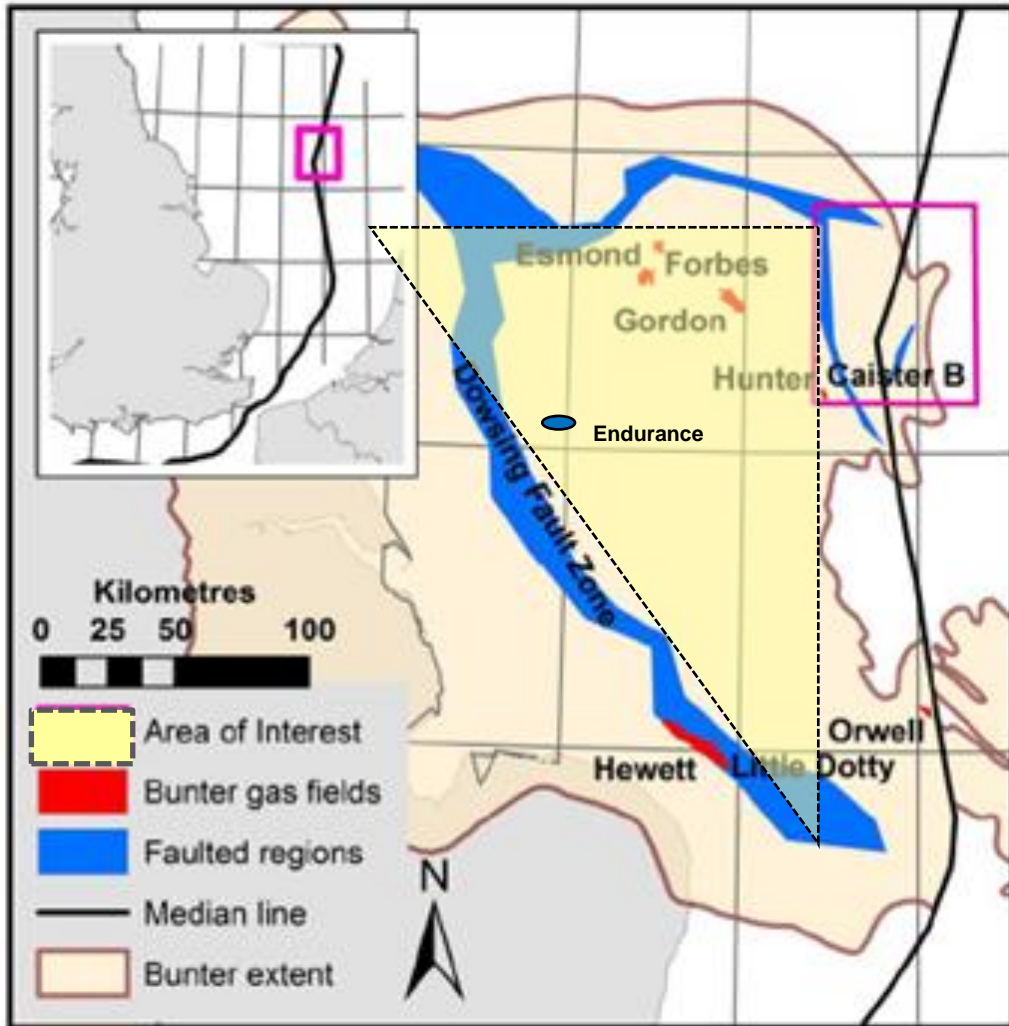
Figure 3.3: Depth Structure Map over Endurance Storage Site



A Regional Structural Framework Model (RSFM) was built to provide structure horizons over the full stratigraphic column from seabed to Top Rotliegend. This provides a common link between the different models that are likely to be built, the geological model, simulation model and geomechanical model. Although a geomechanical model has not been built in this update the RSFM allows later geomechanical models to be constructed if required. A cross section through the RSFM is given in Figure 4.1.

Greater Bunter aquifer that extends over an area approximately 20,000km² and which is bounded by the Dowsing Fault Zone to the west and the thinning to the east across of the Base Cretaceous Unconformity on the Cleaver Bank High in the Dutch sector of the Southern North Sea (Figure 3.4).

Figure 3.4: Extent of the Greater Bunter Aquifer that is Hydraulically Connected to Endurance and surrounding gas fields (original figure from Ref 4)



4 Integrated Geoscience Report

4.1 Summary

This chapter provides a summary of the methodologies, results and conclusions of the geological, structural and sedimentological interpretation of the regional and sub-regional data that has been gathered for the Endurance structure.

The structure of interest (identified as Endurance, previously known as 5/42) is a four-way dip-closure straddling blocks 42/25 and 43/21 in the UK sector of the North Sea, some 60 miles east of Flamborough Head. This structure is a saline aquifer, approximately 22km long, 7km wide and over 200m thick. The crest of the reservoir is located at a depth of approximately 1020m below the sea bed. Reservoir datum pressure and temperature (at 1300mTVDSS) were estimated at 140.0bar and 55.9°C, respectively. A layer of mudstone called the Röt Clay provides the primary seal. This in turn is overlain by more than 90m of a salt layer known as the Röt Halite at the base of the 900m thick Haisborough Group which provide the secondary sealing capability. None of the overburden faults visible on seismic penetrate the Röt Halite.

The subsurface description of the Endurance structure relies on regional seismic and well data. There have been three wells drilled on the structure, two are abandoned hydrocarbon exploration wells drilled between 1970 and 1990, the third was a dedicated CCS appraisal well drilled in 2013 by Carbon Sentinel Limited, which had a comprehensive data evaluation programme designed to quantify and characterise various aspects of the structure for its use for permanent secure CO₂ storage. Several other exploration and appraisal wells drilled with various objectives surround the structure as shown in Figure 3.3.

The Bunter sandstone within structural closure (the “Storage Site”) is primarily composed of very-fine to fine-grained sandstone with excellent porosity and permeability. The Storage Site is estimated to have a net pore volume of over 4.6Bm³ and the 53.6MT of CO₂ planned for production by the White Rose power plant over 20 years will occupy approximately 2% of this volume under reservoir conditions.

4.2 Geological and Structural Setting

4.2.1 Geological History

Endurance acquired its current structural configuration as a result of the development of the underlying Zechstein Halite diapir (Figure 3.3 and Figure 4.1).

The development of the SNS Basin is characterised by a complex history of basinal subsidence and episodes of uplift and erosion (Ref 7). The Triassic is divided into three main sedimentary successions that include the Bacton Group, the Haisborough Group and the Penarth Group. Figure 4.2 shows the lithostratigraphic nomenclature for the Triassic. Top Bunter is one of largely coarse-grained deposits, comprising red sandstones, shales and mudstones that make up the Bacton group. The Bacton Group is immediately overlain by the Haisborough Group which comprises mainly alternating beds of fine-grained clastics and evaporates that act as excellent top seals for CO₂ injected into the Endurance structure. The Bunter Shale formation which underlies the BSF provides a basal seal. The Penarth group at top Triassic is representative of the marine transgression that marks the transition from the Triassic to the Jurassic (Ref 1).

Zechstein movement was initiated at various times during the history of the SNS basin. The majority of the salt movement is likely to have begun in late Jurassic and early Cretaceous times and the mechanism is

well understood. It is related to underlying faulting. The general model is one of extensional faulting being accommodated by the overlying salt, but weakening the overburden through differential loading. Once the overburden becomes weaker than the increasing buoyancy force of the underlying salt, the salt itself will start to flow.

Another salt diapir is present to the southeast of the Endurance structure and the Triassic sands and shales outcrop at the seabed around the salt core (Figure 4.1). Interpretation of seismic data suggests that the Bunter sandstone is continuous in the saddle between the Endurance structure and this diapir.

Tertiary structural inversion (uplift following deep burial) has brought much of the SNS to shallower levels and this has led to poorer quality reservoirs than would be the case in the absence of this inversion. Structural inversion followed by glacial erosion has also resulted in the absence of most of the post Middle Jurassic interval within the vicinity of the Endurance structure and beyond.

Figure 4.1: WNW-ESE Cross-section through the Endurance Structure and Salt Diapir to SE

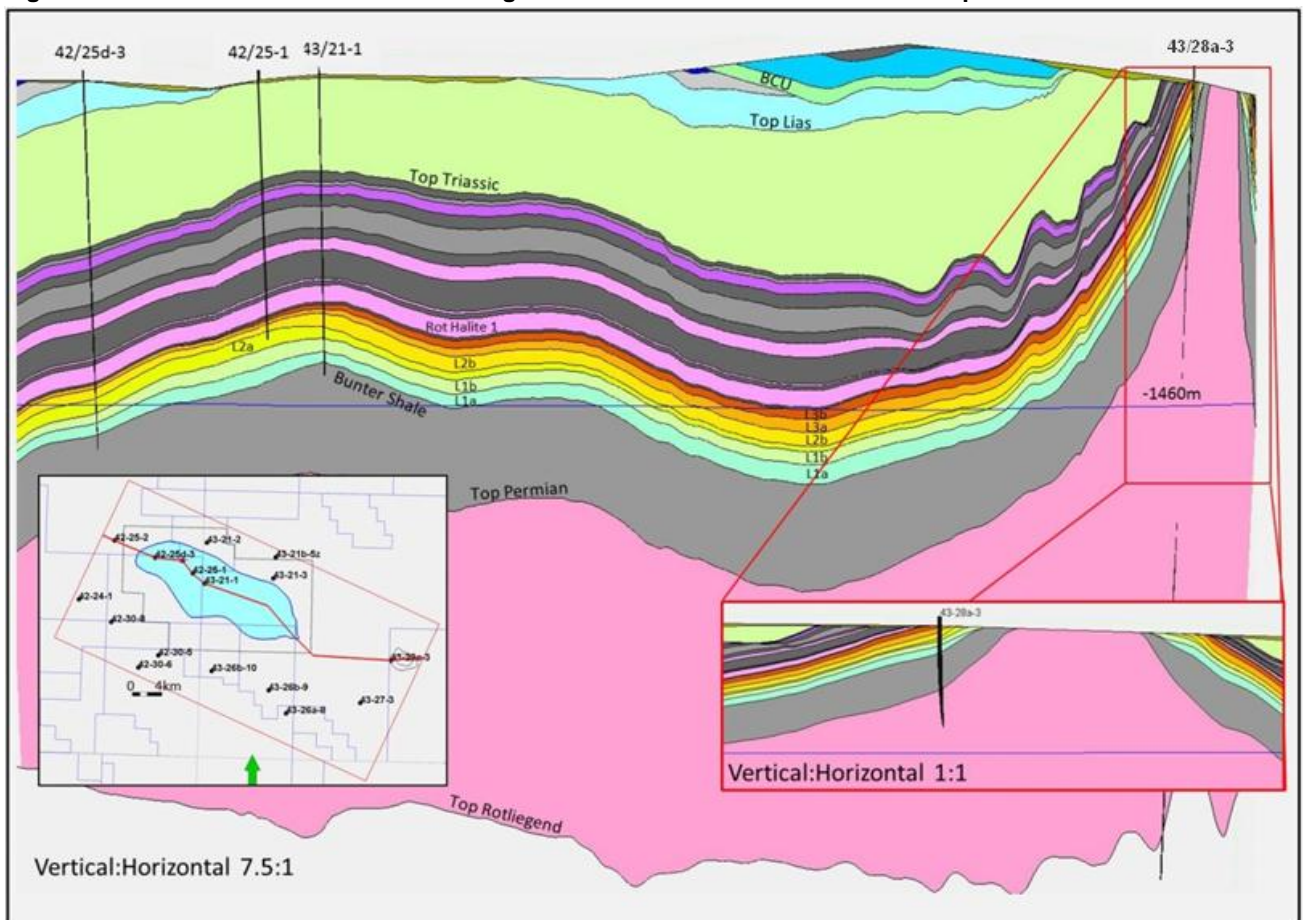


Figure 4.2: Lithostratigraphic nomenclature scheme for the Triassic of the SNS (after Ref 8)

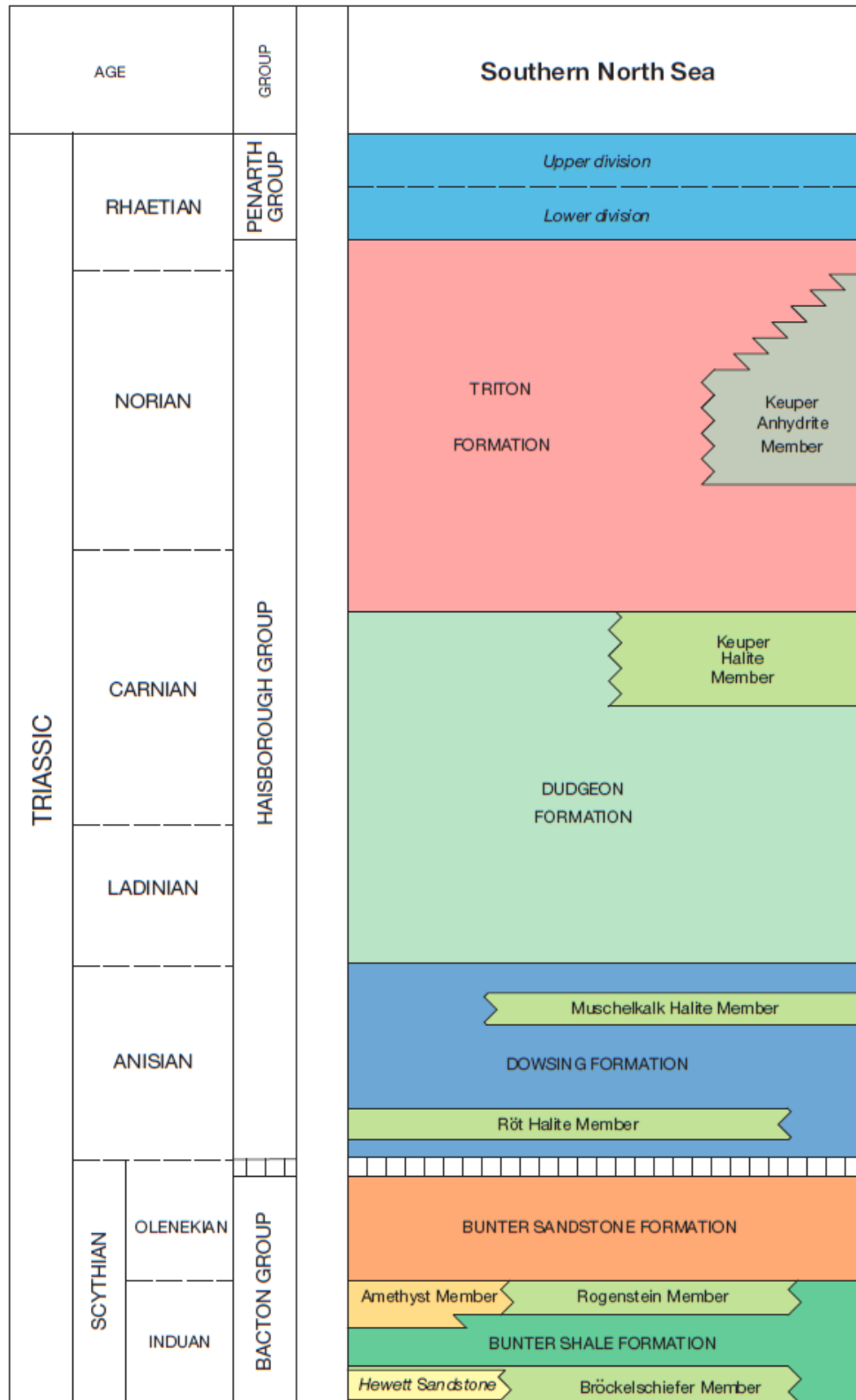


Figure 4.3 highlights the subdivision of the Endurance structure into three overlapping volumes mainly for the purposes of the MMV plan and this is adopted henceforth in this document. These three overlapping volumes are detailed separately in the following three sections:

4.2.2 Endurance Storage Site

The Storage Site comprises the BSF within the Endurance structure. The lithologies above and below Bunter sandstone are mainly shales and evaporites, hence they are all envisaged to have a good sealing quality (Figure 4.5). The areal dimensions of the Storage Site shown in Figure 4.6 are taken from the most likely Top Bunter depth map which closes at 1460m TVDSS.

Figure 4.3: Section Illustrating the Limits of Storage Site, Storage Complex and Monitoring Area. [Plan View Shown in Figure 4.4, below]

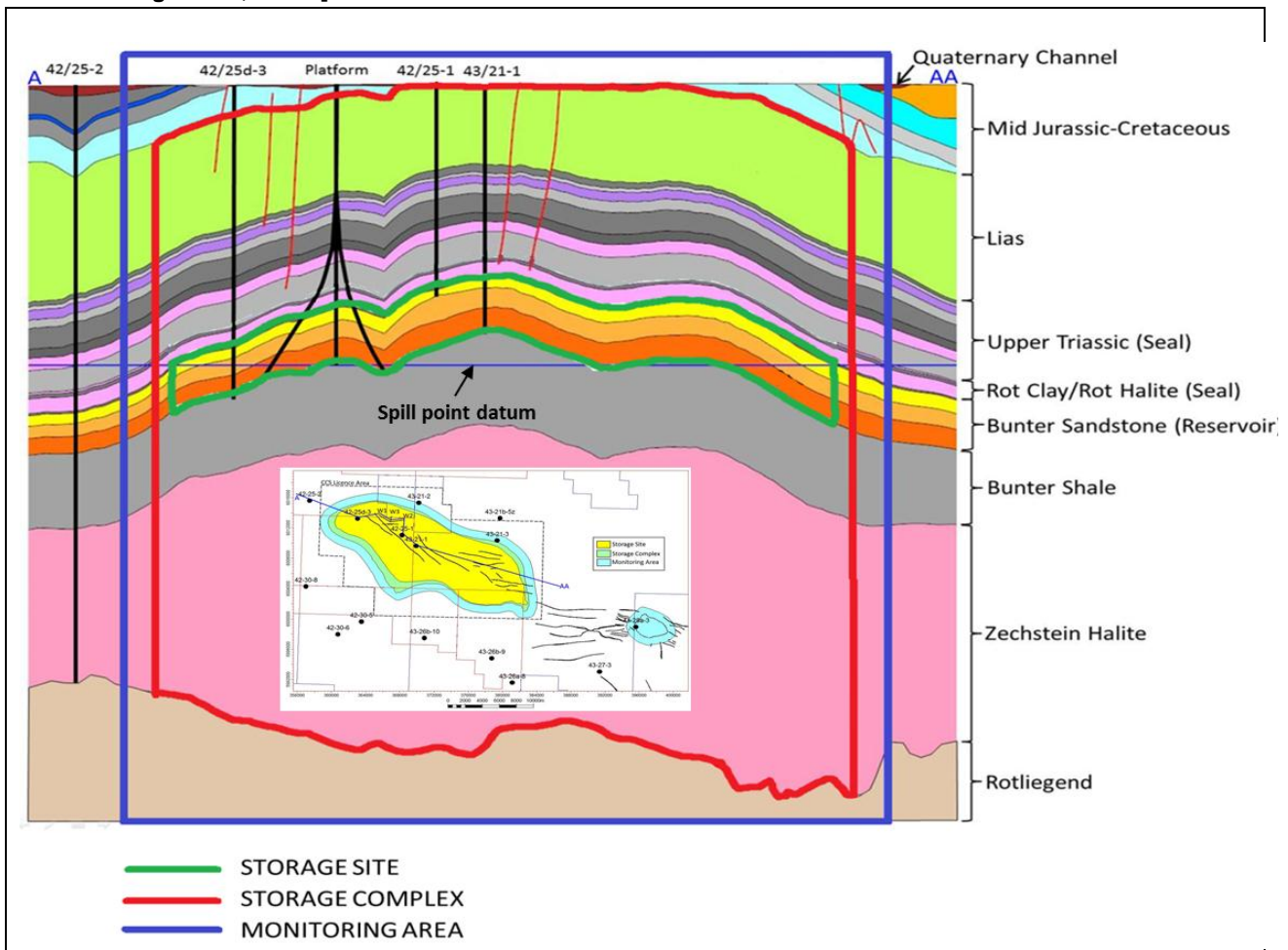


Figure 4.4: Plan of the limits of Storage Site, Storage Complex & Monitoring Area [Section Illustrating the Limits Shown in Figure 4.3, above]

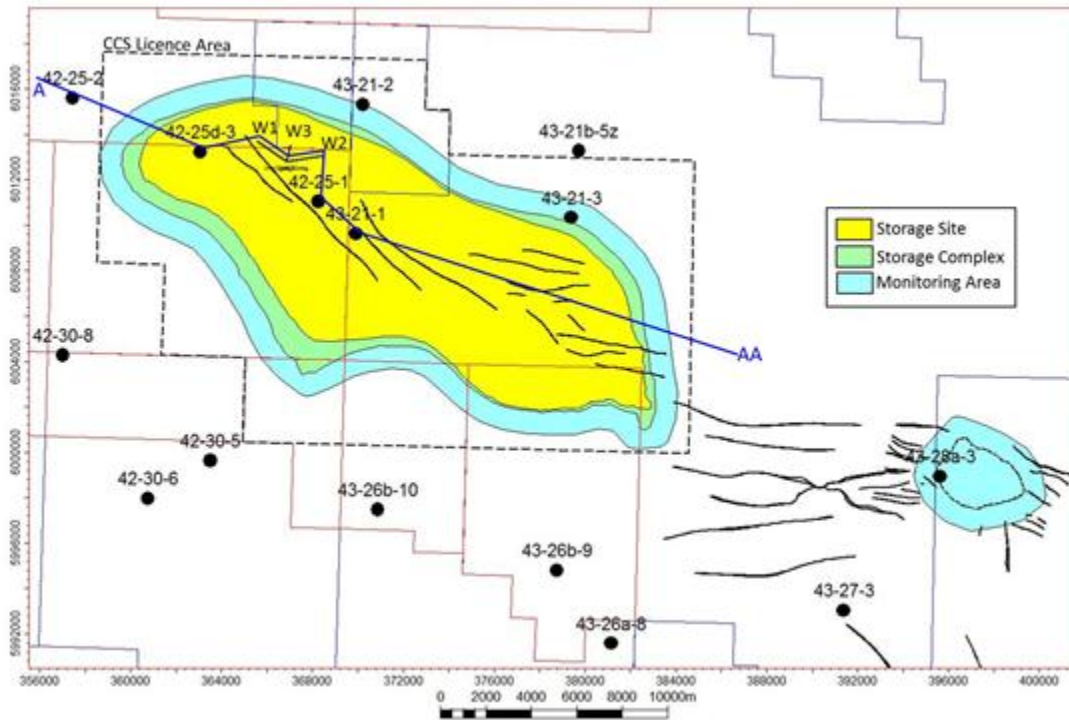


Figure 4.5: Lithostratigraphy of the Storage Site and Complex

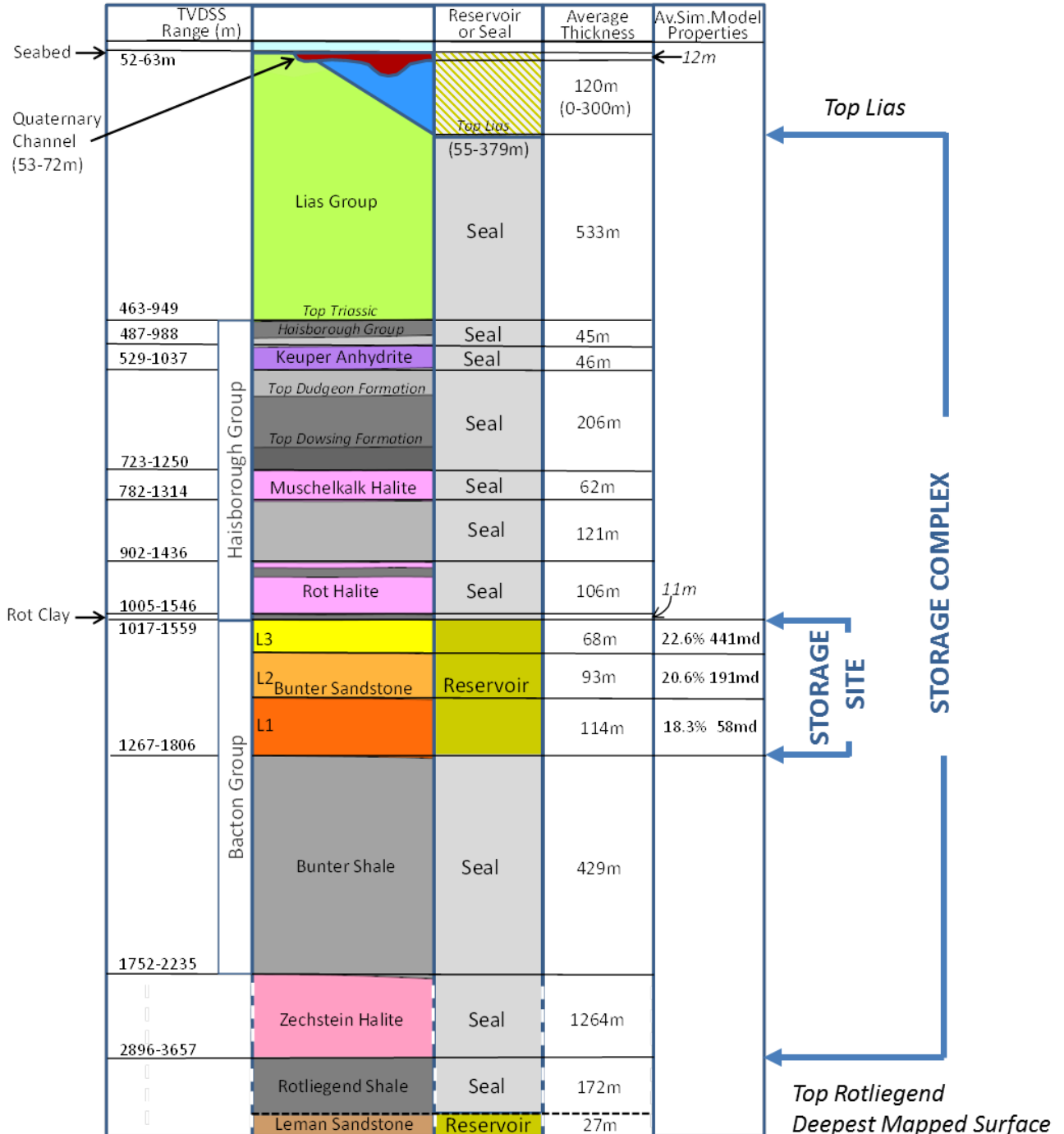
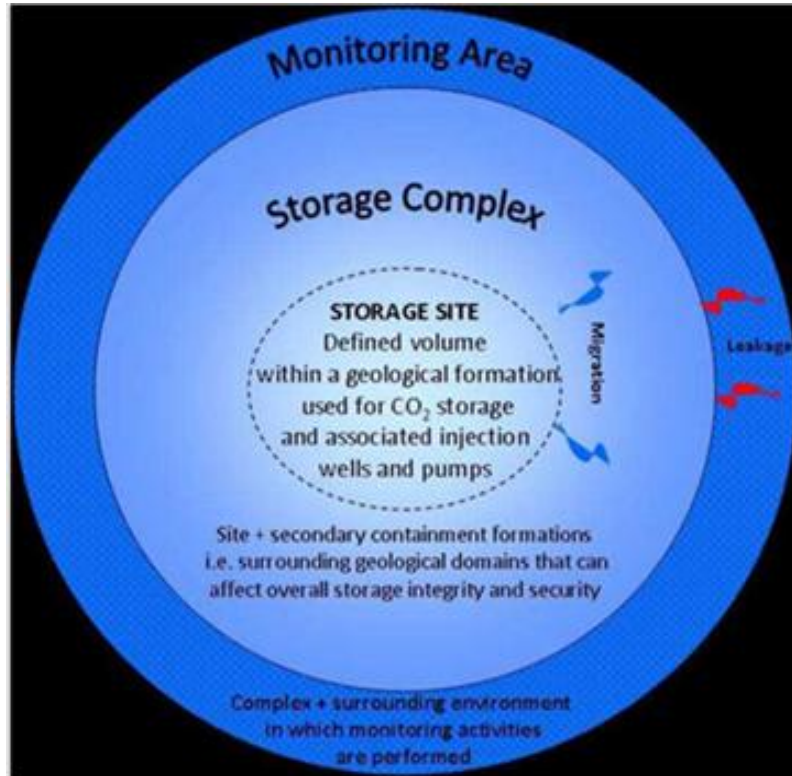


Figure 4.6: Map view of CO₂ Storage Definitions

4.2.3 Endurance Storage Complex

The Storage Complex is defined from the Top Rotliegend to the top of the Liassic and encompasses the Storage Site.

The Upper Rotliegend is likely to provide a further basal seal; however, the base of the formation and the top of the underlying Leman Sandstone reservoir could not be mapped seismically with any confidence. Consequently the base of the storage complex has been placed at the deepest confidently mappable horizon, namely the Top Rotliegend.

The areal dimensions of the Storage Complex for the Endurance structure is taken from the closure of the high Net Pore Volume (NPV) case on the top Bunter Sandstone at -1553m TVDSS. The Storage Complex includes all the overburden geological formations directly above the Röt Clay seal up to the Top of the Liassic, the shallowest sealing interval.

4.2.4 Endurance Monitoring Area

The Monitoring Area will include the Storage Site and Complex – both vertically and areally. The areal extent will ensure that any Lateral migration of CO₂ beyond the Bunter Sandstone spill point which lies to the east and south of the structure is highly unlikely to occur as a result of White Rose CO₂ injection. The areal extent of the Monitoring Area will, however, ensure that any such migration would be detected.

Vertically the monitoring area includes stratigraphy outwith the Storage Complex area. This includes the Middle Jurassic to Cretaceous strata which outcrop at the seabed on the margins of the salt diapir core west of the Endurance anticline. It also includes Quaternary channels which locally erode older stratigraphy.

4.3 Geological Characterisation of the Endurance Storage Site and Storage Complex

4.3.1 Geological and Structural Setting

The Endurance structure is one of several structural closures of the Bunter Sandstone Formation (BSF) found within the Triassic Southern North Sea (SNS) basin. It is a large four-way dip closure and acquired its current structural configuration as a result of the development of the underlying Zechstein Halite diapir (Figure 3.3 and Figure 4.1). It is situated between Blocks 42/25d and 43/21, and has been penetrated by three exploration and appraisal wells drilled between 1970 and 2013. Several other exploration and appraisal wells drilled with various objectives surround the structure as shown in Figure 3.3.

As mentioned above the Triassic is divided into three main sedimentary successions: the Bacton Group (course grain deposits), the Penarth Group and the Haisborough Group. The Haisborough group, which overlies the Bacton Group, comprises the Dowsing, Dudgeon, and Triton formations. The Dowsing formation is Dolomitic and at its base is the Rot Halite member which is well developed throughout the SNS basin. There is a thin basal transgressive unit within the Rot Halite called the Rot Clay. The Rot Clay directly overlies the Endurance structure and is also generally considered to be of considerable extent. Bunter Shale provides a basal seal.

Figure 4.7: Endurance Storage Sites Showing Lease Boundary

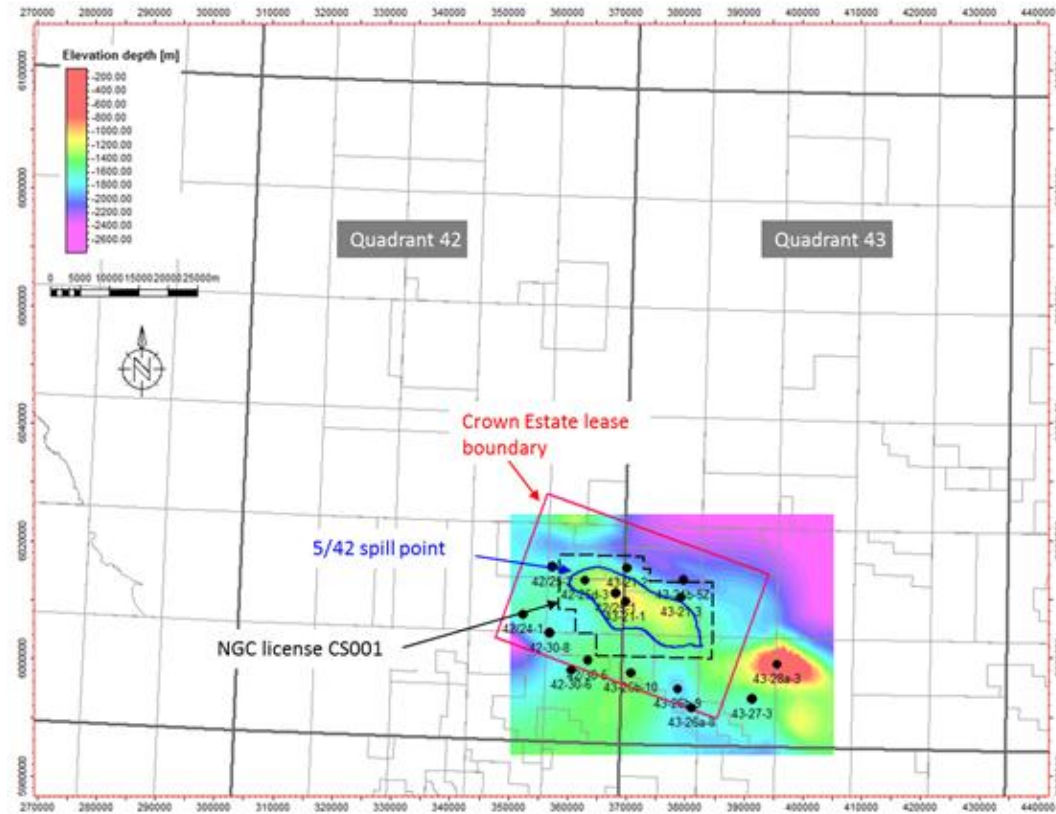


Figure 3.3 shows the Top Bunter depth structure map over Endurance Storage Site showing licence block boundaries (broken black line) as well as exploration and appraisal wells within the AOI. Note only wells 42/25d-3, 42/25-1, and 43/21-1 have penetrated the Endurance structure. Note outline of the Garrow field located below the Endurance structure.

Interpretation of seismic data has provided further insight into the relative sequence of events that led to the present day structural configuration. Figure 4.4 highlights the subdivision of the Endurance structure into three overlapping volumes mainly for the purposes of the MMV (Monitoring, Measurement and Verification) plan and this is adopted henceforth in this document.

The following sections give summaries of the structural interpretations.

4.4 Geological Horizon Mapping

The seismic responses of the key stratigraphic intervals from the 3D OBC survey and the 2D survey (covering the seabed outcrop to the South-East of Endurance) were calibrated to data obtained from approximately 20 wells in the AOI. A total of 6 seismic horizons were interpreted from these extensive seismic to well ties, they are:

Top Chalk; Top Chalk is marked by an increase in acoustic impedance and is represented by a low amplitude trough (red) on seismic. The trough varies in amplitude and continuity, becoming more discontinuous in shallower sections.

Base Cretaceous; The Base Cretaceous was difficult to interpret because of the poor quality of the shallow 3D seismic section. It was picked on a prominent peak throughout the 3D and 2D surveys. It is interpreted to outcrop on the seafloor on the flanks of the structure.

Top Triassic; The Top Triassic is represented as a high amplitude peak which varies considerably, from strong and continuous in the 3D J07 tile of the PGS Mega Merge data, to weak and indistinct in the West K06 and J06 tiles and 2D surveys.

Top Bunter Sand; The Top Bunter Sandstone was the main horizon of interest and this horizon was correlated with well control through synthetic seismograms. It was picked on the prominent blue peak tied into the synthetic seismogram in well 43/21-1 where the upper part of the Bunter Sand has low acoustic impedance associated with high porosity of the sand (Figure 4.8). However, on the flanks of the structure there is an abrupt change in the polarity of the reflection so that it becomes a strong red trough (Figure 4.9).

The Top Bunter Sand horizon was picked as a peak in the high parts of the structure and as a trough in the lower parts. The change from peak to trough occurs almost instantaneously. The boundary is shown on the Top Bunter Sand two-way time structure map in Figure 4.10. The interpretation was continued on the 2D surveys to the southeast and an additional well tie was achieved at 43/27-1, in which the Top Bunter Sand is also a peak.

Top Zechstein; Top Zechstein Group represents the top of evaporite and carbonate rocks of Late Permian age. The Top Zechstein is represented by a sharp impedance contrast between the Bunter Shales and anhydrites of the Top Zechstein, resulting in a strong, continuous trough on seismic across the majority of the survey area.

Top Rotliegend (base Zechstein); Decrease in acoustic impedance resulting in a high amplitude peak on seismic was observed where anhydrites of the Zechstein group overlie clastics of the Rotliegend. The Top Rotliegend is a consistent pick through the AOI with the exception of regions below salt walls and swells, where the horizon becomes steeply dipping due to time pull-up leading to more uncertainty in the horizon pick.

Figure 4.8: Synthetic Seismogram Well 43/21-1, Illustrating Top Bunter Peak

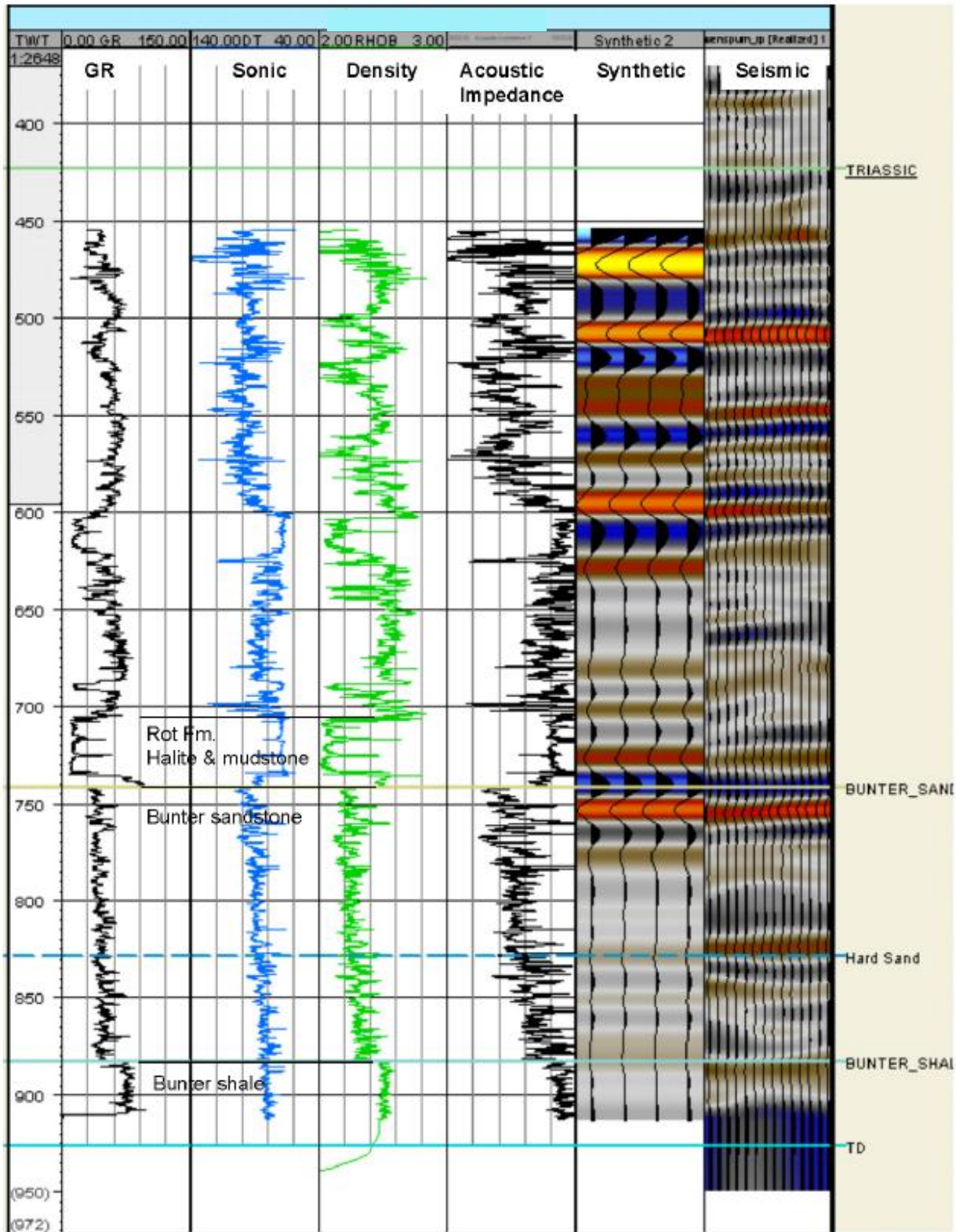


Figure 4.9: Seismic Correlation from 43/21-1 to 43/21-2

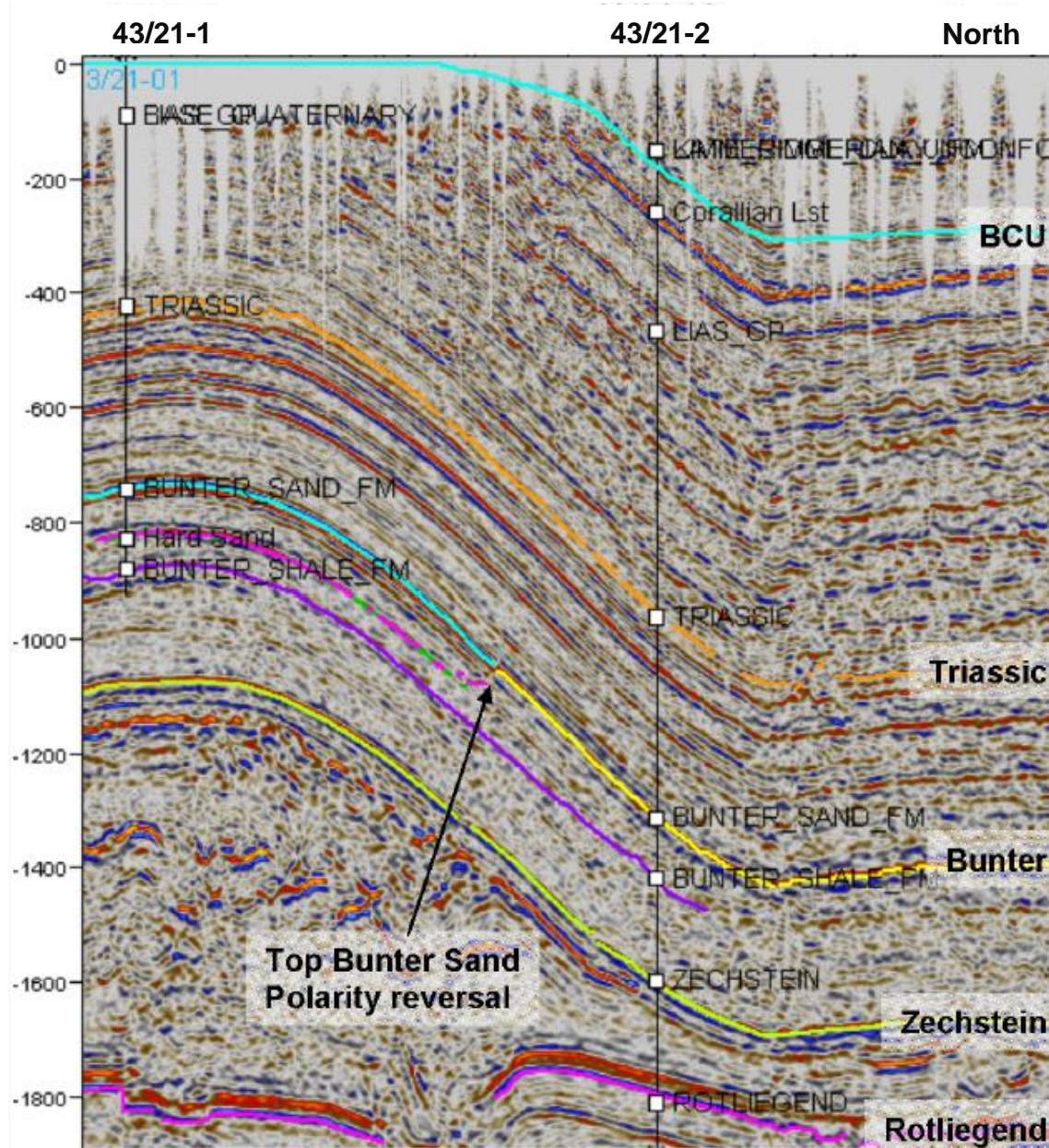


Figure 4.10: Endurance Top Bunter depth surface with wells and Phase Reversal Polygon (PRP)

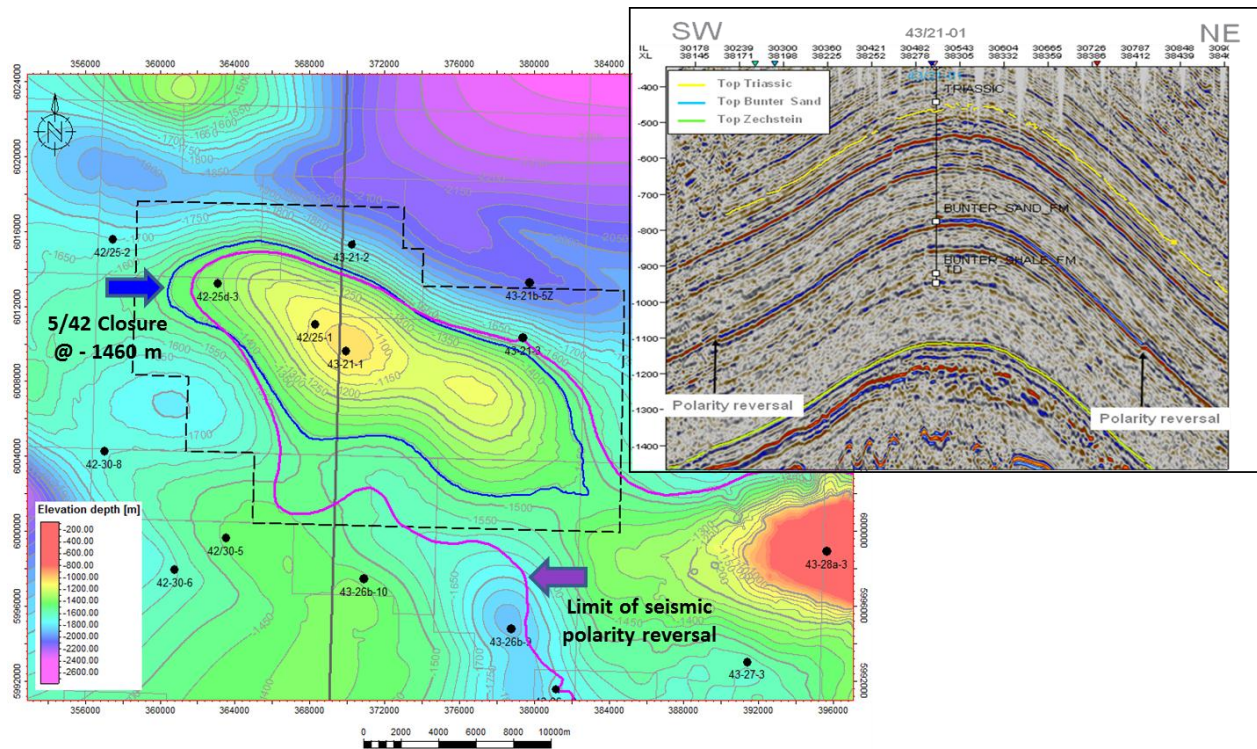
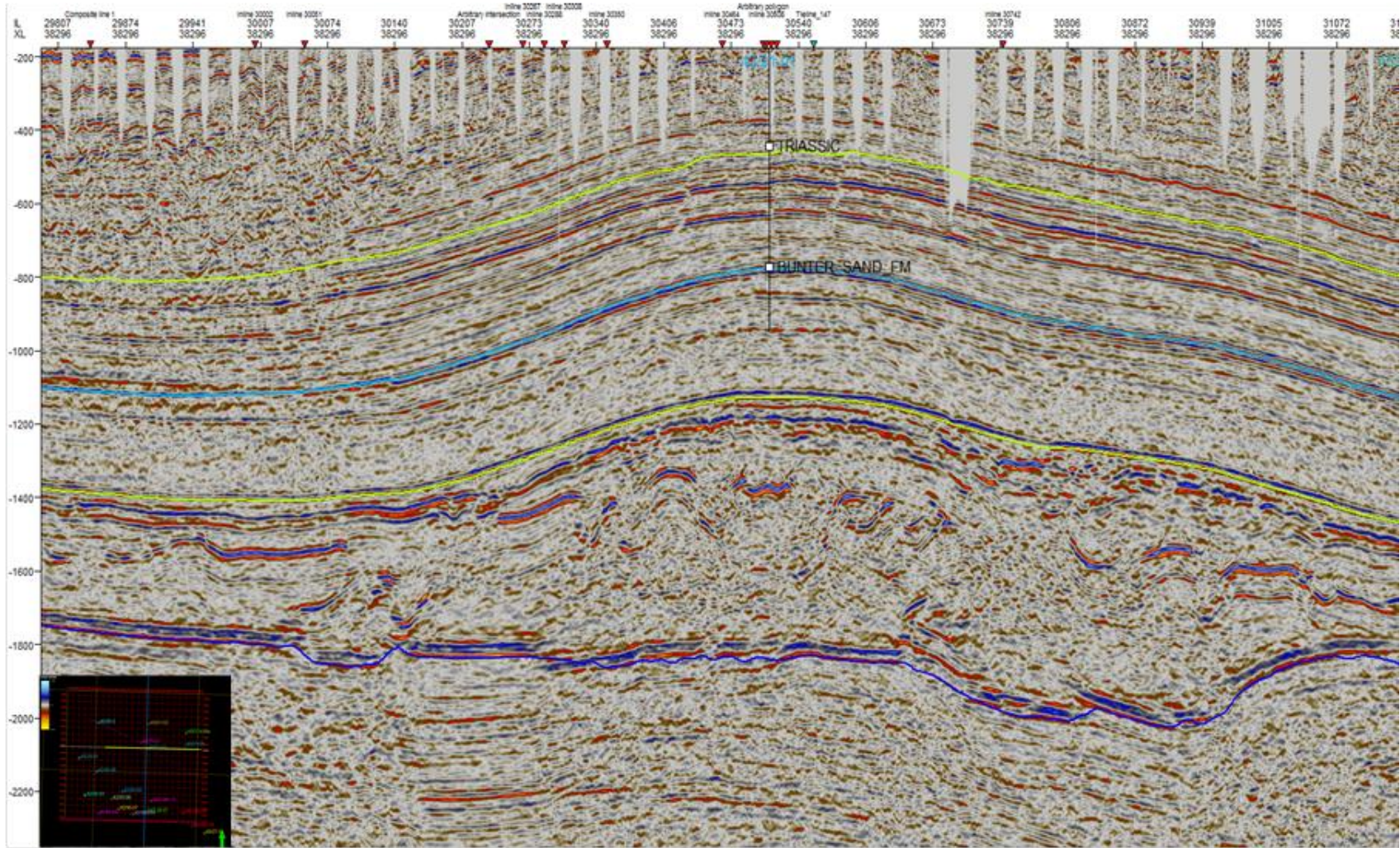


Figure 4.11 shows a West-East oriented crossline from the 3D OBC survey. Due to insufficient spatial sampling by the seabed receiver cables of the near surface geology, seismic gaps are observed in the shallowest 500ms of two way travel time (equivalent to about 590m TVDSS). The survey sampling was sufficient to image the top of the Triassic interval and deeper geological intervals down to Carboniferous depths. Figure 4.11 shows interpreted horizons for top Triassic (light green), top Bunter Sand (cyan), top Zechstein (green) and top Rotliegend (blue). The line intersects the 43/21-1 well at the crest of the Endurance Bunter Sand structure which provides control for the interpretation.

In the context of the seismic gaps in the shallowest data from the OBC survey it is worth noting that a new 3D seismic streamer based data set taken and processed during 2012-14 became commercially available in early 2015 and a 5 km x 5 km pilot area over the crest of Endurance was acquired for assessment. This assessment has indicated that the structural differences seen in this 5 km x 5 km pilot study area with the new data set have minimal impact on the objectives of site characterisation and would have no or minimal impact on the established static, dynamic and geomechanical modelling workflows.

Figure 4.11: 3D OBC Xline 38296 with well 43/21-1 on the crest and projected well 43/21-3 on the north eastern flank



The Cretaceous chalk interval and all younger stratigraphic units are absent over the crest due to uplift and erosion as a consequence of basin inversion during the Tertiary and subsequent glacial erosion.

Figure 4.12 is a 2D seismic tie line running North-West to South-East across the main longitudinal axis of the Endurance anticline (through the 43/21-1 crestal well) and down to the Bunter seabed outcrop (43/28a-3 "outcrop" well). As well as the top Triassic, top Bunter Sands, top Zechstein and top Rotliegend interpreted on the 3D OBC data, overlying reflectors have been interpreted: base Quaternary channels (red), top Chalk (light blue), base Cretaceous (pale purple), Lower Jurassic Lias (blue). The sea bed (yellow) has also been interpreted on this line and sand waves over the core of the anticline can clearly be observed.

A series of TWT (Two Way Time) base maps for Top Triassic, Top Bunter sand, Top Zechstein and Top Rotliegend horizons are shown in Figure 4.13 through to Figure 4.16. For each map, polygons delimiting the static model AOI (red) and the live data area for the 3D OBC grid (blue) are also shown to highlight the total data coverage afforded by the various seismic volumes and thus the degree of grid interpolation required for each horizon. For the Top Triassic, Top Bunter sand and Top Zechstein maps, the original gridded surfaces from the 3D Ravenspurn seismic grid are included and show elements of data interpolation outside the live OBC area.

Figure 4.12: 2D Site Survey Tie Line (147) [change colour of structural close]

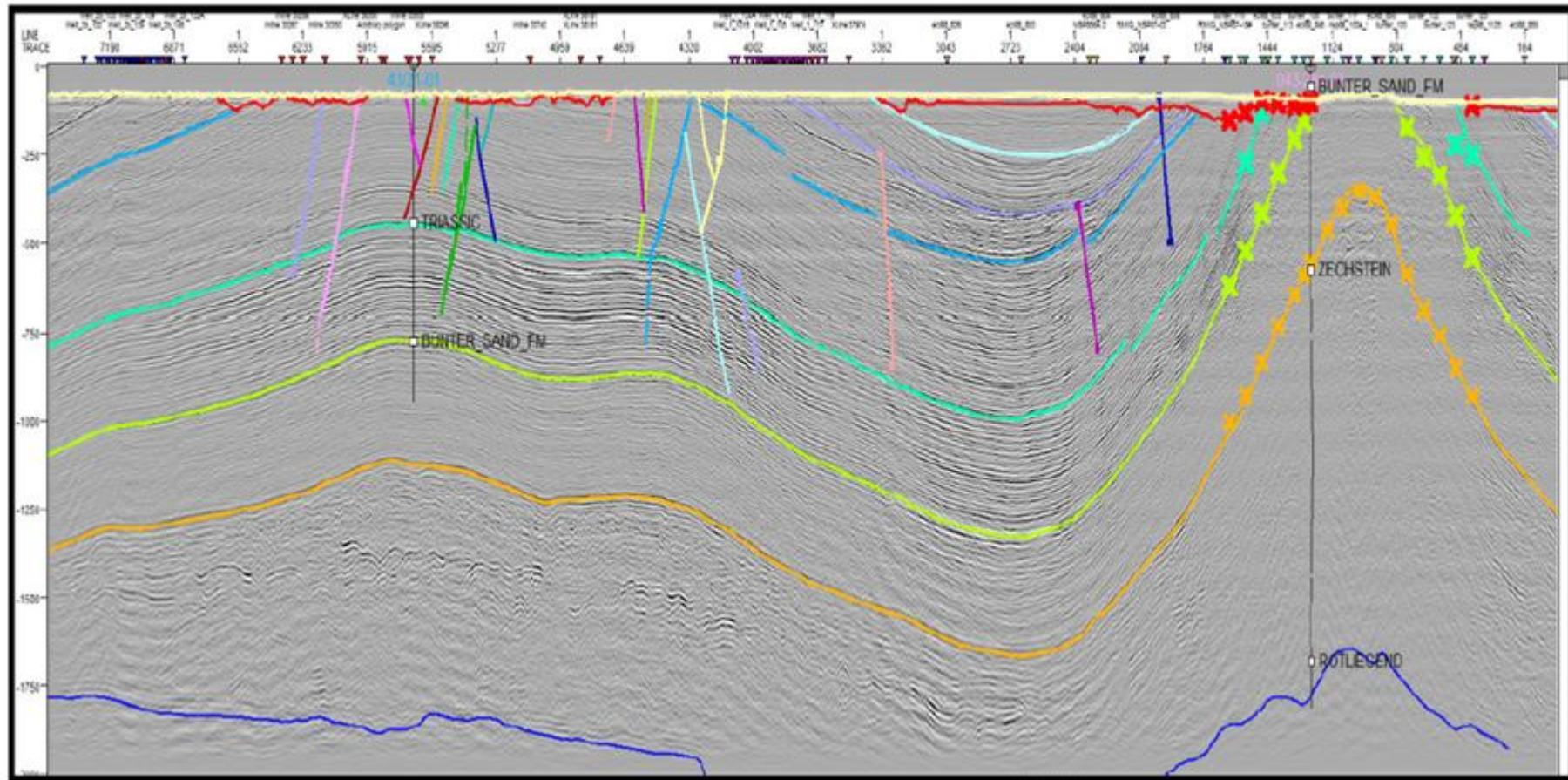


Figure 4.13: Composite Top Triassic TWT Interpretation

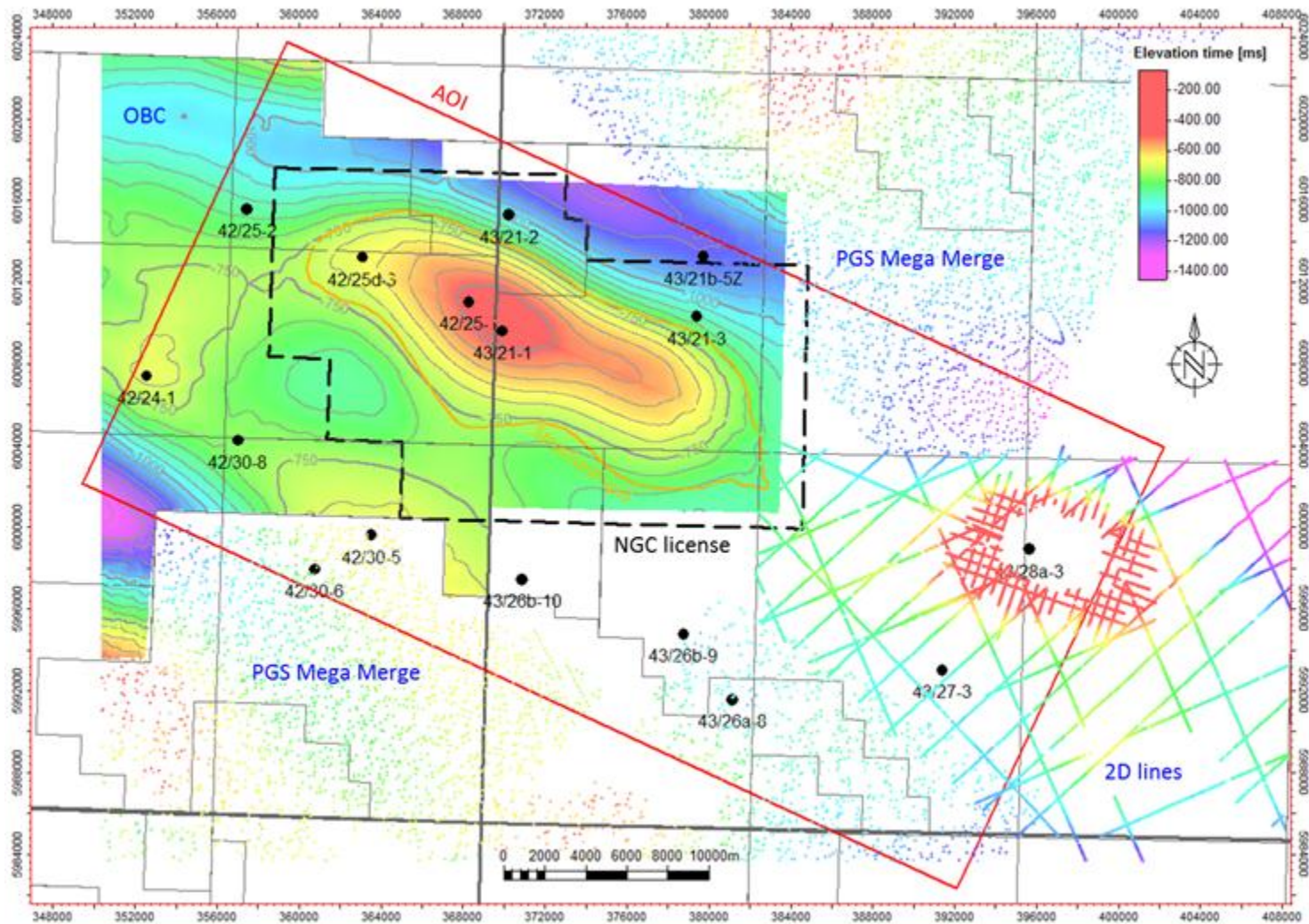


Figure 4.14: Composite Top Bunter Sand TWT Interpretation

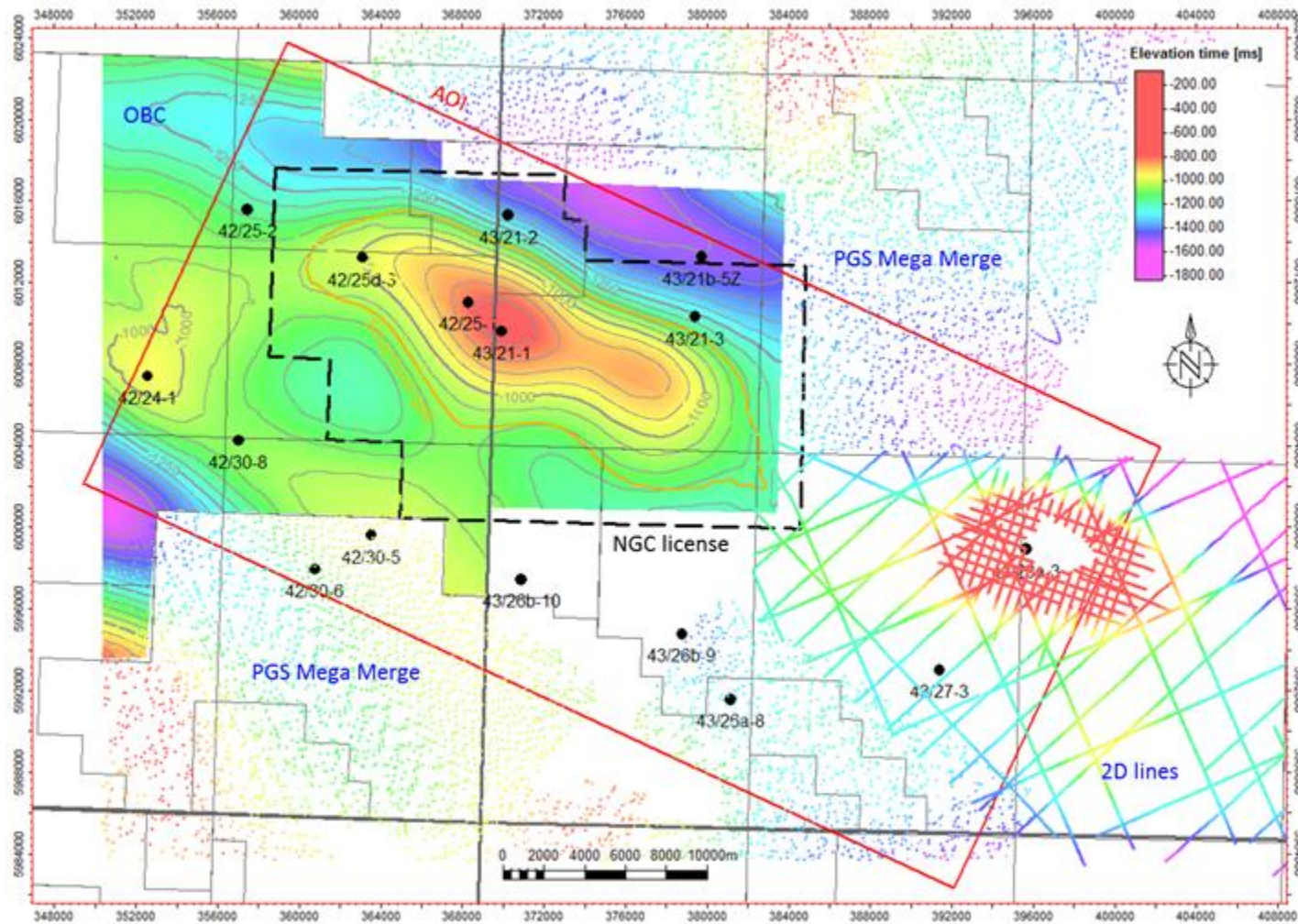


Figure 4.15: Composite Top Zechstein TWT Interpretation

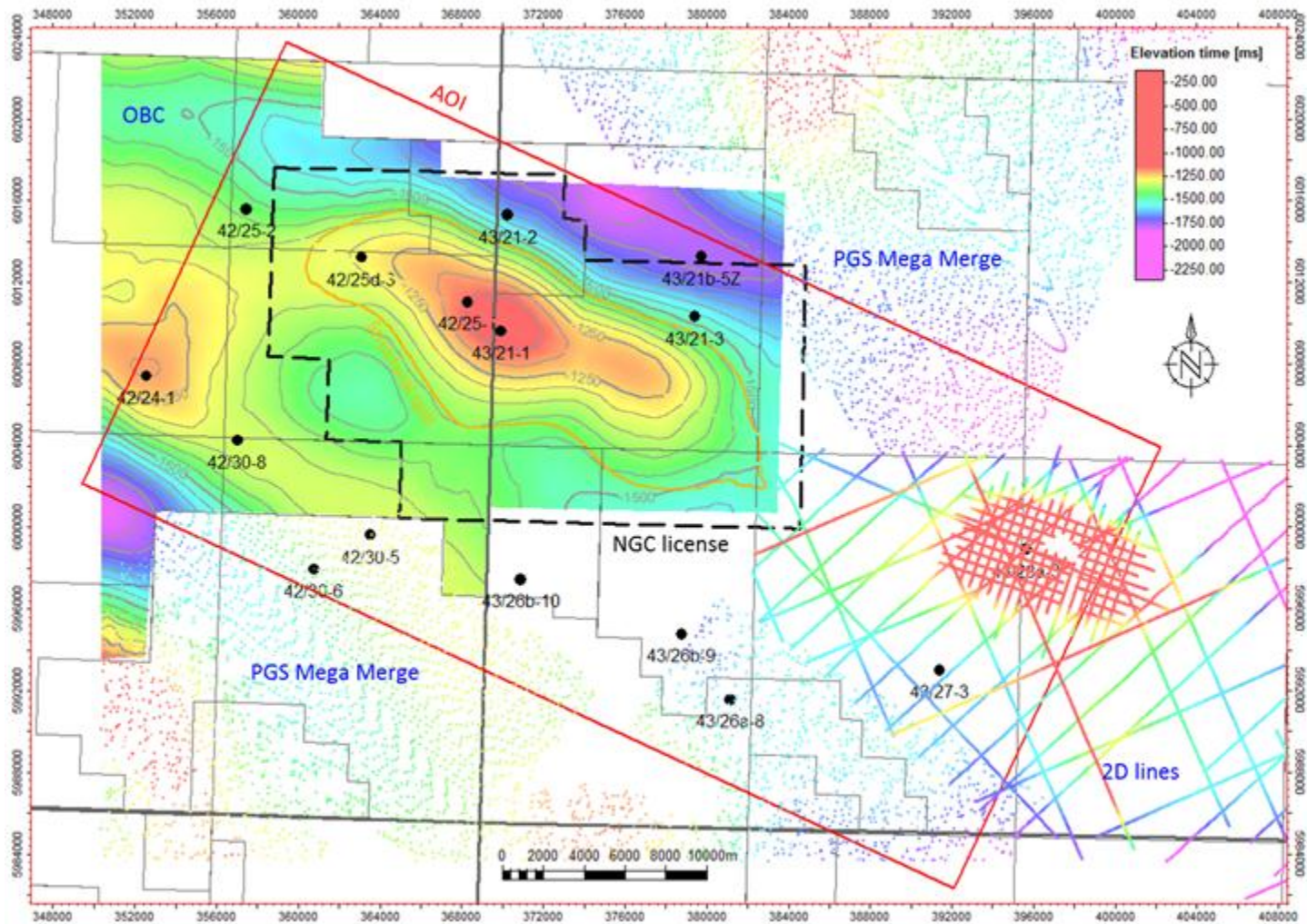
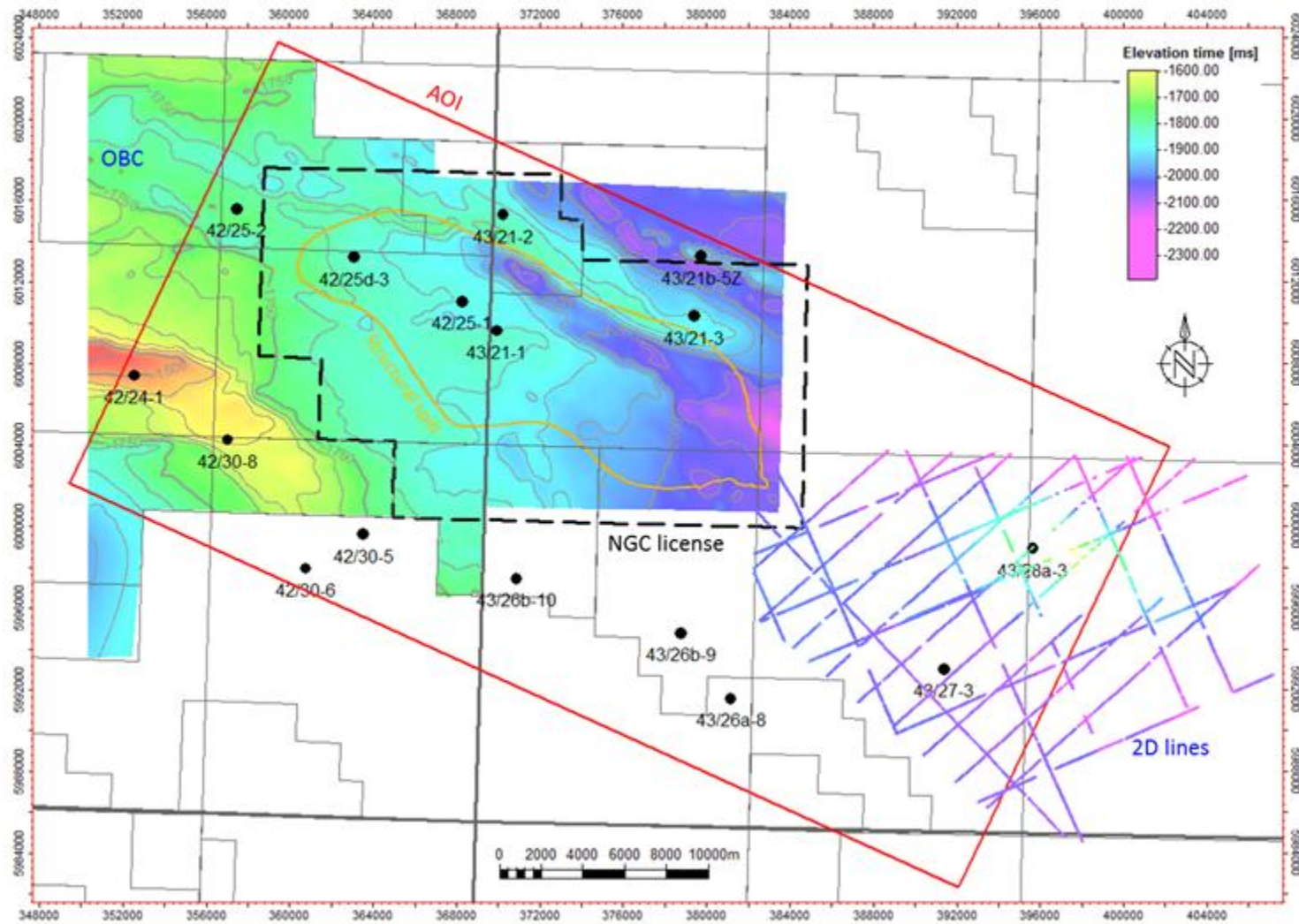


Figure 4.16: Composite Top Rotliegend TWT Interpretation



4.4.1 Depth Conversion and Uncertainties

Time horizons have been depth converted using a V_0k type layer-cake model based on well checkshot velocities. Interval velocity grids were calculated for each layer from the well depths and seismic times.

A constant sea velocity of 1480 m/s was used to the seabed, then velocity layers modelled to Top Triassic, then to Top Bunter Sand, and then to Top Zechstein. For these layers, a linear regression analysis of well velocities estimated the interval velocity at the top of the layer (V_0 or intercept) and the acceleration term of the velocity within the layer (k or gradient). Figure 4.17 shows the initial layer-based linear fit (shown as solid black lines) of the V_0k function to the well velocities. V_0 points were then gridded over the AOI while the k term was held fixed. Each of the bounding horizons were then depth converted in turn, top down, with depth residuals (between predicted and actual well tops) projected back onto the V_0 velocity grids before proceeding down to the next horizon. This process creates a 3D velocity model through which seismic time objects can be converted to depth and vice versa.

This method was used prior to drilling the 42/25d-3 appraisal well in summer 2013 to prognose depths for the two seismic reflectors (Top Triassic and Top Bunter Sands). Other prognosed depths were derived from isochoring from surrounding wells (Table 4.1). The uncertainties quoted in Table 4.1, below are $\pm 25\text{m}$ and $\pm 29\text{m}$, these being derived from 1 standard deviation (SD) of well top residuals. The wellsite tops for Top Triassic came in 11.5m deep to prognosis and the Top Bunter Sands 32.6m deep. Figure 4.18 is the data acquisition summary for the 42/25d-3 well and shows the actual versus prognosed differences.

Figure 4.17: Initial linear fit of well velocities

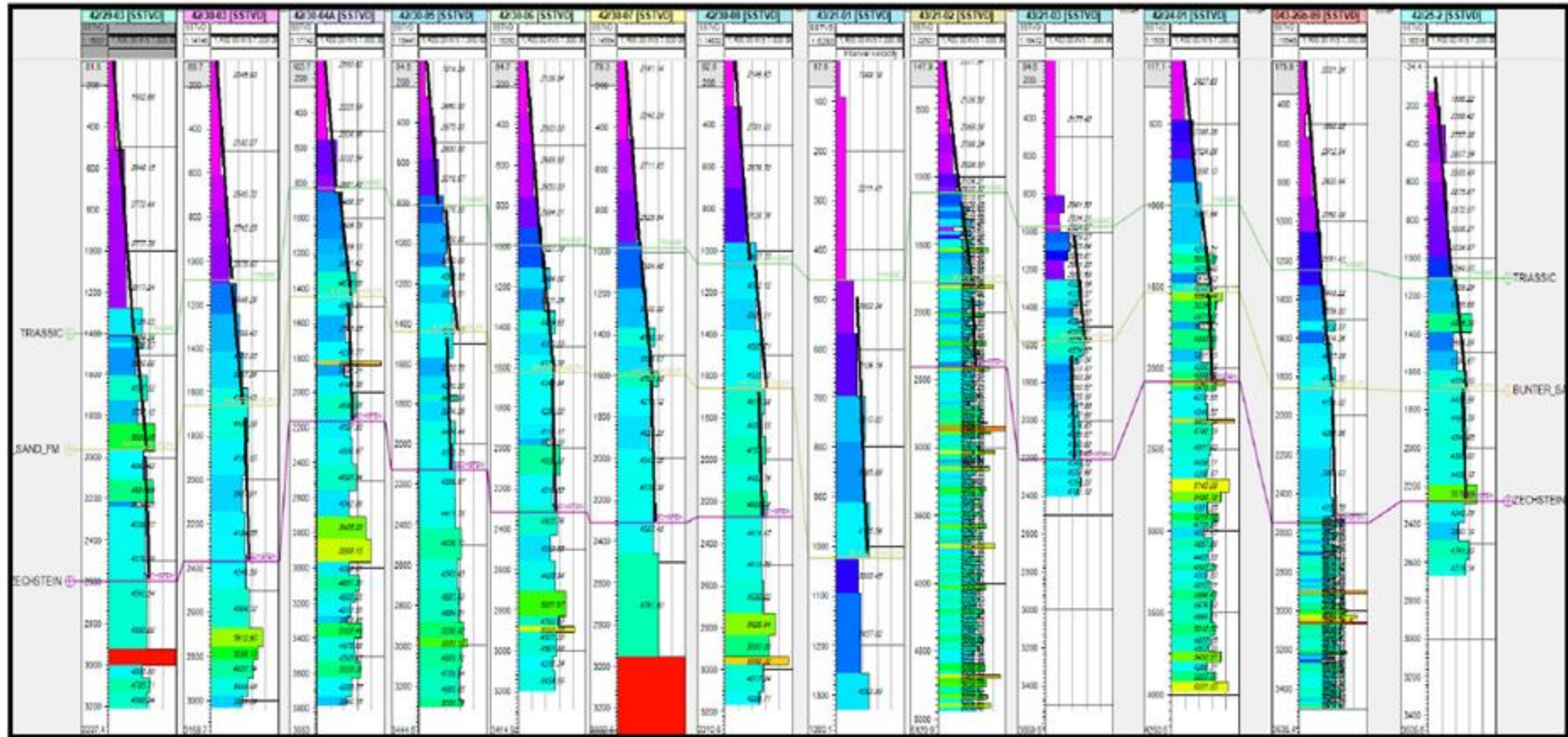
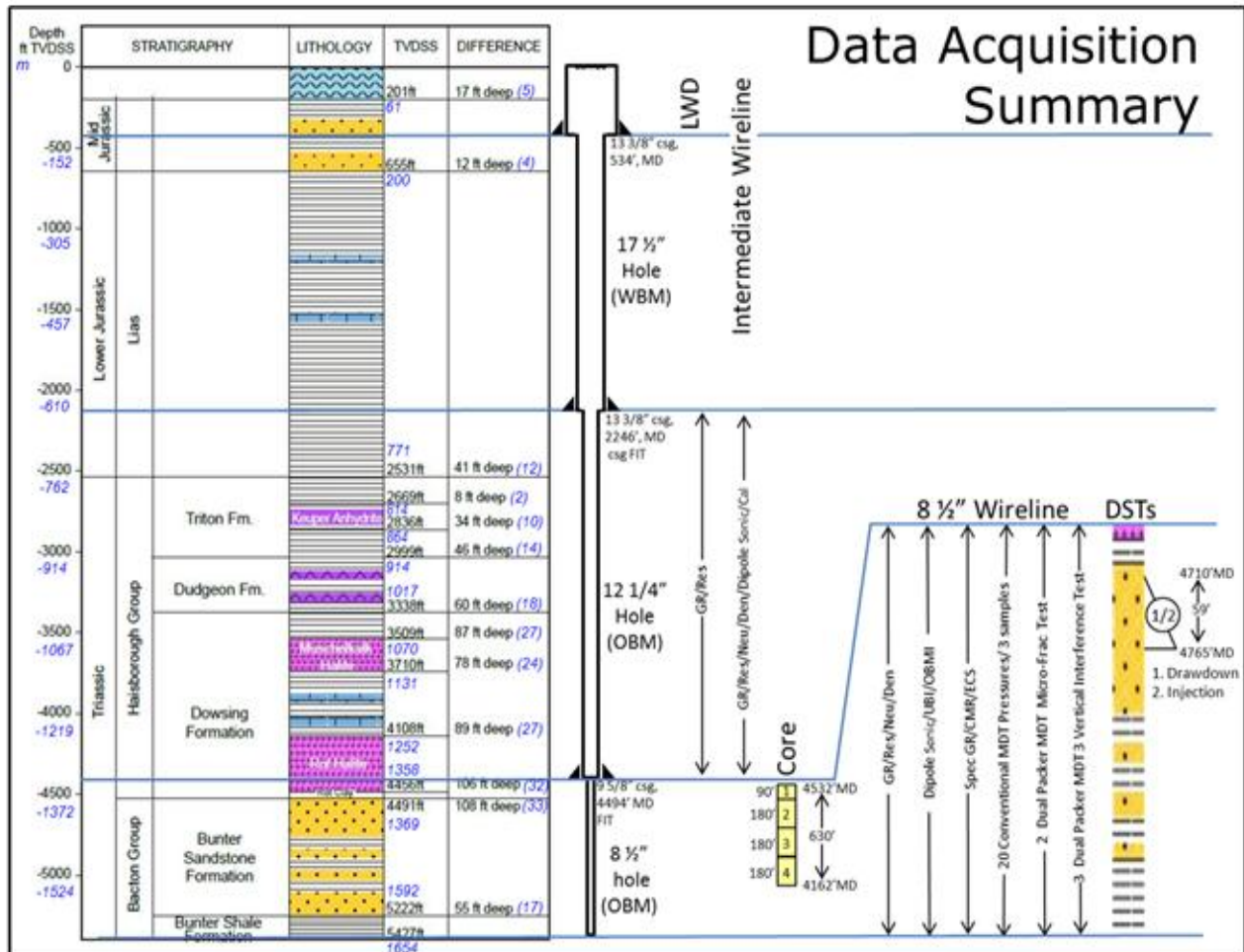


Table 4.1: Prognosed Depths Compared with Actual Depths as Reported at the 42/25d-3 Wellsite

Lithostratigraphical Prognosis			Actual Depth (wellsite)		
Formation Top	TWT [s]	Depth [m SS]	Uncertainty [m SS]	Depth [m SS]	Difference [m] (-=deep to prognosis)
Seabed		-56 (LAT)		-61.3	
Middle Jurassic		-56	+9 to -25m	-61.3	-5.3
Lias Group		-196	+/- 25m	-199.6	-3.6
Top Triassic (Haisborough Group)	0.680	-759	+/- 25m	-770.5	-11.5
Triton Anhydritic (Stag FWR)		(-759)		-783.0	-24
Top Keuper Anhydrite Member		-811	+/- 25m	-812.6	-1.6
Base Keuper Anhydrite Member		-854	+/- 25m	-862.0	-8.0
Dudgeon Formation		-900	+/- 25m	-913.5	-13.5
Dowsing Formation		-999	+/- 25m	-1015.9	-16.9
Muschelkalk Halite Member		-1043	+/- 29m	-1068.9	-25.9
Base Muschelkalk Halite Member		-1107	+/- 29m	-1129.3	-22.3
Upper Röt Halite Member		-1225	+/- 29m	-1250.0	-25.0
Main Halite Member				-1286.0	
Röt Clay Member		-1326	+/- 29m	-1358.2	-32.2
Bunter Sandstone Formation	0.997	-1336	+/- 29m	-1368.6	-32.6
Bunter Shale Formation		-1575	+/- 29m	-1592.0	-17.0
TD		-1655		-1655.7	-0.7

Figure 4.18: Overview of 42/25d-3 data acquisition and results including actual compared to prognosed depths



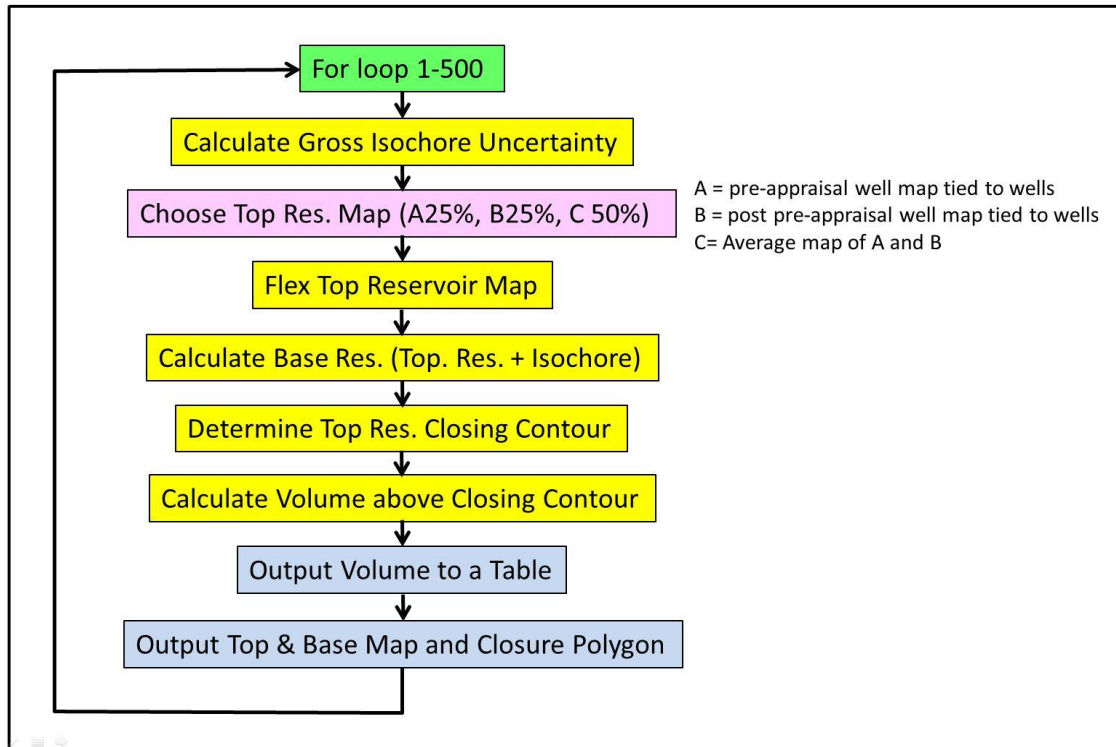
Alternative depth conversion methods were explored post-drilling the 42/25d-3 appraisal well as a means of providing a range of depth map predictions. Predicted depths from these alternative methods were found to be in the range already established by modifying parameters in the V0k method and thus confirm V0k as a reliable method for generating the geological structural model depths.

The uncertainty in depth conversion is reflected directly in the estimates of the structure volume and the NPV of the Storage Site. NPV uncertainty analysis shows that the Gross Rock Volume (GRV) is the most uncertain parameter, creating an NPV range of -16% to 11%. It is however appropriate here to outline the workflow used to generate the gross rock volume.

4.4.1.1 Gross Rock Volume Uncertainty Workflow

The Petrel workflow used for generating the range of gross rock volume is illustrated in Figure 4.19. Five hundred (500) realisations have been created in which multiple Top Bunton structures and Bunton Sandstone isochores are combined to estimate the GRV uncertainty range. The key elements of the workflow are summarised below.

Figure 4.19: Gross rock volume uncertainty workflow



Three maps have been inputted into the workflow; these are listed below.

1. **Low Case Map (MAP A):** represents the pre 42/25d-3 map, tied to the Top Bunter depth point in this well using a 2km radius of adjustment (Figure 4.20). This map was depth converted without the northern flanking wells 43/21-2 and 43/21-3 which were seen to have anomalous velocities. The spill point for this map was -1460m TVDSS.
2. **High Case Map (MAP B):** represents a post 42/25d-3 map (Figure 4.21). For this case the depth conversion was revised incorporating northern flanking wells 43/21-2 and 43/21-3, creating a deeper structure that moved the spill down to -1520m TVDSS.
3. **Mid Case Map (MAP C):** is an average of the low and high cases (Figure 4.22) and was created to provide a realisation over the middle ground between the end member cases. It has a spill point of -1490m TVDSS.

Figure 4.20: Low Case Top Bunter Structure depth map (Map A)

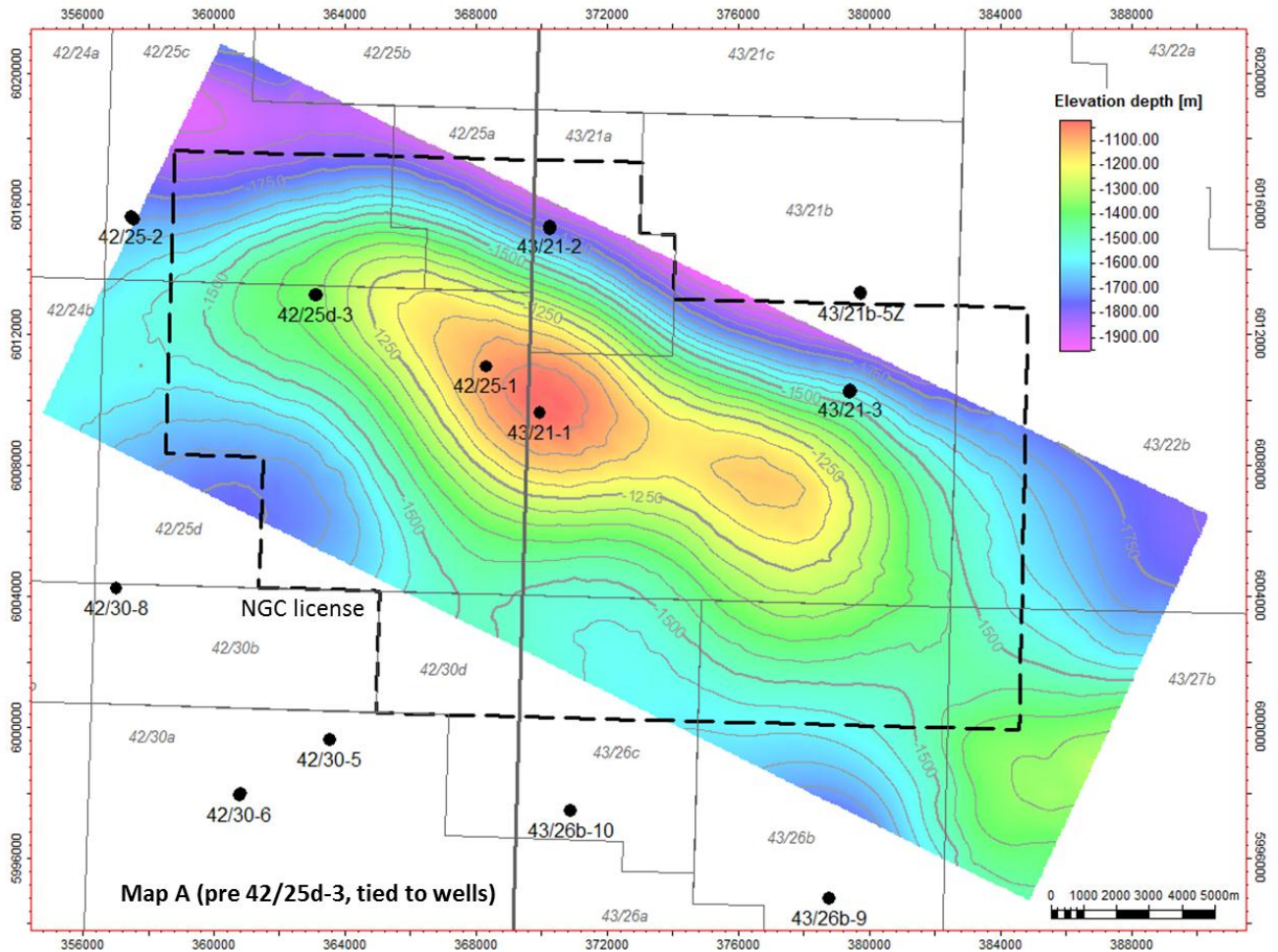


Figure 4.21: High Case Top Bunter Structure depth map (Map B)

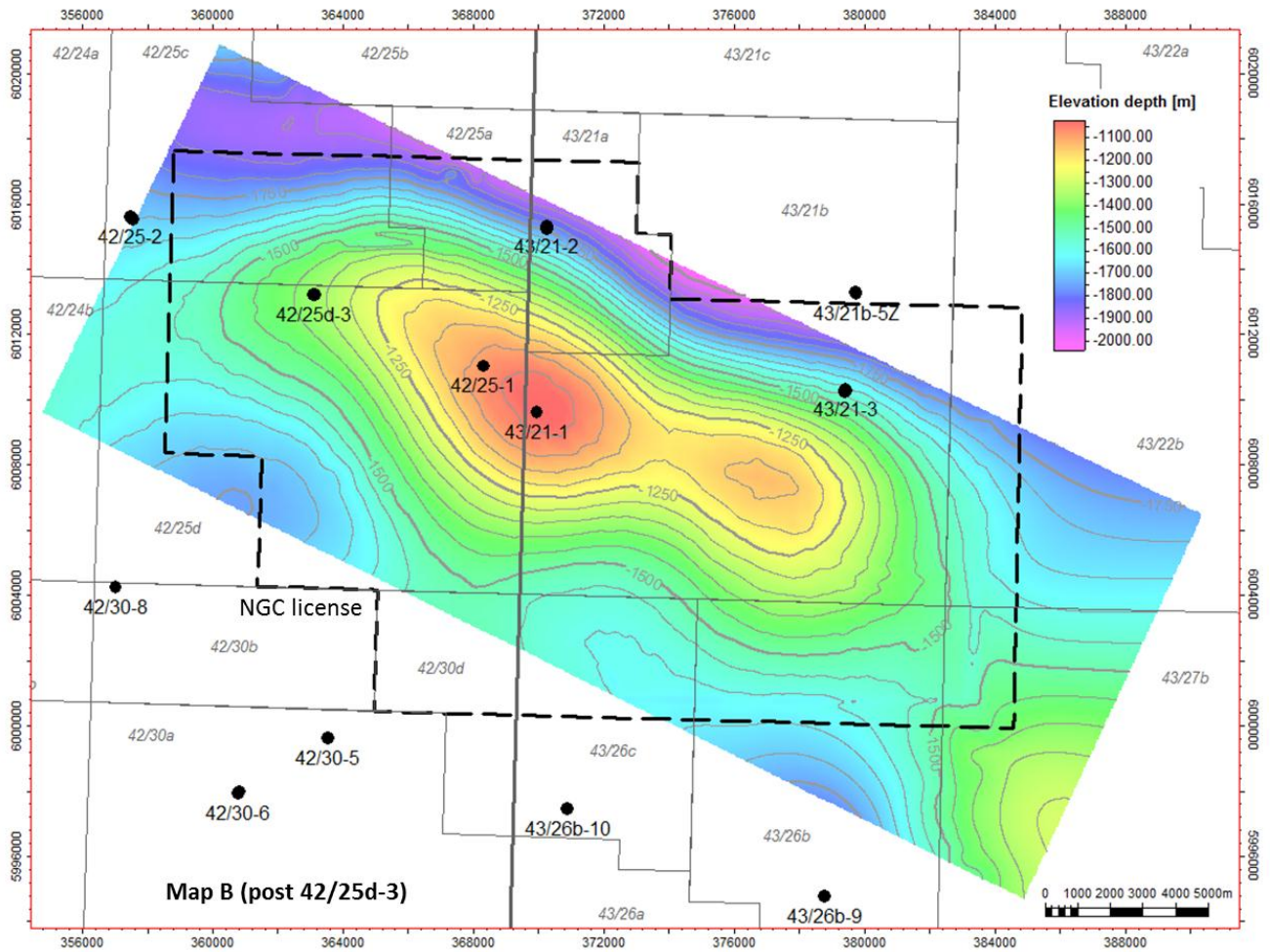
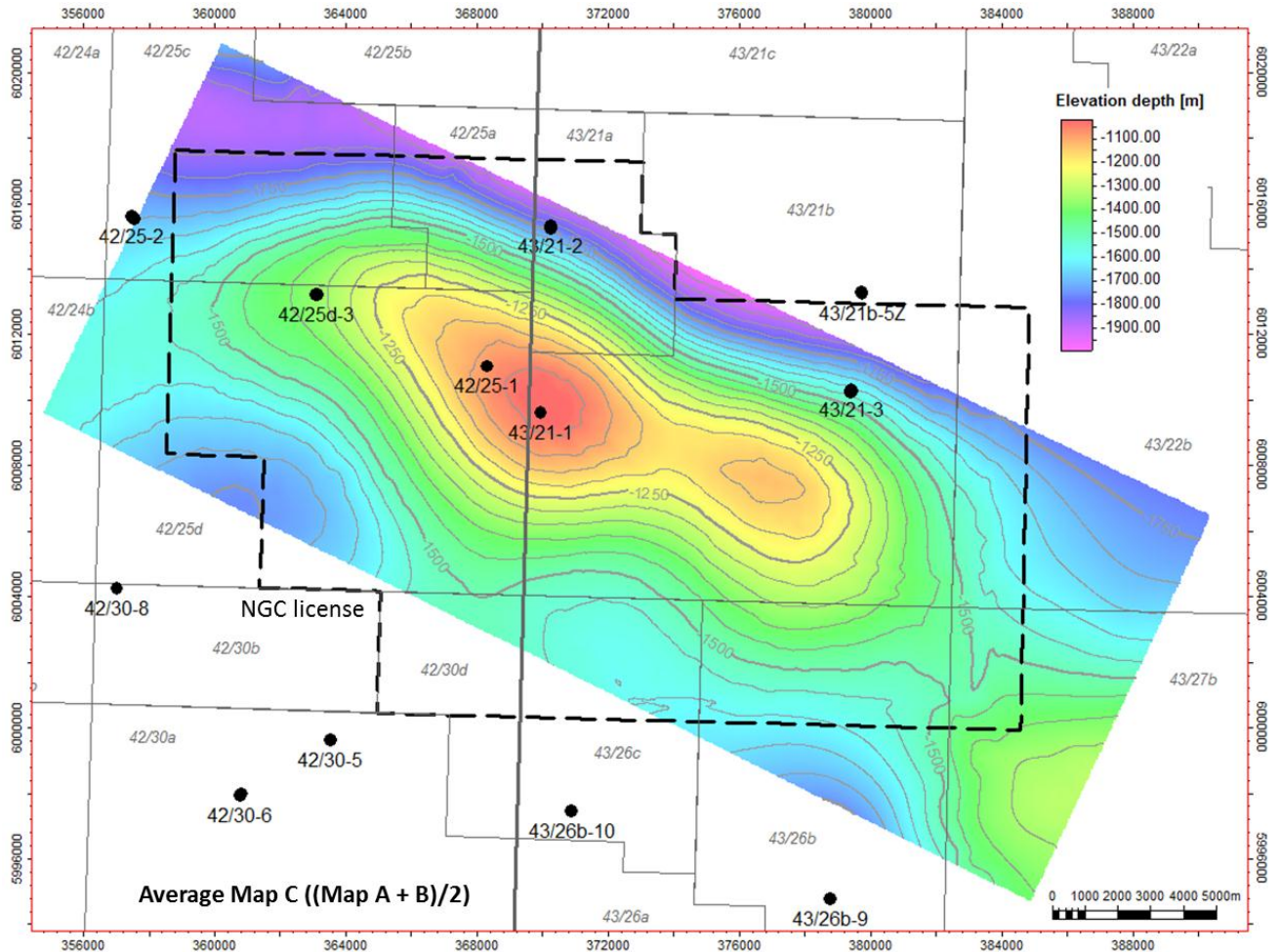


Figure 4.22: Mid Case Top Bunter Structure depth map (Map C)



In the first part of the workflow a Bunter Sandstone isochore is generated whose thickness was $\pm 10\%$ of the base case isochore thickness. This isochore is then added onto to a Top Bunter structure to create a Base Bunter structure. The top structure map is based on either a low, mid or high Top Bunter structure cases (Maps A, C or B). The low and high case maps were each chosen 25% of the time leaving the mid case map being selected 50% of the time.

Once a map has been selected it is flexed in the workflow to create top reservoir depth variation. The method of flexing the map is similar to the method used to vary isochore thickness described above. A maximum top reservoir depth error surface is multiplied by a factor that ranges between -1 and +1 and then added to the selected top reservoir depth surface:

$$\text{Uncertainty Top Structure} = \text{Top Structure} + (\text{Error Surface} \times \text{Factor})$$

The error surface was based on the maximum depth error of 44.6m derived from the pre 42/25d-3 depth conversion process. The west-east cross section in Figure 4.29 illustrates the three input maps (Maps A, B and C) and the maximum and minimum depth surfaces that have been created by the uncertainty

workflow. The depth uncertainty is greatest to the south east of the structure in the vicinity of the saddle that separates Endurance from the outcrop diapir structure. The estimated Endurance closing contours ranges from -1416m to -1553m TVDSS (137m range).

A similar cross section in Figure 4.24 shows the complete range of top and base reservoir structural uncertainty maps created by 500 runs of the Petrel GRV uncertainty workflow.

Figure 4.23: West-East cross-section across the Endurance structure illustrating the input depth surfaces and structural uncertainty

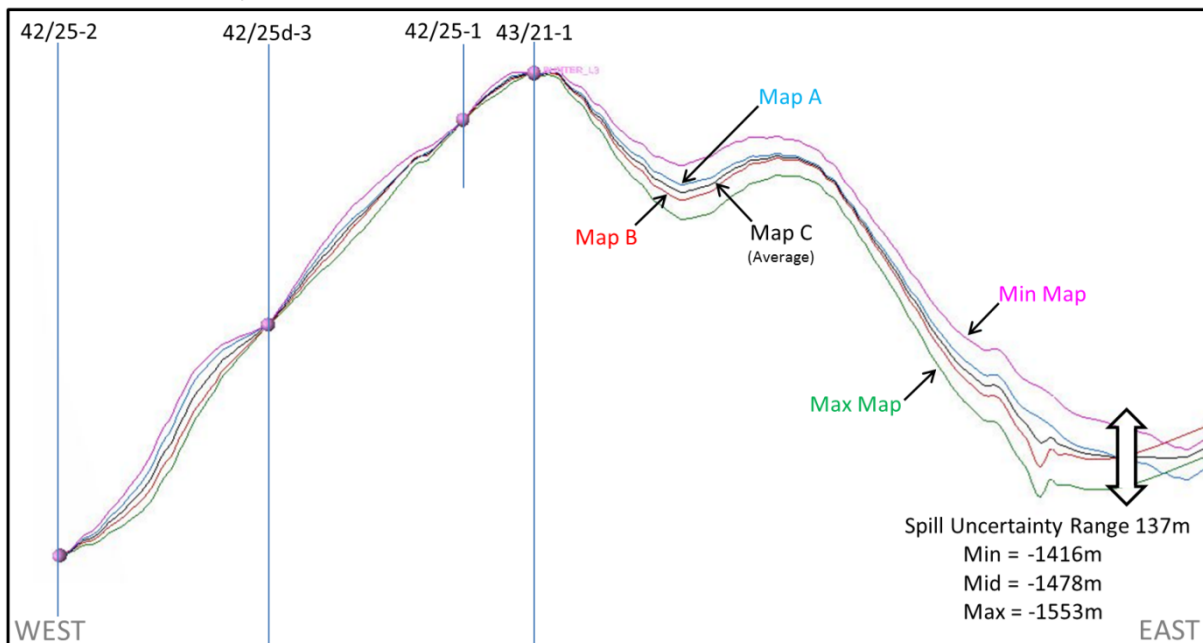
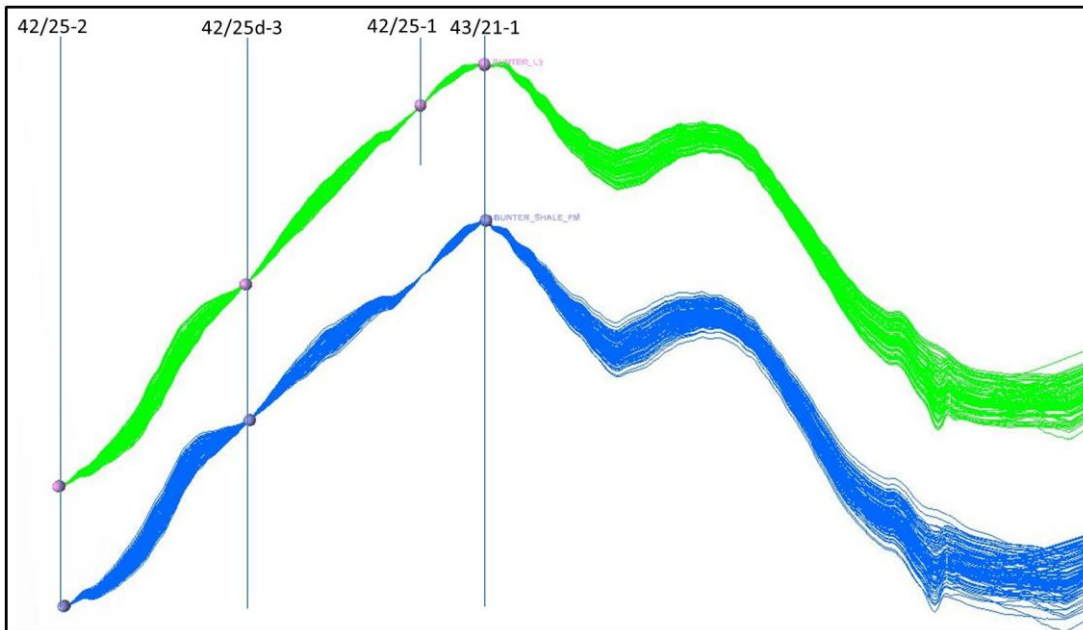


Figure 4.24: West-East cross section across the Endurance structure illustrating the complete range of top and base reservoir depth structures created by 500 runs of the uncertainty workflow.



Once a structure has been selected and flexed for structural uncertainty, the lowest closing contour was determined using a simple routine that tests for volume in a narrow polygon beyond the maximum possible spill of -1553m at progressively shallower levels (Figure 4.25). The spill point in the workflow is defined at the level where volume is no longer detected within the spill volumetrics polygon. Spill occurs mostly to the east but some of the larger structures spill to the south (Figure 4.26a). At this point the workflow saves the spill level for the particular realisation and uses it to calculate GRV of the Bunter interval.

Figure 4.25: Routine for determining the maximum closing spill contour of a structure.

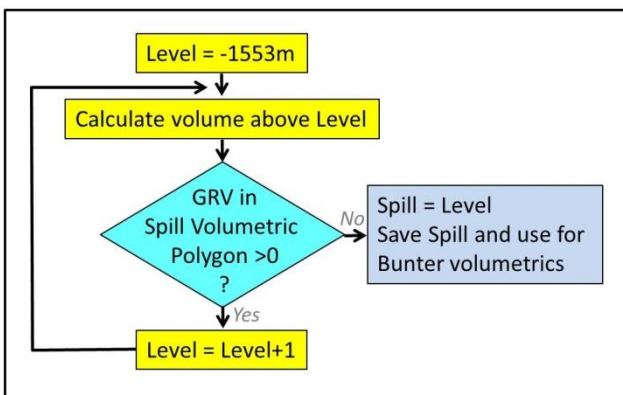
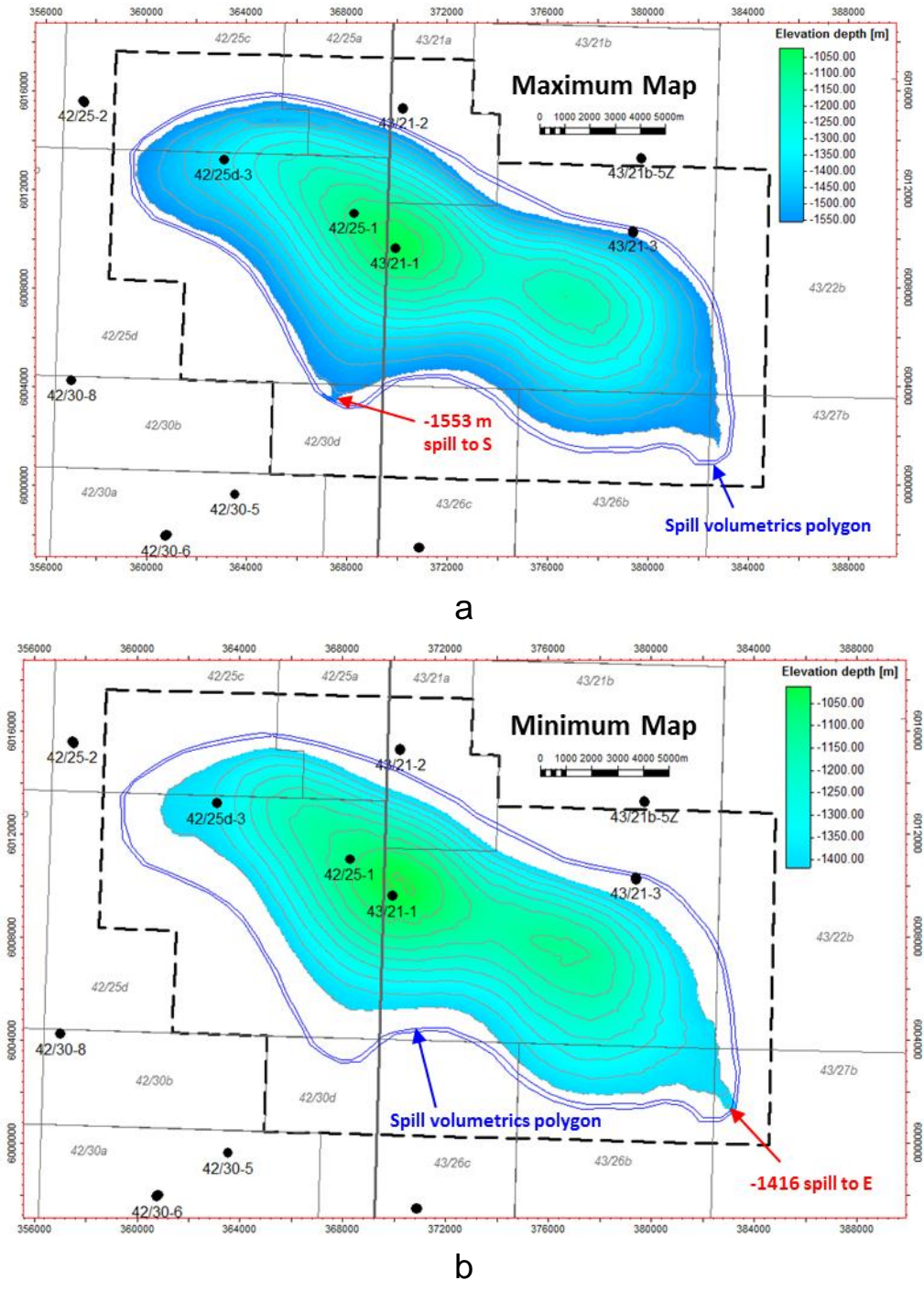


Figure 4.26: Top reservoir structure for the maximum (a) and minimum (b) maps illustrating the spill volumetrics polygon



4.4.2 Structural Configuration and Faulting

Over the Endurance structure a North West - South East grain is observed consistent with the deeper Palaeozoic trend observed at Carboniferous/Permian level. Normal displacements in top Triassic reflectivity can clearly be traced down towards top Bunter but appear to sole out above the Röt Halite interval (Figure 4.27). There is no evidence of faults extending into the Bunter aquifer within the closure of the Endurance anticline. Even with the data dropouts affecting near surface continuity, it is likely that these faults would extend vertically up close to seabed, and this is confirmed on 2D high resolution appraisal well site survey seismic (Figure 4.28). Further interpretation using lately acquired Polarcus 3D seismic data provide additional confidence in this interpretation. Figure 4.29, below, shows comparison of fault interpretation for 2D Tieline, 3D Polarcus and 3D OBC data sets.

Faulting appears constrained to the axial part of the crest and this is thought to be related to sediment cover extensional forces due to underlying Zechstein salt swelling. Fault offsets in general appear relatively small and in the order of 10m to 40m, the lower limit representing the resolution of the seismic data. With increased proximity to the large Zechstein salt diapir to the south-east of Endurance, the faulting style increases in its complexity and frequency with a "concertina" style noted from many of the 2D lines that traverse the area surrounding this feature. A series of upward and downthrown Triassic blocks are noted here over the crest of the salt swell.

Figure 4.27: SW-NE arbitrary section (3D OBC volume)

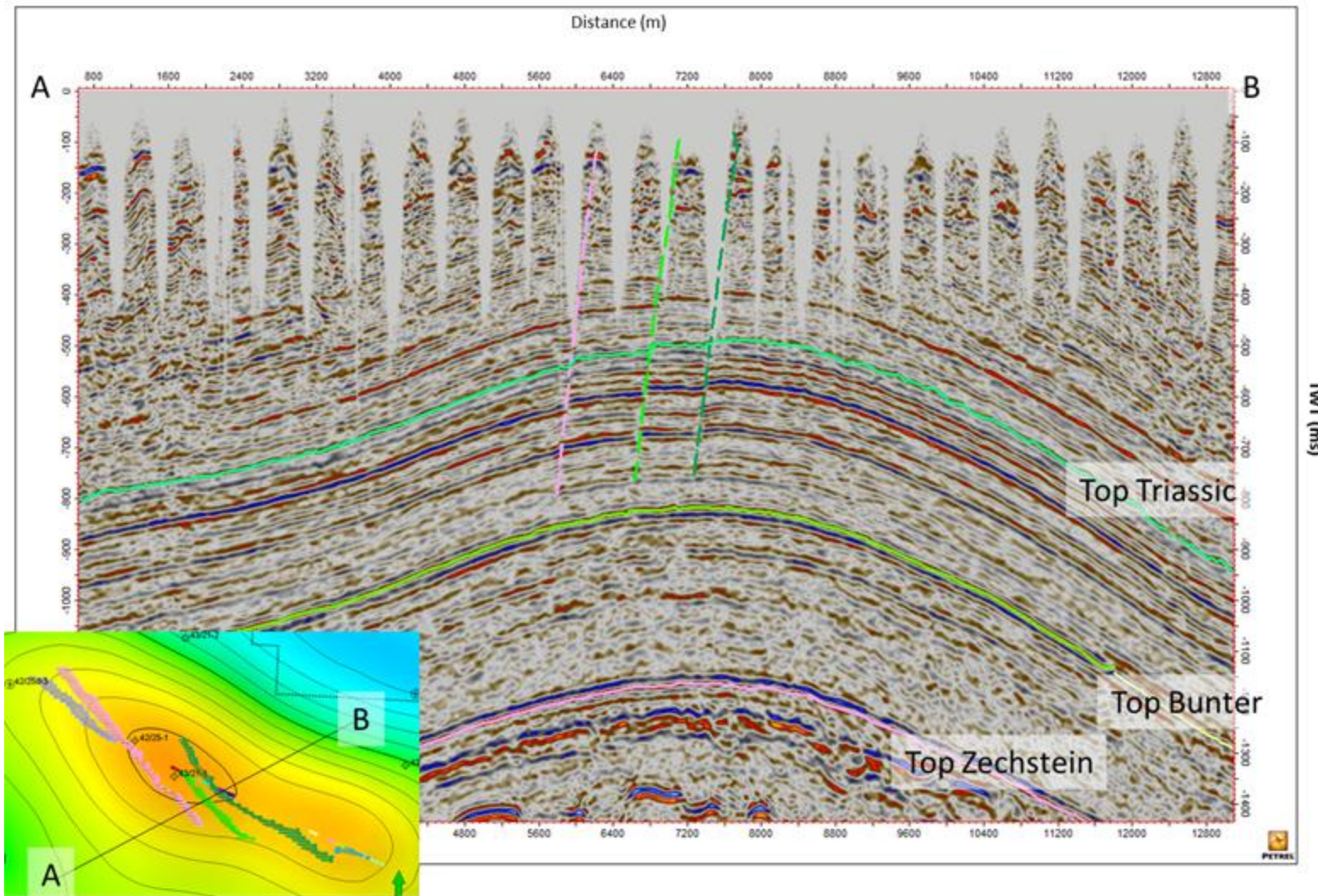


Figure 4.28: 43/21-3 P2 Site Survey Tie Line

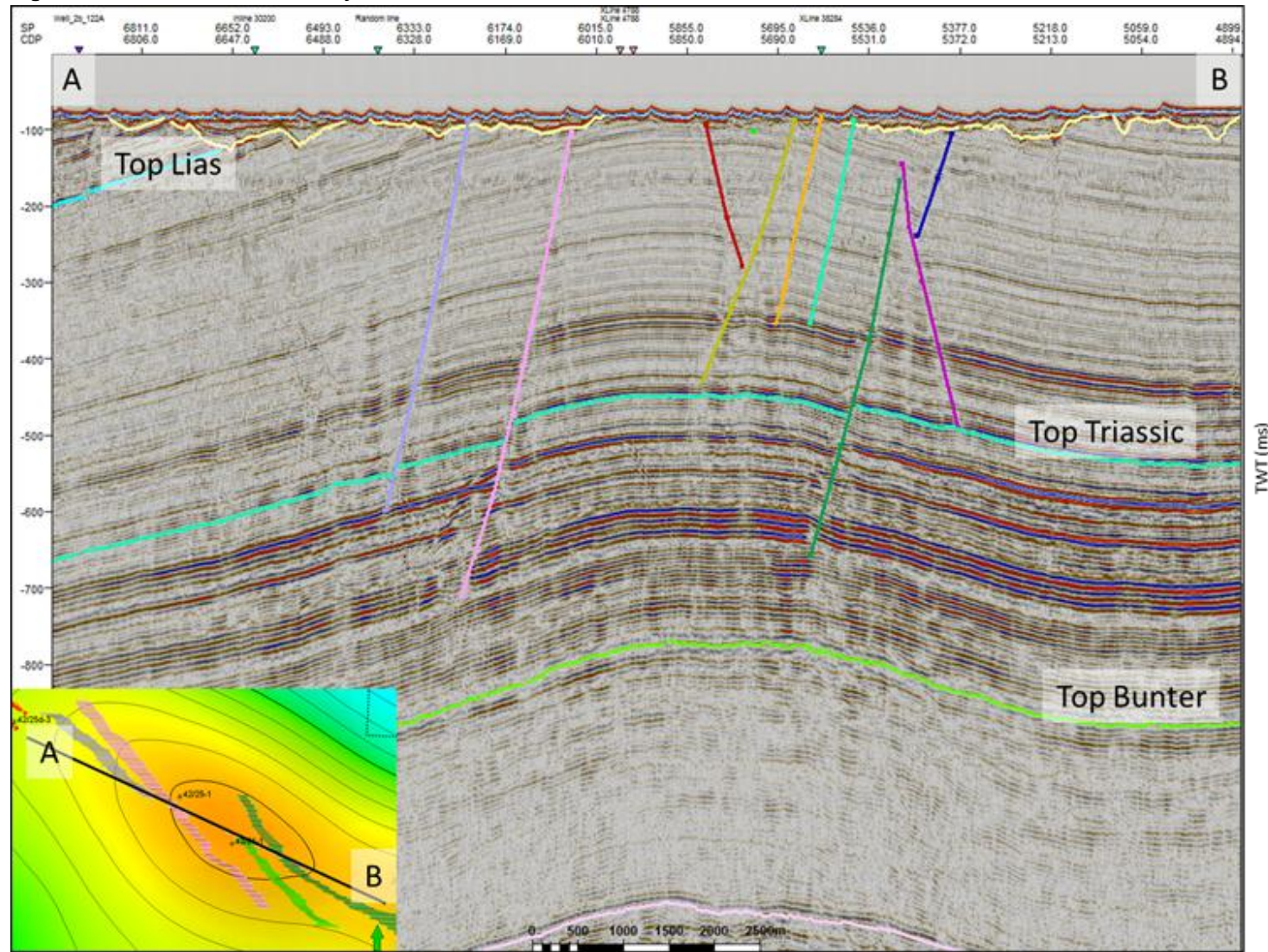
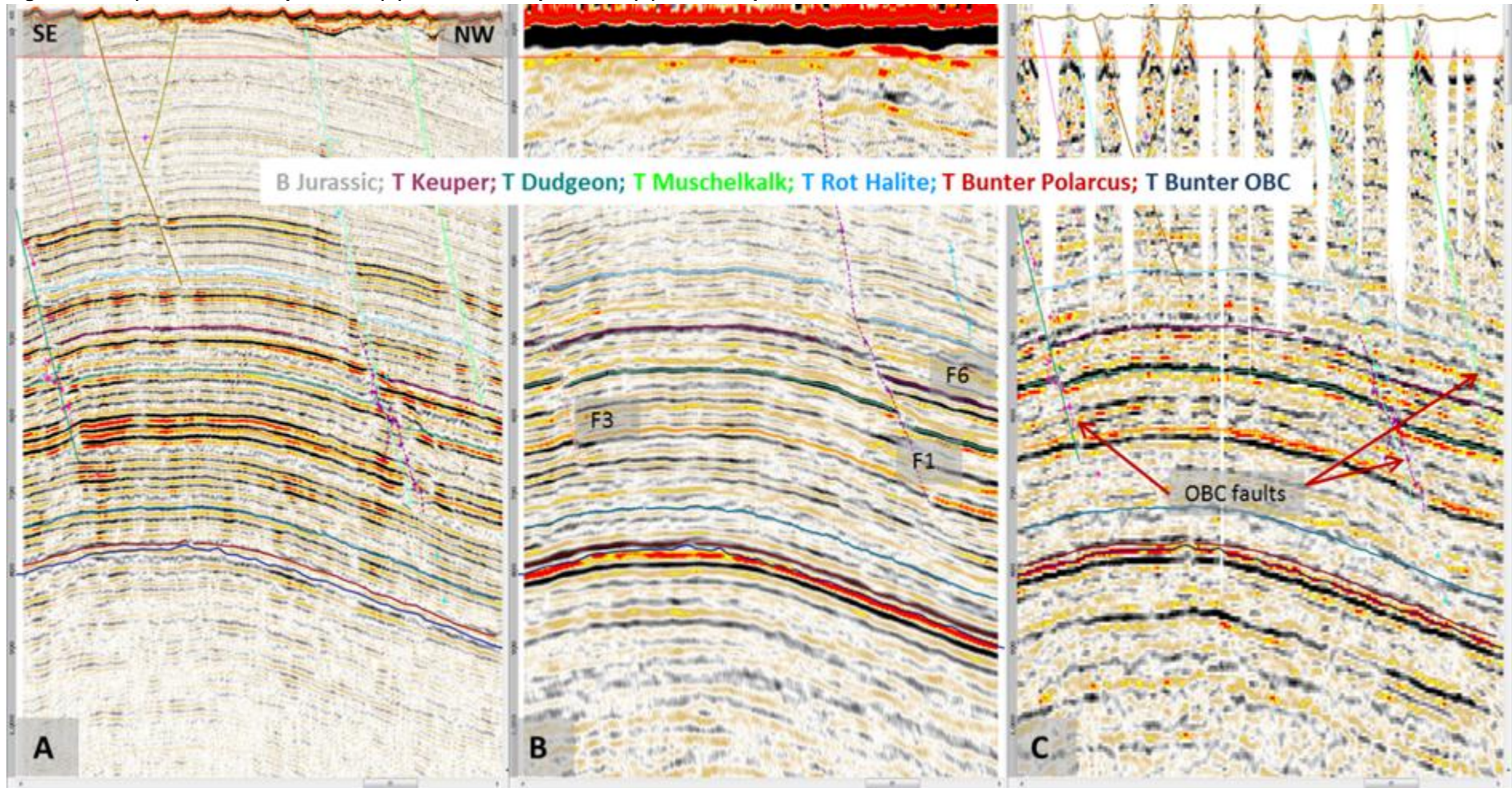


Figure 4.29: A) Tieline 2D interpretation, (B) Polarcus interpretation, (C) OBC interpretation with OBC faults and Tieline faults



4.5 Depositional Setting and Sedimentological Framework

The Bunter Sandstone was deposited in a broad, land locked and gradually subsiding basin situated between 20° and 30° north of the equator. The climate was semi-arid with rivers and streams draining into the basin from surrounding highs and terminating in a playa lake situated within the basin centre. During drier periods, aeolian processes redistributed the sands, and mudstones were desiccated. Expansion of the playa lakes during wetter periods resulted in deposition similar to that of the underlying Bunter Shale Formation and presumably also similar to that of the overlying Röt Clay. Figure 4.30 illustrates the gross regional palaeo geographic setting during Bunter deposition.

The Bunter Sandstone comprises a number of large-scale fining-upwards units in which predominantly fluvial and aeolian sandstones fine upwards into siltstone and claystone alternations of the playa margin facies. Low permeability facies such as clay rich playa mudstones and playa margin flood plain siltstones, deposited during periods of low energy or lake expansion, are abundant in the Lower Bunter. Coarser-grained deposits are more common in the middle and upper parts of the Bunter Sandstone.

Sedimentological logging of the Bunter section in 42/25d-3 supports a depositional model with a general preponderance of coarser-grained fluvial and Aeolian facies. This is probably due to the proximal position of the 42/25d-3 in relation to the regional transport directions (Figure 4.30 and Figure 4.31) compared to the wells 44/26 and 42/25. Well 44/26-1 for example lies farther south than 42/25d-3 and consists exclusively of siltstones, very fine sandstones and minor mudstones and therefore represents a more distal location. Sedimentological interpretation from the short core (16m) recovered from well 42/25-1, the closest well to 42/25d-3, show sandstones that comprise finely interbedded sequence of sand sheet, playa margin, aeolian and fluvial laminated facies. The absence of well-developed finer-grained facies in 42/25d-3 has hindered the subdivision of the Bunter Sandstone into lower-order stratigraphic units based on sedimentology. This has, however, been achieved using chemostratigraphy, where the BSF has been divided into three main units (L1, L2, & L3 from the base up, equivalent to P1, P2, & P3).

The 42/25d-3 core log has been split into six facies successions which include fluvial deposits (mainly sheetfloods) subject to occasional aeolian reworking. The dominant lithology is very-fine to fine-grained sandstone. The only Mudstone bed seen in 42/25d-3 is about 0.35ft (10 cm) thick, comprising muddy siltstones with irregular top and base, and interpreted as laterally inextensive. A bed of presumed reworked ooids from the underlying Rösenstein section is thought to be regionally extensive, and forms a distinct calcareous horizon several feet thick. Nodular anhydrite cement is common at numerous horizons.

Although the depositional interpretation has centred around the 42/25d-3 appraisal well, data and analysis from wells around the Endurance structure, have been used to constrain the interpretation.

Figure 4.30: Schematic representation of Bunter Sandstone depositional environments in the region around the 42/25d-3 well

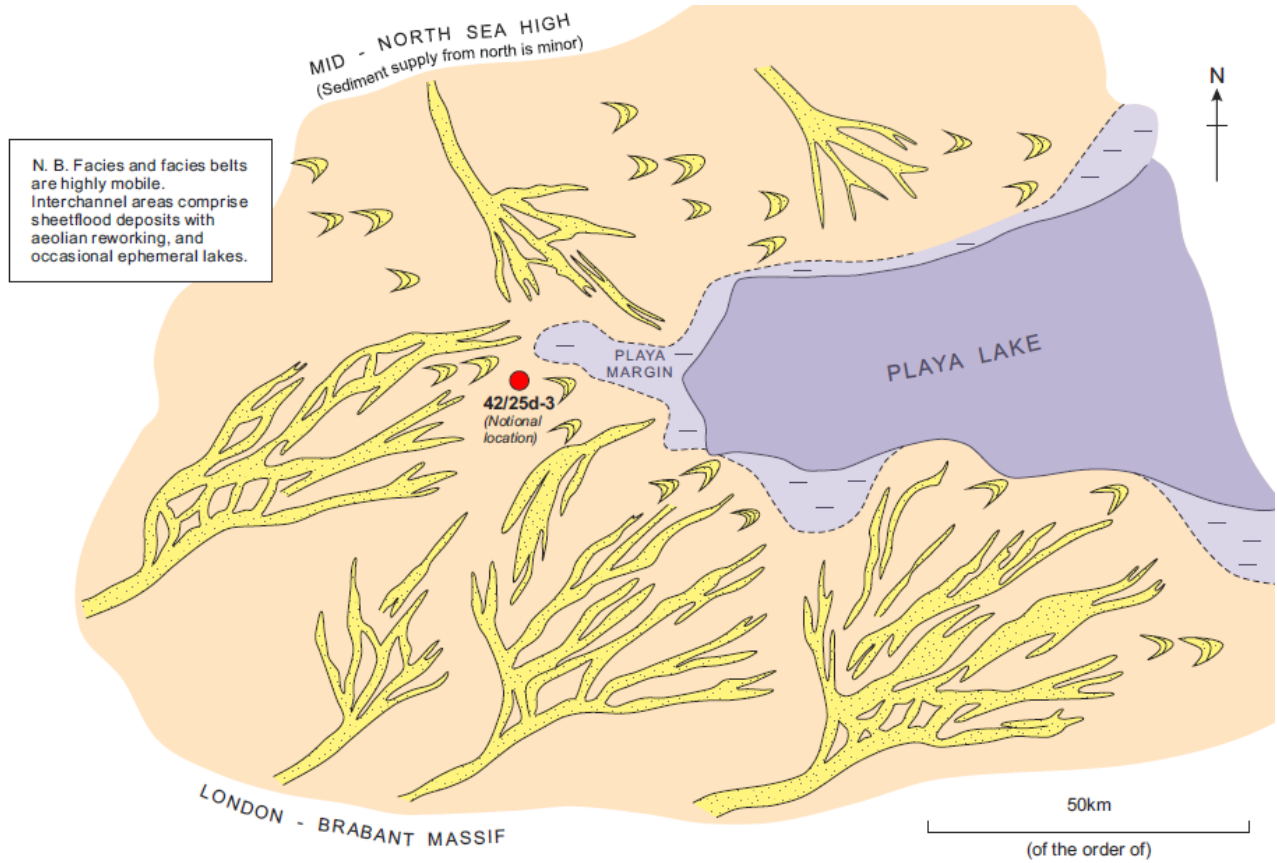
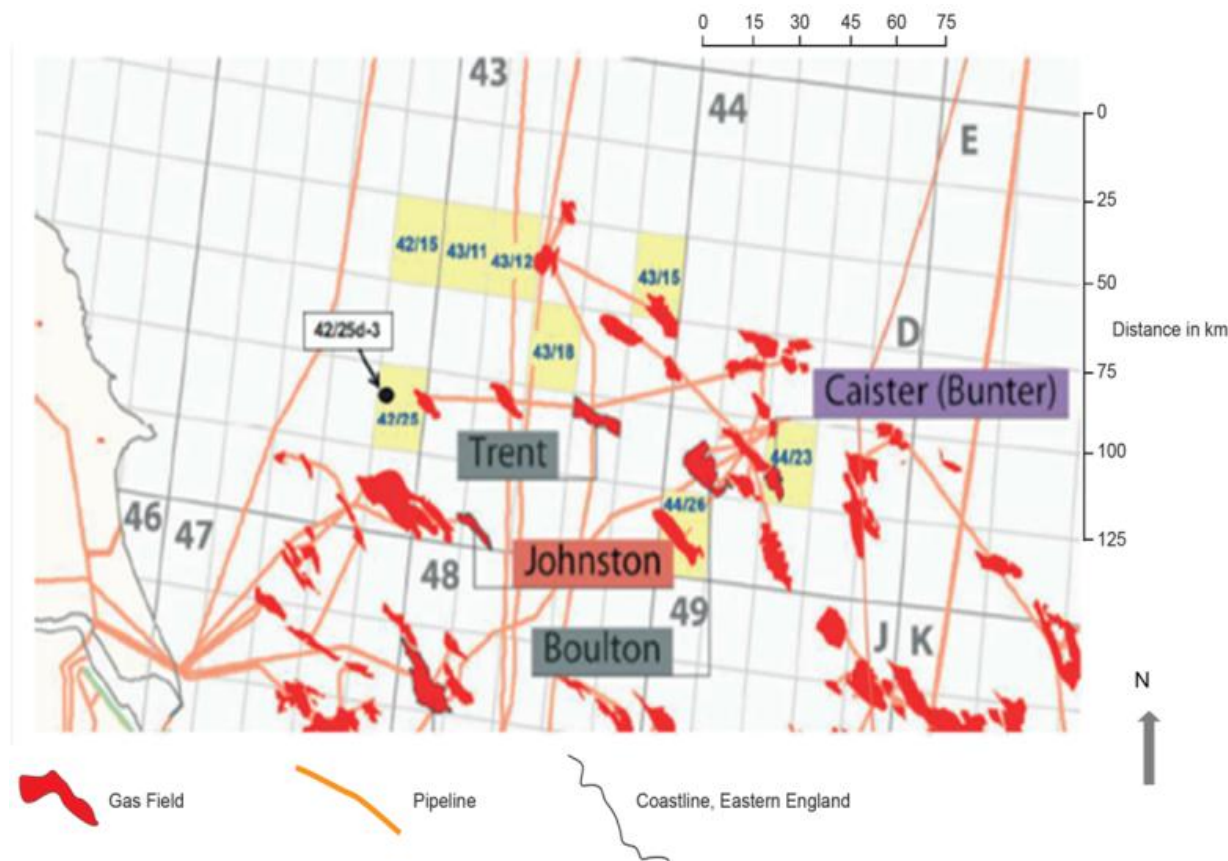


Figure 4.31: Location map



The location map shown in Figure 4.31 is an extract highlighting (in yellow) the blocks that include wells included in an earlier sedimentology study (2011). The position of well 42/25d-3 is also indicated.

4.5.1 Petrographic and Chemostratigraphic Input

4.5.1.1 Chemostratigraphic Input

In the absence of microfossils, obvious regional shale breaks and repeatable log character, chemostratigraphy provided the best means of correlating the sandstone packages. Mineral characterisation of rock samples from the Triassic Bunter Sandstone successions encountered by wells 42/25d-3, 42/25-1, 42/30-6, 43/21-1, 43/21-2 and 43/21-3, established four chemostratigraphic packages and six chemostratigraphic units within the study interval as outlined in Table 4.2. The mineral characterization was based on changes in the feldspar, heavy mineral and mica content within the study interval as shown in Figure 4.32 and Table 4.2 (which shows the key elemental ratios used in the chemostratigraphic interpretation).

Two hundred and ninety-five Bunter sandstone samples have been analysed for this study, using Inductively-Coupled Plasma - Optical Emission Spectrometry (ICP-OES) and Inductively-Coupled Plasma - Mass Spectrometry (ICP-MS), with the samples prepared by an alkali fusion procedure. Data was

acquired for ten major elements, e.g., Si, Ti, Al, etc., twenty-four trace elements, e.g., Ba, Be, Co, etc., and fourteen rare earth elements, e.g., La, Ce, Pr, etc. . The precision error in data acquisition for the majority of these elements is found to be c. 5%, though the precision error for the W, Ti and Sn data ranges from 10% to 20% and these have been excluded from later interpretations. With respect to the standard reference materials, the absolute accuracy of all the data were generally considered to lie within the range of error achieved for multi-determinations of the same sample.

The chemostratigraphic zonations have formed the foundation for the correlation of the study wells as illustrated in Figure 4.34. The main features of the chemostratigraphic correlation are as follows:

- Package P3/L3 occurs in all wells and is consistently defined by its low Be/Al and high K/Rb, implying that it has increased levels of k-feldspar and decreased mica content than package P2/L2; Unit P3a/L3a is recognised in all wells and is characterised by higher K/Al values than the overlying P3b/L3b. Unit P3b/L3b is absent in well 42/25d-3;
- Package P2/L2 is defined in all wells by its high Be/Al and lower K/Rb values: these geochemical characteristics imply package P2/L2 has lower K-feldspar contents than the underlying P1/L1 and overlying P3/L3 packages; Unit P2a/L2a is well defined in all wells by an increased Be/Al values and decreased K/Al values compared to the overlying unit P2b/L2b (also defined in all wells);
- Package P1/L1 is consistently defined in all wells except well 42/25-1 (which did not penetrate the full sequence) by high K/Rb coupled with low Be/Al; Unit P1a/L1a is generally recognised in all wells except 42/25-1 by an increase in K/Al and Be/Al compared to the overlying unit P1b/L1b; Unit P1b/L1b is characterised by low Be/Al values which increase over this unit to a high on the boundary with package P2/L2; and
- Package P0 is defined in wells 42/25d-3, 43/21-1 and 43/21-3 by both low K/Rb and Be/Al values, with the top of the package defined by increased K/Rb values. This change probably implies that package P1/L1 contains more K-feldspar than P0, with P0 considered to be equivalent to the Bunter Shale which underlies the Bunter Sandstone.

Table 4.2: Chemostratigraphic Zonation Of Wells 42/25d-3, 42/25-1, 42/30-6, 43/21-1, 43/21-2 and 43/21-3 within the Bunter Sandstone

Heading Left	Heading Right	Heading Right	Heading Right	Heading Right	Heading Right	Heading Right	Heading Right
P3	P3b		1113	1667	1056	1818	1614
	P3a	1406	1125	1712	1077	1859	1642
P2	P2b	1425	1141	1781	1095	1893	1670
	P2a	1470	1172	1832	1153	1917	1714
P1	P1b	1534		1856	1201	1950	1751
	P1a	1578		1921	1258	2012	1796

All depths are in metres and are measured depths. Note P0 is not included because it lies within the Bunter shale.

Figure 4.32: Key geochemical profiles for well 42/25d-3

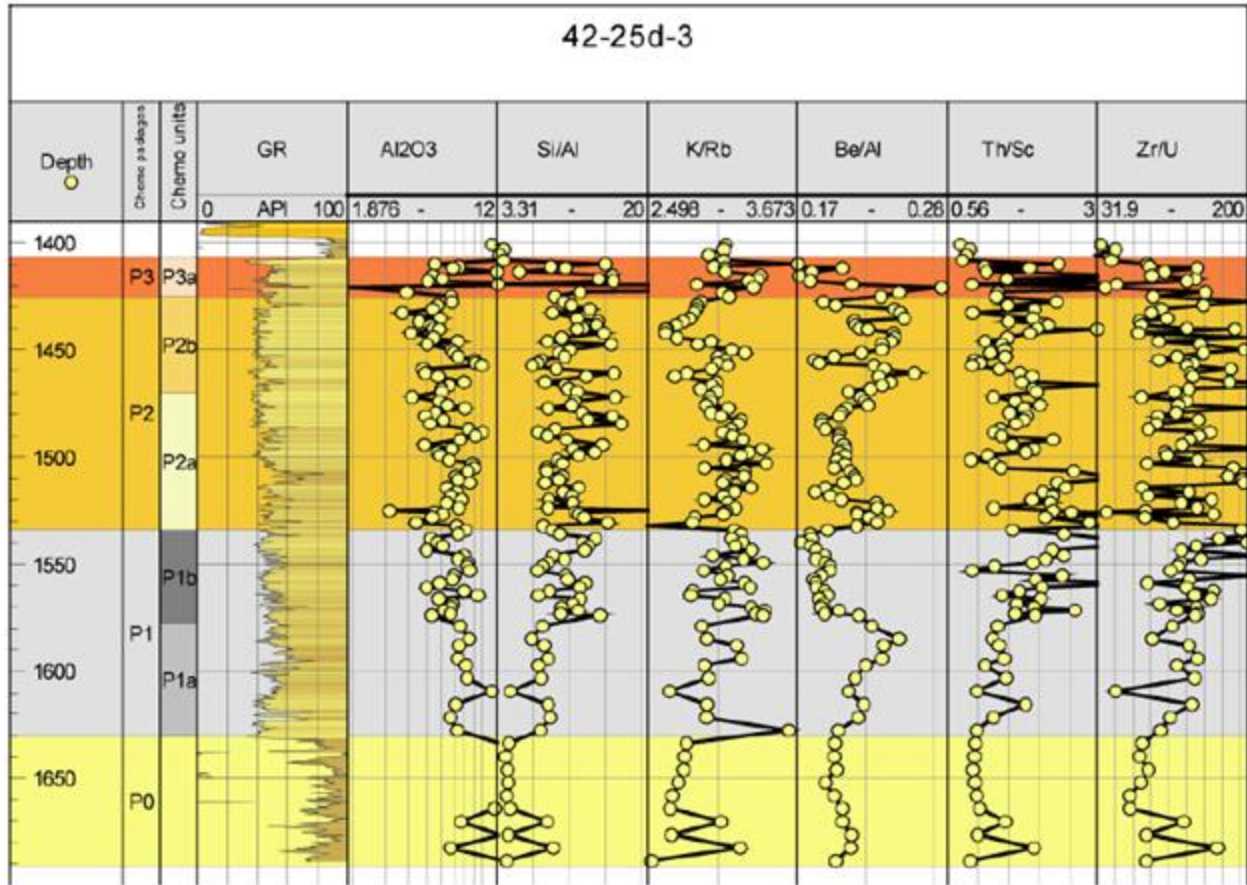


Table 4.3: Key Elements Ratios and Their Mineral Affinities

Element Ratio	Interpretation
K/Al	K feldspar/illite mica
K/Rb	K feldspar/illite mica
Be/Al	Micas/clay
Si/Al	Sand/clay
Zr/U	Zircons

Figure 4.33: A 6 Layer Inter-Well Correlation Incorporating Chemostratigraphic Sub-Layers



4.5.1.2 Petrographic Input

Optical petrographic analysis was performed on fifty core plugs recovered from the Triassic section of well 42/25d-3 to aid sedimentological interpretation and characterisation of reservoir and sealing quality. The four cores cover the lower part of Röt Halite, and the full Röt Clay section and a significant proportion (167 m) of the Bunter Sandstone.

Within the Bunter Sandstone, detrital grains are dominated by quartz and feldspar, with lithic fragments of varying granitic compositions and altered volcanic material. Small volumes of mica and heavy minerals occur. Major authigenic cements include dolomite and anhydrite. Calcareous ooids reworked from underlying Rößenstein are abundant near the top, forming a distinct horizon with potentially reactive calcite mineralogy.

The petrography of the Röt Clay shows detrital grains comprising illite-rich clays and silt-grade quartz, with subordinate plagioclase and traces of alkali feldspar. Cements within the Röt Clay include dolomite, anhydrite and minor halite.

The Röt Halite is made up of coarsely crystalline halite with anhydrite present in trace amounts.

4.5.2 Reservoir Quality and Correlation

The average porosity of the extensively cored appraisal well 42/25d-3 ranged from 0.17 in the Lower Bunter to 0.24 in the Upper Bunter, with corresponding estimated average permeabilities of 100md and 800md. Similar values were observed in the crestal wells 42/25-1 (>0.13 porosity and 100mD horizontal permeability) and 43/21-1 (0.20 – 0.33 porosity and 205 – 2100mD permeability). The high values of

porosity and permeability are suggestive of a post-depositional dissolution of detrital grains (most notably feldspars) and halite cements. Furthermore, although the reservoir lies at a relatively shallow level (1000-1500m) it is well documented that the Bunter Sandstone in the SNS was buried to a much deeper depth prior to being inverted in the Late Cretaceous to Early Tertiary. Based on the distribution of facies porosity from well 42/35d-3 core, reservoir quality was found to be largely independent of depositional facies. Apart from an overall slight reduction in reservoir quality downwards through the sequence, which results primarily from a reduction in grain size and an increase in the proportion of impermeable mudstone beds, the reservoir quality is remarkably uniform on large scales (Figure 4.34). The formation as a whole can be approximated to a single “tank”, with occasional laterally impersistent barriers to vertical permeability associated with thin mudstone horizons, and more widespread baffles associated either with concentrations of such mudstones (e.g. within playa margin facies), or cemented horizons.

The overriding control on reservoir quality appears to be diagenetic, related to post-depositional cementation and possibly dissolution. Anhydrite, dolomite and halite have all been recognised as potential cementing phases. Wells with cemented sandstone (wells 42/24-1, 42/25-2, and 43/21-3 in Figure 4.34) occur on the margin of the Endurance anticline where porosity ranges from being completely occluded to very low (0.05). This cementation appears to be more strongly developed at the top of the reservoir and creates a strong phase reversal on seismic data at the Top Bunter level. The phase reversal boundary is approximately conformant with the Endurance structure, lying close to the structural spill at least at the western end of the structure (Figure 4.16).

The Bunter sands have excellent porosity and permeability within the PRP boundary and are heavily cemented – and thus reservoir quality significantly deteriorates – outwith the PRP. Figure 4.34 shows the large differences in porosity (right hand track) between cemented and uncemented wells. The precise origin of the sharp interface between cemented and uncemented Bunter sandstone as represented by the PRP is not clear. The Thermohaline Circulation Model (TCM) to explain the absence of significant halite cement within the PRP in Endurance. The model envisages convection currents of lower salinity brine preferentially removing halite by dissolution. These convection currents are driven by differential heating of the reservoir through the underlying Zechstein salt.

Simulation of temperature distribution within the Endurance storage complex using highly idealised models have been performed to test the predictions of the TCM. The results agree broadly with the TCM predictions. The seabed above the salt diapir (outcrop) was predicted to be slightly warmer than further away. The temperature difference decreases down to 10°C within a 3 km radius around the diapir centre – 10°C being the assumed seabed annual average temperature (Figure 4.35).

The resulting temperature trends confirm the differential heating of the Bunter Sandstone through the underlying Zechstein Salt, producing brine density variation of up to 3kg/m³ across the structure which is sufficient to trigger thermal convection. The temperature values, ranges and distributions used for this analysis are subject to significant uncertainty and depend on the grid resolution and various assumptions employed in the modelling. Nevertheless the work has been useful in that it lends support to the TCM mechanism.

All available data also show no evidence to support an interpretation of the PRP as a palaeo gas-water contact (GWC). Whilst the PRP boundary is approximately conformant with the Endurance structure, this is not the case regionally, see Figure 4.36, particularly at the 3/44 structure to the east of Endurance which is water bearing but has the phase reversal cutting across the structure close to the crest. Gas

chromatograph readings and processed logs failed to show any evidence of trapped residual gas which would be anticipated if hydrocarbon gas had been present in the structure. Similarly water samples from 42/25d-3 appraisal well recorded no evidence of hydrocarbon gas. Rock strength data from a mini-frac in Röt Clay cap rock from 42/25d-3 appraisal well indicate it is geomechanically strong. Wireline logs suggest the Röt Clay is consistent in both thickness and shale quality. Seismic interpretation shows no faults penetrating the Bunter reservoir over the Endurance structural closure that could act as potential leak paths for hydrocarbons.

The PRP boundary was used in reservoir models as a limit to the extent of better reservoir quality rock. The cemented sandstone margin of the Endurance structure is referred to as the hardground.

Figure 4.34: Cementation in the Endurance area wells. Note the L1, L2, L3 zonations are equivalent to P1, P2, P3 chemostratigraphic packages

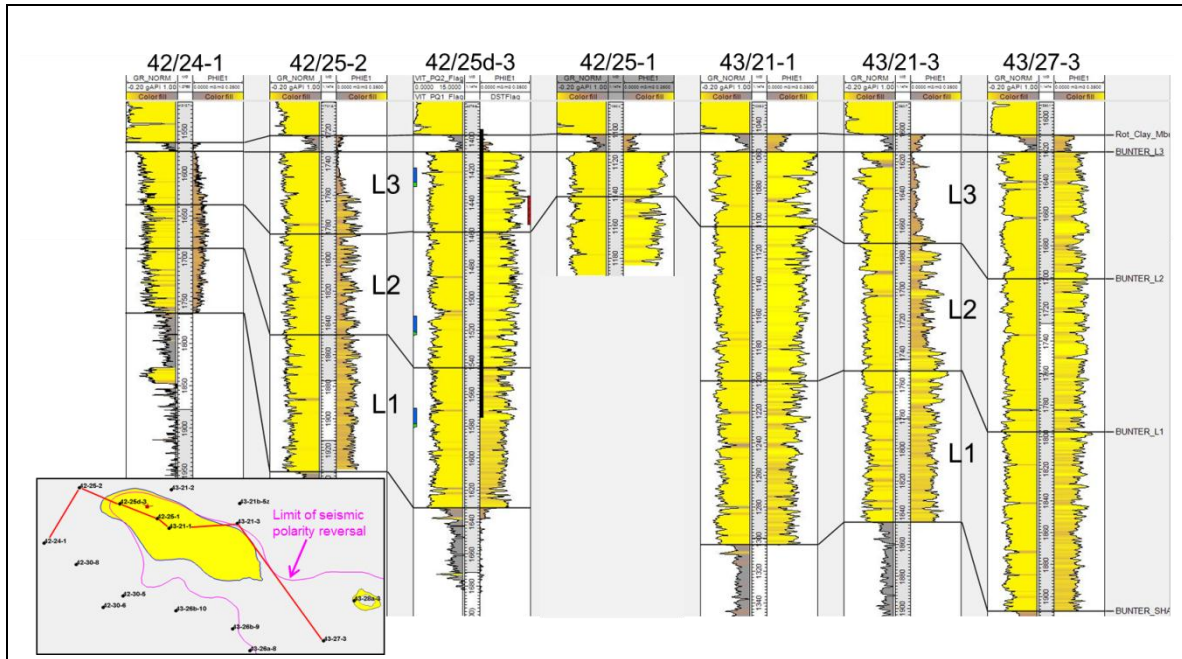


Figure 4.35: Estimated Temperature Distribution along North West-South East Cross-Line

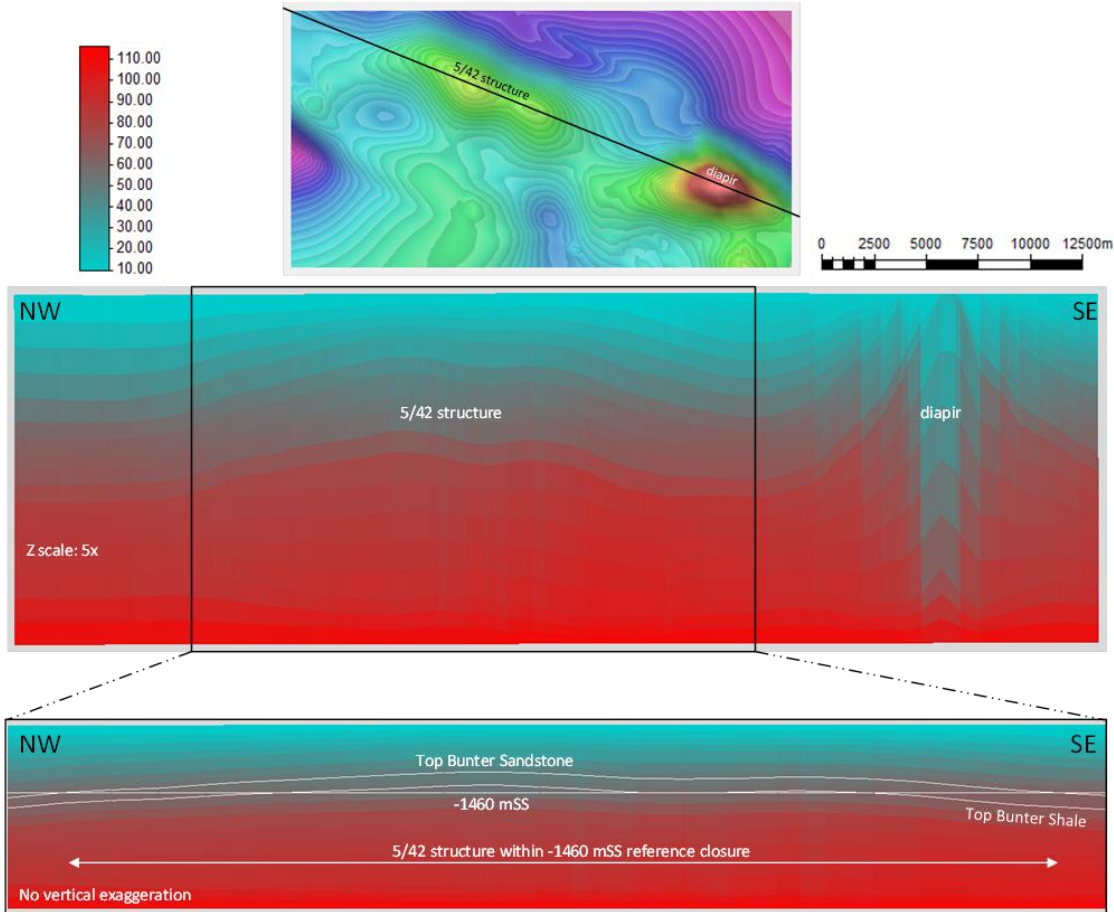
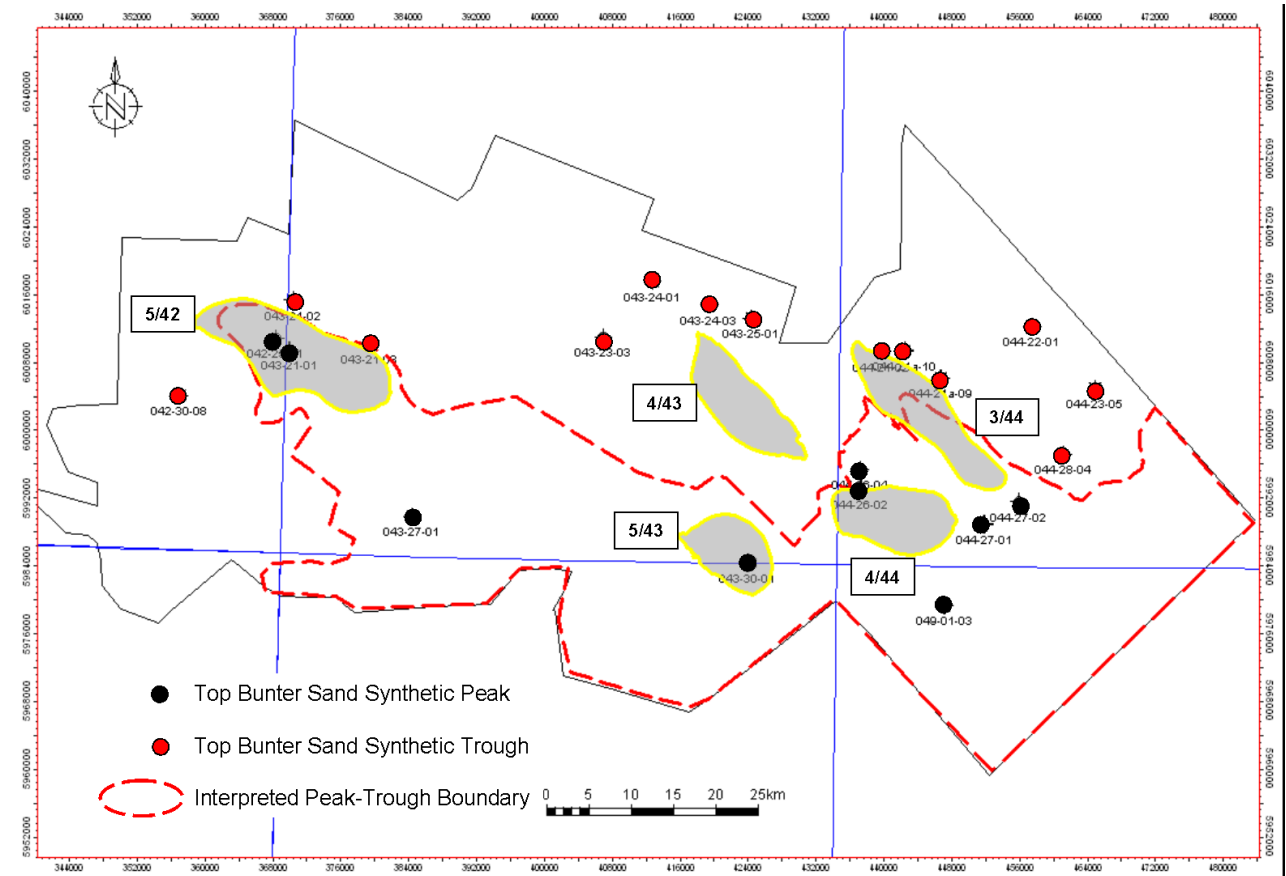
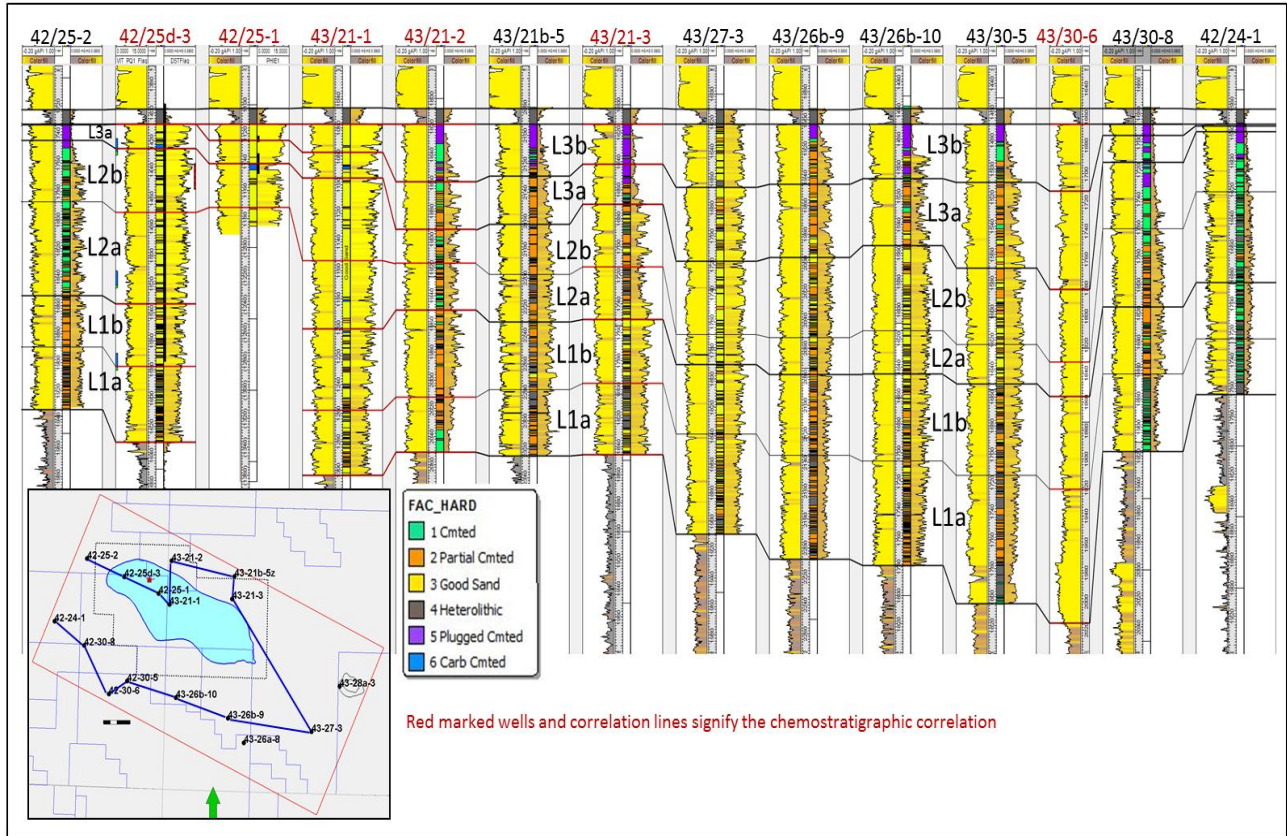


Figure 4.36: Outline of Endurance and the regional extent of the PRP



As already noted in the section on Chemostratigraphic input, the Bunter sandstone has been subdivided into 3 main zones, P1/L2 at the base, P2/L2 in the middle and P3/L3 at the top of the Bunter Sandstone. Each of these zones have been further split into two sub-zones; a lower “a” zone and an upper “b” zone. The chemostratigraphic correlation in Figure 4.34 was expanded by interpolation to the wells without chemostratigraphic analysis, as illustrated in Figure 4.37 (note again the redesignation of the original chemostratigraphic zonations as L1, L2 and L3).

Figure 4.37: Endurance area Bunter Sandstone correlation



4.6 Stratigraphic and Structural Framework

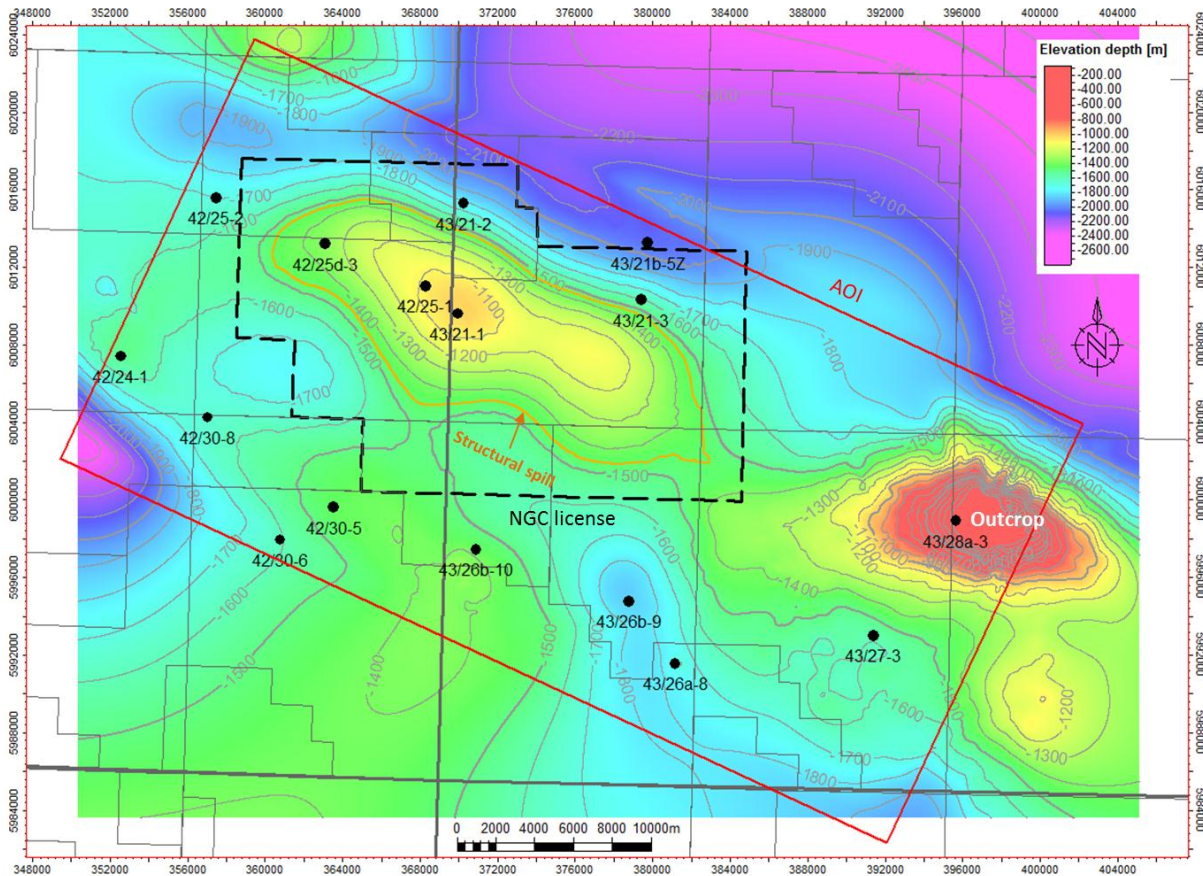
An RSFM covering the full stratigraphic column from seabed to Top Rotliegend was built using the Build Simple Model process in Petrel, without faults. The RSFM provides a common platform for the geological, simulation and geomechanical models. The structural framework shared by the RSFM and the geomechanical models is shown in Figure 4.38. The geological and simulation models focus only on the horizons in the black rectangle except the geomechanical model, which uses the entire RSFM (see Figure 4.62). The overburden faults have only been included in the geomechanical model.

Figure 4.38: Petrel RSFM horizons

Index	Horizon name	Color	Calculate	Horizon type	Conform to another horizon		Status	Well tops	Input #1
1	Seabed		Yes	Conformable	No	1	Done	Seabed (Tops_Aug14_LA)	Seabed
2	Base_Quat		Yes	Erosional	No	1	Done		Base_Quaternary
3	Chalk_Grp		Yes	Base	No	1	Done	Chalk_Grp (Tops_Aug14_)	Top_Chalk
4	Base_Chalk		Yes	Base	No	1	Done	Base_Chalk_Grp (Tops_A)	Base_Chalk
5	BCU		Yes	Erosional	No	1	Done	BCU (Tops_Aug14_LATE)	BCU
6	Corralian_Lmst		Yes	Base	No	1	Done	Corralian_Lmst (Tops_Aug)	Corralian_Lmst
7	Base_Corr		Yes	Base	No	1	Done	Base_Corrallian_Lmst (Top	Base_Corrallian_Lmst
8	Mid_Jurassic		Yes	Base	No	1	Done	Mid_Jurassic (Tops_Aug1	Mid_Jurassic
9	Lias_Gp		Yes	Base	No	1	Done	Lias_Gp (Tops_Aug14_LA)	Liassic
10	TRIASSIC		Yes	Base	No	1	Done	TRIASSIC (Tops_Aug14_)	Triassic
11	Haisboroug		Yes	Base	No	1	Done	Haisborough_Gp (Tops_A)	Haisborough_Gp
12	Top_Keup		Yes	Base	No	1	Done	Top_Keuper_Anhydrite_M	Top_Keuper_Anhydrite_Mbr
13	Base_Keu		Yes	Base	No	1	Done	Base_Keuper_Anhydrite_	Base_Keuper_Anhydrite_Mbr
14	DUDGEON		Yes	Base	No	1	Done	DUDGEON_FM (Tops_Au	Dudgeon_Fm
15	DOWSING		Yes	Base	No	1	Done	DOWSING_FM (Tops_Au	Dowsing_Fm
16	Top_Musc		Yes	Base	No	1	Done	Top_Muschelkalk_Halite_	Top_Muschelkalk_Halite_Mbr
17	Base_Mus		Yes	Base	No	1	Done	Base_Muschelkalk_Halite	Base_Muschelkalk_Halite_Mbr
18	Rot_Halite		Yes	Base	No	1	Done	Rot_Halite_3 (Tops_Aug1	Rot_Halite_3
19	Rot_Halite		Yes	Base	No	1	Done	Rot_Halite_2 (Tops_Aug1	Rot_Halite_2
20	Rot_Halite		Yes	Base	No	1	Done	Rot_Halite_1 (Tops_Aug1	Rot_Halite_1
21	Rot_Clay_		Yes	Base	No	1	Done	Rot_Clay_Mbr (Tops_Aug	Rot_Clay_Mbr
22	BUNTER_		Yes	Erosional	No	1	Done	BUNTER_L3b (Tops_Aug	Buntetr_L3
23	BUNTER_		Yes	Base	No	1	Done	BUNTER_SHALE_FM (To	Buntetr_Shale_Fm_corr_4328a3
24	PERMIAN		Yes	Base	No	1	Done	PERMIAN (Tops_Aug14_L	Permian
25	Rotliegene		Yes	Base	No	1	Done	Rotliegenes (Tops_Aug14	Rotliegend

The RSFM has lateral cells dimensions of 100mx100m within the 44 x 47 km AOI and is rotated by -25° to be parallel to the Endurance structural grain. No layering was applied so each zone is in effect one layer thick. The RSFM is designed to include 16 surrounding Bunter Sandstone well penetrations (Figure 4.39). A cross section through the RSFM is given in Figure 4.1.

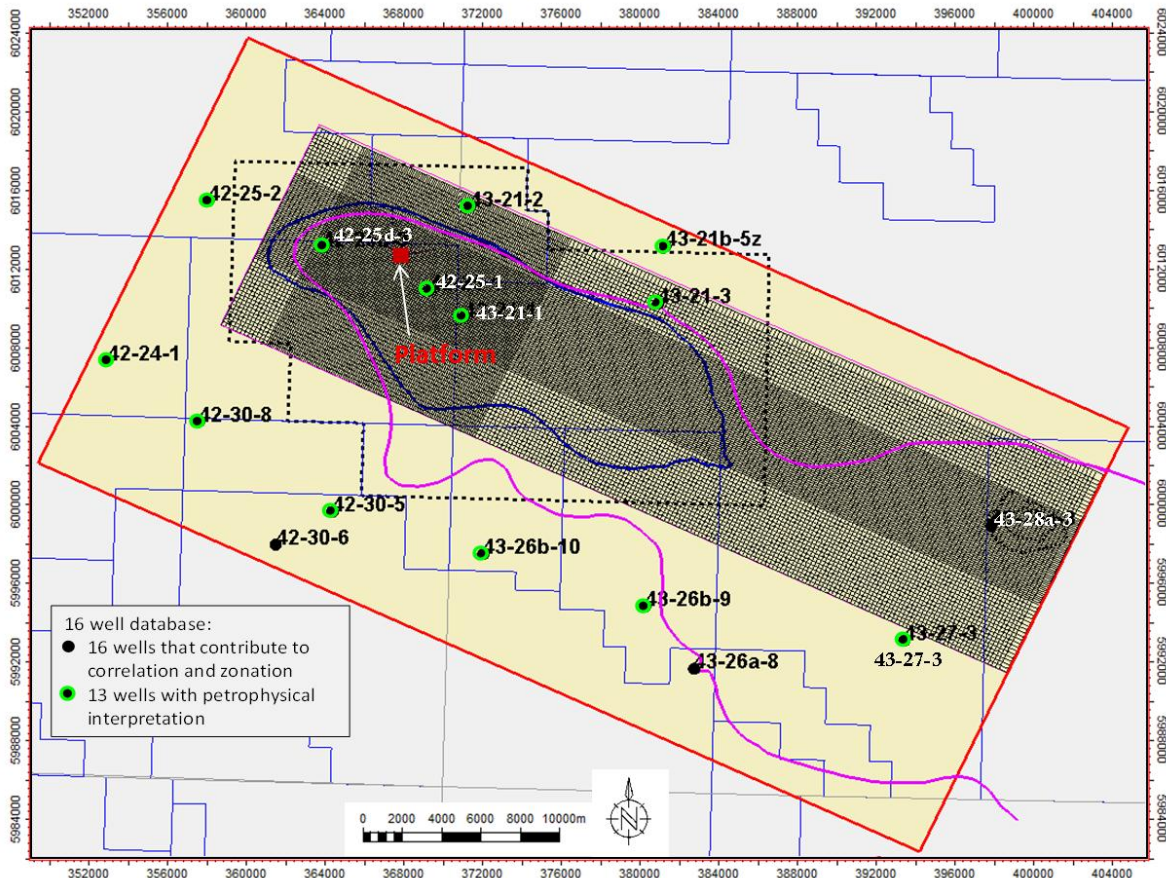
Figure 4.39: Top Bunter depth structure with the RSFM AOI



Note the full RSFM spans an area of 42 x 47 km.

Out of a total of 16 wells in the AOI (Figure 4.40), 13 were subjected to petrophysical analysis for rock properties; the remaining three have incomplete data sets and have been used for correlation only. Additionally, the AOI includes the Bunter Sandstone seabed outcrop that overlies a Zechstein salt diapir 14 km southwest of the Endurance structure.

Figure 4.40: Well database



4.7 Primary and Secondary Seals

Above the Bunter Sandstone lies a thick sequence of shales and evaporites belonging to the Haisborough Group which constitutes the main regional sealing unit (Figure 4.41 and Figure 4.42). The overburden formations have consistent lithologies and only subtle thickness variations. In 43/21-1 a Muschelkalk thinning is attributed to a fault that is visible on the seismic.

Figure 4.41: Triassic lithostratigraphy (after SNS Atlas)

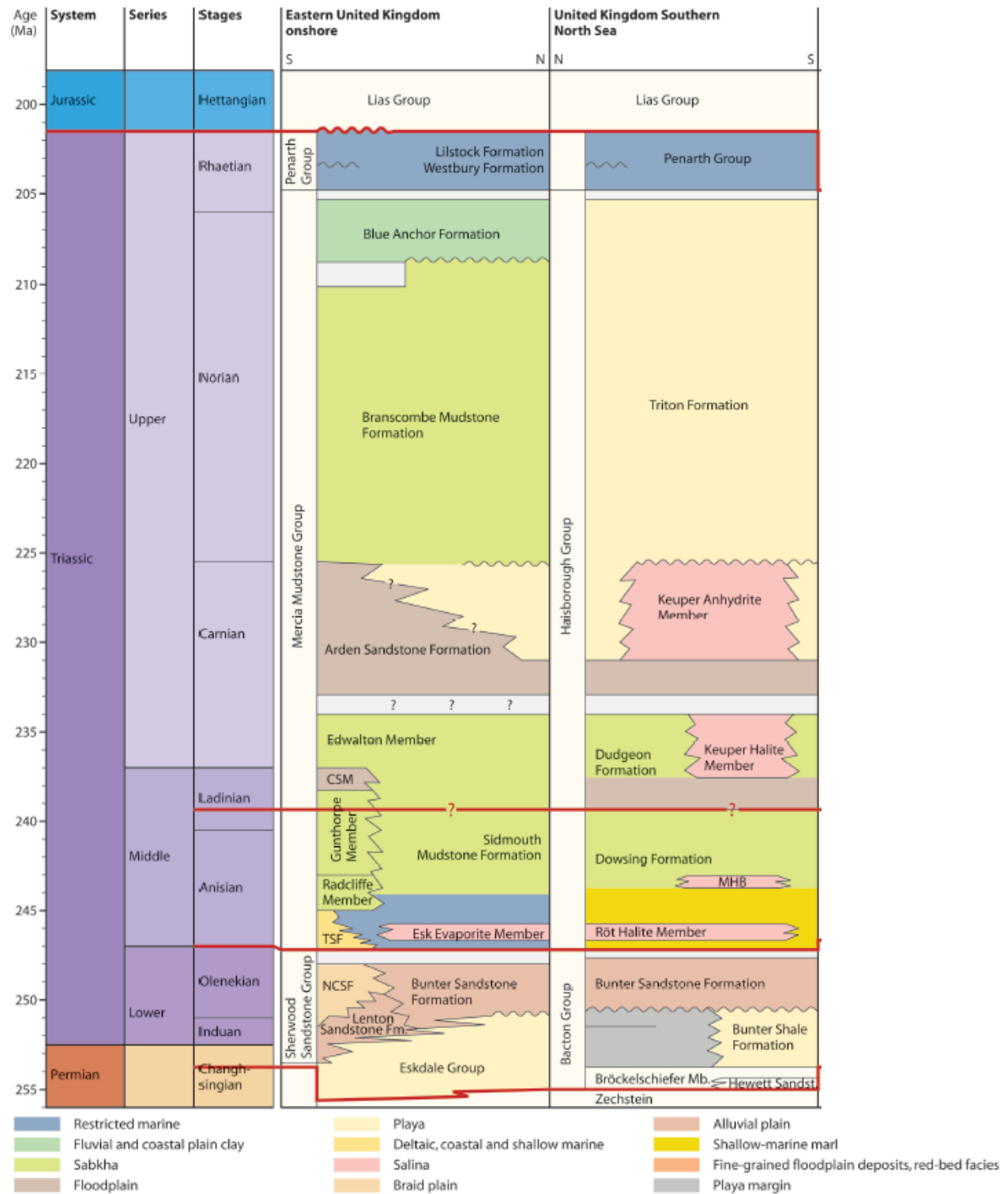
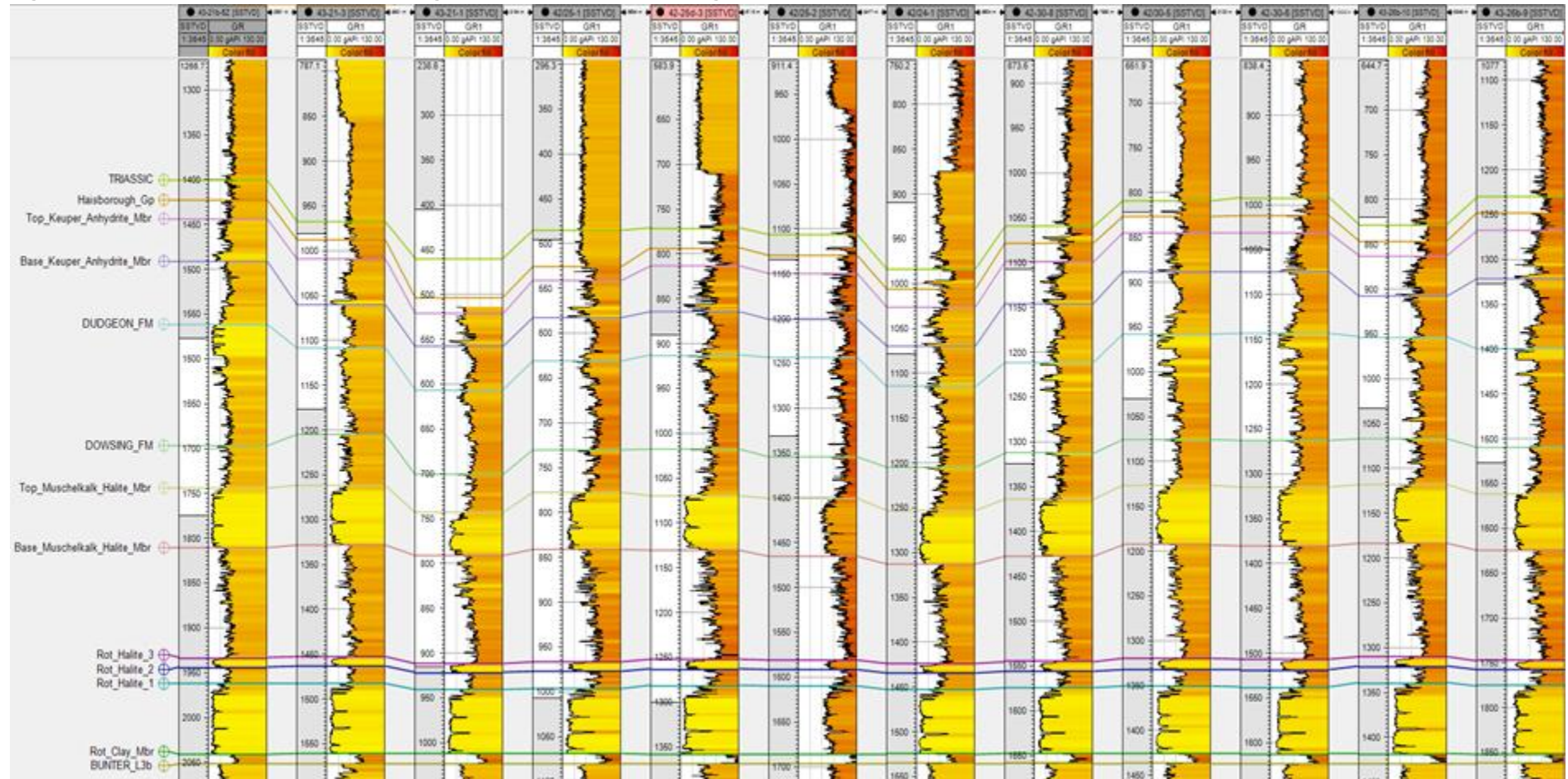


Figure 4.42: Overburden correlation in the regional wells. Note the thinning of Muschelkalk in 43/21-1 due to a fault



At the base of the Haisborough Group and directly overlying the Bunter sands lies the Röt Clay Member approximately 10m thick (as an average) over the Endurance structure. This constitutes the cap rock as well as the primary seal and it is immediately overlain by the Röt Halite Member with interbedded shales and halite layers. The Röt Halite is at the base of an 800m thick sequence of anhydrites and shales comprising, *inter alia*, the Muschelkalk Halite, the Dowsing Shale, the Dudgeon Formation, and the Keuper Anhydrite, that constitute the secondary sealing unit (see Figure 4.3 and Figure 4.6).

Long term (>10,000 years) exposure of the Röt Clay to a CO₂ cap is expected to cause minimal diffusion into the Röt Clay and will not result in any measurable migration outside the Storage Site nor any change in the mechanical properties of the Röt Clay.

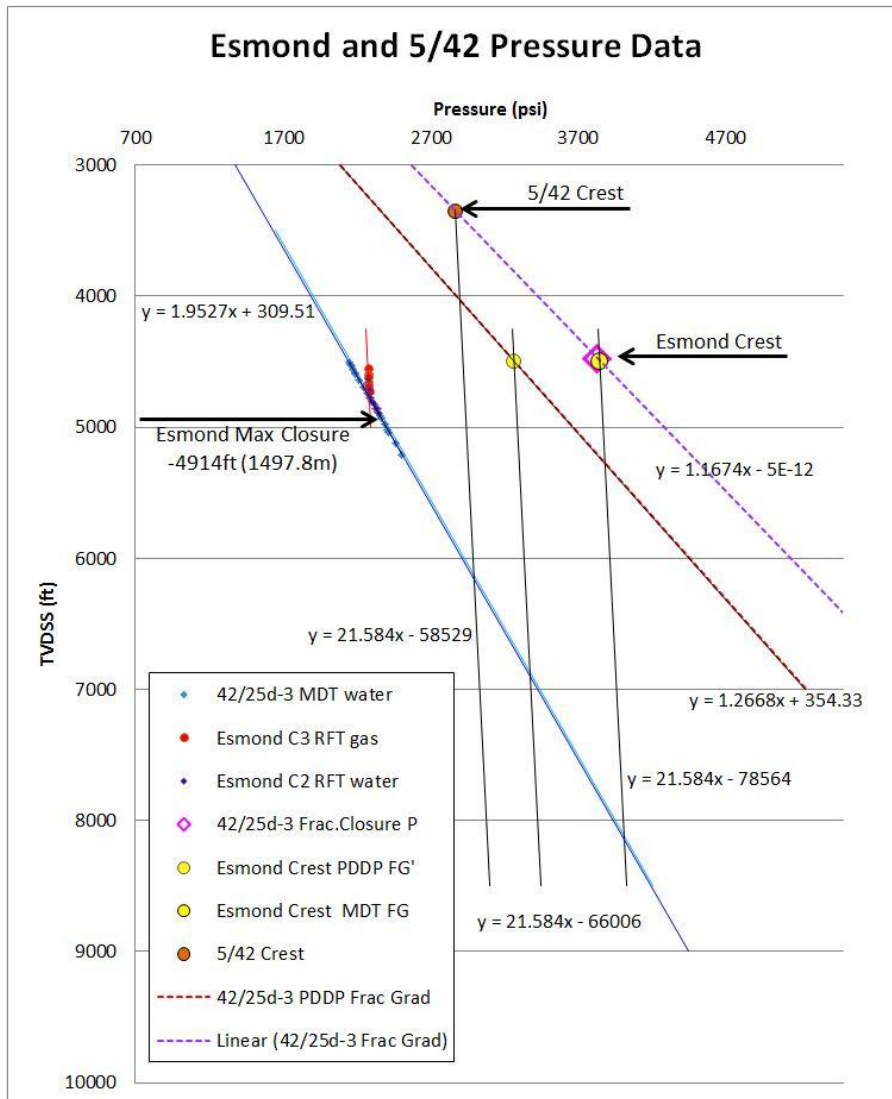
The Röt Clay shale appears to be a competent seal based on all available data: 42/25d-3 mini-frac data, Esmond Field analogue, petrography and geomechanics.

4.7.1 Characterisation

The fracture closure pressure of the Rot Clay – a measure of sealing potential – recorded during a MDT (Modular Formation Dynamic Tester) mini-frac test that was conducted on the appraisal well 42/25d-3 is 264bar (3830 psi) at -1362.8m TVDSS (4471ft TVDSS). This is the best direct evidence that the Röt Clay is geomechanically strong and theoretically capable of trapping a sizeable CO₂ column and also withstanding a significant increase in differential pressure due to CO₂ injection.

Figure 4.43 shows the Endurance structure being capable of supporting a theoretical hydrocarbon gas column in excess of 2500ft (760 m).

Figure 4.43: Esmond and Endurance pressure data



The Esmond Gas Field lies about 45km northeast of Endurance (Figure 4.50). It is a simple 4-way dip anticlinal closed Bunter Sandstone reservoir formed by swelling of underlying Permian salt. The reservoir is around 100m thick and sealed by the Rot Claystone about half the thickness of that seen in Endurance region. The Rot Clay interval actually comprises two shales separated by a thin 7m sandstone which has been labelled the Rot Sandstone (RSS) (Figure 4.51). The lower shale has been labelled Rot Clay 1 (RC1) and is 6m thick (43/13a-C1). The Upper Shale has been labelled Rot Clay 2 (RC2) and is 12m thick. The crest of the reservoir is about 350m deeper than Endurance at -1369 m. The initial GWC lay at -1453.8 m, yielding an initial gas column of 85 m. Estimated GIIP was 325 bcf, of which 313 bcf is has been recovered at a recovery factor of 93% (Encore 2009). Eight crestal producers were drilled with production commencing in 1985 and finishing in 1995 when the field was abandoned. An appraisal drilled into the Esmond reservoir 13 years after production had ceased found that the Bunter sandstone had recovered from an abandonment pressure of 10.3bar (150 psia) in 1995 to 120.7bar (1750 psia) in 2008,

indicating the presence of an active connected aquifer (initial pressure was 157.2bar i.e. 2280 psi). More importantly, formation pressure data shows differential pressures across the Rot Clay interval with the Rot Sandstone having maintained its abandonment pressure of 10.3bar, suggesting that the thin Rot Sandstone is clearly isolated from the main Bunter Sandstone Reservoir and that the thin 6m of Rot Clay 1 is acting as a seal in its own right, holding back a differential pressure of 110bar (1600 psi) between Rot Sandstone and Bunter Sandstone. This provides a useful analogue for the Endurance structure where the Röt Clay is approximately twice as thick and it will be required to withstand a pressure increase of no more than 40bar due to CO₂ injection from the First Load (White Rose).

The gamma ray (GR) logs in the Esmond Field and Endurance wells suggest similar shale character and sealing capability for the Röt Clay (Figure 4.51). Spectral GR does show some subtle differences in clay mineralogy between the two structures. The Endurance area show a higher Rot Clay GR region to the south, around well 42/30-5, which suggests a higher shale content and similar if not better sealing potential than Esmond.

Also, the sonic log data from Esmond ties in with an increasing westerly transit time trend observed in the Endurance area which suggests a greater degree of burial and compaction thus a greater sealing capability of the Röt Clay at Endurance compared to Esmond.

Figure 4.44: Block boundary and wells map illustrating the location of the Esmond Gas Field relative to the Endurance structure.

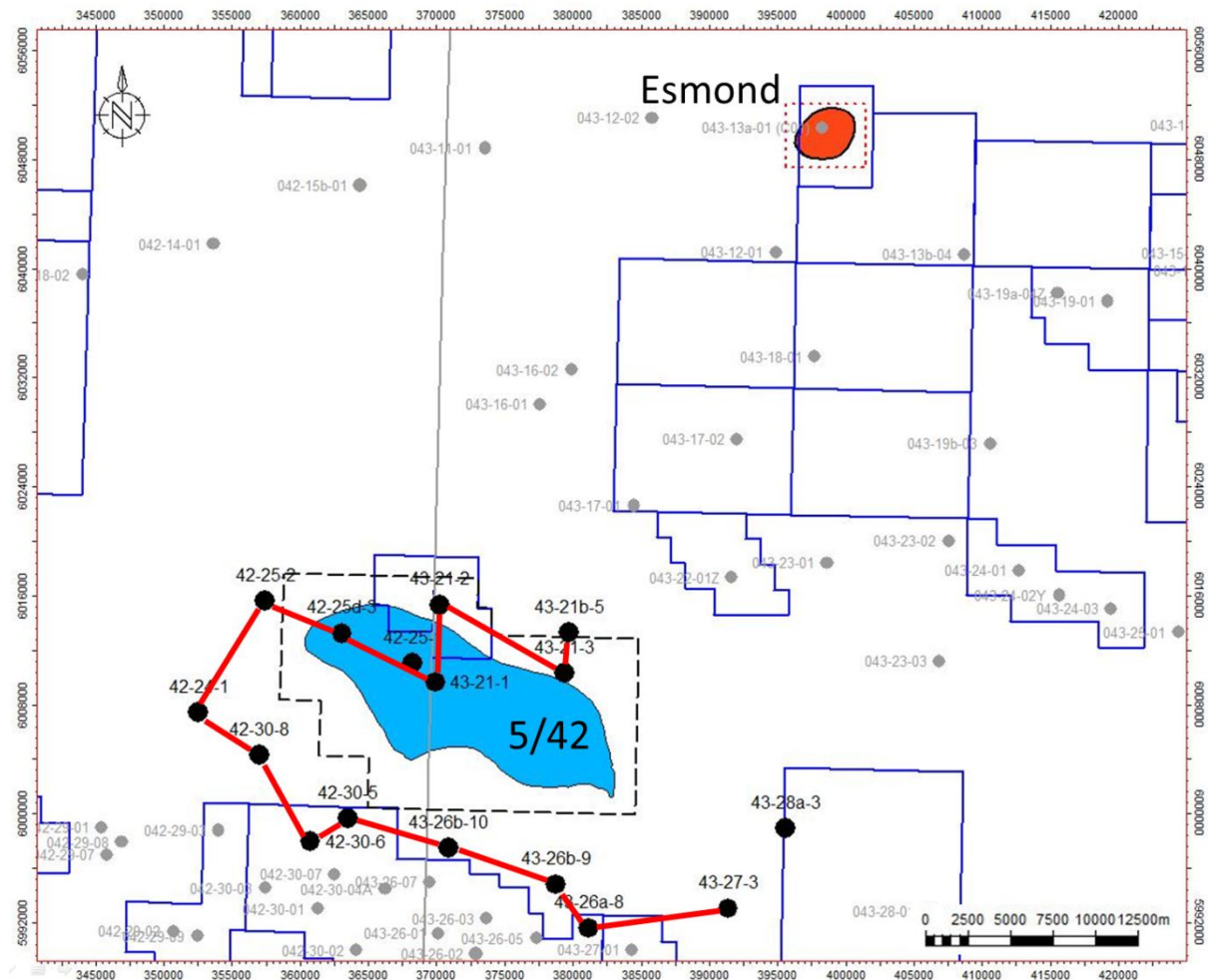
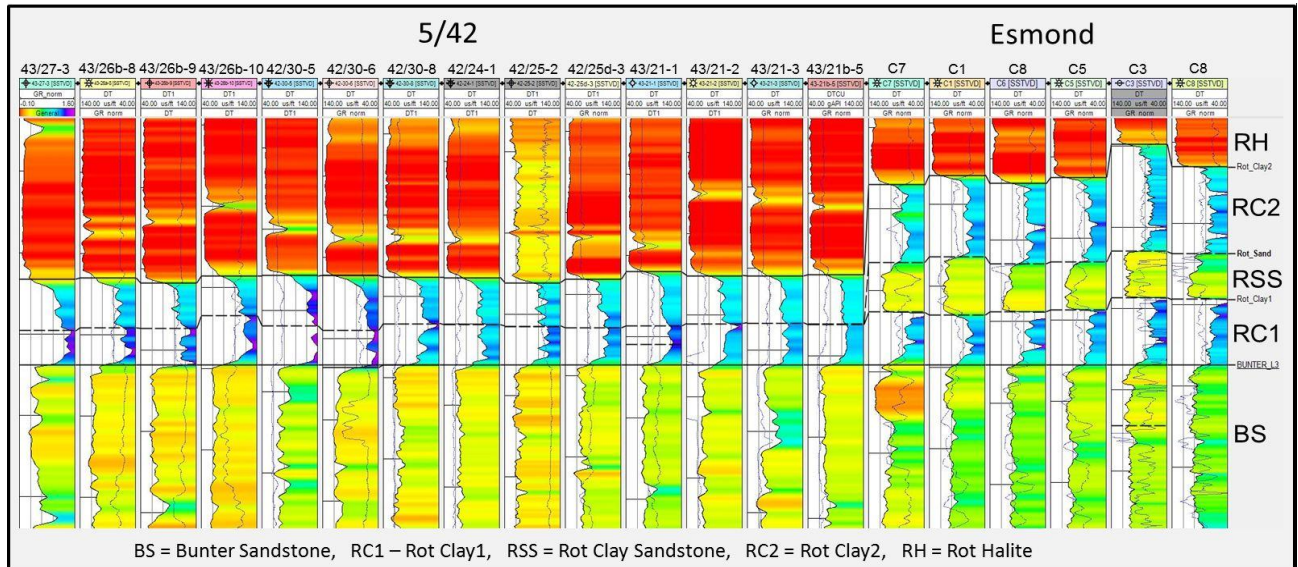


Figure 4.45: Normalised GR correlation of wells from the Endurance and Esmond areas over the Röt Claystone



4.7.2 Core & Cuttings Analysis

The sedimentological and petrographic work undertaken by Blackburn and Robertson (2014) on the 42/25d-3 cores concluded that the Röt Clay and the succeeding Röt Halite have been deposited in a playa lake environment.

The red mudstones of the Röt Clay were interpreted as a transgressive horizon at the base of the playa lake. A significant amount of dolomite cement (up to 27%) intimately mixed with the clays was also reported in the three Röt Clay samples analysed. Other components identified are silts and anhydrite that mix with the illite (main clay mineral) in varying proportions depending on the sample.

The evaporitic sequence of the Röt Halite comprises mostly halite with inclusions and irregular thin laminae of anhydrite. Small proportions of silts, clays and dolomite may also be present although there is uncertainty regarding their presence.

4.8 Reservoir Facies Modelling

In the absence of a meaningful correlation between the primary depositional facies and the reservoir quality (see Section 4.5.2), a set of “electro facies” was defined based on wireline log data alone and was used in the facies modelling. Six electro facies (Figure 4.46) were picked on the gamma-ray, sonic and resistivity logs in 13 wells within the greater Endurance area, including 42/25d-3, and interpreted for trends that could be then used for modelling. The facies are interpreted to relate primarily to post-depositional diagenetic processes that occlude the original porosities.

Figure 4.47 illustrates the porosity distributions for the six facies types. Two of the six facies represent varying degrees of cemented sand (Facies 3 and Facies 4), whilst four are un-cemented facies (Facies 1, Facies 2, Facies 5 and Facies 6). The porosity range, cut off and definitions applied to each facies (Figure

4.47) have been informed by results of 42/25d-3 core sedimentology, petrography and chemostratigraphy. The Heterolithic facies is truncated at 0.17 porosity because 42/25d-3 core sedimentology showed that the bulk of the low porosity facies (<0.17) are playa margin facies.

Petrography provided clarification on the partially cemented facies which comprise both dolomite and anhydrite cements. The dolomitic cements occur in the three Endurance wells 42/25-1, 42/25d-3 and 43/21-1, near the top of the reservoir. Their lateral continuity is uncertain, but they are likely to be patchy as the 42/25d-3 well test indicated (there was no evidence of boundaries in the volume investigated by the test, which was calculated to extend to a radius of 1.2 km.). Chemostratigraphy suggested that halite is more prevalent in cemented wells (42/25-2 and 43/21-3) than in un-cemented wells (42/25d-3 and 43/21-1).

Figure 4.46: GR, electrofacies and porosity in cemented and uncemented wells

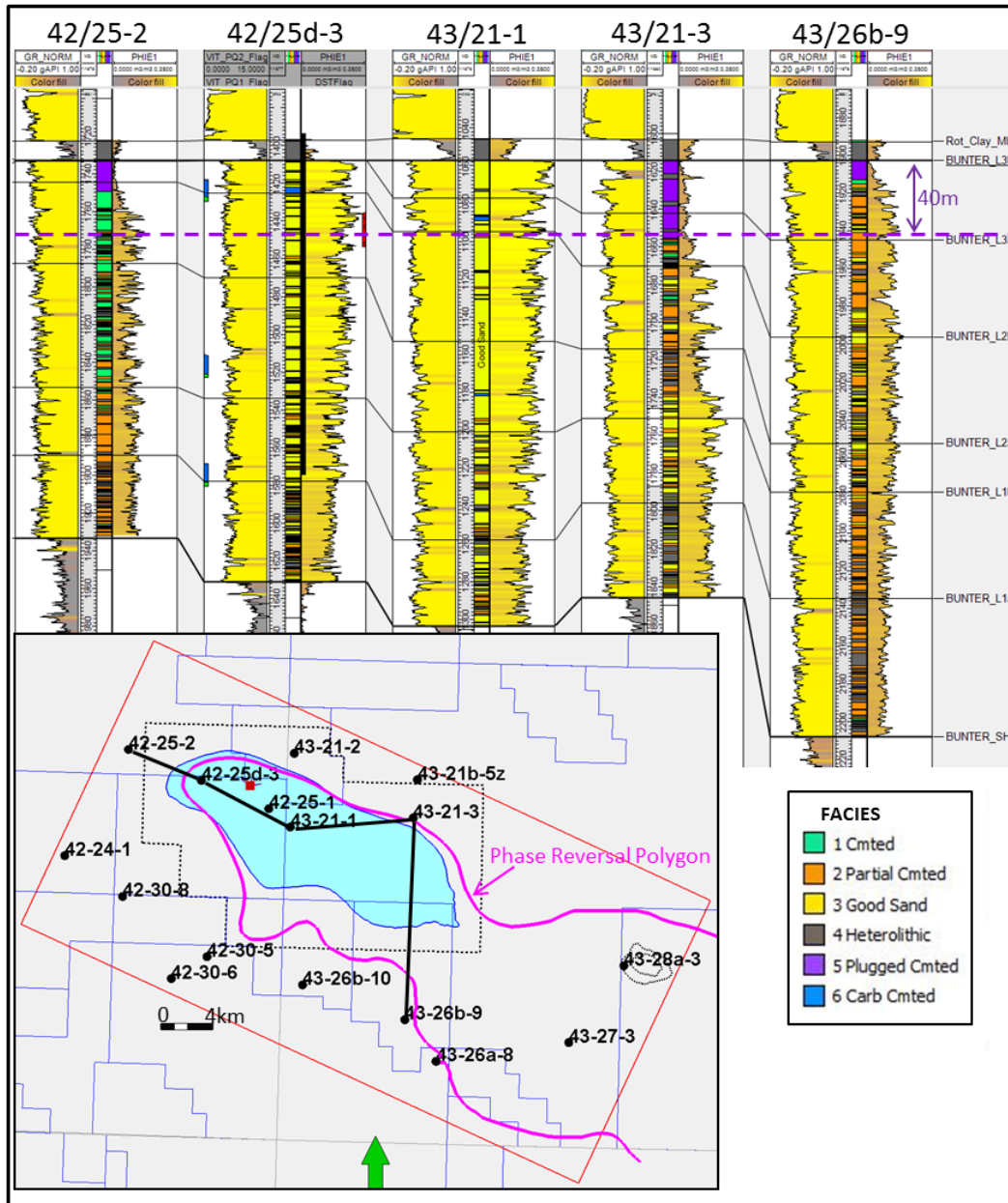
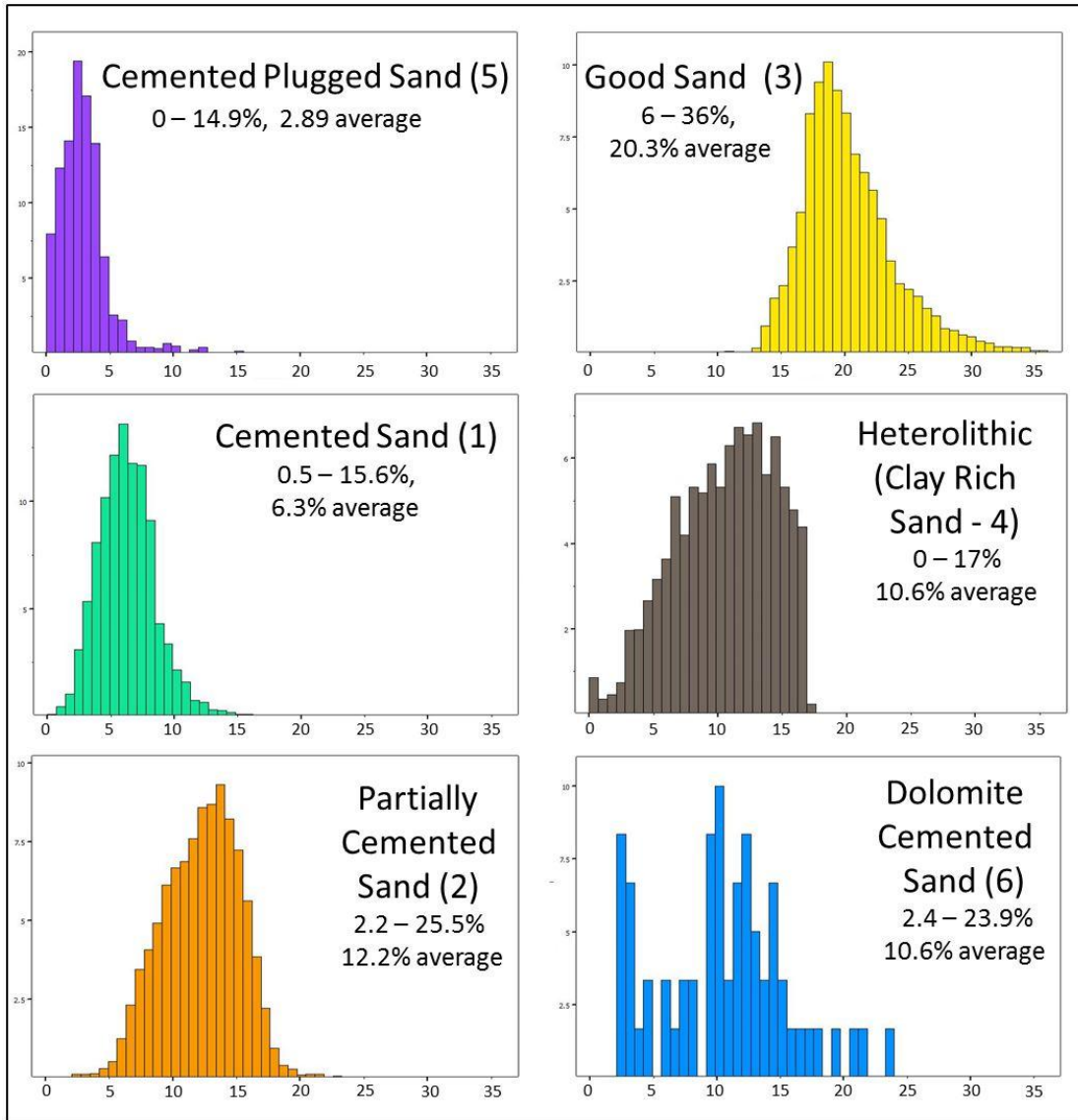


Figure 4.46 shows cemented wells outside the PRP: 42/25-2, 43/21-3 and 43/26b-9; and uncemented wells inside the PRP: 42/25d-3 and 43/21-1.

Figure 4.47: Facies porosity distributions



The electrofacies and the cementation trends described above were captured in the facies modelling. The primary aim in facies modelling was to capture the seismic phase reversal boundary (i.e. the PRP) that appears to control the distribution of cemented facies as discussed above. All other facies trends are secondary to this major trend. The PRP was modelled as a vertical boundary between the cemented and un-cemented sands. Various sensitivities cover the PRP geometry and the amount and lateral distribution of cemented sands within the Endurance structure (Figure 4.48). Facies modelling follows four steps:

1. Creation of a Hardground Region Parameter: Five hardground parameters were created in order to capture, as illustrated in Figure 4.48, the phase reversal boundary uncertainty which are then used in step 2 to distribute the facies types. These hardground parameters are:
 - Vertical Hard Region (VHM): created with the seismic phase reversal polygon defining a “cookie cutter” style region of un-cemented rock surrounded by cemented rock (Figure 4.48A).

- Diffuse Vertical Hardground Region (DVHM): similar to the Vertical Hardground Model except that it has a fuzzy margin (Figure 4.48B). This model acknowledges the fact that Good Sands do exit outside the phase reversal polygon in small proportions that get smaller away from the polygon.
 - Patchy Hardground Model 1: distributes patches of cemented sand within the phase reversal polygon with a trend probability parameter that shows the 25% probability of cemented sand with the phase reversal polygon (Figure 4.48C).
 - Patchy Hardground Model 2: is similar to the PHM1 except the probability parameter used to distribute patches of cemented sand was increased to 50% within the phase reversal polygon (Figure 4.48D).
 - Easterly Trending Hardground Model (ETHM): distributes progressively higher proportions of cemented sand toward the east of the AOI (Figure 4.48E).
2. Distribution of sand facies types within the cemented/un-cemented areas of the Hardground Region. Five individual facies trends were included in this step, namely: (a) Gross facies trends related to the seismic phase reversal boundary (b) Plugged Cemented Trend (c) Cemented Sand Trend (d) Dolomite Cemented Sand Trend (e) Heterolithic Trend.
 3. Distribution of Heterolithic Facies which are independent of the Hardground Region: Heterolithics are distributed using Truncated Gaussian Distribution (see the cross section in Figure 4.49B for an illustration).
 4. Final Facies Model - Combination of the sand facies model created in step 2 and the Heterolithic model created in step 3. Heterolithic facies were allowed to overwrite sandstone "facies". Figure 4.49C provides an illustration of the combined final facies model.

Figure 4.48: Hardground Facies Models

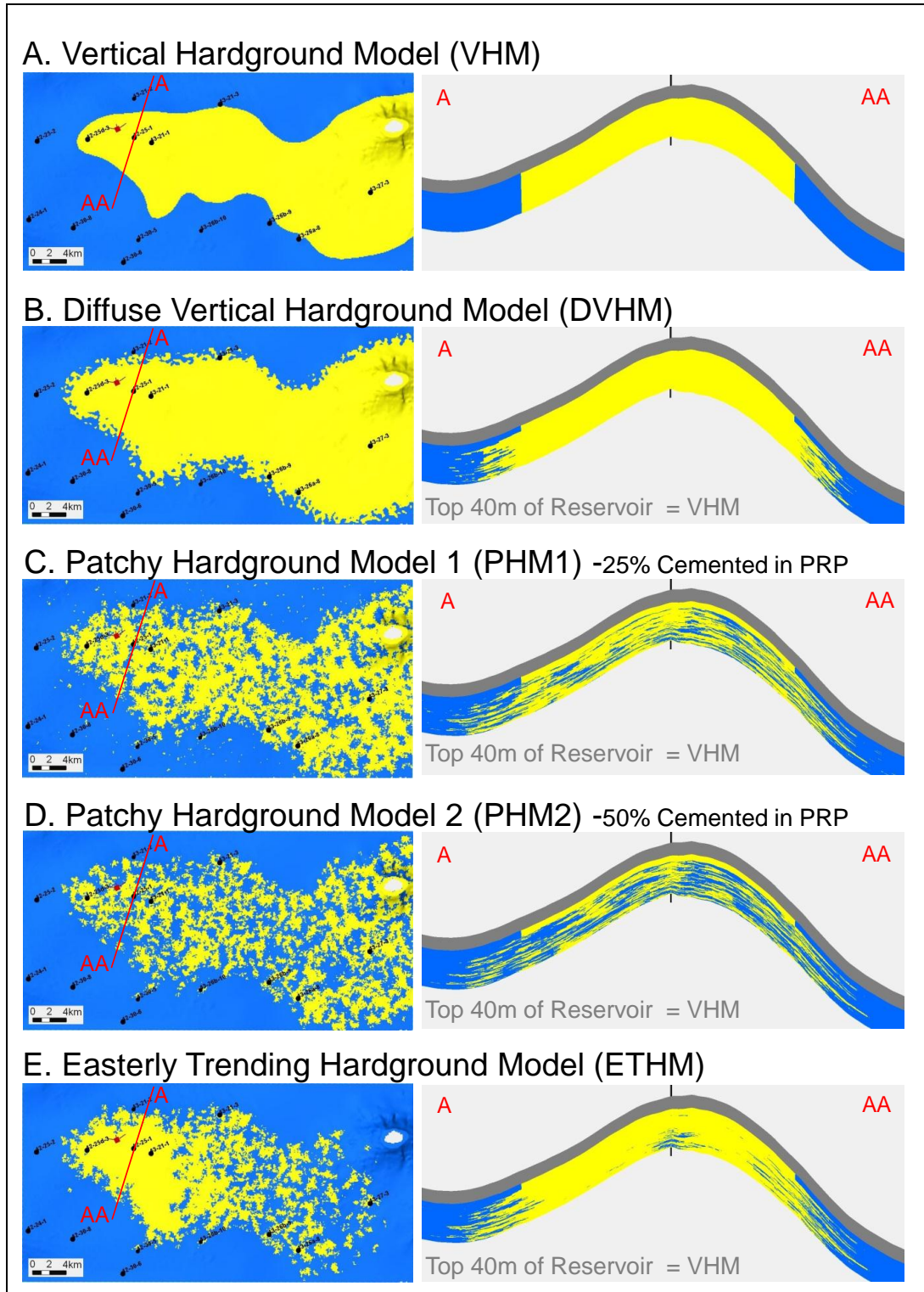
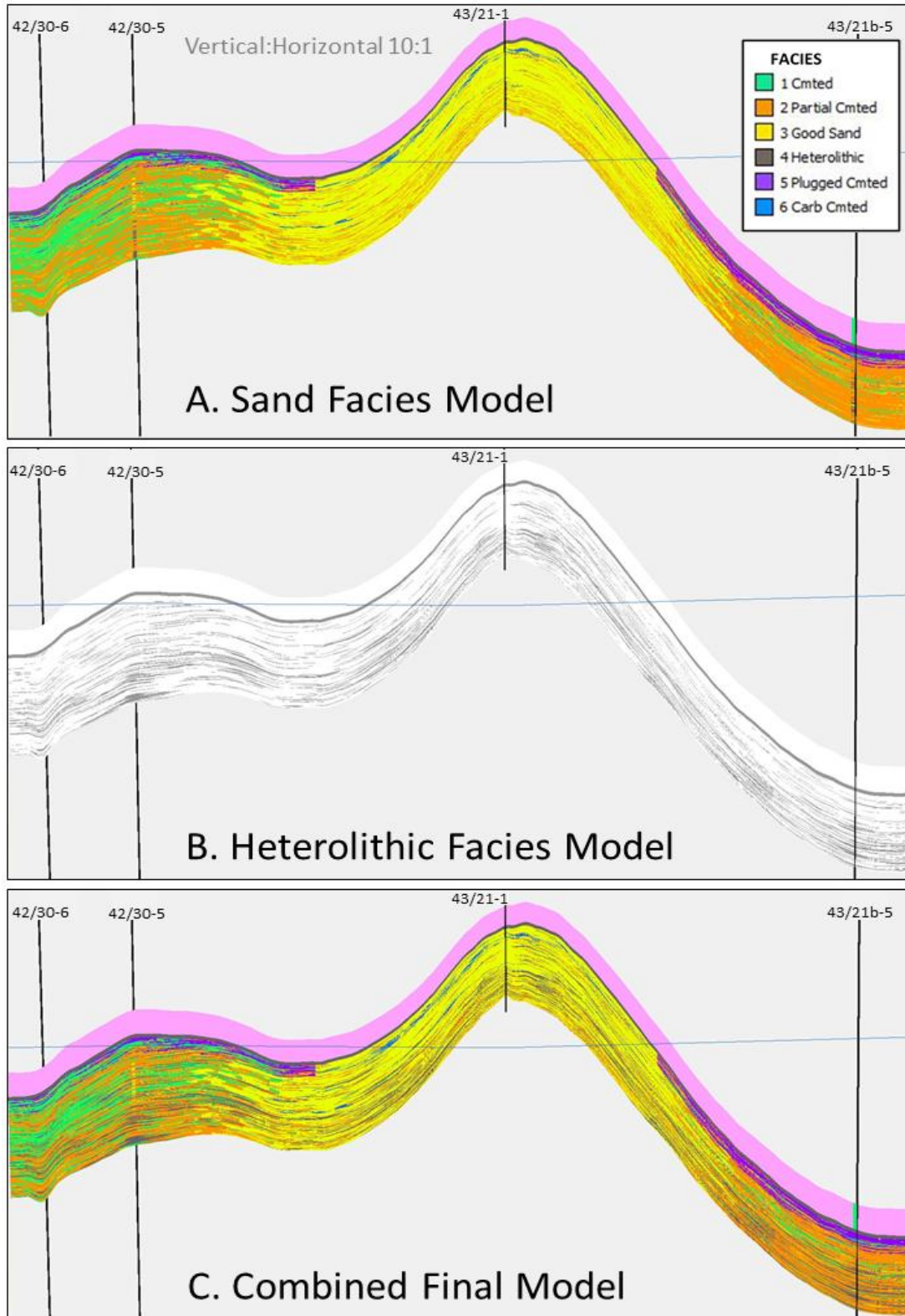


Figure 4.49: Southwest to northeast cross section across the Endurance model illustrating the sand “facies” model (A), the heterolithic model (B) and the combined facies model (C).



4.9 Reservoir Properties

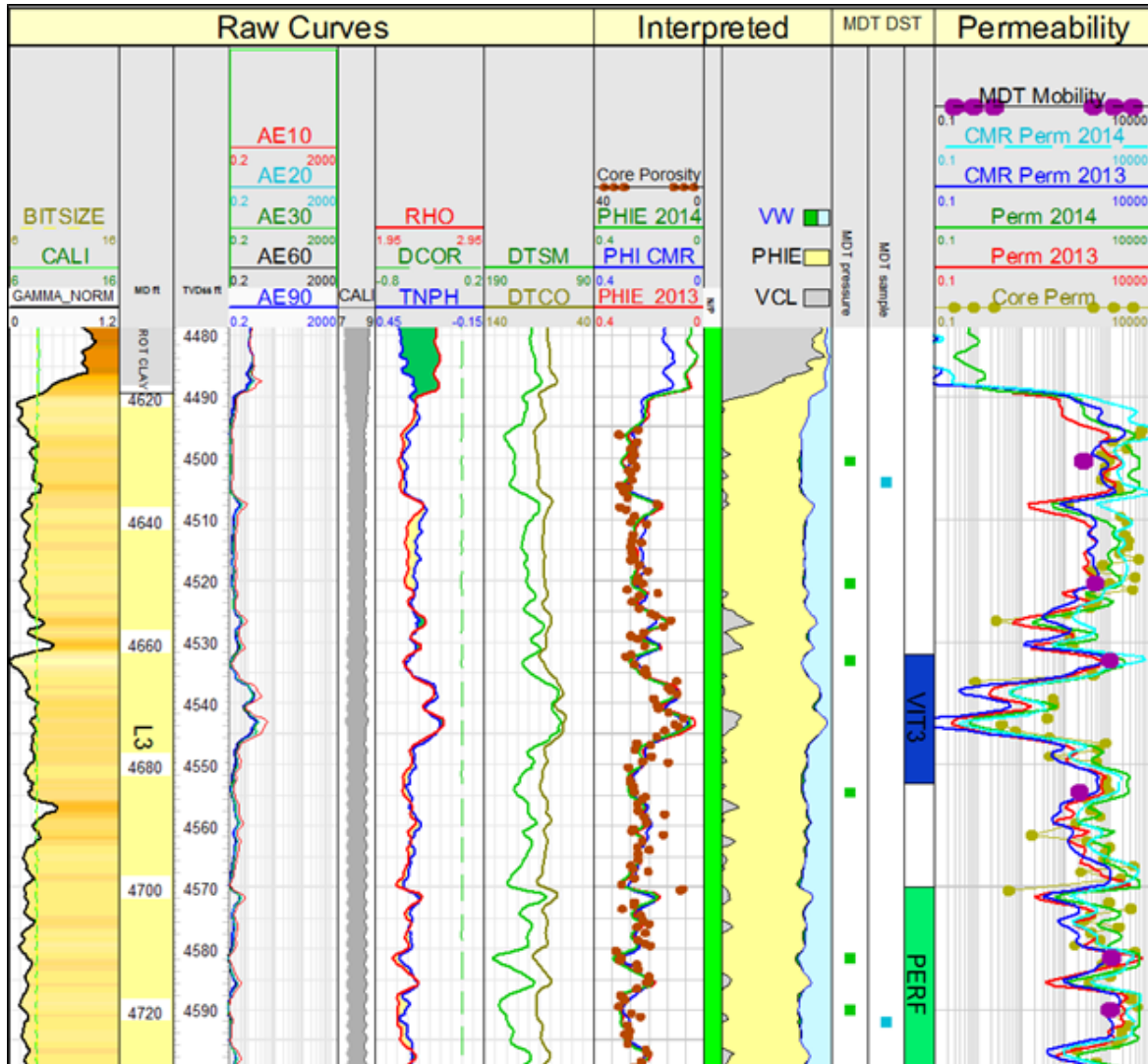
Reservoir porosity and permeability were determined using a combination of logs from 13 wells and core analysis data from two wells (42/25-1 and 42/25d-3).

4.9.1 Porosity

The sonic log was the only porosity curve common to all wells and in conjunction with the core data was used to calculate porosity across the structure. Where available, the density log was used to confirm the sonic porosity. The method involved the integration of a set of preliminary matrix and fluid coefficients in the wells with strong core control and a range of available curves (cored wells and wells with density as well as sonic logs). A preliminary porosity was then calculated and compared to a 'resistivity porosity', after which final adjustments to the matrix coefficients were made. Figure 4.50 shows an example of the excellent agreement achieved between core porosity and porosity calculations from the sonic, density and resistivity logs.

Porosity was modelled in the Geological Model stochastically within each of the six facies described above. The variogram ranges are half the ranges used for facies modelling to capture the heterogeneity observed within each facies. Porosity depth trends were applied for facies that showed porosity decreasing with increasing depth.

Figure 4.50: Petrophysical summary of upper part of Bunter sandstone section.

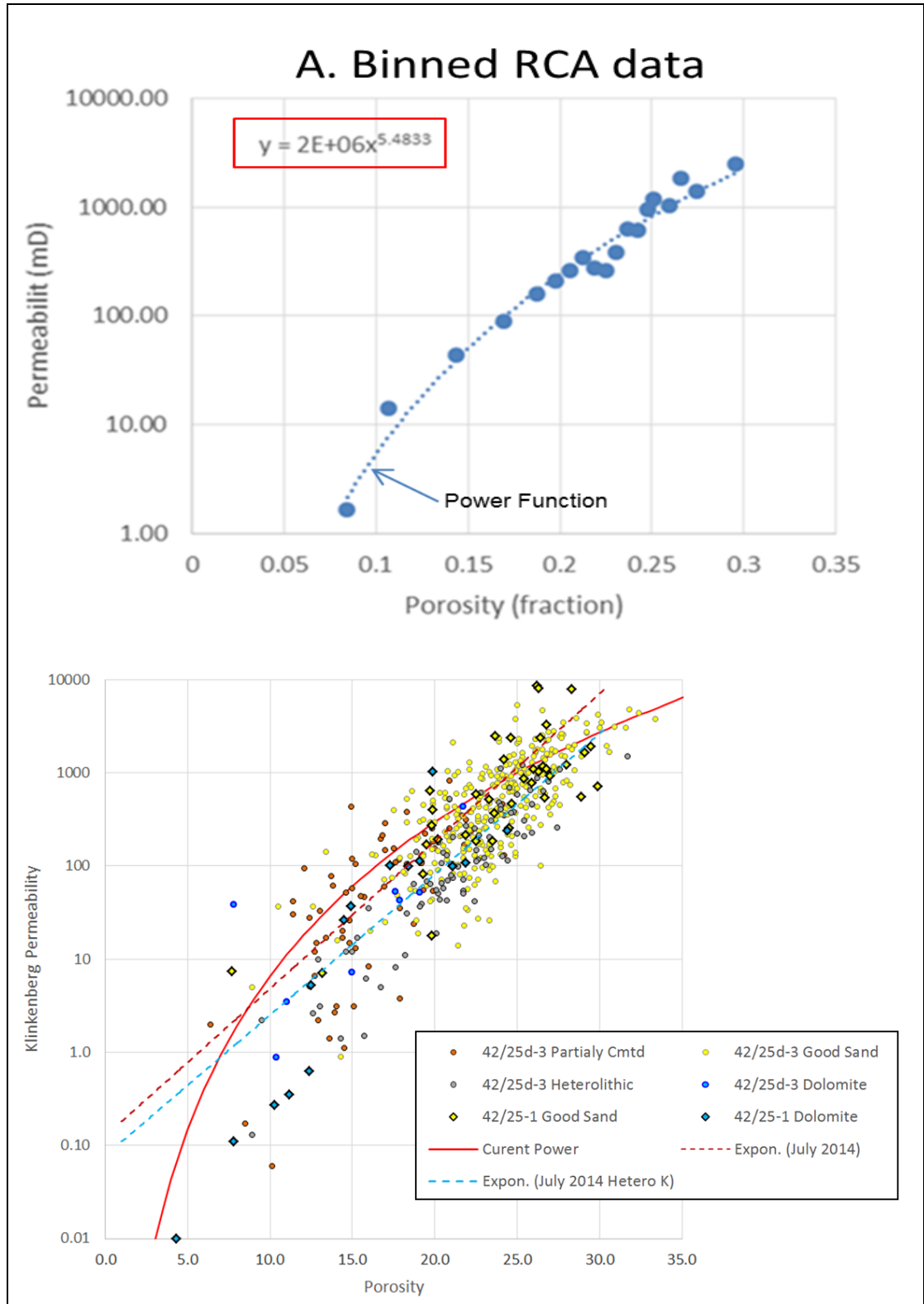


Note: in track 8 comparison of core porosity with calculated porosity curves using density, sonic and resistivity logs.

4.9.2 Permeability

Permeability was based on a permeability prediction algorithm derived from a porosity-permeability cross-plot of core data from wells 42/25-1 and 42/25d-3. Figure 4.51 shows the resulting function fitted to the binned data on a semi-log plot (top plot) and against the raw data cloud (bottom plot). It should be noted that the power function based on the binned data shown in Figure 4.51 has been the one adopted for model development because it gives a reasonable fit at very low values of permeability as compared to a conventional linear or exponential functions.

Figure 4.51: RCA (Routine Core Analysis) permeability vs porosity trend function



4.9.3 Net to Gross

The Net-To-Gross (NTG) cut-off is uncertain in CO₂ storage given the short period of injection compared to hydrocarbon charge. This uncertainty was captured using a range of porosity cut-offs, following established standards in oil and gas exploration using the poro-perm power function shown in Figure 4.51:

- 4.56% - (0.1mD) – equivalent to typical light natural gas threshold;
- 7% - (1mD) – equivalent to a typical light oil threshold; and
- 12% (17.9mD) – defined as being a threshold above which the reservoir volumes are insensitive.

In the NPV uncertainty analysis, 4.56%, 7%, and 12% were treated as low, mid and high cases, respectively. The porosity cut-offs yielded deterministic minimum, maximum and average NTG values of 0.752, 0.993, and 0.927 respectively. The 7% cut-off is viewed as the reference case for deterministic estimates of NPV. The contribution of NTG to the NPV uncertainty range was relatively low (-5.3 to +0.7%).

4.9.4 Temperature

The temperature gradient has been estimated as 3.05°C/100m and equates to a temperature of 55.9°C at a reference depth of 1300m TVDSS.

A number of temperature measurements were made in the 42/25d-3 appraisal well. The reliability of the measurement varies depending on the accuracy of the various tools and the time spent by the tools at the depth of interest during measurement. This latter point relates to the time required for the tool to heat (if moving down the hole) or cool (if moving up the hole) to the local temperature. The sets of measurements at which the tools were given most time at any given depth were those associated with:

- the Modular Dynamic Tester (MDT) measurements of pressure i.e. the MDT long duration test (20 depths);
- Wireline Head Thermometer (WHT) measurements (6 depths, the first two measurements were anomalous and therefore excluded from the final analysis; the anomaly was probably caused because the thermometers were not reset from those used in the previous hole section);
- water sampling (3 depths) – see Section 4.11.2;
- Mini-frac (1 depth in Röt Clay and 1 depth in Lower Bunter sands) – see Section 7.2.5; and
- the Vertical Interference Tests (VIT) (3 depths) – see Section 8.1.2.2.

Measurements associated with the highest tool running speeds include:

- Logging Head Thermometer measurements – made after a short circulation time and could therefore have been affected by frictional heat generated during drilling as well as the relatively low volume of drilling fluid used which had insufficient time to cool at the surface; and
- Quartz gauge measurements – MDT short duration points (20 depths).

The MDT long duration temperature measurements are considered most representative of the geothermal gradient and a plot of the data is shown in Figure 4.52.

Re-arranging the Equation shown on this figure gives:

Equation 4.1 $T_c = 0.0305D + 16.29,$

where T_c is the temperature (C), D is the True Vertical Depth Sub-Sea (TVDSS m) from which the datum pressure above was estimated.

4.9.5 Pressure

The MDT pressure data are shown in Figure 4.53 in which the gradient of the line is displayed along with that obtained from the Repeat Formation Tool (RFT) run in the 42/25-1 crestal appraisal well run in 1990. For a reference depth of 1300m TVDSS on Figure 4.52, the pressure was determined to be 140.0 ± 0.4 bar.

Figure 4.52: Temperature Gradient Measured in 42/25d-3

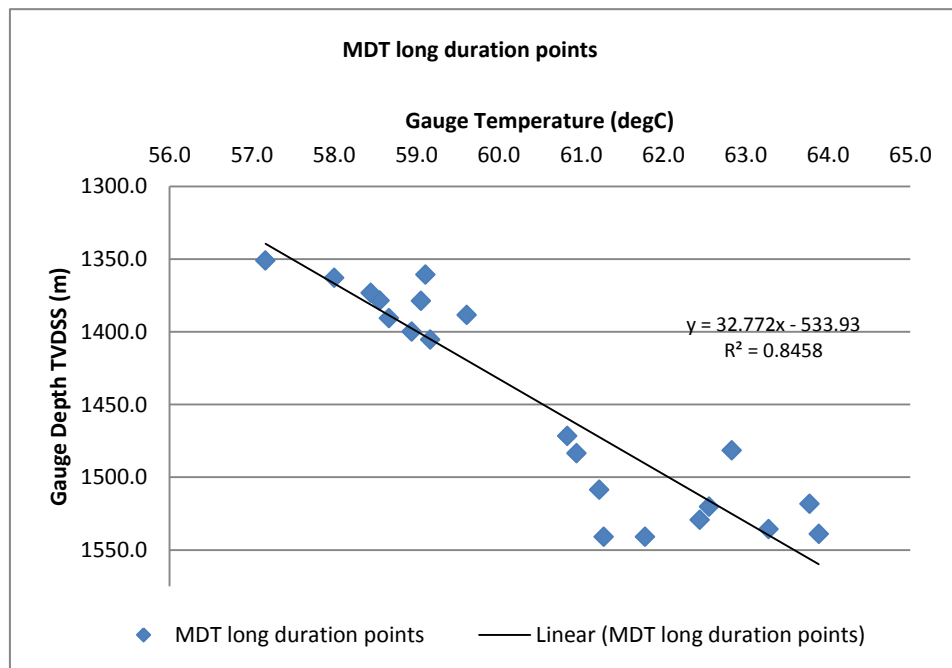
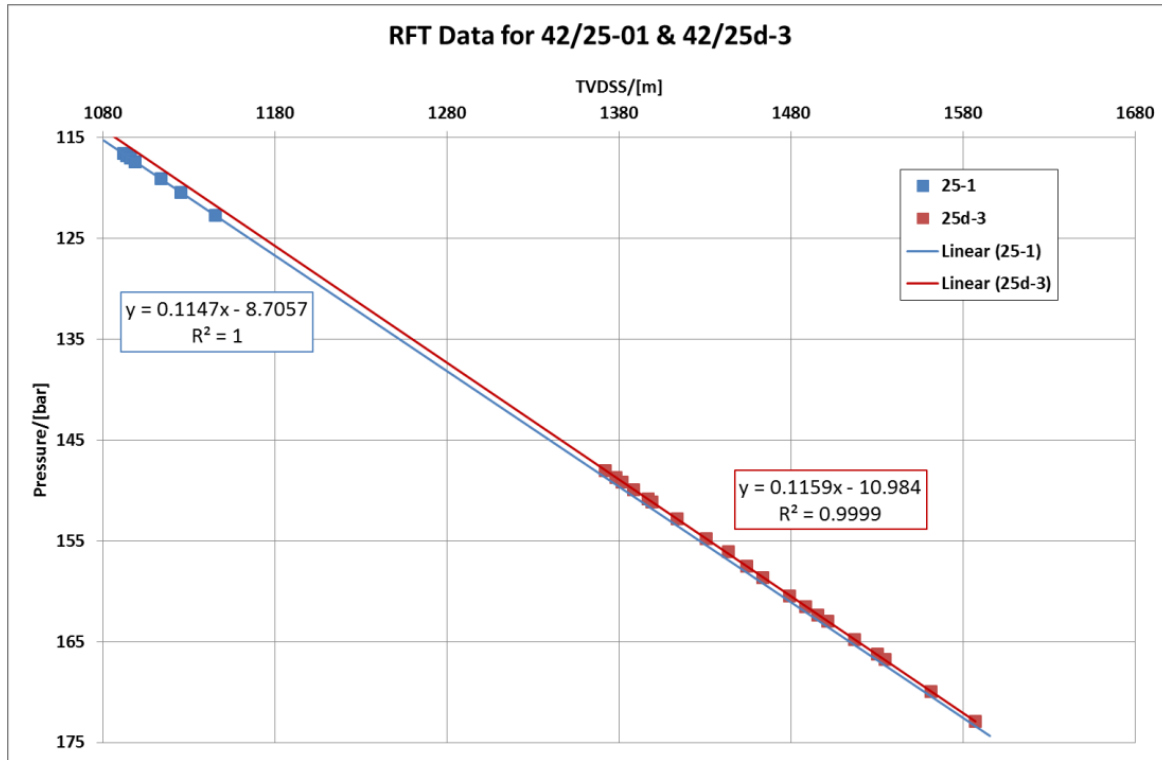


Figure 4.53: RFT Pressure Data from 42/25-1 and MDT Pressure Data from 42/25d-3



The decrease in reservoir pressure seen between the two fitted trendlines is about 0.8bar at 1300m TVDSS. There is a suggestion that this drop in pressure is due to expansion of the Greater BSF to fill the void created by gas production from some of the Bunter hydrocarbon gas fields, in particular the Esmond field some 50 km to the north of Endurance. This important observation suggests that Endurance is connected to an aquifer volume around 100 times larger than itself and thus indicating the availability of a large pressure “sponge” during CO₂ injection.

4.10 Volumetric Ranges and Uncertainties

4.10.1 Net Pore Volume Range

The deterministic NPV analysis has been based on the seven facies models and three NTG models as illustrated in Table 4.4. The NPV ranges from 3.6 to 5.1 Bm³, with an average of 4.5 Bm³. The DVHM model with a mid-case porosity cut-off of 7%, which yielded NPV of 4.6 Bm³, is regarded as the most likely case as it distributes predominantly un-cemented rock throughout the model within the PRP (Figure 4.46) – the 4 wells within the PRP (42/25d-3, 42/25-1, 43/21-1 and 3/37-3) having largely un-cemented Bunter intervals. The structural uncertainty has been assessed via Petrel uncertainty workflows that calculate the spill point for each of the 500 maps generated as already discussed in Section 4.4.1.1. The current model spill is -1460m with a range of -1416m to -1553m resulting from the uncertainty workflow.

Given that the area within the PRP in Figure 4.46 is very large and only penetrated by 4 wells, most of the modelling has focussed on downside scenarios where poorer quality cemented sands could be present

away from the wells. The PHM2 model that yields a NPV of 3.6 Bm³ with a low case porosity cut-off (12%) is therefore regarded as an extreme low case.

Table 4.4: Deterministic model volumetrics and average properties

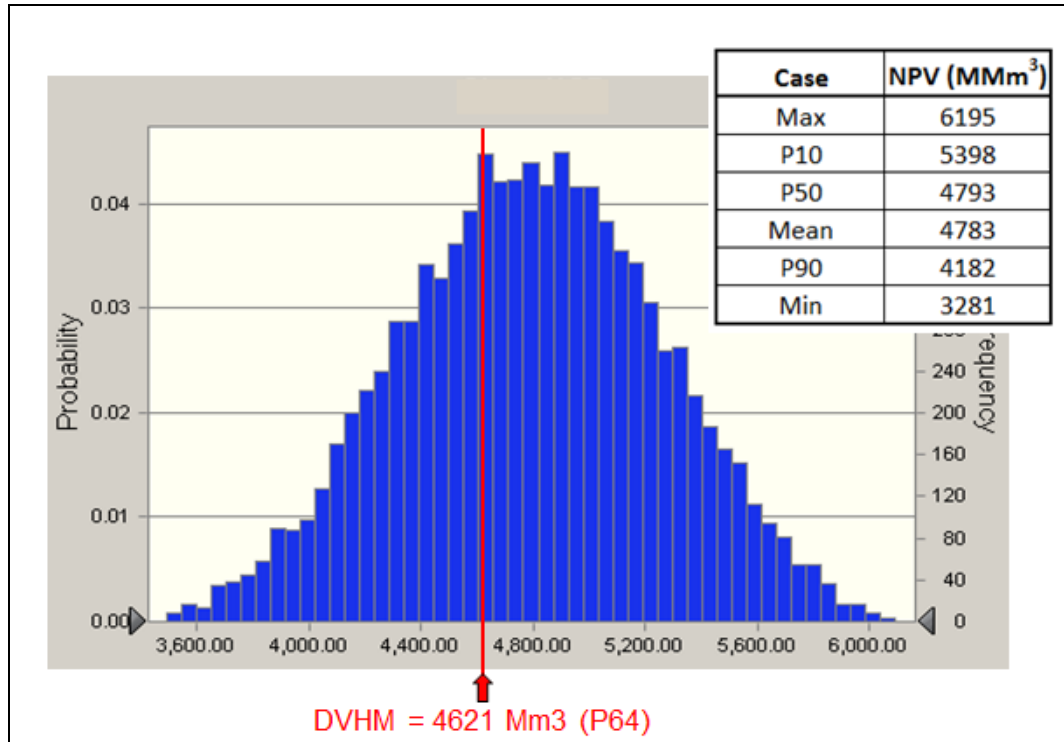
Model	Cut Off %	GRV Bm ³	NRV Bm ³	NPV Bm ³	N:G	Por
DVHM_up	4.7	24.6	24.4	5.097	0.993	0.209
DVHM_up	7.0	24.6	24.2	5.087	0.987	0.210
DVHM_up	12.0	24.6	23.4	4.999	0.951	0.214
VHM	4.7	24.6	24.2	4.629	0.987	0.191
VHM	7.0	24.6	23.7	4.596	0.964	0.194
VHM	12.0	24.6	21.2	4.347	0.863	0.205
DVHM	4.7	24.6	24.2	4.654	0.986	0.192
DVHM**	7.0	24.6	23.7	4.621	0.964	0.195
DVHM	12.0	24.6	21.3	4.384	0.866	0.206
ETHM	4.7	24.6	24.1	4.583	0.981	0.190
ETHM	7.0	24.6	23.2	4.517	0.974	0.194
ETHM	12.0	24.6	20.7	4.267	0.842	0.206
PHM1	4.7	24.6	24.0	4.380	0.976	0.183
PHM1	7.0	24.6	23.1	4.326	0.940	0.187
PHM1	12.0	24.6	19.9	4.011	0.810	0.202
PHM2	4.7	24.6	23.7	4.098	0.964	0.173
PHM2	7.0	24.6	22.5	4.026	0.915	0.179
PHM2	12.0	24.6	18.5	3.636	0.752	0.197
Minimum			18.5	3.636	0.752	0.173
Maximum			24.4	5.097	0.993	0.214
Average			22.8	4.459	0.927	0.196

**Most likely case.

The NPV uncertainty range was established by Monte Carlo simulation using representative distributions of GRV, NTG and porosity. To create the GRV range, a combination of structure, spill level and gross Bunter isochore were varied. The most likely NTG value was taken from the deterministic base case (with 7% NTG cut off) and minimum and maximum values from the extreme values of the deterministic range.

NPV ranged from a minimum of 3.281 Bm³ to a maximum of 6.195 Bm³ with a P50 case of 4.793 Bm³ (Figure 4.54). The most likely deterministic case (DVHM with a 7% porosity NTG cut off) has an NPV of 4.621 Bm³ and represents a P64 case on the distribution range.

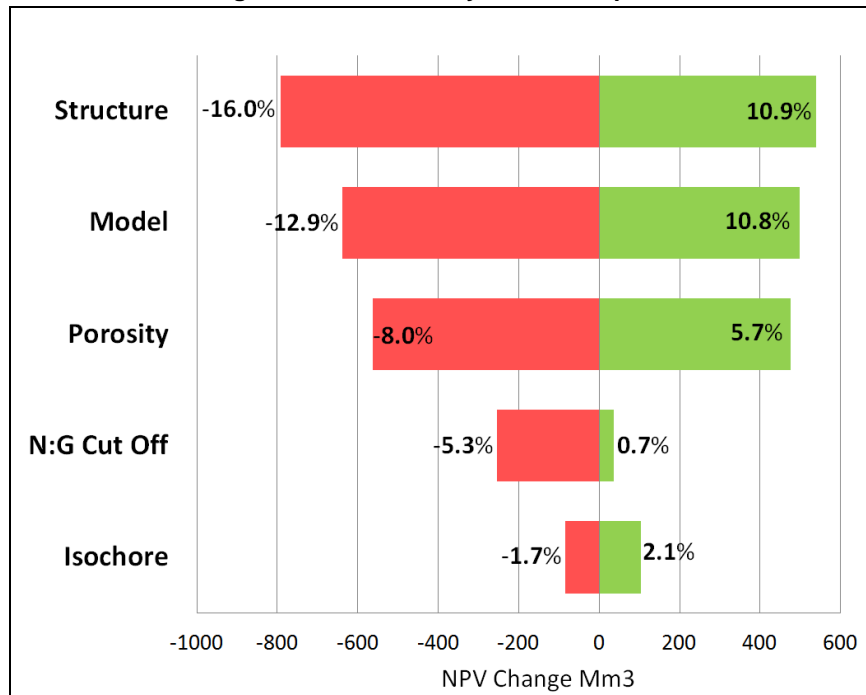
Figure 4.54: Stochastic distribution of Endurance NPV (DVHM denotes the most likely deterministic case)



4.10.2 Net Pore Volumetric Uncertainty

Figure 4.55 shows a tornado plot illustrating the net pore volume uncertainty. The reference value is based on a GRV of 26.307 Bm³ (mid case result of the structural uncertainty workflow) combined with the reference values for facies, porosity, NTG and the gross Bunter isochore. Top Bunter reservoir structure has the greatest impact on the NPV followed by the facies model and average porosity.

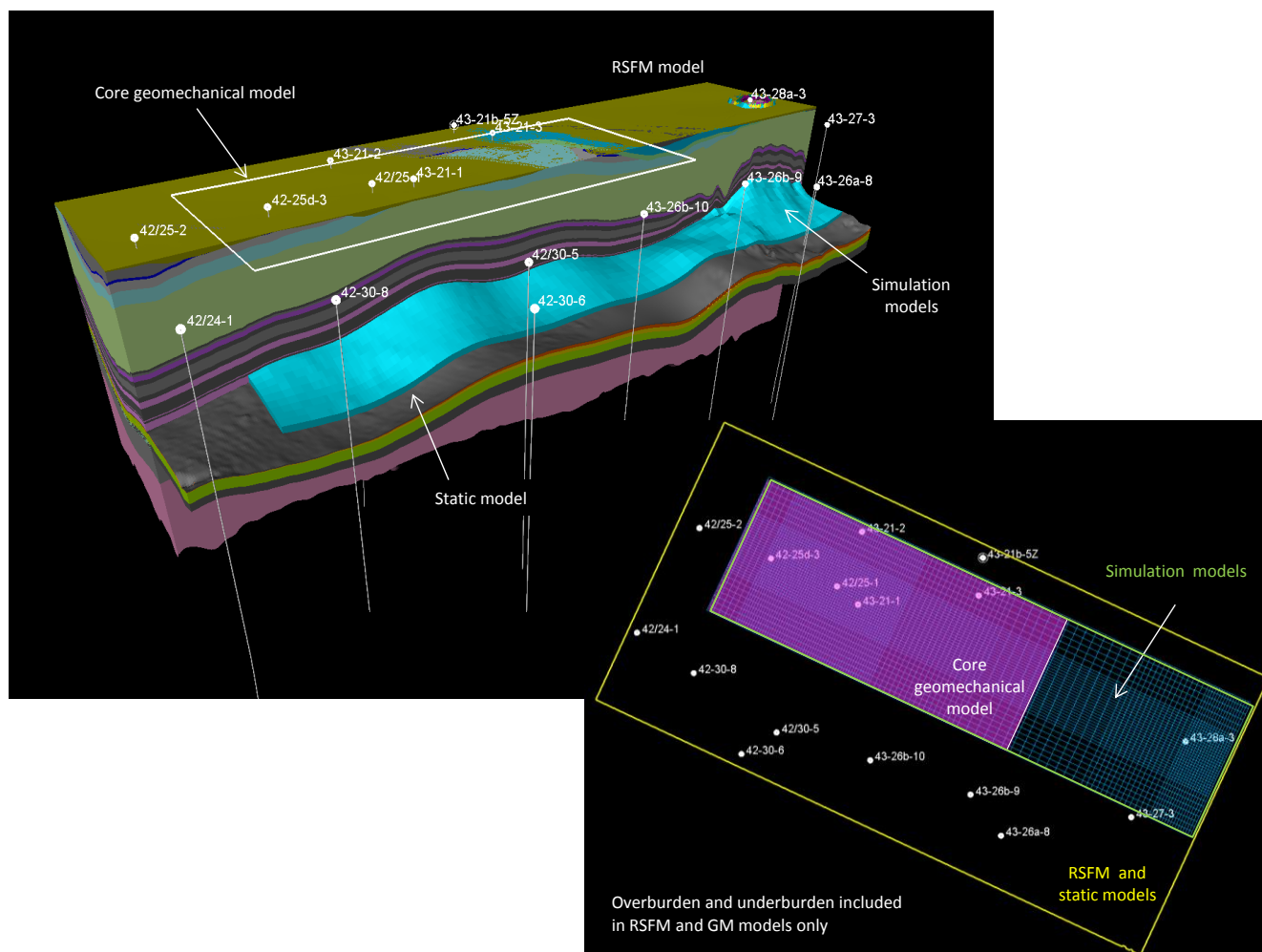
Figure 4.55: Tornado chart illustrating the effect of the key volumetric parameters on NPV



4.10.3 Geological Models

A number of Petrel models that represent sectors of the RSFM have been built (Figure 4.56). These models have different lateral and vertical extents depending on the objective and the spread of the inputs constraining them, and are described in more detail in the following sections.

Figure 4.56: Extent of the Geological Models



4.10.4 Regional Structural Framework Model

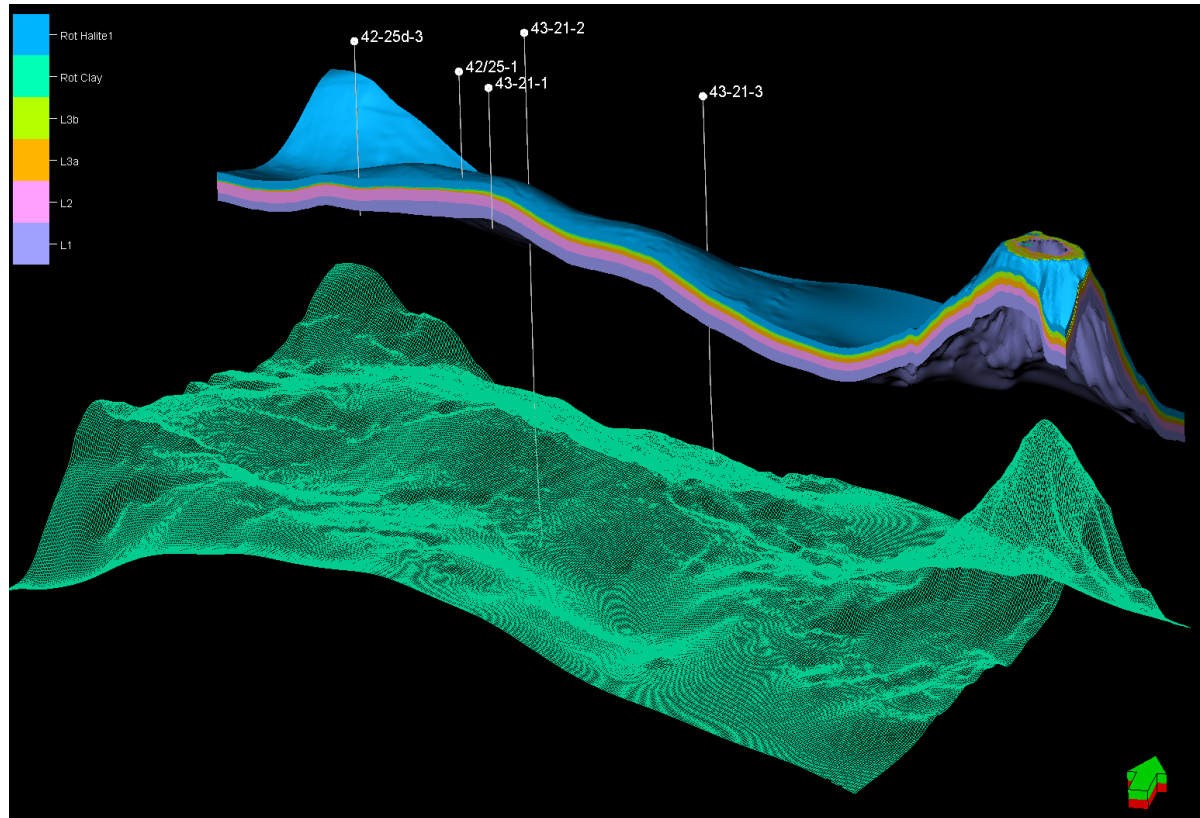
The RSFM has been described in Section 4.6. The stratigraphy includes the latest chemostratigraphic correlation that shows L3b pinching out in the west of the structure.

4.10.5 Static (Geological) Model

The static model has the same areal extent as the RSFM but it extends only from Top Röt Halite to Top Bunter Shale. The reason for such a large areal extent is to include all the regional wells that constrain the stratigraphy and inform the rock property modelling (Figure 4.57).

The model includes the following zones: Röt Halite 1, Röt Clay, Bunter L3b, L3a, L2 and L1, each of them further divided in layers. The lateral resolution is 100m x 100m (same as RSFM) with an average layer thickness of just over 1 m. Figure 4.57 illustrates the zonation in a cropped view of the static grid (top, in colours) whilst the base skeleton (bottom, in green) gives a visual of the horizontal resolution.

Figure 4.57: Static Model Geometry



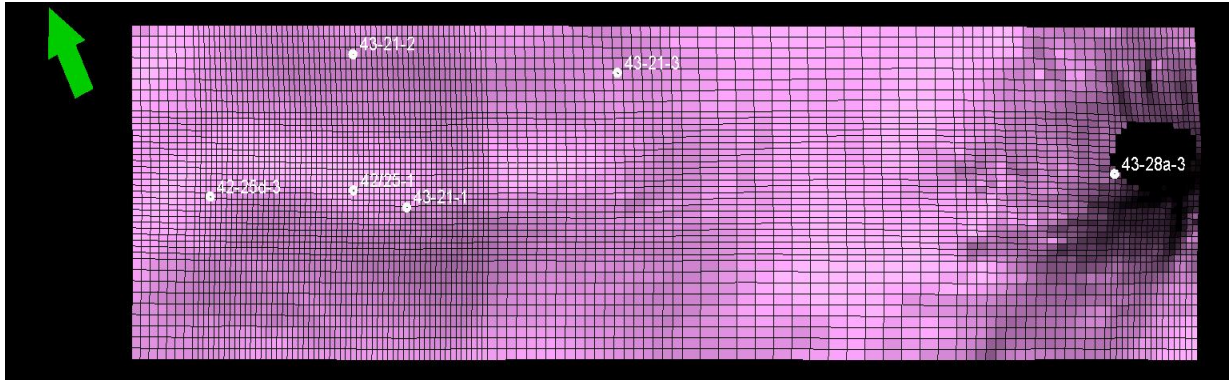
The model contains five facies models or sensitivity cases as described in Section 4.8. The porosity parameters (arrays) are conditioned to the facies; thus five porosity models have also been generated. Each of the facies – porosity pairs is associated with three NTG parameters: low, reference and high, corresponding to the different porosity cut-offs, hence a total number of 25 facies and rock property models are part of the geological model.

4.10.6 Simulation Models

The simulation grids are less areally extensive covering only the Endurance structure width and extending as far as the outcrop to southeast (Figure 4.58). Unlike the other grids that have constant cell size, the simulation grids are tartan-like with smaller cells over the main structure and the outcrop, and larger cells on the flanks.

This approach enables a proper evaluation of the areas of interest whilst still maintaining a manageable total number of cells and simulation run times. Relatively quick simulation runs are key to evaluating as many sensitivity cases as required to properly understand the dynamic uncertainties.

Figure 4.58: Reference Simulation Grid



These grids are usually described by the resolution in the core, finer areas (Endurance crest and around the outcrop) as the cell sizes are variable outside. Different ‘tartan’ geometries have been tried during this study and three, all following the pattern shown in Figure 4.58, but with different resolutions, have been exported to Eclipse and used in the dynamic simulations:

- Fine Grid: approximately 100 x 100 m;
- Reference Grid: approximately 200 x 200 m; and
- Coarse Grid: approximately 400 x 400 m.

All static rock property models for porosity and NTG have been upscaled onto the simulation grids and then exported for simulation. The corresponding permeability arrays have been generated directly in Eclipse by applying the porosity – permeability transform to the 3D porosity models. The resulting permeability models are then scaled to match appraisal well 42/25d-3 average well test permeability of 271mD.

4.10.7 Geomechanical Models

Two geomechanical (GM) models have been built:

- large GM grid that extends further than the RSFM (not shown in Figure 4.56) to incorporate the log properties from all the regional wells. These properties are then sampled into the smaller core GM grid; and
- core GM grid that covers only the Endurance structure (shown in Figure 4.56). Due to the smaller size, this is the grid used in all the geomechanical runs.

These grids are populated with parameters as part of the geomechanical modelling described in Section 4.11.2. As with the simulation models, three different resolutions (at constant cell size) have been generated: 100 x 100, 200 x 200, and 400 x 400 m.

4.11 Geochemistry

Insights into the geochemical interactions between the Endurance Storage Site and injected CO₂ during the injection as well as the longer term post-closure phases were obtained using both laboratory testing and numerical modelling.

4.11.1 Laboratory Testing

The tests described below form part of a larger core analysis programme, but are being highlighted here because of their relevance to the understanding of the potential geochemical processes that may occur within Endurance upon CO₂ injection.

4.11.1.1 Permeability as a function of throughput

The test was performed to establish the effect on Bunter sandstone permeability to continuous exposure to mobile CO₂.

It involves continuous injection of CO₂ through three brine-saturated Bunter sandstone samples, each at a non-damaging flow rate of 10 ml/min for a maximum of 25 pore volumes (PVs) and under Endurance temperature and pressure conditions. The three samples: 4H (28.7mD, 0.181 porosity), 8D (483mD, 0.215 porosity), and 8E (1104mD, 0.256 porosity), represent low, medium and high permeability values respectively.

Comparison of pre and post-flow sample permeability measurements indicate permeability in all three samples reduced by an average of -19.2% – sample 4H, with the lowest permeability, showing the greatest reduction of -26.1% whilst sample 8E, with the highest permeability, showing the least reduction of -12.6%. SEM (scanning electron microscope) analysis of sample #8D (4936.30') showed expelled particles during flow, consisting mainly of illite/mica, quartz, potassium feldspar, plagioclase and other mineral fragments in a matrix of iron carbonate precipitate.

This test suggests that exposure of the Endurance formation to supercritical CO₂ under *in situ* conditions will lead to salt deposition in the pore throats. Injected CO₂ will absorb water from the formation brine causing solid salt to precipitate. As the formation brine is highly saline, this process occurs very quickly. The SEMs of samples and filters all show mobilised clay fines and also amorphous/microcrystalline iron carbonate (likely to have been leached from the iron minerals present in the rock e.g. hematite, chlorite) which may have contributed to the reduction in the permeability. This reduction in permeability is not considered sufficient to cause permanent impairment of CO₂ injectivity and further assessment of this phenomenon along with likely mitigation measures has been performed using numerical modelling (see Section 4.11.2).

4.11.1.2 Impact of CO₂ exposure on rock mechanical properties

A range of rock mechanical characterisation tests have been performed to evaluate the potential for weakening of the Bunter sandstone and the Röt Clay as a result of exposure to supercritical CO₂. No CO₂ exposure tests were carried out on the Röt Halite.

The samples were first saturated in simulated formation water and then surface dried to ensure the CO₂ would contact the face of the core samples and invade into the pore spaces under pressure. Samples were exposed to CO₂ for up to 60 days at 1500psi pressure and 40°C.

Tests completed for the Bunter sandstone sample included Thick Walled Cylinder (TWC), advanced TWC, and triaxial testing. For the Röt Clay, Single Stage Triaxial (SST) and Acoustic Travel Time (ATT) testing

has been performed in addition to Brazilian tensile strength and Brinell hardness testing. The findings may be summarised as follows:

- Bunter sandstone: exposure to CO₂ produced differing effects as both decreases and increases in rock strength have been observed. Increases in unconfined compressive strength (UCS) tend to be greater in magnitude than when a decrease occurs; but a marked increase is seen at 1543.6m as shown in Table 4.5 for the TWC test. Such variations are likely to be facies/mineralogy related; and
- Röt Clay: exposure to CO₂ increased the surface hardness as measured by the Brinell hardness test, especially with increased exposure time. The Brazilian tensile strength test results however showed no clear trends. SST tests run on 3 sets of CO₂ 30 day aged claystone plugs showed UCS values of 348bar to 825bar.

Table 4.5: Comparison between Bunter sandstone rock strength pre and post-exposure to CO₂

Plug Ref.	Plug Depth M brt	TWC Yield bar	TWC Collapse bar	Plug Ref.	Plug Depth m brt	TWC Yield bar	TWC Collapse bar	Delta Yield bar	Delta Collapse bar
Fresh state (connate brine) saturated plugs				30-day scCO ₂ aged plugs					
4	1438.42	293.0	306.8	5	1438.46	355.7	378.0	62.7	71.2
13	1458.95	509.5	555.9	14	1459.00	479.0	513.9	-30.5	-42.0
28	1501.48	452.3	470.5	29	1501.53	486.1	504.6	33.8	34.1
D1	1538.52	495.5	562.9	D2	1538.56	518.6	575.1	23.1	12.2
E1	1543.85	765.6	860.5	E2	1543.90	907.8	1009.4	142.2	148.9
F1	1556.35	611.0	656.0	F2	1556.42	583.5	651.3	-27.5	-4.7

Notes:

Delta Yield (TWC) = TWC Yield (CO₂ exposed – TWC Yield (fresh state)

Delta Collapse (TWC) = TWC Collapse (CO₂ exposed – TWC Collapse (fresh state)

4.11.2 Geochemical modelling and simulation

The numerical models incorporate detailed mineralogical descriptions of the Bunter Formation (derived mainly from petrographic analysis) and of the Endurance brine composition from a comprehensive analysis of formation water samples taken during testing of the 42/25d-3 appraisal well testing. Simulations were performed using a thermodynamic model (called PHREEQC) and the GEM-GHGTM reservoir simulator with coupled geochemical code which has been adapted specifically for use in Green House Gas storage modelling. These models have been used to assess the risk to Storage Site integrity of the dissolution of primary cements in the Röt Clay and the Bunter Sandstone, the potential of carbonation reactions to permanently sequester CO₂, and the extent of near-well brine evaporation and associated halite precipitation on CO₂ injectivity and the effectiveness of water-wash as a possible remediation measure.

4.11.3 Mineralogy and Fluid Chemistry

This section summarises the mineral composition of the Endurance Storage Site and its overlying seals and also the fluid chemistry of the formation brine.

4.11.3.1 Geochemical Composition of Bunter Formation

The mineralogy data came from petrographic and diagenetic analysis of representative cores of the Röt Halite, the Röt Clay, and the Bunter Sandstone recovered from the 42/25d-3 appraisal well as presented in Table 4.6. Sample depths and the corresponding volume fractions are listed in Table 4.6. The average composition for each zone was used in the simulation model.

Based on the mineralogy analysis in Table 4.6, eight mineral components were chosen for the conceptualisation of mineralogy in the geochemical model. They are quartz, illite, calcite, dolomite, K-feldspar, anhydrite, halite, and albite. Among these albite is used as a surrogate for plagioclase as it is not included in the GEM database.

Table 4.6: Mineral Composition of Bunter Formation from Petrographic Analysis

plug	Depth (ft)		Illite/Smectite	Illite+Mica	Kaolinite	Chlorite	Quartz	K Feldspar	Plagioclase	Calcite	Dolomite	Siderite	Magnesite	Halite	Anhydrite	Pyrite	Hematite	Total
20	4551.00	Röt Halite	0.0	0.0	0.0	0.0	TR	0.0	0.0	0.0	0.0	0.0	0.0	99.7	0.3	0.0	0.0	100.0
34	4565.15		0.0	0.0	0.0	0.0	0.5	0.0	0.0	0.0	0.0	0.0	1.4	28.0	70.1	0.0	0.0	100.0
56	4586.90	Röt Clay	0.0	23.6	0.0	4.2	11.5	TR	1.9	0.0	14.8	0.0	0.0	0.0	43.2	0.0	0.8	100.0
76	4607.55		0.0	36.8	0.0	3.2	20.9	TR	4.8	0.0	27.2	0.0	0.0	0.0	5.5	0.0	1.6	100.0
84	4615.00		0.0	35.2	0.0	2.4	31.1	2.2	2.3	0.0	18.5	0.0	0.0	2.5	4.0	0.0	1.8	100.0
86	4616.90		0.0	TR	0.0	TR	62.7	5.9	2.1	0.0	1.3	0.0	0.0	1.9	26.0	0.0	TR	99.9
139	4670.00	L3	0.0	5.0	TR	0.7	15.3	0.7	1.6	62.8	4.2	0.0	0.0	0.0	8.7	0.0	1.1	100.0
170	4701.00	L2	0.0	3.3	0.0	0.8	66.4	7.1	6.3	0.3	3.9	0.0	0.0	7.1	4.3	0.0	0.4	99.9
219	4749.95		0.0	3.9	TR	0.6	75.0	4.9	5.6	0.0	6.8	0.0	0.0	2.6	0.0	0.0	0.6	100.0
269	4800.10		0.0	13.1	TR	2.1	56.2	4.2	11.8	0.0	4.3	0.0	0.0	2.8	2.9	0.0	2.6	100.0
343	4874.00		0.0	9.5	TR	2.1	64.4	4.4	10.8	0.0	1.4	0.0	0.0	3.6	2.0	0.0	1.9	100.0
399	4929.95		0.0	7.9	TR	1.2	63.1	6.1	8.8	6.1	1.3	0.0	0.0	3.2	1.5	0.0	0.7	99.9
459	4990.00		0.0	7.3	TR	1.5	67.2	4.6	8.0	4.4	1.3	0.0	0.0	2.8	2.0	0.0	1.1	100.0
521	5052.20	L1	0.0	5.0	TR	0.8	69.8	7.1	8.2	TR	1.9	0.0	0.0	5.2	1.3	0.0	0.7	100.0
573	5104.00		0.0	12.1	0.0	0.8	63.5	4.0	10.6	3.8	1.0	0.0	0.0	2.4	1.1	0.0	0.9	100.0

4.11.3.2 Formation water composition

The analysis of water samples taken from 42/25d-3 appraisal well shows all water samples were highly saline sodium chloride dominated brines (TDS 300,000 ± 10,000 mg/L) with significant concentrations of common rock constituents, calcium, magnesium and sulphate.

Comparing the depth at which samples were taken for water analysis in Table 4.7 and Table 4.8 with the depth where the cores were sampled for mineralogical analysis in Table 4.6 it is found that three water samples match or are close to the core samples; two in Bunter Sandstone L1 and L2 (4722ft and 5167ft)

and one in Röt Clay (4589ft). As the thermodynamic model is 0D (zero dimensional), and as the 2D radial geochemical model is a homogeneous model, the initial aqueous concentration data were chosen based on the rock and formation water data from the three depths.

Table 4.7: Physicochemical Parameters

	units	L1a	L2a	L3b		Röt Clay
Sample Reference		1.04	1.09	1.13	2.1	2.14
Sampling Point / Depth	ft	5167.5	4722	4634	Separator Water Line	4589.37
Physicochemical Parameters						
pH immediate @ 20.7 ± 1.2°C Initial		6.20	5.25	5.34	-	4.55
Resistivity @ 20°C	ohm.m	0.0461	0.0466	0.047	0.0466	0.0465
Density @ 20.00 ± 0.08°C	kg/L	1.1958	1.1881	1.1868	1.1976	1.1976
TDS - Measured @ 0.2 µm - By Mass	mg/kg	256146	247659	247730	259680	258925

4.11.3.3 CO₂ Composition

The normal White Rose CO₂ stream composition is discussed in Section 8.3.4. For the geochemical modelling, however, the injection stream was assumed 100% CO₂ and other components in the normal stream were ignored.

Table 4.8: Formation Water Composition

Sampling Point / Depth	ft	5167.5	4722	4634	Separator Water Line	4589.37
Chloride	mg/kg	154146	148780	148164	155600	155405
Fluoride	mg/kg	0.15	0.12	0.1	0.13	0.14
Sulphate	mg/kg	296	359	385	360	364
Bromide	mg/kg	473	460	444	438	470
Nitrate	mg/kg	<4	<4	<4	<4	<4
Iodide	mg/kg	<4	<4	<4	<4	<4
Phosphate	mg/kg	<20	<20	<20	<20	<20
Total Carbonate (as Bicarbonate) Immediate	mg/kg	38	37	43	-	39
Formate	mg/kg	<2	<2	<2	<2	<2
Acetate	mg/kg	<2	<2	<2	<2	<2
Propionate	mg/kg	<3	<3	<3	<3	<3
Butyrate	mg/kg	<4	<4	<4	<4	<4
iso	mg/kg	<4	<4	<4	<4	<4
Cl:Br	mg/kg	326	323	334	355	331
Lithium	mg/kg	7.9	8	7.6	8.4	8.5
Barium	mg/kg	2	1	1	1	1
Strontium	mg/kg	108	111	103	117	116
Calcium	mg/kg	8858	8610	8037	8985	9129
Magnesium	mg/kg	2543	3014	3192	3138	3103
Sodium	mg/kg	85512	79664	79953	83763	84792
Potassium	mg/kg	1400	1469	1483	1553	1525

Sampling Point / Depth	ft	5167.5	4722	4634	Separator Water Line	4589.37
Iron	mg/kg	<1	<1	<1	2	1
Copper	mg/kg	3.9	1.7	1.3	1	1.7
Zinc	mg/kg	7.8	8.5	7.9	8.9	8.8
Manganese	mg/kg	2.6	1.6	1.5	1.7	1.7
Aluminium	mg/kg	<0.6	<0.6	<0.6	<0.6	<0.6
Ammonium	mg/kg	<10	<10	<10	<10	<10
Lead	mg/kg	1.1	1.3	1.4	1.4	1.5
Chromium	mg/kg	0.3	0.4	0.4	0.7	0.7
Nickel	mg/kg	<0.2	1.8	1.6	<0.2	0.4
Cadmium	mg/kg	0.2	0.2	0.2	0.1	0.2
Cobalt	mg/kg	0.15	0.16	0.16	0.09	0.08
Silver	mg/kg	<0.04	<0.04	<0.04	<0.04	<0.04
Vanadium	mg/kg	0.07	0.07	0.08	0.07	0.06
Arsenic	mg/kg	1.2	1.3	1.5	2.1	2.4
Boron	mg/kg	9	10	9	10	10
Phosphorus	mg/kg	<6	<6	<6	<6	<6
Silicon	mg/kg	3	3	3	4	4
Sulphur	mg/kg	84	104	112	107	106
Total Barium	mg/kg	2	2	1	2	1
Total Iron	mg/kg	<1	1	<1	3	1
Soluble Mercury	µg/kg	0.4	0.2	0.2	0.3	<0.2
Total Mercury	µg/kg	0.3	0.2	0.2	0.3	<0.2
Total Cl- equivalent	mg/kg	154597	149271	148670	156071	155906
Total Na+ equivalent		101403	96204	96174	101021	102133
Total NaCl equivalent		255999	245474	244845	257092	258039

4.11.3.4 Thermodynamic data

The rate law used for the mineral dissolution and precipitation reaction is (Bethke, 1996):

Equation 4.2
$$r_{\beta} = \hat{A}_{\beta} k_{\beta} \left(1 - \frac{Q_{\beta}}{K_{eq,\beta}} \right)$$

where r_{β} is the rate, \hat{A}_{β} is the reactive surface area for mineral β ; k_{β} is the rate constant of mineral reaction β , $K_{eq,\beta}$ is the chemical equilibrium constant for mineral reaction β and Q_{β} is the activity product of mineral reaction β .

The CMG-GEM software models changes to formation porosity due to mineral dissolution and precipitation by tracking the associated changes in void volume.

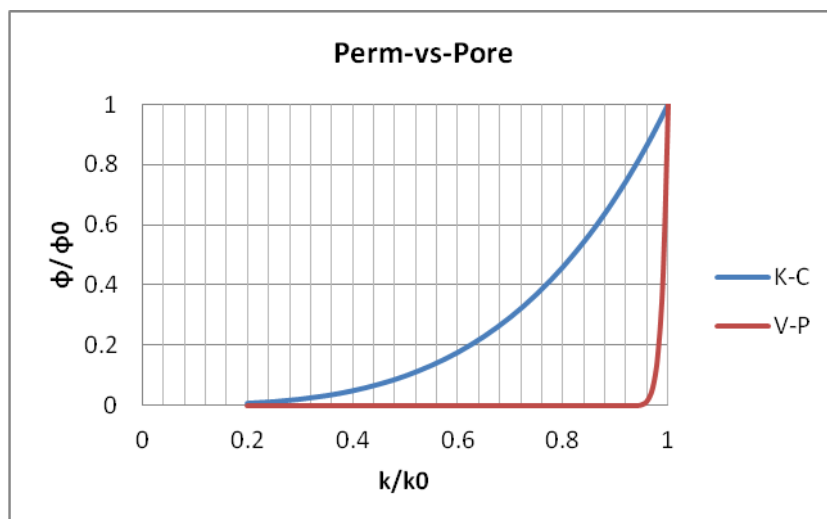
The phase behaviour and properties of reservoir fluids are modelled in the WinProp pre-processor within the CMG-GEM package.

4.11.3.5 Porosity-permeability relationship in dynamic simulation

The Kozeny-Carman perm-poro model (K-C model) was used to predict permeability change induced by mineral dissolution or precipitation. Comparison of simulation results generated using the K-C model and the Verma and Pruess's 'tubes-in-series' model (V-P) showed no noticeable difference between the two – even though this is not apparent from Figure 4.59.

The poro-perm correlation presented in Figure 4.51 has not been used in the prediction of permeability following salt precipitation or dissolution reactions because although this function holds for the consolidated formation rock it may not be applicable for permeability changes that occur as a result of halite precipitation, where it is not known where the halite will deposit (in pore bodies and/or pore throats, and whether once precipitated it will be static, mobile, or mobile until hydrodynamically trapped).

Figure 4.59: Comparison of K-C and V-P permeability-porosity models when $\phi_c=0.90\phi_0$ when $k=0$, and $n=8$



4.11.3.6 Interaction among CO₂, formation water, reservoir and seal facies

The chemical reactions for the PHREEQC modelling were chosen based on the minerals identified in Figure 4.59 and the brine composition in Table 4.8. The primary concern is formation damage in the near wellbore zone and the impact that CO₂ saturated brine could have on the integrity of the cap rock. Thus only the precipitation/dissolution of halite, dolomite, anhydrite and calcite minerals was considered in the main thermodynamic modelling activity.

4.11.3.7 Equilibrium batch 0D modelling (PHREEQC)

PHREEQC was used to run batch geochemical simulations to identify the main chemical reactions in the formation and to validate the equilibrium state based on the water composition data and rock mineral analysis data before building the more complex 2D GEM geochemical model.

In total, six sets of calculations were performed using PHREEQC. Initial calculations were performed to identify the initial equilibrium water composition, and how this varied compared to the supplied water

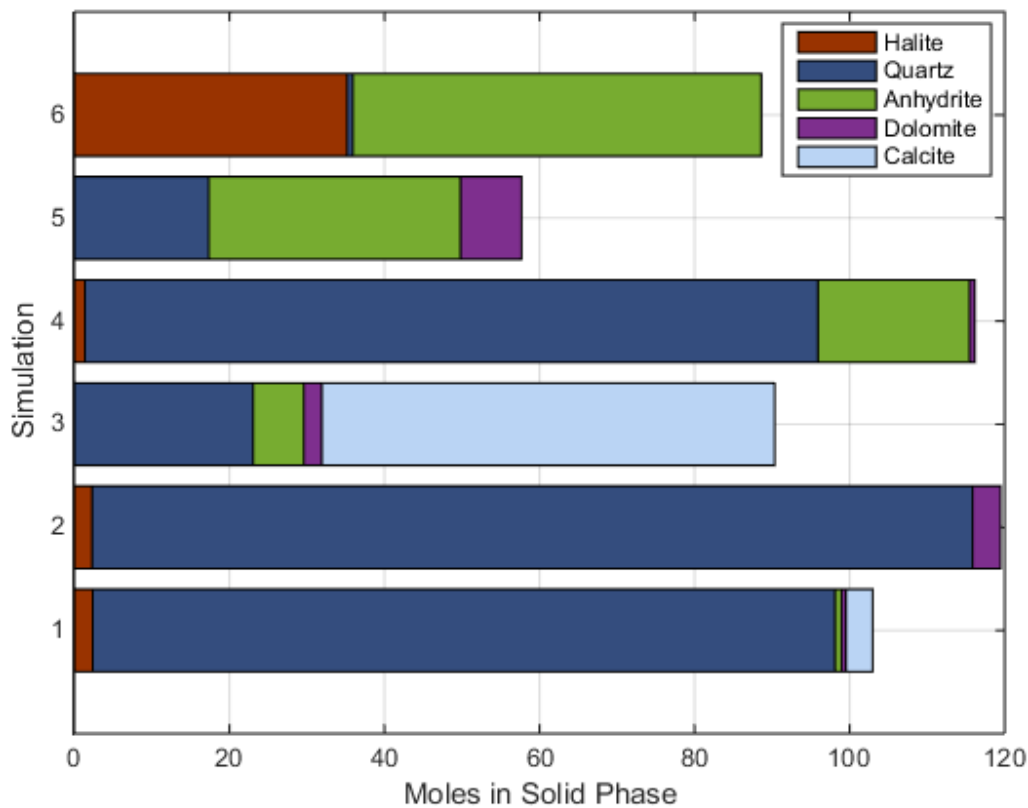
composition. Subsequent calculations then considered the impact of dissolving CO₂ in this brine. The six sets of calculations correspond to six locations in the sequence at various depths, and their corresponding water compositions. These include the Röt Halite, Röt Clay (two intervals) and L3, L2 and L1 intervals of the Bunter sandstone. All simulations were performed using 1L of water at 57.2°C and 142bar. The conditions are identified in Table 4.9.

Table 4.9: Selected brine and aquifer sections for PHREEQC simulations

Simulation 1	Simulation 2	Simulation 3	Simulation 4	Simulation 5	Simulation 6
Brine @ 5167 feet	Brine @ 4722 feet	Brine @ 4634 feet	Brine @ 4634 feet	Brine @ 4589 feet	Brine @ 4589 feet
L1 @ 5104 feet	L2 @ 4750 feet	L3 @ 4670 feet	Röt Clay 1 @ 4617 feet	Röt Clay 2 @ 4587 feet	Röt Halite @ 4565 feet

Figure 4.60 shows the new mineral compositions as a result of the equilibration process (identifying only minerals that are present in fractions > 10%).

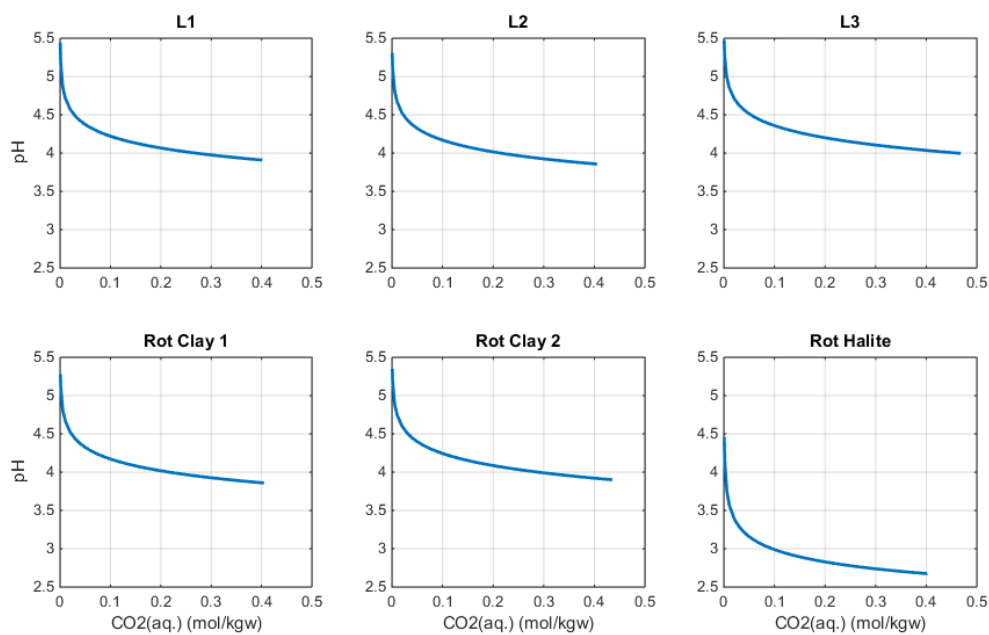
Figure 4.60: Equilibrium mineral fractions from PHREEQC simulations in graphical format



Having established the initial equilibrium conditions, the effect of varying CO₂ concentration on the mineral composition of each of the six scenarios was simulated. The CO₂ solubility for the analysed system is

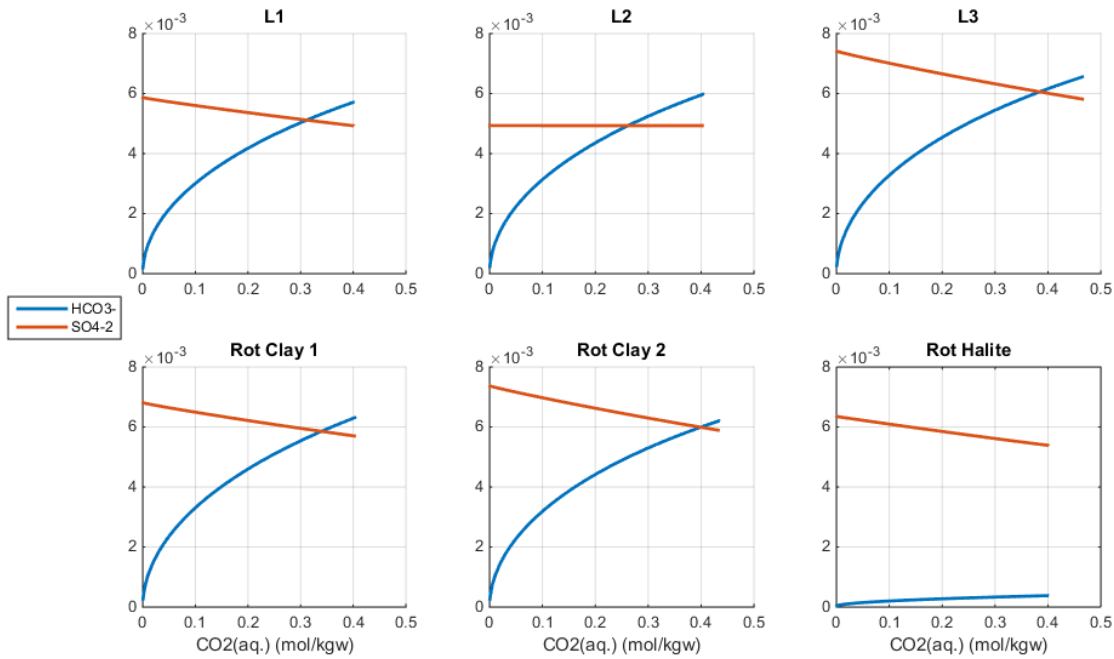
between 0.4 and 0.5 mol/kgw for all intervals. The addition of CO₂ to the formation brine creates carbonic acid, and this results in a drop in brine pH, as shown in Figure 4.61. The pH decreases for increasing amounts of CO₂ (dissociation of carbonic acid). For the Röt Halite, lower pH values are reached because there are no carbonate minerals present to buffer the brine.

Figure 4.61: pH vs CO₂ concentration for 6 scenarios



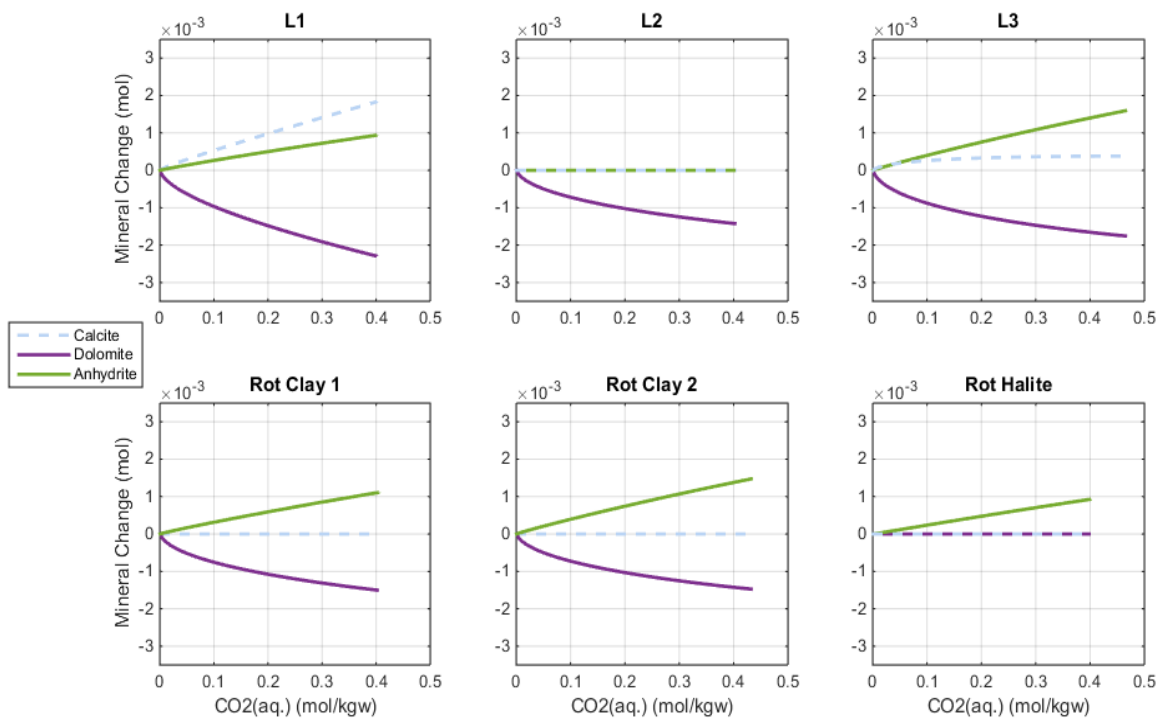
Na and Cl ions have the largest molalities within solution (with molalities an order of magnitude larger than Ca, Mg, and K ions) and represent the dominant species (they set the maximum CO₂ solubility). Increasing CO₂ concentration increased the number of other ions (especially H and HCO₃ ions and led to further dissociation of carbonic acid) in addition to carbonate dissolution (dolomite) and precipitation (calcite). On the other hand, SO₄ ion concentration decreased as anhydrite precipitated (see Figure 4.62).

Figure 4.62: Molalities of HCO₃ and SO₄ ions vs CO₂ concentration for 6 scenarios



The changes in brine composition are driven by the mineral reactions, and these are shown in Figure 4.63.

Figure 4.63: Mineral changes resulting from increase in CO₂ concentration for 6 scenarios



The simulations predict, in general, that only dolomite may dissolve under conditions applicable in Endurance, with all other minerals precipitating.

4.11.3.8 Kinetic batch 0D modelling (PHREEQC)

The last section has identified equilibrium endpoint conditions for a range of CO₂ concentrations. The next sets of calculations include kinetic reaction rates and are used to identify the evolution of the mineralogy over a 10,000 year period.

The Pitzer database (a database summarising a set of parameters, which are used to characterise the interactions amongst ions and solvents and thus predict the behaviour of ions dissolved in natural waters) was used in all quantitative predictions as it is the database applicable for the conditions in Endurance. However, the Pitzer database includes only a limited set of minerals and sensitivities were therefore performed with the default PHREEQC database to assess the long term evolution of secondary minerals such as hematite, chlorite, kaolinite and K-feldspar which are not included in the Pitzer database.

Simulation was initialised by equilibrating the formation water with the minerals present in each reservoir section. Then, 0.5 mol/kgw of CO₂ was added and kinetic calculations performed for a period up to 10,000 years. Because the final state of the system was reached before 200 years, results have been plotted for this transient period only.

From Figure 4.64, the amount (moles) of dissolved dolomite is higher than the precipitated calcite for all reservoir sections except for Röt Halite where neither mineral is present. Therefore, there is no net mineralisation of CO₂ in the reservoir. From Figure 4.65, halite precipitation is predicted as the fastest mineral reaction and stops after 5 years. Wherever halite precipitation occurs it has a mineral change that is many orders of magnitude larger than the combined mineral change of the remaining three primary minerals (i.e. dolomite, calcite, and anhydrite).

The rock volume changes over the course of the reactions indicate that the decrease in volume due to dolomite dissolution was higher than the increase in volume due to precipitation of calcite and anhydrite combined. This means that porosity is likely to increase in areas where halite does not precipitate, namely L3 and Röt Clay 2. However, this porosity increase would be below detectable limits (<0.001%1 pore volume of fluid) Halite precipitation is the main reaction likely to cause a measurable porosity change – a porosity decrease of approximately 0.1% for 1 pore volume of fluid.

Figure 4.64: Calcite, dolomite and anhydrite precipitation (positive) and dissolution (negative) vs time

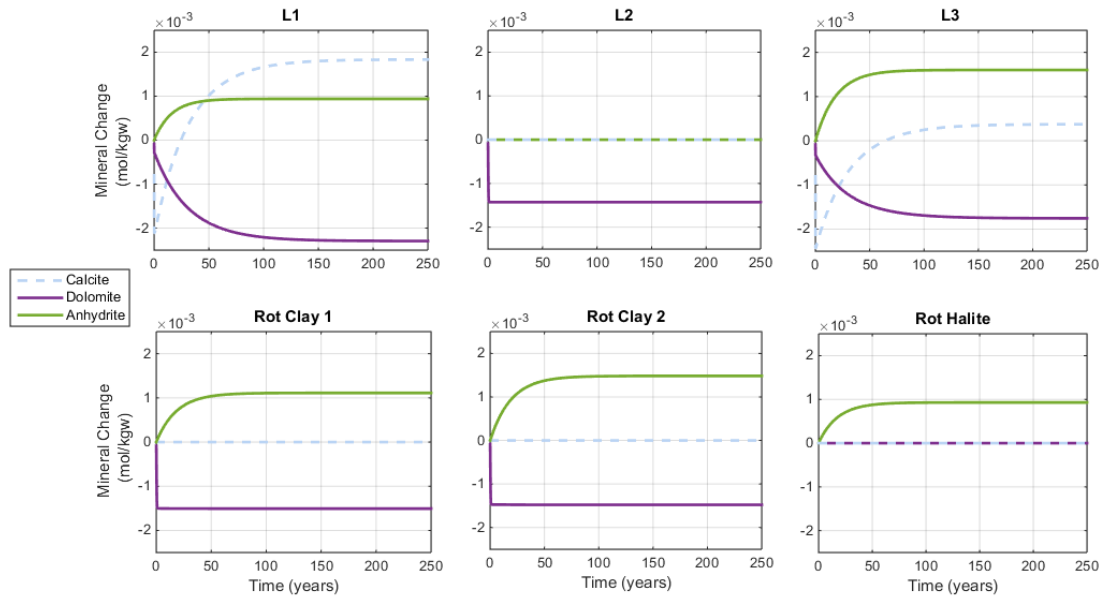
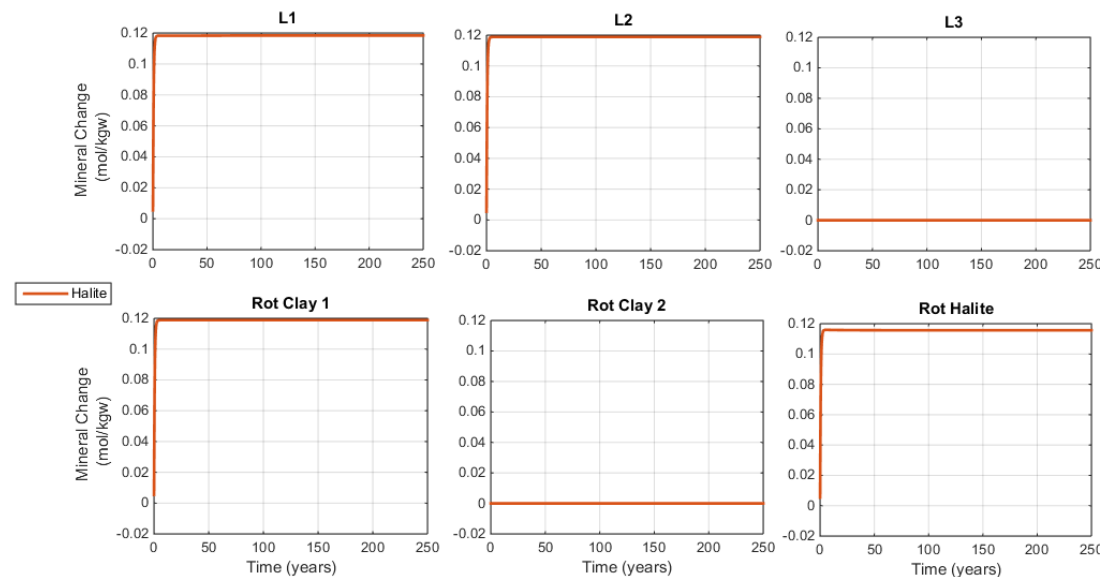


Figure 4.65: Halite precipitation (positive) and dissolution (negative) vs time



Kinetic Simulation Using PHREEQC default database: the above calculations have been repeated using the default PHREEQC database, but now including other minerals that may be involved in reactions not included in the Pitzer database. The results of this second set of calculations are considered as qualitative only since the PHREEQC database is applicable for salinity conditions only up to 1 mol/kgw, whereas the Pitzer database can handle salinities of over 6 mol/kgw – 4/52 aquifer salinity is approximately 4.3 mol/kgw.

Of the original reactions, calcite, dolomite and anhydrite all undergo dissolution whilst halite was precipitated (Figure 4.66). The other mineral reactions, including dissolution of chlorite and K-feldspar, and precipitation of kaolinite were much slower (Figure 4.67). Note that mineral reactions are shown for the full 10,000 years of the calculations, since the slow reaction kinetics mean that equilibrium is not reached over that period.

Although the default PHREEQC database is not as accurate for Endurance salinity system as compared to the Pitzer database, there is no predicted long term dissolution of major minerals that would affect reservoir or cap rock integrity. Chlorite dissolution at a very low rate may continue for 10,000 years but the volume change is likely to be very small.

Figure 4.66: Calcite, dolomite, anhydrite and halite precipitation (positive) and dissolution (negative) vs time using the default database, and with inclusion of other mineral reactions in the calculation

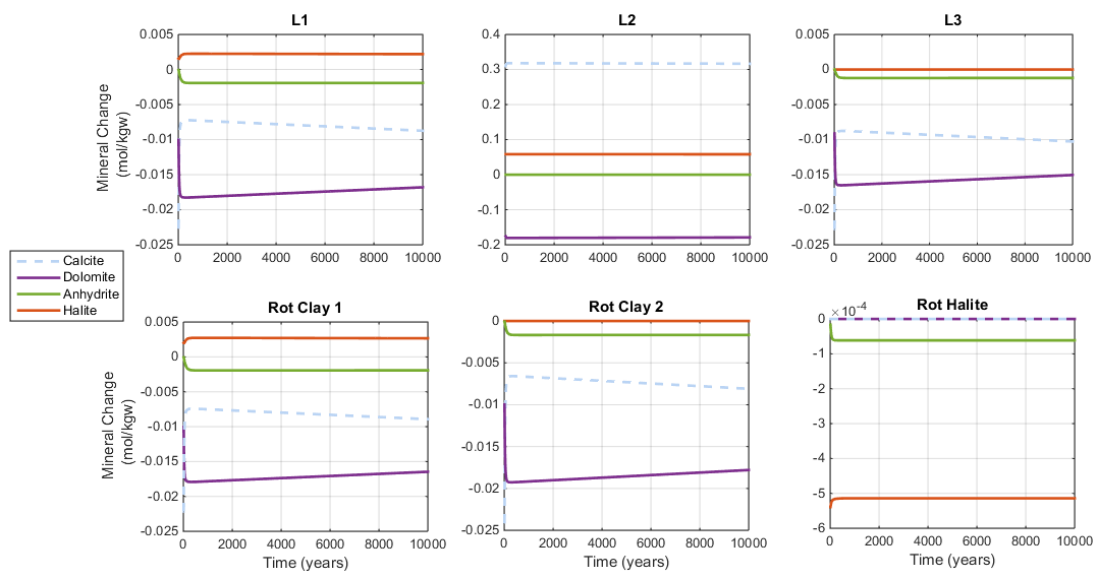
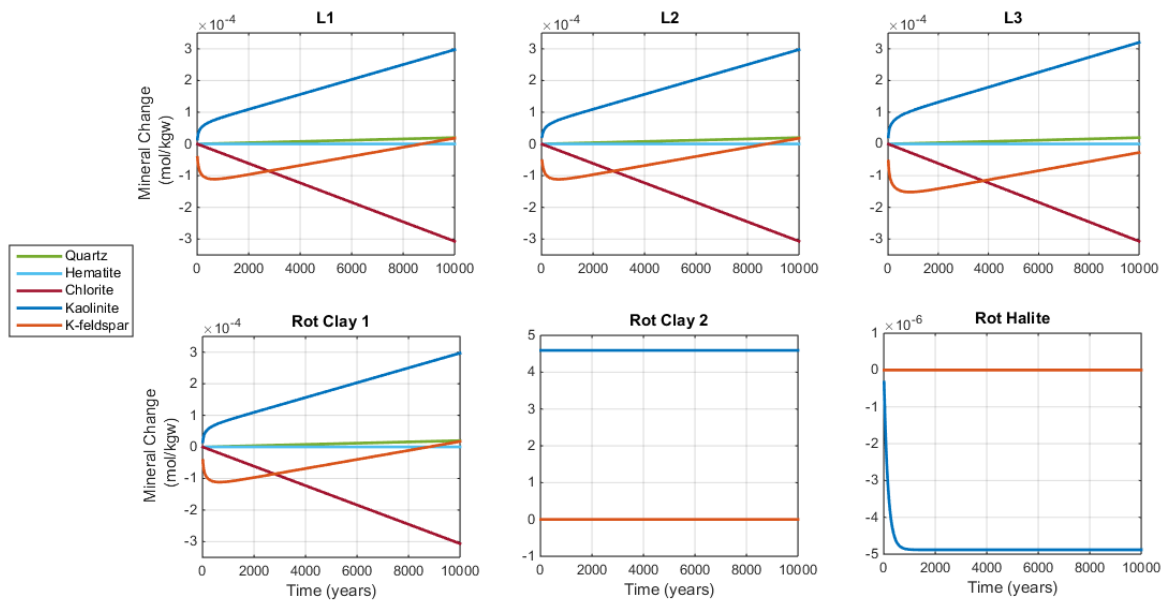


Figure 4.67: Quartz, hematite, chlorite, kaolinite and K-feldspar (positive) and dissolution (negative) vs time using the default database



4.11.3.9 Summary of Kinetic batch 0D modelling (PHREEQC)

The more accurate Pitzer modelling identifies that halite and anhydrite precipitation is likely to occur (even excluding the effects of evaporation), and that short term calcite dissolution may give way to calcite precipitation, driven by the more long term effects of dolomite dissolution. No dissolution reactions are predicted when CO_2 saturated brine contacts the Röt Halite. Contact of CO_2 saturated brines with the Röt Clay may lead to early time dissolution of dolomite, but this is likely to stop by the end of White Rose CO_2 injection period. Long term dissolution of dolomite would only take place in the Bunter sandstone intervals, and the volume changes due to this reaction are predicted to be small. Furthermore, dolomite cement exists as isolated nodules in the Bunter sandstone and does not contribute significantly to the overall rock strength, its dissolution is unlikely to have any impact on Storage Site integrity. The net trapping of CO_2 as a solid mineral phase is likely to be less than 1 % of White Rose CO_2 injection.

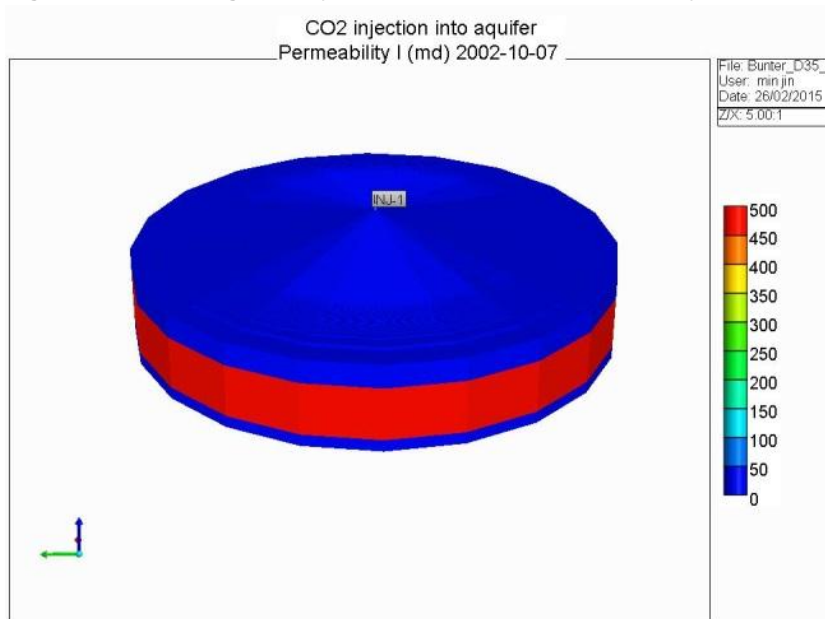
4.11.3.10 Fluid Flow and Geochemical Reaction Coupled Modelling (GEM)

The coupled flow and geochemical simulations were performed using GEM-GHG software by Computer Modelling Group Ltd. GEM-GHG is a general Equation-of-State (EoS), three-dimensional compositional reservoir simulator for modelling multi-phase flow of multi-component fluids, and specifically adapted for use in Green House Gas (GHG) storage modelling.

The 2D simplified model is built with a radial mesh of 48 layers: 2 layers of cap rock, 45 layers of Bunter Sandstone, and one layer of underburden. Two regions were defined to represent cap rock (Röt Halite and Röt Clay) and Bunter Sandstone. The underburden had the same properties as the cap rock. The dimension of the model is 4000m in radius, 375m in thickness with a dip angle of 2 degrees. The top of the model is at the depth of 1200 m. A numerical aquifer is connected at the out boundary of the model and the spill point is at the outermost column of cells at a depth of about 1480 m. The injector is in the

centre of the model as shown in Figure 4.68. The perforations go through the L2 and L3 zone (layer 22 to 47). Injection of CO₂ is simulated at 0.6MTPA for 15 years. A pre-injection run was carried out for formation equilibrium.

Figure 4.68: Model geometry and cross-section with porosity distribution for the 2D GEM model



Fluid flow and rock properties: Table 4.10 gives a summary of the rock and fluid properties for the two model geometries used. Measured Endurance relative permeability and capillary pressure curves (Figure 4.67) have been used for the simulations whilst the Viking-2 data was used as a sensitivity.

Table 4.10: Input data for simulation models illustrated in Figure 4.74 [above]

Grid type		1D Radial model	2D Radial model
Grid dimension	I x J x K	699x1x3	
grid size	ni x di	495x0.02	642x5
Röt Fm.	nk x dk	1x100	1x80, 1x20
BSS Fm.	nk x dk	1x225	45x5
Under burden	nk x dk	1x50	1x50
datum	m	1300	1300
Pressure	kPa	14120	14120
Pressure gradient	bar/m	0.115	0.115
Temperature	C	57.2	57.2
Temperature gradient	Degree C/m	0.0316	0.0316
Pore compressibility	1/kPa	5.0x10 ⁻⁷	5.0x10 ⁻⁷
Porosity (o/u burden)		0.1	0.1
Porosity (BSS)		0.22	0.22
Permeability (o/u' burden)	mD	0.0001	0.0001
Permeability (BSS)	mD	500	500
Deepest inj. point	m	1459	1459

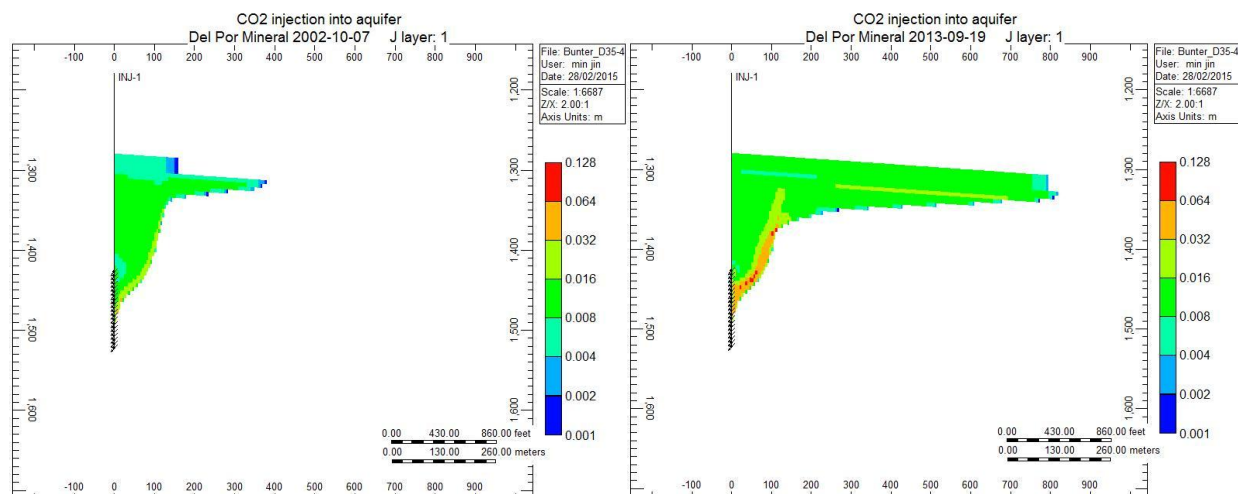
Grid type		1D Radial model	2D Radial model
Top perforation	m	1292	1292

Chemical reaction model: three aqueous reactions and six mineral reactions were selected, based on the PHREEQC modelling above and reactions reported in the literature for minor minerals.

Results:

Figure 4.69 shows the porosity change due to mineral reactions. The main porosity change induced by CO₂ injection was from halite precipitation (mainly from brine evaporation) because of a combination of relatively high Na and Cl concentrations relative to the other components and the relative low rates of other reactions.

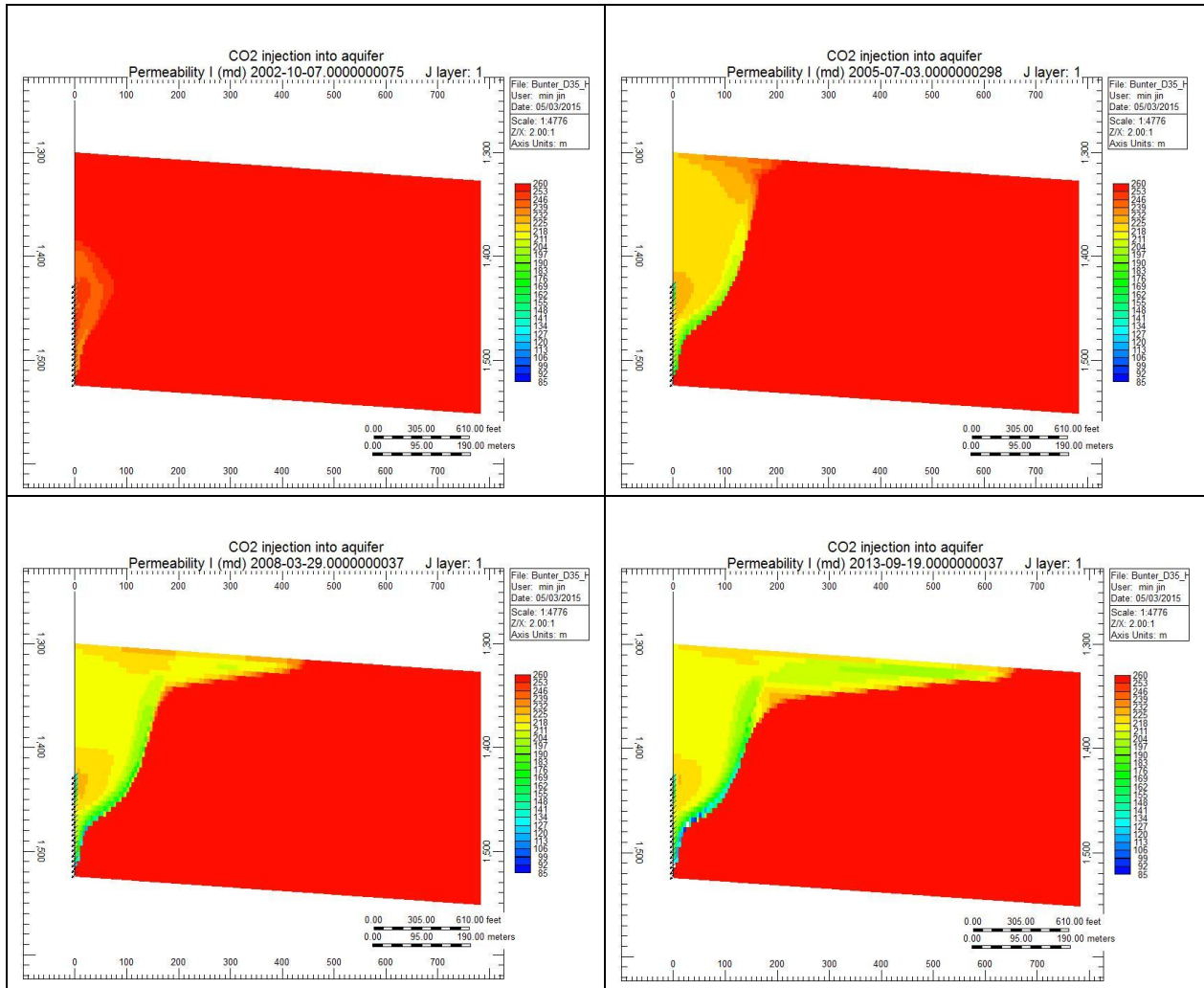
Figure 4.69: Porosity change due to CO₂ injection and salt precipitation after 100 and 5000 days. The figure indicates the gradual formation of a low permeability flow barrier near the perforations which forced a change in CO₂ migration path during the rest of injection



As shown in Figure 4.69, a low porosity zone was formed gradually at the edge of CO₂ plume in the 2D model. The pronounced vertical solid saturation trend and the emergence of a localized region with very large salt precipitation near the lower portion of the dry-out front was caused by a backflow of brine towards the injector under capillary force, which provides a continuous supply of salt that increase the local salinity and the precipitable salt. Gravity override effects accelerated the accumulation of solids.

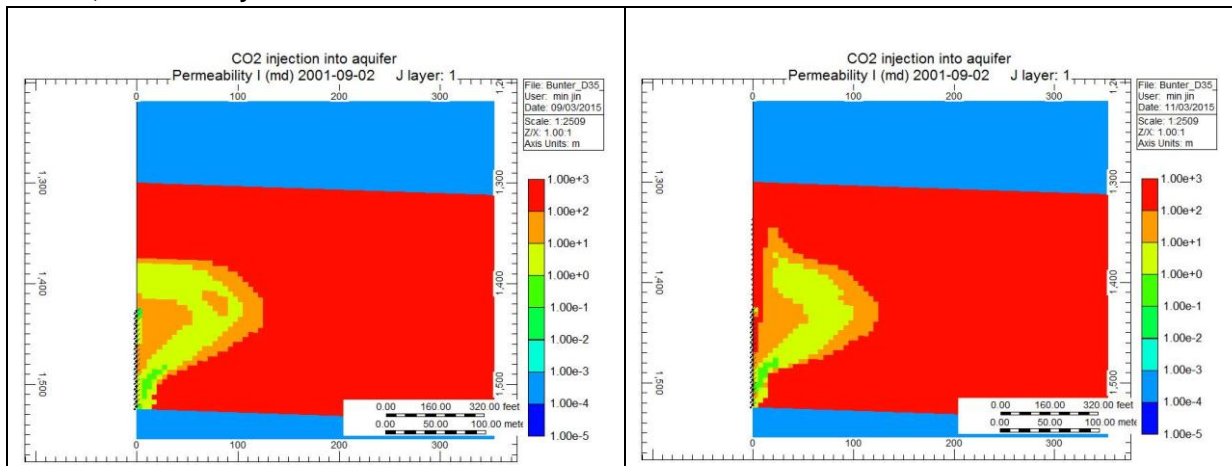
The permeability reduction due to halite precipitation at different time steps is shown in Figure 4.70. The permeability in the front at 5000 days was predicted to reduce to about 1/3 - 1/2 of its initial value whilst a region with an impaired permeability can be seen to develop along the top perforations.

Figure 4.70: Permeability reduction due to the halite precipitation at different time steps (a) 1000, (b) 2000, (c) 3000, and (d) 5000 days. The permeability at the front after 5000 days reduced to about 40% of its initial value



A freshwater flush, which reduces the brine salinity near the wellbore before CO₂ injection (re-injection water flushing), was simulated to assess its effectiveness in alleviating injectivity impairment, caused by salt precipitation during CO₂ injection. The pre-flush water was injected for 10 days. Figure 4.71 shows a comparison of the permeability reduction in the model without pre-flush (left) and with pre-flush (right) after 600 days. In the model with pre-flush a low salinity region was created that established a pathway for CO₂ migration and pressure release. The maximum well bottom hole pressure (BHP) after 3 years of CO₂ injection was reduced by about 40% compared to the model without the pre-flush.

Figure 4.71: Comparison of permeability reduction between (a) no water flush model and (b) pre-flushed model, after 600 days



4.11.4 Summary of Fluid Flow and Geochemical Reaction Coupled Modelling

The impact of halite deposition was to channel the CO₂ but there was no significant change in injection pressure. Where extreme modelling assumptions have been made, a 20% reduction in injectivity was predicted over a three year period. The coupled flow and geochemical simulations suggest that the impact of halite precipitation on injectivity during continuous and sustained injection of CO₂ at a constant rate will not to be significant.

4.11.4.1 CO₂ Exposure in Analogous Reservoirs: Literature survey

Published works have been examined to understand the interaction of CO₂ with sandstone reservoirs that share key features (sandstone mineralogy, highly saline brine, halite seal, etc) with the Endurance Storage Site to discover relevant lessons that could be incorporated into operational planning.

The introduction of CO₂ into saline aquifers could give rise to geochemical processes such as CO₂ dissolution in brine forming a weak acid which reacts with the minerals of the aquifer and the caprock, leading to mineral precipitation and dissolution reactions that span varying timescales.

In the short term it is near-well precipitation of minerals that presents the greatest challenge since this can lead to reduced porosity and permeability and thus decrease the injectivity. Although salt precipitation due to CO₂ injection have been observed to reduce rock permeability by up to 70% in reservoir condition laboratory experiments using brine salinities ranging from 150,000 – 350,000 mg/l, all the instances of CO₂/reservoir interactions examined by the review (including CO₂ Storage Sites as well as CO₂-EOR operations) relate to brine with salinities that are much lower than found in the Endurance reservoir (~300,000 mg/l) (see Figure 4.72).

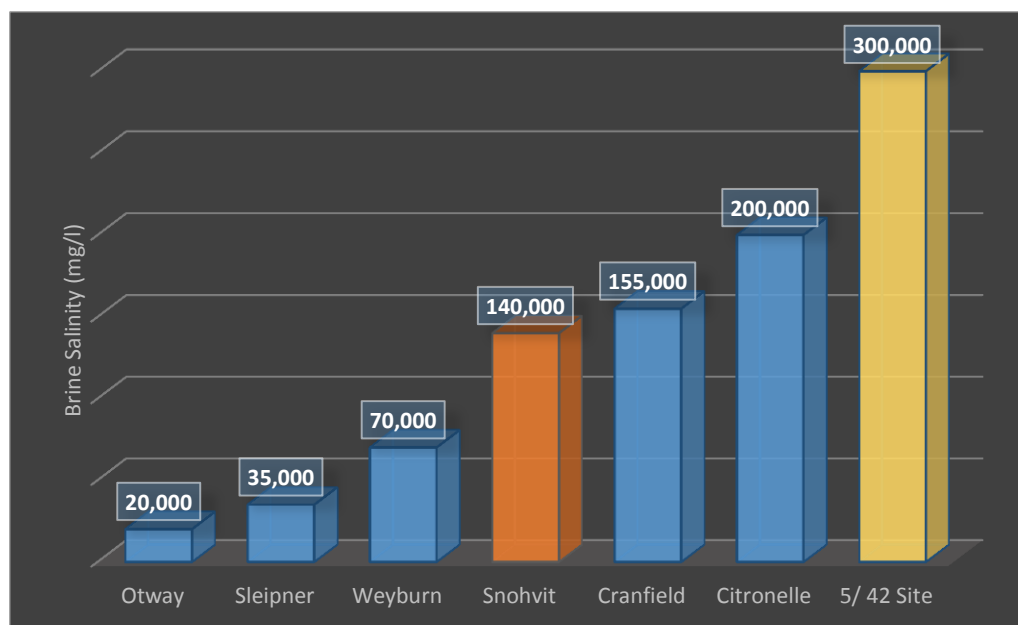
Only one out of the six studied sites reported injectivity problems (Snohvit), however, this particular case was mainly due to fluvial reservoir heterogeneities and limited high permeability channel sandstone connected to large volume of poorer injectivity reservoir. At Snohvit, the extent of good reservoir was less than predicted because of the presence of faults which sealed lateral connectivity and blocked access to the larger reservoir volume. The dislodging of fine particles (i.e. clays and other particles not contributing

to the grain framework) due to CO₂ injection in addition to salt precipitation were also claimed to have contributed to the reduction in injectivity at Snohvit. The injectivity impairment was temporarily ameliorated by injection of MEG (monoethylene glycol). However, no data on the actual levels of overall injectivity change nor on the geochemical reactions involved has been published but it was stated that the impact of mineral precipitation was “minor”.

Petrographic analysis indicate the Endurance Storage Site contains high amounts of detrital feldspar (13.8% K-feldspars and 10.9% plagioclase) as well as carbonate (9.6%) and anhydrite (2.2%) cements and trace amounts of diagenetic halite. Geochemical modelling of Endurance (Section 4.11.2) suggests that only dolomite carbonate cements will dissolve as a result of brine acidification due to injected CO₂ dissolution. However, dolomite occur in relatively small amounts as isolated nodules and is not part of the load-bearing framework of the Endurance Bunter sandstone and therefore the impact of its dissolution on injectivity or Storage Site integrity is likely to be immeasurably small. The detrital feldspars are on the other hand integral to the load-bearing framework but alteration of siliciclastic minerals takes much longer than carbonate alteration and it's unlikely to have an impact on the injection phase timescales. Studies of analogue reservoirs which remain water wet have, however, shown that over geological time-scales all feldspars can be dissolved and replaced by authigenic clays. For example, the average feldspar content in reservoir sandstones in the Otway Basin, Australia, is highly dependent on the CO₂ content of the reservoir – high CO₂ reservoirs have <1% feldspar whilst low CO₂ reservoirs have ~25% detrital feldspar (Higgs et al, 2014). Long term geological modelling of CO₂ interaction with the Endurance Storage Site suggests that K-feldspar will dissolve rapidly in the first few hundred years followed by a long period of slower precipitation which will restore the initial K-feldspar content after approximately 10, 000 years (see Figure 4.67).

Experimental studies on CO₂ injection into Rotliegend gasfields (alluvial fan Slochteren Formation) of Netherlands, Germany, and Poland also hold some lessons for the Endurance Storage Site even though the reservoir mineralogies of these fields differ from that of Endurance. Short term effects (30 day, 300bar, and 100°C) include partial dissolution of feldspar, anhydrite, carbonate, kaolinite; followed by precipitation of halite as the porewater dries into the CO₂. Addition of 100 ppm and 5000 ppm H₂S trace quantities produced significant growth of anhydrite with pyrite, and severe halite precipitation. The injection of pure CO₂ led to 10 – 30% increase in reservoir permeability whilst caprock permeability increased by 3x to 10x – although it was still in the micro Darcy range and provided a good seal. With 100 ppm and 5000 ppm H₂S added to the CO₂ stream, permeability increased after 30 – 80 days by between +3% for reservoir and 30% for the caprock as halite precipitation come to be dominated by mineral dissolution of the rock framework. The CO₂ stream specification for transportation to and storage at Endurance precludes processing streams with these high levels of H₂S.

Figure 4.72: Bar Chart Illustrating The Brine Salinity of the Endurance Reservoir Compared to Other CO₂ Storage and CO₂-EOR Operations. Red at Snohvit indicates injectivity problems partly related to near well mineral precipitation. Ketzin not included due to gas phase injection



4.12 Overview of plausible leakage pathways

All available evidence suggests that White Rose CO₂ injected into the Endurance structure will be securely and permanently stored. It is nevertheless important to consider the consequences to storage integrity of significant deviations of Storage Complex behaviour from what current interpretation of available data would suggest as this usually forms the basis for risk assessment and the development of the MMV and corrective measures plan. A number of possible CO₂ leakage pathways have been analysed under alternative evolution scenarios of the Storage Complex based on plausible assumptions about selected geological features and the injection wells penetrating the Bunter sandstone.

4.12.1 Reservoir Leakage Through the Primary Seal and Secondary Seals

4.12.1.1 *via Faults/Fractures*

All the faults above Endurance structure interpreted from seismic sole out above the Rot Halite secondary seal and none was interpreted to penetrate the Bunter sandstone (see Section 4.4.2). Since the faults seen on the seismics do not extend through the deepest secondary seal and then through the primary seal into the reservoir, the possibility that there are existing sub-seismic fractures through the primary seal is now considered. If these fractures connect to a sufficient number of shallower sub-seismic fractures, or if they connect the reservoir to shallower faults that are visible on the seismics (Figure 4.73), possibly a pathway for CO₂ leakage could be formed – it should be noted that there is no evidence to suggest that the shallow faults are open. In order for leakage outside of the Storage Complex to occur, these fractures must not have been closed by creep of the salt, the fractures are closed but not fully sealed due to the roughness of the fracture surfaces, or these existing fractures must be re-opened.

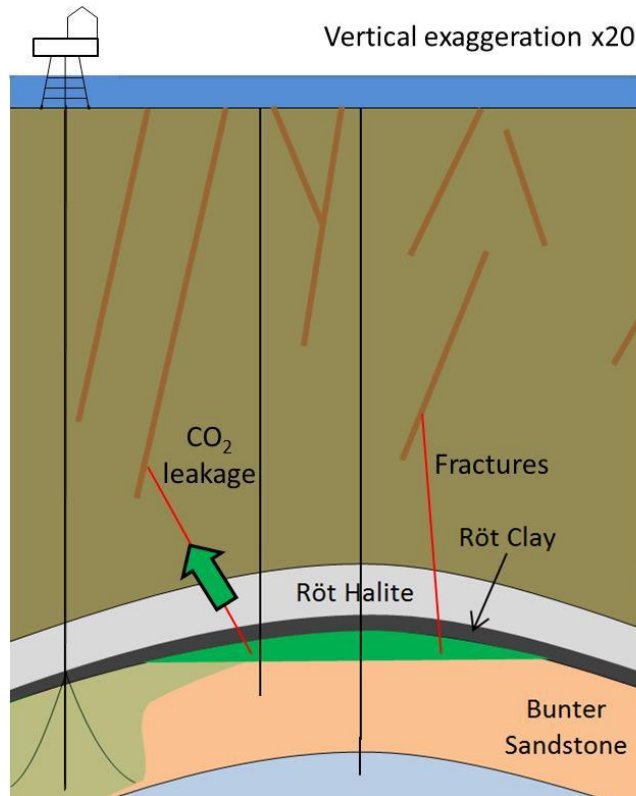
It is unlikely that the sub-seismic fractures have not been closed by creep of the salt as demonstrated by the high overpulls recorded when drilling well 42/25-1 through the Röt Halit. Leakage might occur on closed fractures that are not fully sealed due to the roughness of the fracture surfaces. This might occur in the Röt Clay and overburden, but it is less likely to occur in the halite.

The fracture closure pressure of the Röt Clay is higher than the expected peak BHP (Ref 12), so opening of fractures by pressure increase around the wells, and throughout the wider reservoir should not be possible. There are unlikely to be weaker areas of rock in which the fracture closure pressure is significantly lower because key controls on the closure pressure are the weight of the overburden and the regional tectonic stress field. This expectation is supported by comparison of the fracture closure pressures in the Bunter Sandstone and the Röt Clay, which are similar despite their significantly different lithologies. The fracture closure pressure in the Röt Halite is also likely to be higher than the peak reservoir pressure for the same reason. This expectation is supported by calculations of the fracture gradient with depth using the method of Matthews and Kelly. The calculated fracture gradient is consistent with the results of the mini-frac tests on the Röt Clay and Bunter Sandstone, so there is confidence in the calculation results for the Röt Halite.

It is possible that there could be thermal fracturing of the sandstone around the injection wells. The injection horizons should be located sufficiently far from the Röt Clay that there is no risk of fracturing it. Fractures through the Röt Clay could potentially occur if the extent of thermal fracturing has been underestimated, however it is exceedingly unlikely that thermal fractures could extend right through the Röt Halite. Even if this was to occur, the reservoir gas pressure, and hence the gas pressure in the fracture, would not be sufficient to hold the fracture open in the halite.

Overall, it is very unlikely that there is a pre-existing sub-seismic fracture CO₂ leakage pathway, or that existing fractures could be widened by CO₂ injection and thereby become leakage pathways. However, there is residual uncertainty due to the limit of resolution of seismic data.

Figure 4.73: Schematic Illustration of Leakage through the Primary Seal and Secondary Seals via Faults/Fractures Scenario



4.12.1.2 Diffuse Leakage

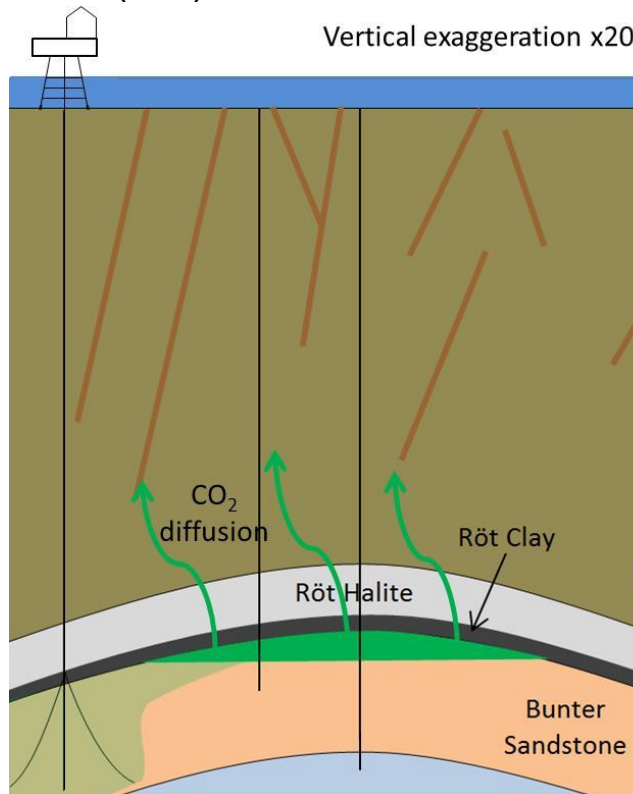
There are two possible mechanisms for diffuse leakage. The first is diffusion of CO₂ dissolved in brine (Figure 4.74), and the second is diffuse release of CO₂.

Rates of diffusion of dissolved CO₂ through the primary seal and secondary seals are expected to be very low due to the nature of the lithologies, as supported by the documented function of these formations as seals for the Bunter Sandstone gas fields in the SNS. Rates of diffusion might be increased if unconnected micro-fracturing is present, but would still be low. The highest potential flux would be associated with increased diffusion through micro-fractures into the larger faults that are visible on the seismics, if the larger faults are open. However, as already discussed, this is unlikely to be the case.

Free CO₂ would also be able to enter micro-fractures and thereby migrate over an area as wide as the area of micro-fracturing. Such migration could be considered diffuse. Where the micro-fractures connect to form a continuous pathway to the sea bed or an open fault, the initially diffuse migrating CO₂ would become progressively focussed, so that any CO₂ emissions at the seabed would tend to be at a number of localised points across a wider area. Alternatively diffusion could be increased through a combination of movement of a free CO₂ phase through micro-fractures, dissolution and diffusion through the rock into another micro-fracture.

Residual uncertainty remains because there is only limited spatial data on the properties of the rocks, and micro-fractures cannot be detected by seismics.

Figure 4.74: Schematic Illustration of Leakage through the Primary Seal and Secondary Seals by Diffusion Scenario (AE3.b).



4.12.2 Well Failure

4.12.2.1 Injection Wells

This scenario assumes that one of the injection wells will suffer early well seal failure, or significant accidental damage to the sea-bed exposure of the abandoned well, e.g. as a result of trawling activities post-abandonment (Figure 4.75). Three variants are explored:

1. failure/ damage during injection;
2. failure/damage on injection cessation; and
3. failure/damage a few hundred years after injection cessation.

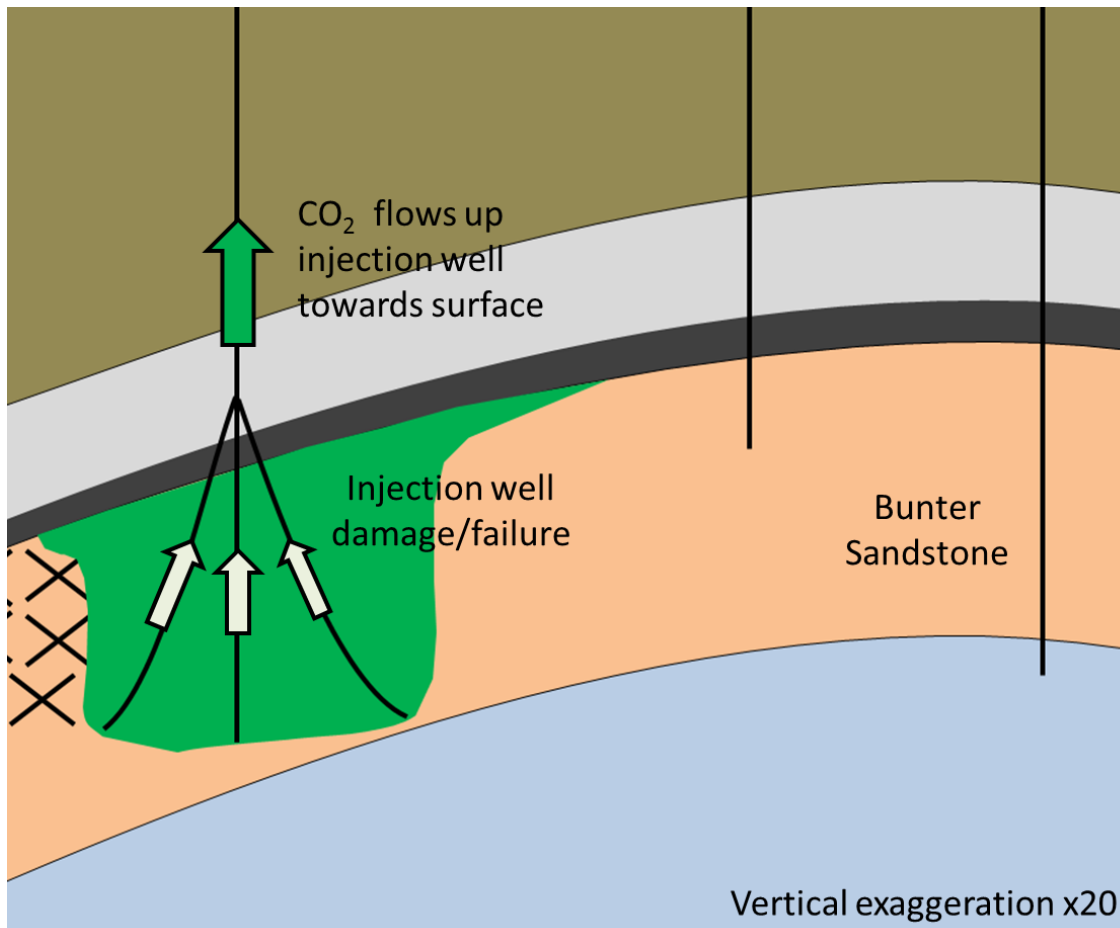
Operational issues that might affect the integrity of the wells and the success of sealing include:

- stresses on the wells due to daily changes in the CO₂ flux as the power station output is changed, and when the wells and / or power station are shut down for maintenance;
- if fluid phase changes were to occur in the wells;
- fracturing of borehole cements by induced seismicity and thermal fracturing associated with injection; and

- casing corrosion due to water washing and the resultant CO₂ – water mix in the wells.

Specific abandonment plans are being developed for the injection wells to provide the required long-term sealing and containment of CO₂. For example these include use of CO₂ resistant cement formulations and the possible removal of sections of the casing and surrounding cement by milling to ensure seals are in direct contact with the rock. If abandonment sealing of the wells was not successful, leakage of free CO₂ could only occur during the early post-closure period when there is free CO₂ around the wells. Once the majority of CO₂ has migrated to the top of the reservoir, significant leakage will not be possible.

Figure 4.75: Schematic Illustration of Well Failure: Injection Wells Scenario. Lower part of injection well only shown



Leakage of free CO₂ could be followed by longer term leakage of brine up the wells until the reservoir pressure returns to equilibrium. This brine could include a small amount of dissolved CO₂.

4.12.2.2 Other Wells

This scenario considers leakage from one of the other wells, and in particular the two abandoned crestal wells (42/25-1 and 43/21-1) (Figure 4.76). It also includes leakage from NGCL's abandoned appraisal well located on the flanks of Endurance (42/25d-3). However leakage from this well is much less likely since it

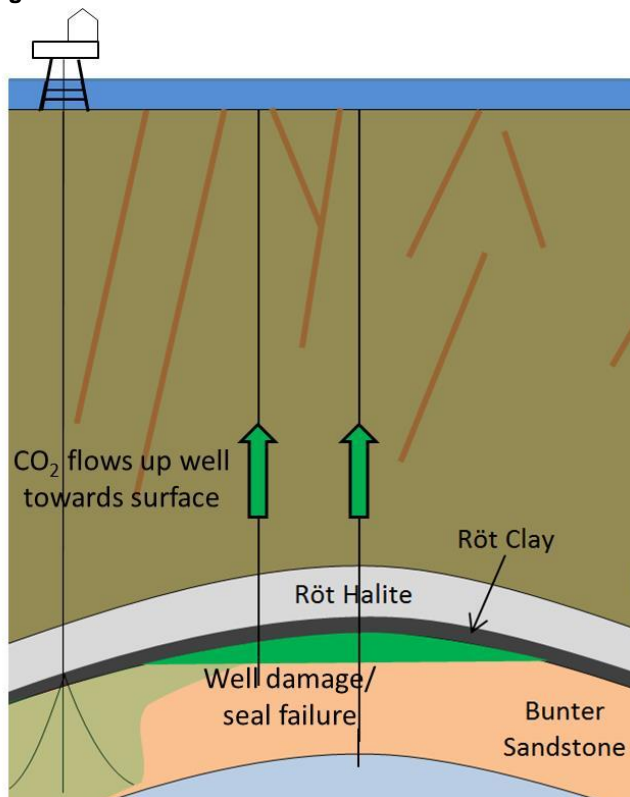
is down-dip of the most likely injection location and therefore may never be exposed to free CO₂. Three variants are explored:

- failure during injection;
- failure on injection cessation; and
- failure a few hundred years after injection cessation.

Although the crestal wells have been abandoned using multiple plugs, their abandonment was not optimised for long-term CO₂ storage, and they will be permanently exposed to the free CO₂ trapped at the crest of the anticline. Therefore there is a greater risk of leakage from these wells than from 42/25d-3 or the injection wells, although the risk may still be low.

The general conclusion is that the abandonment method of the two legacy wells will provide a robust mechanical seal to prevent leakage of injected CO₂. Any remedial work that may be required on these legacy wells will most likely be restricted to the setting depth of the 13-3/8" as the open hole below this casing shoe (548m in 42/21-1 and 557m in 43/25-1) would have closed over.

Figure 4.76: Schematic Illustration of Well Failure: Other Wells Scenario (AE5.b)



4.12.3 Conclusions Regarding Leakage Paths

Interpretation of a wide range of geophysical and well data show that the White Rose Storage Site is a large anticlinal Bunter sandstone structure formed over a Zechstein Halite diapir within the Triassic Haisborough Group of the Southern North Sea basin. It is overlain by a 10m thick Röt Clay of proven sealing quality and a 75m Röt Halite within the 900m thick Haisborough Group which also includes the Muschelkalk halite, Keuper anhydrite, and a number of shale layers that provide secondary sealing capability. All of the overburden faults visible on seismic terminate above the Röt Halite.

Sedimentological, log and core analyses show that the Storage Site is predominantly very-fine to fine-grained sandstone which is interspersed with thin mudstones that are interpreted to be laterally impersistent. Overall, the Storage Site is a homogeneous body of sand of excellent porosity and permeability. The net pore volume of the Storage Site estimated using the most likely structural closure of 1460m TVDSS is 4.6 Bm³, less than 2 % the maximum total White Rose Project CO₂ volume of 53.6MT.

5 Petrophysical Workflows & Coefficients

5.1 Summary

This Chapter provides a description of the petrophysical workflows and coefficients that have been used to generate reservoir properties from which have subsequently been used to build the static reservoir model. The 'best case' results of the interpretation are presented in addition to a discussion of the uncertainty ranges.

Petrophysical interpretation of Endurance and regional data demonstrate excellent reservoir quality within the White Rose CO₂ Storage Site and hence very good storage potential. Interpreted data came from thirteen wells, three of which penetrated the Bunter sandstone within the Endurance structure (43/21-1 drilled in 1970, 42/25-1 drilled in 1990, and the more recent CO₂ storage appraisal well 43/25d-3 drilled in 2013). The three wells that intercept the Bunter sandstone below the seismic phase reversal show pore occlusion by halite/anhydrite minerals; this leads to relatively poor reservoir quality at these depths. Some pore occlusion also occurs at the top of the Bunter although the general trend of reservoir quality is gradual deterioration with depth due to the effect of compaction. In general, the extent of halite/anhydrite cementation and its later dissolution is the primary control on rock quality in addition to depth of burial.

Core data was available for evaluation from only two of the 13 wells (well 42/25-1 and 42/25d-3). The average core corrected porosity was determined as 0.22 although when evaluate across all the wells porosity can exceed 0.30. The three wells drilled into the structural closure all show a ratio of NTG close to 100%. The sensitivity to porosity and NTG in 42/25d-3 and 42/25-1 is very weak. The sensitivities in the uncored wells in the AOI are much greater, largely due to data limitations.

The comprehensive coring programme in the 42/25d-3 appraisal well, which involved the recovery of full diameter cores across the full length of the Bunter sandstone, has enabled the development of a porosity-dependent permeability prediction algorithm, which can be used to extrapolate petrophysical properties in reservoir models.

5.2 Available Data

The available log database is summarised in Table 5.1 and indicates a range of reservoir properties derived from thirteen wells within a rectangular AOI around the Endurance structure; see Figure 4.39 in which the broken black line shows the licence block boundary straddling quadrants 42 and 43. Only three of these wells penetrated the structure, namely 43/21-1 drilled in 1970, 42/25-1 drilled in 1990, and the more recent appraisal well 43/25d-3 drilled in 2013. Well 43/21b-5z has only cased-hole sonic compressional and shear logs available, which are of poor quality and have not been used for quantitative analysis. Wells 42/30-6 and 43/28-3 only have gamma ray logs across the Bunter Sandstone. The data for 42/25d-3 was acquired for the purpose of appraising the Bunter sandstone interval. Therefore the data for this well is of a much higher quality (and quantity) compared to the older wells and includes a full range of conventional logs as well as NMR, ECS (elemental spectroscopy) and FMI (borehole image).

Table 5.1: Summary of available data by well

Well	Date	Gamma	Sonic	Resistivity	Density	Neutron	NMR	Core
42/24-1	1990	Y	Y	LLD				
42/25-1	1990	Y	Y	ILD	Y	Y		Yes
42/25-2	1995	Y	Y	LLD	Y			
42/25d-3	2013	Y	Y	HRLA	Y	Y	Y	Yes
42/30-5	1985	Y	Y	ILD				
42/30-8	1988	Y	Y	ILD				
43/21-1	1970	Y	Y	LL7	Y			
43/21-2	1991	Y	Y	ILD				
43/21-3	1994	Y	Y	RD				
43/21-5	2009	Y	Y	LWD				
43/21-5z	2009	sonic through casing only						
43/26-9	1991	Y	Y	ILD				
43/26-10	1998	Y	Y	RIPD	Y			
43/27-3	1991	Y	Y	RILD				

All the other wells (except 42/25-1) were drilled to appraise deeper Permian and Carboniferous targets. The wells were designed such that the Bunter section was drilled as an intermediate borehole. As a result, log coverage was largely limited to basic gamma, resistivity and sonic. Well 42/25-1 was drilled to target the Bunter structure and has a full range of conventional logs as well as core. However, the full Bunter section is not penetrated.

Data for ten of these wells was downloaded from the Schlumberger wells database that was built as part of a large regional project (Miersemann 2010); it included raw data as well as ELAN (computer based probabilistic method) interpreted porosity and lithology curves. Raw log data from the remaining three boreholes (42/25-2, 43/21b-5, 5z) has been purchased from IHS.

The log quality is acceptable over most intervals. Depth shifts were applied to the LL7 curve for well 43/21-1 in order to match the other logs. Minor adjustments were made to sonic and density curves over intervals of cycle-skipping and bad hole. The sonic log in 43/26b-10 appears to be in error (reading too slow) at the top of the Bunter where it is not consistent with the resistivity and density logs. The curve has not been edited, but has been discarded for quantitative evaluation.

Core was acquired in wells 42/25-1 and 42/25d-3 and the following depth shifts have been applied to match the log depths (Table 5.2):

Table 5.2: Shifts applied to Core Depths to match Log Depths

Well	Core Number	Depth From ft	Depth To ft	Shift ft	Depth From m	Depth To m	Shift m
42/25-1	1	3664	3678	11.5	1117	1121	3.5
	2	3713	3766	5	1131.7	1148	1.5
42/25d-3	1	4532	4621	3.5	1381	1408.5	1
	2	4622	4801.3	2.5	1408.75	1463.5	0.75
	3	4802	4981.3	2.2	1518.3	0.67056	0.7
	4	4982	5163.6	1.75	1518.5	1574	0.53

5.3 Petrophysical Evaluation

A detailed and high resolution model of the evaluation of 42/25d-3 has been developed using the acquired comprehensive log and core data set and is described below. Minor iterative changes have been made to the calculated log curves of the wells 42/25-1 and 43/21-1, which are high on the structure, above the halite cemented zone. However, no changes have been made to the calculation of the log curves for the remaining deeper wells, which were first outlined in Garnham 2013¹.

5.3.1 Clay Volume Determination

The gamma ray curve has been used to derive a Vclay curve and a 'normalised' GR curve. Linear normalisations have been used.

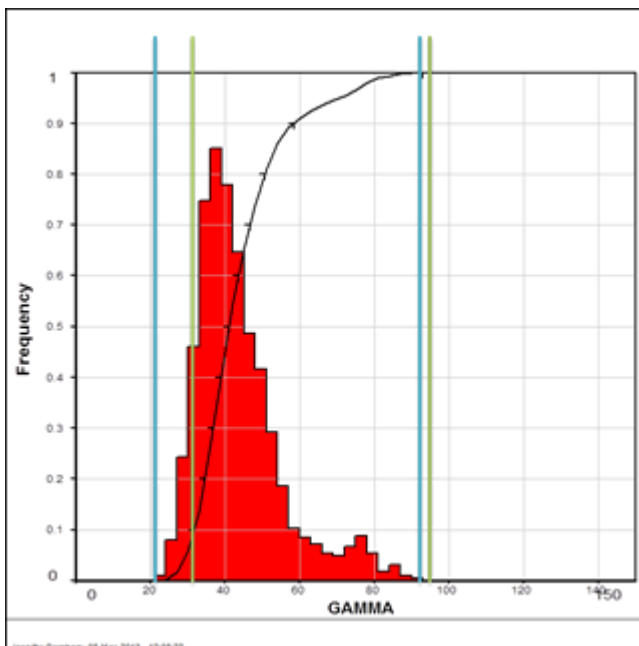
The objective of normalising the gamma is to enable quantitative comparison of the gamma response across the structure. This has been achieved by taking the lowest GR value within the Bunter sandstone as the zero point and just above the maximum GR value of the Rot Clay as the 100% point.

The objective of generating a Vclay curve is to quantify the clay content of the Bunter. The fluvial Bunter sandstones have a poorly sorted and complex detrital content. The gamma ray log responds largely to clay content, but also to non-clay minerals and detrital grains (such as feldspar and granitic grains/clasts). Therefore the baseline zero Vclay point is set above the minimum GR value of the Bunter at approximately the 15th percentile. The maximum Vclay is set just above the maximum of the Rot Clay. The normalisation to derive both curves is illustrated below in Figure 5.1 in which the blue lines represent the maximum and minimum values used for the GR_NORM curve and the green lines represent the maximum and minimum values used for the VCL curve. The end-member values of the gamma ray for each of the wells are shown in Table 5.3 below.

Table 5.3: End member values of gamma ray log used to determine Vclay and normalised gamma

Well	Bunter 100%	Rot Clay 0%	Bunter Mean	Normal GR		Vclay	
				GR min	GR max	GR Min	GR Max
42/24-1	22.4	87.8	42	22	92	32	90
42/25-1	32.8	112	47	32	117	42	115
42/25-2	64	143	83	64	150	75	148
42/25-3	24.8	152	57	30	145	47	140
42/30-5	22.4	106	45	22	110	35	115
42/30-8	22.4	117	44	22	117	35	120
43/21-1	28	96	45	28	100	38	100
43/21-2	18	81	30	18	85	25	85
43/21-3	19.2	84	41	19	88	30	92
43/21-5	88	159	108	88	165	100	160
43/26-9	27	137	54	27	142	40	140
43/26-10	26.2	130	49	26	135	40	140
43/27-3	27.4	130	53	27	135	40	140

Figure 5.1: Gamma Ray distribution plot of Bunter sandstone and Rot Clay



The comprehensive range of log data gathered in 42/25d-3 enabled a comparison between Vclay calculated from gamma ray and Vclay calculated from density/neutron (DN) crossplot technique. It was observed that the Vclay from DN was slightly lower than the Vclay from gamma ray, especially in the deeper part of the Bunter. Therefore in this well Vclay has been calculated using a minimum of both methods, which is believed to be closer to the true Vclay content of the rock. The density and neutron clay end members are 2.58 g/cc and 30% respectively.

5.3.2 Porosity Determination

Two different methods have been used to calculate porosity in these wells. The cored wells use a density porosity method that is calibrated to core porosity. The uncored wells use a sonic porosity which is optimised to match the density porosity, where available, and is consistent with low resolution resistivity porosity.

Porosity in 42/25-1 and 42/25d-3 have been calculated using the density log calibrated to core porosity. The equations used are: $PHIT = (RHOMA - RHOB)/(RHOMA - RHOFI)$; and

$$PHIE = (RHOB - RHOMA - V_{clay}(RHOCI - RHOMA))/(RHOFI - RHOMA)$$

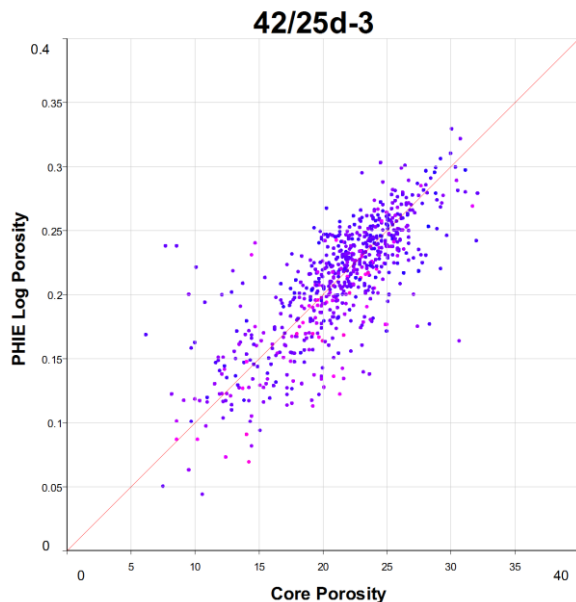
Table 5.4: Density Coefficients used to Calculate Porosity

Well	RHOMA	RHOFI	RHOCI
42/25-1	2.64	1.2	2.58
42/25d-3	2.67	0.98	2.58

Core porosity is often regarded as being close to $PHIT_{(density)}$ by assuming that aggressive core cleaning processes liberate clay-bound water. However, the core cleaning and drying process has been very carefully controlled for 42/25d-3, and it is regarded as unlikely that clay-bound water has been liberated. Therefore in this well, core porosity is assumed to be very close to $PHIE_{(density)}$ and the value of RHOFI has been optimised by minimising the difference between overburden-corrected core porosity (PHI_{ob}) and PHIE (Figure 5.2). RHOMA is taken from the modal core grain density values.

$$PHI_{ob} = \text{Core porosity} \times 0.96$$

Figure 5.2: Overburden Corrected Core Porosity vs. PHIE from Logs



The porosity calculation in the other wells is limited by the available data. The sonic log is the only porosity curve that is common to all wells and has been used to calculate porosity on the structure. Where available, the density log has been used to confirm the sonic porosity.

The Bunter sandstone in this structure is known to have a complex and variable mineralogy. In particular halite is known to have precipitated as a cement phase in some of the wells. Each mineral phase responds differently to the sonic and density logs, which leads to uncertainty in the porosity calculation. Schlumberger (Miersemann 2010) have approached this problem by using a multi-mineral approach to solve for porosity and mineralogy. However, the rocks have many unknown minerals and only two curves with which to accurately derive a multiminer solution (i.e. an underdetermined solution). Furthermore, the solution is difficult to replicate and verify.

A pragmatic, deterministic method has been adopted by this study. Porosity is calculated using the sonic log. Preliminary matrix and fluid coefficients are defined in the wells with strong core control and a range of available curves (cored wells and wells with density as well as sonic logs). A preliminary porosity is calculated and compared to a 'resistivity porosity', after which final adjustments to the matrix coefficients are made.

The resistivity porosity is calculated by reconfiguring the Archie equation using the assumption that the reservoir fluid is 100% water:

$$Porosity = \frac{Rwa^{1/m}}{Rt}$$

Where Rw = water resistivity;
 Rt = True Resistivity (from deep resistivity curve); and
 a, m = Archie exponents.

Resistivity porosity is a low resolution curve as it is derived from the deep resistivity log which has a large sample volume and low vertical resolution. However, in this context it is useful to help verify the sonic porosity, as the resistivity tool is not influenced by the mineral composition of the matrix. The sonic porosity coefficients are listed below in Table 5.5:

Table 5.5: Sonic Porosity End-Members

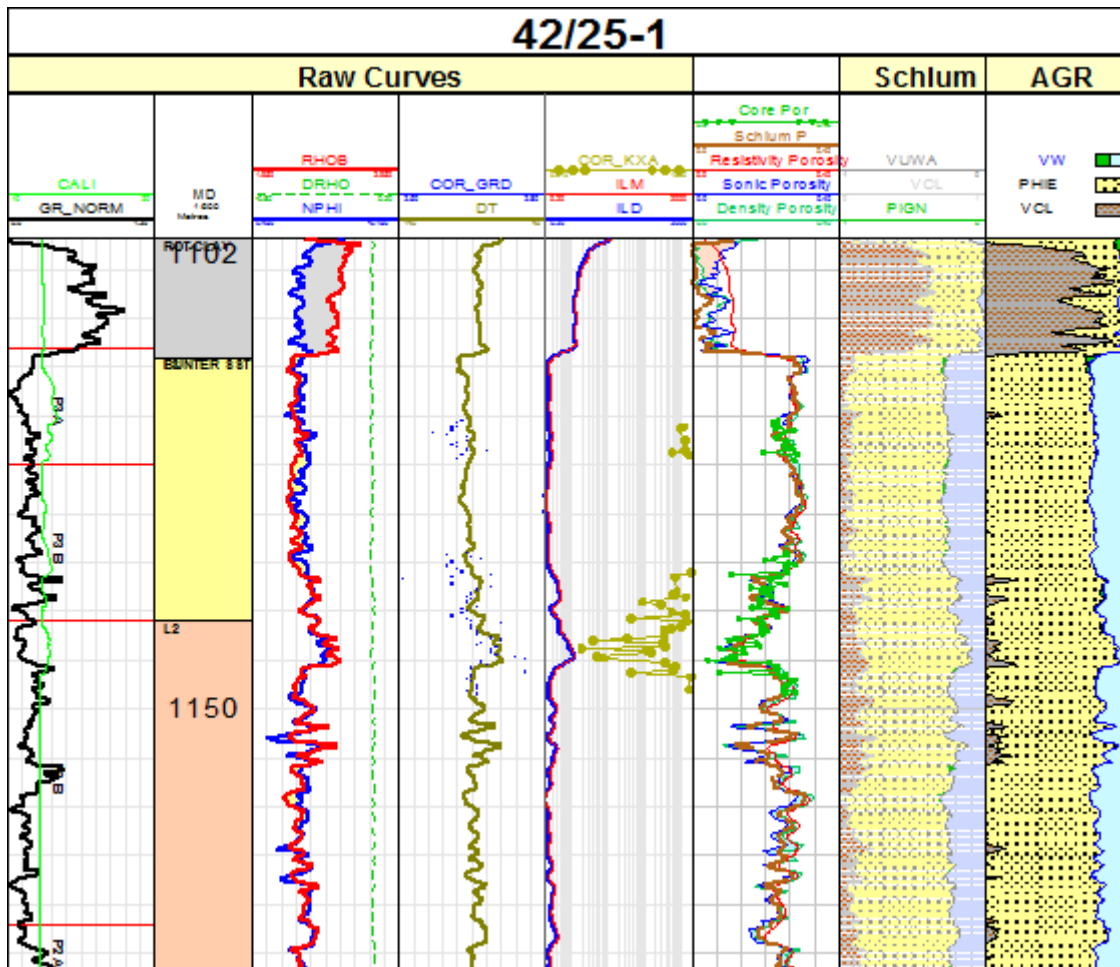
Well	Dtma	DTfl	DTcl
42/24-1	53.5	189	70
42/25-2	55.5	189	70
42/30-5	55	189	70
42/30-8	54	189	70
43/21-1	55	189	80
43/21-2	55	200	70
43/21-3	55	189	75
43/21-5	54	189	70
43/26-9	55	215	75
43/26-10	55	200	75
43/27-3	55	200	75

The sonic log in well 43/26-10 displays anomalous and incorrect values in the upper 23 feet of the Bunter Sandstone, therefore a resistivity porosity is used across this interval.

An example of porosity calculations from the sonic, density and resistivity logs are displayed below in Figure 5.3 and compared against the ELAN output porosity curve from Schlumberger (Miersemann 2010) and the core porosity. All the log calculations are consistent with the overburden-corrected core porosity.

Note that Schlumberger multimimeral porosity (brown) and core plug porosities (green points, which have been depth shifted to match log depths) are also shown in track 6 (sixth column).

Figure 5.3: Comparison of calculated porosity curves using density, sonic and resistivity logs



5.3.3 Permeability Prediction

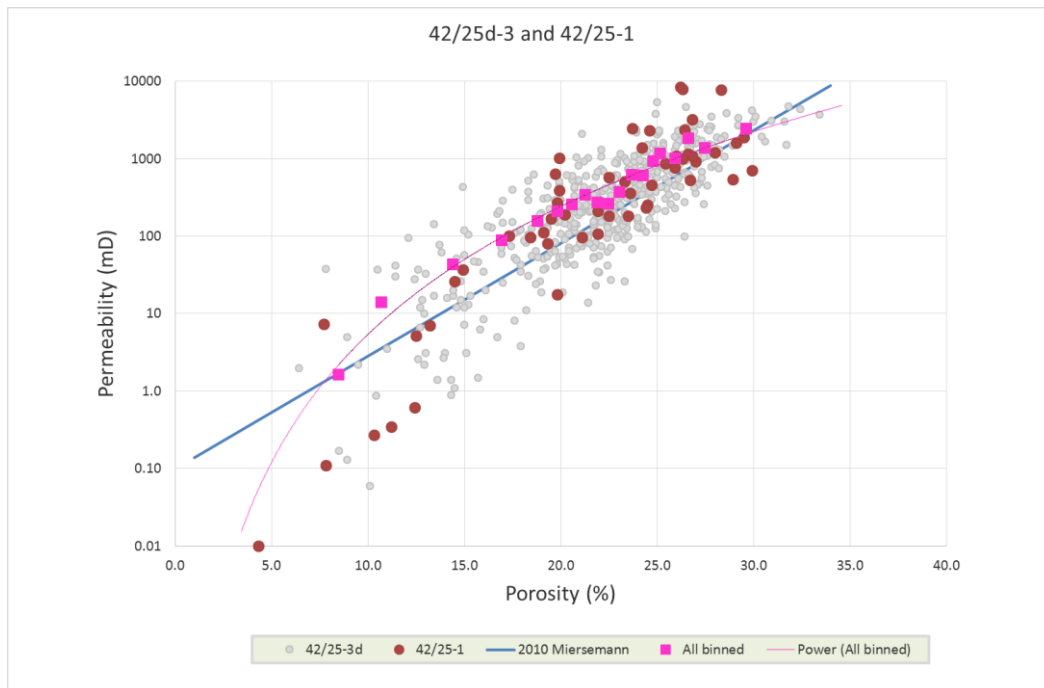
The acquisition of full diameter core in 42/25d-3 across the majority of the reservoir interval and the subsequent analysis of porosity and permeability from plugs has enabled the derivation of a permeability prediction algorithm. The algorithm is dependent on porosity and can be extrapolated for use in the reservoir models.

The plugs (cylinders of approximately 37mm diameter and 57mm length) were cut horizontally to the bedding orientation at a spacing of approximately one 270mm. (Further plugs were also cut vertically to the bedding at a spacing of approximately one meter, but the permeability values were excluded from the analysis to derive an algorithm). The plugs were cleaned and dried prior to analysis. A cleaning study was performed to ensure that delicate clays and soluble minerals (halite) were not damaged by the cleaning process.

A plot of porosity versus permeability (logarithmic) shows the range of the data, which covers a similar range to the smaller data set derived from 42/25-1 (Figure 5.4). A prediction algorithm can be derived by a

regression through the data, similar to the algorithm derived by Miersemann (2010). However, a simple regression of all the data on a logarithmic/linear plot statistically generates a prediction trend which will produce a geometric average of the permeability data. Reservoir behaviours are observed to conform more closely to the arithmetic average of permeability. Therefore, in this study, a binning technique has been used to derive a prediction that is closer to the arithmetic average. The data is sorted according to porosity and subdivided into a number of bins. The arithmetic average of porosity and permeability are calculated for each bin; which are subsequently plotted on a logarithmic/linear crossplot. The prediction algorithm is derived from a regression of the binned data. The binned data points are plotted (pink) alongside the plug data from both wells (Figure 5.4). The blue trendline illustrates the previous prediction algorithm (Miersemann 2010), the pink trendline is a power law regression through the binned data.

Figure 5.4: Porosity versus Permeability crossplot from 42/25-1 and 42/25d-3.



The pink curve was adopted as the 2014 permeability prediction algorithm.

The final algorithm is as follows:

$$\text{Permeability} = 2000000 \times (\text{porosity } 5.4833) \quad (\text{porosity is decimal}).$$

A comparison of the predicted permeability from the porosity log using this algorithm and core permeability is shown in the left-hand plot from Figure 5.5, the red line, represents a line of unity.

The output from the CMR log (magnetic resonance, NMR) can also be processed to generate a permeability curve using the modified Timur-Coates equation

$$\text{Permeability} = a \times ((\text{FFV}/\text{BFV})^c) \times ((10 \times \text{PHI_CMR})^b)$$

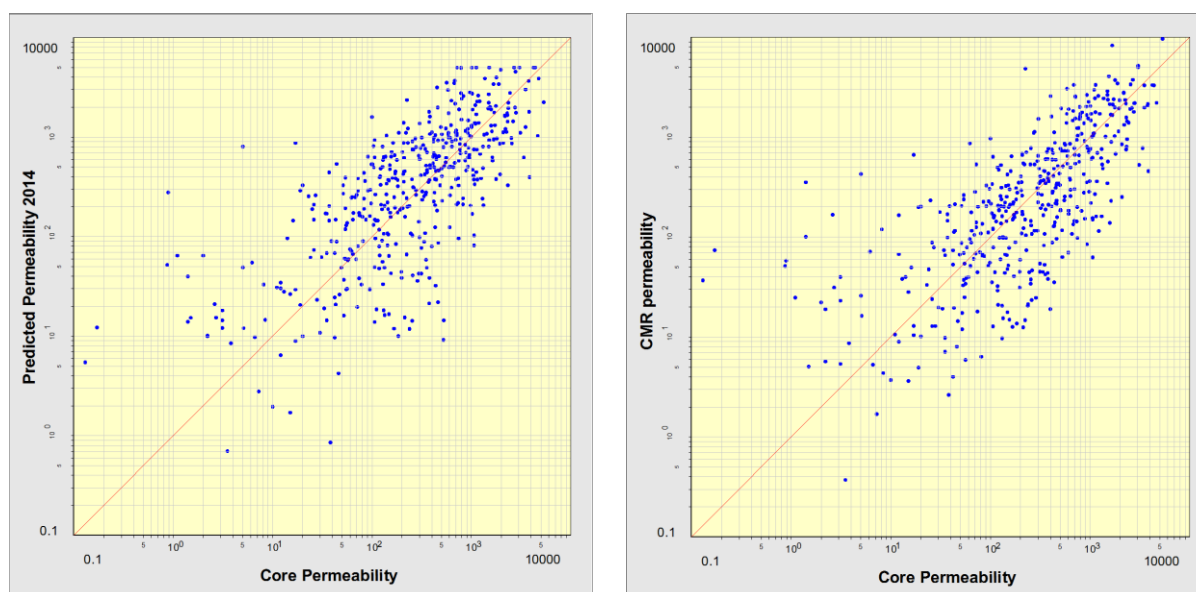
Where FFV = Free Fluid Volume;

BFV = Bound Fluid Volume;
 PHI_CMV = Total Porosity from CMR; and
 a, b, c = coefficients.

The default values for the coefficients a, b, c are 1, 4, and 2 respectively. These values were used in Garnham 20132 to derive a first pass CMR permeability log. However, the calculation can be calibrated using core analysis data to optimise these coefficients. The calibrated coefficients a, b, c are 12.6, 1.47, 2.76.

The modified Timur Coates equation has been used to build an updated CMR permeability curve (Figure 5.5, right-hand plot), which is observed to be consistent with the core analysis data, and with the updated prediction algorithm previously described (Figure 5.5, left-hand plot).

Figure 5.5: Comparison of Core Permeability Versus. Predicted Permeability from Algorithm (left) and Core Permeability Versus. Optimised Cmr Permeability (right)



It is recommended that the permeability algorithm derived from core analysis data is used as the reference case permeability curve. This algorithm has the advantage that it can be implemented in a reservoir model where porosity is distributed as a property. However, the permeability from CMR can be viewed as an alternative, independent, deterministic realisation, which can be used to understand uncertainty ranges.

5.3.4 Net Reservoir Determination

In conventional hydrocarbon exploration the definition of “net” is usually taken to be, “reservoir rock that is capable of storing hydrocarbon under the current conditions of reservoir pressure, temperature and fluid type”.

In order for a rock to be considered net, the reservoir fluid (oil or gas) must be able to enter part of the pore network as a result of buoyancy or capillary forces overcoming the pore entry thresholds which are

functions of fluid-fluid interfacial tensions, fluid contact angles and pore sizes. Once the fluid is in the pore network, however, the strength of fluid-fluid and rock-fluid molecular interactions can significantly affect the permeability of the fluid through the pore network. Due to the relatively weaker inter molecular forces in gases relative to liquids the permeability to gas is generally greater than permeability to liquid under the same pressure gradients. The phenomenon is the well-known Klinkenberg effect. Consequently, it is generally observed that gas molecules are able to enter lower permeability reservoirs than would oil; therefore the threshold permeability, used to define net, is lower for gas than oil. These thresholds are determined by capillary pressure measurements on core plugs and are converted to reservoir conditions using empirical understanding of the behaviour of the two fluid phases in a capillary system. Very often a rule of thumb approach is used, whereby the threshold permeability to oil is defined at 1mD and the threshold permeability to gas is defined as 0.1mD.

For the purposes of the White Rose project the fluid type is CO₂, but its physical behaviour within a brine-filled pore network is less well researched. Hence, it is not yet possible to accurately define a threshold permeability to determine net reservoir. Therefore a range of thresholds have been applied.

The threshold values used are expressed in terms of porosity, as permeability is not directly calculated from the logs and these porosity based threshold values can be compared with previous interpretations (Miersemann 2010), where a threshold value of 12% porosity has been used. The relationship between porosity and permeability that has been used to derive these thresholds has been outlined above. The three porosity values used are listed below:

1. 4.65% (0.1mD) – equivalent to typical light natural gas threshold;
2. 7% (1mD) – equivalent to a typical light oil threshold; and
3. 12% (Miersemann 2010) – defined as being a threshold above which the reservoir volumes are insensitive.

5.3.5 Water Saturation

The calculation of water saturation is not relevant to this study, as no hydrocarbons are present. No gas was identified whilst drilling any of the wells above the structural closure. Rock properties and capillary pressure testing indicate that there is potential for the reservoir to accommodate a high gas/CO₂ saturation.

5.3.6 Electrofacies

A simple log-derived facies scheme (electrofacies) has been developed to assist geological modelling. The logs within the Bunter Sandstone are responding largely to diagenetic controls, rather than primary depositional facies. Therefore the electrofacies relate to post-depositional diagenetic processes which have created varying amounts of cementation and porosity reduction. The derivation of the facies scheme is fully described in Garnham 20131.

The majority of the wells have only three log curves and the electrofacies scheme is limited to these curves to ensure a consistent approach across the region. The workflow uses a 'rules-based' categorisation, which is then interactively fine-tuned to overcome intervals of poor or ambiguous log responses, see Table 5.6.

Table 5.6: Summary of Log-Derived Facies

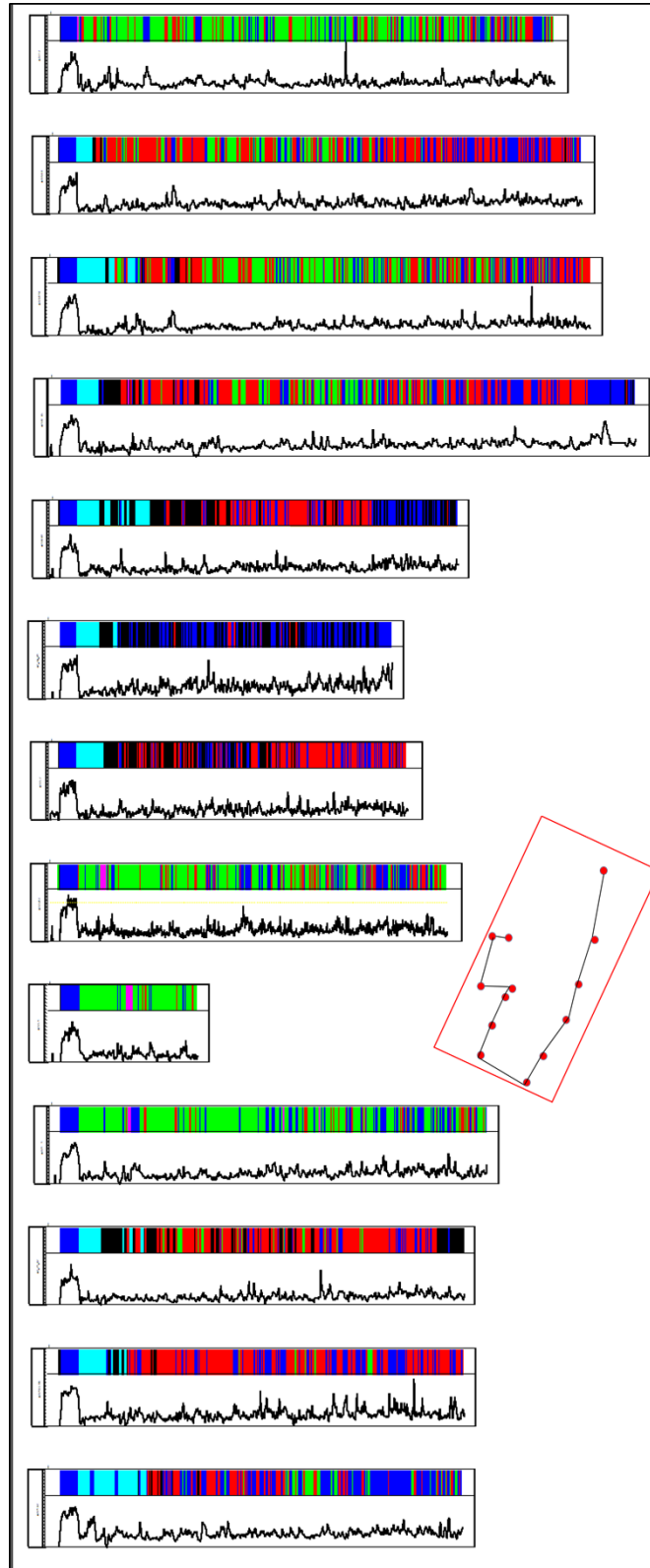
Facies	Log Character	Geological Interpretation
1	RT > 0.2 ohmm	Cemented Sand
2	Remainder, not defined by other facies rules	Partially Cemented Sand
3	DT > 80 μ s/ft	Good Sand
4	GR_Norm > 0.3	Heterolithic & Clay-Rich Sand
5	very high resistivity, very low sonic	Cemented Plugged Sand
6	Very low GR, low porosity	Dolomite Cemented Sand

Facies 1 – 5 are automatically picked using the log threshold criteria shown in Table 5.6. The resistivity threshold for Facies 5 is set per well (usually $R_{deep} > 15 - 20$ ohm). Facies 6 corresponds to a thin, correlatable layer toward the top of the Bunter Sandstone and is picked by hand per well. Small adjustments are made by hand and include small intervals of high porosity (>17%) that automatically are binned into Facies 4 and are transferred to Facies 3 prior to incorporation in the geological model (Wright 2014).

In a series of integrated CPI log plots (Figure 5.6), the crestal wells, 42.25-1, 42/25-2 and 42/25d-3 show predominantly good facies (green). All other wells, except 43/27-3 show cemented, plugged sand (turquoise) at the top of the Bunter. Heterolithics are observed to increase with depth in all wells and are the dominant facies in 42/24-1. The wells to the south and east of the structure show better reservoir quality than those to the north and west.

The plugged, cemented facies (5) is believed to be caused by occlusion of the pore space by halite and anhydrite (Chemostrat 2014, Blackburn and Robertson 2014) and corresponds to a seismic inversion (Dingwall et al. 2103). Early models implied total plugging of the pore space below the seismic inversion had occurred. However, the log interpretation demonstrates that total pore occlusion only occurs in the upper parts of the reservoir and the deeper layers can have moderate to good reservoir quality.

Figure 5.6: Summary of Bunter Sandstone Facies Picks by Well



5.4 Results by Wells

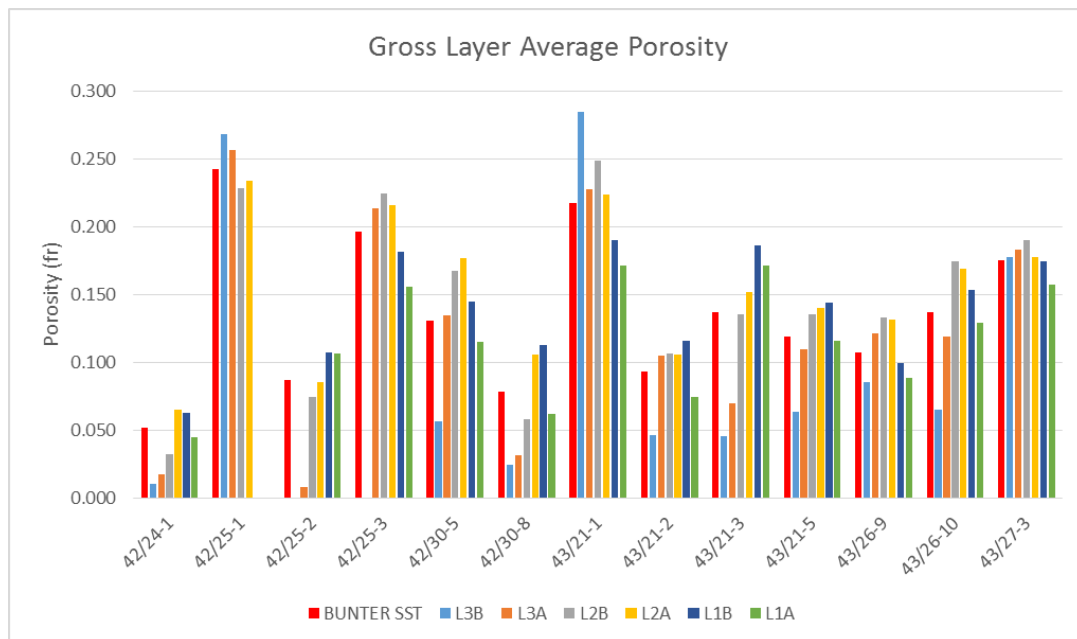
A summary of the properties of the Bunter sandstone calculated for the wells in the AOI is given below (Table 5.7). The net porosity cut-off used to generate this table is 7 percent.

Table 5.7: Average Reservoir Properties for Bunter Sandstone Interval using a 7% Porosity Cut-Off

Well	Zone	MD From m	MD To m	TVD From m	TVD To m	Gross Thickness	Net Thickness	NTG	Average Net PHIE	Average Net PHIT	Average Total PHIE
42/24-1	BUNTER SST	1574.0	1764.0	1535.6	1725.5	189.9	45.9	0.242	0.082	0.098	0.052
42/25-1	BUNTER SST	1113.5	1185.0	1075.1	1146.6	71.5	71.1	0.995	0.243	0.243	0.242
42/25-2	BUNTER SST	1733.0	1933.0	1662.5	1861.8	199.9	133.2	0.666	0.112	0.127	0.087
42/25-3	BUNTER SST	1408.0	1631.2	1368.7	1591.0	223.3	221.0	0.990	0.198	0.197	0.197
42/30-5	BUNTER SST	1468.7	1805.0	1399.0	1734.2	336.2	298.1	0.887	0.142	0.158	0.131
42/30-8	BUNTER SST	1687.4	1917.0	1617.0	1845.8	229.5	117.2	0.511	0.110	0.124	0.078
43/21-1	BUNTER SST	1057.3	1303.5	988.3	1234.3	246.3	246.1	0.999	0.218	0.240	0.217
43/21-2	BUNTER SST	1818.0	2051.0	1747.2	1979.6	233.0	158.2	0.679	0.115	0.127	0.093
43/21-3	BUNTER SST	1614.0	1846.0	1543.9	1774.9	232.0	189.4	0.817	0.158	0.169	0.137
43/21-5	BUNTER SST	2092.0	2325.0	2050.9	2283.8	232.9	204.5	0.878	0.130	0.147	0.119
43/26-9	BUNTER SST	1903.0	2208.0	1861.9	2166.9	305.1	264.3	0.866	0.117	0.137	0.108
43/26-10	BUNTER SST	1469.5	1779.0	1429.5	1739.0	309.5	273.1	0.882	0.151	0.167	0.137
43/27-3	BUNTER SST	1621.0	1909.0	1583.8	1871.6	288.0	286.8	0.996	0.176	0.194	0.176

The proportion of NTG is very high in most of the wells and approaches a value of one in the three wells in the Endurance structure.

Table 5.8: Average Layer Porosity without Cut-Offs



The average porosity of the Bunter Sandstone ranges from 5 – 24%. The highest porosities are seen in the youngest layers (L3B and L3A) of the three shallow wells within the Endurance structure (42/25-1, 42/25d-3 and 43/21-1) (Table 5.8). The wells to the South and East of the region have the best porosity in the middle of the Bunter Sandstone, e.g. 43/26-10 shows the highest porosity in layers L2A and L2B, but the deeper wells to the North and West of the structure have the best porosity in the deepest layers, e.g. 43/21-3.

The porosity appears to be controlled by three factors:

- diagenesis – especially pore-occluding halite/anhydrite growth;
- primary depositional facies and clay content; and
- depth of burial.

5.4.1 Diagenesis

The upper layers of a number of the wells in the AOI have been severely affected by pore-occluding minerals, hence the average porosities of layers L3B and L3A are lower than the deeper layers. In these wells an interval of Bunter sandstone between 3m to 40m thick has porosity calculated to be below 2%. The indications from the petrography and logs is that these intervals have their primary porosity occluded by halite/anhydrite cements (Blackbourn and Robertson 2014). The cements appear to be localised to the upper parts of the reservoir and do not appear to have affected deeper layers in these wells. Note that Blackbourn and Robertson (2014) have proposed that these halite/anhydrite cements have been largely removed from the pore space by dissolution in the shallower wells on the structure.

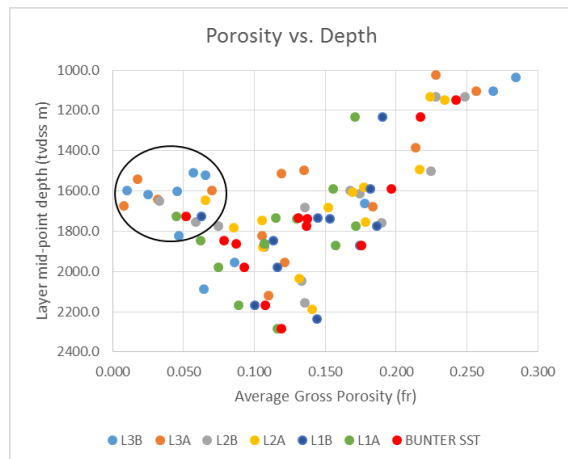
5.4.2 Primary Depositional Facies

The low quality depositional facies (playa mudstones and marginal facies) are more common in the deeper stratigraphic levels and the sediments indicate a 'cleaning upwards' profile (Wright 2014), which is reflected in the general porosity decrease with depth seen in the three crestal wells. However, Wright (2014) also demonstrated that reservoir quality in the sandy facies was independent of facies type.

5.4.3 Depth of Burial

The deeper wells in the AOI generally have a lower porosity, which reflects the depth of burial. A plot of porosity vs. depth demonstrates the burial trend (Figure 5.7), but shows some scatter. The data points circled are the layers affected by later diagenesis. However, other deviations from the trend can be explained by the non-uniform inversion, where wells to the South and East of the field have been uplifted by a greater amount than wells to the North and West (Garnham 2013, Dingwall 2013).

Figure 5.7: Average Layer Porosity vs. depth. Circle shows wells affected by halite / anhydrite / dolomite pore-occluding cements



5.5 Uncertainties and Sensitivities

The uncertainties on porosity and net thickness are co-related, as the calculation of net thickness uses a porosity threshold. However, their uncertainty is addressed independently using deterministic methods.

5.5.1 NTG Sensitivity

The final results are presented using a range of porosity cut-offs to define net reservoir. Most wells show a net thickness between 200m to 300m using either the 4.65% or 7% porosity threshold (Figure 5.8). However, net thickness is significantly reduced in many wells when a stricter 12% cut-off is applied. It should be noted that the NTG of the three wells within the Endurance structure is close to 1, even using the 12% cut-off.

The sensitivity of this net cut-off has been further examined in a step by step process for each of the wells (Figure 5.9). The plot shows the calculated value of NTG for each well using porosity thresholds ranging from 0% to 15%. The wells on the Endurance structure (and 43/27-3) are insensitive to the porosity cut-off. However, other wells, especially those to the west of the AOI are very sensitive to the cut-off.

Figure 5.8: Comparison of Net Thickness and NTG for each Well Using Three Porosity Cut-Offs

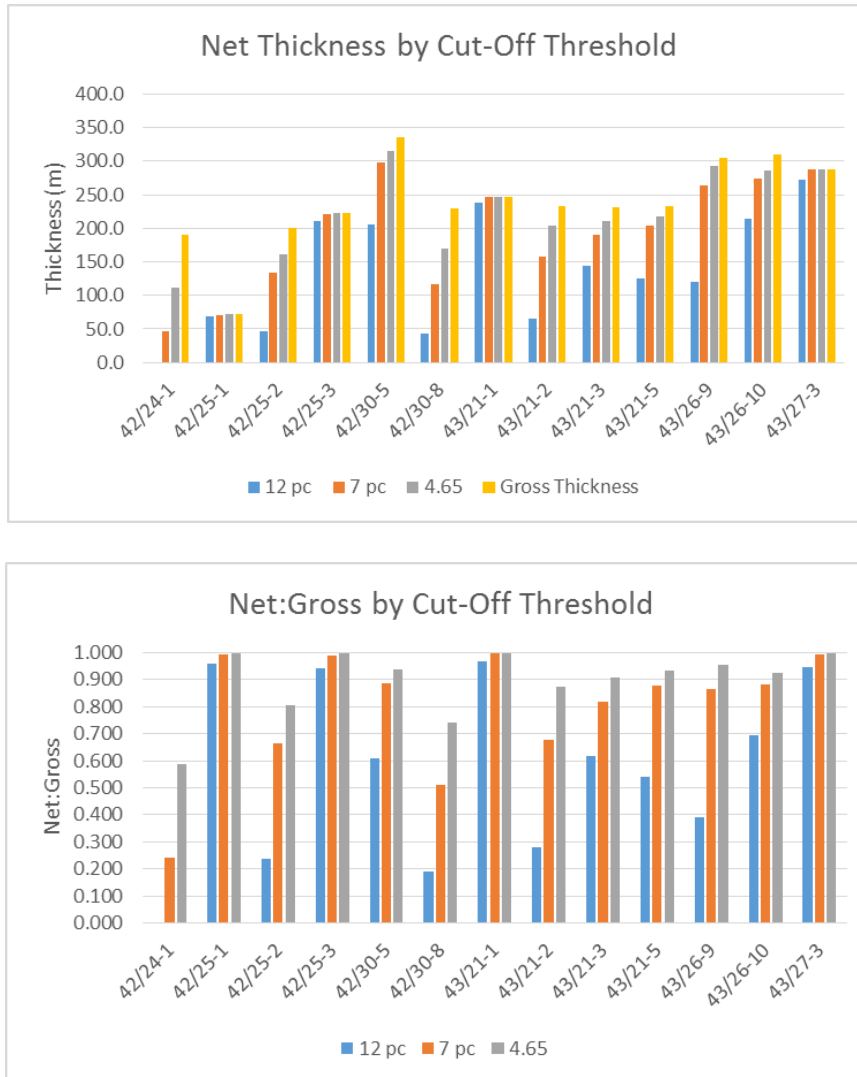
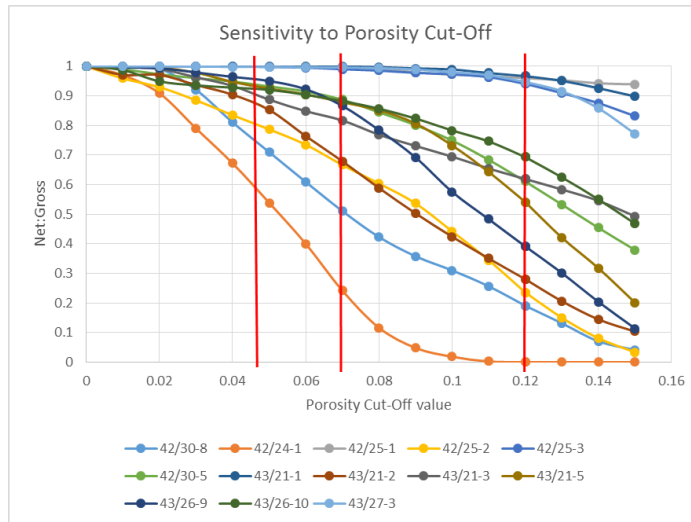


Figure 5.9: Sensitivity of NTG value across the entire Bunter Sandstone using a range of Porosity Cut-offs from 0% to 15%.



Note: the red lines show the 4.65%, 7% and 12% values provided in the tabulation

It is concluded that the Bunter Sandstone in the Endurance structure is insensitive to the porosity cut-off for the majority of the structure. However, there may be some sensitivity in the deeper intervals, where the overall porosity will be lower.

5.5.2 Porosity Sensitivity

The sensitivity of the porosity calculation is addressed separately for the cored wells and uncored wells respectively.

5.5.2.1 Cored Wells

The log porosity calculated in the cored wells uses a fixed matrix density, taken as the modal grain density from core analysis. A fluid density is then optimised by performing a regression of log density upon core porosity. The systematic uncertainty is explored by adjusting the matrix density by +/- one Standard Deviation of the core grain density. Each adjustment requires a further recalculation of the fluid density to ensure that the core porosity is honoured. The values used for the two cored wells and the resultant porosities demonstrate a very low sensitivity (approximately 0.2%) (Table 5.9).

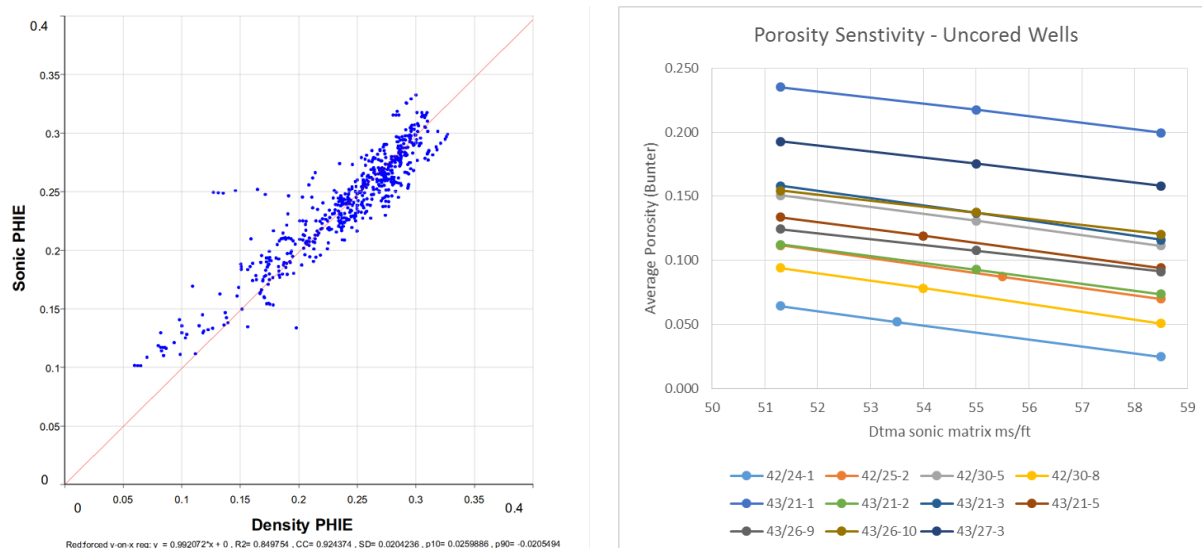
Table 5.9: Sensitivity of Porosity in Cored Wells

Well	Case	RHOMA	RHOfl	Average Bunter Porosity	Porosity Difference
42/25-1	high	2.602	1.29	0.2427	-0.0018
	reference	2.64	1.2	0.2409	
	low	2.678	1.04	0.2363	0.0046
42/25-3	high	2.695	0.9	0.1985	-0.0019
	reference	2.67	0.98	0.1966	
	low	2.645	1.07	0.1958	0.0008

5.5.2.2 *Uncored Wells*

Porosity in the uncored wells is derived from the sonic log. In order to determine a systematic uncertainty, the variance of the sonic log compared to the density log is used. The crossplot of density porosity versus sonic porosity (Figure 5.10, left-hand plot) shows the Standard Deviation of the data to be 0.0204 porosity units. The sonic matrix values required to obtain porosity +/- one Standard Deviation are 51.3 ms/ft and 58.5 ms/ft respectively. High and low porosity values have been calculated in all the wells using these end members (Figure 5.10, right-hand plot). The porosity difference compared to the reference case averages 1.9%, with a high of 2.7% and a low of 1.2%.

Figure 5.10: Sensitivity of Sonic Porosity



Note: the left-hand plot shows density vs. sonic porosity and the right hand Plot shows the range of porosity using high and low values of DTma set at one Standard Deviation.

In addition to systematic uncertainties the important lithological uncertainty needs to be addressed. Variable amounts of diagenetic halite, anhydrite and dolomite are present (Blackbourn 2012, Purvis and Okkerman 1996, Blackbourn and Robertson, 2014). Whilst the amounts present are not known, the maximum (30%) and minimum (0%) are known. If zero diagenetic minerals are present, then DTma will be

set to the default value of 55 ms/ft. Theoretical values of DT_{ma} can be calculated for varying proportions of each mineral in the maximum case, and are found to range between 53 – 59.5 ms/ft, which are very similar to the systematic range described above. Therefore the uncertainty in porosity due to diagenetic effects is also likely to be +/- 2% porosity.

5.6 Conclusions

The evaluation of petrophysical data from well 42/25d-3 has demonstrated that the Endurance structure has excellent reservoir quality and good storage potential.

Regionally, the reservoir quality is more variable, and the wells which intercept the Bunter Sandstone below the seismic phase reversal show pore occlusion by halite/anhydrite minerals. The extent of halite/anhydrite cementation, and its later dissolution, is the primary control on rock quality in addition to depth of burial. The pore occlusion always occurs at the top of the Bunter Sandstone and in most wells moderate to good quality reservoir is present beneath the occluded zone.

Porosity can exceed 30% and permeability can be above 1000mD. The three wells drilled above the structural closure all show a ratio of NTG close to 100%.

The sensitivity to porosity and NTG in 42/25d-3 and 42/25-1 is very low. The sensitivities in the uncored wells in the AOI are much greater, largely due to data limitations.

6 Geomechanical Modelling

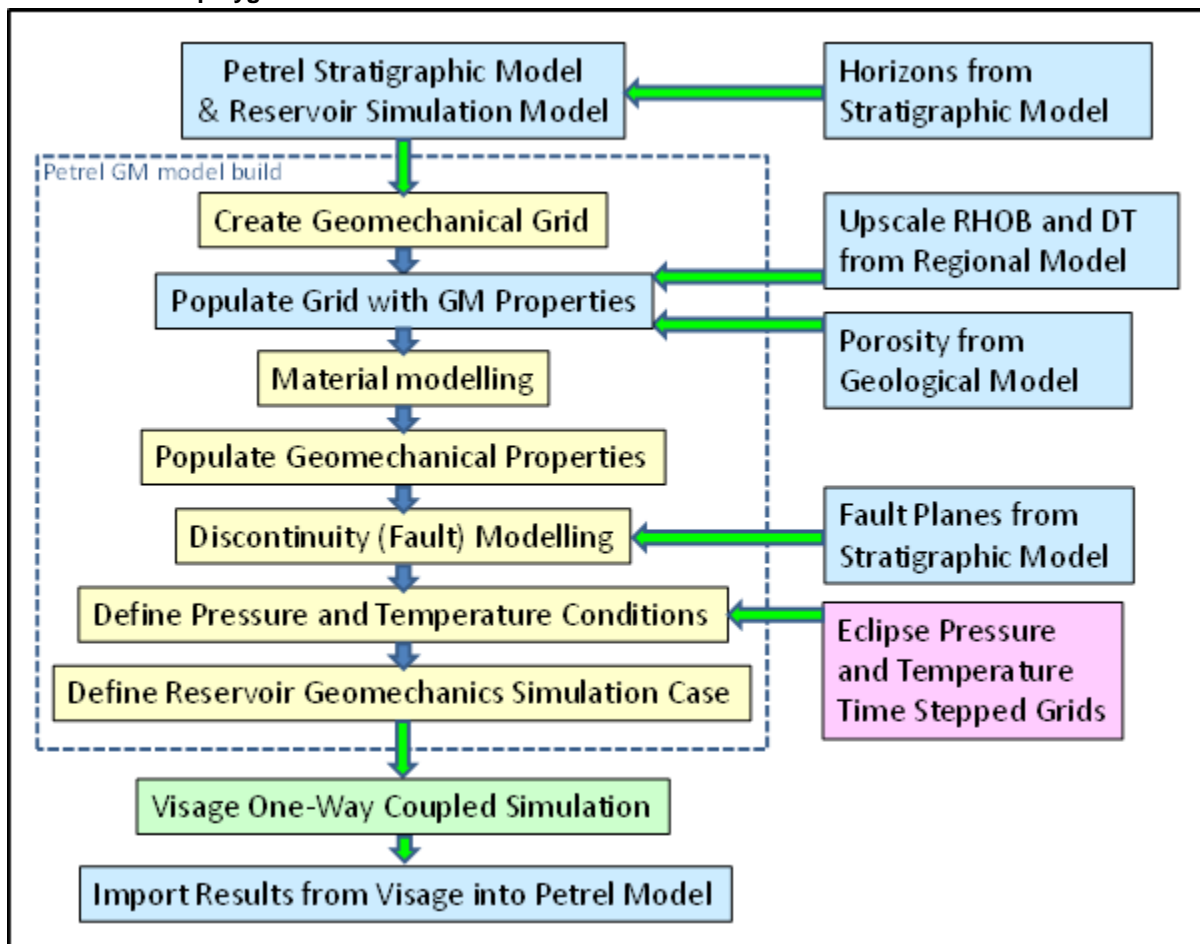
6.1 Summary

A geomechanical model (GM) of the Endurance storage complex has been built using a workflow that utilises the Petrel Geomechanics software. The GM is built on a substrate of the RSFM, which was developed as part of the static geological modelling of the Endurance structure. This modelling is large scale in that the grid has 200m x 200m cells covering the whole of the storage complex from Zechstein halite to seabed with some additional side volumes for GM boundary condition compliance. The grid is populated with properties derived from log and core data with some modifications based on the geomechanical core testing results and other published sources. Once the GM has been built it can then be integrated with the VISAGE finite-element geomechanics simulator to analyse the impact of White Rose CO₂ injection on stress, deformation, and failure properties and behaviours of the Endurance storage complex.

6.2 Introduction

The Petrel geomechanical modelling workflow followed in this study is highlighted (within the dashed blue polygon) in Figure 6.1

Figure 6.1: Coupled Reservoir Modelling Workflow with the Geomechanical Model workflow highlighted in the dashed blue polygon



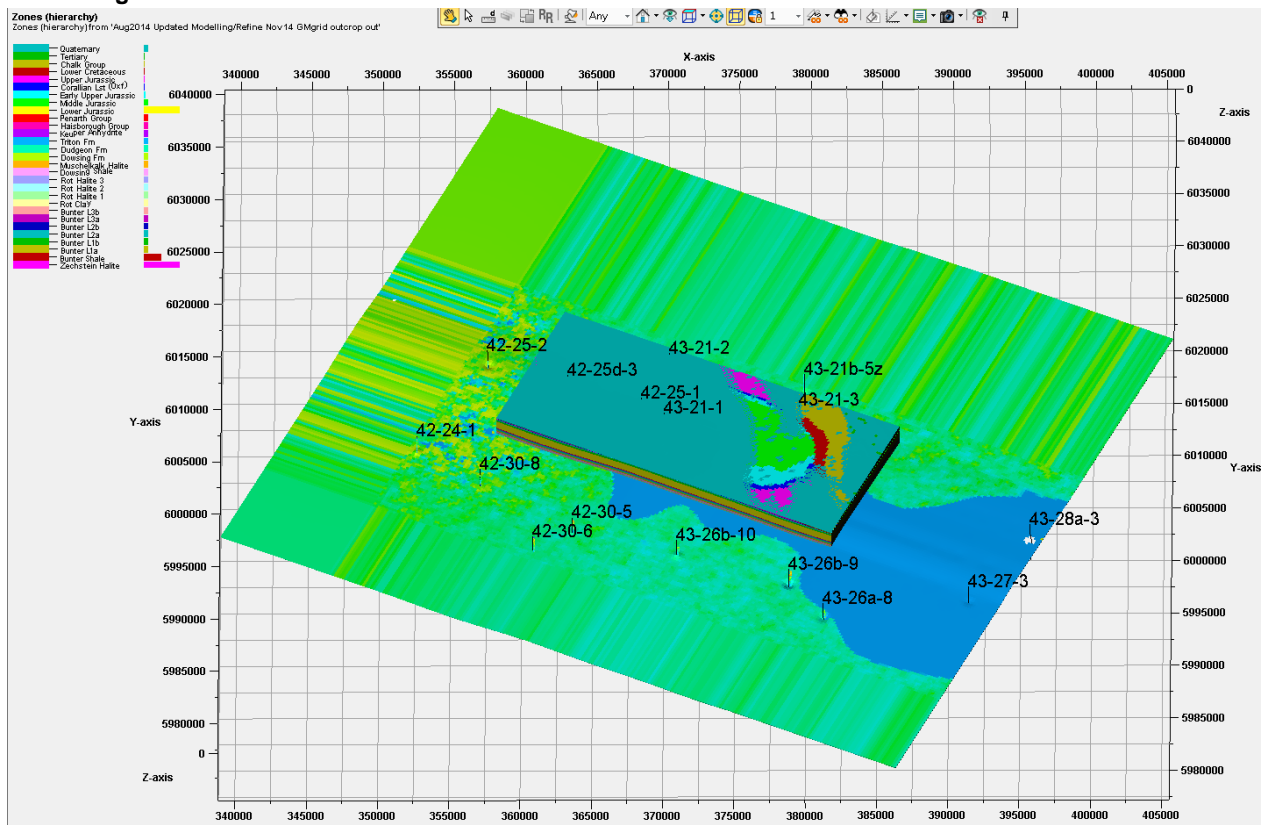
6.3 Pre-Geomechanical Model (Pre-Gm)

Prior to building the geomechanical model (GM) a pre-geomechanical model (pre-GM) was constructed that covered the same area of AOI as the simulation model but included the full stratigraphic column from Seabed to Top Rotliegend. The preGM provides the core of the GM grid described later.

The pre-GM grid *Refine Nov14 GMgrid outcrop out* was extracted over the Endurance structure area from the larger grid *Aug14_Rev_200X200M_PossFuture_GMgrid* that also included the Bunter outcrop at seabed approximately 25Km south east of the Endurance structure. An additional grid was created called *Large GM grid* that had the same cell size as the preGM grid but covered a much larger area (see Figure 6.2). The purpose of this was two-fold:

1. to include additional wells outside the Endurance closure area; and
2. to provide a distribution of properties over the full area that would be covered by the final geomechanical grid.

Figure 6.2: Refine Nov14 GMgrid outcrop out with zones property and Large GM grid with Density property over a larger area



6.4 Results of Geomechanical Tests from 42/25d-3

The prime source of the data to generate the elastic properties is from density and sonic logs . However, the recently acquired geomechanical tests from 42/25d-3 performed by FracTech for Baker Hughes

(FracTech 2015a, 2015b and 2015c) have also been used to condition the property ranges used in the modelling. This section provides a brief summary and discussion of these results.

6.5 Test Process

A comprehensive suite of geomechanical tests were performed on the three lithologies of interest; Rot Halite, Rot Clay and Bunter Sandstone. Details on the test types, testing processes, sample locations and results are presented in FracTech 2015a, 2015b and 2015c. The key test results used during this work are listed below in Table 6.1.

Table 6.1: Key FracTech 2015 test results used in the geomechanical modelling

Test	Rot Halite	Rot Clay	Bunter Sandstone
Confined Strength UCS, Friction angle (FANG) 290, 725 and 1450 psi confinements	UCS reasonable at 1877 psi, FANG of 43.74°. Lower confinements (73, 145, 290 psi).	UCS average of ~8500 psi, FANG of 30.38°	Fresh state and 30 day CO ₂ aged cores. UCS average of ~6500 psi, FANG of 41°
Confined Strength UCS, Friction angle & Elastic properties (E, ν). 290, 725 and 1450 psi confinements	E values very low at ~0.1 Mpsi and not used. Lower confinements (73, 145, 290 psi).	E consistent across all confining stresses, ~2.0 Mpsi. ν 0.12-0.19 depending on confining stress (lo to hi respectively)	Fresh state and 30 day CO ₂ aged cores. E 1.3-2.2 and ν 0.15-0.2 depending on confining stress (lo to hi respectively).
Linear Thermal Expansion Coefficient Average of 20-40 °C and 40-60 °C measurements	4.0 E-05 1/C. Published values also around 4.0 but Senergy (2011) reports a strong decrease with decreasing T C	1.4 E-05 1/°C	1.2 E-05 1/C

6.6 Test Results

6.6.1 Rot Halite

Most of the FracTech results are regarded as good. However, the halite Young's modulus is extremely low (average ~0.1 Mpsi) and Poisson's ratio is potentially low (0.27). The halite plugs are heterogeneous with anhydrite crystals and stringers and a number of small anastomosing microfractures possibly representing halite crystal boundaries. It is not clear if these microfractures are also present in-situ or whether they have formed during coring, handling or plugging. Table 6.1 shows the typical appearance of the Rot Halite plugs. The finely crystalline halite/anhydrite appears grey and the more coarsely crystalline halite is a white colour.

Published information on halite mechanical properties is sparse and variable. Some examples are provided below in Table 6.2 along with the FracTech results and the final sets of properties used in various simulation runs. The Linear Thermal Expansion Coefficient (LTEC) for halite at the expected temperature range is approximately three times higher than most rocks (4E-05/C) meaning that cooling will have a greater effect on the halite stress compared to other rocks. The strong trend in LTEC decrease with lower temperatures reported by Senergy (2011) was not seen during the FracTech testing indicating that 4E-05/C is a robust estimate for this phase of modelling.

The main issue is choosing the appropriate values for Young's and Poisson's in the Rot Halite. On a geological timescale, halite will generally deform and equalise the stresses to be lithostatic. However, the

various published results, FracTech data and AGR TRACS log derived values shown in Table 6.2 indicate a higher Young's and lower Poisson's. This is probably because the tests are conducted at shorter timeframes and at lower temperatures than occur in the Earth's crust. In reality, the salt will deform by viscous behaviour due to one or more creep mechanisms over months or years.

Creep data for the halite was obtained by FracTech (see Table 6.2) which indicates the expected non-linear viscous / plastic behaviour. However, VISAGE only treats salt as a linear elastic material so to get lithostatic stress type behaviour (at least at small strains) a low Young's (e.g. 0.6bar E05) and a high Poisson's ratio (e.g. 0.45) are used by default in VISAGE. To cover this uncertainty and compensate for the lack of non-linear creep functionality for salt within VISAGE, it was decided to run two cases in VISAGE to encompass the ranges of Young's modulus and Poisson's ratio (see Table 6.2).

Note that only the Rot Halite 1 and 3 layers were regarded as containing enough salt to be treated as a halite from a geomechanical perspective. The Zechstein salt was also given two sets of values. The shallower Muschelkalk Halite was not explicitly defined as a salt layer during this modelling as it was not regarded as a significant factor. However, it could be included in future work if required.

Figure 6.3: Typical Appearance of Rot Halite Plugs, Pre and Post Testing (from Fractech (2014c))

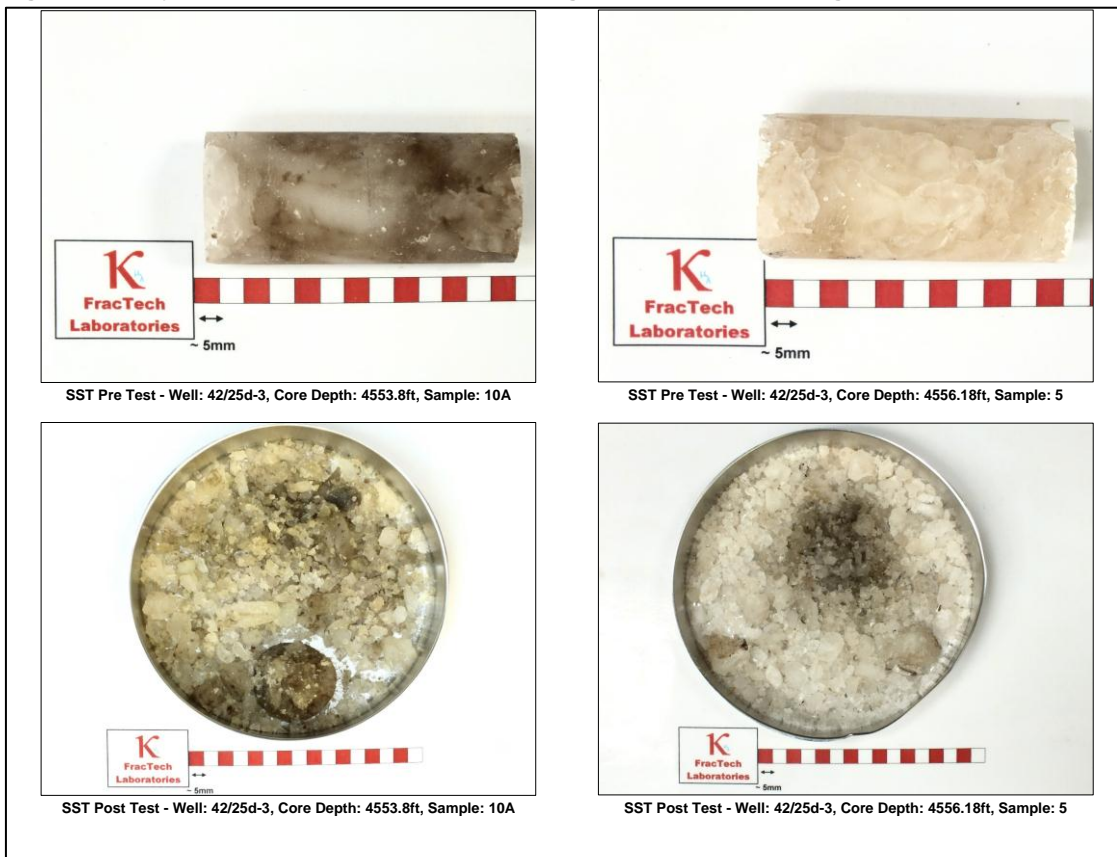
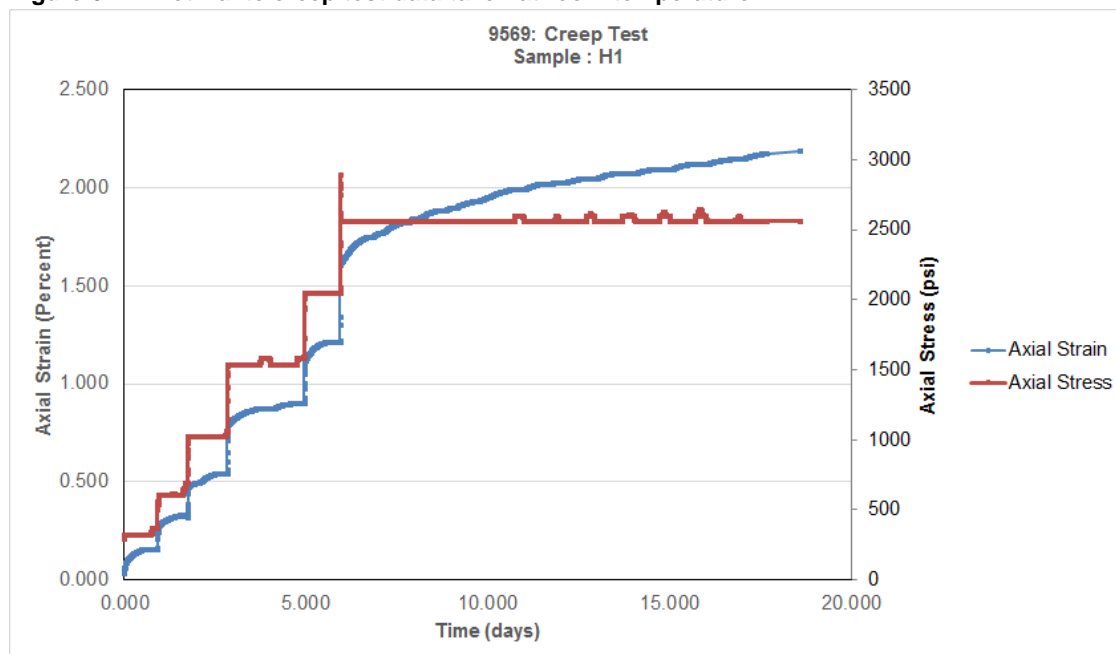


Table 6.2: Published, Measured and Modelled Halite Geomechanical Property Ranges in the Reservoir Volume.

Reference	Young's (E) 10bar	Poisson's Ratio	UCS (bar)	Friction Angle (ϕ)	Linear Thermal Expansion Coefficient (1E-5/ $^{\circ}$ C)
Senergy (2011)	3.12 (P50)	0.22 (P50)	32	22 $^{\circ}$	4.0, but highly temperature dependent.
FracTech (2015) core values (static)	0.0689. Samples disaggregating?	0.27	129	44 $^{\circ}$	4.0 average; from 3.85 at 20 $^{\circ}$ C to 40 $^{\circ}$ C and 4.24 at 40 $^{\circ}$ C to 60 $^{\circ}$ C
AGR TRACS log values (dynamic)	3.45	0.28 or 0.36	595	-	-
Liang et. al. 2007	0.52 (zero confining stress)	0.31	185 (range 150 to 320)	31 $^{\circ}$	-
VISAGE AGR TRACS Weak Rot Halite 1 & 3. Averages	0.6 constant	0.45 constant	110 to 140 (Av 129). Not used.	39 $^{\circ}$ Not used	4.0
VISAGE AGR TRACS Reference Rot Halite 1 & 3. Averages	3.1 to 3.4 (Av 3.3)	0.28 constant	110 to 140 (Av 129). Not used.	39 $^{\circ}$ Not used	4.0

Figure 6.4: Rot Halite creep test data taken at room temperature



6.6.2 Rot Clay

The Rot Clay properties are more straightforward to assess although the core was fractured in places (possibly during handling) so plugging was not easy. The Rot Clay is a lacustrine claystone with some silty

material comprised of quartz and feldspars. Cements also occur and are composed of dolomite, anhydrite and minor halite. The dolomite is a pervasive microcrystalline phase that can comprise up to 27% of the rock. All of the cements are regarded as forming during early post deposition times (Baker Hughes 2015).

The published, FracTech, log derived and geomechanical property ranges are shown below in Table 6.3.

Table 6.3: Published, Measured and Modelled Rot Clay Geomechanical Property Ranges in the Reservoir Volume

Reference	Young's (E) 10 ⁵ bar	Poisson's Ratio	UCS (bar)	Friction Angle (φ)	Linear Thermal Expansion Coefficient (1E-5/°C)
Senergy (2011)	1.11 (P50)	0.29 (P50)	283 (P50)	34° (P50)	0.33
FracTech (2015) core values (static)	1.38	0.17 average	531	30°	1.4
AGR TRACS log values (dynamic)	2.94	0.28 or 0.36	370	-	-
VISAGE AGR TRACS ref Rot Clay. Averages	1.1 to 2 (Av 1.4)	0.22 to 0.26 (Av 0.24)	256 to 1165 (Av 502)	34° to 39° (Av 36)	1.4

6.6.3 Bunter Sandstone

Most of the samples and tests conducted by FracTech were performed on the Bunter Sandstone. This unit is comprised of high quality aeolian and fluvial sandstones with some interbedded playa margin silts and clays. The detrital mineralogy is heterogeneous but dominated by quartz and various lithic fragments. Authigenic cements include (in descending order of importance) dolomite, anhydrite, hematite and quartz and feldspar overgrowths. Halite cement is also present in many places and can locally be the dominant cementing phase (Baker Hughes 2015).

The published, FracTech, log derived and VISAGE geomechanical property ranges are shown below in Table 6.4. The modelled Young's and UCS values vary considerably because the underlying porosity model used to control the sonic and density property distributions contains variations to represent more cementing with depth and/or on the flanks of the structure.

Table 6.4: Published, Measured and Modelled Bunter Sandstone Geomechanical Property Ranges in the Reservoir Volume

Reference	Young's (E) 10 ⁵ bar	Poisson's Ratio	UCS (bar)	Friction Angle (φ)	Linear Thermal Expansion Coefficient (1E-5/C)
Senergy (2011)	1.3 (P50)	0.26 (P50)	195 (P50)	35° (P50)	0.9
FracTech (2014) core values (static)	1.45	0.19 average	462	41°	1.2
AGR TRACS log values (dynamic)	2.95	0.27 or 0.36	397	-	-
VISAGE AGR TRACS ref Rot Clay. Averages	0.75 to 3.24 (Av 1.25)	0.19 to 0.37 (Av 0.25)	8.3 to 4115 (Av 390)	24° to 46° (Av 36)	1.2

6.7 Geomechanical Model Build

6.7.1 Make Geomechanical Model

The Make Geomechanical Model is run from the Pre-GM model and creates a GM with additional cells on the margins to account for regions adjacent to the reservoir to ensure even distribution of stress (Figure 6.5). In the case of the preGM, the overburden from top reservoir to seabed, was already modelled so additional overburden cells were not required. However, additional cells have been added along the sides of the grid (sideburden) and below the base of the grid (underburden). The part of the GM grid occupied by preGM is referred to as the embedded grid.

For the side burden, an additional 10 cells have been added whose sizes increase geometrically by a factor of 1.5 toward the margin of the model (Figure 6.6). Additionally the model places plates with stiff properties on the grid's lateral margins. These have been made to be 50m thick.

For the underburden an additional 8 layers have been added from the base of the model to -9000m TVDSS and further 17 layers from -9000m to -45000m TVDSS. The layers geometrically increase in thickness by a factor of 1.5 (Figure 6.7).

The GM model is approximately 52km long x 40km wide x 45km deep and contains 2.3 million cells.

Figure 6.5: Geomechanical Grid

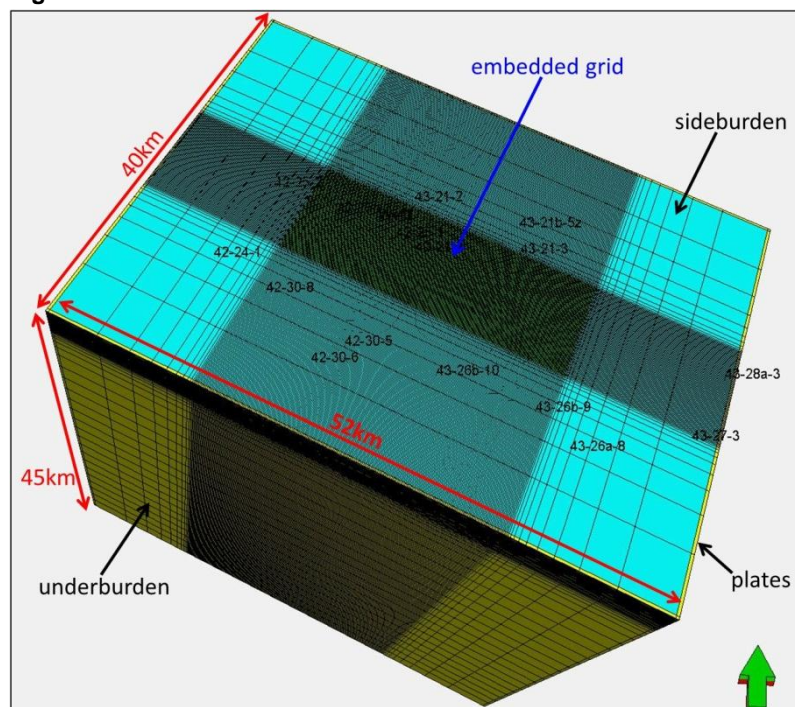


Figure 6.6: Sideburden tab of the Make Geomechanical Grid process

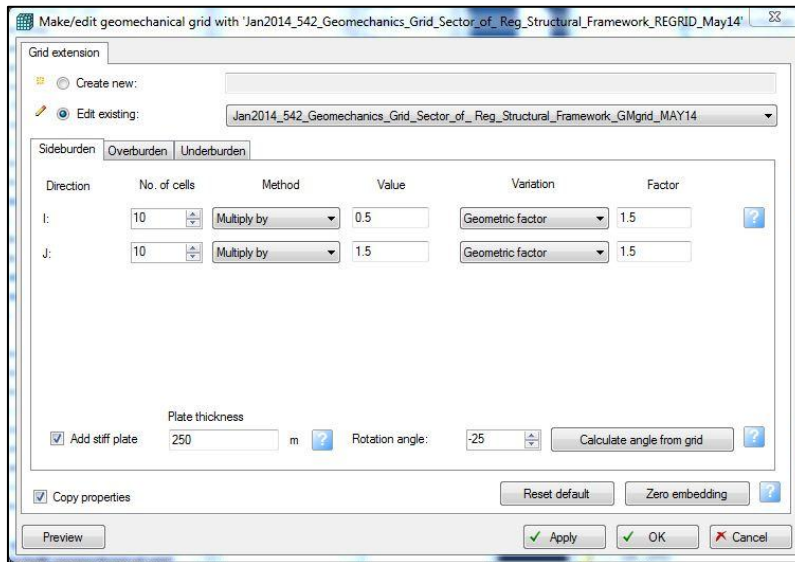
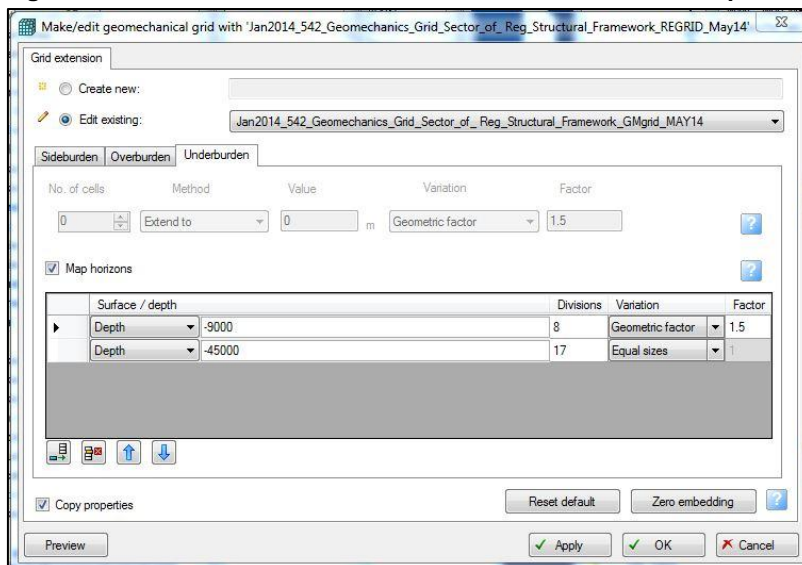


Figure 6.7: Underburden tab of the Make Geomechanical Grid process



6.8 Distributed Sonic and Density

The GM grid needs to be populated with Geomechanical properties which stem from sonic and density log measurements in the wells (Figure 6.5). Prior to using the wells for modelling they were edited. This involved removing spurious values which commonly occur at the start and end of logs. The edited logs were re-named DT_gm and RHOB_gm in Petrel. Full waveform sonic data was only available in well 42/25d-3. The Vs log from this data was used later on in the modelling process to calibrate calculated Vs.

Table 6.5: Available logs for creating geomechanical properties

Well	Compressional Sonic DT	Shear Sonic DTSM	Density RHOB
42/24-1	X		X
42/25-1	X		X
42/25-2	X		X
42/25d-3	X	X	X
42/30-5	X		X
42/30-8	X		X
43/21-1	X		X
43/21-2	X		X
43/21-3	X		X
43/21b-5z	X		X
43/26b-9	X		
43/26b-10	X		
43/26a-8	X		
43/27-1			X

The DT_gm and RHOB_gm logs could not be up-scaled and populated directly into the GM grid since only 4 out of the 14 wells listed in Table 6.5 lie in the embedded grid. The remainder penetrate the sideburden of the GM grid. The sideburden cannot be used directly for property distribution since zones in sideburden have been extrapolated laterally and lie in the incorrect structural location relative to the well data (Figure 6.8).

To overcome this problem a grid with the same dimensions and horizons as the geomechanical grid was created but with 200x200m cells throughout and local ties to the well data in the sideburden areas (*Large GM grid*, see Figure 6.10). This allowed the correct upscaling and distribution of the log derived properties from all available wells. The lack of coincidence of the large scale layering between *Large GM grid* and the GMGrid at the wells was handled via the zone mapping process during upscaling (see Figure 6.8).

For non-reservoir layers in *Large GM grid*, Kriging interpolation in the petrophysical modelling process in Petrel was used to distribute upscaled DT_gm and RHOB_gm logs from all available wells with data. For the reservoir layers only, both DT_gm (copied and renamed DT_gm_PHIEcokrig76) and RHOB_gm (copied and renamed RHOB_gm_PHIEcokrigminus97) were co-kriged with porosity using correlation coefficients 0.76 and -0.97 respectively (Figure 6.9). The porosity property used was DVHM_PHIE1 which was previously up-scaled to Large GM grid from the geological grid (Aug14_Rev_Regional_GEOLOGICAL_Model_for_Upscaling).

Figure 6.8: Comparison of zones from the GM grid (colour) and the Large GM grid (lines)

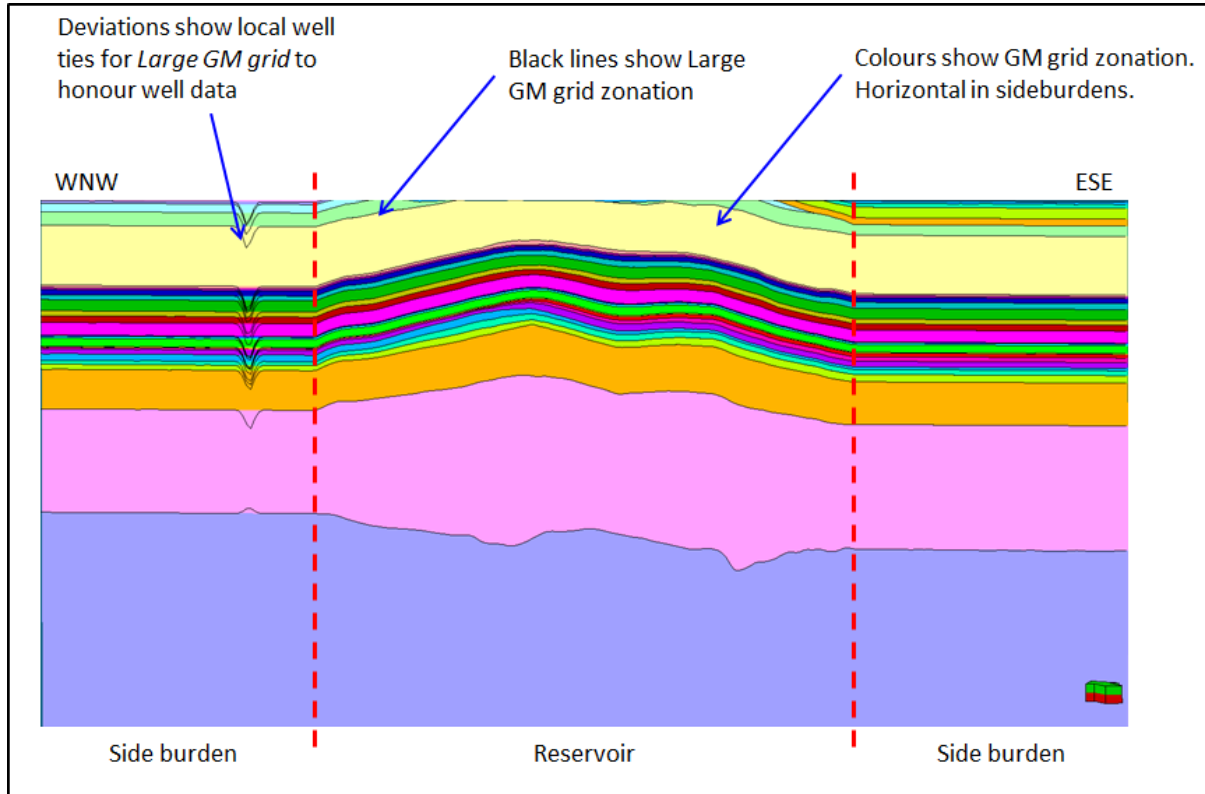
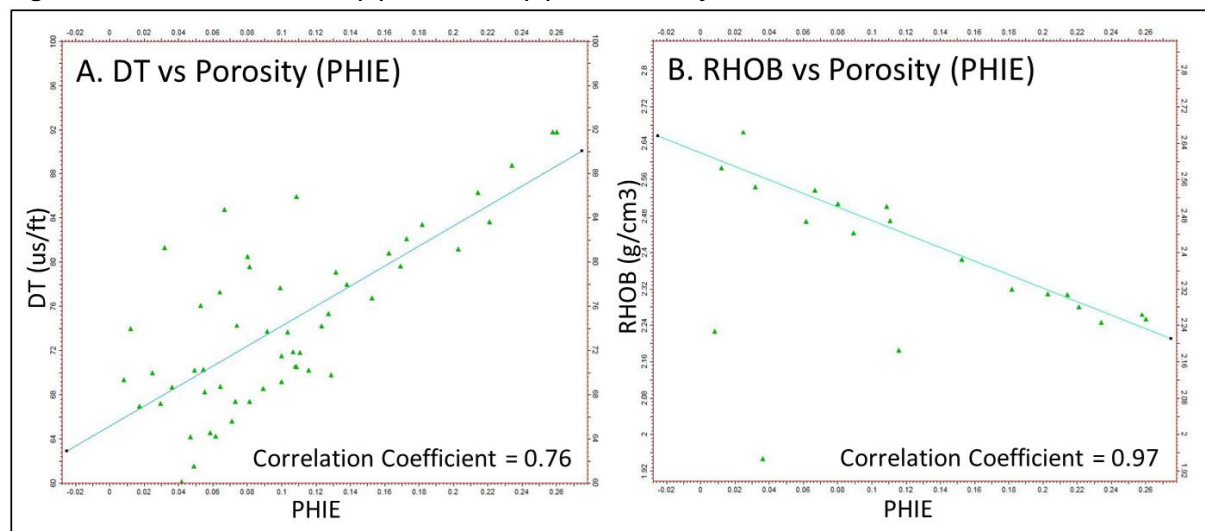


Figure 6.9: Correlation of DT (A) and RHOB (B) with Porosity within the Bunter Sandstone



The full sequence of steps for creating and upscaling the density and sonic properties is shown in Figure 6.10 to Figure 6.14. It can be seen from Figure 6.10 that the porosity in the Bunter Sandstone units appears striped in the sideburden areas. This is because the geological grid is not defined over the sideburden areas so the values are extrapolated. However, this is not regarded as a significant issue for the geomechanical modelling.

Figure 6.10: Porosity properties in Geological Grid

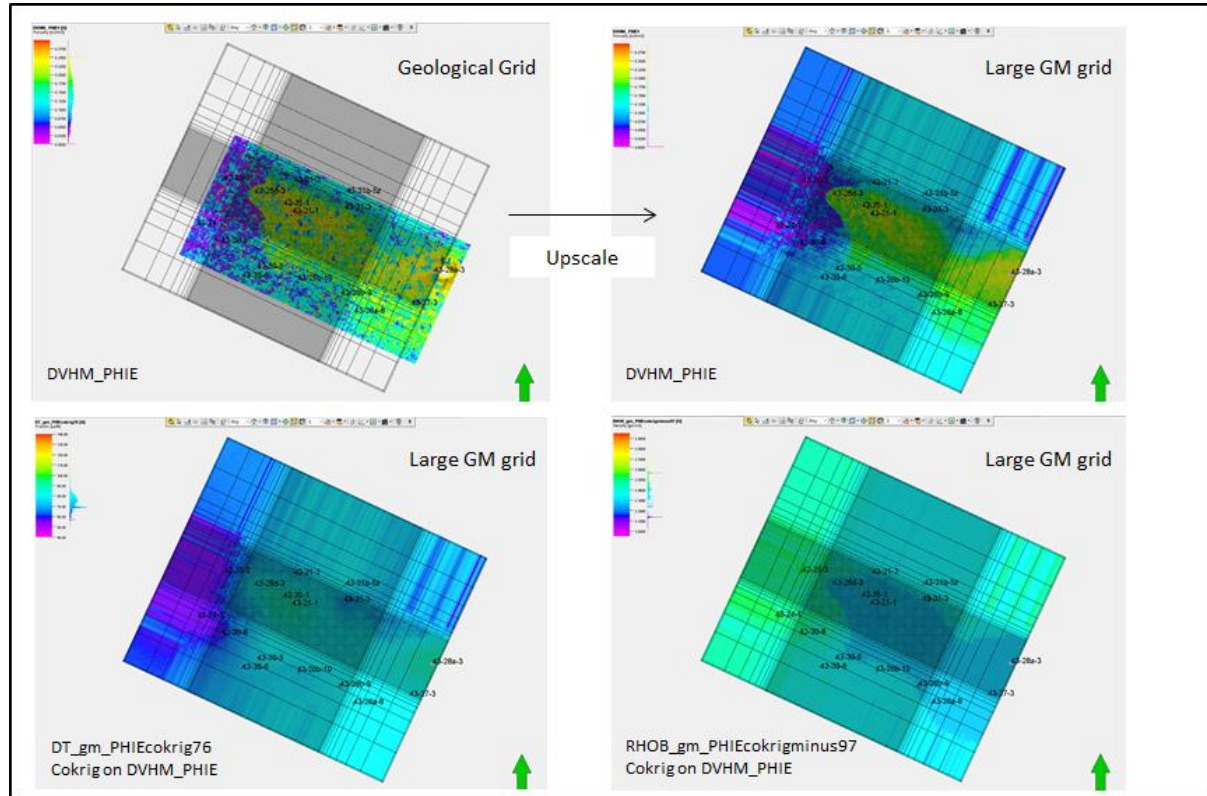


Figure 6.10 shows the porosity properties in Geological Grid (Top Left); after upscaling to the Large GM grid (Top Right). Bottom Left and Bottom Right show the co-kriged DT and RHOB properties respectively within the Bunter Sandstone in Large GM grid.

Figure 6.11 and Figure 6.12 show the sequence of steps required to get sonic and density properties created over the interval of interest (Seabed to Base Zechstein) using log data distributed by kriging in most layers and collocated co-kriging to porosity in the Bunter Sandstone. The co-kriging was used in the Bunter Sandstone to capture the rapid changes in sonic transit time and density that were conceived due to changes in cement distribution on the flanks of the Endurance structure (see Figure 6.10).

Figure 6.11: Sequence of Steps (first 4) Required to Get Sonic and Density Properties

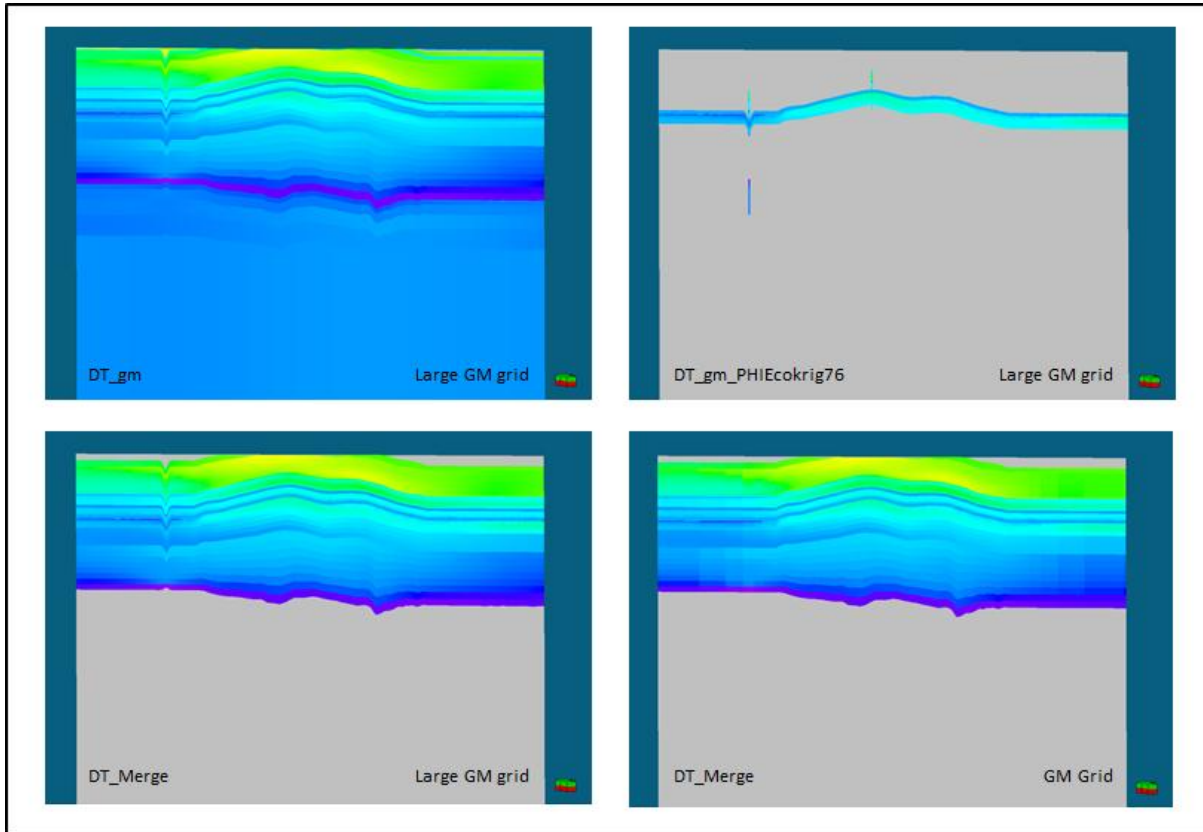


Figure 6.11: top left shows DT_gm upscaled from logs distributed using kriging; top right shows DT_gm_PHIEcokrig76, upscaled and distributed using kriging and conditioning to DVHM_PHIE within Bunter Sandstone; bottom left shows DT_Merge from combining DT_gm and DT_gm_PHIEcokrig76; bottom right shows DT_Merge upscaled from Large GM grid to the GM grid.

Figure 6.12: Sequence of Steps (last four 4) Required to Get Sonic and Density Properties

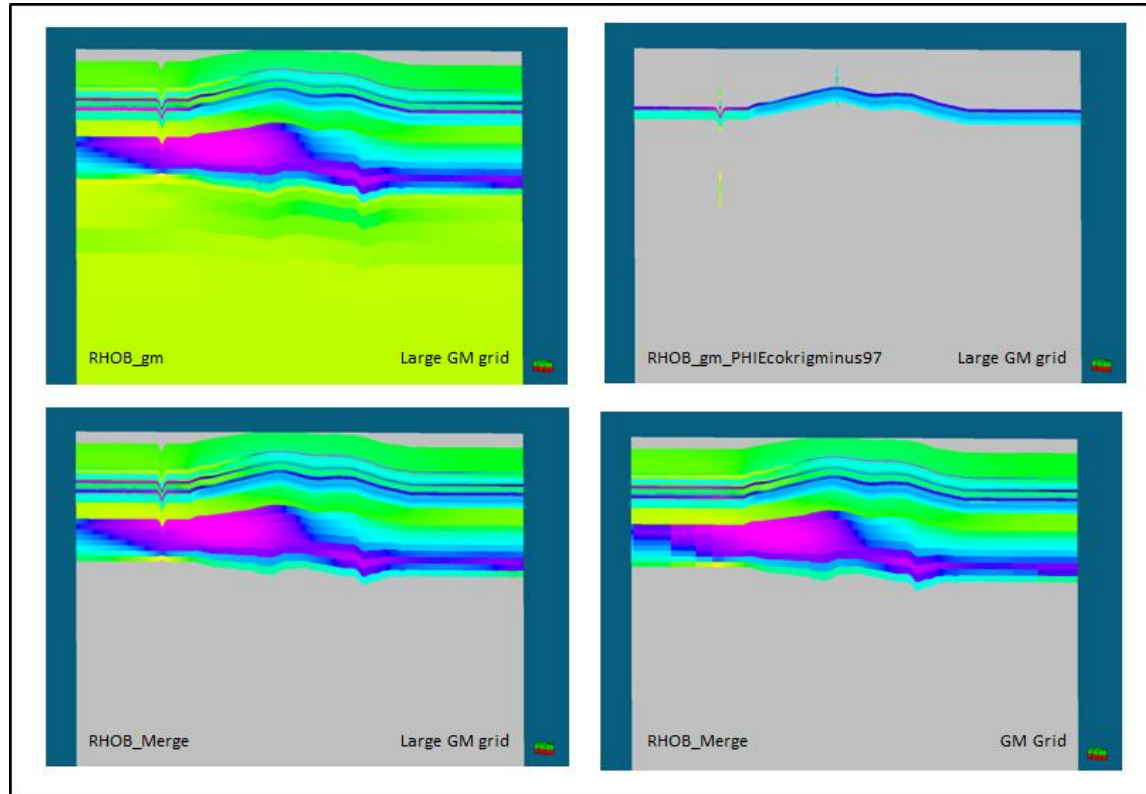


Figure 6.12: porosity properties in Geological Grid: top left shows RHOB_gm upscaled from logs and distributed using kriging; top right shows RHOB_gm_PHIEco-krigminus97 upscaled and distributed using kriging and conditioning to DVHM_PHIE within Bunter Sandstone; bottom Left shows RHOB_Merge from combining RHOB_gm and RHOB_gm_PHIEco-krigminus97; bottom right shows RHOB_Merge upscaled from *Large GM grid* to the GM grid.

6.8.1.1 Fully Populated Velocity (VP_Log) and Density (Density_Merge) Properties

After generation of the kriged log derived sonic transit time and density properties from Seabed to Zechstein (shown in Figure 6.11 and Figure 6.12), it was necessary to create additional properties that had values over the entire geomechanical grid interval. Given that logs were only available over a restricted interval compared to the grid size, simple linear trends were used as 'background' properties. Note that DT_Merge was converted to VP_Log using the following equation:

$$Vp_Log \text{ (m/s)} = 1E+6/(3.28*DT_Merge)$$

The linear trend functions for VP and Density were defined as follows:

$$Vp_Linear_Trend = 1 / (\Phi_LinerTrend / 1500 + (1 - \Phi_LinerTrend) / 4500)$$

$$Density_Trend = \Phi_LinerTrend * 1.05 + (1 - \Phi_LinerTrend) * 2.65$$

Where the Petrel equations are:

$$DP = \text{Depth}()$$

$$\text{Phi_LinerTrend} = (((DP * -1) - 5331.5) / -171.68) / 100$$

$$\text{Phi_LinerTrend} = \text{If}(\text{Phi_LinerTrend} < 0, 0, \text{Phi_LinerTrend})$$

The porosity-depth trend was estimated from good quality Bunter Sandstones from 7 wells in the Endurance area (Figure 6.13A). Effective porosity (PHIE) was converted to total porosity (PHIT) using a relationship from porosity logs in 42/25d-3 (Figure 6.13B). The total porosity depth trend is illustrated in Figure 6.13C.

Figure 6.13: Porosity versus Depth relationship for the Endurance area

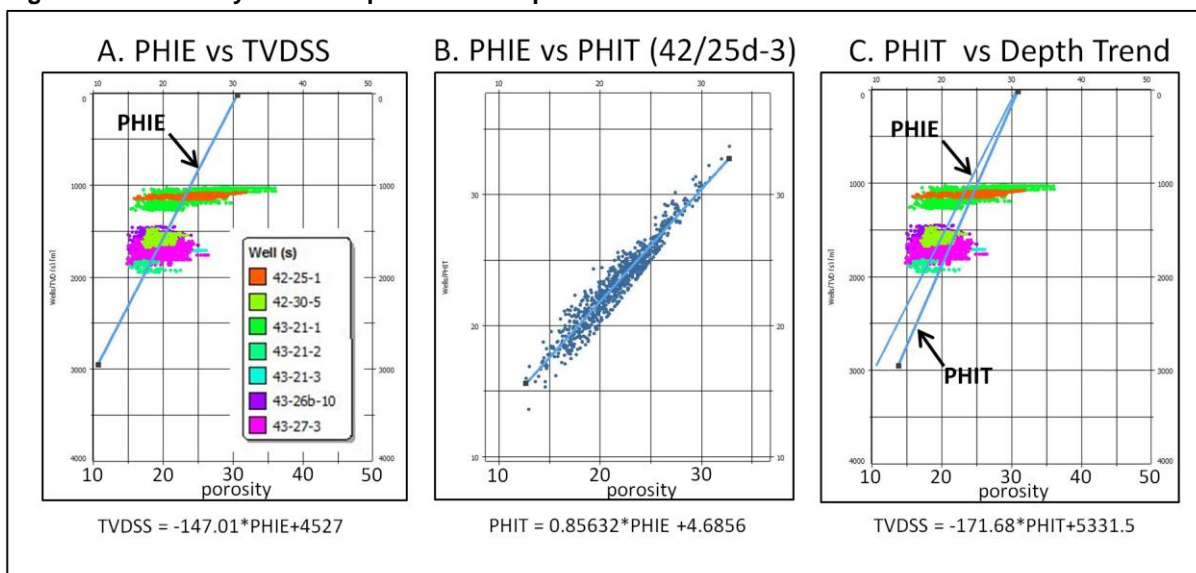


Figure 6.14, below shows the steps taken to create the final VP_Linear_Merge and Density_Merge properties used in the subsequent log derived geomechanical property calculations

Figure 6.14: Sequence of Steps to create the final VP_Linear_Merge and Density_Merge

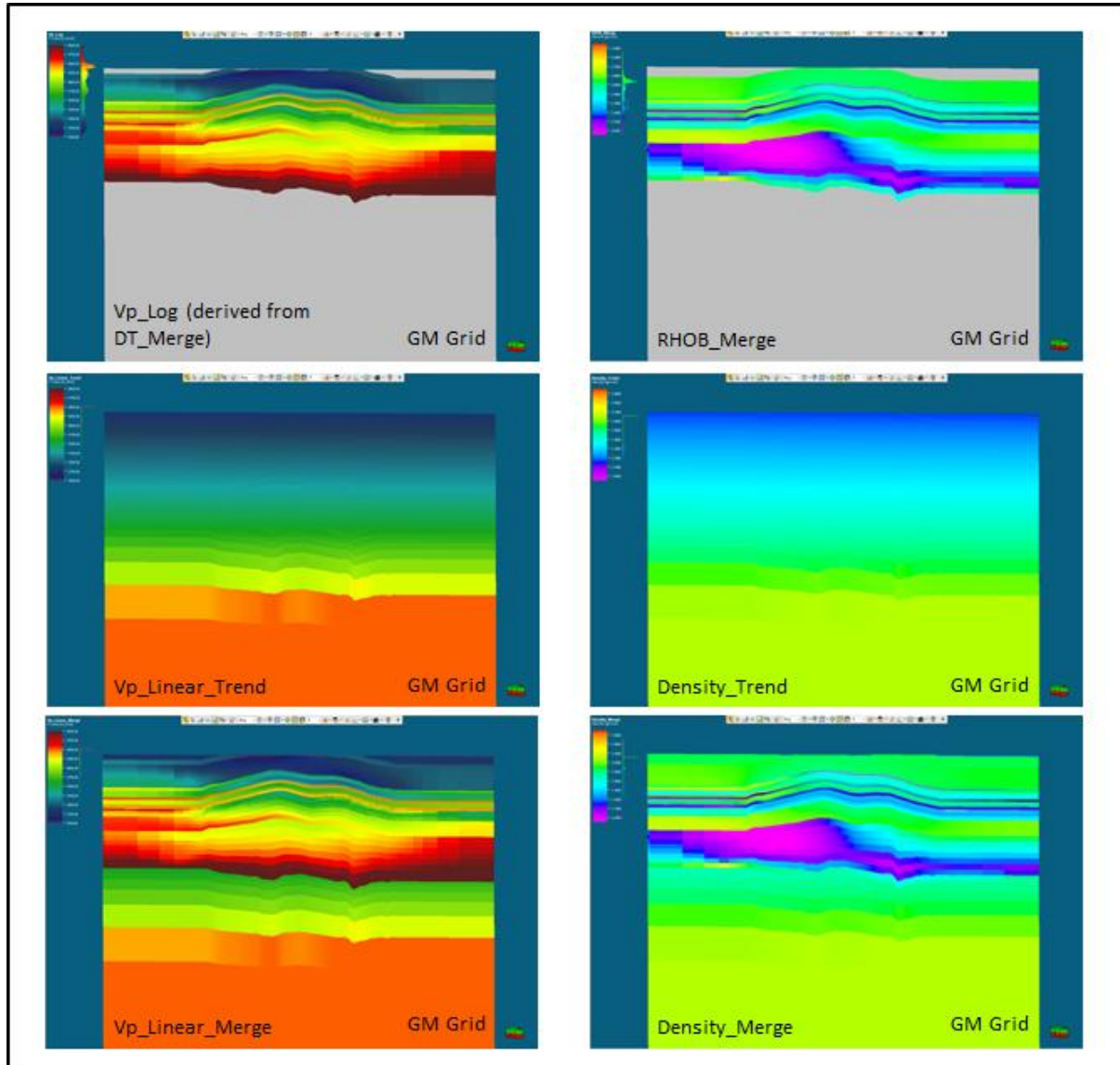


Figure 6.14: the frames on the left side from top to base show VP_Log derived from DT_Merge and a linear depth trend of VP (VP_Linear_Trend) combined to a single property (VP_Linear_Merge). The frames on the right side, from top to base show RHOB_Merge and a linear trend of density with depth (Density_Trend) combined to a single property (Density_Merge). Both properties were used for geomechanical property generation.

6.9 Geomechanical Property Calculations

The parameters described below are used in the VISAGE modelling described in Coupled reservoir modelling report, C001-27-11-99-S001-036. Geomechanical properties derived from sonic logs are termed dynamic as the sonic data is acquired using high frequencies affecting the in-situ rocks. According to Mossop (2012) this generally corresponds to the undrained conditions used in some laboratory tests

(usually referred to as static measurements). Mossop (2012) also suggests that although most geomechanical models utilise static laboratory tests obtained under drained conditions, these are only relevant when modelling the linear elastic response of reservoirs undergoing active depletion. In most other linear elastic modelling situations the dynamic or undrained static values are more appropriate. Because the Endurance store will be pressurised rather than depleted, the log derived properties have generally been used during this modelling. However, where the log derived values are deemed inappropriate or to model some specific behaviours, certain geomechanical property values have been changed in VISAGE to be more in line with the static data obtained by FracTech (discussed below).

In all these estimates, isotropic elasticity is assumed although in reality many real rocks display anisotropic material properties.

6.9.1 Shear Velocity (Vs)

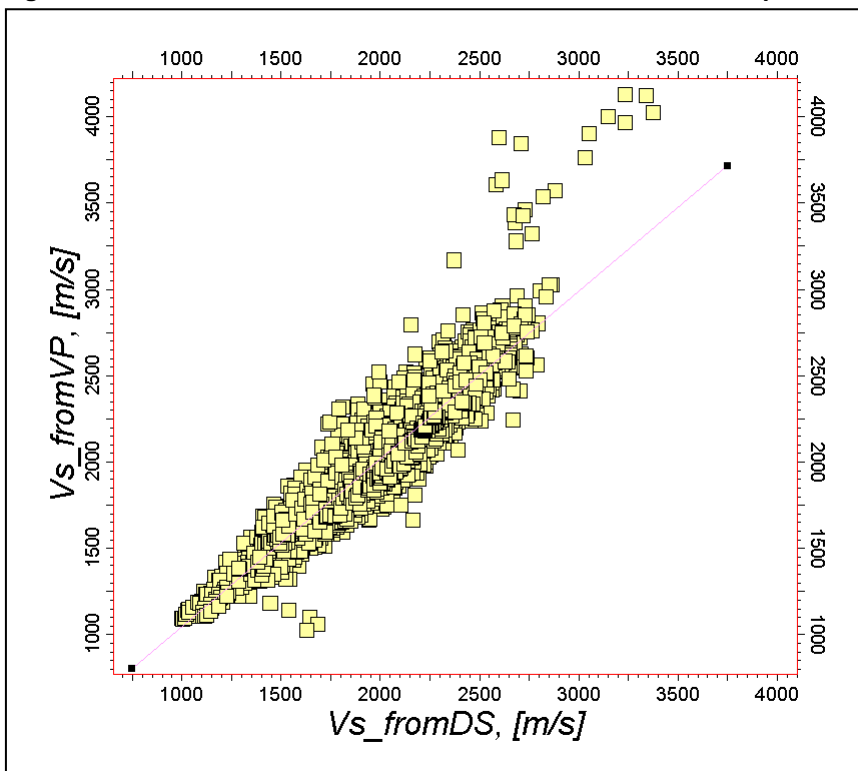
In combination with VP_Linear_Merge and Density_Merge this is the third and last input parameter used in the geomechanical property calculations. Although some shear sonic data was acquired in 42/25d-3, an adequate version can be derived in any well with compressional sonic using the following equations;

$$Vs_Merge = 0.716579 * Vp_Linear_Merge - 726.417$$

$$Vs_Merge = 1.06549 * Vs_Merge - 68.8356$$

A comparison between measured and calculated values in 42/25d-3 is shown in Figure 6.15.

Figure 6.15: 42/25d-3 Shear Data: Measured versus Derived from Vp



6.9.2 Linear Elastic Parameters

These parameters are used in isotropic linear elastic materials for calculating the changes in in-situ stress and strain in a rock mass during depletion or pressurisation in a reservoir sequence.

6.9.2.1 Shear Modulus (G)

The shear modulus (G) is a measure of the relationship between shear stress and shear strain.

$$G_{\text{dyn}} = (\text{Density_Merge} * 1000) * \text{Pow}(\text{Vs_Merge}, 2)$$

$$G_{\text{dyn}} = G_{\text{dyn}} / 1\text{E}+9 \quad (\text{Converts data from Pascals to Gigapascals – GPa})$$

6.9.2.2 Bulk Modulus (K)

The bulk modulus (K) defines the relative change in volume of a body relative to an applied stress.

$$K_{\text{dyn}} = (\text{Density_Merge} * 1000) * \text{Pow}(\text{Vp_Linear_Merge}, 2) - 4/3 * G_{\text{dyn}}$$

$$K_{\text{dyn}} = K_{\text{dyn}} / 1\text{E}9 \quad (\text{Converts data from Pascals to GPa})$$

6.9.2.3 Young's Modulus (E)

Young's Modulus (E) is sometimes termed the modulus of elasticity and relates the axial strain to the axial stress. This is a key component of linear elastic strain computations.

$$E_{\text{dyn}} = 9.0 * G_{\text{dyn}} * K_{\text{dyn}} / (G_{\text{dyn}} + 3 * K_{\text{dyn}}) / 1\text{E}+9 \quad (\text{Dynamic E, Output in GPa})$$

$$E_{\text{sta}} = 0.032 * \text{Pow}(E_{\text{dyn}}, 1.632) \quad (\text{Static E})$$

The E_{sta} values were generated prior to the 42/25d-3 rock mechanics data becoming available. Most values were very low and were not used in the final set of geomechanical runs as they were regarded as too low to be realistic. Two variants of E were created for use in VISAGE modelling:

E_ref uses the E_{dyn} values in the halite unit as these are in line with published values but halves the other units E values to be more in line with the FracTech measurements.

$$E_{\text{Ref}} = \text{if}(\text{Zones_hierarchy}=17 \text{ or } \text{Zones_hierarchy}=19 \text{ or } \text{Zones_hierarchy}=28, E_{\text{dyn}}, E_{\text{dyn}} * 0.5)$$

E_ref_Wk_Hal Similar to E_{ref} but uses the default VISAGE E values for salt in the Rot Halite and Zechstein Salt units. This helps the salt to equalise the stresses more readily leading to a lithostatic stress regime.

$$E_{\text{Ref_Wk_Hal}} = \text{if}(\text{Zones_hierarchy}=17 \text{ or } \text{Zones_hierarchy}=19 \text{ or } \text{Zones_hierarchy}=28, 6, E_{\text{dyn}} * 0.5)$$

6.9.2.4 Poisson's Ratio

Poisson's ratio (Poisson's ratio (ones_hierarchy=17 or Zones_hierarchy=19 or Zones_hierarchy=28,6,E_dyn*0.5)tein Salt units. This helps the salt to equalise the stresses more readily leading to a lith

$$v_dyn = (3.0*K_dyn-2.0*G_dyn)/(6*K_dyn+2.0*G_dyn)$$

v_ref uses the v_dyn values in the halite unit as these are in line with published values but reduces the other units v values by 20% to be more in line with the FracTech data and other published measurements.

$$v_Ref=if(Zones_hierarchy=17 \text{ or } Zones_hierarchy=19 \text{ or } Zones_hierarchy=28,v_dyn,v_dyn*0.8)$$

v_ref_Wk_Hal uses the default VISAGE (uses the default VISAGE 17 or Zones_hierarchy=19 or Zones_hierarchy=28,v_dyn,v_dyn*0.8) reduces the other units v values by 20% to blithostatic stress regime.

$$v_Ref_WkHal=if(Zones_hierarchy=17 \text{ or } Zones_hierarchy=19 \text{ or } Zones_hierarchy=28,0.45,v_dyn*0.8)$$

6.9.3 Non-linear Failure Parameters

These parameters are used in conjunction with those defined above in yield type failure (e.g. Mohr Coulomb). This is relevant for the non-linear analyses and faults used in some realisations.

6.9.3.1 Unconfined Compressive Strength (UCS)

The UCS is a measure of the stress at which a sample fails due to shear from axial compression at zero confining stress. The following relationship is empirical and calibration to core derived data is usually done.

$$G_dyn_Mpsi=(G_dyn*145037.73773)/1000000 \quad (G \text{ in millions of psi})$$

$$UCS=0.12*Pow(6.894757*G_dyn_Mpsi, 2.3)/6.894757*1000 \quad (\text{Dynamic})$$

$$UCS=UCS*0.06894757293178 \quad (\text{Converts psi to bar})$$

For VISAGE modelling the UCS values were modified to incorporate input from the FracTech data and published values. Values in bar.

$$UCS_ref=if(Zones_hierarchy=17 \text{ or } Zones_hierarchy=19 \text{ or } Zones_hierarchy=28,UCS*0.3,if(Zones_hierarchy=20,UCS*1.67,if(Zones_hierarchy>=21 \text{ and } Zones_hierarchy<=26,UCS*1.91,UCS)))$$

$$UCS_ref=if(Zones_hierarchy=17 \text{ or } Zones_hierarchy=19 \text{ or } Zones_hierarchy=28,if(UCS_ref>200,200,UCS_ref),UCS_ref)$$

6.9.3.2 Friction and Dilation Angles

Friction angle defines the angle between an axis of motion and the axis of maximum stress at which deformation occurs. It is used in defining the slope of the failure envelope (e.g. Mohr-Coulomb) in normal vs. shear stress space.

$$\text{FANG} = \text{ASIN}((\text{Vp_Linear_Merge} - 1000) / (\text{Vp_Linear_Merge} + 1000)) \quad (\text{Degrees})$$

The dilation angle indicates the propensity of a material to dilate when undergoing shear. It is usually less than the friction angle and is set to half the friction angle for all materials used in VISAGE.

$$\text{DANG} = \text{FANG} / 2 \quad (\text{Degrees})$$

6.9.3.3 Tensile Strength

Tensile strength is the strength of a material under a tensile (negative or stretching) stress. The value is usually very low in natural materials compared to other strengths and forces. Some failure criteria require a tensile strength cut-off (TSTR) to avoid over predicting tensile strength.

$$\text{TSTR} = 6.896 \quad (\text{bar})$$

6.9.4 Additional Geomechanical Parameters

6.9.4.1 Biot's Elastic Constant

Biot's elastic constant or factor is a value between 0 and 1 that defines the impact of pore pressure on the effective stress. In a true zero porosity material Biot's factor is zero whereas in a fully compliant porous solid with connected pores it is close to 1. VISAGE assumes a value of 1 for all materials and this was used here as that maximises the impact of pressurisation on the effective stress. However, many rocks can have values between 0.75 and 0.9.

6.9.4.2 Linear Thermal Expansion Coefficient (LTEC)

The LTEC defines the degree of axial strain of a unit of rock due to a change in temperature. This can be a constant or a function of temperature (see Section 6.6.1 for a discussion on Halite LTEC). The default for VISAGE is 1.3E-05/°C. This is close to the values measured for Rot Clay and Bunter Sandstone reported by FracTech for temperature ranges of 20°C to 40°C and 40°C to 60°C. However, the FracTech Rot Halite values and several published sources (e.g. Senergy 2011) indicate the halite LTEC should be 4.0E-05/°C. This will have a noticeable impact on the strain (and in-situ stress) if the rock is cooled, as is likely during CO₂ injection. 4.0E-05/°C was used during this study for the Rot Halite 1, Rot Halite 2 and Zechstein Salt layers.

6.10 Conclusions

A GM of the Endurance Storage Complex has been built using a workflow implemented in the Petrel Geomechanics software to build the grids and populate it with properties derived from log and core analysis of wells in the Endurance structure and complemented with data from the literature. The next

phase of geomechanical modelling involves coupling this GM with the VISAGE finite-element simulator for analysis of the effect of dynamic pressure and temperature responses due to White Rose CO₂ injection on the stress, deformation, and failure properties and behaviours of the Endurance Storage Complex.

7 Geomechanical Simulation

7.1 Introduction

Modelling of coupled reservoir processes was performed using the VISAGE software, a finite-element geomechanics simulator that integrates a structural and rock properties model of the Storage Complex with output from dynamic reservoir simulation within the Petrel geomodelling platform. The aim of this modelling was to assess the geomechanical integrity of the Endurance structure during and after the injection of White Rose CO₂.

The modelling incorporated pressure increases based on White Rose CO₂ injection scheme of 2.68MTPA. Temperature was modelled with a geothermal gradient and cooling in a plume above a candidate injection well injection site at mid Bunter Sandstone level. The potential for fault related failure was addressed by modelling the mapped overburden faults with three different sets of fault properties (Strong, Weak and Very Weak). In addition one crestal fault was extended (i.e. shifted downwards) so that it intersected the upper Bunter Sandstone layers to simulate the possibility of a sub-seismic fault intersecting the Bunter. It should be noted this scenario is not a situation which has been seen on seismic but has been run as a potential worst-case scenario.

The Petrel Geomechanics workflow used to build the Geomechanical Model (GM) of the Endurance Storage Complex which incorporates the RSFM – the output of the static geological modelling – and the rock mechanics test results have been described in the previous section. As Figure 6.1 shows the GM build represents the first phase of the coupled reservoir modelling workflow. The next phase involves importing this geomechanical framework into VISAGE simulator for analysis of dynamic responses.

The key issues investigated are as follows:

- investigation of optimal rock properties for modelling incorporating core test results;
- stress initialisation in the Rot Halite, Rot Clay and Bunter Sandstone at virgin pressure conditions calibrated to the 42/25d-3 Rot Clay and Bunter Sandstone minifrac data;
- overburden uplift during and at the end of injection using one way coupled runs from 4 pressure steps (initial, +5 years, +10 years, +20 years);
- impact of cooling at the injection site on the stresses and strains; and
- potential tensile fracturing, shear fracturing and fault reactivation in the Rot Clay and shallower levels.

It was decided not to perform fully coupled (VISAGE-Eclipse) simulations that would modify the reservoir and overburden permeabilities due to decompaction, tensile fracturing or fault reactivation as they have a relatively low probability of occurrence with the proposed White Rose injection rates and associated pressures.

7.2 VISAGE Model Setup

The VISAGE engine is the finite element numerical geomechanics simulator that is setup and accessed via the Petrel Reservoir Geomechanics Module. As described in Chapter 6, special grids are created and geomechanics properties initialised that are used in simulations where effects of changes in pore pressure and/or temperature are modelled. The simulations can be defined in three ways:

1. Initialisation: the simulator calculates the initial strains and intra-grid stresses at T₀ depending on the combinations of boundary condition stresses and elastic properties provided; this is a necessary step for all simulations;

2. One Way Coupling allows timesteps from T_1 to T_n where pressure and/or temperature and/or saturation output from a flow simulator is used to determine the changes in rock strain, displacement and stress at each timestep. Calculations on the mode of rock failure are also made for each cell at each step; and
3. Two Way Coupling uses an active simulator (Eclipse) job to update the matrix permeabilities as a result of the changes in strain and possible failure modes caused by changes in pressure and/or temperature and/or saturation. The Eclipse simulation run then forms the input to the next geomechanical model time-step.

Only steps 1 and 2 were run here as the Bunter Sandstone is regarded as high quality and detrimental matrix poro-perm changes from geomechanical processes are unlikely as the reservoir is being pressurised.

The sections below describe the steps of the Petrel Reservoir Geomechanics processes.

7.2.1 Material Modelling

This contains the Reservoir Geomechanics library of standard materials (shale, sandstone, salt, chalk, faultrock etc.) with specific geomechanical parameters that can be used to populate some or all of the grid. PlateMaterial is used on the cells at the outer edge of the model to provide stiff plates that the boundary stresses act on.

No properties were modified, but some new ones were created and used in certain runs. These new materials are listed below:

- | | |
|--|--|
| ■ PlateMaterial_Rev <isotropic,None> | Decreased Young's from 50 GPa to 25 Gpa; |
| ■ Material <Isotropic,None> | Generic linear elastic rock material; |
| ■ My Material <isotropic,Mohr-Coulomb> | Generic non-linear rock material; |
| ■ Fault Material Imported <> | Weak fault rock properties; |
| ■ Fault Material Imported[1]<> | Very weak fault rock properties; and |
| ■ Salt Mod Thermal <isotropic,None> | Salt with LTEC set to 4E-05/C. |

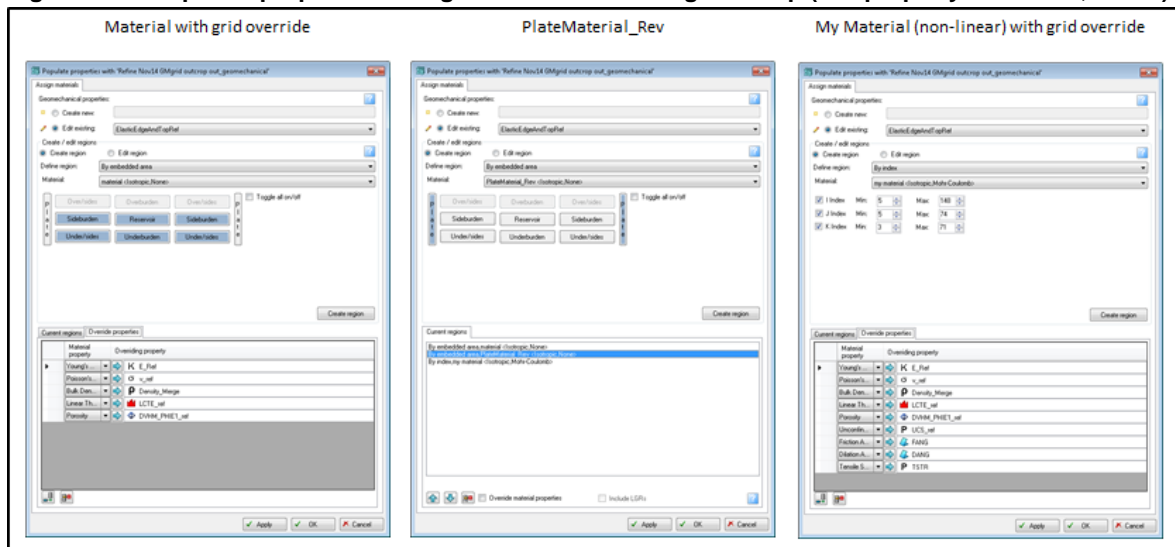
7.2.2 Populate Properties

This stage creates a set of geomechanical properties in each region of the geomechanical grid according to rules of priority. Each item in the list (region) overwrites any previous properties defined in the same embedded areas. Each region is assigned a default material from the library and a subset of the embedded areas (reservoir, side burdens, under burdens, under / sides and side plates). The overburden and over/sides areas are defined explicitly in this model and are incorporated in the reservoir and sideburden areas. The parameters within these materials can be overwritten by one or more properties defined on the grid. This is where the properties described above are used. Anywhere the grid property is not defined, the material properties are used instead.

An example of the regions definition and material plus property assignments are shown below in Figure 7.1. The three columns of pictures correspond to the relevant tabs used to setup three different materials for a property collection called Geomechanical properties; from left to right these are:

- Material <isotropic,None> Covers whole grid with grid property override for Young’s Modulus, Poisson’s and Density within the reservoir, side and under burden sections;
- PlateMaterial_Rev <isotropic,None>. Relatively stiff material (25 GPa Young’s Modulus) used for side plates only.
- My Material <isotropic,Mohr Coulomb>. Non-linear material defined over the same area as Material <isotropic,None> but excluding the cells at the grid margin. Grid property override parameters as above plus UCS, FANG, DANG and tensile strength cut-off (TSTR).

Figure 7.1: Populate properties dialog boxes for ElasticEdgeAndTop (see property collection, below)



Two property collections were created for the final iteration of the modelling:

- ElasticEdgeAndTopRef Modified dynamic elastic properties; and
- ElasticEdgeAndTopWkHal Modified dynamic elastic properties with weak halite.

The processes adopted to create these properties are described in detail in Chapter 6, above.

7.2.3 Discontinuity Modelling

This stage is used to define the locations and properties of any faults or Discrete Fracture Networks (DFNs) that need to be incorporated. DFNs were not used here as there is little or no evidence of natural fracturing in the sequence. However, there are a number of north-west striking faults interpreted from seismic data in the overburden and these were included. The process works by selected surfaces representing the faults and assigning fault material properties from the library to them (see Figure 7.2 Left hand side). The modelling here used three variants, (Weak, Very weak and Strong), and the values assigned to each are given below.

NS = Normal Stiffness bar/m and SS = Shear stiffness bar/m.

Imported Fault material	Weak.	NS: 500	SS: 200
Imported Fault material [1]	Very weak.	NS: 50	SS: 20

Figure 7.3: Linear pressure functions used in Petrel

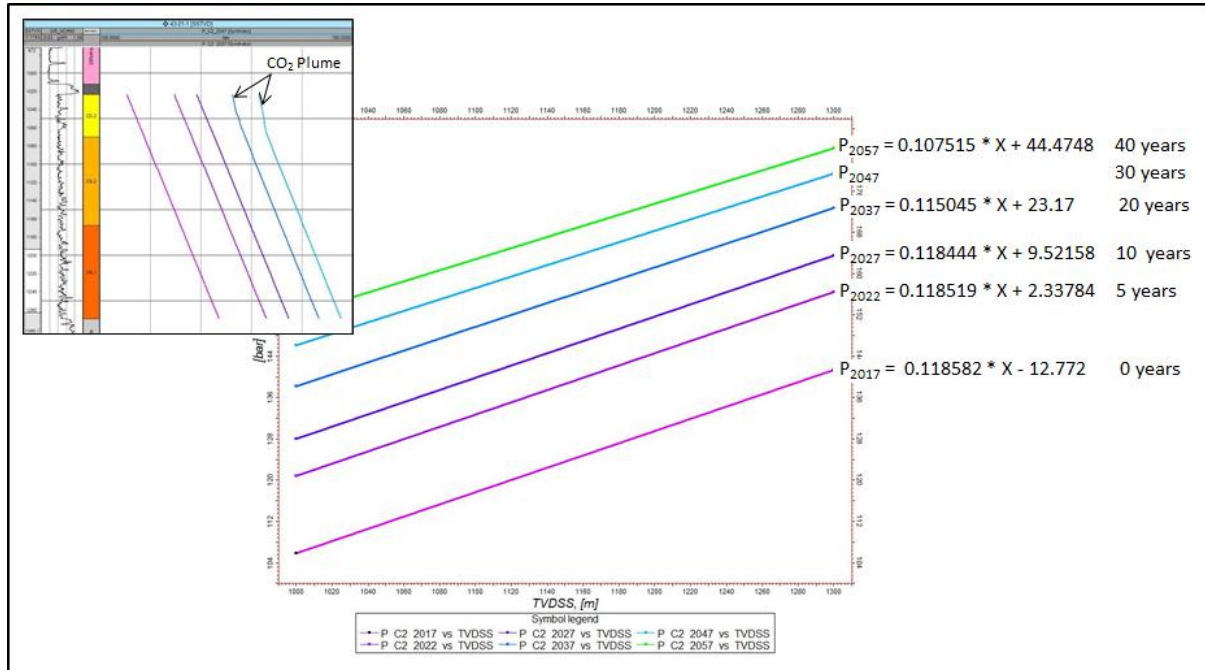
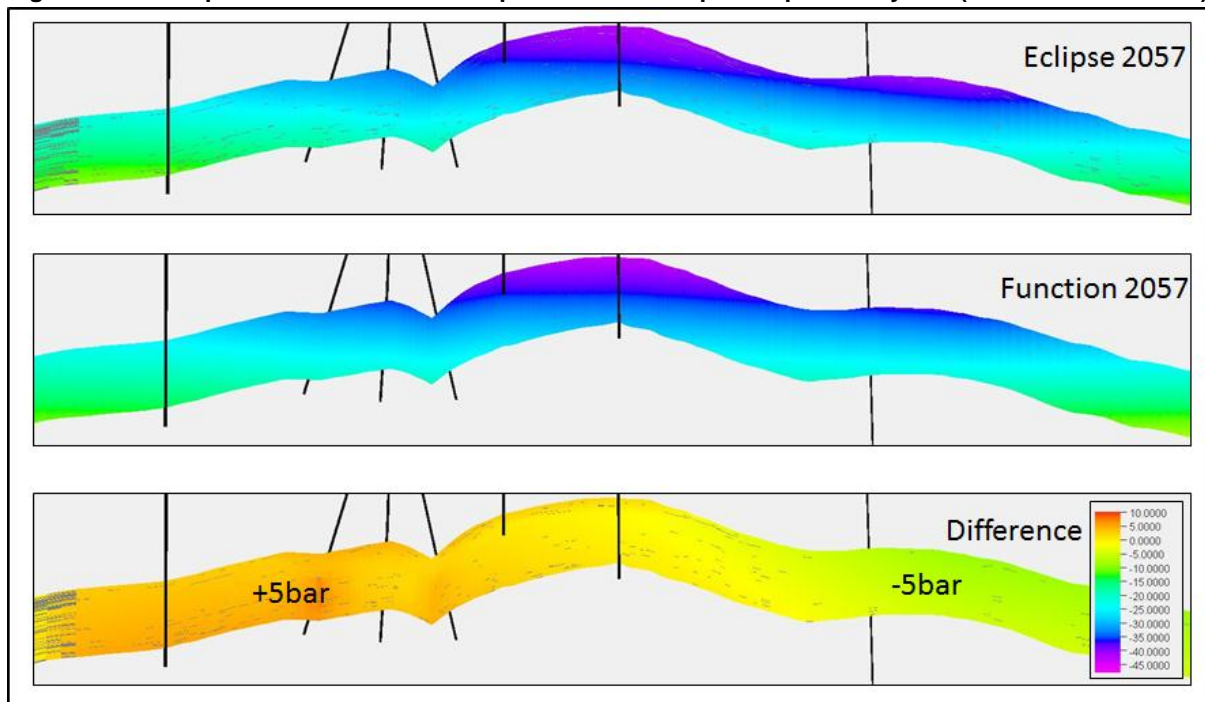


Figure 7.4: Comparison of linear function pressure and Eclipse output at 40 years (maximum difference)



The pressure properties were given the relevant date stamps (2017, 2022, 2027, 2037 and 2057).

Temperature was defined in Petrel as follows:

$$\text{TEMP_Jan_01_2017}=(0.038*\text{Elevation_general})+10$$

This property was then copied and given the relevant date stamps (2017, 2022, 2027, 2037 and 2057). As this property just defines the geothermal gradient, later versions of the temperature property incorporated a cooling effect due to the CO₂ plume. This was achieved using the following steps:

1. Create a vertical polygon from the approximate location of the *Well 3 60 degree inclination* injector perforations to the base of the Rot Clay (note Well 3 is one of the prospective moderately deviated injection wells intended for the first load);
2. Create a 'Distance from Well_3_Plume' property using Geometrical modelling;
3. Create a 'Well_3_Plume_Temp_Grad' property using this equation:

$$\text{Well_3_Plume_Temp_Grad}=\text{if}(\text{Distance_from_Well_3_Plume}>250,1,\text{Distance_from_Well_3_Plume}/250);$$
 and
4. Update the 2022 and subsequent temperature properties by using a formula of the form:

$$\text{Plume_Cooling_TEMP_Jan_01_2022}=15+(\text{TEMP_Jan_01_2022}-15)*\text{Well_3_Plume_Temp_Grad}.$$

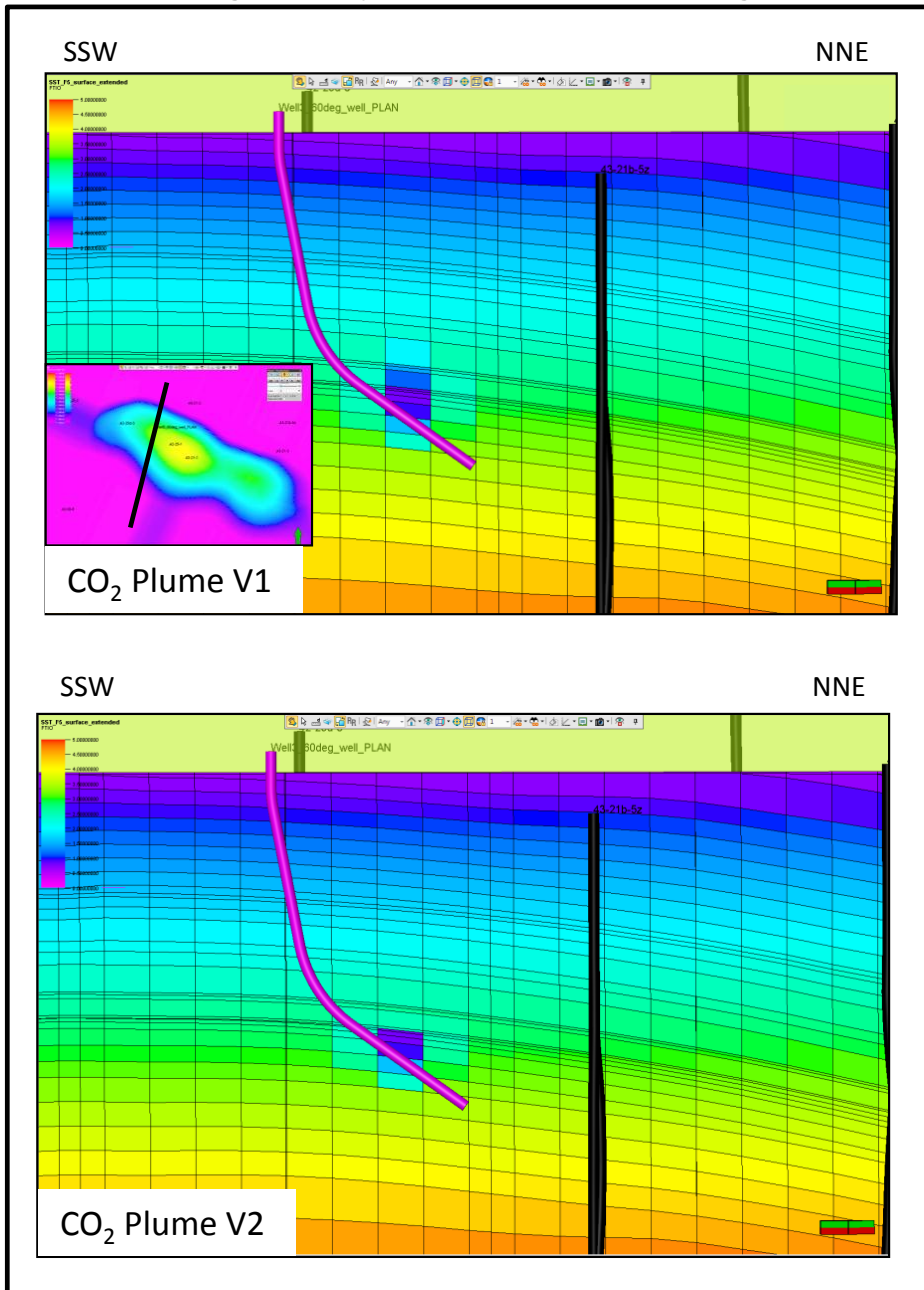
A second version of the CO₂ plume to represent the smaller temperature change in the Rot Clay and Rot Halite due to conductive cooling was created by using the following additional calculator steps in place of steps 3 and 4 listed above.

5.
$$\text{Well_3_Plume_Temp_Grad_V2}=\text{if}(\text{Zones_hierarchy}=20 \text{ and } \text{Well_3_Plume_Temp_Grad}<0.8,0.8,\text{if}(\text{Zones_hierarchy}=19 \text{ and } \text{Well_3_Plume_Temp_Grad}<0.9,0.9,\text{if}(\text{Zones_hierarchy}\leq 18 \text{ and } \text{Well_3_Plume_Temp_Grad}<1,1,\text{Well_3_Plume_Temp_Grad}));$$
 and
6. Update the 2022 and subsequent temperature properties by using a formula of the form:

$$\text{Plume_Cooling_V2_TEMP_Jan_01_2022}=15+(\text{TEMP_Jan_01_2022}-15)*\text{Well_3_Plume_Temp_Grad_V2}.$$

The resulting temperature properties for the two CO₂ plume versions are shown in Figure 7.5. Note these are very simplistic cooling properties based on an estimate of cooling at a single cell with a linear change to the geothermal gradient over adjacent cells. The first version made no account of the fact that the plume would not convectively cool the Rot Clay and Rot Halite. Although version 1 of the CO₂ plume case is not regarded as likely, further plume temperature / thermal fracturing modelling in the near injector region is recommended to more accurately model the temperature effects.

Figure 7.5: Temperature property. Upper: Initial version of CO₂ plume. Lower: Second version of CO₂ plume with minimal cooling in Rot Clay and Rot Halite. Section is through the Well3_60deg_PLAN trajectory

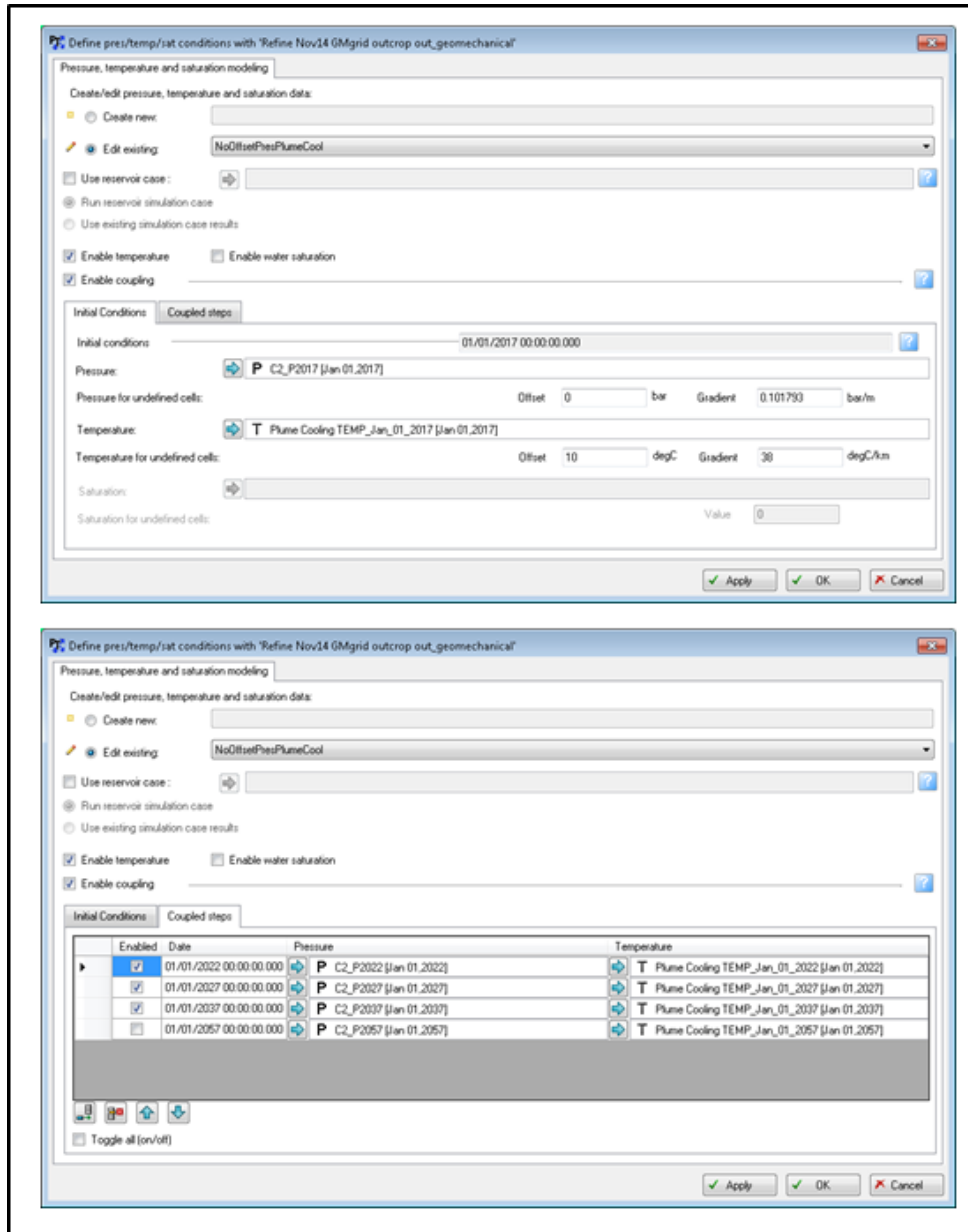


Saturation changes were not modelled during this phase of work as they were not deemed important for the first order geomechanical effects during first load modelling.

The Reservoir Geomechanics process for defining a set of saturation and temperature properties is shown below in Figure 7.6. The first tab sets up the pressure data and whether temperature and saturation are also included. Pressure and temperature gradients are also setup to provide values in the undefined cells.

The second tab details the number of steps in a one-way coupled run, in this case pressure and temperature.

Figure 7.6: Define pres/temp/sat conditions dialog boxes



7.2.5 Define Boundary Conditions

Boundary conditions are initially defined by using gravity, a constant minimum horizontal stress (Sh) gradient and a constant maximum horizontal stress (SH) to Sh ratio (SH/Sh). However, this applies the same stress parameters across all layers and in most sequences, changes in the Young’s modulus, Poisson’s ratio and LTEC will have an effect on the stress system. From the 42/25d-3 mini-frac data (Bailey 2013), high quality closure stress (in this case Sh) estimates were obtained in the Rot Clay and

Bunter Sandstone (Bailey 2013). These values along with some estimated lithostatic values for the Rot Halite are shown below in Table 7.1.

Table 7.1: 42/25d-3 mini-frac data and estimated Rot Halite stresses

Unit	Depth mTVDss	Sh bar	Sh bar/m	Sh psi/ft	Regional SH/Sh
Rot Halite 1	-1318	319	0.2424	1.072	1.00
Rot Clay	-1363	264	0.194	0.856	1.20
Bunter Sandstone	-1520	262	0.172	0.762	1.15

From Table 7.1 it is clearly difficult to create a single gravity/boundary stress based boundary condition that would satisfy all these variations. Therefore, three separate boundary conditions were created to initialise stresses in cells at 42/25d-3 that are close to the 42/25d-3 well stress values in each unit. These three sets of boundary conditions were used in iterative optimisation runs at the first time step only to ensure a match to the measured stress values in each unit. After the values were deemed acceptable (+/- 5%), the Total stress tensor data from each run were exported to properties and concatenated using the criteria listed in Table 7.2.

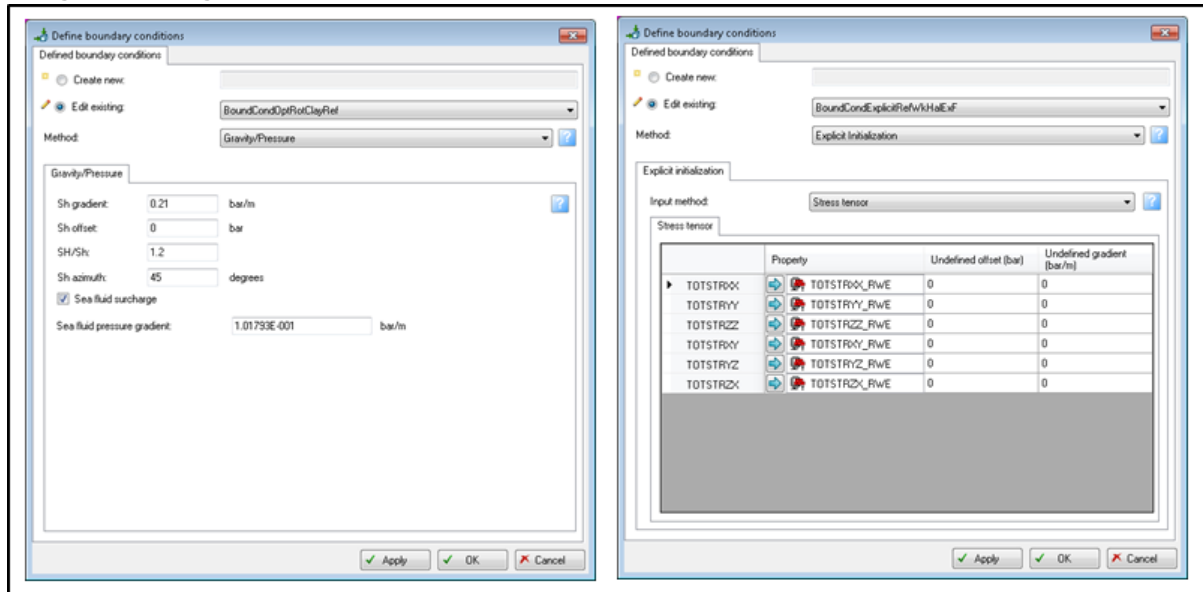
Table 7.2: Concatenation Criteria

Unit	Optimisation stress property
Rot Halite 1 & 3 and Zechstein Halite	Halite stresses
Bunter Sandstone	Bunter Stresses
Rot Clay and other units	Rot Clay stresses

This concatenated total stress data was then used in an explicit initialisation of stress for the runs with CO₂ injection.

The stress orientation was set to 45° for Sh (i.e. 135 for SH) based on regional data and the World Stress Map (Bailey 2013, Senergy 2011). It is not likely to vary significantly across the structure although alternate directions are possible.

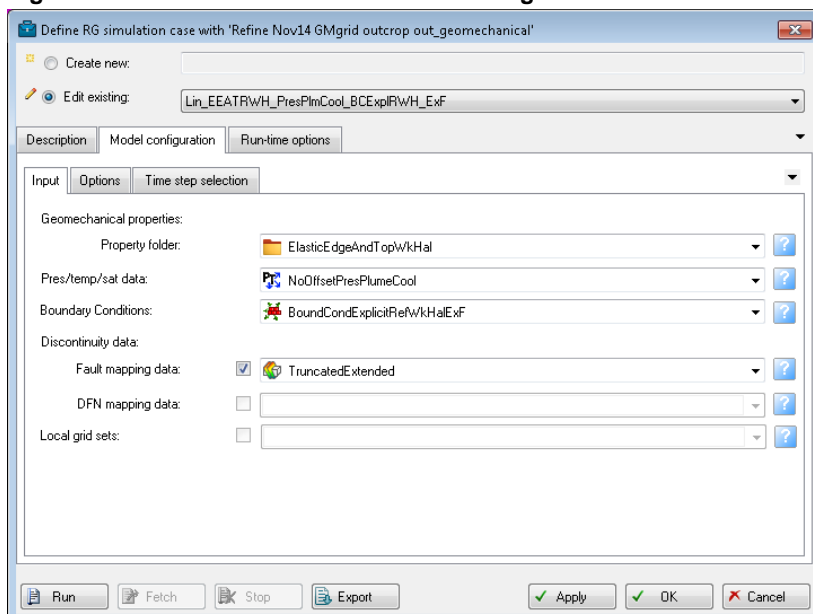
Figure 7.7: Boundary condition process. LH Side: GravityPressure method. RH Side: Explicit Initialisation using pre-existing stress tensor properties



7.2.6 Define Reservoir Geomechanics Simulation Case

This is the step where the various properties, discontinuities, pressures and temperatures and boundary conditions are selected to form a geomechanical model run (see Figure 7.8). Additional parameters can be set in the options tab relating to matrix solver iterations, convergence tolerances etc. but the defaults were used here. Note the parallel processing option for 4 cores (set on the Run-time options tab) was used on all runs. The Time step selection tab allows runs to be restarted and ended using pre-existing run steps. These were not used here.

Figure 7.8: Define RG Simulation case dialog box



The runs were designed to explore the following key sensitivities:

Halite elastic parameters	(Dynamic values and weak values)
Variation in LTEC	(High in halite, constant low value)
Cooling effects from a CO ₂ plume (Clay and Rot Halite)	(~30°C cooling in Rot Clay and Rot Halite, ~5°C cooling in Rot Clay and Rot Halite)
Fault normal stiffness and shear stiffness (strength) variations	(Strong, Weak, Very Weak)
Single fault extension into the Bunter Sandstone	(Not extended, extended)

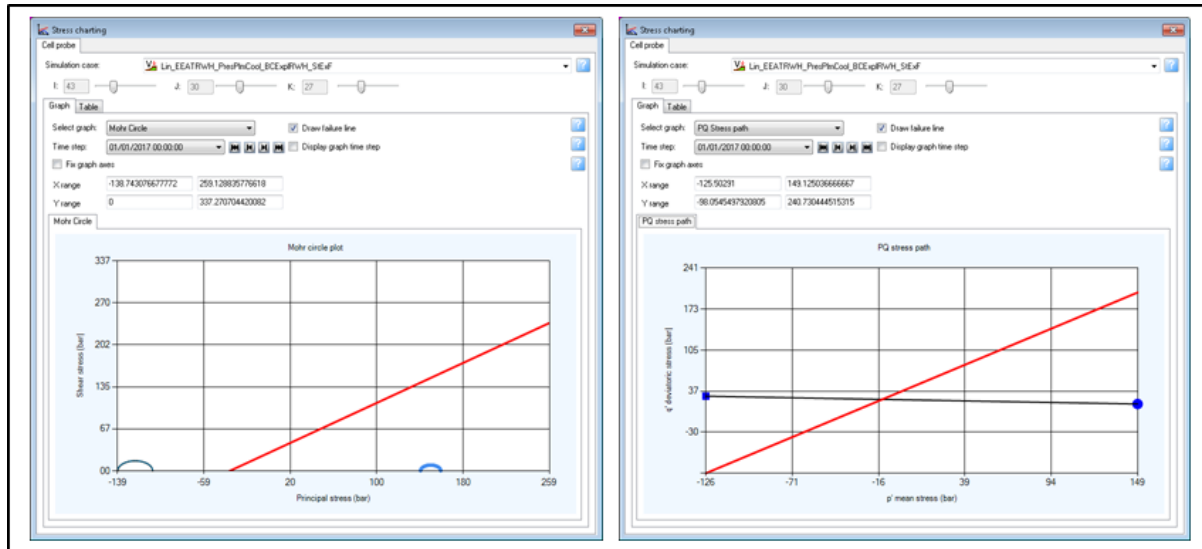
Many additional sensitivities are possible and several were investigated in earlier runs but these are generally regarded as second order effects or the parameters have a relatively low uncertainty. These are listed below:

Sh orientation variations	(45° +/-20°)
Elastic properties	(Dynamic vs. static)
Porosity	(Log derived vs. constant)
Tensile stress cut-off	(Not investigated)

7.2.7 Stress Charting and property generation

The stress charting process allows interrogation of the VISAGE run results once they have been loaded into Petrel. This allows the stress path (total stress changes with pressure changes) and Mohr circle vs. failure envelope plots to be generated for single cells in the model. In addition, the principal stress (S1, S2, S3), vertical stress (SV), SH, Sh, Von Mises stress and Sh azimuth and SH azimuth data can be generated and loaded into the grid as properties. This is more useful for QC purposes than the stress tensor data obtained from the 'convert simulation to 3D property' process where stress and strain properties are defined as XX, YY, ZZ, XY, YZ and ZX components. The typical appearance of the charts is shown below in Figure 7.9 for the halite cell above the first version of the CO₂ plume. For this particular cell, the stable, near lithostatic conditions in the semicircle on the right are significantly affected by the cooling so that, at later times, the circle has increased slightly and moved into the tensile region beyond the failure envelope. The stress path shows a similar crossing of the failure envelope.

Figure 7.9: Mohr Circle (LH side) and stress path (RH Side) plots for cell 43-30-27 (Rot Halite 1 above CO₂ plume)



7.3 Simulation Cases and Results

The modelling process is iterative to allow convergence on the appropriate grid geometry, geomechanical properties and boundary condition combinations. Therefore, only the most relevant recent results are presented. The results are summarised in Table 7.3. The first phase of runs has been designed to push the models to displaying failure or noticeable increases in displacement or elastic strain. After assessing the likelihood of these failure cases, a more informed decision on defining a reference case was then possible.

There are a large range of output properties that can be generated from a VISAGE simulation. Some of the more important ones are described below and used to illustrate the changes in strain, displacement and possible failure modes in the model.

Table 7.3: Summary of key VISAGE runs for Endurance structure with Phase 1 injection pressure changes

VISAGE Run Name	Notes
LIN_EEATRWH_PRESKOOL_BCEXPWRWH_NOF	Initial Case - No faults, weak halite, explicit stress initialisation, simple CO ₂ cooling at perforations, Tensile failure in Rot Halite 1 from cooling above injection.
LINEEATRWH_PRESPLMCOOL_BCEXPWRWH_WKF	Pessimistic Limit Case - Very weak faults, one overburden fault extended into Bunter Sandstone, weak halite, explicit stress initialisation, V1 of CO ₂ plume cooling above Well 3 (affects halite). Some failure seen in Bunter fault and in cooled Rot Halite. All faults failing in upper cells - (Jurassic). Quarternary also failing but this interval is very weak in the model and probably not realistic.
NONLIN_EEATRWH_PRESPLMCOOL_BCEXPWRWH_WKEXF	Pessimistic Limit Case - Non-linear run of LINEEATRWH_PRESPLMCOOL_BCEXPWRWH_WKF. Some differences to linear case, especially in increased elastic strains around faults.
LIN_EEATRWH_PRESPLMCOOL_BCEXPWRWH_EXF	Limit Case - Weak faults, one overburden fault extended into Bunter Sandstone, weak halite, explicit stress initialisation, V1 of CO ₂ plume cooling around Well 3. Some failure in upper 1-2 layers

VISAGE Run Name	Notes
	(spurious?). Also failure in the two halite cells above plume.
LIN_EEATREF_PRESPLMCOOL_BCEXP_LRRH_EXF	Limit Case - Weak faults, one overburden fault extended into Bunter Sandstone, reference (strong) halite, explicit stress initialisation, V1 of CO ₂ plume cooling around Well 3. Some failure in upper 1-2 layers (spurious?). Also failure in the 3-4 halite cells above plume. Greater likelihood of cooling related tensile failure in salt with higher Young's Modulus and lower Poisson's Ratio compared to weak halite.
LIN_EEATRWH_PRESPLMCOOL_BCEXP_LRWH_STEXF	Optimistic Limit Case - Strong faults (VISAGE default), one overburden fault extended into Bunter Sandstone, weak halite, explicit stress initialisation, V1 of CO ₂ plume cooling around Well 3. Some minor failure in upper layers on Endurance crest (spurious?). Also tensile failure in 2 cells in halite above the plume. No obvious changes in stresses around faults.
LIN_EEATRWH_PRESPLUMECOOLV2_BCEXP_LRWH_F	Reference Case - Weak faults, no fault extension, weak halite, explicit stress initialisation, V2 of plume cooling around Well 3. Some minor failure in upper layers on Endurance crest (spurious?). Some minor stress changes and strain around OB faults but no thermal or fault related yielding below layer 10. No significant failure modelled.
NONLIN_EEATRWH_PRESPLUMECOOLV2_BCEXP_LRWH_F	Reference Case - non-linear run. Very similar results to linear case (LIN_EEATRWH_PRESPLUMECOOLV2_BCEXP_LRWH_F).

7.4 Limit Cases

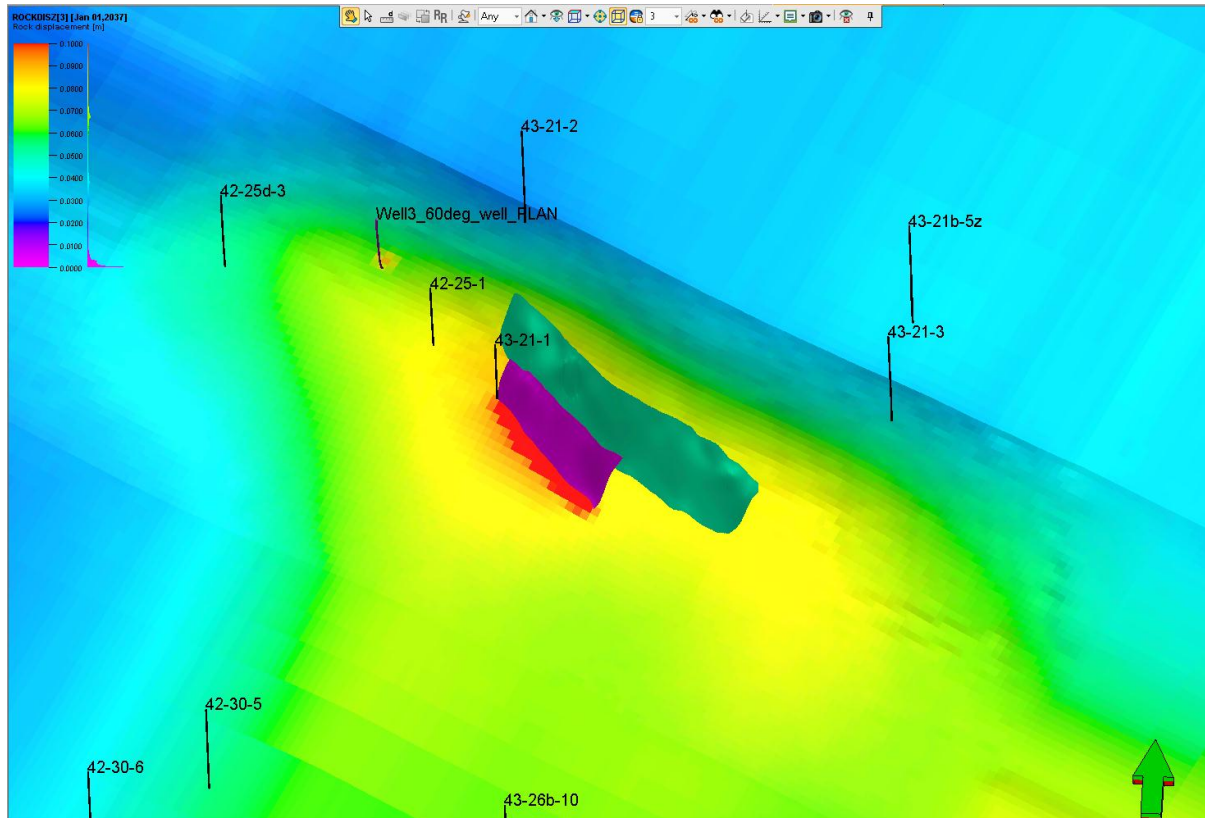
Limit cases are those where the model is modified to induce different types of failure and/or increased displacement and strain that could lead to the generation of seal breach and the formation of a leak pathway. The results of one way coupled geomechanical modelling do not directly calculate the impact of changes in strain and displacement on the permeability so this is a qualitative assessment.

7.4.1 Rock Displacement

This parameter has three variants defining displacement of the rock in the X, Y and Z directions. The X and Y displacements are usually minimal and only have significant values in localised areas where there is significant cooling, steeply dipping layers or weak layers / faults with movement. The ROCKDISZ property defines the degree of vertical subsidence or uplift in the model.

For Endurance the maximum uplift across all cases varies from 0.09m to 0.15m. This uplift is generally concentrated around the crest of the structure; however, it also occurs below the cooled zone and above the crestal fault (SST_F5_surface_extended) that was shifted down into the Bunter Sandstone and assigned Very Weak faultrock properties. This is shown in Figure 7.10. Note that the other faults that only occur in the overburden do not show this increased uplift even though they are also Very Weak. The Weak faults case also shows extra uplift above SST_F5_surface_extended although the magnitude is much less marked. There is no extra uplift above any fault in the Strong extended faults case.

Figure 7.10: Vertical rock displacement (ROCKDISZZ) indicating the amount of uplift in case LINEATRWH_PRESPLMCOOL_BCEXPWRWH_WKF at the Rot Clay level. Note the increased uplift around the cooled area and above the extended fault



7.4.2 Yield Mode

This is the invariant yield criteria yielding mode where 0 =no failure (pink), 1 = tension (dark blue), 3 = shear (green) and 5 = cap (red). Cap is compressive or compactive failure of the rock although none of the models display cap failure. All models display some minor tensile and some shear failure in the layers exposed at the crest of the model (layers 9 and 10 and above). However, this is regarded as an artefact of the grid geometry near seabed as the deeper layers are exposed on the crest of the structure and the failure also occurs in the pre-injection initialisation step. This yield in the crest can be seen in Figure 7.11 for the No Fault case at the 2017 and 2037 timesteps. All the other cases have some degree of failure in layers 9 and 10 at the crest. However, the only significant failure in deeper layers occurs in the Rot Halite 1 and 3 above the CO₂ plume in some models and some shear failure for certain additional overburden layers in the Very Weak faults case (see Figure 7.12). Note that in the Very Weak faults case this yield adjacent to the faults also occurs in the 2017 timestep indicating that the faults are too weak as they are showing yield prior to injection.

Figure 7.11: YIELDMOD values for the No Faults case (LIN_EEATRWH_PRESCOOL_BCEXPWRH_NOF). Note yield occurs in layers 9 and 10 only

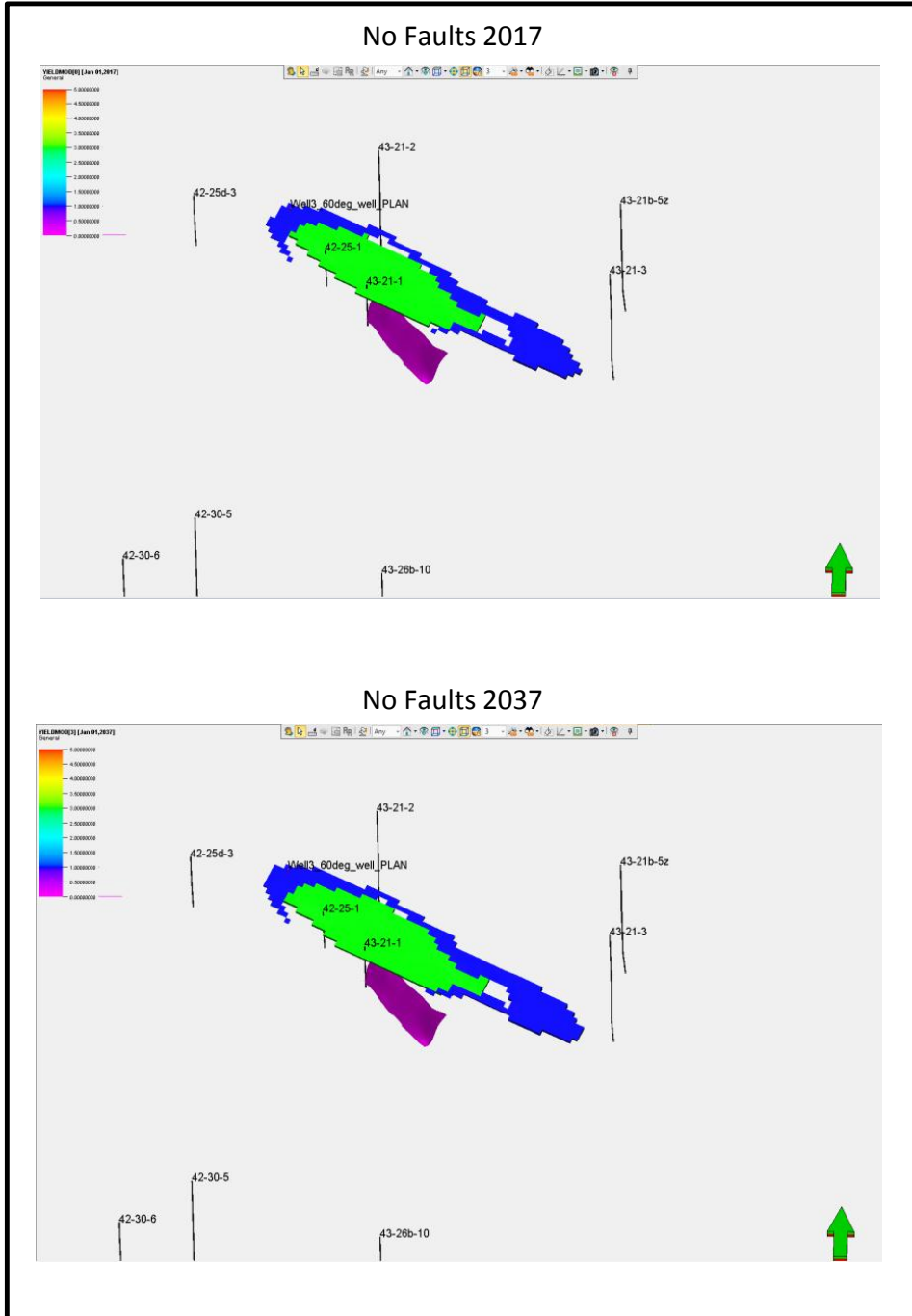


Figure 7.12: YELDMOD yield modes for the Weak Faults case (LINEEATRWH_PRESPLMCOOL_BCexplrwh_WKF) in 2037. Layers 9 and 10 excluded. Note that the 2017 timestep displays a similar yield distribution

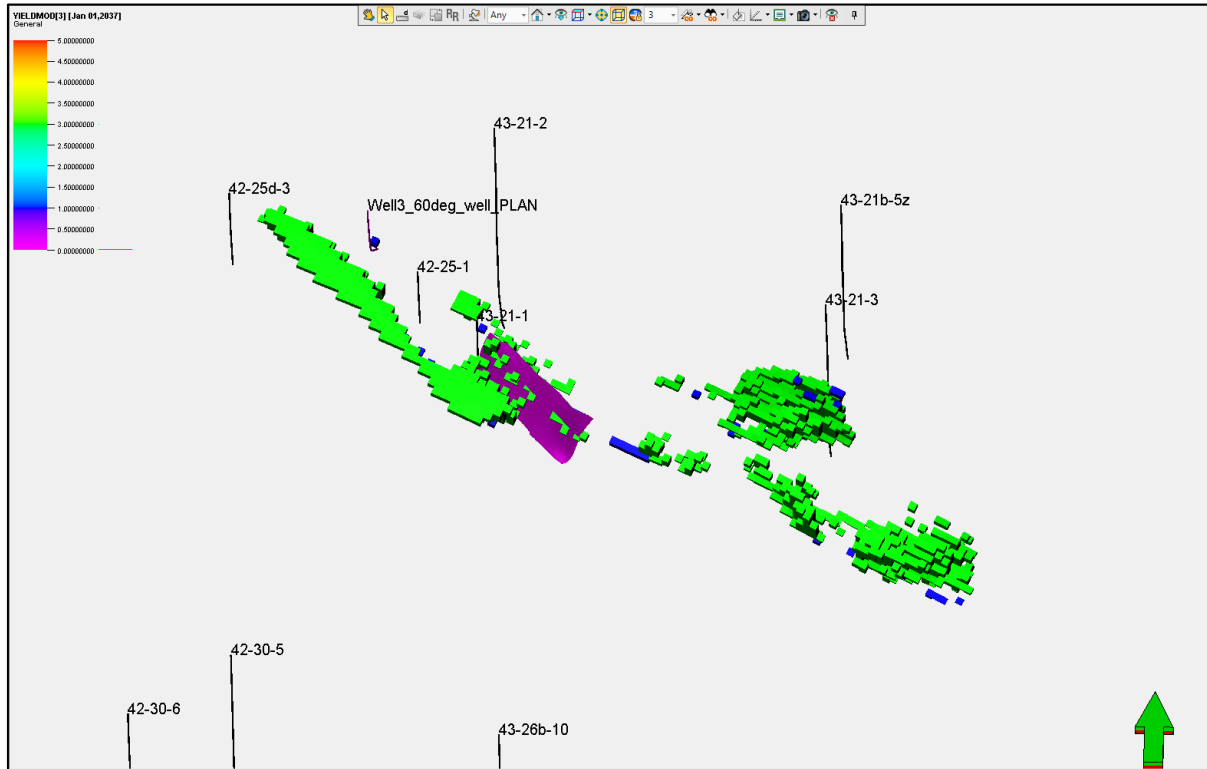
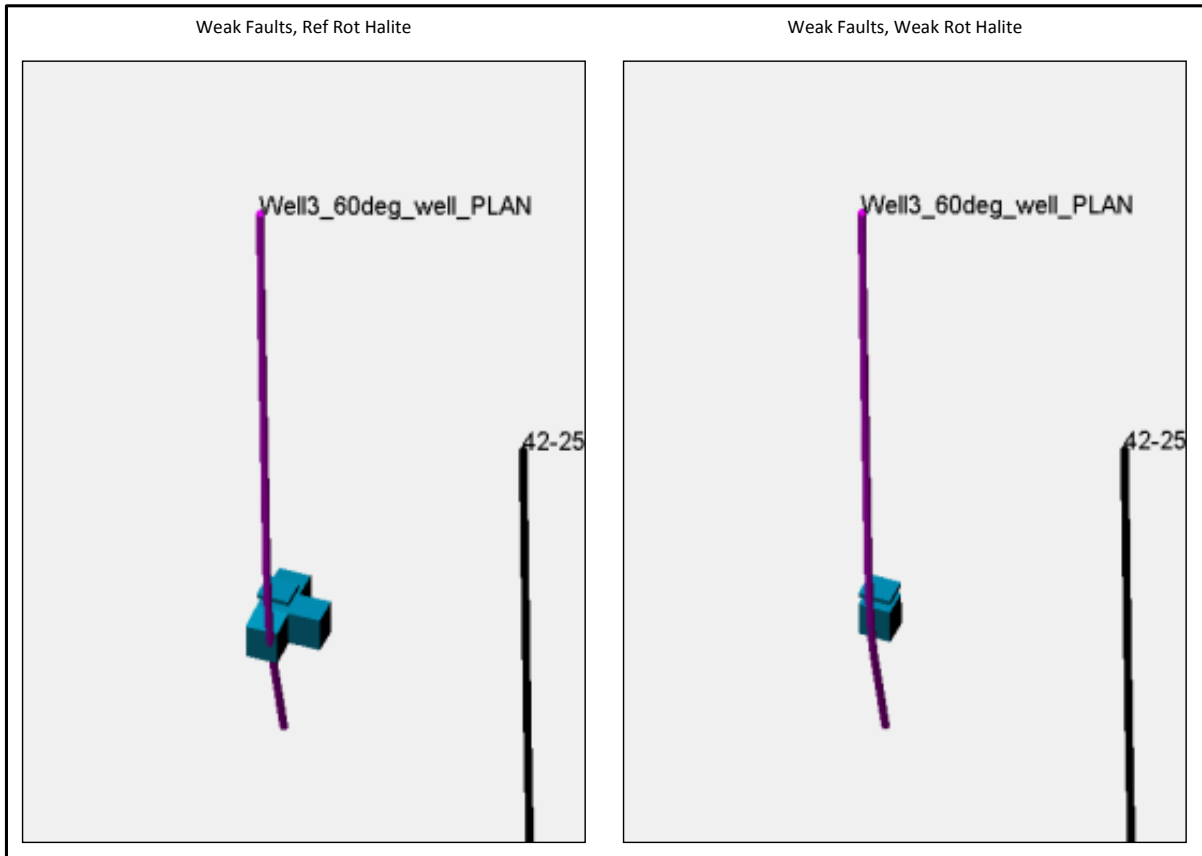


Figure 7.13 shows the increased area of CO₂ cooling related tensile failure associated with the higher Young's and lower Poisson's (Ref Rot Halite case) properties compared with the reduced area of tensile failure with the lower Young's higher Poisson's (Weak Rot Halite case).

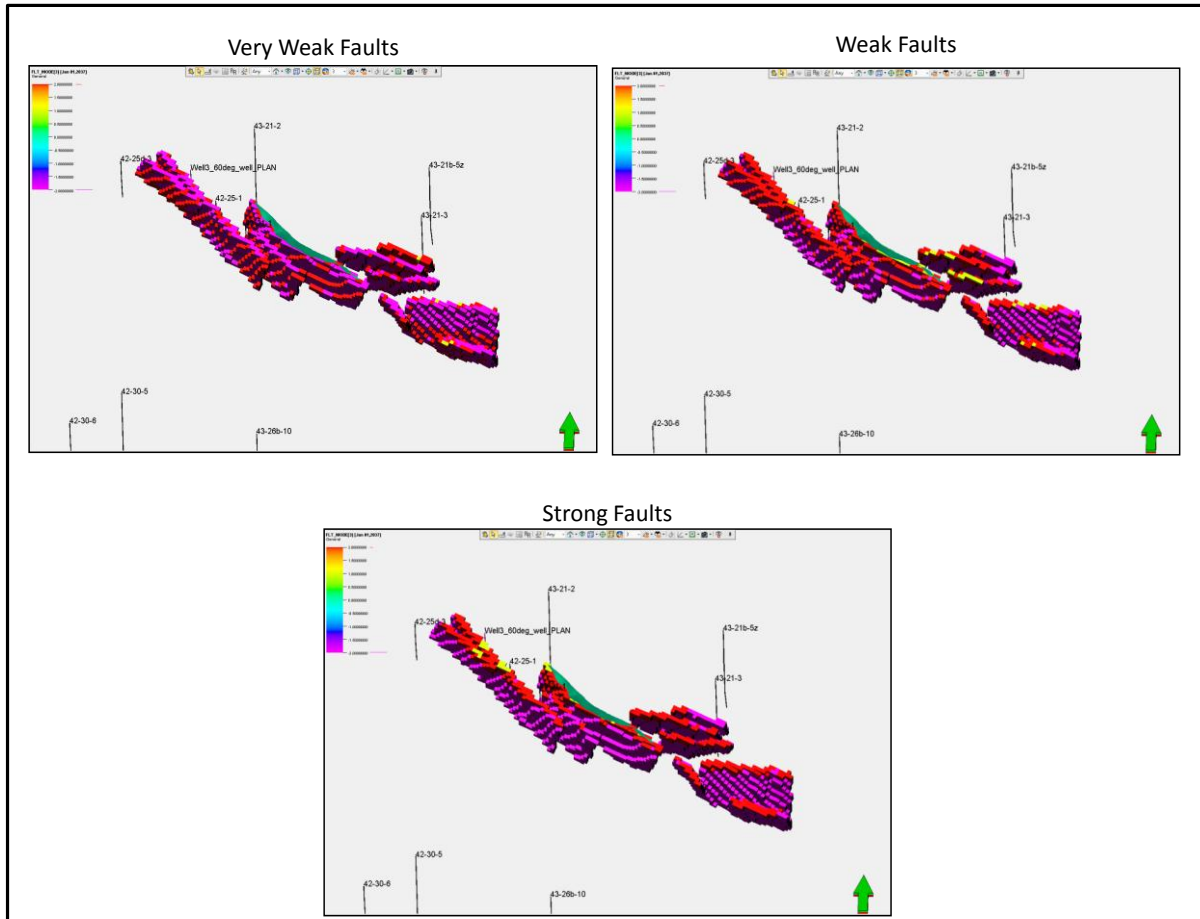
Figure 7.13: YELDMOD yield values in Rot Halite for first CO₂ plume model. LH Side: Reference Rot Halite E and u (LIN_EEATREF_PRESPLMCOOL_BCEXPLRRH_EXF). RH Side: Weak Rot Halite E and u (LIN_EEATRWH_PRESPLMCOOL_BCEXPLRWH_EXF). All failure is tensile



7.5 Fault Yield Mode

For any model run containing active faults, this property can be generated. The value range is; -2 = elastic shear (pink), -1 = elastic tension (blue), 1 = yielding tension (green/yellow) 2 = yielding shear (red). There are some differences in the yield mode between the three different fault property cases (see Figure 7.14). More yielding shear occurs throughout all the layers cut by faults in the Very Weak Faults case (LINEEATRWH_PRESPLMCOOL_BCEXPLRWH_WKF) whereas in the Weak (LIN_EEATRWH_PRESPLMCOOL_BCEXPLRWH_EXF) and Strong faults (LIN_EEATRWH_PRESPLMCOOL_BCEXPLRWH_STEXF) cases, most yield is elastic shear apart from some yielding tension and yielding shear in the uppermost 2-3 layers.

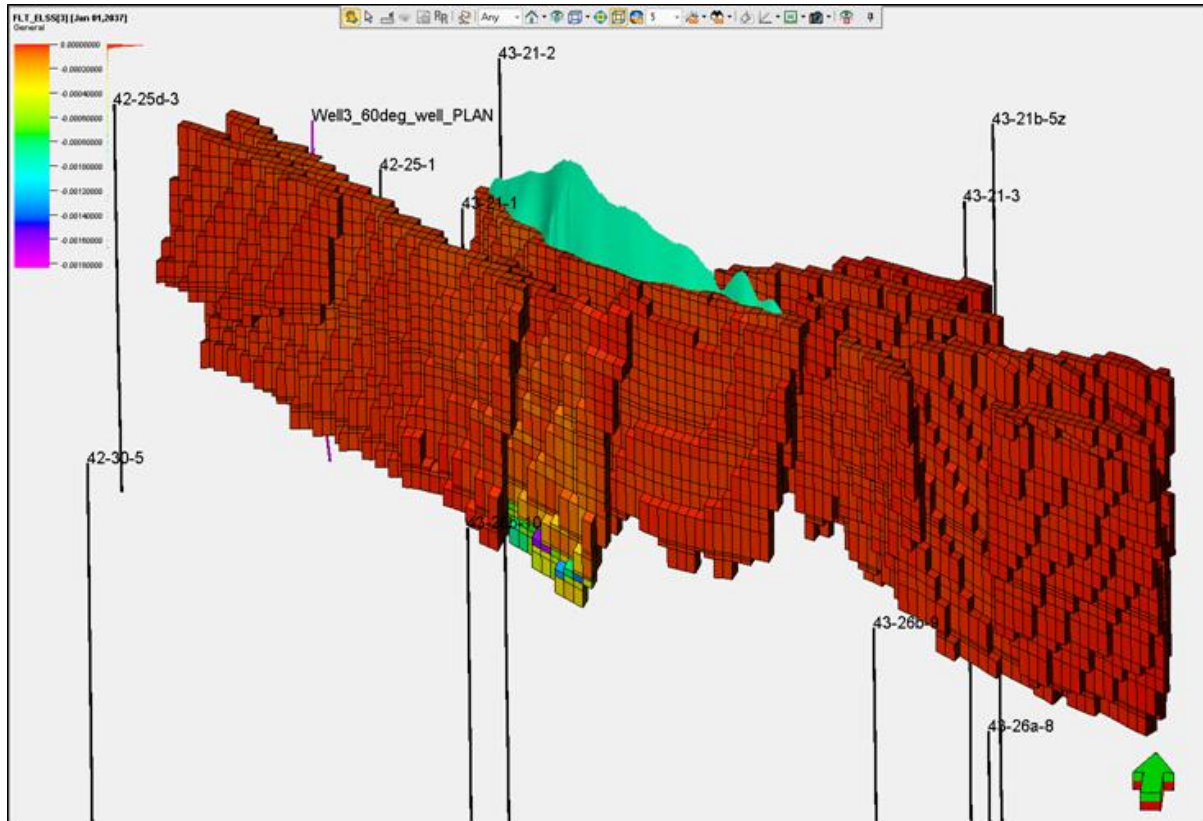
Figure 7.14: Fault Yield Mode properties for the Endurance structure extended faults



7.6 Fault Elastic Shear and Normal Strains

This is a measure of the amount of elastic shear strain affecting the fault cells. It can be seen from Figure 7.15 that the only noticeable values are at the base of the extended Very Weak faults case, mainly within the Bunter Sandstone. This strain links to the increased vertical displacement above the extended fault shown in Figure 7.10. There is also an increase in shear strain seen at the same location in the Weak Faults case but the magnitudes are lower. The fault normal strain magnitudes show a similar distribution to the shear strain values. Note the absolute magnitude of strain increase is still very low.

Figure 7.15: Fault Elastic Shear Strain (FLT_ELSS) for the Very Weak extended Faults linear case (LINEATRWH_PRESPLMCOOL_BCEXPWRH_WKF)



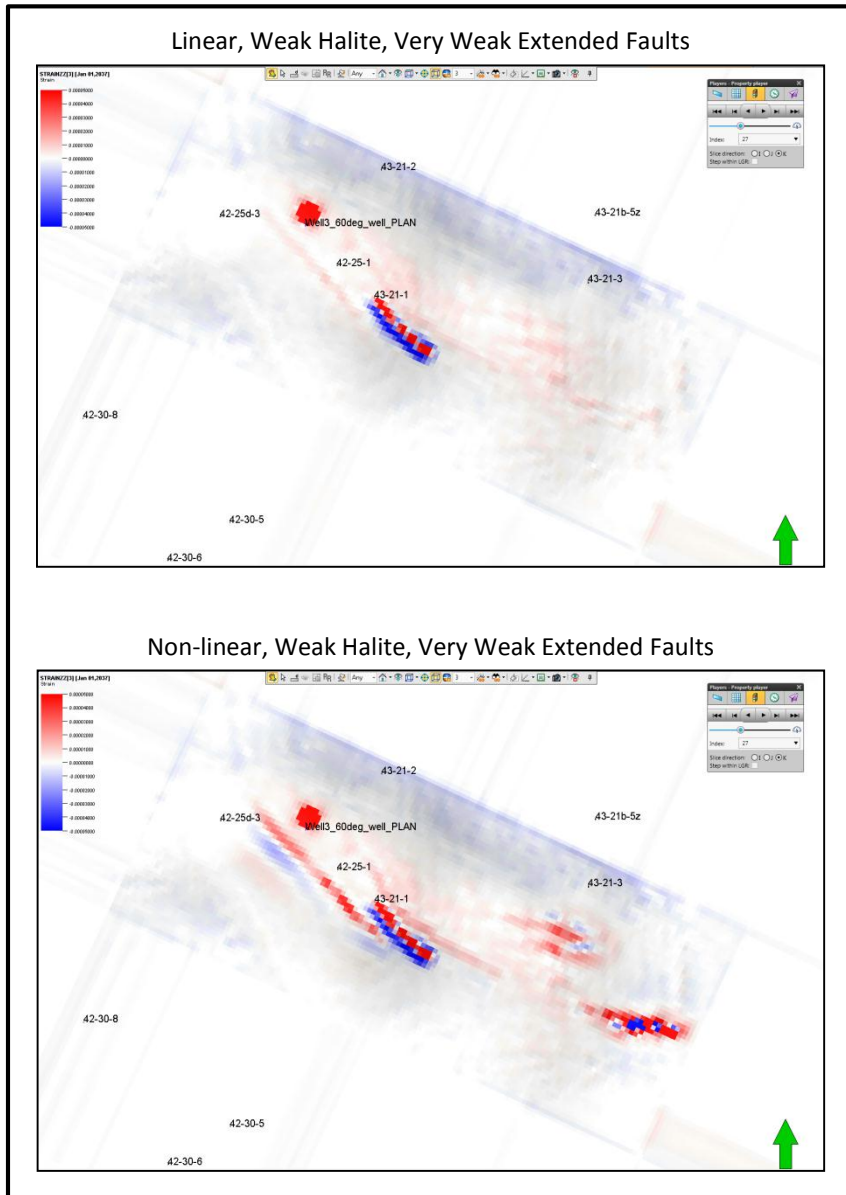
7.6.1 Very Weak Faults, non-linear case

This case (NONLIN_EEATRWH_PRESPLMCOOL_BCEXPWRH_WKEXF) was executed to determine whether any plastic deformation strains and displacements, which were more significant than the linear (elastic) case, were generated in the model. The case chosen was the Weak Extended Faults, Weak Halite, first version plume cooling case as that had the bulk of the elastic failure in the linear case.

The vertical displacement and intra Bunter Sandstone vertical strains are very similar to the linear case. However, in the overburden around the faults at timesteps 2022-2037, there is noticeably more vertical elastic strain (STRAINZZ) in the matrix which is x10-100 larger in places. There is also slightly more elastic shear strain (FLT_ELSS) in the faulted cells in the non-linear run. Note that the non-linear runs shows minimal development of plastic strain as the bulk of the strain is elastic.

The reason for the increase in vertical elastic strain in the overburden at timesteps 2022-2037 is not clear as all the inputs were the same as the linear case. It is possible that additional elastic strain is accumulating in the matrix after some additional elastic or plastic strain has occurred on the faults. Note that the absolute amounts of STRAINZZ and FLT_ELSS concerned are small (typically 1E-04 to 1E-05) so it is also possible that the strains are at the accuracy limit of the modelling processes. Also note that the extra strain is also manifest at the initialisation time step indicating it is related to the excessively weak faults slipping as soon as they are loaded.

Figure 7.16: Very Weak extended faults, CO₂ plume V1. Vertical elastic strain (STRAINZZ) at timestep 2037 Rot Halite 1 level. Upper: Linear run (LINEEATRWH_PRESPLMCOOL_BCEXPWRH_WKF). Lower: Non-linear run (NONLIN_EEATRWH_PRESPLMCOOL_BCEXPWRH_WKXF)



7.7 Reference Cases

These cases were devised to represent a more likely combination of parameters in the Endurance store. The key parameters and case names are listed below.

Weak Halite

Weak faults (not extended)

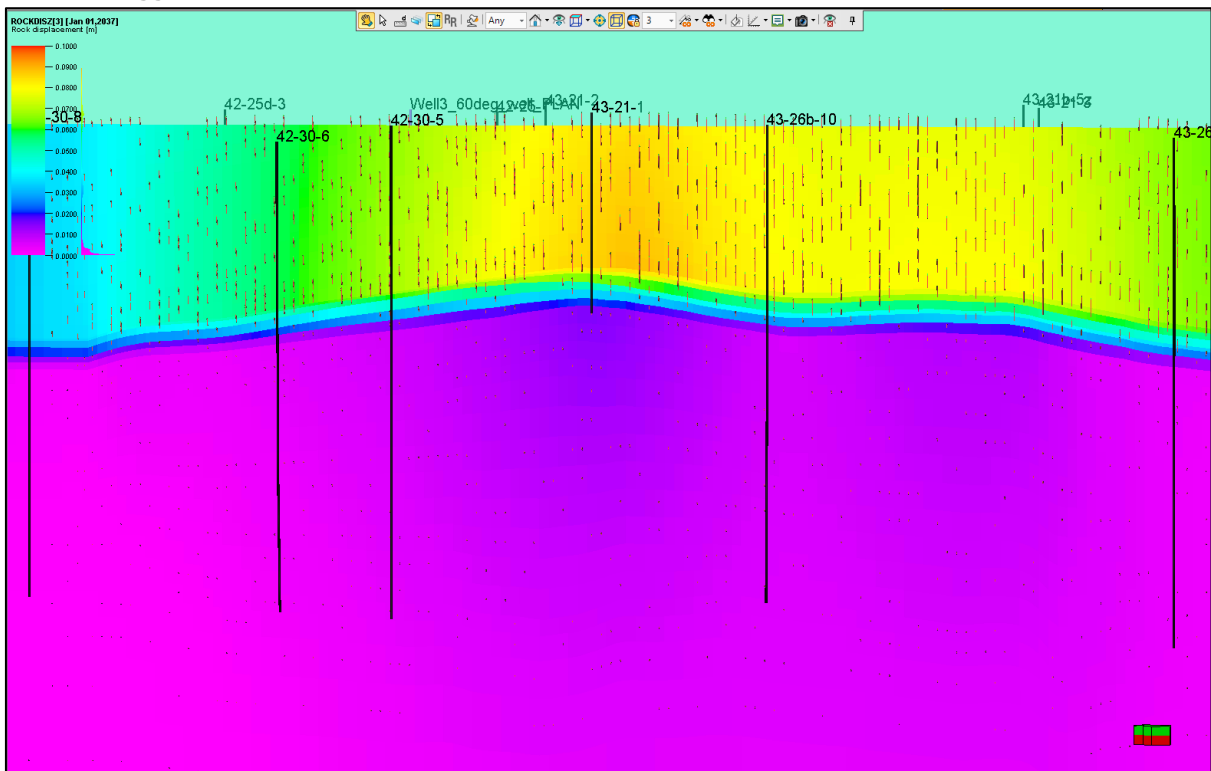
Plume cooling (second version)

Linear: LIN_EEATRWH_PRESPLUMECOOLV2_BCEXPWRWH_F

Non linear: NONLIN_EEATRWH_PRESPLUMECOOLV2_BCEXPWRWH_F

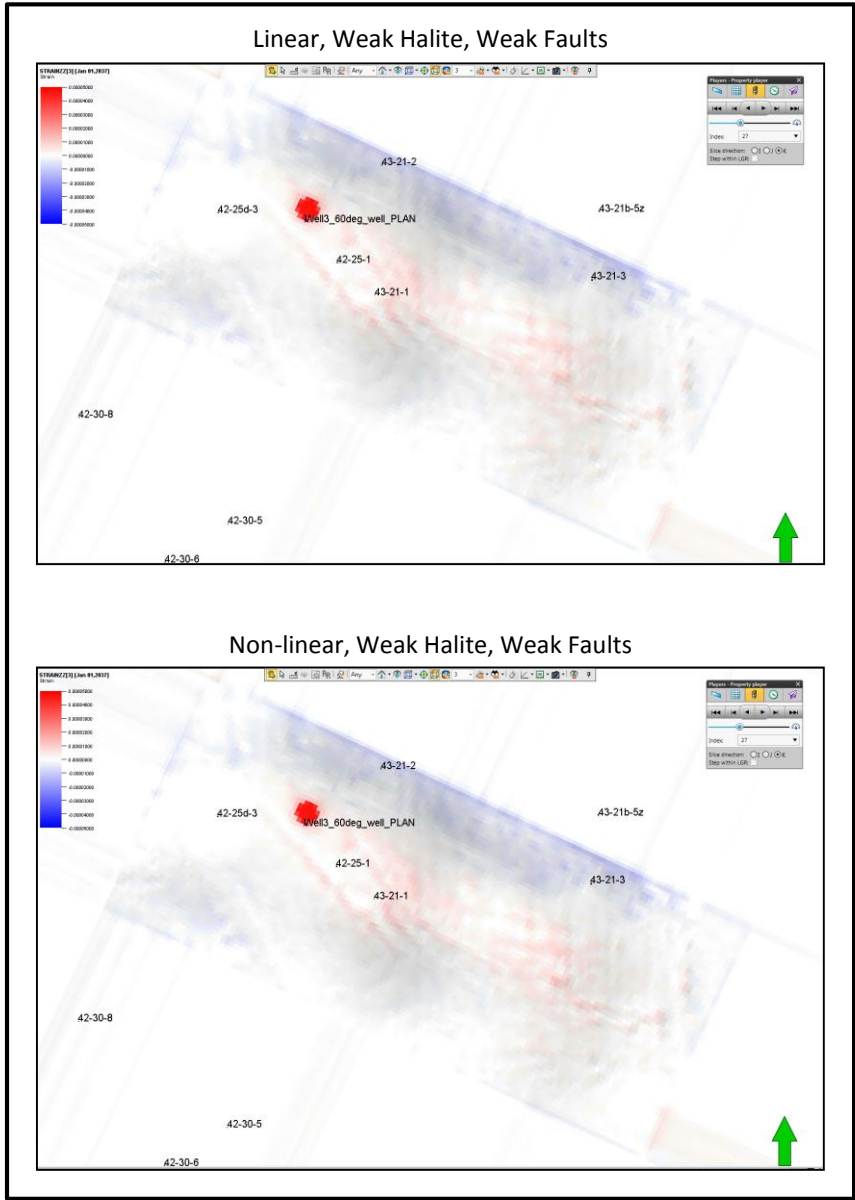
The vertical displacement in both cases is similar to the other cases with Weak faults (approx. max vertical displacement of 0.085m at the crest at the Rot Clay level). In the linear case, if layers 9 and 10 are excluded, there is no tensile failure in the Rot Halite above the CO₂ plume and no tensile or shear yield associated with the overburden faults. The linear case displacement property is shown in Figure 7.17, but the non-linear case vertical displacement property is virtually identical.

Figure 7.17: Vertical displacement property and vectors for the linear Reference case (LIN_EEATRWH_PRESPLUMECOOLV2_BCEXPWRWH_F). Crestal EW section, W on left. Vertical exaggeration x3



The non-linear case shows a similar distribution of smooth displacement and very slight strain changes above the Bunter Sandstone compared with the linear case although some minor differences in vertical strain occur that follow a similar pattern to those described in Section 7.6.1 albeit with much reduced differences. There is slightly more elastic shear strain within the faulted cells compared to the linear case but most of that elastic shear strain is minor and the higher values in the non-linear case mainly occur in layers 9 and 10 where boundary conditions dominate.

Figure 7.18: Weak faults case, CO₂ plume V2. Vertical elastic strain (STRAINZZ) at timestep 2037 Rot Halite 1 level. Upper: Linear run (LIN_EEATRW_H_PRESPLUMECOOLV2_BCexplrwh_F). Lower: Non-linear run (NONLIN_EEATRW_H_PRESPLUMECOOLV2_BCexplrwh_F)



7.8 Summary and Conclusion

For each case, the coupled model in-situ stress system was modelled in stages with three optimisation runs; two to match the 42/25d-3 Rot Clay and Bunter Sandstone minifrac data and a third run to optimise isotropic lithostatic salt stresses. These three separate property sets were combined into concatenated total stress models for use in the main modelling cases.

For the White Rose CO₂ the main conclusion is that there is little risk of significant strain and/or failure of the Röt Clay and Röt Halite seals as a consequence of Endurance structure being subject to the predicted pressure and temperature changes.

In order to assess worst case conditions, two cases were created to check the point at which the model would indicate noticeable strain or yield failure; these were:

1. weak and very weak faultrocks with a fault extended into the upper part of the Bunter Sandstone resulted in minor increased strain and localised displacement in the overburden and in the upper Bunter Sandstone layers; extended faults have not been mapped from seismic and the Very Weak faultrock is regarded as highly unlikely; and
2. cooling of the Röt Clay and Röt Halite above a simplistic CO₂ plume leads to tensile failure (fracturing) of some Röt Halite cells immediately above the plume. The Röt Clay and clay rich Röt Halite however do not show this tensile failure. To reiterate, the degree of cooling modelled is very unlikely and the slower process of conduction would dominate over convection unless there is already a leak pathway.

The simulations considered a number of 'limit' cases where the fault locations, fault strength and degree of cooling were pushed up to or possibly beyond realistic ranges to get some failure. Even in these cases the increased strain or failure appears to be minor and localised and is not likely to create a significant leak pathway. Note that little difference was generally observed between the linear and non-linear runs. These results are summarised below:

Shifted one crestal fault into the Bunter Sandstone, applied very weak shear and normal stiffness values. The shear and normal stiffnesses were reduced to values just above zero to simulate cohesionless faults. At the end of simulation this localised the increase in displacement to 16 cm around the shifted fault hanging-wall. Additional localised increases in shear and tensile strain on faults in the overburden were also observed (compared to the faults with stiffer properties). Most cases with the very weak faults displayed strains even at the initialisation step which indicates the values are probably too low. Even if that strain is possible, it is probably not enough to create a connected leak pathway. Some increase in elastic strain occurred around overburden faults in the non-linear case compared to the linear case.

Aggressive plume cooling around and above the injection well: The cooling in the Röt Halite and Röt Clay cells above the perforations was to 22°C which is higher than from conduction alone. Localised failure of a few Röt Halite 1 and Röt Halite 3 cells occurred via tensile fracturing. In the Weak Halite case, this is in one Röt Halite 1 cell and one Röt Halite 3 cell. In the Reference Halite case this tensile failure increases to four Röt Halite 1 cells because of the more stiffer and brittle properties. The Röt Clay and clay rich Röt Halite 2 do not show this tensile failure.

Given that the scenarios described above are unlikely, there is very little likelihood of significant strain and related yield of the Röt Clay and Röt Halite in the Endurance structure due to the White Rose CO₂ injection.

The basic conclusion is that with the White Rose CO₂ load of 2.68MTPA (as a maximum over 20 years), the Endurance structure when modelled with reasonable properties shows only minor uplift of 9 cm at the crest. In reality, cumulative injection of the first load over 20 years will be less than the maximum possible aggregate of 53.6MTPA.

8 Reservoir Engineering Field Report

This section describes the use of analytical and full field simulation models as well as regional information to assess the capacity, injectivity, hydrodynamics and containment of the Endurance structural closure for the safe and permanent storage of White Rose CO₂

CO₂ enters the formation through perforations in the pipe as a horizontal flow. The density of CO₂ in the brine field in the aquifer at reservoir conditions will be considerably less than the native brine, so buoyancy will force the CO₂ to migrate upward until it reaches the cap rock.

Once at the cap rock, the CO₂ will flow along the top of the Bunter sandstone formation until it reaches the crest of the brine in the aquifer where it will start to form a secondary gas cap.

There are many important aspects associated with the injection of CO₂ into a saline aquifer, not least of which is the effect on reservoir pressure. If pressure is not managed correctly, there will be a risk of fracture of the reservoir and cap rock that would compromise the integrity of the store.

Other important aspects of are the different types of trapping mechanism which can occur:

- structural and stratigraphic, which is largely a function of the geology of the reservoir and its cap rock;
- residual, a function of relative permeability;
- solubility, which depends on the CO₂/brine phase behaviour; and
- mineral trapping.

The first three mechanisms listed above will be considered in this section. The fourth, mineral trapping is largely down to geochemical reactions which are thought to take place over the timescale of hundreds to thousands of years and have not been considered in this study.

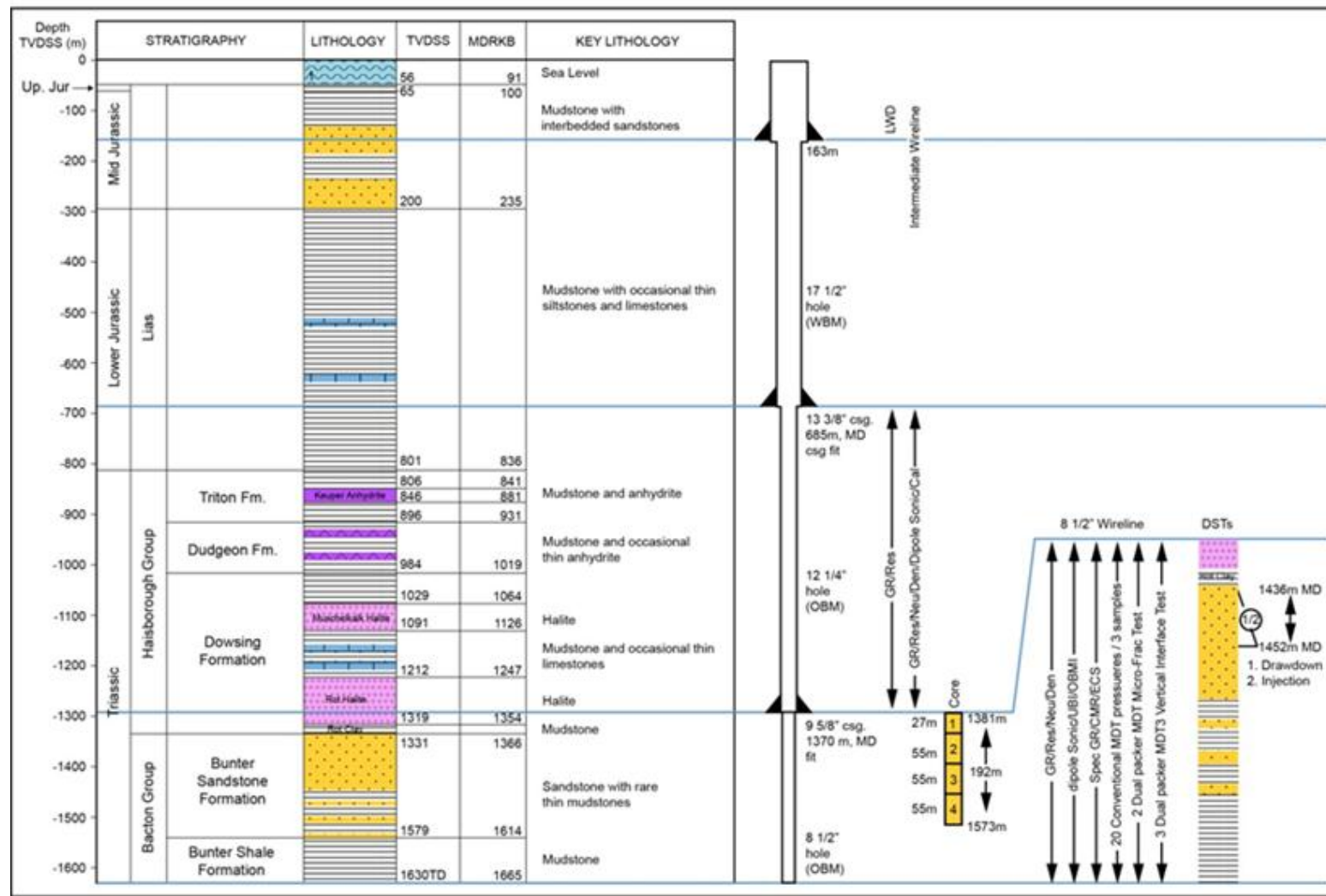
8.1 Appraisal of Endurance structure with Well 42/25D-3

To obtain a storage permit application from the UK regulator, DECC, NGCL will have to satisfy the relevant legislation to meet the requirements of Directive 2009/31/EC of the European Parliament and of the Council of 23 April 2009 on the geological storage of carbon dioxide and amending Council Directive 85/337/EEC, European Parliament and Council Directives 2000/60/EC, 2001/80/EC, 2004/35/EC, 2006/12/EC, 2008/1/EC and Regulation (EC) No 1013/2006.

A key statement within the guidance is: *The goal of the characterisation of the storage site and complex is to assess the site's capacity, injectivity, hydrodynamics, containment and ability to be monitored in order to ensure safe and permanent storage of CO₂.*

This statement drove the objectives of the appraisal of well 42/25d-3; the data gathering program is summarised in Figure 8.1, below.

Figure 8.1: Bunter Sandstone Formation Stratigraphy and 42/25d-3 Appraisal Well Data Gathering Program



The following list some of the data gathered and how they address the objectives.

- capacity;
- the static capacity of the reservoir, as measured by the pore volume, helps define the NTG ratio and porosity measurements from the gamma ray and neutron logs;
- injectivity;
- a multi-rate injection test was undertaken following on from the production flow test to prove injectivity; filtered sea-water was used as the injectant as a substitute for dense phase supercritical CO₂.
- hydrodynamics;
- the key parameters affecting hydrodynamics are the absolute and relative permeability of the CO₂ and brine; the relationship between absolute permeability and porosity was refined through logs and core measurements whilst relative permeability was measured for the first time by special core analysis of some of the core samples; and
- containment.

A number of activities have proved containment:

- the parallel geomechanical modelling study completed in February 2015;
- specialist logs for data gathering;
- testing of the cap rock and reservoir core sample for data gathering;
- monitoring; and
- a four dimensional (4D) seismic tools was employed to monitor plume development. The data from some of the specialist logs, such as dipole sonic, produced images of the reservoir as it is filled.

The key components of well 42/25d-3 appraisal programme are now summarised in the following sections.

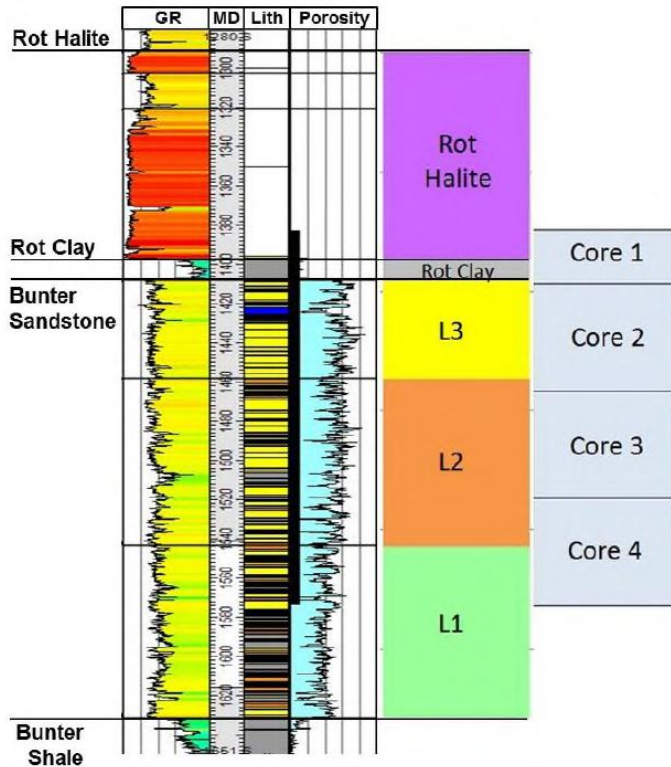
8.1.1 Core Analysis

Four cores were recovered from well 42/25d-3 totalling a length of 192.51m (631.6ft) (Figure 8.2). Core 1 (84.6ft.; 25.79 m) recovered the lower part of the Röt Halite and the whole of the Röt Clay unit including the first few feet of the top Bunter sandstone, whilst Cores 2, 3, and 4 recovered 166.73m (547ft) of the Bunter sandstone section. All cores were delivered to Weatherford Laboratories (UK) Limited in July, 2013 for core analysis. The core analysis was divided into broadly two parts: the conventional (or routine) core analysis (RCA) and the special core analysis (SCAL).

The RCA involved photographing, CT scanning, spectrographic gamma ray, as well as core plug permeability, probe permeametry measurements, porosity, grain density and particle size analysis in addition to plug selection for further SCAL work. A cleaning study to determine the effect cleaning agents had on the halite within the core plugs and Mercury Injection Capillary Pressure tests were also completed.

The SCAL study was preceded by an Interfacial Tension study to determine how a synthetic formation water would react with CO₂ at reservoir conditions, as well as a study to determine the effect of critical flow velocity. Subsequently the SCAL study identified irreducible water saturation and relative permeability curve parameters for use in dynamic modelling based on capillary pressure and 1-D core performance modelling results.

Figure 8.2: 42/25d-3 Well Schematic Showing Cored Interval
42/25d-3



8.1.1.1 Conventional Core Analysis

The main objective of the RCA was to determine basic rock properties of the cores recovered from appraisal well 42/25d-3 and to prepare plug samples for use in more specialised core analyses. The basic rock properties measured during RCA include porosity, permeability, grain density and grain size distribution. The following sections give brief summaries of the RCA programme in a broadly chronological order.

Core Preparation: Core 1 was cored using 4” diameter half-moon sleeves and delivered to the laboratory cut into 3ft lengths, immersed in plastic tubes containing a bland mineral oil, capped at each end. Following CT scanning, these were removed from the tubes and transferred to custom made stainless steel troughs, immersed under Isopar L oil. This prevented the core from de-hydrating whilst allowing its surface to be viewed as required. Cores 2, 3 and 4 were approximately 3.5” in diameter and arrived at the laboratory in 30ft aluminium inner sleeves which were then cut into 3ft lengths to enable the core sections to be handled. Other operations associated with core preparation: Core Gamma run, CT Scanning, Core Handling, Samples Preservation, Conventional Core Plug Sample Preparation, Special Core Analysis (SCAL) Plugs Preparation, and Plug Sample Analysis.

Permeability was determined by use of a Weatherford Laboratories DGP-300B Steady State Nitrogen Permeameter at an effective confining pressure of 400 psig. These were used in conjunction with the callipered length and diameter to calculate permeability from Darcy's equation.

As an internal quality control, one in ten plugs were re-run during analysis of the samples, and prior to running the plugs, check plugs of predetermined permeability covering a range from 0.18mD to 6000mD were analysed, with each check plug corresponding to a mass flowmeter in the permeameter.

Helium Porosity and Grain Density: porosity of the clean, dry unsleeved plug samples was determined by direct measurement of grain volume at ambient conditions and bulk volume determined by mercury displacement. The sleeved plugs underwent an additional direct pore volume measurement using a confining pressure of 400 psig.

Grain volume was determined using a Weatherford Laboratories DHP-100 Boyle's Law porosimeter. Bulk volume for the mounted plugs was calculated from the sum of the measured grain volume and direct pore volume. Grain density was calculated from the weight and measured grain volume, taking care that all sleeving materials volume and weight were subtracted. The porosity measurements were repeated to ± 0.02 psi.

Cross plots of horizontal permeability and vertical permeability vs. porosity are presented in Figure 8.3 and Figure 8.4.

Figure 8.3: 42/25d-3 Helium Porosity vs Horizontal Permeability

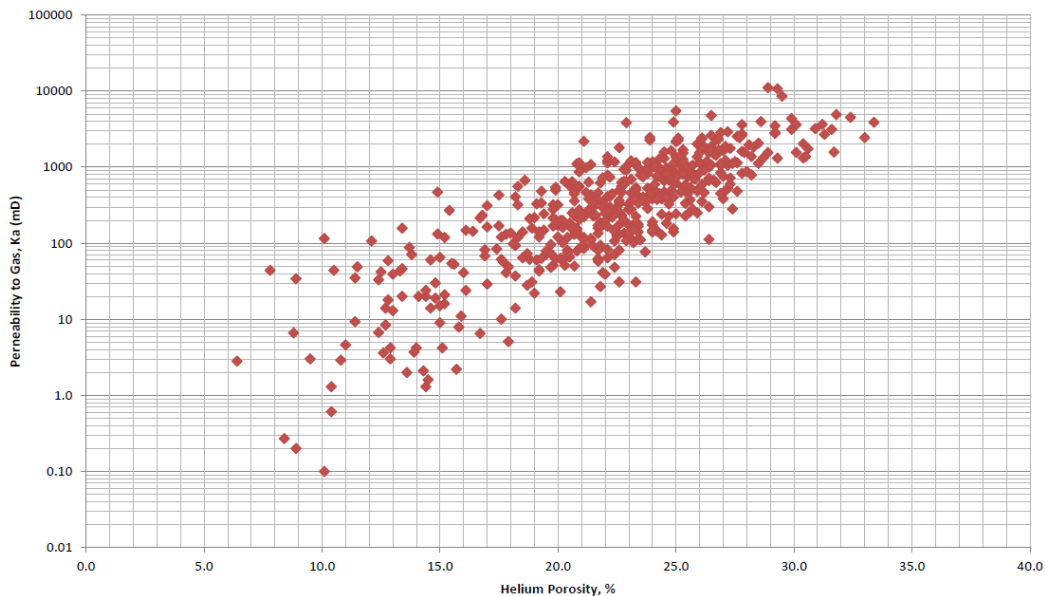
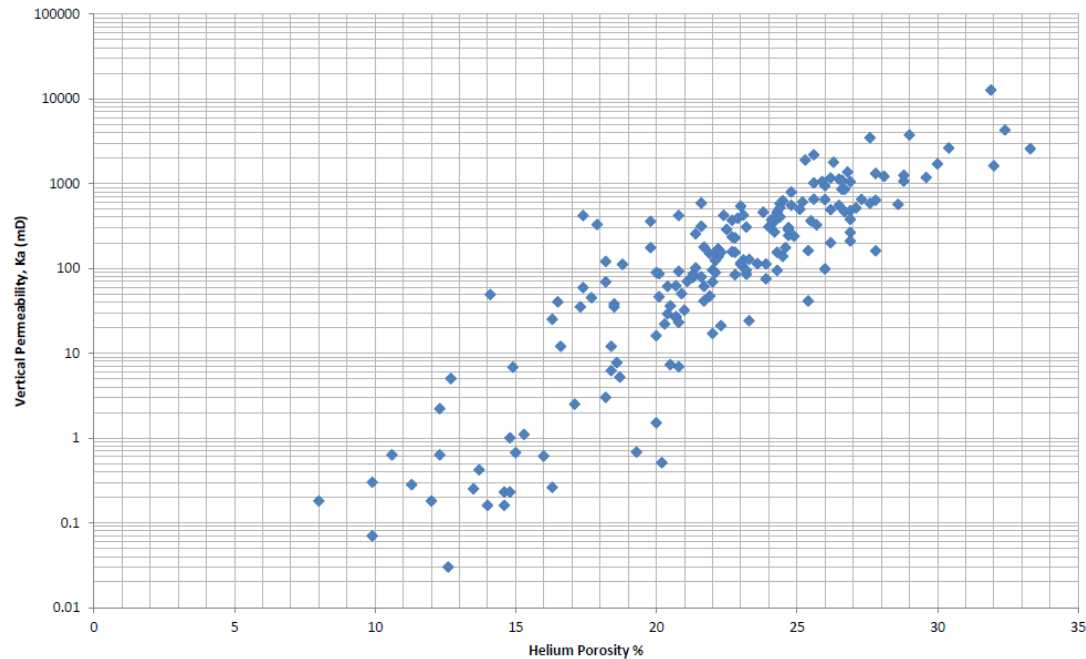


Figure 8.4: 42/25d-3 Helium Porosity vs Vertical Permeability



Fifteen plugs were re-measured independently for porosity after an assessment of the original preliminary data showed that the measured porosities for these samples fell outside the accepted error margins in comparison to the calculated length x area porosities. Re-measurement put back the new lengths, diameters and porosities into the accepted error margin. The initial deviations were attributed to plugs misshaped by chipped edges or sides, fractures or slight ridges along plug lengths.

Klinkenberg Permeability

Klinkenberg Permeability was determined by use of a Weatherford Laboratories DGP-300B Steady State Nitrogen Permeameter at two minimum sleeve pressures of 400 psig (28barg) and 2600 psig (179barg).

Measurements were repeated a minimum of four times on each sample at different mean pore pressures to enable the calculation of Klinkenberg permeability (Kl). Permeability to CO₂ was plotted vs 1/mean pore pressure and the best fit line extrapolated to infinite mean pore pressure to provide the Kl.

Example Klinkenberg permeability data are presented in Figure 8.5 and Figure 8.6 for sample 94 (4624.90ft) at confining pressures of 28barg and 179barg respectively.

Figure 8.5: Klinkenberg plot for sample 94 (4624.90ft) at a confining pressure of 28barg
Klinkenberg Plot

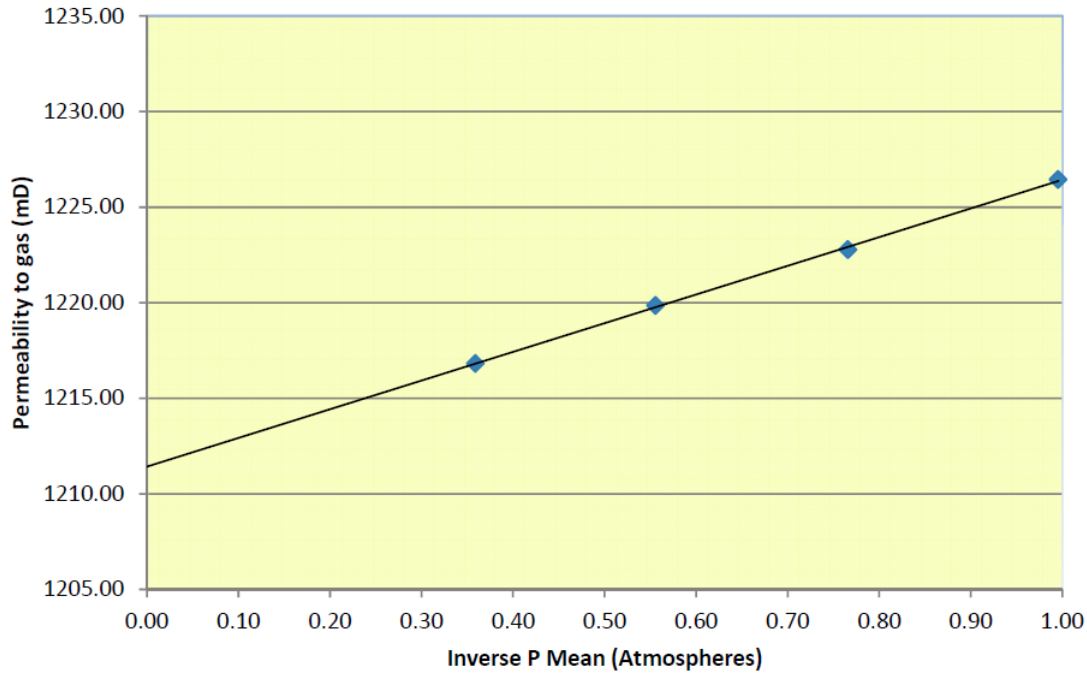
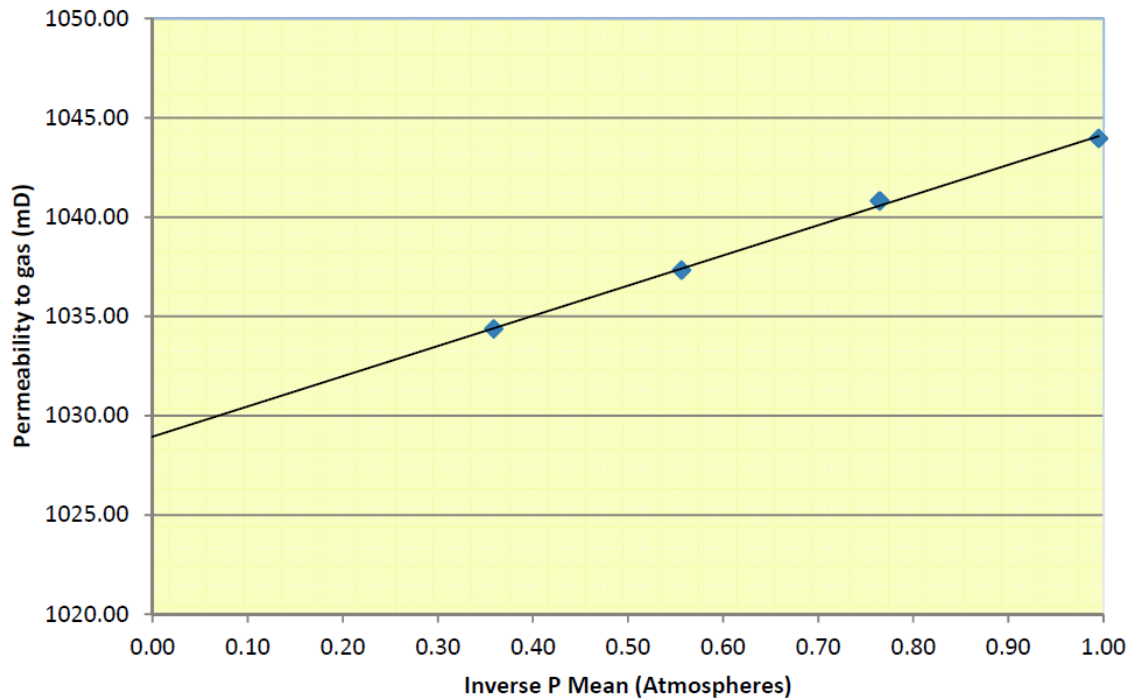


Figure 8.6: Klinkenberg plot for sample 94 (4624.90ft) at a confining pressure of 179barg



Slabbing: on completion of all sampling and plugging the core was slabbed 1/3 to 2/3 to expose maximum dip dry. The slabbed core was placed into plastic gutters to support it without movement.

Core Photography: following slabbing, salt was leaching to the surface of the core, obscuring the sedimentological features. In order to improve this, each section was carefully sanded and smoothed prior to quickly taking the core photograph under white light.

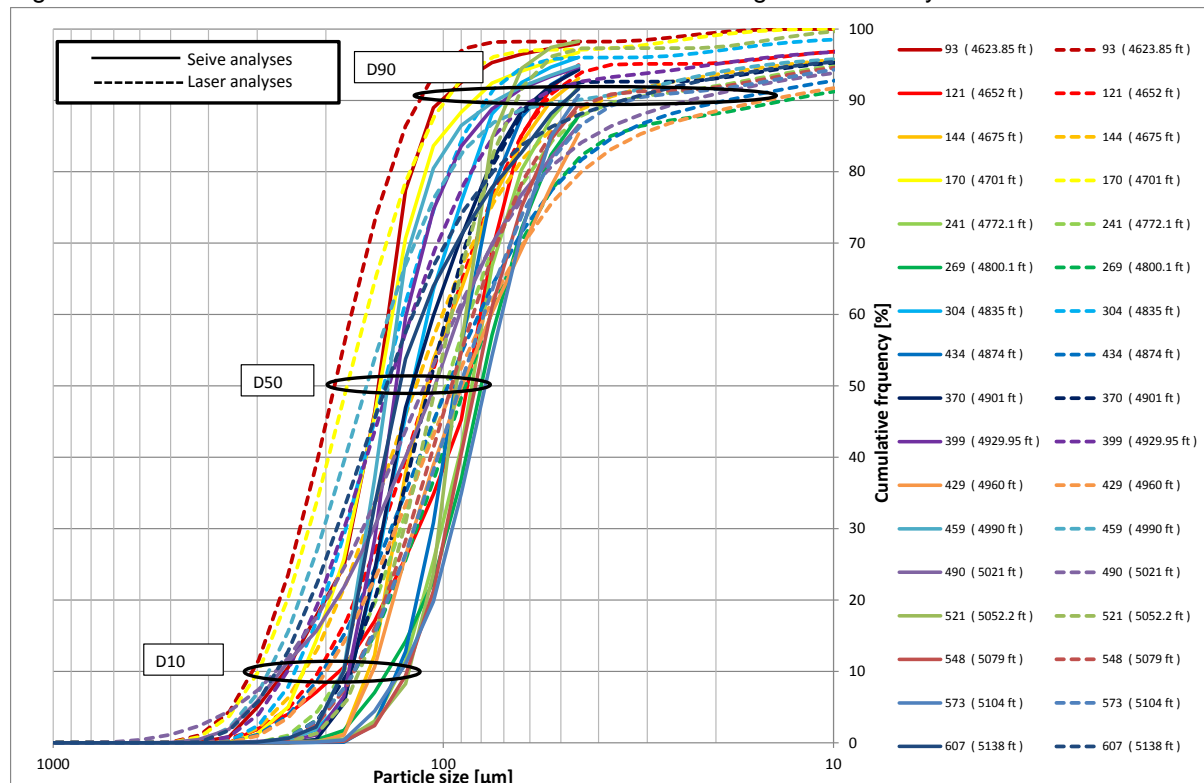
Resination: following core photography, a second slabbing cut was performed. A 2cm thick “biscuit-slice” was taken along the entire cored interval from the photographed face of the 1/2 cut core section. The slice was placed into plastic presentation trays, labelled with well name, core number, box number, and all routine porosity and permeability data. Clear Epoxy resin was then used to seal the core into the trays for archive purposes.

Particle Size Analysis: laser particle size analysis and sieve analysis were performed on 17 plug samples. Sieve Analysis is a procedure used to assess the particle size distribution of a granular material by weight whilst laser particle size analysis is used to assess the particle size distribution of a granular material by laser diffraction.

Sieve analysis is applicable for particles larger than coarse silt (45 microns) whilst Laser particle size analysis is applicable for particles from 2mm to 0.02 microns.

Graphical laser particle size analysis and sieve analyses data is presented in Figure 8.7.

Figure 8.7: - Particle size distribution from laser and sieve grain size analysis



Unconventional RCA Studies: additional studies (which may be termed unconventional RCA) have been performed at Weatherford Laboratories in Norway to support the routine core analysis carried out in the UK using 30 core plugs. The main outlines of the study are:

- perform a non-standard cleaning study on plug samples and sister end trims, perform basic rock properties on plugs samples and prepare sister end trims for Scanning Electronic Microscope;
- the Bunter formation contains potential native halite minerals and has a highly saline formation water. This study was meant to assess the extent to which the removal of native and/or precipitated salts produced changes in basic rock properties and to ascertain the most appropriate method of cleaning Bunter core for RCA;
- trims from samples were taken through three cycles of cleaning and basic petrophysical properties determined after each cleaning cycle; all the samples that survived through all cycles of cleaning show a tendency to an increase in permeability but the increase was not significant (see Figure 8.8). Standard cleaning procedures were therefore considered appropriate for cleaning Bunter cores for RCA; and
- seal unit-cap rock tests meant to determine pore throat size distributions and as a characterisation tool for geological and petrophysical parameters including:
 - a) water permeability measurements at 400 psi net confining pressure;
 - b) pore squeeze to 2600 psi net confining pressure;
 - c) water permeability measurements at 2600 psi net confining pressure;
 - d) measurement of bulk volume by Archimedes principal; and
 - e) grain volume and porosity measurements.
- Capillary pressure by mercury injection or Mercury Injection Capillary Measurements, MICP: this is to determine pore throat size distributions and for use as a characterisation tool for dynamic models. Before performing MICP, cleaned Bunter core samples were oven dried and their pore volume, density, and porosity determined.

This test program was shared between Weatherford's Stavanger and Trondheim laboratories. Tests (a) to (d) above were performed at the Stavanger lab; the remaining at the Trondheim lab. The original test program at Trondheim lab had to be curtailed because of damage (ranging from complete plug dissolution to fracturing) to all but one of the 19 samples due to prolonged storage in cold isopropanol. It is therefore important to note that even if great care was taken when collecting grains of the damaged samples stored in isopropanol into the thimbles prior to soxhlet cleaning, some grains would have been lost. This will affect the interpretation of the results for grain density and porosity. The results are summarised in Figure 8.9 and Figure 8.10.

Figure 8.11 shows the plot of mercury pressure versus mercury saturation. The pore throat size distribution is given as a plot in Figure 8.12. The pore throat distribution size varies from 0.752 microns to 13.463 microns, corresponding to an injection pressure that varies from 2.52 psia to 62.25 psia. The J-function is plotted against saturation in Figure 8.13.

Table 8.1 is a summary of the measured petrophysical properties obtained as part of the additional RCA study. The table shows the range (from minimum to maximum values) of each measurement and also indicates the applicable test program.

Figure 8.8: Klinkenberg corrected CO₂ permeability, kL, vs. Helium porosity, ϕ_{He}

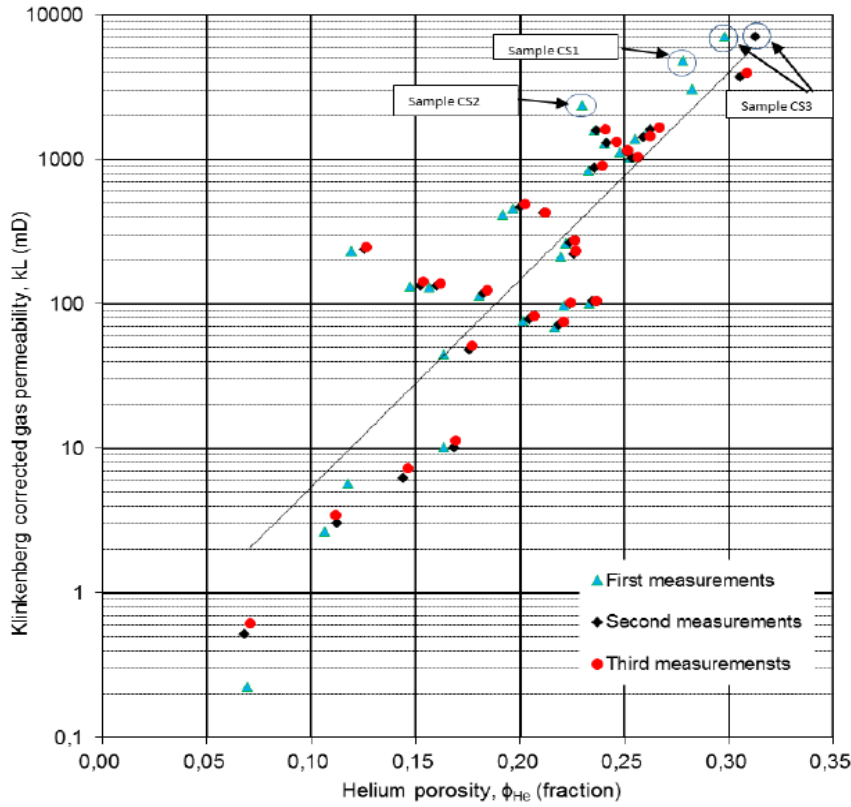


Figure 8.9: kw at 400 psi NCP vs. porosity obtained at Trondheim Lab

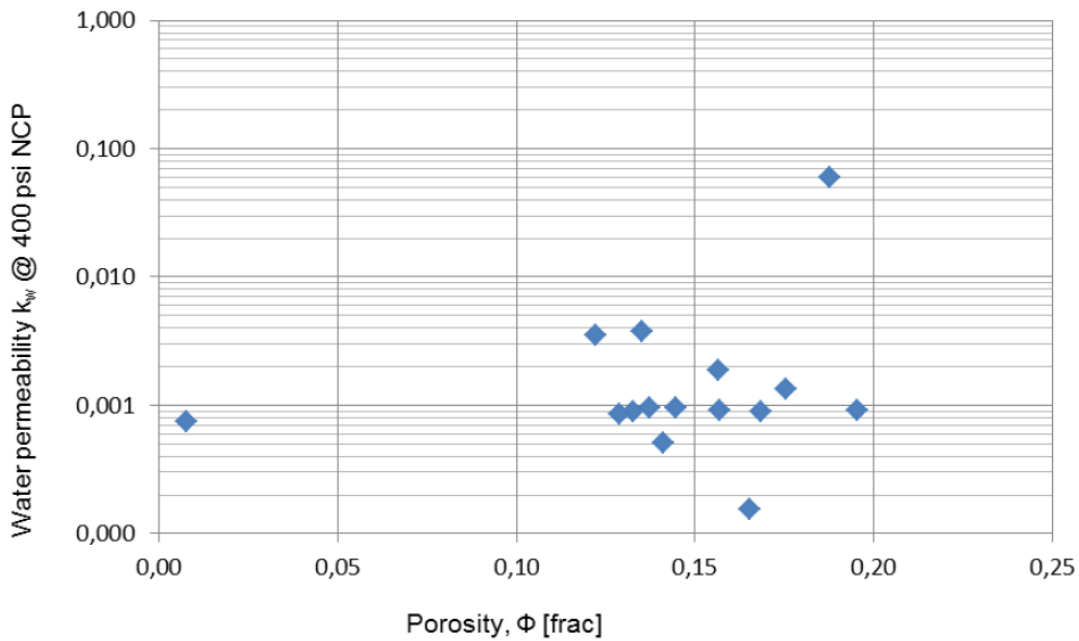


Figure 8.10: k_w at 2600 psi NCP vs. porosity calculated at 2600 psi NCP

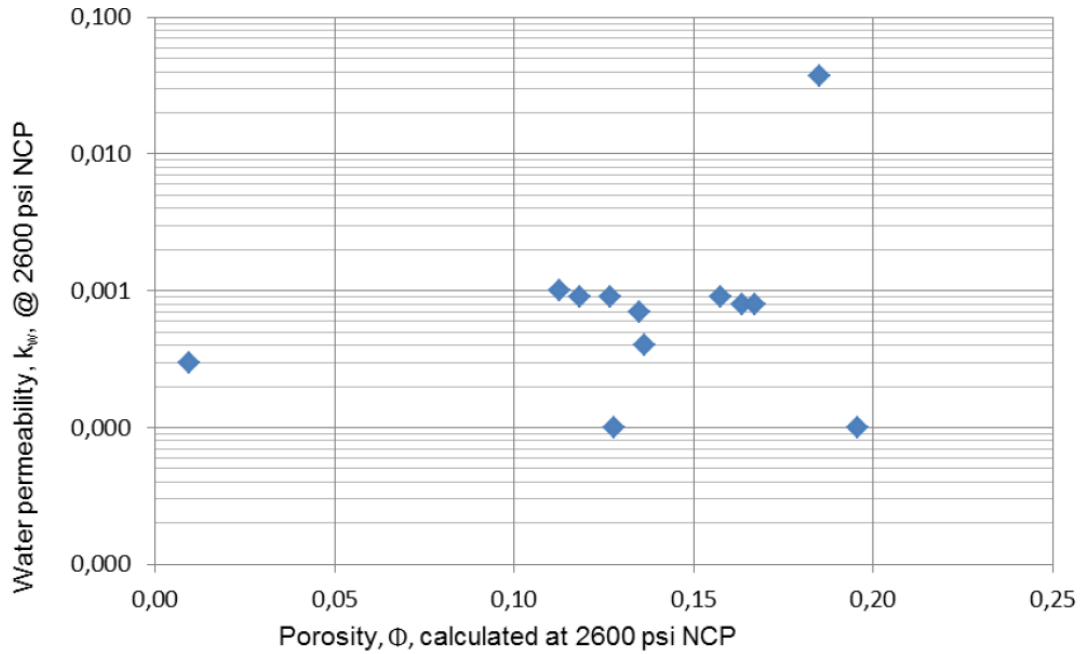


Figure 8.11: Pressure vs. saturation obtained from MICP

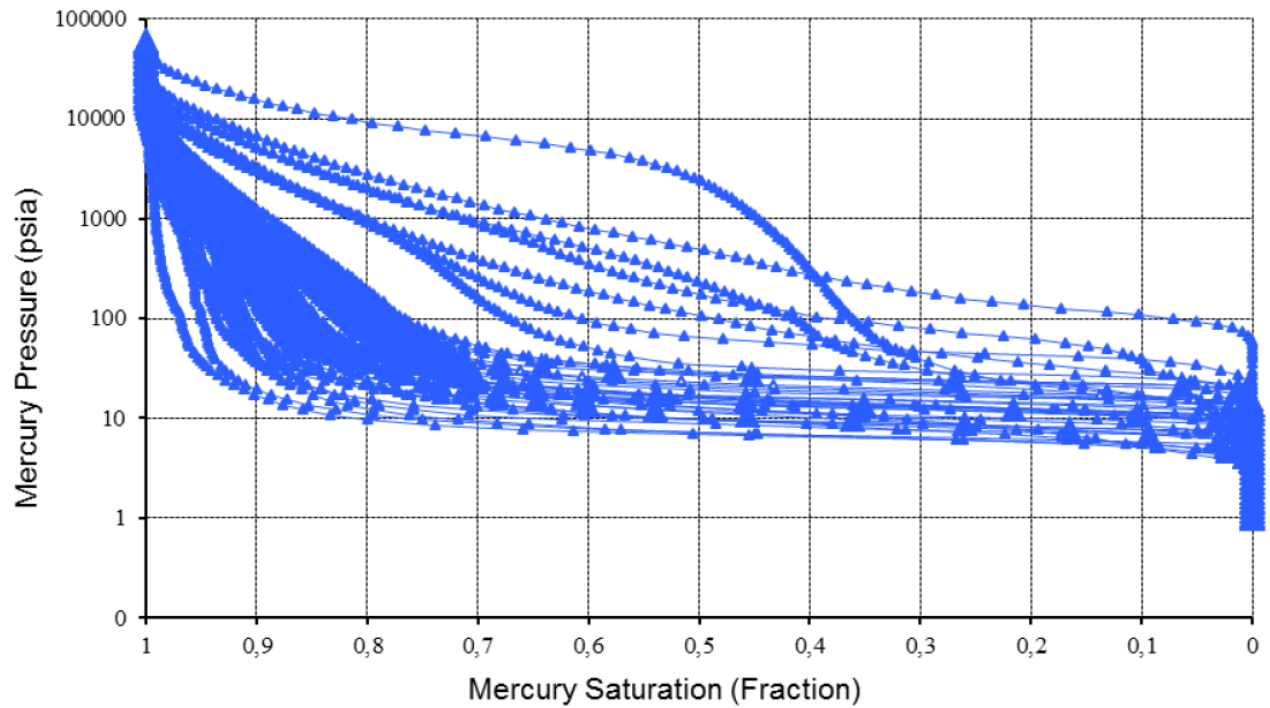


Figure 8.12: $dS_w/d\log$ pore throat size vs. Pore throat size obtained from MICP

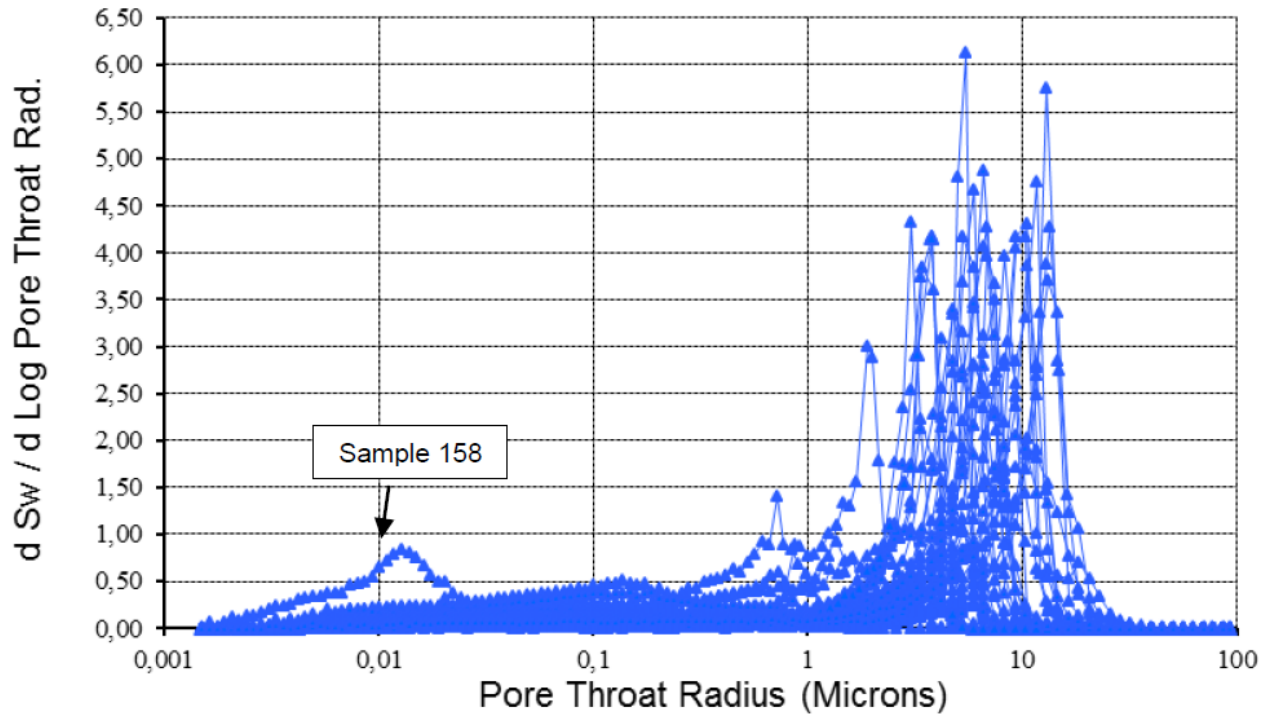


Figure 8.13: J-Function plot ($J(1-S_{HG})$ vs. Saturation)

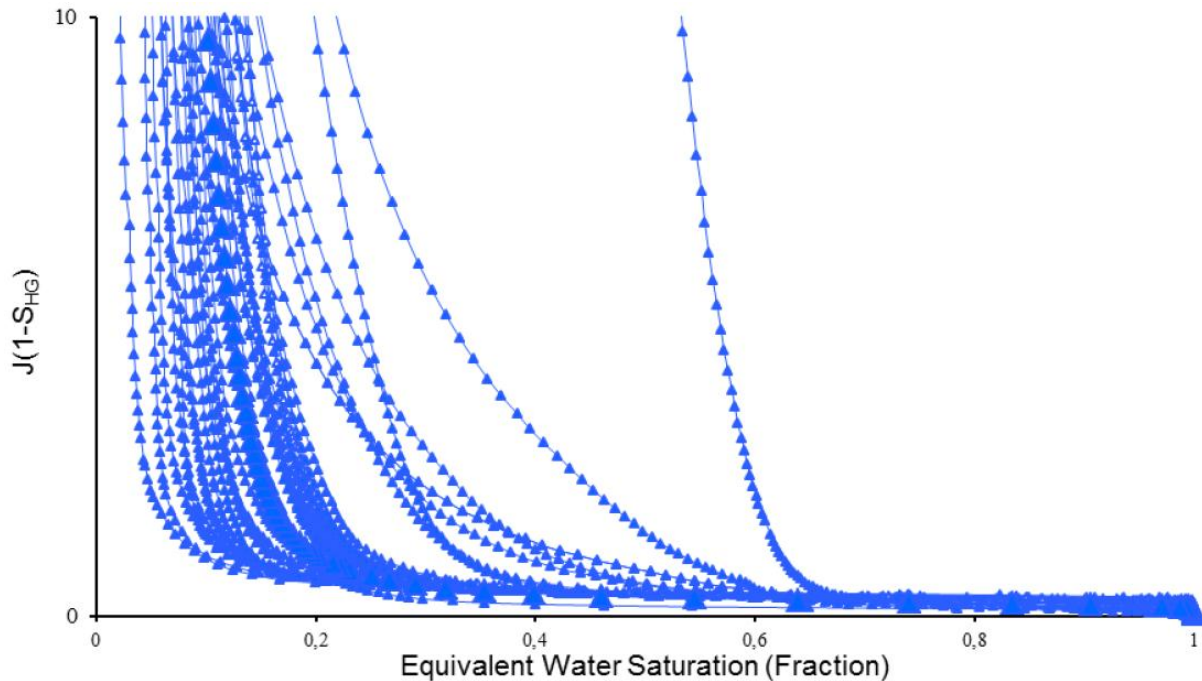


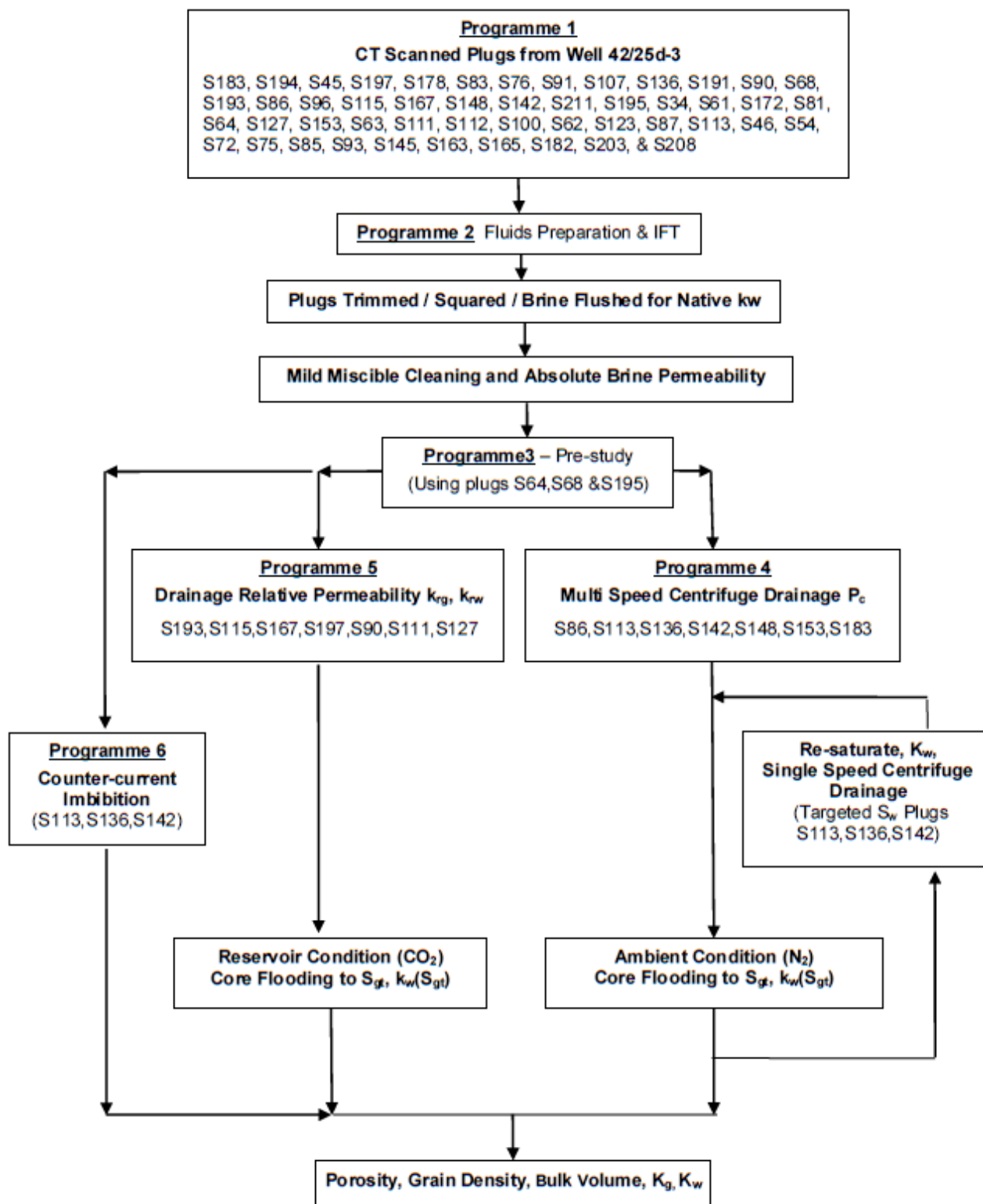
Table 8.1: Measured Petrophysical Properties from Additional RCA study

Petrophysical Properties	Range	Test Programme
Cleaning study: first measurement Klinkenberg corrected gas permeability, K_L , [MD]	0.225 - 3061	(1)
Cleaning study: first measurement Helium porosity [%]	6.90 – 28.2	(1)
Cleaning study: second measurement Klinkenberg corrected gas permeability, K_L , [MD]	0.519 – 3758	(1)
Cleaning study: second measurement Helium porosity [%]	6.80 – 30.5	(1)
Cleaning study: third measurement Klinkenberg corrected gas permeability, K_L , [MD]	0.615 – 3969	(1)
Cleaning study: third measurement Helium porosity [%]	7.10 – 30.9	(1)
Water permeability @ 400 psi	0.0002 – 2.7	(2)
Porosity at ambient	1.0 – 20.0	(2)
Archemedes bulk volume [ml]	14.93 – 68.77	(2)
Water permeability at reservoir net confining pressure, 260 psi	0.0001 – 0.037	(2)
Porosity at reservoir net confining pressure, 260 psi [%]	0.93 – 15.6	(2)
MICP porosity [%]	2.60 – 30.20	(3)

8.1.1.2 Special Core Analysis

The Special Core Analysis (SCAL) programme was undertaken to measure the range of trapped CO_2 saturation, CO_2 and water relative permeability data relevant to dynamic modelling of CO_2 movement in the reservoir. The programme consists of ambient condition tests using centrifuge, unsteady state displacements, together with reservoir condition measurements using supercritical CO_2 . For reservoir condition testing, all measurements were made at a reservoir temperature of 57°C and a reservoir (pore) pressure of 2030 psig (140barg). Analytical grade CO_2 was used as the injection gas. An outline of the SCAL programme is given in Figure 8.14. Brief descriptions of each element of the SCAL programme and the associated results are outlined as follows:

Figure 8.14: SCAL Experimental Process Description



Programme 1 – Plug selection

Plug selection involved:

- Plug CT scanning: 12 of the original 49 samples disqualified after X-ray CT scanning, leaving 37 plugs going forward;
- Native State (as-received) Brine Permeability: Brine permeability was measured for all remaining 37 samples using Synthetic Formation Water (SFW) and under a confining back pressure of 145 psig (10barg);
- Sample Cleaning & Routine Core Analysis: Sample cleaning was performed following the procedure described in the cleaning pre-study (Section 8.1.1.1). The results of the RCA have already been presented in Section 8.1.1.1;
- Brine Permeability: dry samples were formation brine saturated, degassed and absolute brine permeability (K_w) measured using a back-pressure of 145 psig (10barg); and
- Mercury Injection Capillary Pressure (MICP): MICP was measured on 36 samples.

Programme 2 - Fluid Preparation

Synthetic Formation Brine a laboratory filtered (0.45 μ m) and degassed SFW was prepared according to the salts given in Table 8.2. Data in the table corresponds to SFW density of 1.24 g/cc and salinity of 248,000 ppm. For measurements using in-situ saturation monitoring, approximately 0.25 mole of CsCl dopant (Molar mass 168.36 g/mol) was used to replace 0.25 mole NaCl (Molar mass 58.44 g/mol). The doped synthetic brine composition is given in Table 8.3 for reference. The measured density of the doped brine was 1.26 g/cc corresponding to a brine salinity of about 264,300 ppm.

Reservoir Fluids: both an impure CO₂ mixture and pure (analytical grade) CO₂ were used at reservoir conditions (57°C at 141bar). The CO₂ mixture was measured to have a density of 0.577 g/cm³ (at 57 °C at 141bar). The CO₂-brine interfacial tension was measured to be 36.8 \pm 0.7 mN/m. This compared to a measured (analytical grade) CO₂ density of 0.596 g/cm³ and CO₂-brine interfacial of 39.5 \pm 0.8 mN/m at the same test conditions.

Table 8.2: Synthetic Formation Brine

Heading Left	Heading Right
NaCl	258.13
CaCl ₂ .2H ₂ O	40.09
MgCl ₂ .6H ₂ O	31.05
KCl	3.48
SrCl ₂ .6H ₂ O	0.42

Table 8.3: Doped Formation Brine

Salt	g/L
NaCl	244.24
CsCl	40.00
CaCl ₂ .2H ₂ O	40.09
MgCl ₂ .6H ₂ O	31.05
KCl	3.48

Salt	g/L
SrCl ₆ H ₂ O	0.42

Programme 3 - Pre-Study

Three plugs (S64, S68, S195) were selected for pre-study testing which includes Critical Velocity tests and Acid Brine Sensitivity test. Critical velocity tests were aimed at identifying the potential for fines movement within the plug and its threshold value. The acid brine sensitivity test was to see if the pore matrix was affected by brine that will become acidified when in contact with CO₂ in the reservoir. The results of the critical velocity test was inconclusive whilst for the Acid Brine Sensitivity test, a small reduction in grain volume (0.64 – 1.14 cm³) was observed for each plug as a result of acid brine flooding – this corresponds to an increase in porosity of about 2 – 6 %. Klinkenberg CO₂ permeability was also observed to increase post-flooding (approximately 10% for S64 & S68 and over 20 % for S195).

Scanning Electron Microscopy (SEM) of native pre-test and post-acidified brine flood end-trims were undertaken to determine if there is evidence for pore structural change following exposure to acidified brine. The most notable and common difference between the pre-test and post-test samples was the absence of halite in the post-test samples. No evidence for change in pore structure was observed.

Programme 4 – Ambient Temperature Tests

All measurements were performed at a laboratory temperature of 22°C with a pore (back) pressure of around 145 psig (10barg). Analytical grade nitrogen (N₂) was used as the injection gas. Primary drainage (air displacing brine) to target Swi was performed by unconfined multi-speed centrifuge tests.

Primary drainage gas-water capillary pressure (P_c) was measured on seven core plugs covering the rock types and permeability ranges for the Bunter sandstone. These data are shown in Figure 8.15. Plotting of J-function curves showed only samples S153 and S142 of the seven tested plugs as being from the same rock type. Plug S148 was chosen to constrain reservoir condition Pc modelling since the base parameters (K, phi) were the closest match available to the composite parameters (S193, S115, S167).

Each plug at Swi was brine flooded to acquire trapped gas saturation and end point brine relative permeability. In-situ saturation monitoring was utilised to quantify both the initial gas saturation and trapped gas saturation. Imbibition end-point data are summarised in Figure 8.16. End-point trapped gas saturation was verified independently using volumetric gas production data and sample (post-study) pore volume measurements.

Targeted brine saturations of 0.30, 0.70 and 0.80 were established on individual plugs (S113, S136 & S142) using the single speed centrifuge method. These plugs were also brine flooded to trapped gas saturation for the measurement of krw at Sgt. The relationship Sgt versus Sgi correlated as expected (see Figure 8.16, targeted S_w data points) but it was clear from ISSM that the saturation distributions were very non-uniform (Figure 8.17 is an exemplar). Because of the non-uniformity in brine saturation, it is unlikely that measured krw is representative. This ambient condition work showed that uniform brine saturation profiles cannot be acquired at high values of brine saturation from centrifugation

Post-study plug characterisation data show that grain volume change was less than 0.1cm³ for all samples. Significant gas permeability loss was observed for sample S136 but remaining samples were within +/-10%

of original values. This was not true for absolute brine permeability which was found to decline by 10% to 30%.

Figure 8.15: Primary Drainage Capillary Pressure, Combined Plot

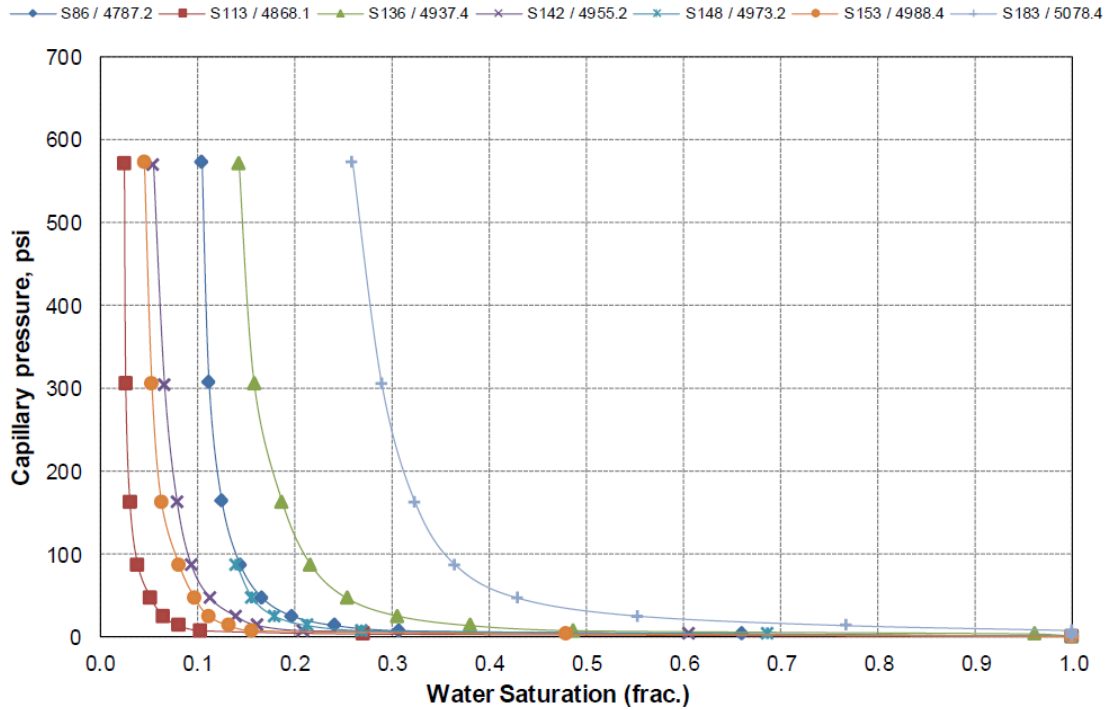


Figure 8.16: Trapped Gas Satration versus Initial Gas Satration

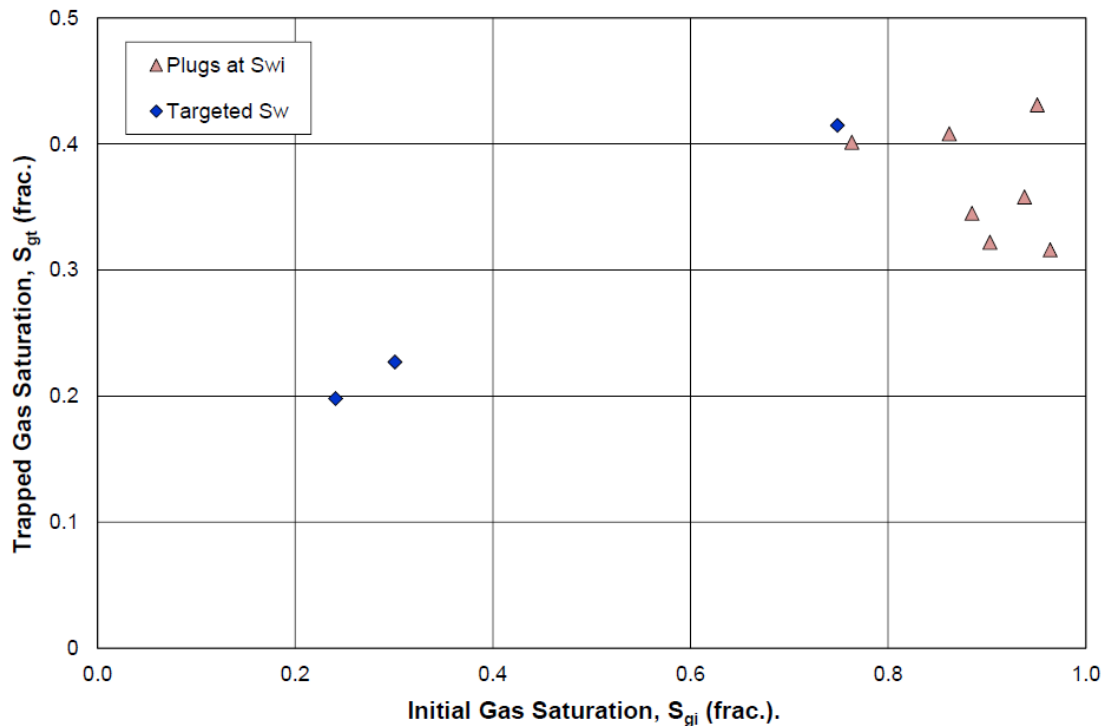
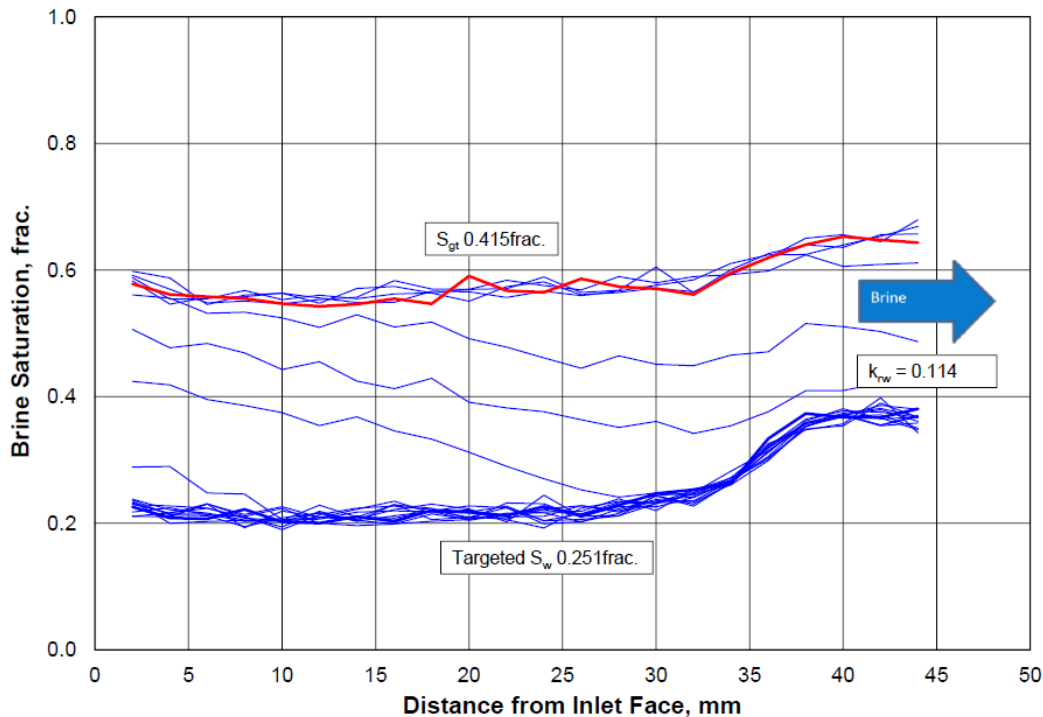


Figure 8.17: Saturation Distribution Targeted S_{wi} 0.3 (Plug S113)


Programme 5 - Reservoir Condition Gas-Water Kr

Unsteady-state primary drainage gas-water relative permeability was measured using two composites and two single plugs. All measurements were performed at a reservoir temperature of 57°C with a reservoir (pore) pressure of 2,030 psig (140barg), using analytical grade carbon dioxide (CO_2) as the injection gas. The first test used a three plug composite core (Composite S193, S115, S167) with a measured absolute brine permeability of 115.7mD (porosity 0.253). The brine saturation distribution was influenced by the component plug individual properties and plug butting (see Figure 8.18). Subsequent tests were therefore performed with single plugs, plug S197 (11.6mD, porosity of 0.152frac) and plug S90 (77.5mD, porosity of 0.267). The final test however reverted back to a composite core (Composite S111, S127) since the rock type was of high permeability. The measured absolute brine permeability for this composite was 1324mD (porosity 0.272).

Measured CO_2 relative permeability was similar for plug S90 and composite S111, S127 (k_{rg} 0.158 and k_{rg} 0.184 respectively at S_g 0.560 and 0.556). Higher CO_2 relative permeability was observed for composite S167, S115, S193 and plug S197. The measured analytical end-point CO_2 -water relative permeability data for these floods are shown in Figure 8.19.

Imbibition brine flooding to trapped CO_2 saturation was also performed starting from low initial CO_2 saturations ($1-S_{wr}$). Initial CO_2 saturations ranged from $0.424 < S_{gi} < 0.579$ resulting in trapped CO_2 saturation (S_{gt}) ranging from $0.255 < S_{gt} < 0.387$. All trapped CO_2 saturation data including ambient and reservoir condition flooding is summarised in Figure 8.20 which also show the correlations of Spiteri et al. (2008) and that of Land. The alternative data provided on this plot came from counter-current imbibition experiments (Programme 6), where the initial saturation is controlled using toluene- CO_2 saturation and

imbibition experiments are undertaken under purely spontaneous processes, allowing toluene to imbibe into the sample under capillary forces. The corresponding brine relative permeability (k_{rw}) at Sgt is shown plotted in Figure 8.21.

As Figure 8.18 shows, coreflood drainage experiments are strongly affected by capillary end effects leading to non-uniformity in saturation distribution along the core length. One way of minimising this effect is by performing experiments at high injection rates. For this study, CO_2 injection rate ranged between $4\text{cm}^3/\text{h}$ (corresponding to a reservoir advance rate of $1.2\text{ft}/\text{day}$) to $400\text{cm}^3/\text{h}$. However, high flow rates are known to induce instabilities at the flood front that are unrepresentative of displacement conditions deep in the reservoir.

To reconcile time and spatially dependent experimental data and generate relative permeability data that is corrected for the effects of laboratory scale capillary pressure, core flood simulation was performed using *Sendra*TM. *Sendra*TM is a proprietary simulator based on a two phase 1-D black oil simulation model together with an automated history matching routine. The simulator recreates the balance of forces in the core experiment, taking as input the capillary pressure and relative permeability data, to match measured experimental production and pressure data. Once a satisfactory match has been obtained, a characteristic reservoir relative permeability is then generated that corrects for the laboratory capillary artefacts.

To improve confidence in simulated relative permeability data, it is usually better to employ capillary pressure data from samples within the same rock type. In the case of Bunter data (except for sample S90), this proved difficult and it became necessary to use an analytical capillary pressure model as an input, where the simulator was given some flexibility to estimate parameters of the capillary pressure model. The model employed is due to Skjaeveland et al (2000) and is as stated in Equation 8.1, recast in terms of water and gas phases. Comparison of P_c generated with the Skjaeveland model and those generated from two laboratory tests – the multi-speed centrifuge capillary pressure (LabPc) and the corrected Mercury Injection Capillary Pressure (MICP) – are shown in Figure 8.22 through Figure 8.24.

$$\text{Equation 8.1} \quad P_c = \frac{c_w}{\left(\frac{S_w - S_{wR}}{1 - S_{wR}}\right)^{a_w}} + \frac{c_g}{\left(\frac{S_g - S_{gR}}{1 - S_{gR}}\right)^{a_g}}$$

where c and a are constants defining the capillary entry pressure (threshold pressure) and curvature exponent, respectively for water and oil (as denoted by subscripts 'w' and 'o', respectively).

Although this model was designed to allow for mixed-wet capillary pressure data in imbibition and secondary drainage processes, it may still be used for strongly wetting systems in primary drainage, by either negating the gas term or by using $c_g = 0$. Table 8.5 lists the Skjaeveland parameters used as input for each coreflood simulation.

Table 8.6 lists the end points used as input to the simulation model. K_L and K_w represents the Klinkenberg and water permeability respectively. Water permeability was lower than the Klinkenberg permeability and also exhibited a decreasing trend as shown in Figure 8.25. This is uncommon in clean sandstone materials and the anomaly creates unusual CO_2 relative permeability when relative permeability is based on water permeability as the absolute – i.e. the effective CO_2 permeability at initial water saturation (S_{wi}) become greater than specific water permeability at 100% water saturation, and hence the relative permeability to CO_2 at S_{wi} would be greater than 1.

Although this phenomenon is apparently counter to conventional hydrocarbon system relative permeability behaviour, as referenced in reservoir engineering literature, there are a number of experimental studies reporting similar observed behaviour. These papers incorporate two different potential hypotheses for the phenomenon. The first theory is that clay minerals may become swollen in the presence of formation water, and that the fresher the water, the more pronounced the effect. The second theory suggests that turbulent flow may be occurring in a water-filled system due to water flowing over and through tight, rough surfaces – postulating that at irreducible water saturation the gas (or oil) path is free from such turbulence since water continues to fill the rough, clay rich surfaces. The dominance of Illite in the Bunter clay mineralogy would underpin the first hypothesised mechanism. Illite swells in the presence of brine and can thus reduce the permeability to this phase whilst in the presence of CO₂ the clays will shrink and allow an enhanced permeability. The second hypothesis has also been described in terms of non-wetting lubrication. Since the CO₂ occupies the largest pores, it is speculated that the CO₂ then sees a reduced drag or surface friction because it is in contact with smoother surfaces. The Bunter sandstone is considered (strongly) water-wet and both mechanisms could therefore be complementing one another in the Endurance matrix.

Simulated relative permeability curves were defined using the Corey model which for water relative permeability is defined as:

Equation 8.2
$$K_{rw} = K_{rw_{max}} \cdot S_{wn}^{Nw}$$

where K_{rw} is the relative permeability to water, $K_{rw_{max}}$ is the maximum relative permeability to water, Nw is the Corey exponent for water, and S_{wn} is normalised water saturation – given as, $S_{wn} = (S_w - S_{wi}) / (1 - S_{wi})$, for a primary drainage process.

The Corey model for relative permeability to gas (in a gas-water system) is defined as:

Equation 8.3
$$K_{rg} = K_{rg_{max}} \cdot (1 - S_{wn})^{Ng}$$

where K_{rg} is the relative permeability to gas, $K_{rg_{max}}$ is the maximum relative permeability to gas and Ng is the Corey exponent for gas.

The Corey exponent for water (Nw) ranged from 4.7 – 6.0, and for gas (Ng) the range was from 2.5 – 3.0. The curves derived from these parameters are presented in Figure 8.27 on Cartesian and semi-log axes (left and right-side, respectively). The curves are also presented as a function of normalised water saturation in Figure 8.26., Figure 8.28 and Figure 8.29 show production and saturation profiles history match for the composite sample S111/S127 using Corey exponents of $Nw=4.7$ and $Ng = 2.7$. They show good matches in production, differential pressure and saturation profiles.

Figure 8.18: Primary Drainage In-situ Brine Saturation S115 S167 S193

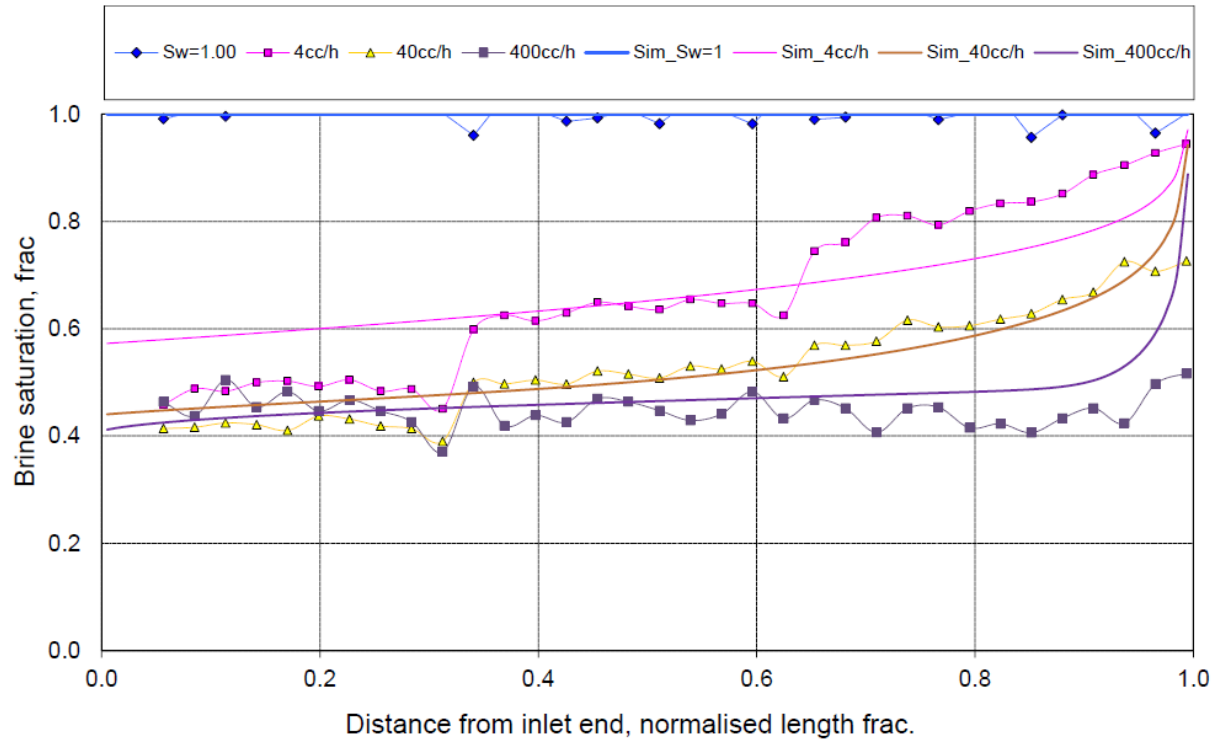


Figure 8.19: Analytical (End-point) Gas Relative Permeability (Programme 5)

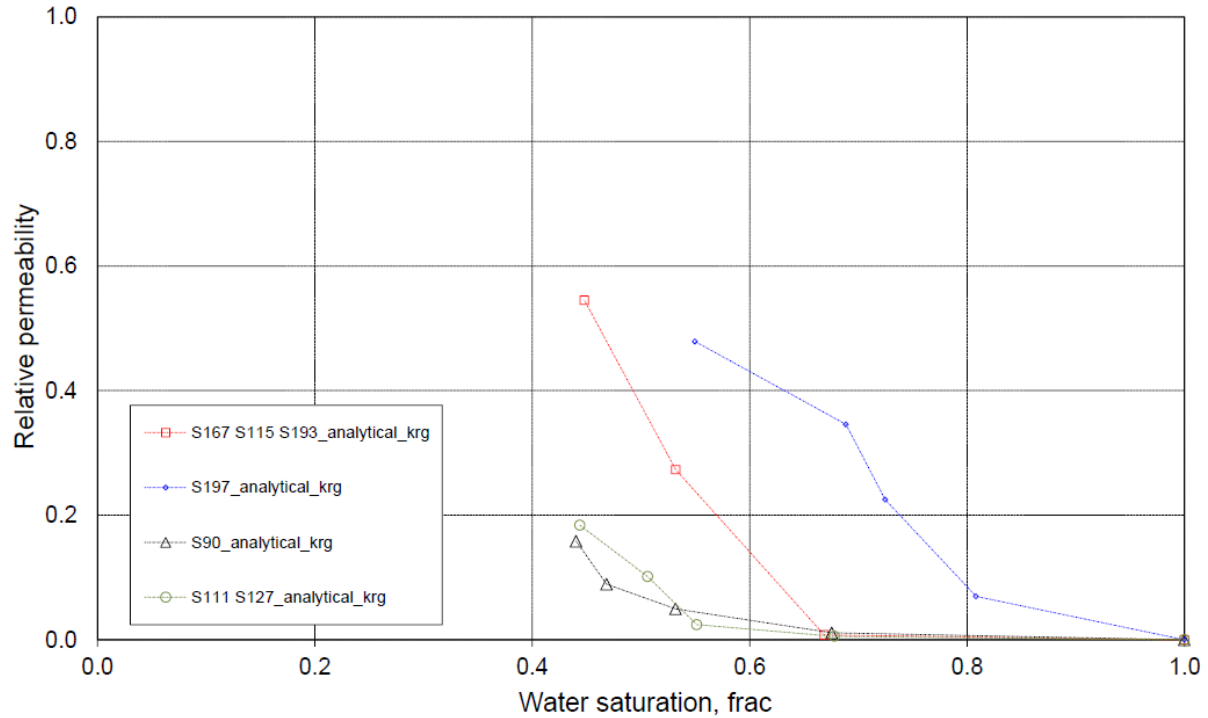


Figure 8.20: Trapped gas saturation (S_{gt}) as a function of initial gas saturation (S_{gi}) – all methods

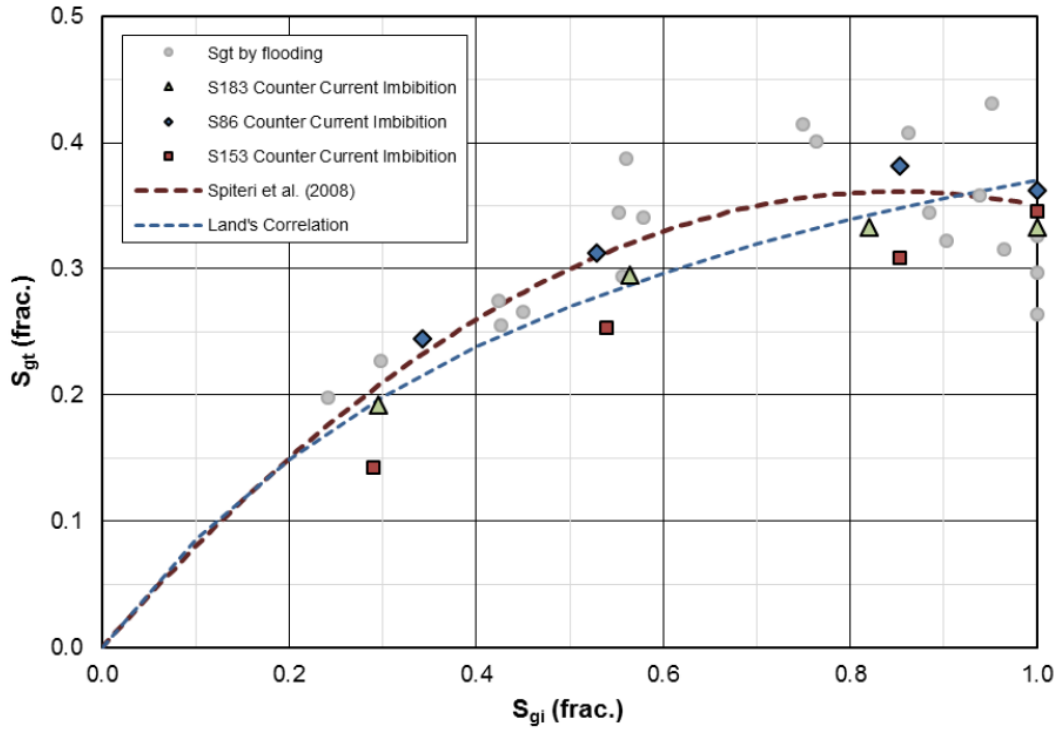


Figure 8.21: Brine Relative Permeability versus S_{w_max} (Programme 5)

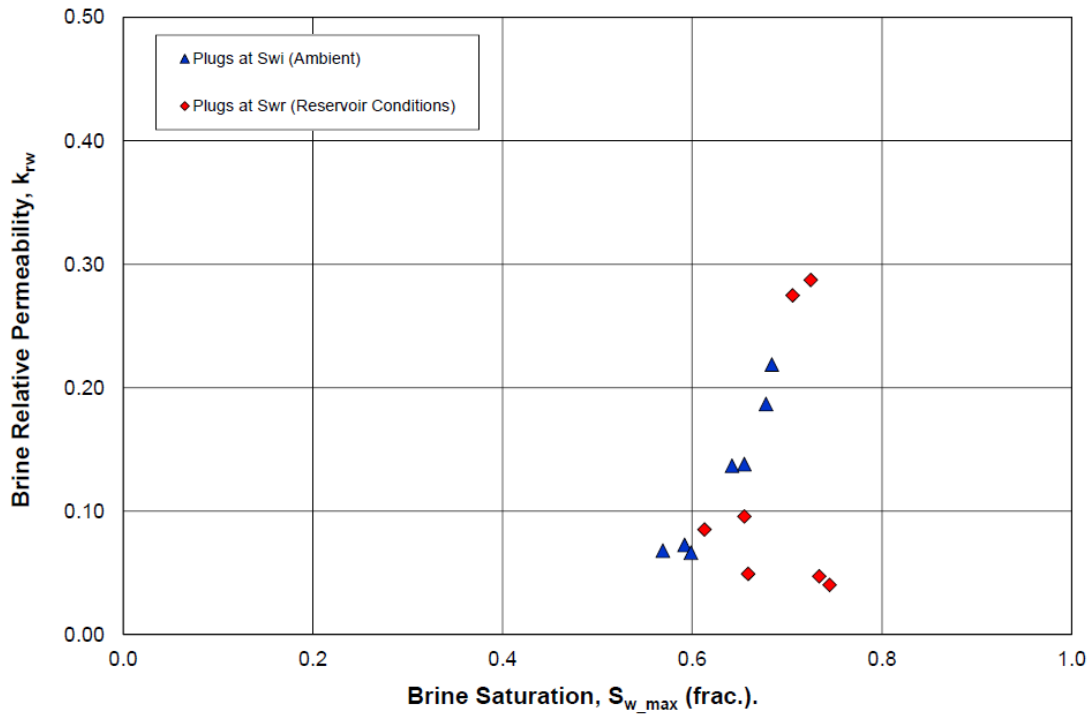


Figure 8.22: Good correlation of centrifuge Pc (lab Pc) and MICP data (S113 & S153)

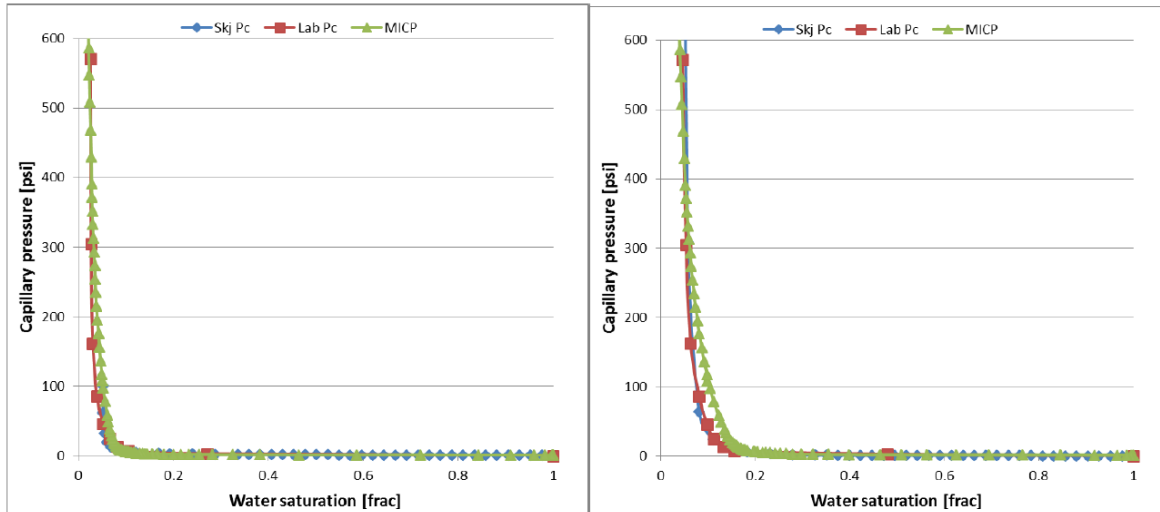
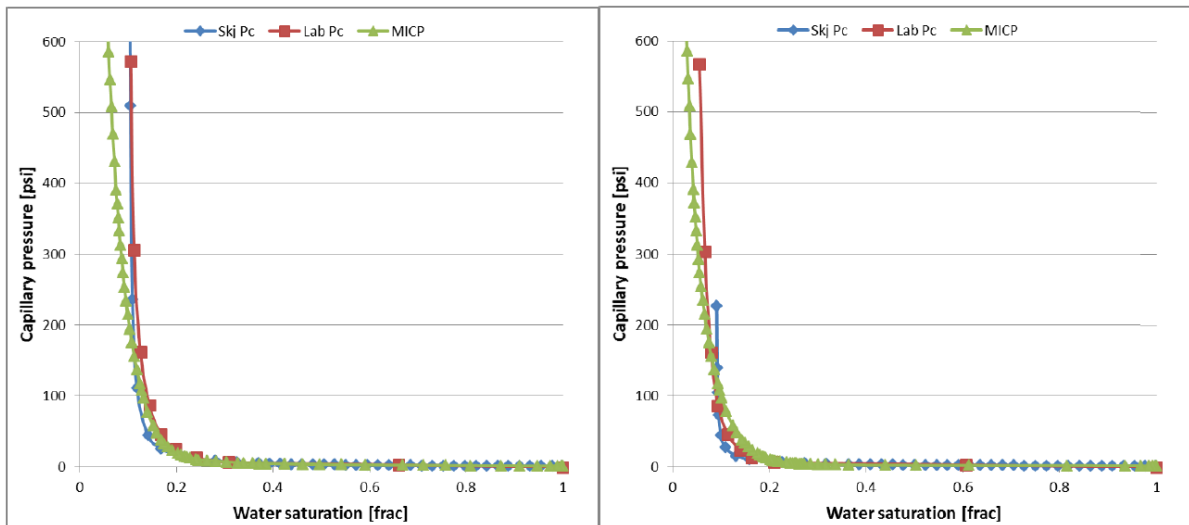


Figure 8.23: Reasonable correlation between centrifuge Pc (lab Pc) and MICP data (S86, S142 & S148)



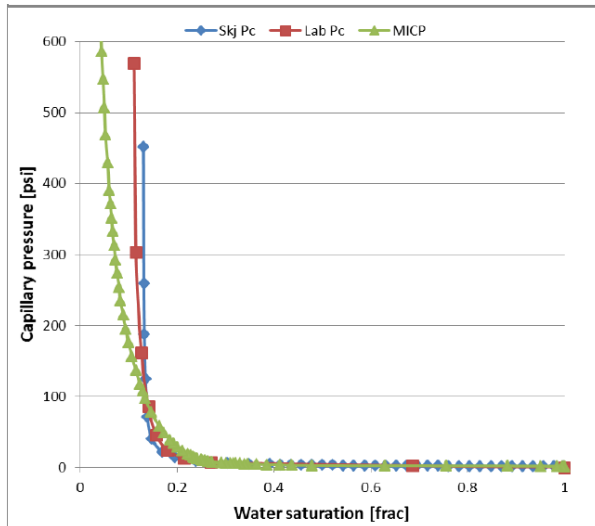


Figure 8.24: Poor correlation between centrifuge Pc (Lab Pc) and MICP (S136 & S183)

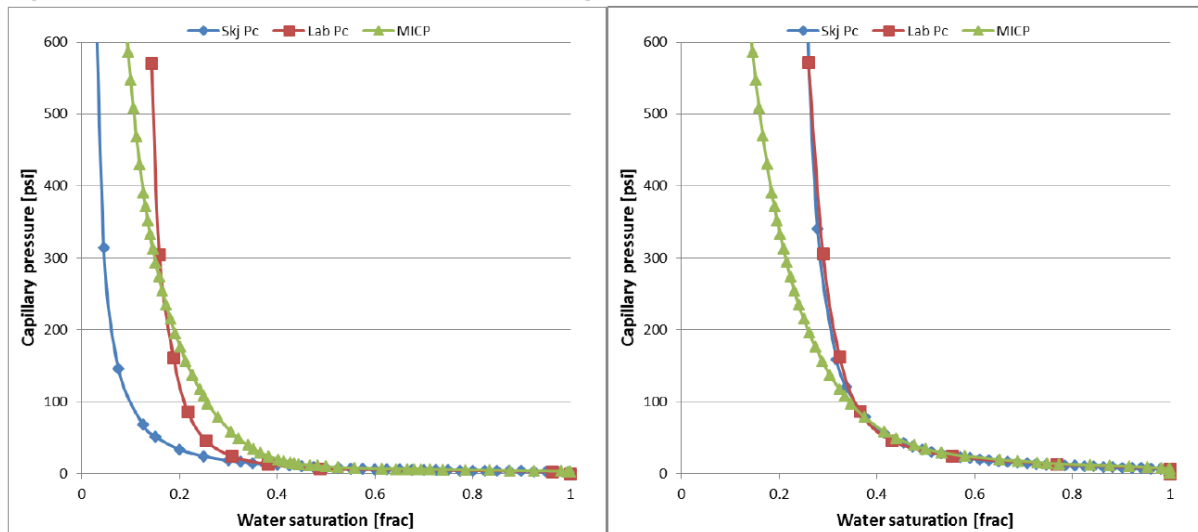


Table 8.4: Skjaeveland Pc Model Parameters

Sample	cw	aw	Swi
S115/S167/S193	1.7	0.2	0.080
S197	4.5	0.2	0.190
S90	-	-	-
S111/S127	0.7	0.5	0.030

Table 8.5: Endpoint Simulation Inputs

Sample	KL	Kw	Krw_max	Kg@max	Krg_max
S115/S167/S193	275	171	0.620	275	1.000
S197	14	6.75	0.482	14	1.000
S90	173	103	0.596	173	1.000
S111/S127	1583	1136	0.718	1583	1.000

Figure 8.25: Water permeability (Kw) versus Klinkenberg gas permeability (KL)

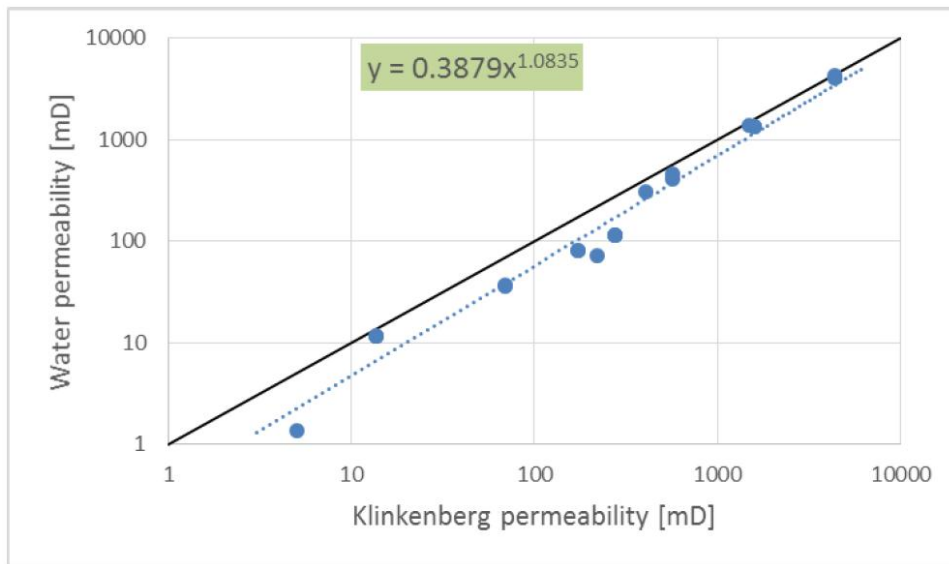


Figure 8.26: Simulated relative permeability curves – indicating the observed exponent variance

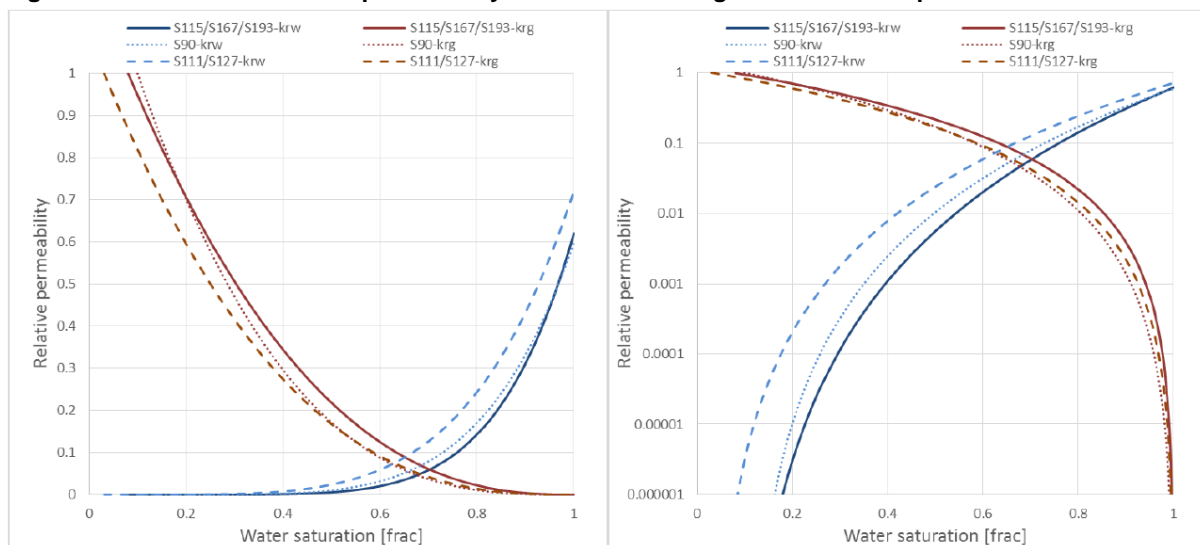


Figure 8.27: Simulated relative permeability curves versus normalised water saturation

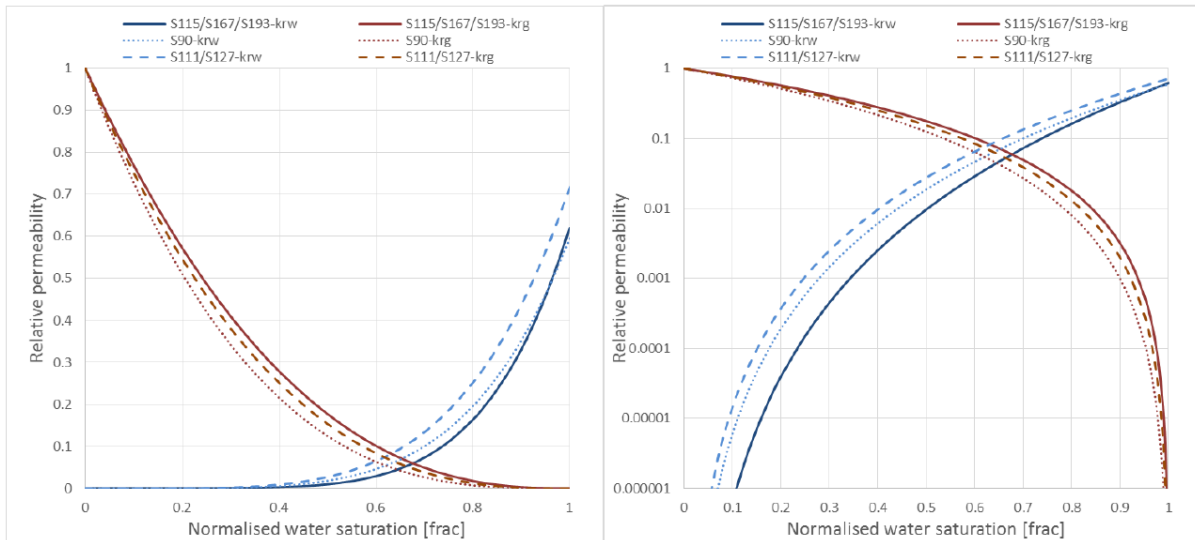


Figure 8.28: Production history match for S111/S127

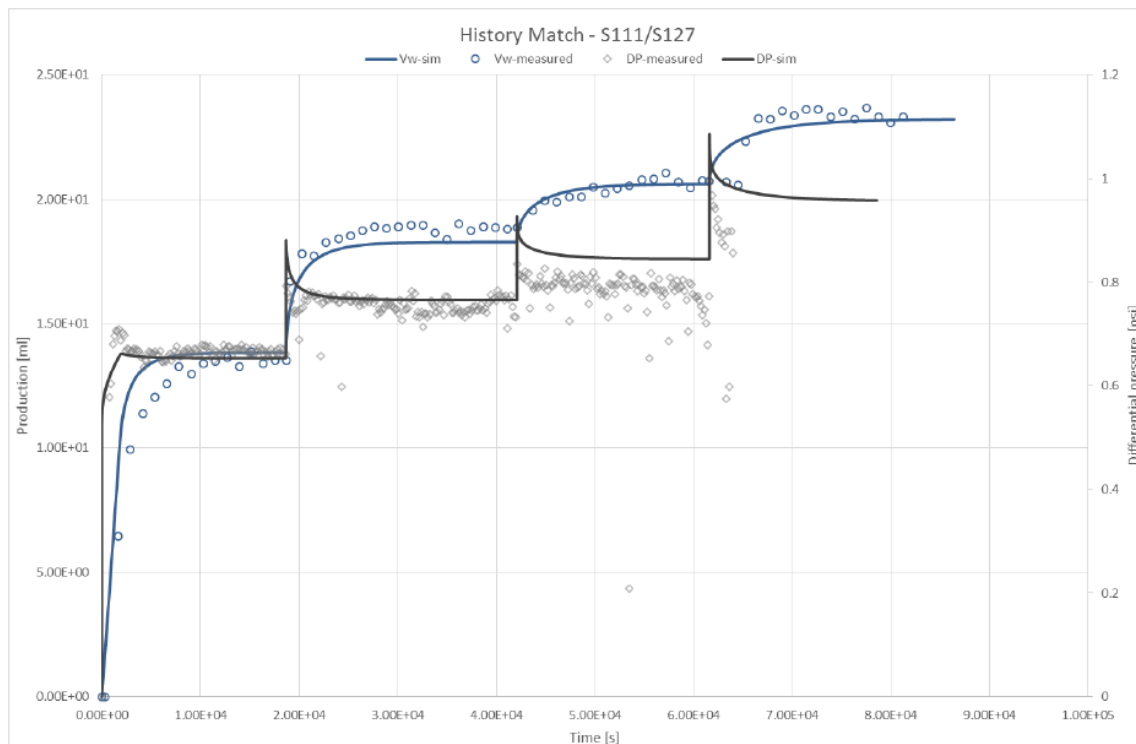
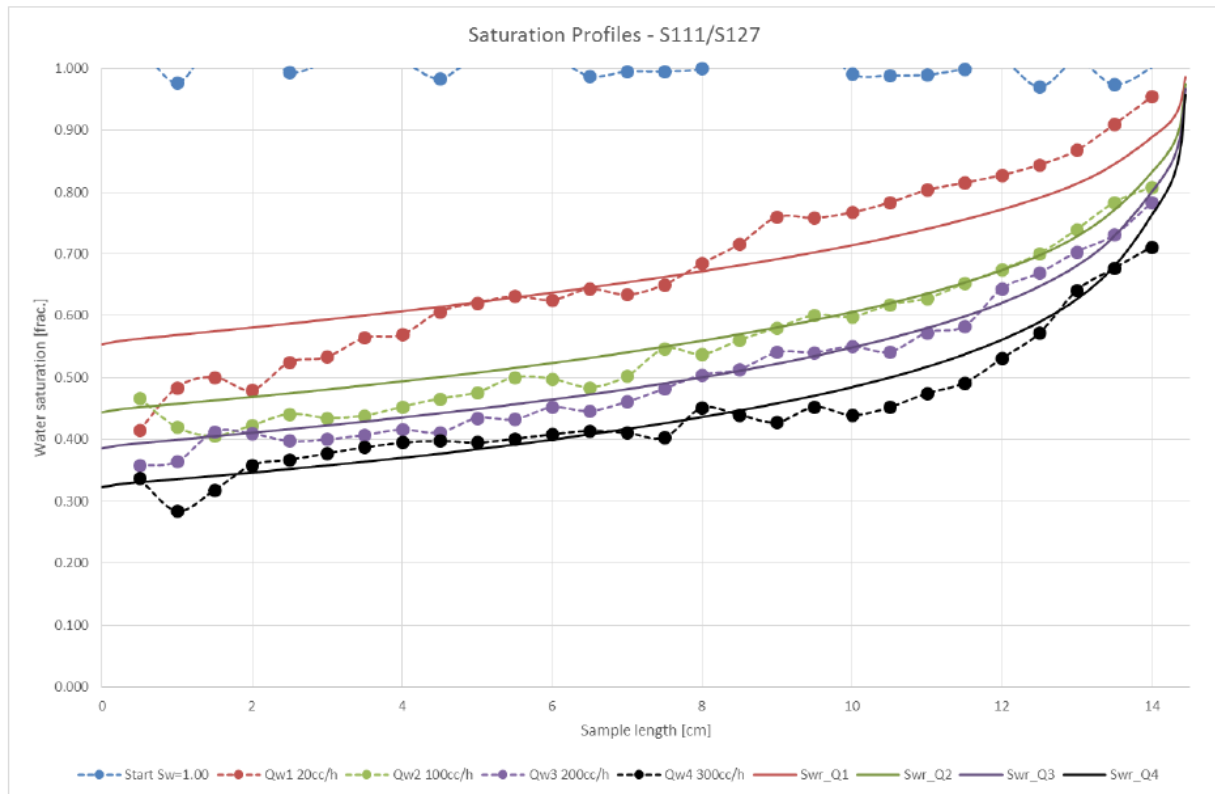


Figure 8.29: Saturation Profiles – S111/S127



8.1.2 Well Testing and Vertical Interference Test Results

8.1.2.1 Well Test Results

As part of the data gathering programme, a well test was completed over the interval 1396.3 - 1414.3m TVDSS to achieve the following:

- determine initial reservoir pressure
- establish key reservoir parameters; permeability, thickness & skin;
- determine the influence of nearby boundaries and/or heterogeneities within the volume of the reservoir investigated by the test;
- investigate vertical connectivity and estimate K_v/K_h (vertical/horizontal) permeability ratio over the tested interval;
- secure good quality formation water samples for chemical & biological analysis and electrical properties;
- carry out a step rate injection test to prove injectivity of the best practicable analogue to supercritical CO_2 (filtered seawater); and
- investigate (injection) rate dependent skin including any plugging, fracturing or dissolution effects seen during testing.

The testing programme consisted of a production period of approximately 24 hours at a rate of 5000 stb/d (795 m^3/day) using an Electrical Submersible Pump (ESP), followed by a shut-in and pressure build-up for 48 hours. Subsequently a multi-rate injection test using filtered seawater (CO_2 was not used due to safety

concerns over handling the fluid in its super-critical state and sourcing a sufficient volume of CO₂) was performed at rates of 5000, 10000 & 15000 stb/d (795, 1590, 2385 sm³/day), followed by a 12 hour pressure fall-off test. The key results calculated from the test include:

- an an initial reservoir pressure of 151.8bar at a depth of 1405.3m TVDSS. This is in excellent match to the same datum pressure estimated using data from the long duration MDT formation pressure testing on wireline of 152 ±0.5bar at the same datum average permeability of 271mD based on a test interval of 230.4 m. This is an excellent match with reservoir properties derived from porosity-permeability trends;
- a negative skin of -1.1;
- no evidence of boundaries in the volume investigated by the test, which was calculated to extend to a radius of 1.2 km;
- a vertical to horizontal permeability ratio (K_v/K_h) of 2.19×10^{-4} , which is considerably lower than that seen on the scales investigated by the VIT (discussed below); this was attributed to the test taking place within a laterally extensive high permeability zone which flows preferentially. K_v/K_h ratio calculated from VIT was used for reservoir simulation;
- multi-rate injection tests generated unexpected results, most likely caused by mechanical blockage of the perforations by debris from the surface equipment;
- a maximum rate-dependent skin of 80; and
- the injection test demonstrated that injection at the specified rates would be possible over the perforated interval despite what was thought to be significant mechanical blockages in the completion.

8.1.2.2 Vertical Interference Test (VIT)

As part of the wireline programme of the 42/25d-3 appraisal well, three VITs were undertaken at depths of 1580.4, 1522.8 and 1429.8m MD to determine formation permeability and quantify vertical to horizontal permeability ratio (K_v/K_h) to a depth of investigation deeper than would be seen using formation pretests (mini-DST). VIT was also used to identify any barriers to vertical flow over the interval tested.

Each test was planned to use four different pump rates of approximately 30 minutes each, followed by a build-up period of one hour. The VITs were interpreted using transient pressure analysis (PTA) and reservoir simulation.

The mini-DST result for the first station (1429.8m MD) was successful and recorded a formation permeability of 24mD from the PTA and 18mD from the numerical simulation, with a high degree of confidence. Stations two and three (1522.8 and 1580.4m MD, respectively) could not be taken with similar confidence due to operational reasons; however the estimated results were within the range expected from the porosity-permeability trend. No barriers to vertical flow over the intervals tested could be detected. K_v/K_h ratios were determined from all three stations, ranging from 0.10 to 0.36. This range has informed the choice of the K_v/K_h range of 0.10 to 0.15 for reservoir simulation purposes.

8.2 SectionSectionExtent and Effective Hydraulic Communication of the Aquifer

Two separate reviews, one looking at the geology of the BSF in the UK SNS within a regional AOI that includes the Endurance Storage Complex, and the other looking at the historical pressure behaviour at Endurance and the nearby Esmond gas field, suggest that it could be in hydraulic communication with an area approximately 20,000 – 23,000km².

A triangle drawn to approximate the area of the BSF bounded by faults to the west (the Dowsing Fault Zone), north and north-east, and the thinning to the east across the Base Cretaceous Unconformity on the Cleaver Bank High in the Dutch sector of the SNS (see Figure 3.4), was shown to extend to a width of 160 km and a height of 240 km, giving an area of about 20,000 km².

Comparison of pressure gradient measurements in the 42/25-1 appraisal well drilled in 1990 and the 42/25d-3 appraisal well drilled in 2013 shows that pressure in Endurance has fallen by 0.7bar in 23 years. This was probably caused by gas offtake from the Esmond field about 50 km north-east of Endurance and the subsequent expansion of the aquifer to replace this void space. A material balance calculation estimated an aquifer with an area of 23,000 km² to be required to result in the observed pressure decrease. If production from other gas fields in the Esmond Complex (Forbes and Gordon) were taken into account then an aquifer of twice the estimated size or compressibility would be required. It is therefore highly probable that Endurance is connected to a large regional aquifer which can help to limit the pressure increase associated with White Rose CO₂ injection and ensures that the sealing integrity of the cap rock is preserved.

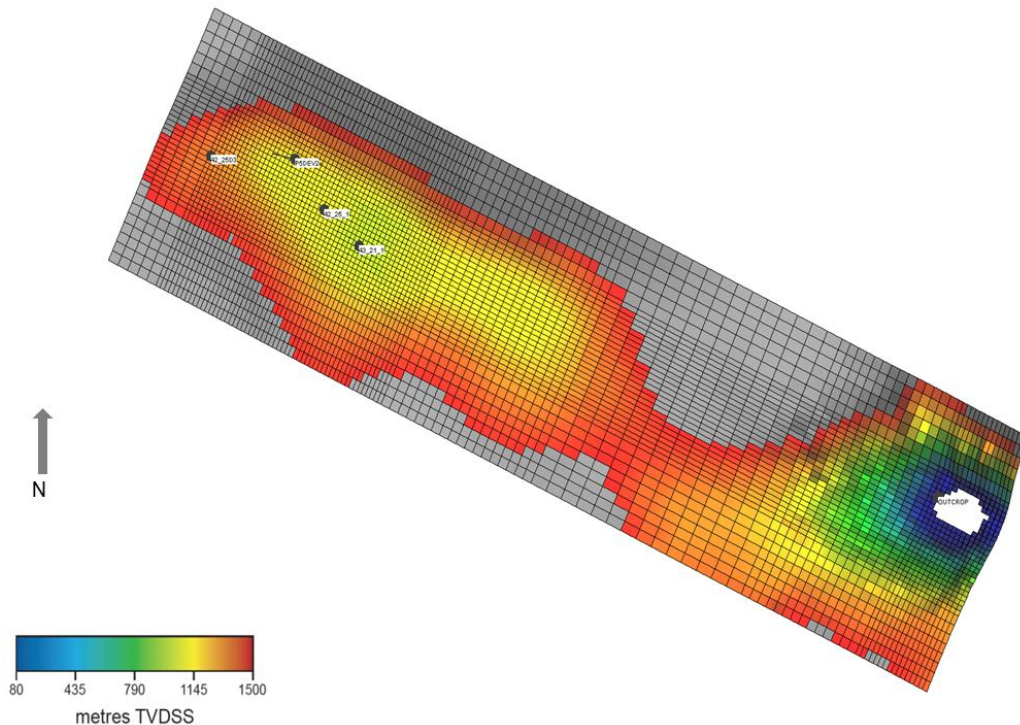
8.3 Dynamic Simulation Models

Dynamic modelling has been performed using the Blackoil ECLIPSE 100 simulator (E100) from Schlumberger. Two classes of simulation models have been built: (a) the Base or Sub-regional simulation model which was used to address issues surrounding general plume development, storage capacity and pressure profile predictions; and (b) Simplified models consisting of the Simplified AOI simulation model and the Simplified injection model which were developed for the purposes of undertaking various sensitivities in an expeditious manner including the impact of reservoir properties on CO₂ migration and pressure profiles and the impact of completion strategy on CO₂ injectivity. The Sub-regional model is next described in detail.

8.3.1 Sub-regional simulation model

The dynamic model for simulation covers an area spanning about 42 km by 11 km, and thereby encompasses and extends beyond the Endurance anticline which measures about 25 km long by 8 km wide along the 1500m TVDSS contour close to the depth of the most likely spill. The outcrop to the east southeast of the Endurance structure has been included in the simulation model to enable the assessment of the effects of potential hydro-dynamic communication between Endurance Structure and the outcrop during CO₂ injection. A Top Bunter depth map view of the resulting grid is shown in Figure 8.30.

Figure 8.30: Grid Model Using 200/400m Cells of Endurance Area of Interest



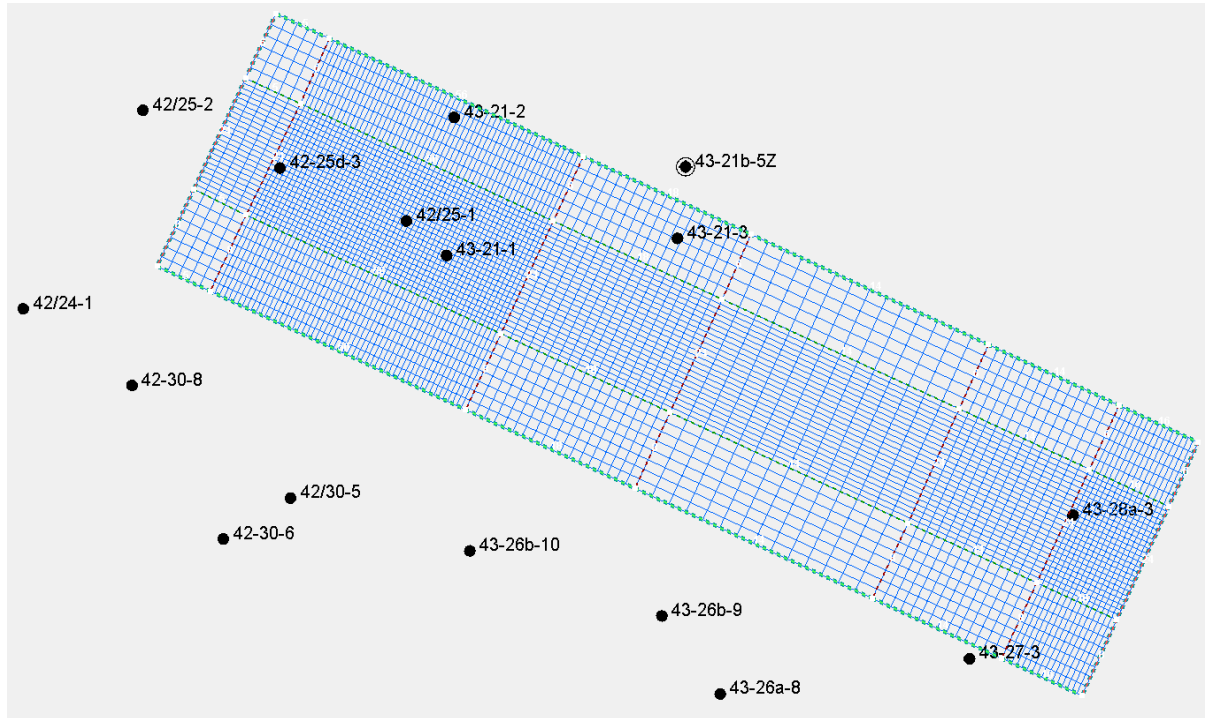
The Bunter sandstone thickness in the AOI varies between 250 and 300 m. The vertical grid cell resolution has been maintained regardless of which aerial resolution was adopted to adequately capture the buoyancy driven migration of injected CO₂. The average vertical grid cell size is about 2 m.

8.3.2 Upscaling for Reservoir Simulation

8.3.2.1 Simulation and Grid Design

A total of 125 cells in the vertical direction ($N_z = 125$) were used to model the whole Endurance structure volume (an average vertical cell size of 2m over a 250m interval). Total grid size therefore increases very rapidly once X- and Y-direction grid cells (N_x and N_y) are accounted for. A 200m by 200m X and Y-directions cells would imply $N_{xyz} \approx 1.4$ million cells. It was decided to use relatively fine grids only in the area between the injection points and the crest of the structure to adequately resolve buoyancy-driven CO₂ migration. Control lines have therefore been drawn parallel and perpendicular to the main axis of Endurance to bound the core area of the model and also the outcrop (Figure 8.31).

Figure 8.31: AOI and Control Lines for Hybrid Gridding



Using these control lines, a hybrid gridding scheme was developed that minimises the overall cell count whilst maximising detail where required. In the core area (and over the outcrop) the finest cell sizes have been implemented, these being:

- 100m by 100m (Fine);
- 200m by 200m (Intermediate); and
- 400m by 400m (Coarse).

Stepping away from the core area in a given direction (X or Y) beyond the control lines, the cell size is allowed to increase by a factor up to two (to minimise material balance errors due to finite difference gradient approximation).

The net result is the total number of grid cells is reduced from $N_{xyz} \approx 1.4$ million to about $N_{xyz} \approx 1.0$ million cells. Whilst this is only a 29% saving in total cells, the reduction in computing time is approximately 80 to 100%. The actual grid dimensions for the three scales considered are shown in Table 8.6.

Table 8.6: Grid Sizes and Dimensions

Case	Core Δ [m]	(N_x, N_y, N_z)	$N_x N_y N_z$	N_{active}
Fine	100	(258, 82, 228)	4,823,568	2,880,734
Intermediate	200	(129, 41, 228)	1,205,892	734,353
Coarse	400	(66, 21, 226)	313,216	194,896

Comparison of simulated CO₂ breakthrough times (the time for CO₂ to reach the 43/21-1 well at Top Bunter) and peak pressure responses between reservoir models incorporating the three grid sizes showed minor differences. Preference has therefore been given to the coarse or intermediate models for the

reservoir engineering modelling runs since they run much quicker (Table 8.7). Where appropriate, verification runs have been done using the fine scale model.

Table 8.7: CO₂ Time to Crest and CPU Time by Grid Size

Model	Break-Through Time [yr]	CPU Time to 2100 [hr]
Coarse	3.5	0.17
Intermediate	3.9	0.53
Fine	4.2	4.05

8.3.2.2 Up-Scaled Parameters

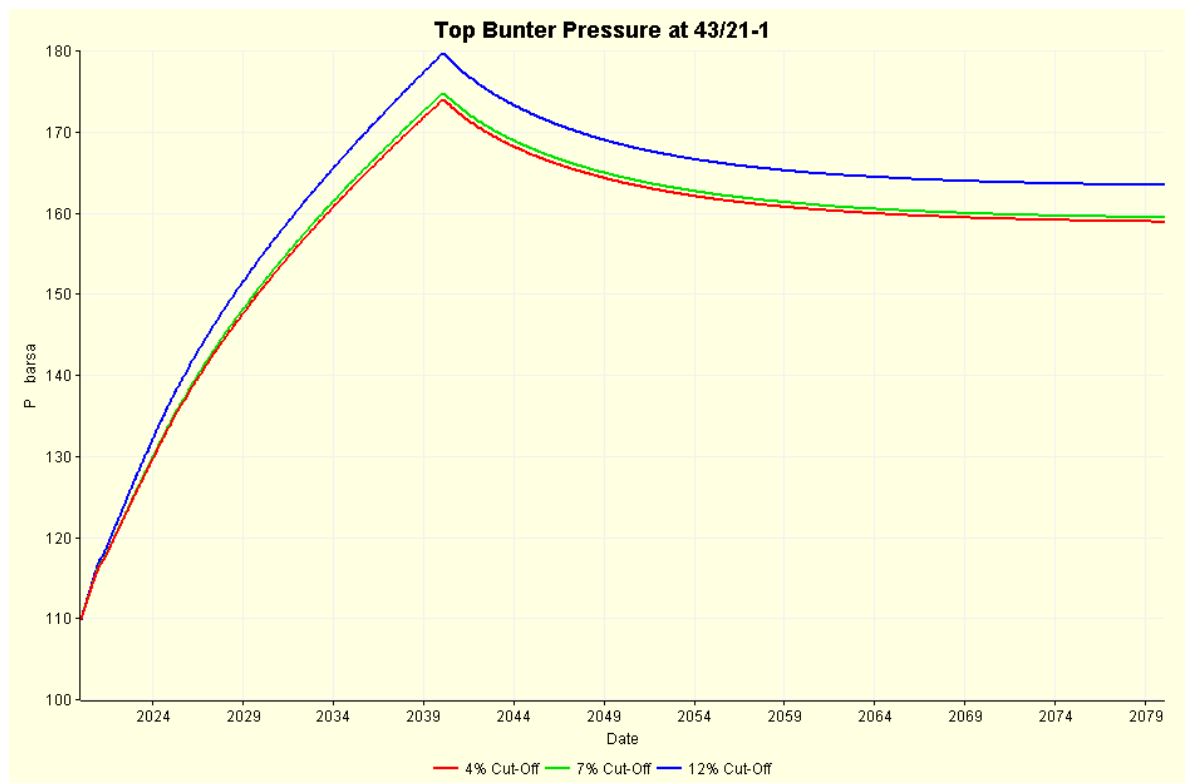
The key parameters required by the simulation model are the NTG ratio, porosity and permeability. NTG and porosity have been upscaled from a fine scale geological model to a coarser scale simulation model using simple pore volume weighted arithmetic averaging. The NTG array depends on the minimum porosity or porosity cut-off below which a volume of rock is considered non-reservoir or non-net. The dynamic effects of porosity cut off was tested on the intermediate grid using the values of minimum porosity shown in Table 8.8 which also shows the resulting average porosity and Water Initially in Place (WIIP).

Table 8.8: Average Porosity and Water Initially in Place versus Porosity Cut-Off

Minimum Porosity/[fraction]	Average Porosity/[fraction]	WIIP 10 ⁹ m ³
0.04	0.189	20.8
0.07	0.192	20.5
0.12	0.202	18.6

As the minimum porosity is increased, the resulting average porosity increases but the WIIP decreases as more of the GRV is moved from reservoir to non-reservoir. The dynamic pressure profile shows the peak and asymptotic shut-in pressures increasing as WIIP decreased with increase in cut off (Figure 8.32).

Figure 8.32: Sensitivity of Crestal Pressure to Porosity Cut-Off



The mid-case porosity cut-off of 0.07 was selected for use in the modelling work.

The Top Bunter porosity map corresponding to that shown in Figure 8.30 is shown in Figure 8.33. Note the minimum porosity here was set to 0.10 and any cells with values less than that are coloured grey. The outline of the seismic phase reversal is clearly visible.

Permeability was distributed based on the upscaled porosity distribution according to Equation 8.4. Regardless of the grid size and permeability upscaling algorithm used, the permeability was multiplied by a factor such that the (arithmetic) average will be close to 271mD for the pore volume within Endurance above 1500m TVDSS. The Top Bunter X-direction permeability distribution corresponding to that shown in Figure 8.30 is shown in Figure 4.35; note a logarithmic distribution has been used [0.3 to 3000.0mD]. It is assumed that areally permeability is homogeneous, i.e. Y-direction permeability equals X-direction permeability. The average K_V/K_H was taken to be 0.15 as indicated by the VIT run in well 42/25d-3.

Equation 8.4 $\log_{10} K = 15.6\phi - 0.9$

Figure 8.33: Top Bunter Porosity Distribution

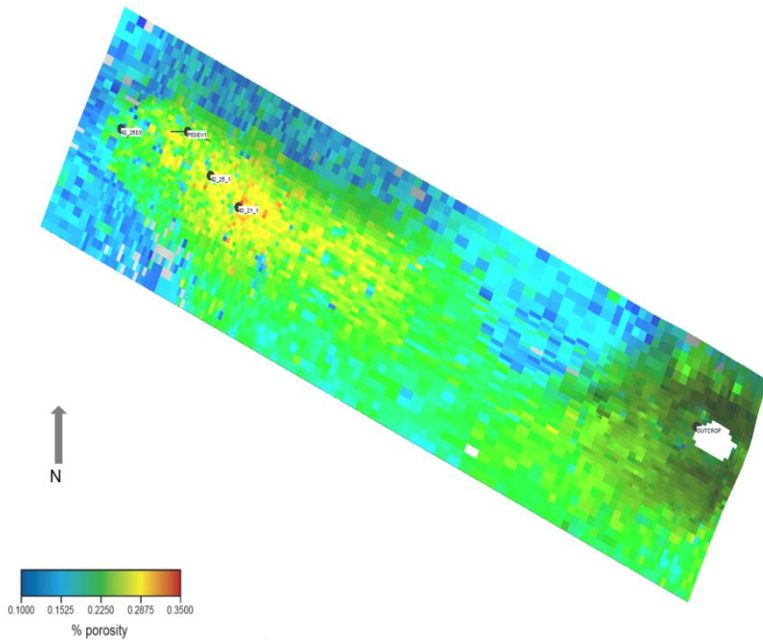
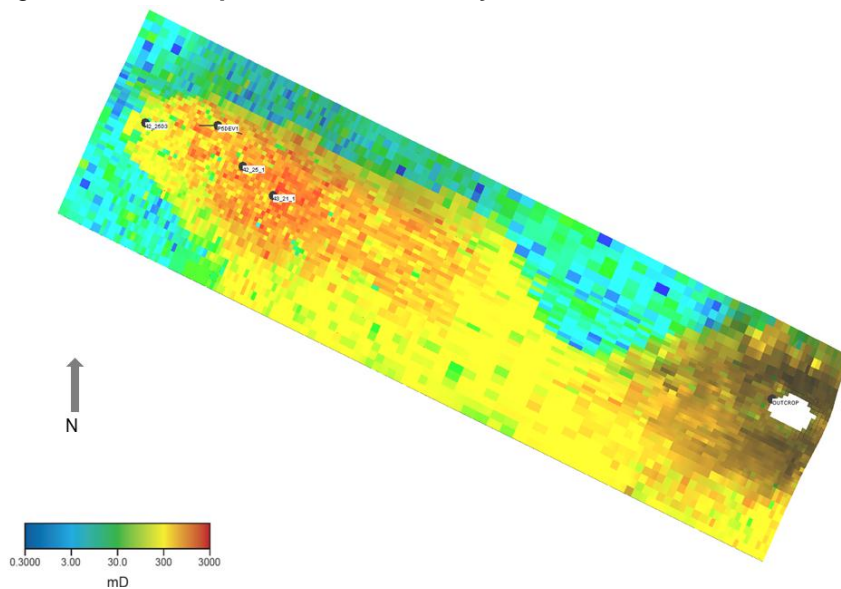


Figure 8.34: Top Bunter Permeability Distribution



8.3.3 Fluid Properties

All simulations have generally been performed at constant reservoir temperature, assuming immiscible CO₂ and brine with no solid phase. The localised (near well bore) cooling of the reservoir from the injection of cold CO₂ was studied using a simple model (see Section 8.3.17). The possible implications of CO₂ dissolution has been considered separately in Sections 248 using somewhat different dynamic modelling

methodologies and software other than Eclipse 100. The details of how fluid properties have been modelled under these conditions will be reported accordingly.

8.3.4 Carbon Dioxide

The CO₂ stream composition used in the reservoir simulation model is a typical composition notionally indicative of the commingled stream from multiple prospective CO₂ emitters (i.e. power stations). This composition is given in Table 8.9 and conforms to the National Grid Safe Pipeline Transportation Specification for CO₂ Mixtures.

Table 8.9: Notional CO₂ Stream Composition

Component	Mnemonic	Mole Percent
Carbon Dioxide	CO ₂	96.0
Argon	Ar	0.6
Nitrogen	N ₂	2.0
Hydrogen	H ₂	0.6
Oxygen	O ₂	0.8

In terms of phase behaviour within the reservoir, the main effect of the impurities is to increase the effective critical pressure and critical temperature of pure CO₂ which are 73.9bar and 31.1°C. As long as the pressure in the system stays above 85.0bar, the mixture will be in its super-critical state.

8.3.4.1 Brine

Brine has been modelled using data derived from brine samples taken in wells 42/25-1 and 42/25d-3. An in situ brine density of 1169.2kg/m³ was determined from the RFT (repeat formation tester) pressure gradient measurement of 0.1147bar/m in well 42/25-1. In situ brine salinity was estimated as 243,000 mg/kg using the Rowe and Chou correlation, an oil and gas industry standard, which takes in density, pressure and temperature as input. The salinity trend observed from the MDT measurements in 42/25d-3 have also been incorporated into the brine model.

The concentration of anions and cations from the three MDT samples along with the sample depths, pressures and temperatures are shown in Table 8.10.

Table 8.10: Concentration of Anions/Cations from MDT Samples

Attribute/	Unit	MDT Water Samples		
Sample		1.04	1.09	1.13
MD	ft	5167.5	4722.0	4634.0
MD	m	1575.1	1439.3	1412.4
Pressure	bar	171.48	155.75	152.65
Temperature	C	64.35	60.21	59.39
TDS	mg/kg	253426	242549	241832
pH		6.84	6.61	6.54
Sulphate	mg/kg	296	359	385
Chloride	mg/kg	154146	148780	148164

Attribute/	Unit	MDT Water Samples		
Fluoride	mg/kg	0.15	0.12	0.10
Bromide	mg/kg	473	460	444
Total BiCarb	mg/kg	51	43	34
Sodium	mg/kg	85512	79664	79953
Potassium	mg/kg	1400	1469	1483
Calcium	mg/kg	8858	8610	8037
Magnesium	mg/kg	2543	3014	3192

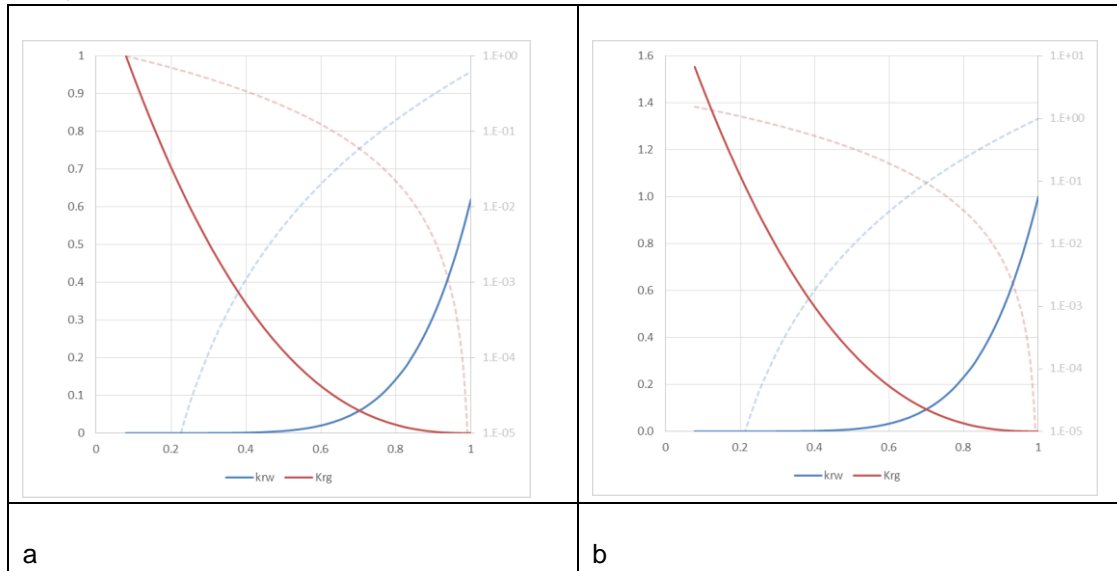
8.3.5 Relative Permeability and Capillary Pressure functions

Both analogue and measured Endurance CO₂-brine relative permeability (K_r) and capillary pressure data were used at different stages in the assessment of the likely dynamic behaviour of the Endurance Storage Site.

8.3.5.1 Measured Endurance Data

The program of experiments that has been used to generate relative permeability from core taken from well 42/25d-3 has already been summarised in Section 8.1.1 of this document. As Figure 8.25 shows the Klinkenberg permeability was found to be always greater than measured effective water permeability and this led to the choice of Klinkenberg permeability as the base permeability for calculating the relative permeability in order to avoid the peculiar situation of having CO₂ relative permeability at irreducible water saturation being greater than 1.0. However, the Endurance Storage Site is currently brine filled, i.e. $S_w = 1$. Therefore, the effective water permeability must be taken to be the absolute permeability K_{abs} , since this is the permeability measured from the dynamic tests undertaken on the 42/25d-3 appraisal well, which include the production well test, the VITs and even the MDT pressure measurements. Because $K_w = K_{abs}$, it means $K_{rw}(S_w=1) = 1$. Selecting (effective) water permeability as the base (absolute) permeability in relation to which relative permeability is defined means the data generated in the SCAL analysis had to be re-based. In Figure 8.35 the re-based relative permeability is compared to the originally generated curve from SCAL laboratory analysis.

Figure 8.35: (a) SCAL Analysis- Water/ CO₂ Relative Permeability Curves and (b) Re-Based Water/ CO₂ Relative Permeability Curves



Note: the dashed lines refer to the logarithmic axis shown as the right-hand y-axis

The Corey exponents and the irreducible water saturation were found to be functions of the Klinkenberg permeability, the Corey exponents being weakly so as Table 8.11 and Figure 8.36 show respectively. The trapped gas saturation S_{gt} is shown in Figure 8.20 to be a function of S_{wi} i.e. $S_{gi} = 1 - S_{wi}$. The Land model of S_{gi} vs S_{gt} in Figure 8.20 was preferred to the Spiteri model because of the tendency of the Spiteri model to generate a maximum at $S_{gi} < 1$ (giving two values of S_{gi} for a single value of S_{gt}) which could cause numerical problems.

8.3.5.2 Capillary Pressure

Mercury Injection Capillary Pressure (MICP) and centrifuge methods were used to measure capillary pressure. It was found that the MICP data was best for determining the entry pressure, i.e. $P_c(S_w=1) > 0$ whereas the centrifuge data was best at describing the behaviour at low (water) saturation. The final capillary pressure behaviour was generated from a Skjaeveland model:

$$P_c = \frac{C_w}{\left(\frac{S_w - S_{wi}}{1 - S_{wi}}\right)^{a_w}}$$

Equation 8.5

Here the coefficients were determined to be $(C_w, a_w) = (1.7, 0.2)$.

Understanding and quantifying the non-zero entry pressure $P_c(S_w=1)$ was a critical step in determining the relative permeability data shown in Figure 8.35 This data was generated using a core flood simulator called SENDRA using the measured capillary pressure data as one of its sets of input data.

Figure 8.37 shows the drainage and imbibition “base” relative permeability data for CO₂ and brine as well as the capillary pressure curve as implemented in ECLIPSE. Note that the values of the key Corey end-

points and exponents have been indicated on the figure. The imbibition water relative permeability follows the drainage curve except that the maximum water saturation is now $1 - S_{gt}$. The imbibition CO_2 relative permeability curve starts at $[S_{wi}, K_{rg}(S_{wi})]$ and terminates at S_{gt} . These dependencies have been modelled using the ECLIPSE End-Point-Scaling functionality (EPS).

Table 8.11: Variation in Endurance Corey Water (N_w) and Gas (N_g) Exponents

Sample	K_L [mD]	N_w	N_g
S193, S115, S167	276.0	6.0	2.5
S197 *	13.6	4.8	2.4
S90	173.0	5.0	3.0
S111, S127	1583.0	4.7	2.7

* Sample S197 was disqualified based on QC-analysis.

Figure 8.36: Irreducible Water Saturation versus Klinkenberg Permeability

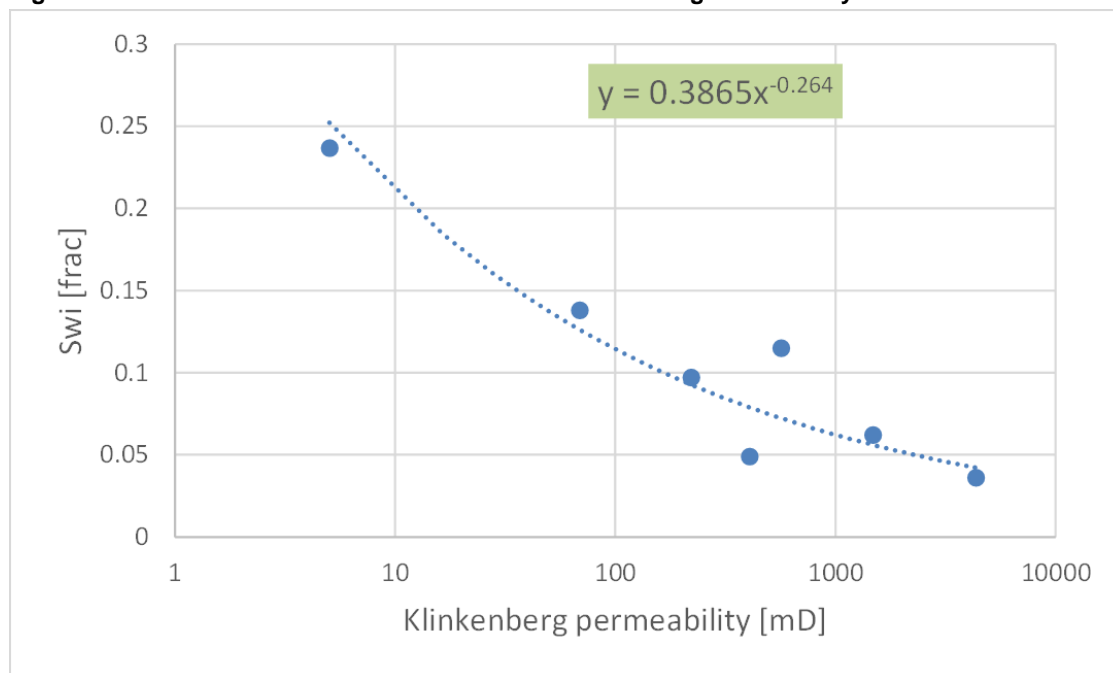
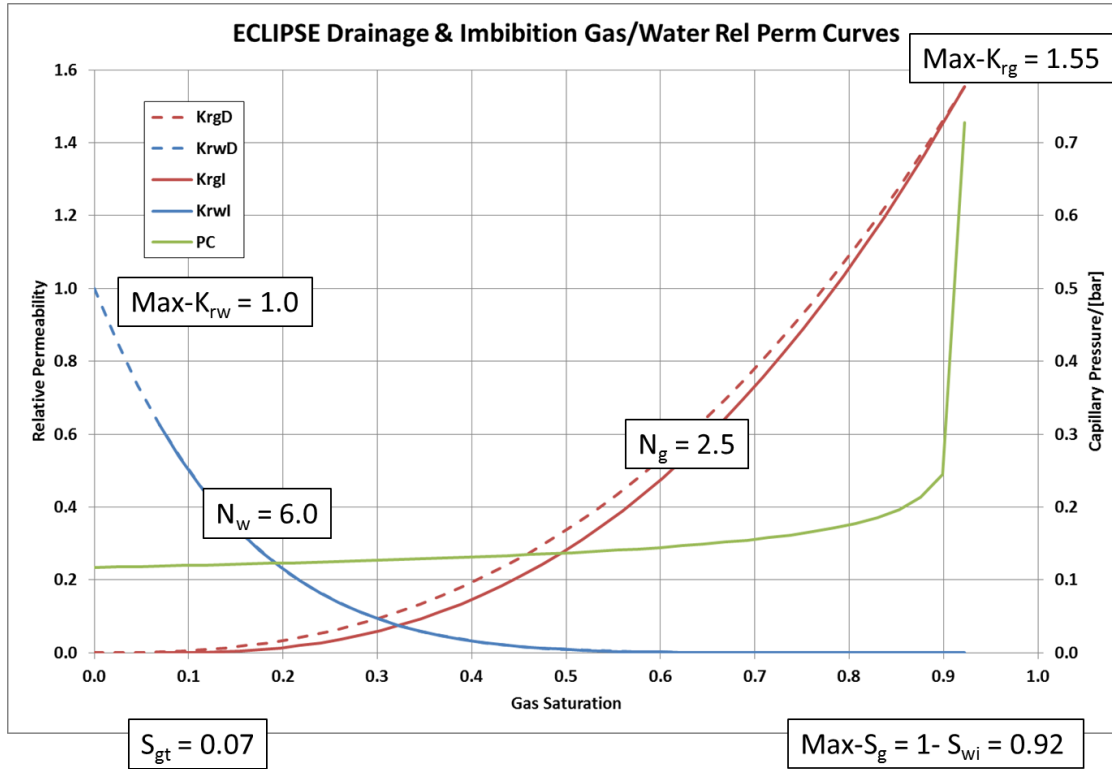


Figure 8.37: Drainage/Imbibition Gas/Water Relative Permeability Data for Endurance



8.3.5.3 Endurance Relative Permeability Analogues

Whilst awaiting Endurance SCAL (special core analysis) results, a literature survey was conducted to assess the suitability of published CO₂/brine relative permeability (Kr) and capillary pressure data for use in the reservoir model. The CO₂-brine Kr data determined using a Viking sandstone reservoir sample as reported in Ref 12 and reproduced in Figure 8.38, is a commonly used analogue data for simulation of CO₂ storage in sandstone formations. There is however significant differences between the physical properties of the Viking sandstone formation compared to the Endurance Bunter sandstone. The Viking sandstone sample was taken from a depth of 1343m where the pressure and temperature are 86bar and 35°C with an average porosity and permeability of 0.195 and 21.7mD and a brine salinity of 28,300 mg/kg. The Endurance Bunter sandstone formation on the other hand has average porosity, permeability and salinity of 0.192 (7% cut-off), 271mD (well test), and 250, 000 mg/kg, respectively.

A closer analogue to the Endurance Bunter sandstone was found in the Ketzin core Kr measurements as shown in Figure 8.39. The Ketzin core was recovered from the Stuttgart formation in the late Triassic Keuper age rocks that overlie the early Triassic Buntsandstein (Endurance Bunter equivalent) formation. In flow tests, the permeability was measured to be between 50 and 100mD whilst tests on core showed values range between 500mD and 1000mD. The brine salinity was reported as 220,000 mg/kg. The values of the Corey coefficients are reproduced in Table 8.12. Results obtained from these analogue data have been interpreted as model sensitivities on Kr behaviour.

Figure 8.38: Viking Relative Permeability and Capillary Pressure Data

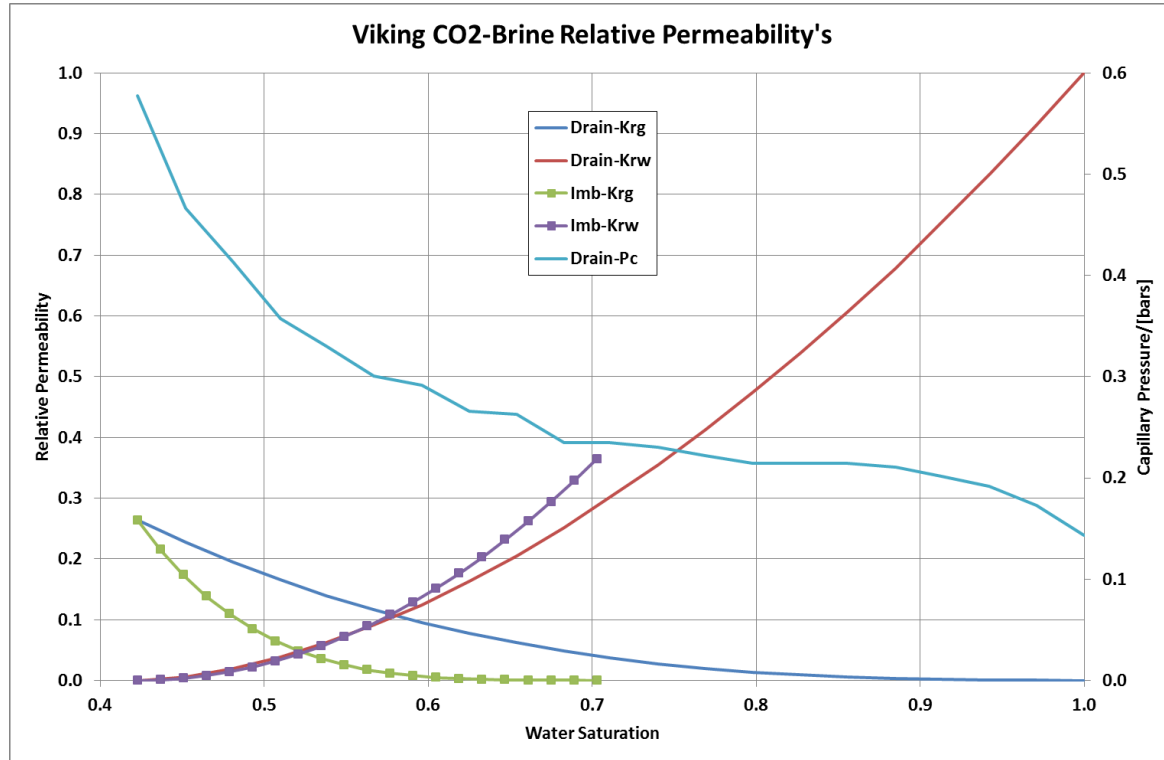
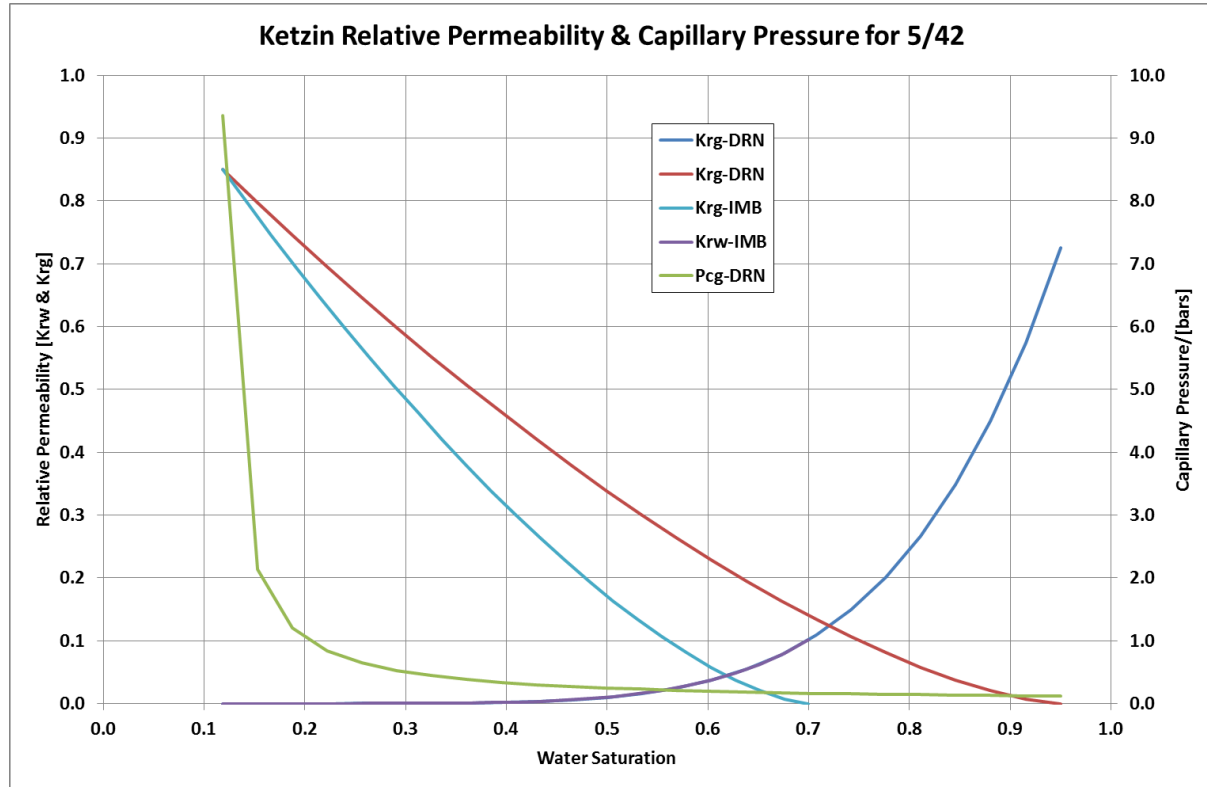


Table 8.12: Ketzin Corey Relative Permeability Coefficients

Parameter	CO ₂	Brine
Exponent	1.50	5.50
Drainage-Residual	0.05	0.15
Imbibition-Residual	0.30	0.15

Figure 8.39: Ketzin Relative Permeability and Capillary Pressure Curves



The capillary pressure function is given by:

$$P_c = \left(\frac{S_w - S_{wi}}{a} \right)^m$$

Equation 8.6

where $a = 0.096$ and $m = -0.989$. Of course Equation 8.6 becomes infinite as $S_w \rightarrow S_{wi}$ so a small offset is introduced to keep P_c finite.

Note the maximum gas (CO_2) relative permeability in Figure 8.39 of $Krg^M = 0.85$ is 3.2 times larger than the corresponding value in the Viking data (Figure 8.38) and so the CO_2 will move proportionally faster towards the crest of the structure.

8.3.6 Initialisation

Pressure, temperature and salinity (via collection of brine samples) measurements were taken from the 42/25d-3 appraisal well.

8.3.7 Pressure Variation

The model uses a datum pressure of 140.0bar at a reference depth of 1300m TVDSS and the pressure gradient is taken to be 0.115bar/m. These values have been derived from the combined interpretation of RFT and MDT pressure measurements in wells 42/25-1 and 42/25d-3 respectively (see Section 8.1.2).

8.3.7.1 Temperature Variation

A reference temperature of 55.9°C at 1300m TVDSS was calculated from a temperature gradient of 0.0305°C/m which was determined from the MDT long duration tests, i.e. pressure points and brine sampling.

The CO₂ injected into Endurance will be somewhat cooler than the reservoir given that it will have travelled along a 90 km pipeline and the seabed temperature in this part of the UK SNS is known to vary between 5 and 15°C winter to summer. The CO₂ will heat as it travels down the injection wells into the reservoir and this has been estimated to be about 10°C although this will of course depend critically on the flow rate. It has been assumed that the minimum temperature of the CO₂ at the perforations is 15°C (in winter). The injection of CO₂ which is cooler than the reservoir temperature is likely to cause thermal fracturing. For this reason the perforation strategy prescribes the perforation of the deeper sections of the injection wells. A 185m perforation interval across the L1 zone of the Bunter sandstone has been shown to support the White Rose maximum design CO₂ injection rate of 2.68MTPA whilst allowing for ample distance between the Röt Clay caprock and any potential thermally induced fractures in order to provide for future perforating should existing perforations become plugged or collapse, or the near wellbore becomes damaged.

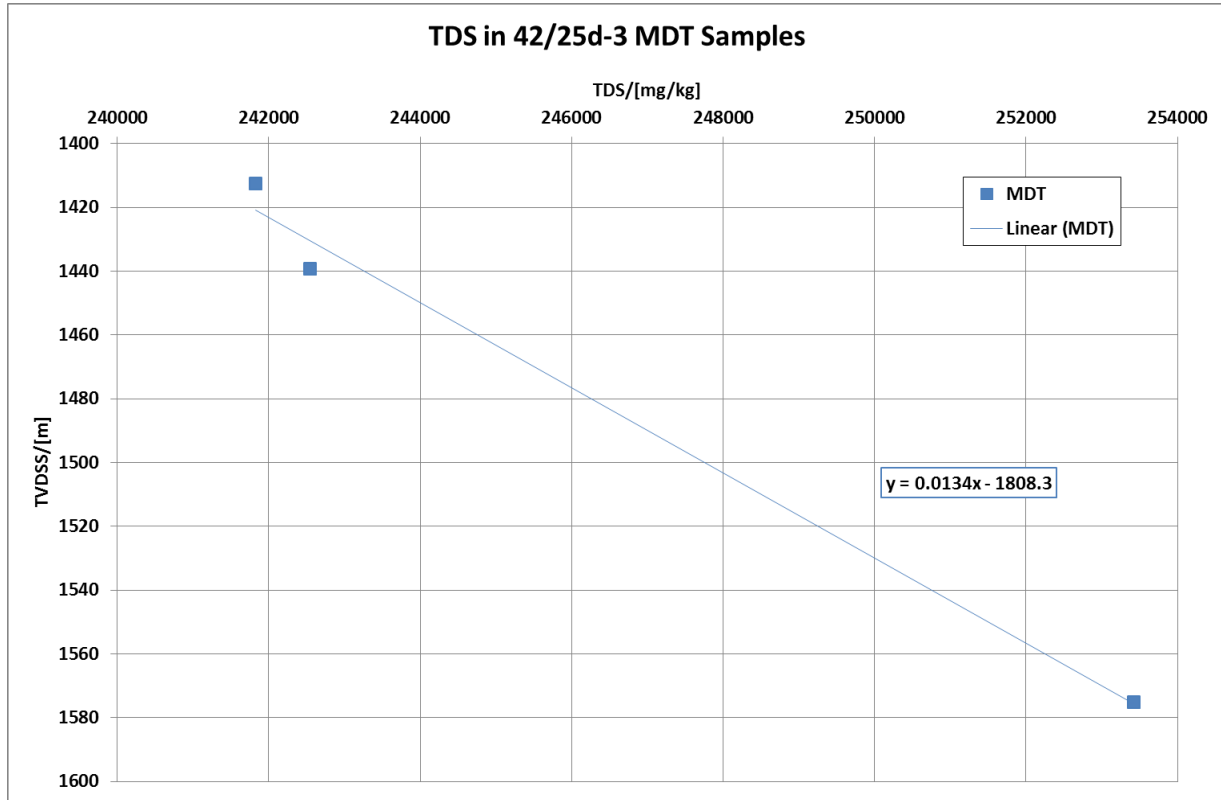
8.3.8 Salinity Variation

Analysis of the MDT brine samples suggests that there is a variation of salinity with depth as shown in Figure 8.40.

Re-arranging the Equation of the fitted trendline gives a Total Dissolved Solids (TDS) (mg/kg) = 74.6 (TVDSS (m) + 1808) so that at the seabed location of the outcrop where TVDSS = 65 m, then TDS ≈ 135,000 mg/kg.

It is uncertain whether the outcrop could maintain such a linear gradient in salinity and have a TDS at seabed of around 135,000 mg/kg (whilst sea-water salinity is around 35,000 mg/kg). Petrographic analysis of cuttings in well 43/28a-3 that passes through the western side of the outcrop suggests flow of meteoric water in the past and also that the high quality Bunter and more recent Quaternary sands are open to flow. The outcrop is by default open to flow and a sensitivity analysis has been performed in which it is considered closed to better characterise its dynamics during and post CO₂ injection.

Figure 8.40: TDS variation with depth from 42/25d-3 MDT samples



8.3.9 Greater Bunter Size and Properties

Even though an area of about 460 km² is being considered with a pore volume of around 20.0x10⁹ m³ (the Endurance pore volume measured to the most likely spill is about 4.8x10⁹ m³), it is considered most likely that Endurance is connected to a much larger volume of the BSF, see Section 8.2 for a summary of the arguments.

To avoid the prohibitive simulation CPU requirement, the greater Bunter was not modelled explicitly. Instead, the Carter-Tracy aquifer model in Eclipse has been used. The two parameters which define the model are the time constant τ (with dimensions of time) and the aquifer influx coefficient β (with dimensions of total influx per unit pressure change). These parameters are defined by:

Equation 8.7
$$\frac{1}{\tau} = c_1 \frac{K_A}{\mu_w \phi_A c_T r_o^2}$$

Equation 8.8
$$\beta = c_2 H f \phi_A c_T r_o^2$$

The variables in Equation 8.7 and Equation 8.8 are defined in Table 8.13 along with values where appropriate. Some of the variables are explained by use of the schematic diagrams shown in Figure 8.41.

Figure 8.41: Schematic of the Carter-Tracy Aquifer Model

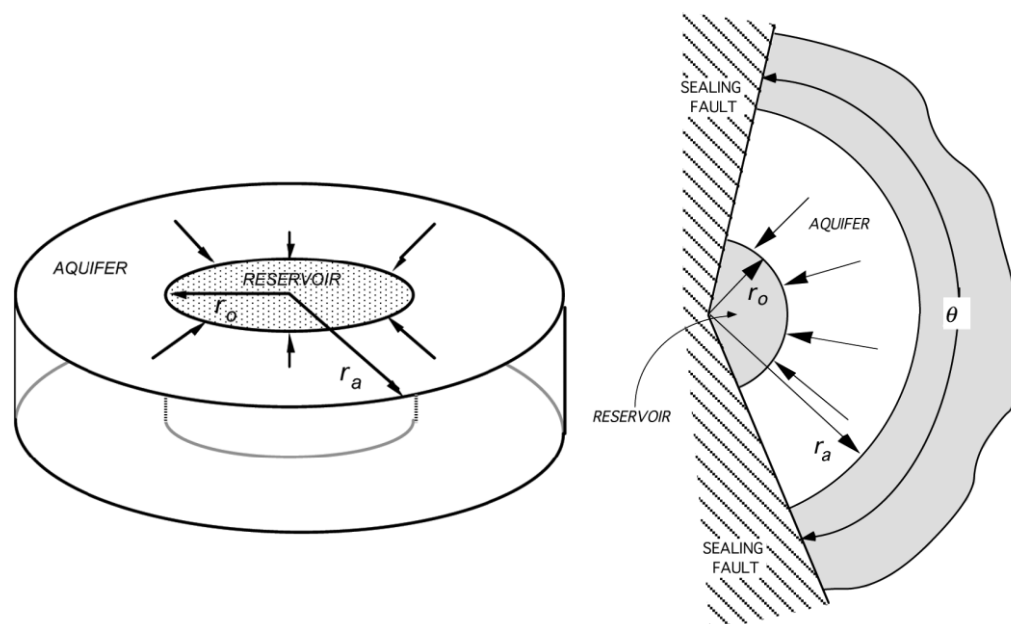


Table 8.13: Parameters in the Carter-Tracy Aquifer Model

Symbol	Parameter	Default Value
K_A	Aquifer Permeability	mD
μ_w	Aquifer Brine Viscosity	1 cP
ϕ_A	Aquifer Porosity	
c_T	Total (Rock and Brine) Compressibility	85×10^{-6} /bar
r_o	Reservoir Radius	11,000 m
H	Aquifer Thickness	250 m
f	Fraction of Angle Subtended	

For the application of the Carter-Tracy model, rather than a rectangular AOI whose major and minor axes are 40 km and 10 km, the AOI is considered to be a circle with a radius of 11 km, i.e. equivalent area (hence the value of r_o shown in Table 8.13). It has been argued that the aquifer attached to 5/4 extends to an area in excess of 20,000 km². This implies a pore volume of about 1×10^{12} m³, assuming an average thickness of 250m and porosity of 0.19. Sensitivity of Endurance dynamic pressure to aquifer property is presented in Section 8.3.14.3.

8.3.10 The Outcrop

The AOI for the dynamic model has been chosen to explicitly include the outcrop so that sensitivity to whether it is connected to Endurance and open to flow or not can be studied. The geological interpretation of the outcrop bathymetry is shown in Figure 8.42 whilst Figure 8.43 shows the map and sides views of the out crop in the simulation model. Note the area of Bunter Sandstone thought to be exposed at the seabed is around 1.4 km². Even if only a fraction of this area is open to flow, it is likely to have significant production for minimal pressure increase, i.e. a very large Productivity Index (PI).

Allowing the outcrop to flow to the sea if the whole system is pressured up is achieved by defining a super-well at the edge of outcrop within the ring of modelled cells with a transmissibility that is 100 times greater than that of a typical well in order to capture the expected high PI.

Figure 8.42: Geological Interpretation of Outcrop Seabed Bathymetry

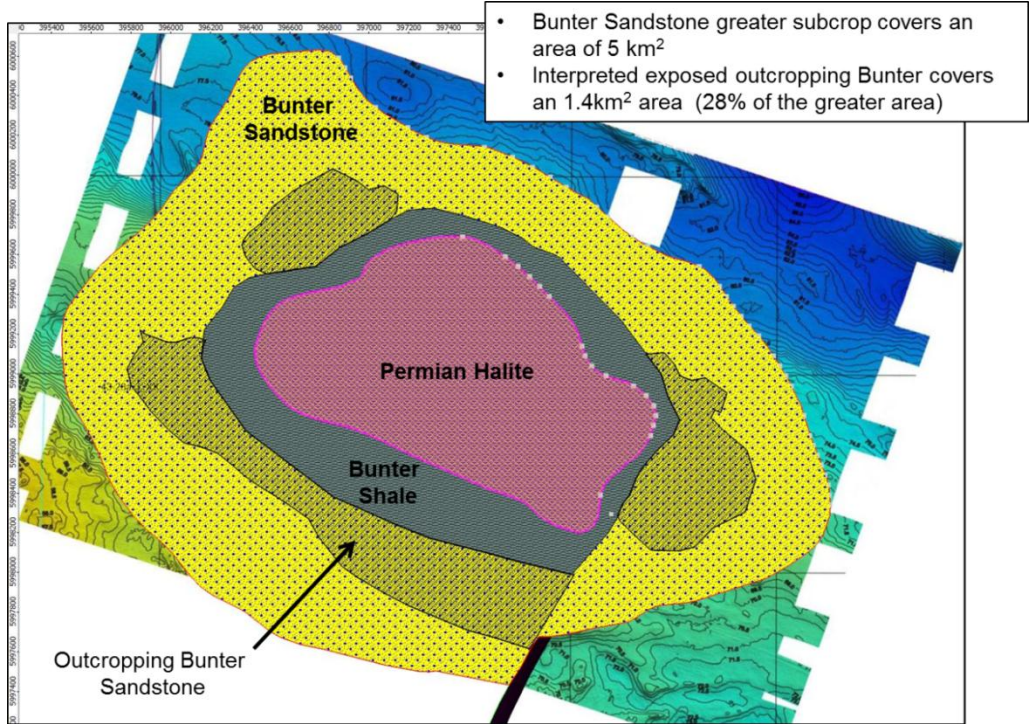
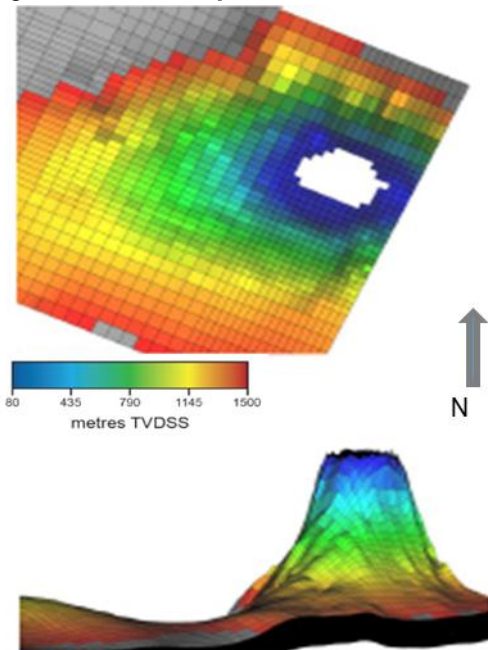


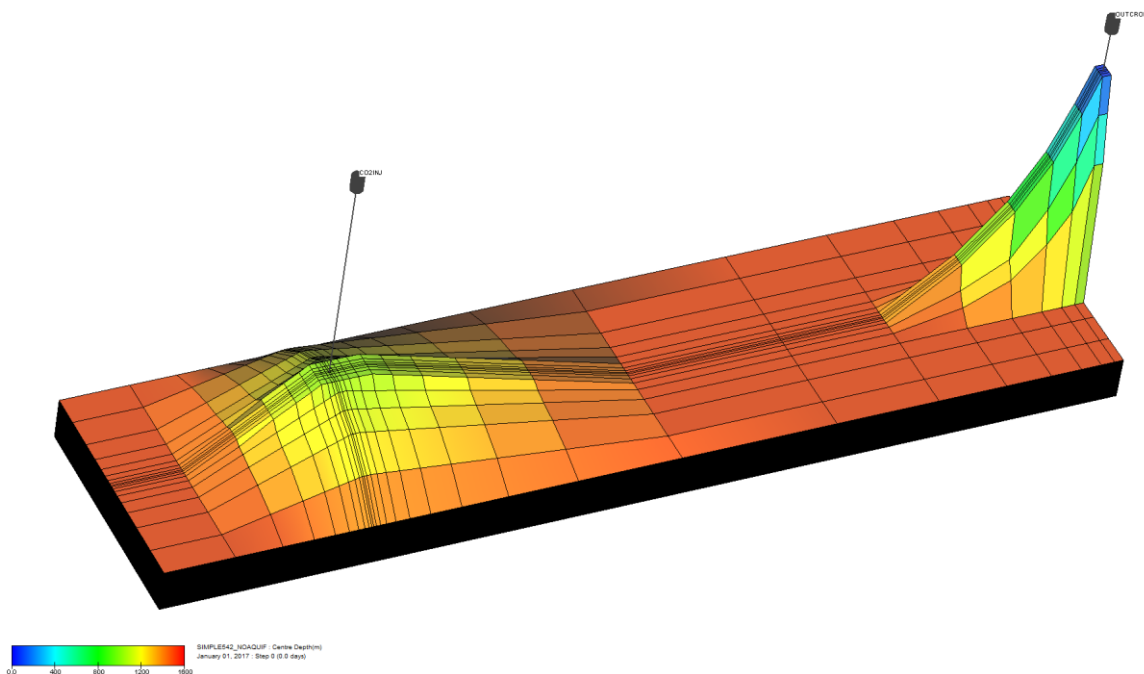
Figure 8.43: Map and Side-Views of the Outcrop in the Simulation Model



8.3.11 Simplified AOI Simulation Model

To allow more sensitivity runs to be made, a simplified simulation model has been constructed which incorporates the key features of the detailed model. Firstly the model is about 50km long, 12km wide and 250m thick. Porosity is made a linear function of depth with 0.28 at Top Bunter and 0.12 at Bottom Bunter. Horizontal permeability is a function of porosity as per Equation 8.4 and vertical permeability is set using $K_V/K_H = 0.15$. The pore volume of the model is adjusted such that the total volume is about the same as the detailed model of $1.9 \times 10^{10} \text{m}^3$. Vertical grid cell resolution is 2m throughout the 125 layers (to make a total thickness of 250m). The areal grid resolution varies as shown in Figure 8.44.

Figure 8.44: Top Bunter Depth of Simplified Model



8.3.12 Simplified Injection Model

Even the fine scale grid considered in Section 8.3.2.1 was too coarse for looking at issues surrounding injectivity which are dominated by near well bore effects. Therefore the type of grid developed in the previous Section has been modified to study sensitivities around injectivity as discussed in Section 8.3.16.

This model has been developed to study injectivity issues by adding finer grid cells to a core area whose extent has been defined by the horizontal departure of a well drilled through the Bunter sand at 50° to 60° orientation from the vertical. A grid size of $(\Delta X, \Delta Y) = (50\text{m}, 50\text{m})$ has been adopted with $(N_x', N_y') = (21, 21)$ cells for this core area. Outside this area, the grid cells are increased by a factor of 1.5 until an area comparable to that of the Greater Bunter in the UK SNS has been covered. A map view of the grid showing the ΔX -values is shown in Figure 8.45 and a cross Section in Figure 8.46.

Both Röt Halite and Röt Clay have been included in this model to permit quantification of the conductive cooling created from injecting cold CO_2 through the wells. Porosity and permeability of the halite layers are

set to 0.001 and 1 μD whilst the values in the clay are set to 0.005 and 10 μD . The porosity in the Bunter sandstone is made a linear function of depth with a value of 0.27 at Top Bunter and 0.14 at Bottom Bunter. Permeability of the Bunter sandstone is calculated using Equation 8.4.

Figure 8.45: Simplified Grid to Study Injection Issues

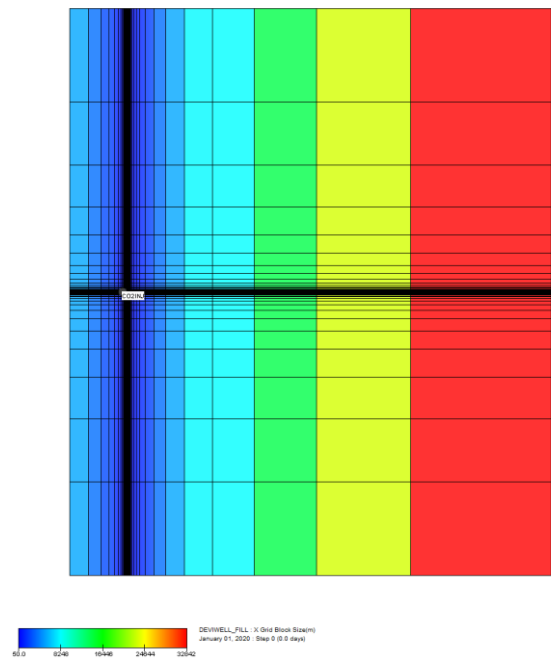
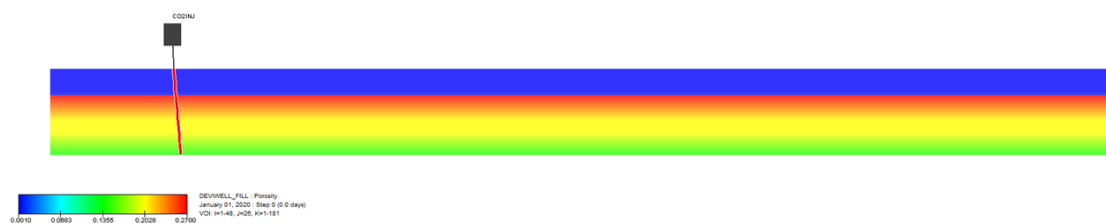


Figure 8.46: West-East Porosity Cross-Section through Injection Model



8.3.13 Wells

The injection wells have been designed to ensure ease of access during potential well interventions: wellheads will be located on a platform and a maximum well trajectory of less than 60° has been adopted to ensure operations can be undertaken via wireline. Since all wells will be set on a single platform it is important to perforate as deep as possible to maximise the separation of the plumes generated from each well whilst ensuring the injected CO₂ remains within the confines of the structure defined by the shallowest possible spill point.

Injecting the CO₂ as deep as possible has other advantages, namely:

- maximises the offset from the cap rock, i.e. delays the CO₂ arrival time to the crest of the structure;
- maximises opportunity for residual and dissolution trapping; and
- minimises risk of thermal fracturing of the cap rock.

8.3.13.1 Well Locations and Trajectories

The location chosen for the platform is at 366882m Easting’s and 6012790m Northing’s in UTM Zone 31 on the ED50 datum.

The deviation of the three specified CO₂ injection wells (55° to 60° from the vertical) is shown in Figure 8.47. The red and purple images in the map overlay are overburden faults. Avoidance of overburden faults was one of the criteria which dictated the well placement.

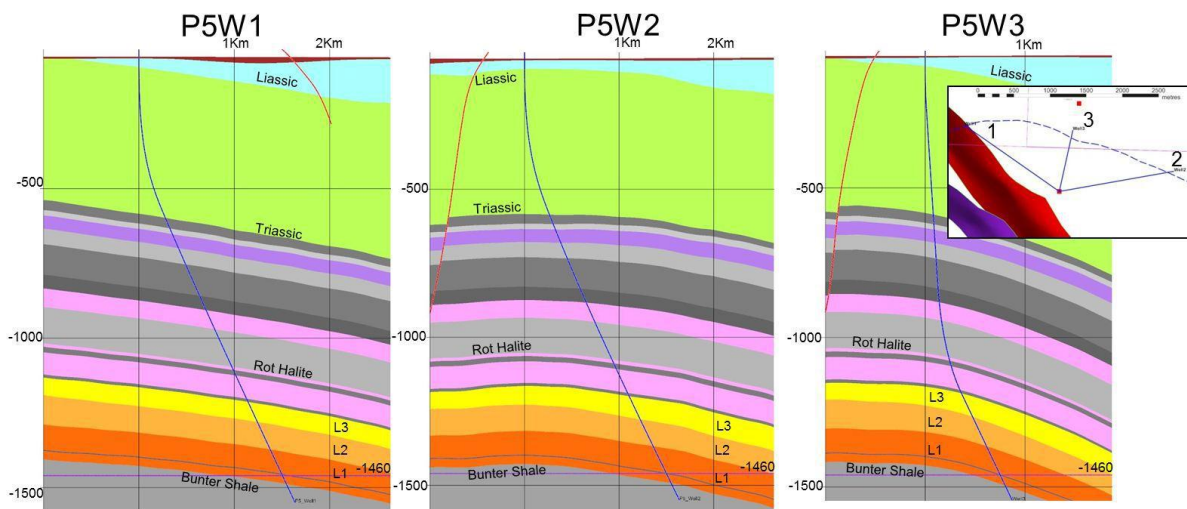
8.3.13.2 Perforation Interval

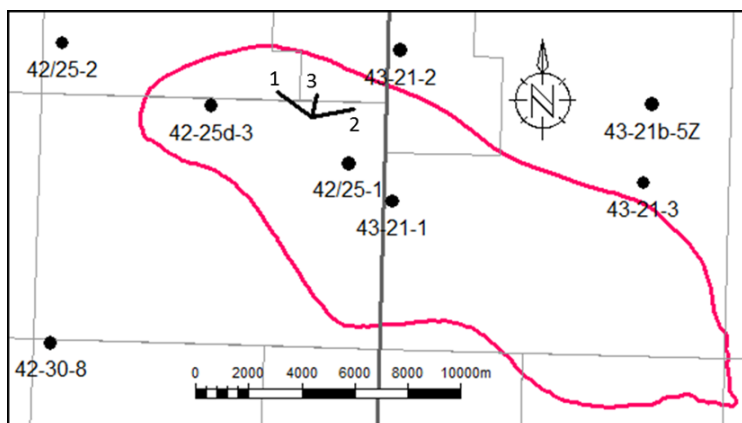
As stated above, the perforation strategy is to perforate the wells as deep as possible. Whilst the relative buoyancy guarantees that CO₂ will migrate upwards, a decision has been made to set the deepest perforation 30m above the shallowest possible spill point of the structure. It is assumed that the topmost perforation will be set in the middle of the L2-Bunter Sandstone.

8.3.13.3 Well Switching

Considering the three injection wells discussed above, the standard operating strategy that has been adopted in the dynamic simulations is to split the maximum injection rate of 2.68MTPA between two of the three wells, i.e. 1.34MTPA/well and then to cycle between the set of wells every six months so that any given well is injecting for 12 out of every 18 months.

Figure 8.47: Well Trajectories from P5 Platform Location (and Location Sketch)





8.3.14 CO₂ Storage Capacity and Reservoir Pressure Profiles

This section describes the determination of the storage capacity within Endurance, bringing together the most up to date interpretation of geophysical and petrophysical data, as well as core analysis data from the 42/25d-3 appraisal well. The most likely NPV and a mid-case irreducible water saturation are first used to estimate the maximum CO₂ storage capacity within the Endurance and then the implications of White Rose CO₂ injection upon Endurance pressure increase under static and dynamic conditions are explored given assumptions about hydro-dynamic connectivity to the caprock and the Greater Bunter aquifer.

8.3.14.1 Endurance Maximum CO₂ Storage Capacity

Equation 8.9 has been used to calculate the maximum pore volume (PV) which could be occupied by CO₂

$$\text{Equation 8.9} \quad V_{\text{CO}_2} = (1 - S_{\text{wi}}) \text{NPV}$$

where S_{wi} is the irreducible water saturation.

The net NPV analysis is based on seven facies and three NTG models over which porosity cut offs are assigned according to the degree of cementation. The low, mid and high NPV are calculated as $4.2 \times 10^9 \text{ m}^3$, $4.6 \times 10^9 \text{ m}^3$, and $5.4 \times 10^9 \text{ m}^3$, respectively. The structural uncertainty was assessed via Petrel uncertainty workflows that calculate the spill point for 500 top structure maps that have been generated stochastically. The current Endurance structural model spill is -1460m with a range of -1416m to -1553m resulting from the uncertainty workflow.

Figure 4.37 has been derived from the analysis of cores recovered from the 42/25d-3 appraisal well and shows S_{wi} as a function of Klinkenberg permeability. Using the average permeability interpreted from the 42/25d-3 well test of 271mD, S_{wi} for the Bunter sandstone within Endurance is estimated as 0.09. Taking account of measurement uncertainty, a conservative $S_{\text{wi}} = 0.15$ has been used to estimate the CO₂ storage capacity.

Using the mid-case NPV, therefore, $V_{\text{CO}_2} = 3.9 \times 10^9 \text{ m}^3$.

Assuming that the in-situ CO₂ density in Endurance is $\rho_{\text{CO}_2} = 700\text{kg/m}^3$, then the mass of CO₂ which could be stored in Endurance is $m_{\text{CO}_2} = \rho_{\text{CO}_2} V_{\text{CO}_2} = 2.7 \times 10^{12}\text{kg} = 2700\text{MT}$. The maximum White Rose CO₂ injection rate is 2.68MTPA for 20 years, i.e. a total of 53.6MT or less than 2% of the theoretical Endurance capacity. Whilst taking up 2% of the total PV may seem insignificant, it must be remembered that Endurance is presently filled with brine of very small compressibility. The next section describes attempts to estimate the associated pressure increase as a result of injection, firstly using simple material considerations and then using more elaborate dynamic simulation models.

8.3.14.2 Pressure Increase in Endurance Due to White Rose CO₂ Injection and Hydraulic Isolation

The magnitude of pressure increase within Endurance as a result of White Rose CO₂ injection is strongly dependent on assumptions about pressure communication between the volume enclosed by the most likely structural close contour and the rest of the Bunter sandstone formation.

This considers a limit case in which Endurance is a closed volume bounded by an impermeable boundary at the most likely structural close of 1460 m.

Equation 8.10 is an expression for the conservation of mass in terms of compressibility factor in which ΔV is the volume of fluid measured at reservoir conditions injected into a closed box of volume V and average compressibility c which as a result of the injection sees an increase of pressure of ΔP .

Equation 8.10 $\Delta V \approx cV\Delta P$

or $\Delta P \approx \Delta V / cV$

The compressibility of brine and rock at the conditions of interest is 3.0×10^{-5} /bar and 5.6×10^{-5} /bar, respectively giving a total effective compressibility of $c \approx 85 \times 10^{-6}$ /bar. The CO₂ density at reservoir condition of 700kg/m^3 ; resulting in a corresponding volume $\Delta V \approx 76.6 \times 10^6 \text{ m}^3$. $V = \text{NPV} = 4.6 \times 10^9 \text{ m}^3$. Therefore the pressure increase resulting from WR CO₂ injection provided by Equation 8.10 is:

$$\Delta P \approx \frac{1}{4.6 \times 10^9} \frac{(76.6 \times 10^6)}{(8.6 \times 10^{-5})} = 194 \text{ bar}$$

A pressure increase of 194bar equates to an average reservoir pressure of approximately 301bar at the end of WR CO₂ injection, which would almost certainly undermine the sealing integrity of the Rot Clay primary seal whose fracture closure pressure has been estimated to be 264bar at 1362.8m TVDSS. However, multiple sources of evidence ranging from seismic interpretation over the Endurance structure, petrophysical data from surrounding appraisal wells, and analysis of production performance of surrounding gas fields strongly suggests that the assumption of an hydraulically isolated Endurance is an extreme limiting case. Endurance is indeed one of several structural closures of the Bunter Sandstone Formation (BSF) that have been created by salt tectonics within the Triassic Southern North Sea (SNS) basin. To the southeast of the Endurance structure lies a salt diapir that outcrops to the sea bed and seismic interpretation suggest that the Bunter sandstone is continuous in the saddle between the Endurance structure and this diapir, see Figure 4.1.

Pressure history from the Esmond gas field, approximately 40 km north of Endurance, as well as pressure measurements within Endurance itself between 1990 and 2013 suggests the existence of an active regional Greater Bunter aquifer whose size has been estimated to be about 50 to 100 times that of the Endurance structure.

Using a 7% porosity cut-off, the total PV of Endurance and the contiguous Bunter sandstone between it and the outcrop is estimated as $20.5 \times 10^9 \text{ m}^3$ (note that this does not include the greater Bunter aquifer volume). Substituting the V term in Equation 8.10 results in a maximum Endurance pressure increase due to WR CO₂ injection of 43.5bar, well below the fracture pressure of the Rot Clay. Because this is simple material balance estimation, there is the implicit assumption that pressure is transmitted instantaneously across the reservoir during injection. In fact, it takes some time for the total pressure perturbation as a result of a unit volume of CO₂ injection to be felt uniformly across the system and there is always a transient non-uniformity in pressure distribution within the system that peaks just after the end of injection. These dynamic effects have been analysed using more detailed full field simulation models and are discussed below.

8.3.14.3 Dynamic Pressure Profiles Associated with White Rose CO₂ Injection; Outcrop Open or Closed.

The concern here is to use the model to investigate the transient pressure profiles within Endurance during WR CO₂ injection using sensitivities that consider:

- whether the seabed outcrop connected to Endurance is open to flow or not; and
- the impact of the size and strength of the Greater Bunter attached to Endurance.

The question of open/closed outcrop is addressed first as having the outcrop open may obscure questions concerning the aquifer size and strength.

CO₂ is injected at a rate of 2.68MT/yr for 20 years, i.e. 53.6MT total, followed by a 20 year shut-in period. Initially the model is limited to include only Endurance and the outcrop giving a total PV of $20.5 \times 10^9 \text{ m}^3$. The pressure calculated at the crest of Endurance that corresponds to the location of the 43/21-1 well is shown in Figure 8.48, for when the outcrop is closed and when open, along with the brine production rate in the latter case.

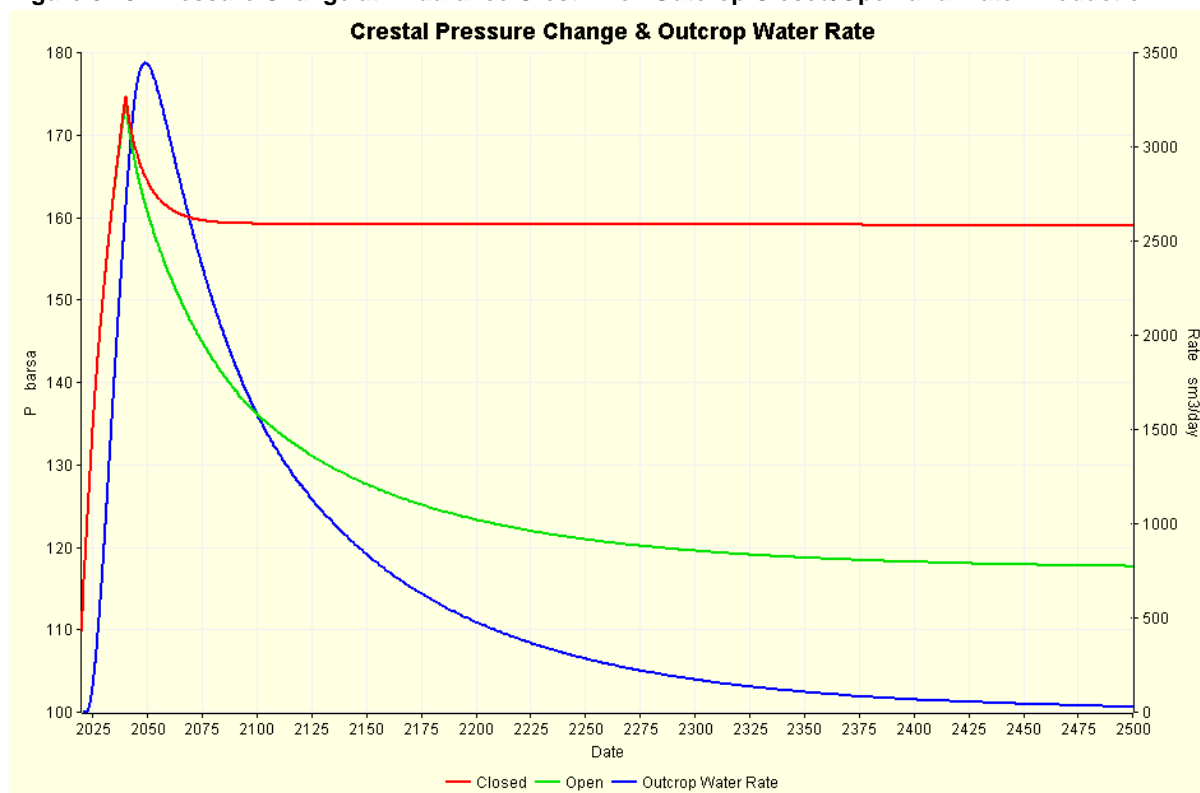
With the outcrop closed the maximum pressure increase is 64.8bar at the end of injection which drops to 49.2bar after shut-in. This shows good agreement between the simulation and the simple material balance model used in the previous section.

With the outcrop open, the maximum pressure at the end of injection is only 0.9bar lower than the closed case, but the pressure then continues to drop as the excess pressure causes flow from the outcrop to continue during the shut-in period. By the year 2500, 460 years after shut-in, the pressure is just 7.8bar over initial pressure.

Brine production starts 2.5 years after the start of CO₂ injection (when the pressure at the outcrop is 0.1bar above its initial pressure), it peaks around 3500m³/d about nine years after shut-in and is still over 3000 m³/d twenty years after cessation of injection. By 2500 the production rate is still more than 30 m³/d.

For the WR project, whether the outcrop is open or closed seems to have little effect on the maximum pressure increase during the injection phase.

Figure 8.48: Pressure Change at Endurance Crest when Outcrop Closed/Open and Water Production



There is a strong argument that Endurance is in hydrodynamic communication with a much larger volume than itself. However, while there appears to be good evidence over the size of the greater Bunter, the strength by which it couples to Endurance is less clear.

The area of the Endurance structure assuming a spill at 1460m TVDSS is about $25 \times 8 = 200 \text{ km}^2$. The area of the simulation model is about $42 \times 11 = 460 \text{ km}^2$. The Greater Bunter area attached to Endurance has been estimated to be probably in excess of $20,000 \text{ km}^2$ or 100 times the Endurance area and 43.5 times the area of the simulation model.

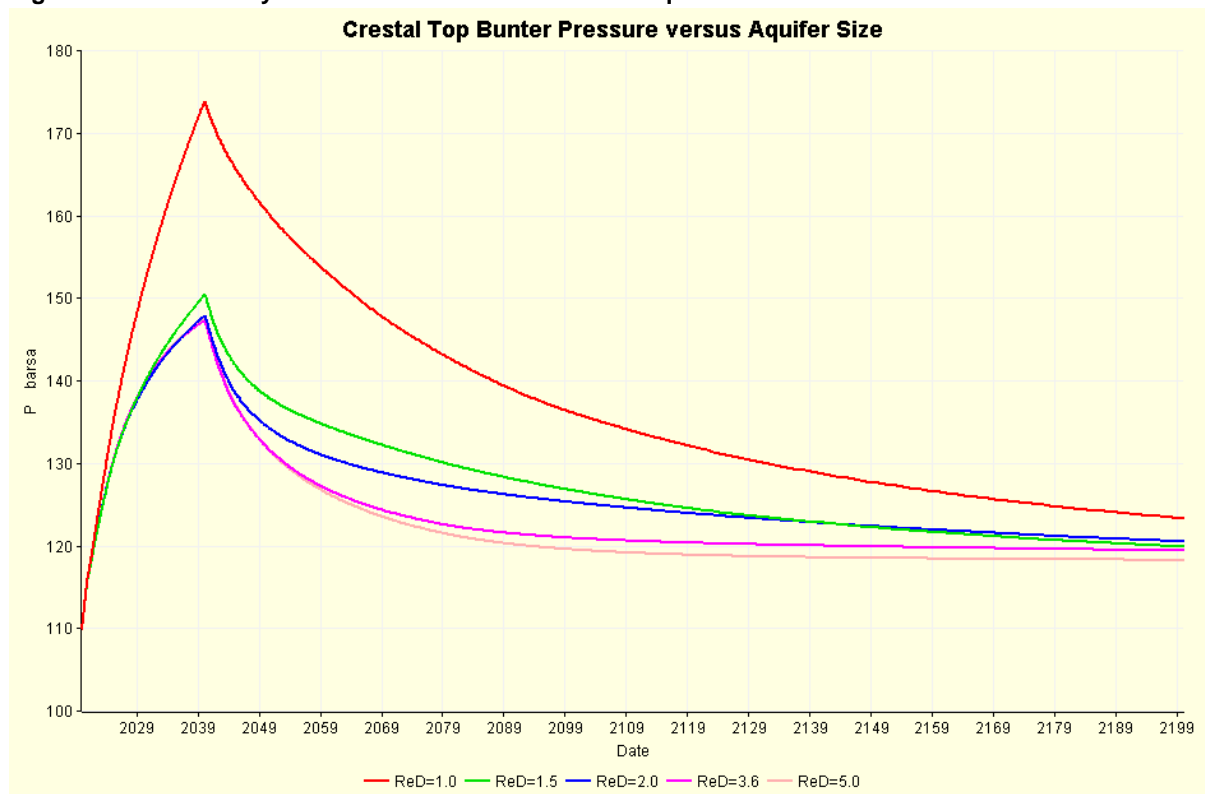
To test a range of additional volumes a finite radial aquifer of variable $r_{eD}/r_{eD} = r_a/r_o$, i.e. ratio of aquifer radius to reservoir radius or the dimensional radius, see Figure 8.41, was attached to all the edge cells of the simulation model. The thickness has been set to 250m and an average porosity of 19.2% was used, that being the average porosity assuming 7% cut-off. The proposed porosity yields an aquifer permeability of 125mD using the poro-perm correlation obtained from interpretation of well logs from 42/25d-3 appraisal well (Equation 8.4). The angle subtended by the aquifer is assumed to be 360° , i.e. full circle, the total compressibility of the rock and brine is $86 \times 10^{-6} / \text{bar}$, the brine has a salt concentration of 250,000 mg/kg and the area of the simulation model converts to a circle of radius 11 km.

The set of r_{eD} investigated is shown in Table 8.14 along with the resulting area (with respect to the AOI) and the total PV of the AOI and attached aquifer. Note that the first row in the table with $r_{eD} = 1.0$ means no additional volume attached, i.e. the green line in Figure 8.48. The pressure response reported at the crestal location is shown in Figure 8.49. Note that at $r_{eD} = 5.0$, the total area of the AOI and aquifer system is only 25 times that of AOI alone, somewhat less than the previously speculated size of the Greater Bunter attached to Endurance.

Table 8.14: Size of Aquifer and Resulting Model Area and Pore Volume

r_{eD}	Area with respect to Model Area	Total PV (10^9 m^3)
1.0	1.00	20.5
1.5	2.25	46.1
2.0	4.00	82.0
3.6	12.96	265.7
5.0	25.00	512.5

Figure 8.49: Sensitivity of Crestal Pressure Increase to Aquifer Size

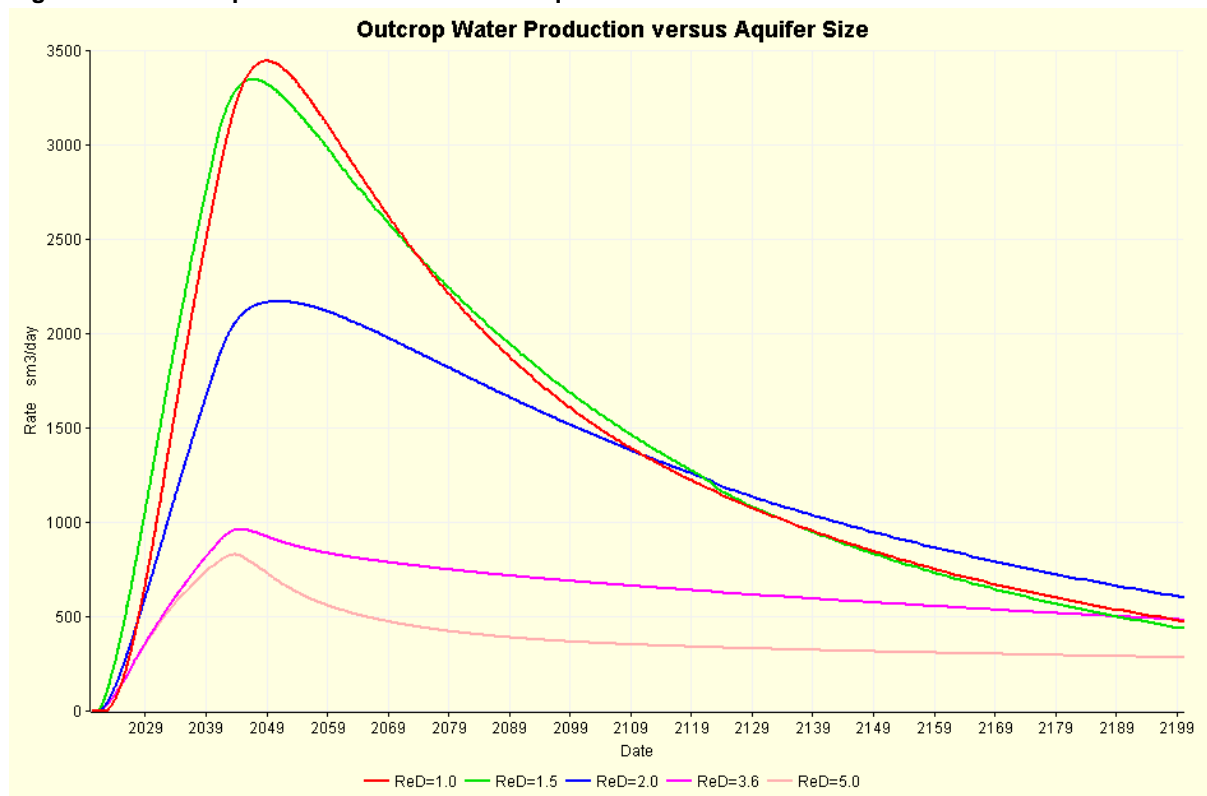


It can be seen once $r_{eD} > 2.0$ the peak increase in pressure at the crest is not significantly reduced from its value of 38.0bar at $r_{eD} = 2.0$. Clearly the asymptotic behaviour during shut-in is changed but some of this change is due to the water production rate from the outcrop which has been open to flow in all these cases; the outcrop production rate versus aquifer size is shown in Figure 8.50. As the attached aquifer becomes larger, it can take-up more of the pressure increases caused by injection meaning less pressure at the outcrop and hence less brine production.

It takes 10 to 12 years to differentiate between the $r_{eD} = 2$ and $r_{eD} > 2$ cases. It would appear to be nearly impossible to differentiate between the $r_{eD} > 2$ cases though this may be easier if porosity and permeability are less than the 19.2% and the 125mD assumed here. This is studied in the next section.

Going forward the $r_{eD} = 3.6$ aquifer size will be assumed unless notified otherwise.

Figure 8.50: Outcrop Production Rate versus Aquifer Size



8.3.14.4 Aquifer Strength

The properties of the attached aquifer, in particular the related porosity and permeability are clearly unknown. A wide range of permeability values have proposed by various sources that ranged from less than 1mD to 250mD.

As stated above, the $r_{eD} = 3.6$ aquifer size has been used, but the porosity and permeability of the Carter-Tracy aquifer are as defined in Table 8.15.

Table 8.15: Porosity and Permeability Used in Aquifer Strength Sensitivity

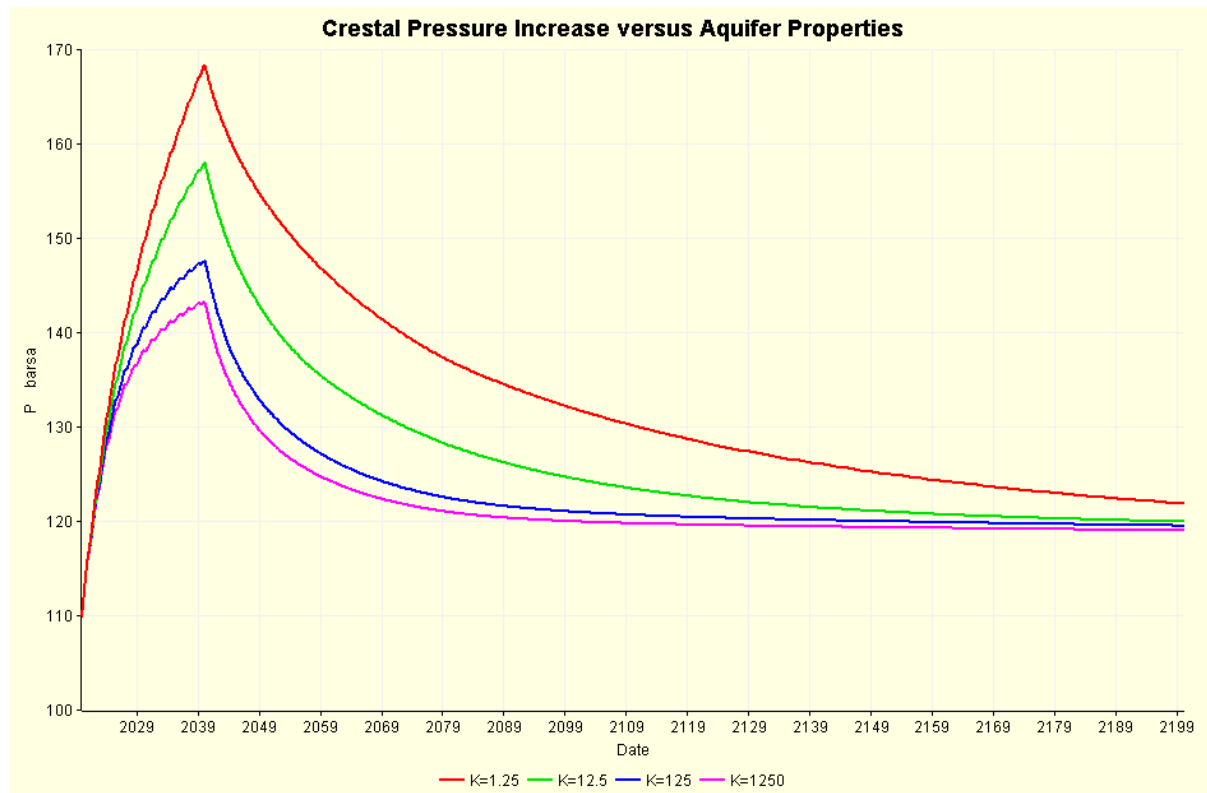
Porosity [%]	Permeability [mD]
6	1.25
13	12.50
19	125.00
26	1250.00

The results of this sensitivity are shown in Figure 8.51. Reducing the quality of the attached aquifer clearly has a detrimental effect on the injection scheme by increasing the crestal pressure seen at the Top Bunter 43/21-1 location. In particular, relative to the $K = 125\text{mD}$ case, reducing the permeability to 12.5mD and 1.25mD makes the peak pressure increase from 37bar to 47bar and 58bar , respectively.

Regarding the most representative aquifer properties, at the Esmond field $45\text{ km North East of Endurance}$, a Greater Bunter aquifer average permeability of 16mD was estimated from material balance calculations that used actual production performance and post shut in pressure build up data. However, much wider range of values has been estimated by a number of authors. Average porosity and permeability for the Greater Bunter of both 0.18 and 250mD and 0.20 and 100mD have been reported. It has also been estimated the average well porosity for wells in the UK SNS Bunter to be 0.187 (from 603 core plugs) – although a great variability of porosity within individual wells was observed; from 0.024 in well $42/10a-1$ to 0.22 in well $42/25-1$. For the $42/25d-3$ appraisal well, the average porosity is approximately $0.20 - 0.27$ at the top and 0.14 at the base.

There is therefore considerable uncertainty around Greater Bunter aquifer properties. Nevertheless, a Greater Bunter permeability of 125mD has been used in simulations from here onward unless explicitly stated otherwise as this is consistent with a porosity of 0.19 from the poro-perm function in Equation 8.4.

Figure 8.51: Crestal Pressure Increase versus Aquifer Properties



8.3.15 Plume Development

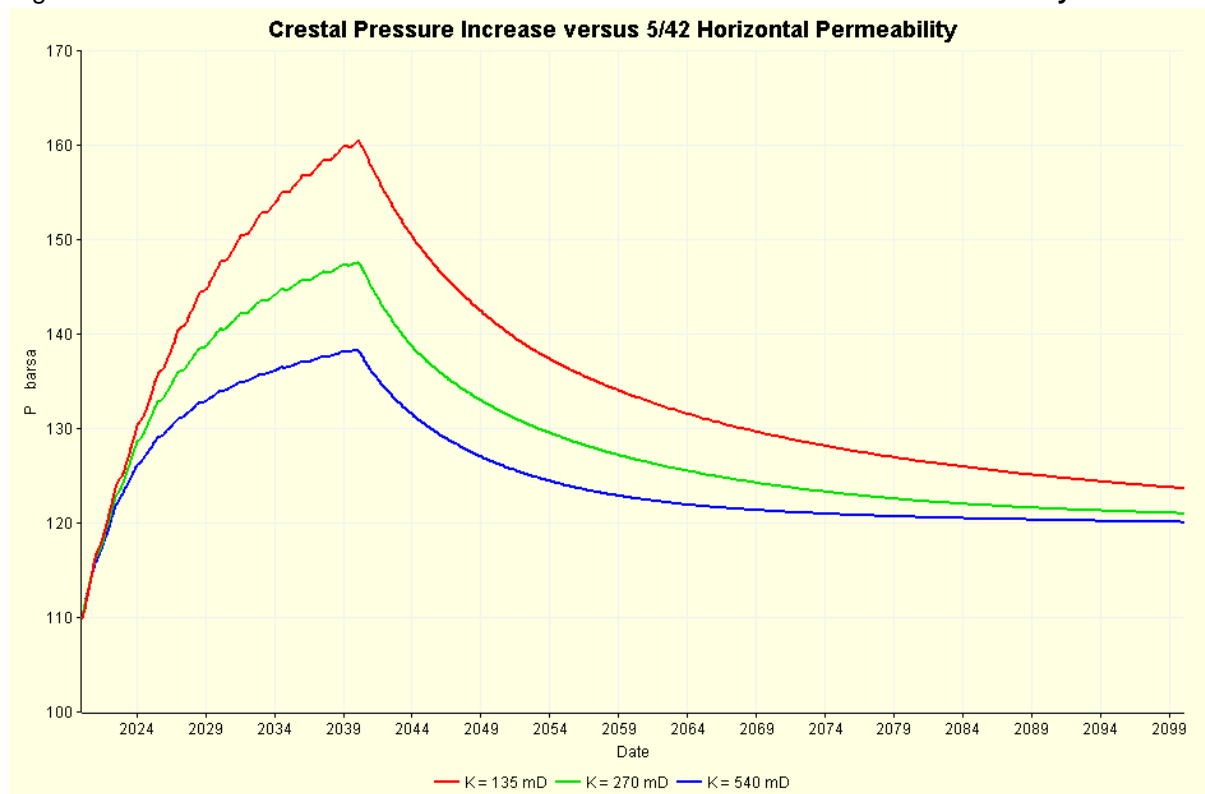
The change in pressure caused by CO₂ injection has been shown to depend mainly on the size and strength of Greater Bunter attached to Endurance. Once the effect of the near wellbore over-pressure required to cause inflow has dissipated, the dense CO₂ will migrate upwards and because of the density difference between it and the native brine, until a seal is encountered. Thereafter CO₂ will flow upwards along the Top Bunter until it pools at the crest of the structure.

The impact of a number of parameters on plume development has been considered and is outlined in the sections that follow.

8.3.15.1 Horizontal Permeability

As with the sensitivity of the aquifer properties analysed in Section 8.3.14.4, varying the horizontal permeability of the Endurance rock will change the crestal pressure increase as shown in Figure 8.52. In varying the horizontal permeability, the earlier constraint on average model permeability imposed by the upscaling method has been temporarily relaxed to permit the use of low (135mD) and high (540mD) case permeability values. The 271mD from 42/25d-3 production well test is taken as the mid case. Note the maximum pressure increase follows the differences seen in Figure 8.51.

Figure 8.52: Crestal Pressure Increase versus Endurance Horizontal Permeability



Part of the increase (for K = 135mD) and decrease (for K = 540mD) in crestal pressure is because of the reduced and increased well injectivity, respectively.

The main effect under study here is the frontal advance of the CO₂ plume because of the reduced/increased *KH* and this is shown in Figure 8.53; the break through time (first CO₂) is listed in Table 8.16.

Table 8.16: Time to First CO₂ at Crest of Endurance versus Permeability

<i>KH</i> /[mD]	First CO ₂ /[yr]
135	5.5
270	3.3
540	1.8

A semi-transparent map view of the Top Bunter depth is shown in Figure 8.54 on which a line can be seen from WNW to ESE across the crest of the structure. This line denotes the set of cross-section displays that follow. The line includes the DEV1 (NW) well as well as the 42/25-1 and 43/21-1 wells. The CO₂ saturations in this mid-case (271mD) cross-section at 6 months after the start of injection, 5 years after, 20 years after (the end of injection) and a further 60 years of shut-in are shown in Figure 8.55, Figure 8.56, Figure 8.57, and Figure 8.58 respectively.

Figure 8.53: CO₂ Saturation at Top Bunter 43/21-1 Location

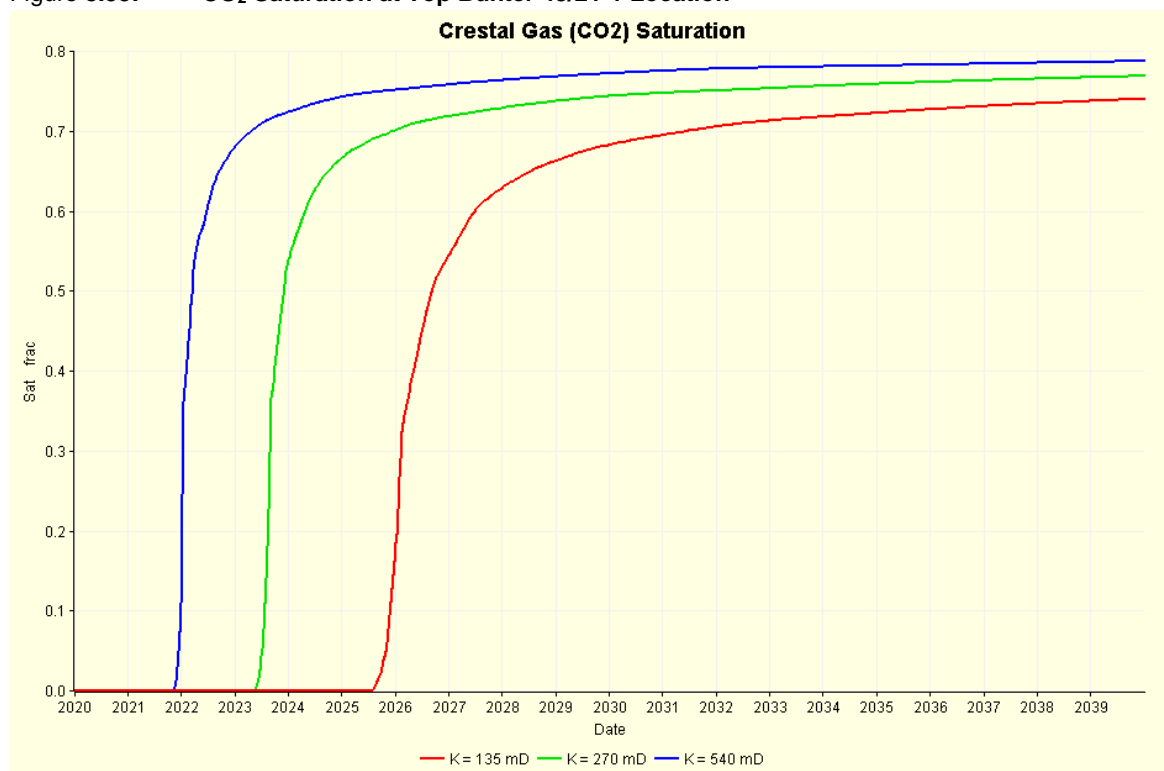


Figure 8.54: Cross-Section through DEV1, 42/25-1 and 43/21-1

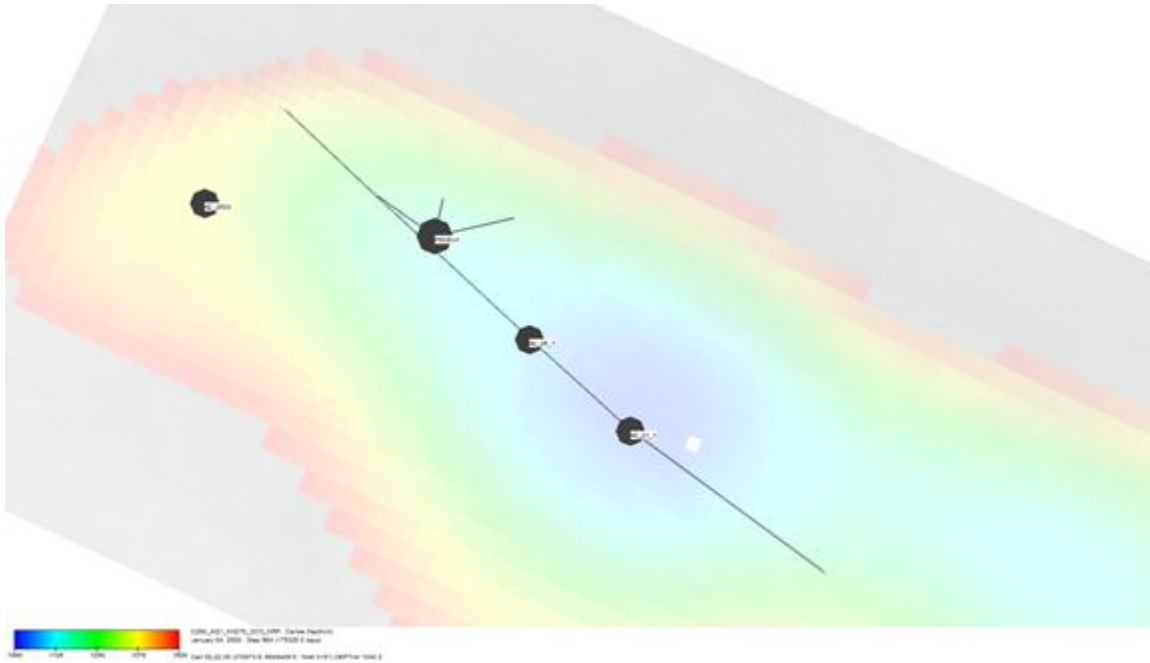


Figure 8.55: CO₂ Distribution after 6 Months of Injection

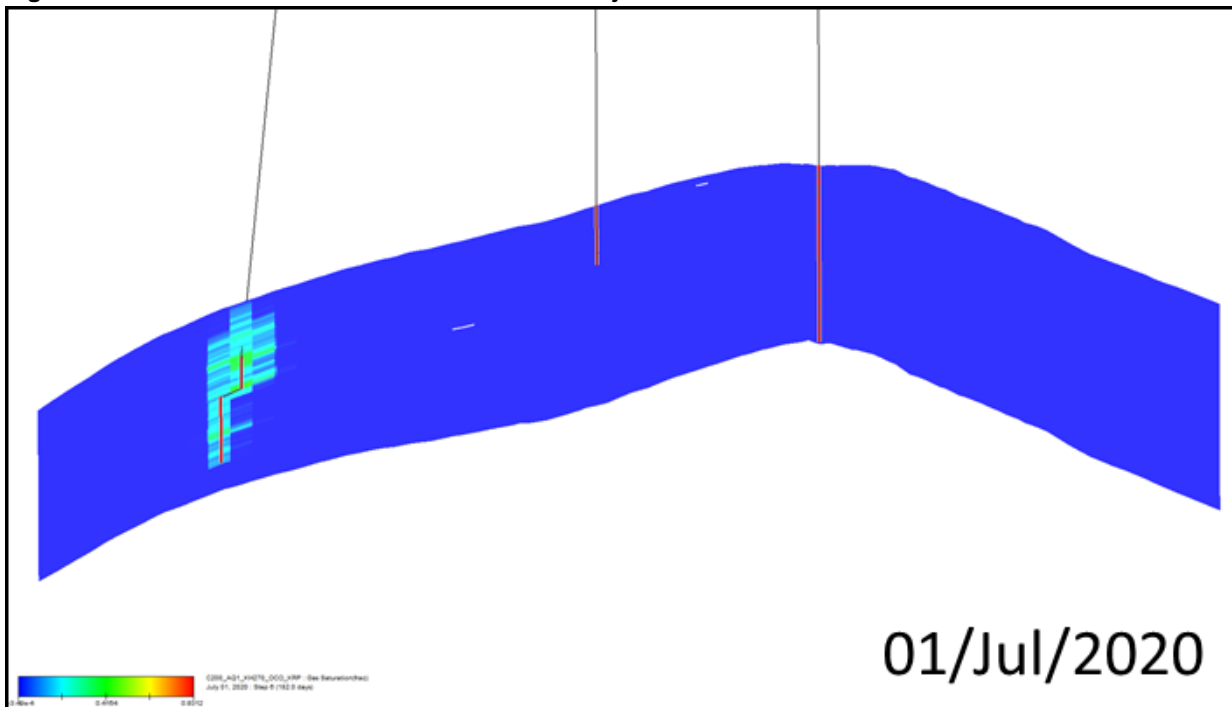


Figure 8.56: CO₂ Distribution after 5 Years of Injection

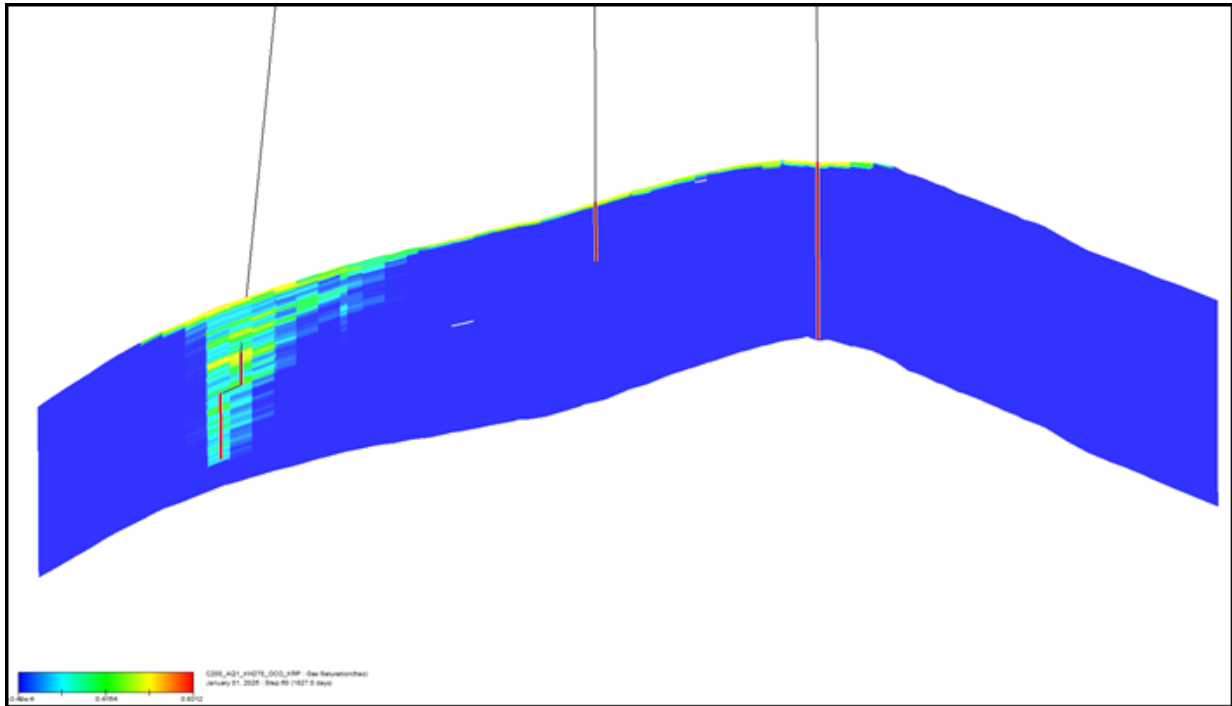


Figure 8.57: CO₂ Distribution after 20 Years of Injection

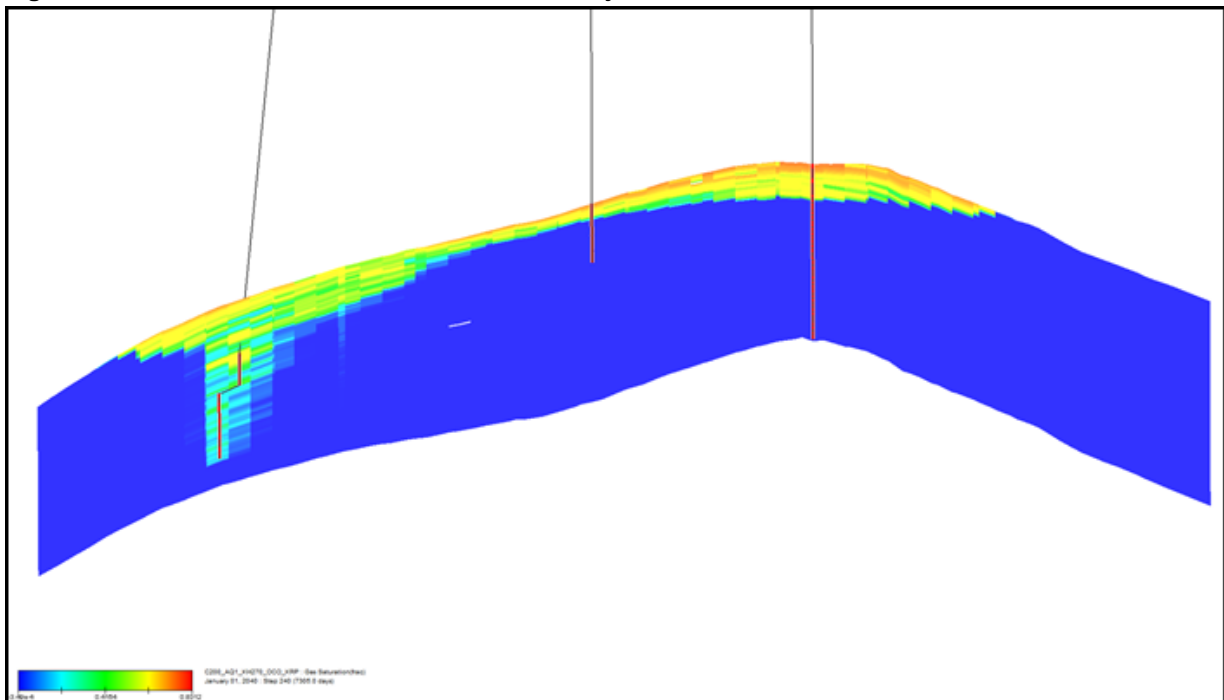
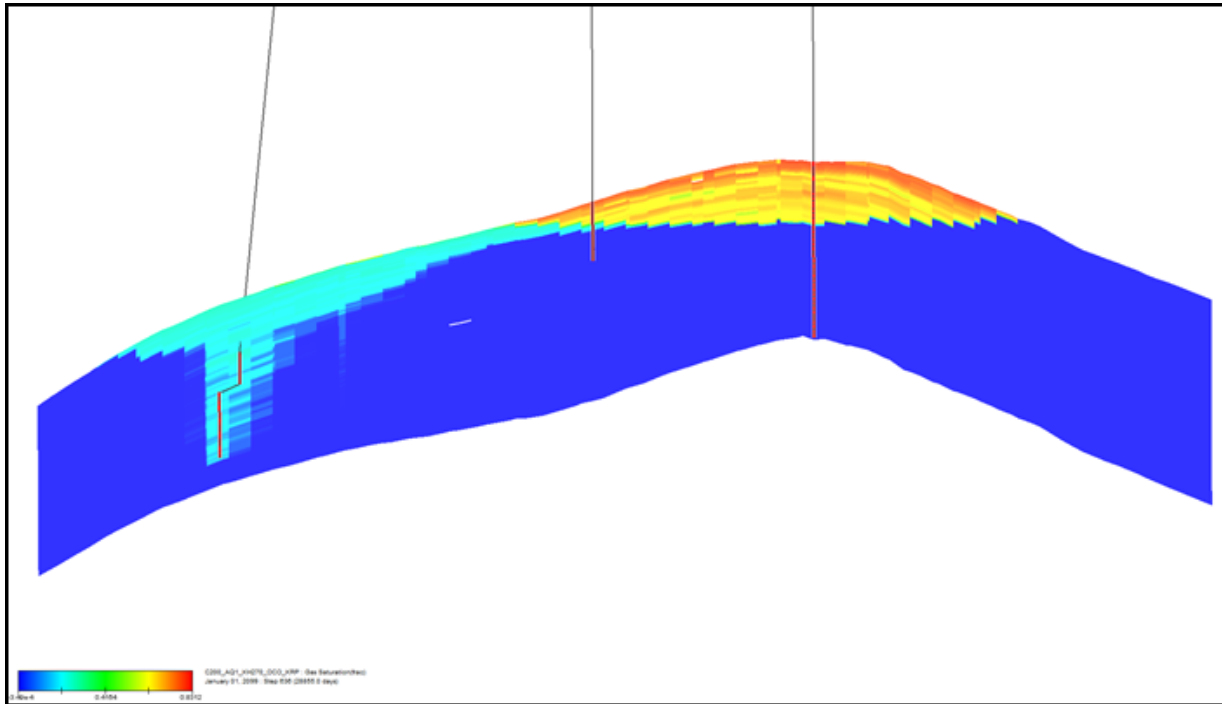
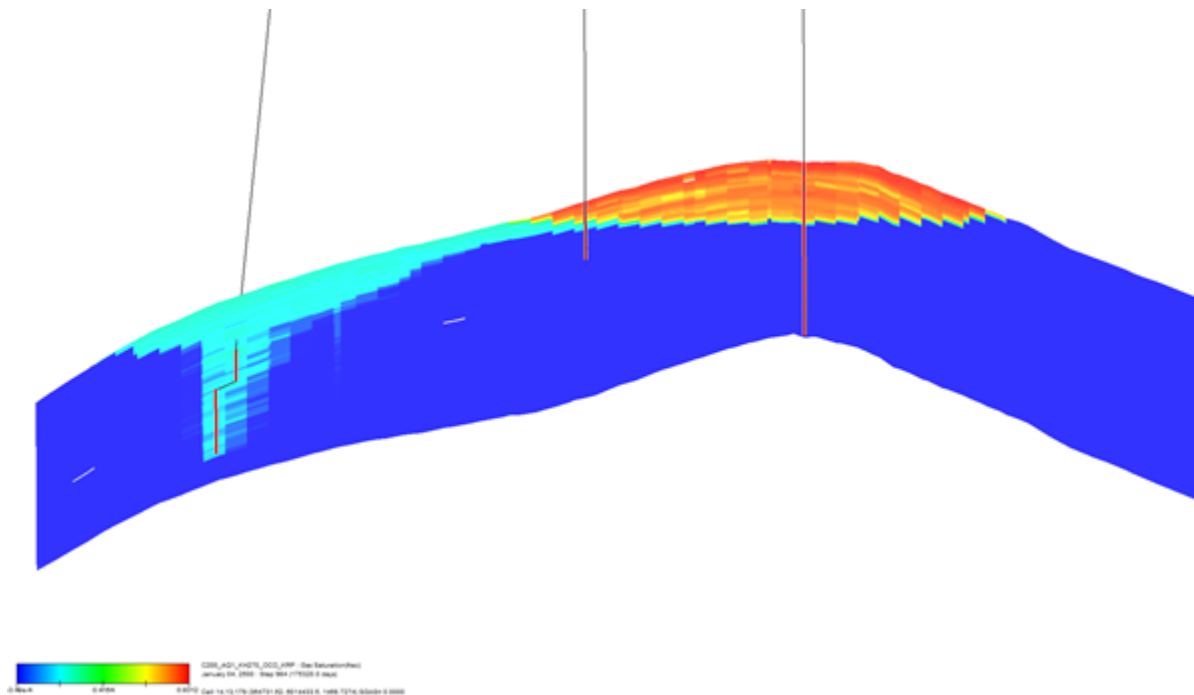


Figure 8.58: CO₂ Distribution after 20 Years of Injection and 60 Years of Shut-In



Even though CO₂ is being injected in the lower half of the Bunter sandstone, it reaches the cap rock in just over 6 months, Figure 8.56. After 5 years, Figure 8.56, the CO₂ cap is starting to become established at the crest of the structure. At the end of injection, Figure 8.57, the area above the DEV1 well shows predominantly green and yellow coloured cells indicating saturations in the range 0.4 to 0.6, i.e. well above the imbibition critical gas saturation $S_{gt} = 0.3$. After shut-in, the mobile CO₂ continues to migrate upward to the cap rock and on to the crest whilst fresh brine imbibes into the area surrounding the well trapping CO₂ at this 0.30 saturation limit as seen in Figure 8.58; the free CO₂ at the crest now approaches its limiting saturation of $S_g = 1 - S_{wc} \approx 0.90$, coloured red in this figure. Running this model onto 01 Jan 2500, 460 years after shut-in, produces the distribution shown in Figure 8.59. Essentially all the CO₂ is now free at the crest or residually trapped elsewhere.

Figure 8.59: CO₂ Distribution after 20 Years of Injection and 460 Years of Shut-In



It is important to remember some of the limitations of this model, namely:

- no CO₂ dissolution in the brine;
- no temperature effects;
- no diffusive flow; and
- no geochemical effects.

Dissolution effects are discussed in Section 8.4 whilst temperature effects are addressed in Section 8.3.17. In particular, diffusion is thought to be the mechanism by which free CO₂ which has pooled at the crest of the structure can dissolve in the underlying fresh brine generating saturated brine which is slightly denser than fresh brine. This density difference (which will be 0.1 to 0.2% in a 250,000 mg/kg brine) can then generate Rayleigh-Taylor instability in which the saturated brine flows down while fresh brine flows up to act as the recipient for additional free CO₂ from the crestal pool. This process in conjunction with long term geochemical reactions between the saturated brine and the rock fabric leading to potential mineralisation of the CO₂ has been suggested by many academic researchers investigating the ultimate fate of the sequestered CO₂. However, all of the experimental research that has been reported has tended to focus on idealised scenarios that use unrepresentative rock matrix and on timescales of days to months rather than thousands of years as is more appropriate for CO₂ sequestration. Whilst modelling and simulation could be used to overcome some of the limitations there is still a great deal of uncertainty as to the accuracy of the results since even the most advanced models are able to account for only a small fraction of the potential geochemical interactions. The approach for investigating the likely dissolution-convection-mineralisation processes as a result of White Rose CO₂ injection into Endurance has been to use 2D sector models to investigate limit cases using proven databases. The results are presented in Section 8.4.

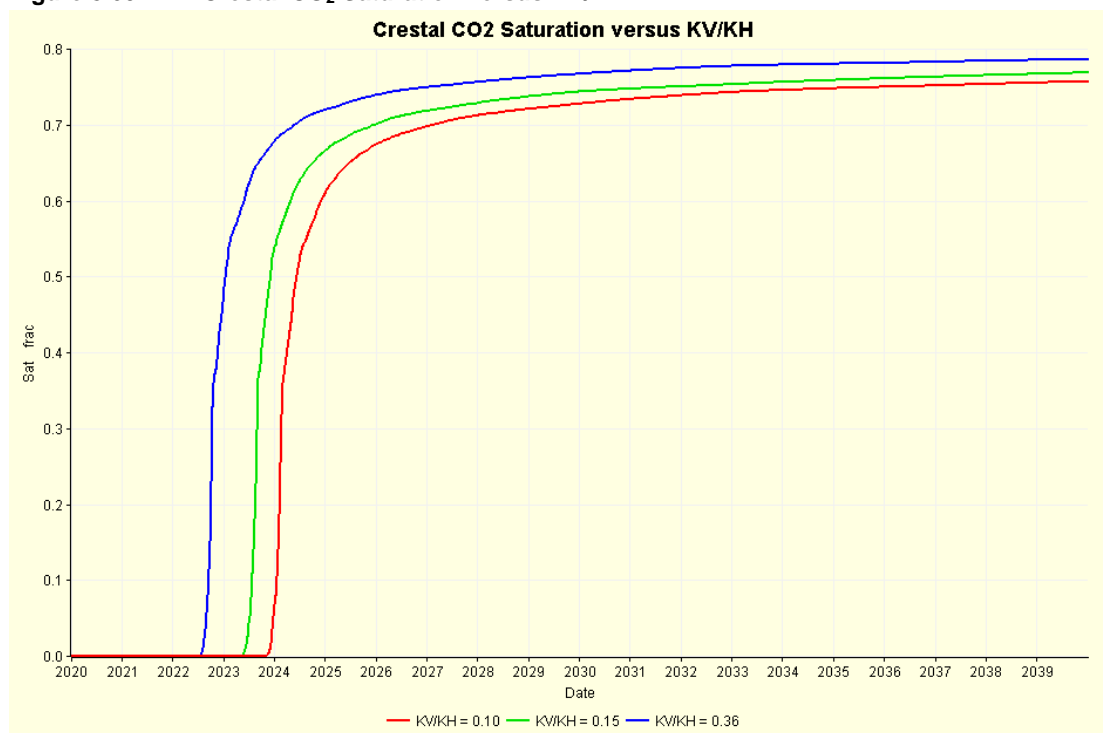
- Vertical/Horizontal Permeability Ratio.

Generally vertical permeability K_V is calculated via a multiplier applied to the horizontal permeability K_H ; the multiplier is the ratio of K_V/K_H . The mid-case value of K_V/K_H has been presented as 0.15 in Section 8.3.2.2; low and high values for K_V/K_H have been derived as 0.10 and 0.36 respectively from vertical interference test (Section 8.1.2.2).

The result of this sensitivity had no material effect on the pressure change measured at the crest of the structure. Varying the ratio did not change the horizontal permeability and it was K_H that was used to calculate well injectivity.

The speed at which the CO_2 plume moves is clearly affected by K_V/K_H as shown in Figure 8.60

Figure 8.60: Crestal CO_2 Saturation versus K_V/K_H



More than doubling the mid-case value from 0.15 to 0.36 does not half the crestal arrival time of the CO_2 but reduced it by around 10 months.

8.3.15.2 Sub-Seismic Baffling

There is no evidence for baffles in any of the three well penetrations nor can faults be seen on seismic within Endurance. This does not preclude the existence of such features being present within the structure.

Therefore, to test the effect of baffles and barriers a simple set of modifications have been employed. First, 1% of the total cells in the intermediate model (representing 7000 cells) were randomly assigned vertical cell-to-cell transmissibility T_z of zero. Cells in the intermediate grid have 200m aerial grid spacing over the core of Endurance. The difference between the case without the barriers and that with the 7000

flow barriers is small, with only a slight delay in the arrival time of the CO₂ at the crest of the structure (Figure 8.61).

Two further cases were constructed where the size and then the orientation of the barrier was changed, the results of which (crestal pressure change and CO₂ saturation) are shown in Figure 8.62. Firstly, the set of 7000 horizontal barriers (as applied through a vertical transmissibility multiplier) studied previously were all extended in size. Rather than being the cross-sectional area of a single grid block (200m by 200 m), the barriers were made three blocks by three blocks, i.e. 600m by 600 m. These values are shown as the pair of blue lines (solid line for CO₂ saturation and dashed line for pressure) in Figure 8.62. The green pair of lines shown on the same figure is for a case where the barriers are vertical in their orientation.

Figure 8.61: Crestal Pressure Change & CO₂ Saturation Without & With Horizontal Barriers

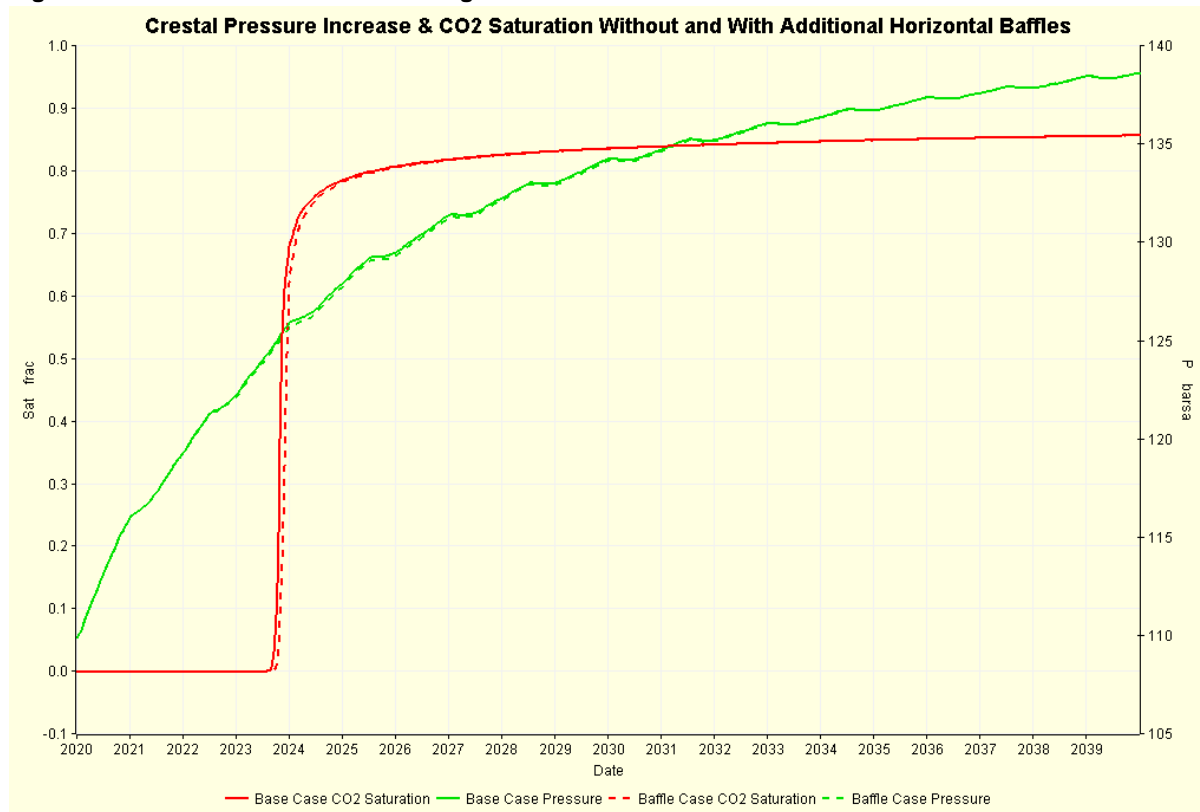
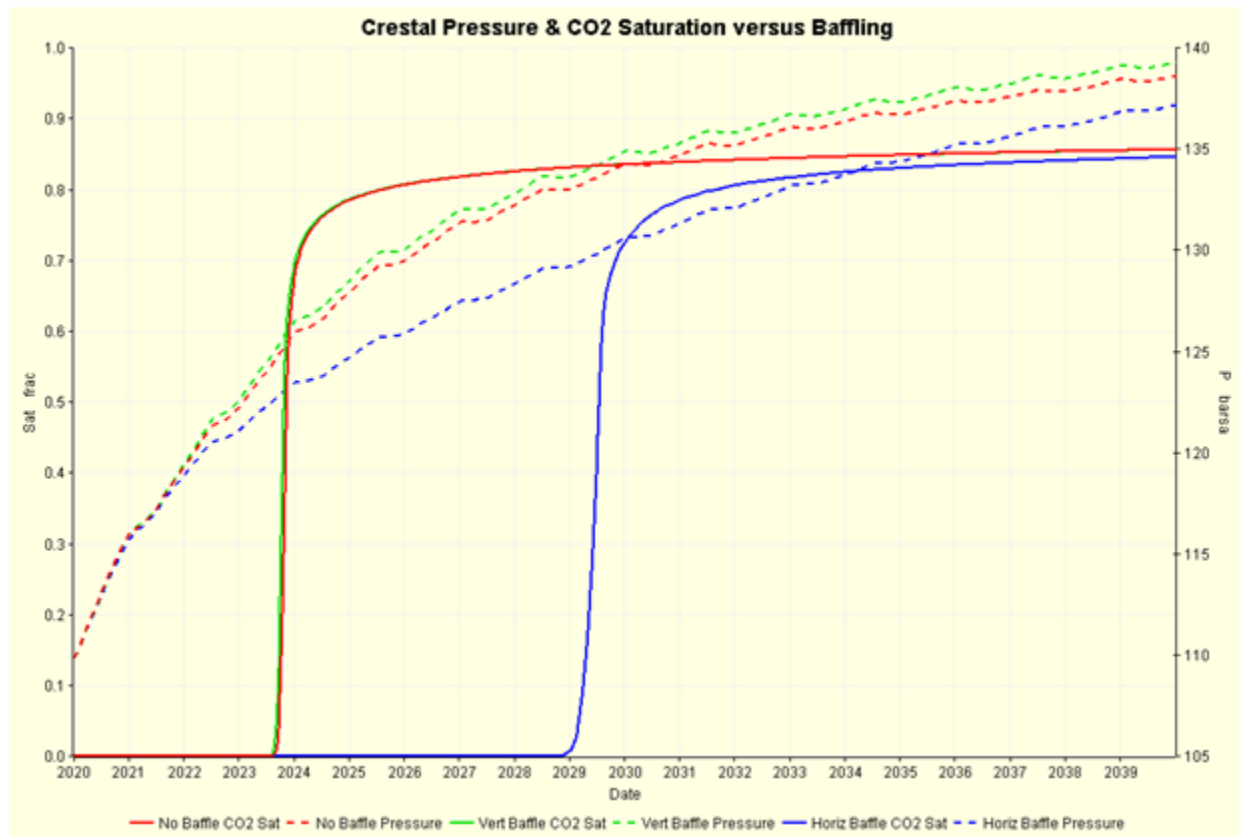


Figure 8.62: Crestal Pressure Change & CO₂ Saturation versus Different Barriers

The vertical barriers are three grid blocks wide, i.e. 600m and five grid blocks high, i.e. 10m. The height is considered to be less than that resolvable on seismic, which is typically 20 m. It is noticeable from Figure 8.62 that the vertical barriers (in green) have little impact on the progress of the CO₂.

The effect of larger horizontal barriers (shown in blue) is much more pronounced (also see Figure 8.63 and Figure 8.64). The arrival time of the CO₂ at the crest has been increased from 3.5 years to over 9.0 years whilst the increase in pressure is also reduced although this difference is gets smaller toward the end of the 20 year injection period.

Figure 8.63: No Baffle CO₂ Cross-Section after 9 years

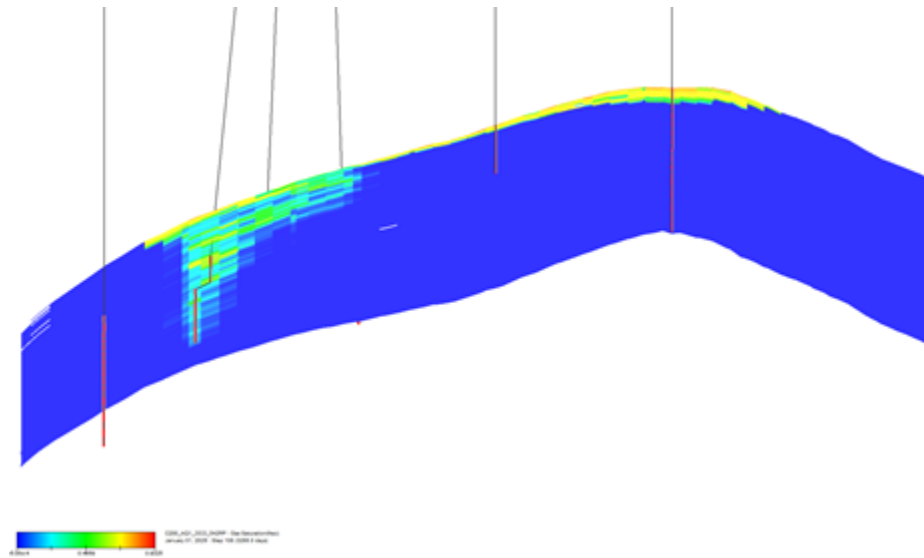
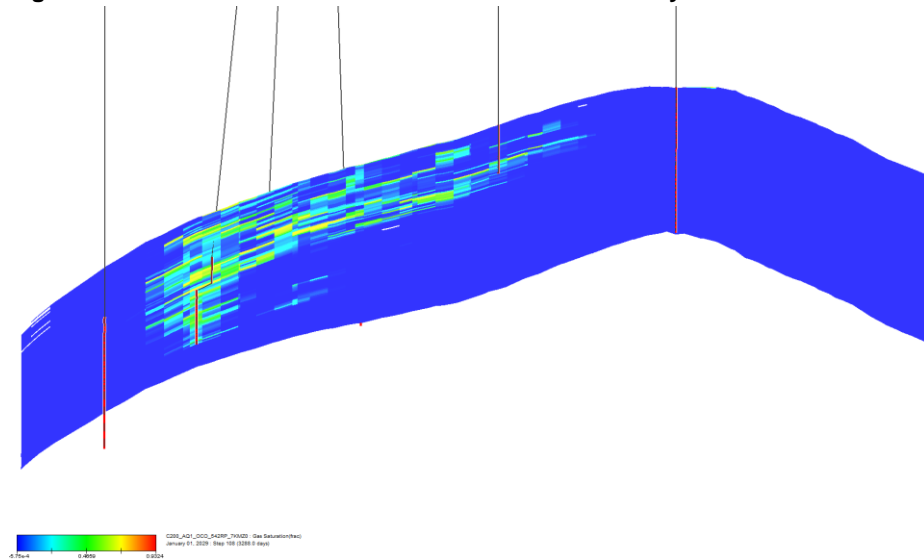


Figure 8.64: Vertical Baffle CO₂ Cross-Section after 9 years



It must be stressed there is little geological evidence for either of the barrier cases presented here, horizontal or vertical; there is evidence for barriers in the Caister Bunter field. That said, most reservoirs are usually found (late in the field life) to be more heterogeneous than first thought.

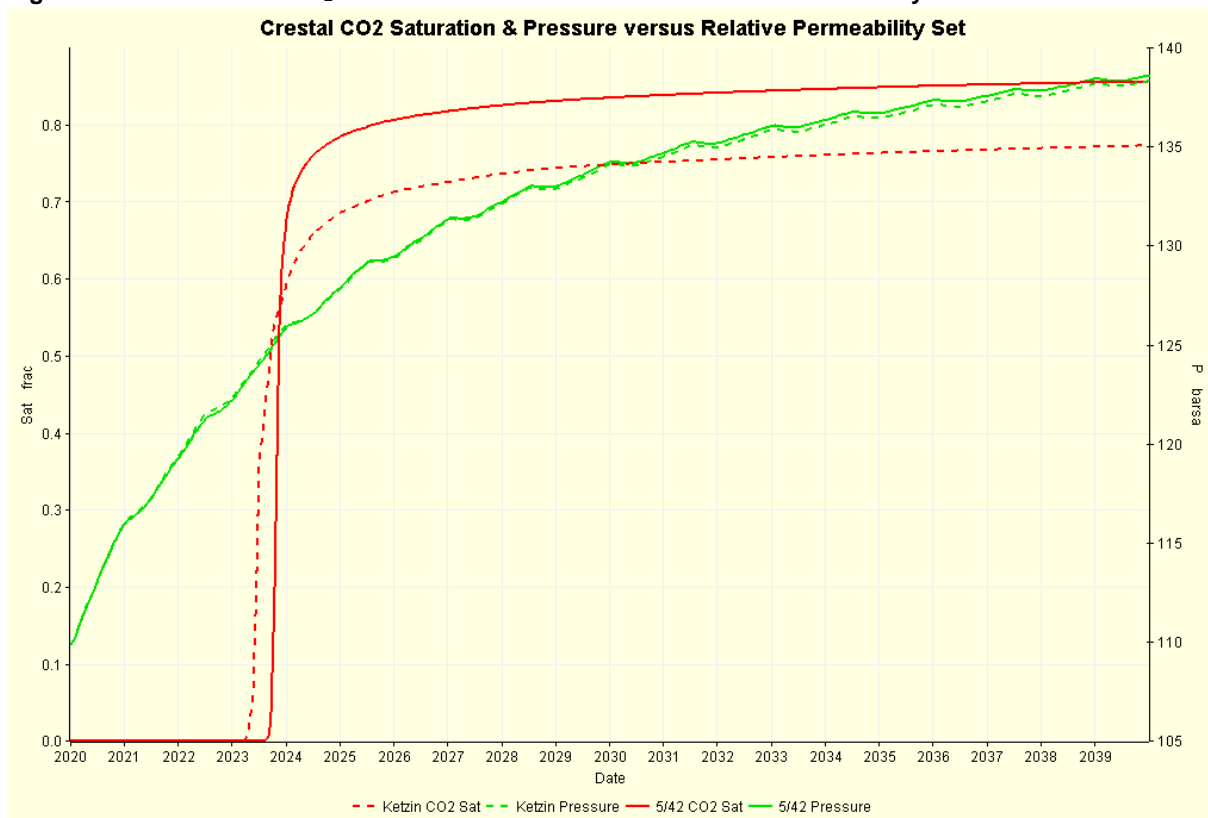
8.3.15.3 Impact of Relative Permeability data on Model Behaviour

The behaviour of the mid-case Ketzin data (dashed lines) is compared with that of the Endurance relative permeability data (solid lines) in Figure 8.65, which shows the CO₂ saturation and pressure at the crest of the structure. The difference in the pressure response was predicted to be minimal. The asymptotic value

of CO₂ saturation was higher for the Endurance data because of the low irreducible water saturation for Endurance at the crest of the structure where the CO₂ is pooling.

One of the interesting results is the delayed arrival of CO₂ at the crest (by 3 months) when using the measured Endurance data set compared to the Ketzin data set. This has been attributed to the CO₂ Corey exponent for the Endurance data ($N_g = 2.5$) being higher than that used in the Ketzin data ($N_g = 1.5$). The Corey exponents control the curvature of the relative permeability curve and comparing Figure 8.39 for the Ketzin data and Figure 4.38 for the Endurance data the CO₂ relative permeability can be observed to be lower for the Endurance data when the CO₂ saturation is less than 50% because of the increased curvature.

Figure 8.65: Crestal CO₂ Saturation & Pressure versus Relative Permeability Set



The CO₂ saturation after 20 years of shut-in (following 20 years of injection) along the WNW-ESE cross-section is shown in Figure 8.66 using the Ketzin data and in Figure 8.67 using the Endurance data; note both figures use the same range of 0.01 to 0.85 hence most cells are greyed-out, i.e. zero CO₂ saturation.

Figure 8.66: CO₂ Saturation Cross-Section after 20 years of Shut-In: Ketzin Rel Perm

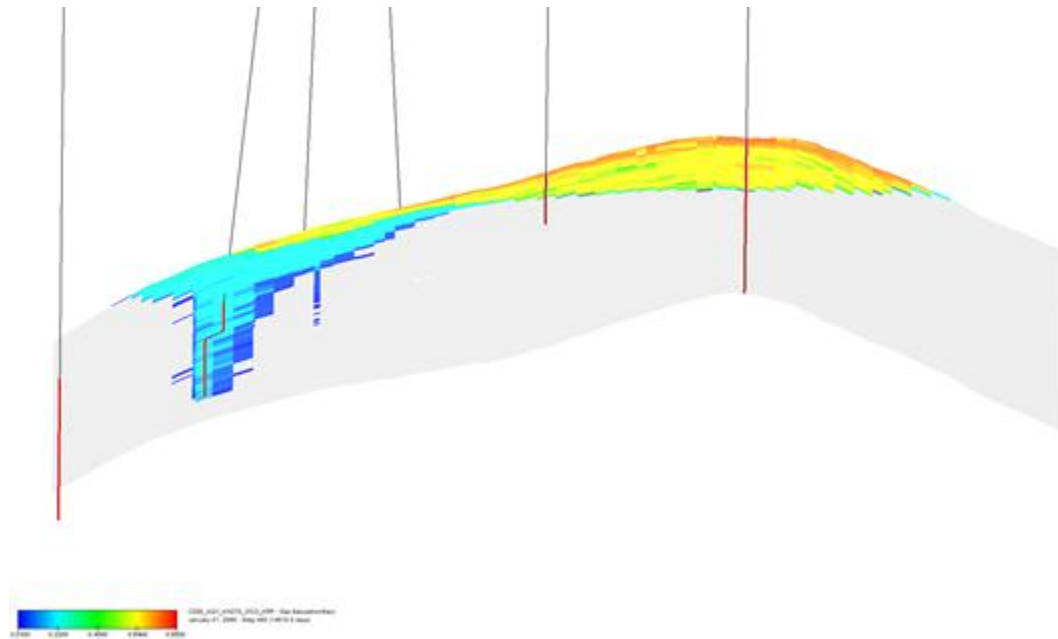
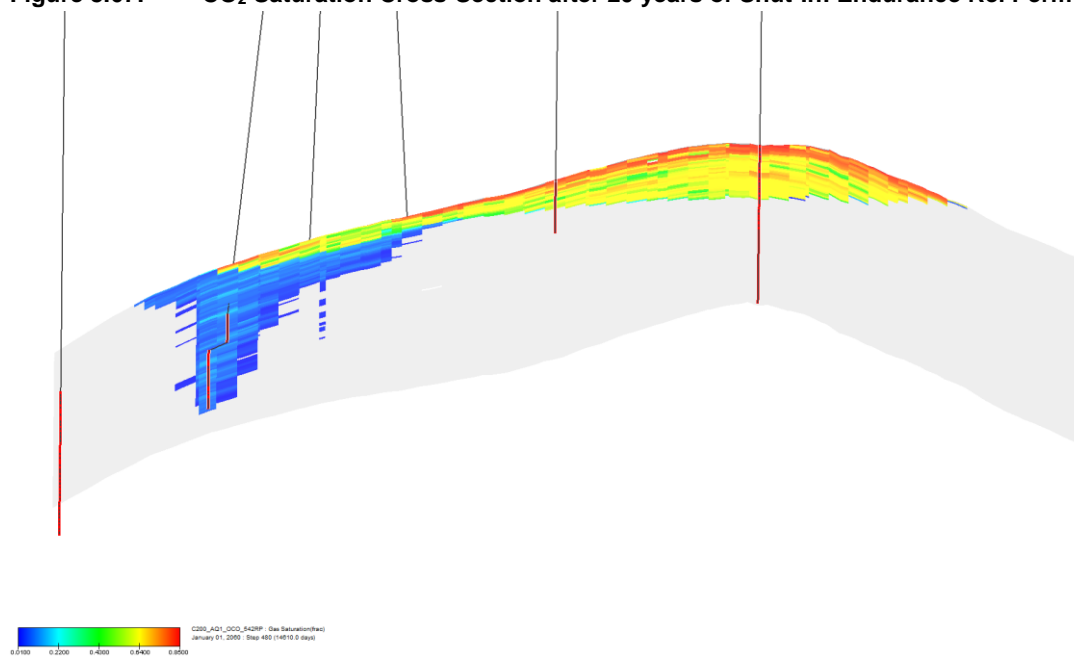


Figure 8.67: CO₂ Saturation Cross-Section after 20 years of Shut-In: Endurance Rel Perm

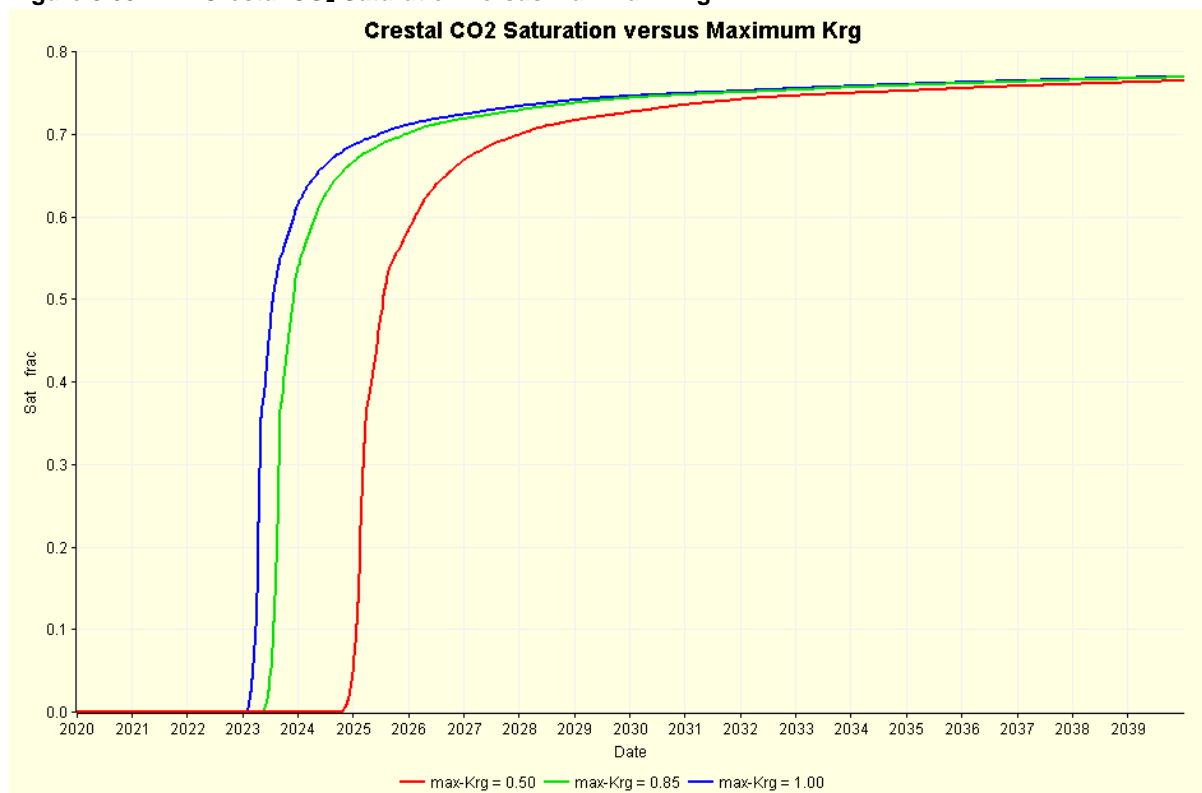


Note the shape of the plume is very similar. What differs of course is the trapped gas saturation which is lower using the Endurance data as shown by the darker blue colours in the vicinity of the injection wells. Whilst there appears to be significant differences between the analogue Ketzin and measured Endurance relative permeability data, in terms of the overall model performance there is little difference between the two.

8.3.15.4 Maximum Gas Relative Permeability

In Figure 8.39 the maximum gas relative permeability is shown as being $K_{rg}^M = 0.85$; this has been taken as the mid-case value. Low and high values have been set to 0.5 and 1.0, respectively, and the resulting crestal CO_2 saturations are shown in Figure 8.68. The effect is as expected and it replicates the changes seen by varying K_H and K_V/K_H .

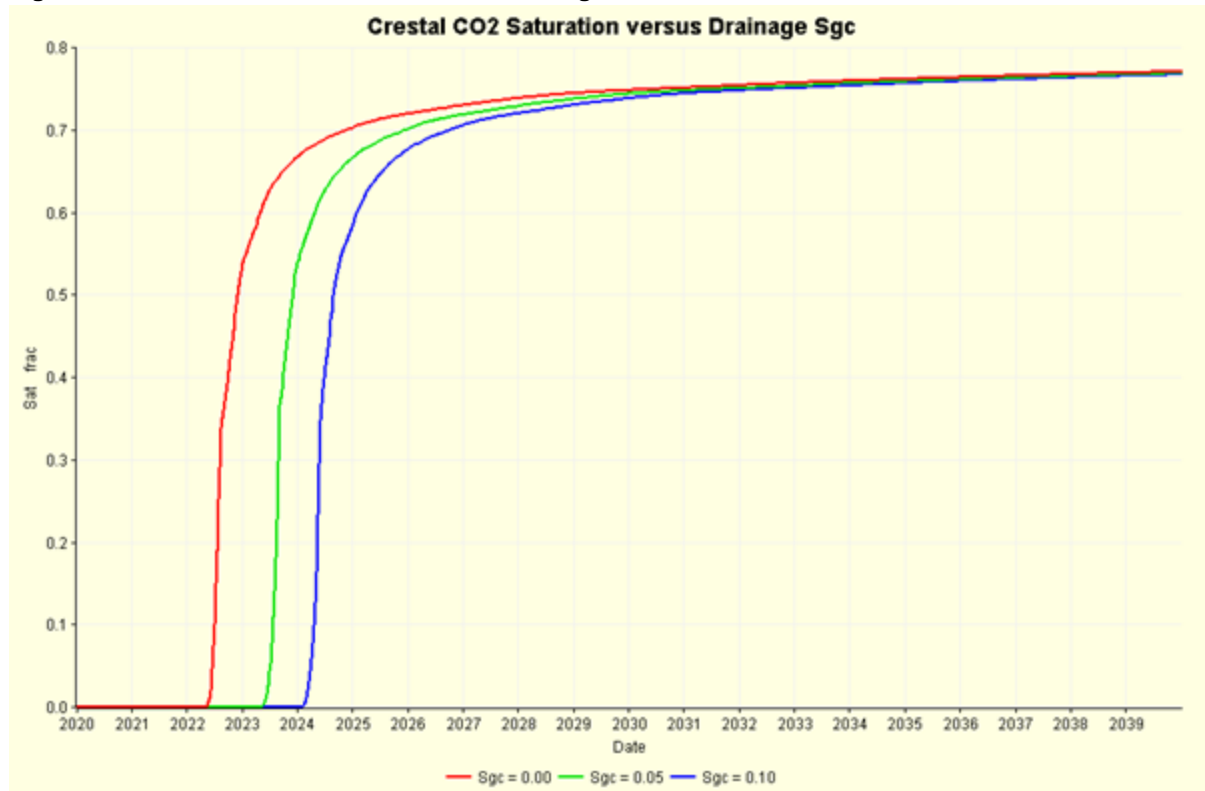
Figure 8.68: Crestal CO_2 Saturation versus Maximum-Krg



There is a change in the maximum pressure increase seen at the crest but the difference between the 0.50 and the 0.85 and 1.00 cases is less than 2.0bar.

8.3.15.5 Drainage Critical Gas Saturation

The default (mid-case) drainage critical gas saturation S_{gc} has been set to 0.05 from Table 8.12. For a low case $S_{gc} = 0.0$ and a high case $S_{gc} = 0.1$. The resulting crestal CO_2 saturation profiles are shown in Figure 8.69. Clearly setting $S_{gc} = 0.0$ means the CO_2 does not have to wait in a grid cell for its saturation to rise before it is free to move onto the next grid cell. This sensitivity has no discernible effect on the maximum pressure increase.

Figure 8.69: Crestal CO₂ Saturation versus Drainage Critical Gas Saturation

8.3.15.6 Imbibition Critical Gas Saturation

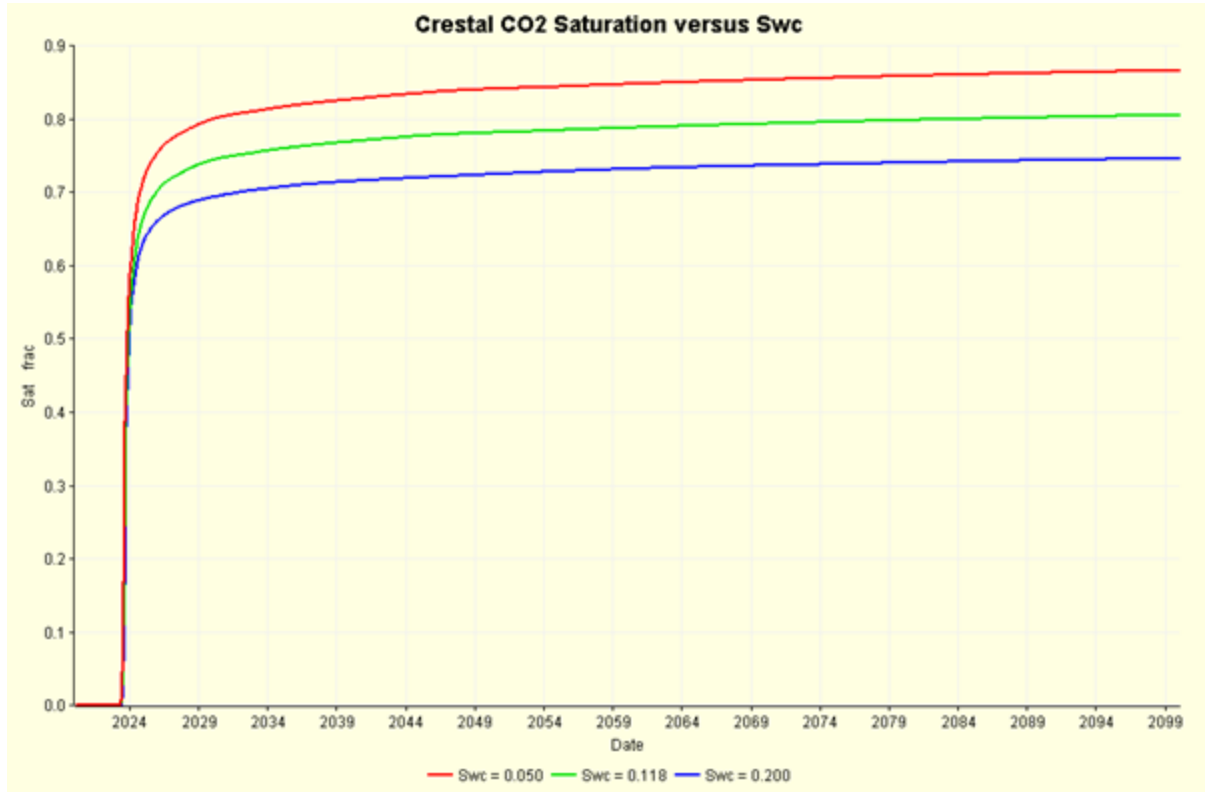
The mid-case value adopted in Table 8.12 has been $S_{gt} = 0.30$; low and high case values were 0.20 and 0.40 respectively. There was no discernible difference in crestal pressure increase or CO₂ arrival time as a result of this sensitivity.

8.3.15.7 Critical Water Saturation

The drainage (and imbibition) critical water saturation S_{wc} quoted in Table 8.12 was 0.15. For sensitivity to critical water saturation the mid-case S_{wc} used was 0.118. Low and high case values of 0.05 and 0.20 were selected and the resulting crestal CO₂ saturation profiles are shown in Figure 8.70.

Varying this parameter does not affect the time at which the CO₂ reaches the crest, rather it changes the maximum saturation $S_g = 1 - S_{wc}$. There is no effect on the pressure change from this sensitivity.

Figure 8.70: Crestal CO₂ Saturation versus Critical Water Saturation



8.3.15.8 Reservoir Location of White Rose CO₂

The downhole (reservoir) volume occupied by the White Rose CO₂ mass of 53.6MT of CO₂ (being 2.68MTPA for 20 years) is predicted to be 84.9x10⁶m³ from the mid case model. Assuming no dissolution or residual trapping and a critical water saturation of $S_{wi} \approx 0.15$, the pore volume required to store this volume is about 100x10⁶m³.

Figure 8.71: WNW-ESE Depth Cross-Section through the core of Endurance

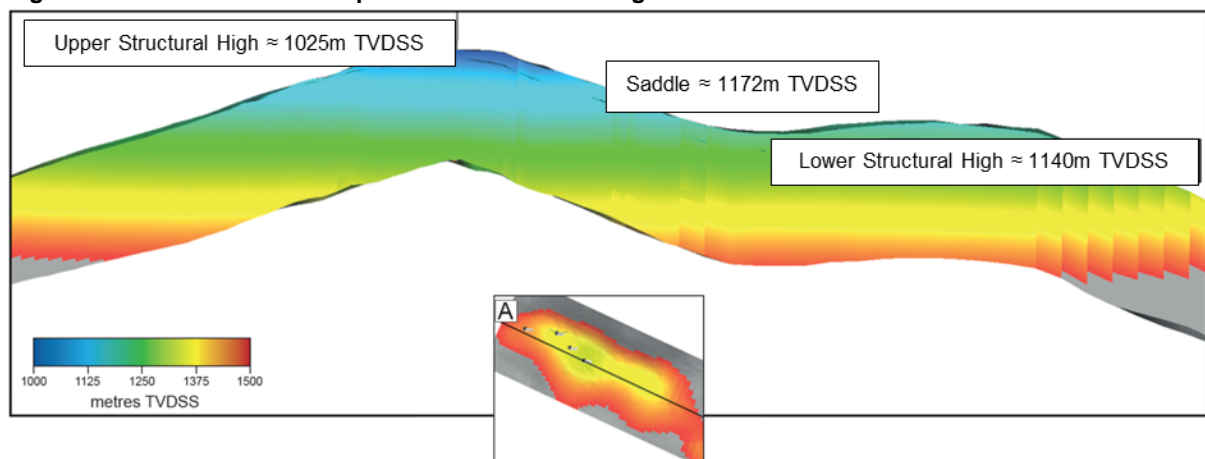


Figure 8.71 shows a cross-sectional depth display along the spine of Endurance. Note the depth of the upper peak (corresponding to the location of the 43/21-1 exploration well), the depth of the lower peak and the saddle between them. The pore volume contained in the upper peak to the spill at the saddle depth of 1172m TVDSS is $362 \times 10^6 \text{ m}^3$, i.e. 3.6x larger than the White Rose volume. So, consideration is given here to whether there is any way CO_2 can get to any part of Endurance other than the upper peak given the current injection locations to the NW of the structure.

It is pertinent here to consider Darcy's Law applied in the vertical direction:

$$v_z = \frac{K_V K_{rC}}{\mu_C} \frac{dP}{dZ}$$

Equation 8.11

Here the effect of capillary pressure and gravity head has been ignored, v_z is the vertical velocity (in m/s), K_V is the vertical permeability (in m^2), K_{rC} is the CO_2 relative permeability, μ_C is the CO_2 viscosity and dP/dZ is the vertical pressure gradient.

The pressure gradient is driven by the density difference between the native brine of $\rho_B \approx 1170 \text{ kg/m}^3$ and the CO_2 density in the reservoir which varies between $600 \leq \rho_C \leq 800 \text{ kg/m}^3$; a mid-case density of $\rho_C \approx 700 \text{ kg/m}^3$ is assumed here to give a density gradient of $dP/dZ \approx (\rho_B - \rho_C) \cdot g = (1170 - 700) (9.81) = 4610 \text{ Pa/m}$ (0.0461bar/m).

The average vertical permeability can be estimated from $K_V = K_H (K_V/K_H) = (271) (0.15) (10^{-15}) = 41 \times 10^{-15} \text{ m}^2$, where $K_V/K_H \approx 0.15$, $K_H \approx 271 \text{ mD}$, and $1 \text{ mD} \approx 1 \times 10^{-15} \text{ m}^2$. At typical reservoir conditions the CO_2 viscosity $\mu_C \approx 0.06 \times 10^{-3} \text{ Pa.s}$.

The vertical velocity of CO_2 can then be estimated to be $v_z = 3.15 \times 10^{-6} K_{rC} \text{ m/s}$, where K_{rC} is the maximum CO_2 relative permeability which when set to 0.85 gives $v_z = 2.68 \times 10^{-6} \text{ m/s}$. The injection rate of 2.68MTPA is equivalent to a reservoir conditions volumetric rate of 11,500 m^3/d or $Q = 0.133 \text{ m}^3/\text{s}$. Therefore the horizontal velocity will be $v_H = Q/(2\pi RH)$ where R is the radial distance from the well where the velocity is being calculated and H is the perforated length through which the fluid is being injected. With the injection wells being deviated 60° from the vertical, the perforated length in the reservoir is about 250m so that $v_H \approx Q/(1500 R) = 90 \times 10^{-6}/R \text{ m/s}$. Therefore, at around 30m from the injection wellbore the (near-constant) vertical velocity will always exceed the falling horizontal velocity so even if one or more of the wells intersected an extremely high permeability streak, the CO_2 cannot avoid its ultimate fate of pooling under the upper peak. A further reinforcing consideration is that the injection rate of 2.68MTPA is a maximum value (of flow from the power station) unlikely to be reached in practice for any extended period of time.

8.3.16 Injectivity

One of the key objectives of the flow test performed on 42/25d-3 appraisal well was to assess injectivity. The test (summarised in Section 8.1.2.1) demonstrate that injection at the specified rates would be possible over the perforated interval although the large pressure spike observed about 1200 s after the start of injection give cause for caution. The timing is significant as it corresponds to the time required for the sea-water from the surface to reach the perforations (at $795 \text{ m}^3/\text{d}$) given the Internal Diameter (ID) of the well tubing.

The pressure spike is thought to have been caused by some contamination carried with the injected sea water. The pressure spiked until a fracture was created and as the injection test continued, and the rate was increased in two further increments, the effect of the blockage was gradually reduced. There is a possibility that the blockage was caused by an interaction between the native brine and the sea-water or as a temperature effect.

8.3.16.1 CO₂ Injection Wells Injectivity

To maximise the opportunity for residual trapping as well as keep colder CO₂ away from the cap rock it is proposed to perforate the lower half of the three injection wells drilled from the P5 platform location. One downside of the lower half perforation strategy is the quality of the BSF degrades with depth so that while porosity at the top of the Bunter often exceeds 0.25, at the bottom of the Bunter it can be less than 0.15, with consequent effect on permeability via Equation 8.4. This has been investigated using the simplified injection model developed in Section 8.3.15.1.

Equation 8.12 $Q = I_i \Delta P$

In Equation 8.12 ΔP is the (depth corrected) pressure difference between the BHP and (average) reservoir pressure into which the (total) rate Q is being injected and I_i is the Injectivity Index.

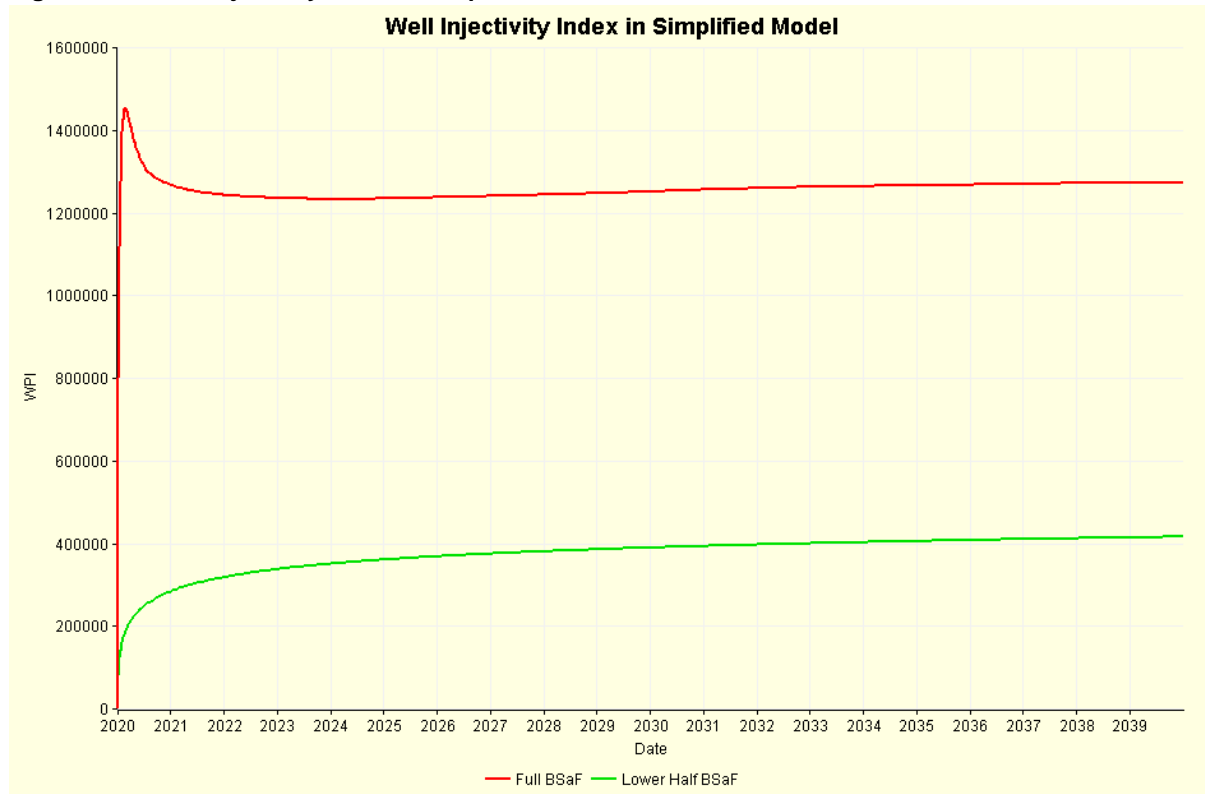
To assess injectivity two simulations were performed with one having the well shown in Figure 8.64 perforated through the whole of the Bunter sandstone and the other having the well just in the lower half. The resulting well Injectivity Index for the two cases is shown in Figure 8.72.

The units for I_i in Figure 8.72 are m³/day/bar which E100 does not append to the outputted property. After the transient (pressure and saturation) changes have declined, the pseudo-steady-state I_i is over three times lower for the case where the whole well has been perforated.

The variation of BHP however needs to be considered in conjunction with the differences in Injectivity Index. In Figure 8.73 the BHP variations for the three CO₂ injection wells are shown for the mid-case model. Note the cyclic nature of the wells which are injecting half the total rate of 2.68MTPA for 12 months out of every 18 months (see Section 8.3.13.3 for summary of well switching scheme).

The transient spike in BHP at the start of each well's 12-months of injection is a relative permeability effect. In the grid cells containing the well completions, the CO₂ saturation and hence the CO₂ relative permeability is low initially. This in turn means the mobility is small and a high pressure difference is required to achieve the desired flow rate. The transient spike is almost the same on the first injection cycle for all three wells. All the wells see an increase in the transient pressure on the second cycle of injection. Thereafter the transient pressure for P5DEV2 is greater than P5DEV3 which is greater than P5DEV1.

Figure 8.72: Well Injectivity Index in Simplified Model



The jump in the transient pressure spike between the first and second cycles of injection was because in the six months period that the well is shut-in, the buoyant CO₂ migrates up-structure and fresh brine imbibes into the vicinity of the shut-in well, trapping CO₂ at a saturation of about $S_{gt} = 0.30$. When CO₂ injection resumes, a new drainage (of the brine) phase begins but with a lower effective CO₂ relative permeability and hence the need for a larger BHP to achieve the required flow rate. After the third and fourth cycles the pattern settles down. Note that the Ketzin Kr data (Figure 8.39) which incorporates the extreme limit of S_{gt} was used for this simulation. In contrast the measured Endurance Kr data (Figure 4.38) has in contrast $S_{gt} \sim 0.10$ which would likely cause a smaller change in CO₂ mobility after fresh brine imbibition and hence reduce the pressure spikes predicted in Figure 8.72.

The differences between the BHP responses of the three wells are due to their relative locations and the way in which CO₂ and brine move during the 12-month injection period and 6-month shut-in period of each well. CO₂ injected in P5DEV1 and P5DEV3 migrates upward in the plane of the wells before heading toward the crest, thereby leaving higher CO₂ saturation behind, whereas the CO₂ injected in P5DEV2 move tangentially away from this well's trajectory toward the crest (Figure 8.72 and Figure 8.75).

Figure 8.73: BHP Variations from Mid-Case Model

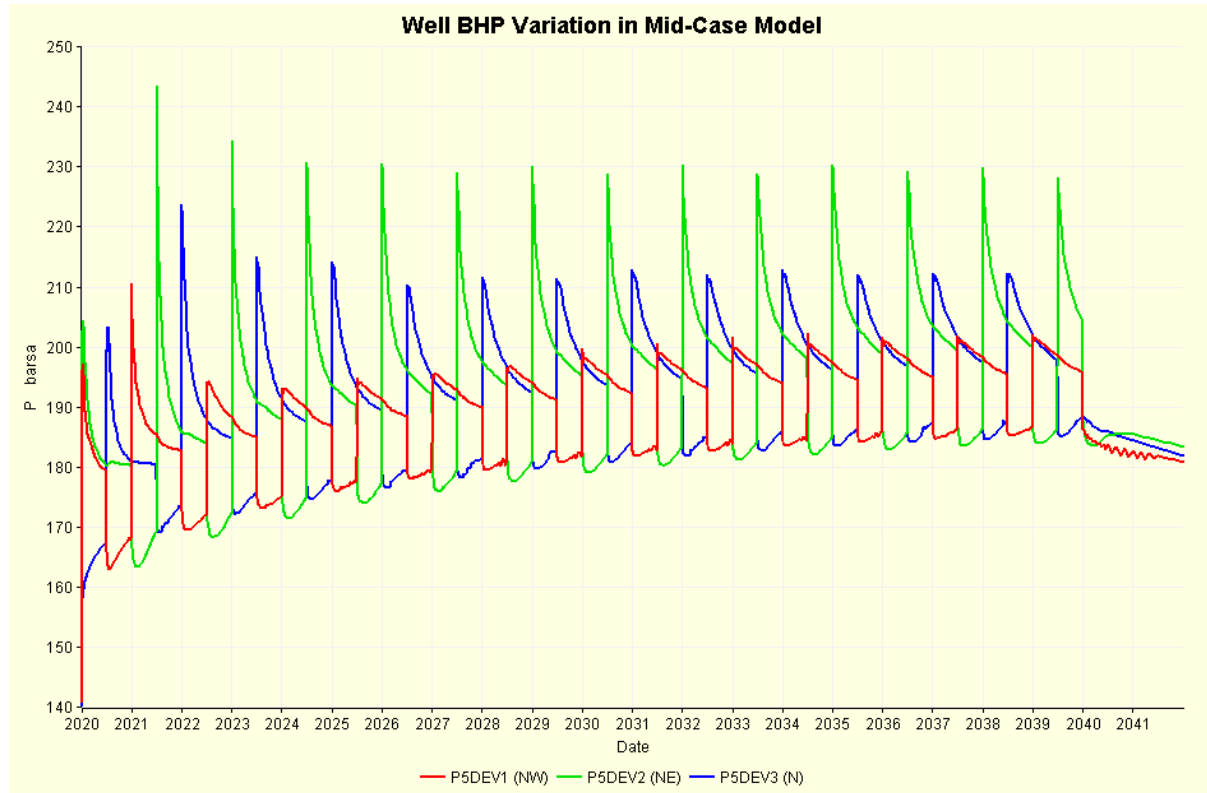
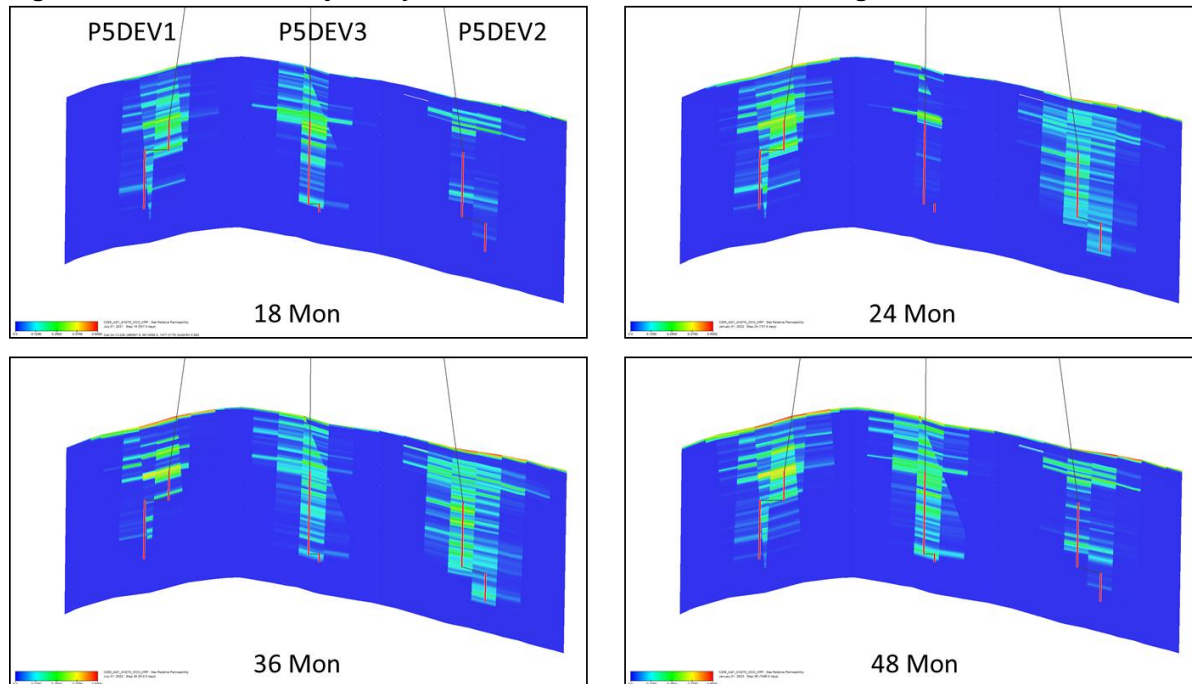


Figure 8.74: Line of Cross-Section through Injection Wells



Figure 8.75: CO₂ Relative injectivity shown on Cross-Section Defined in Figure 8.74



8.3.16.2 Skin Factor

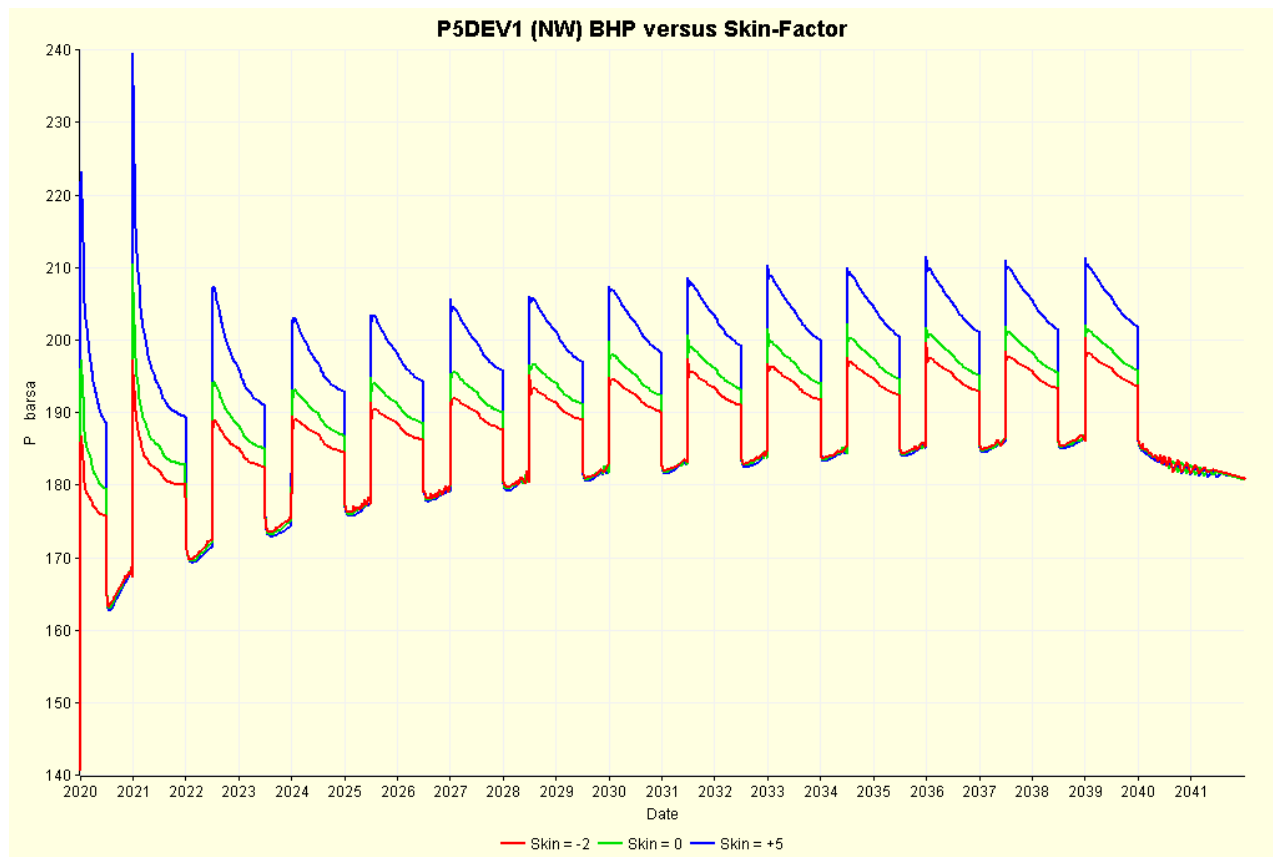
The default skin applied to all the wells is zero. There is a case to suggest that the skin in the actual wells could be negative as a result of thermal fracturing caused by relatively cold CO₂ cooling the rock in the near wellbore – note that the perforation strategy will prevent any thermal fracturing near the Röt Clay caprock by confining perforations to the deeper zones of the Bunter formation. Alternatively, positive skin may result due to mechanical blockage as was seen in the injection phase of the 42/25d-3 well test. For the purposes of understanding the range of possible effects a beneficial case has been simulated using a skin of $S = -2$ applied to all perforations whereas a detrimental case has been simulated using $S = +5$; the mid-case being $S = 0$.

There is no effect of changes in skin (of the range of magnitudes investigated) in terms of the crestal pressure increase or the time taken for the CO₂ to reach the crest of the structure. Skin clearly has an effect on well BHP and the difference is shown in Figure 8.76 for the P5DEV1 only. The other two wells show a similar response.

The beneficial effect of the negative skin (red line) is relatively modest but again it must be stressed the value of $S = -2$ has been assessed based on experience of realistic negative skins rather than detailed modelling.

The detrimental effect of the positive skin (blue line) is potentially of more concern as the assessed value of $S = +5$ is not considered particularly high and yet the second cycle transient response is close to the maximum pressure that would be tolerated to avoid hydraulic fracturing.

Figure 8.76: P5DEV1 BHP versus Skin-Factor



8.3.17 Temperature Effects

The simplified injection model was used to examine how temperature profiles within Endurance might change as a result of injection of cold CO₂.

The CO₂ will be transported to Endurance via a 90 km 24" pipeline and so will cool to the seabed temperature which will vary between 5°C and 15°C winter to summer. Using the steady-state Prosper modelling, it is estimated that the CO₂ will heat by about 10°C between wellhead and the perforations meaning the lowest sandface temperature is estimated to be 15°C compared with a reservoir temperature of about 55°C see Figure 4.58 (the specified CO₂ injection wells are up-structure of 42/25d-3).

Two cases of the simplified injection model have been considered here. The first considers the whole Bunter interval is perforated so see the effect of putting cold CO₂ against the cap rock, see Figure 8.77. The second case is thought to be more likely as only the lower half of the well has been perforated, see Figure 8.78.

Figure 8.77: Temperature Cross-Section after 20 years, All Bunter Perforated

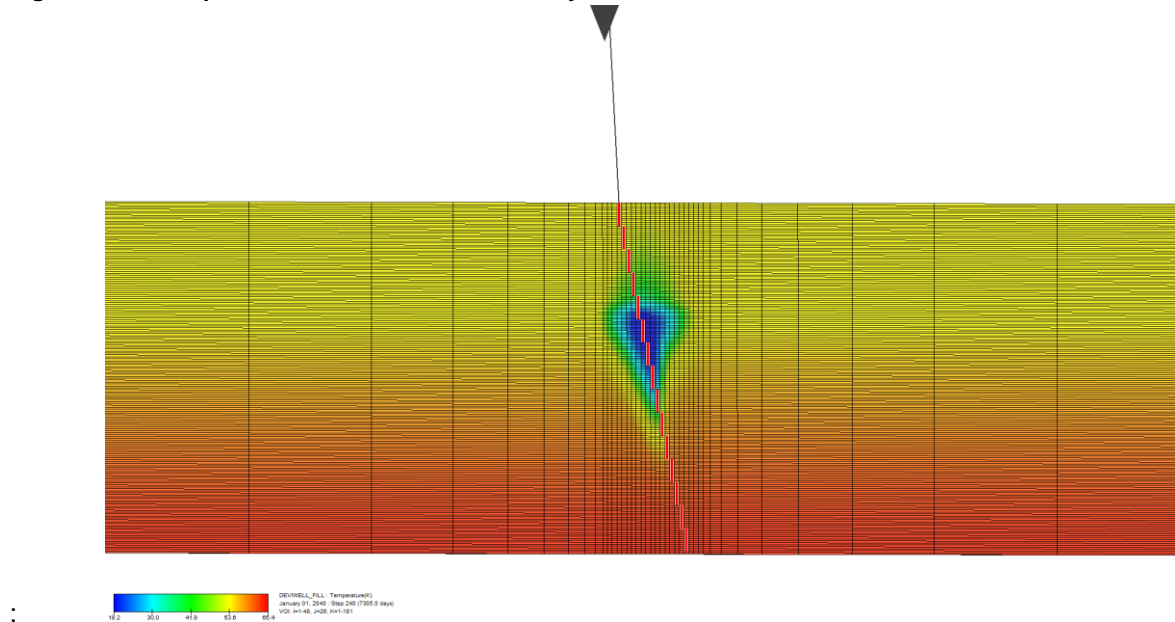
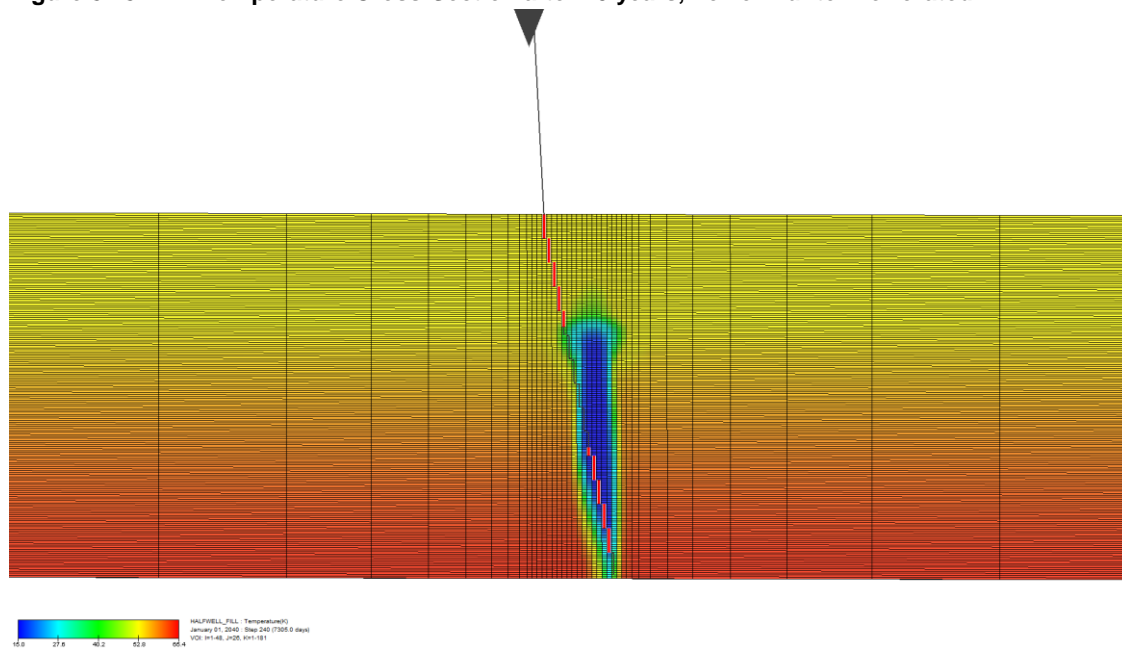


Figure 8.78: Temperature Cross-Section after 20 years, Lower Bunter Perforated



The convective cooling effect of placing cold CO₂ against the cap rock is felt immediately if the top of Bunter sandstone is perforated as is seen in Figure 8.77. This should be compared with the gradual cooling that would be achieved by injecting deeper in the Bunter sandstone. With reference to the detailed simulation models it is noted that the CO₂ takes between 6 to 12 months to flow from top perforation to the cap rock. Therefore the 20 year profile shown in Figure 8.78 would take many months to develop in practice.

8.4 Simulation of the Diffusion-Dissolution-Convection (DDC) process

To recap, the four main CO₂ trapping mechanisms during CO₂ sequestration are described in more detail in Section 10.2.5, are recognised as:

1. mineral trapping, in which the dissolved CO₂ reacts with the brine and the host rock to produce solid minerals;
2. structural trapping, in which CO₂ accumulates beneath an impermeable caprock;
3. residual trapping, in which part of the migrating CO₂ plume gets detached and ultimately trapped by capillary forces; and
4. solubility trapping, in which both structurally and residually trapped CO₂ dissolves in the brine via diffusion and convective processes. This process is characterised below.

The full field simulation approach used in the prediction of CO₂ plume development, specifically the use of analytical aquifer models, does not permit direct modelling of the dissolution of CO₂ in brine under dynamic flow conditions. An alternative scheme that uses a 2D XZ sector model of Endurance has therefore been used to quantify solubility trapping and thereby gain a better insight into the long term fate of White Rose CO₂.

8.4.1 DDC Process Overview and Simulation Model Set Up

CO₂ dissolution in brine occurs by molecular diffusion across the CO₂-brine interface and this process would take place wherever a CO₂-brine interface exists i.e. both CO₂ trapped by capillary forces and CO₂ trapped under the cap rock will undergo dissolution over time. Since the Endurance relative permeability measurement suggests that less than 10 % of White Rose CO₂ is likely to be trapped in residual form, the DDC modelling has focused on dissolution of the CO₂ cap at the crest of the Endurance structure.

Dissolution of CO₂ increases the brine density (by approximately 2.5kg/m³), creating a denser brine layer below the plume. This layer eventually becomes gravitationally unstable so that fingers of dense CO₂-rich brine propagate downward and transport the aqueous CO₂ away from the interface. This density-driven convection increases the rate of mass transport from the free CO₂ phase into the brine phase and is typically orders of magnitude faster than pure diffusion.

The E100 black oil simulator with the diffusion option has been used for modelling the DDC process. The grid is a 2D XZ sector model of Endurance, 2500m × 200m across and consisting of 100, 000 cells (Figure 8.79). The central portion (500 m) of the model is assumed to capture the extent of the CO₂ plume predicted by the full field model (Figure 8.79a). The left and right hand sides are for the reservoir section outside the CO₂ plume footprint area. The simulation model is given a dip angle of 2.3° by varying the depth of cells on the left and right hand sides at the top layer as shown in Figure 8.79. The key parameters for this model are:

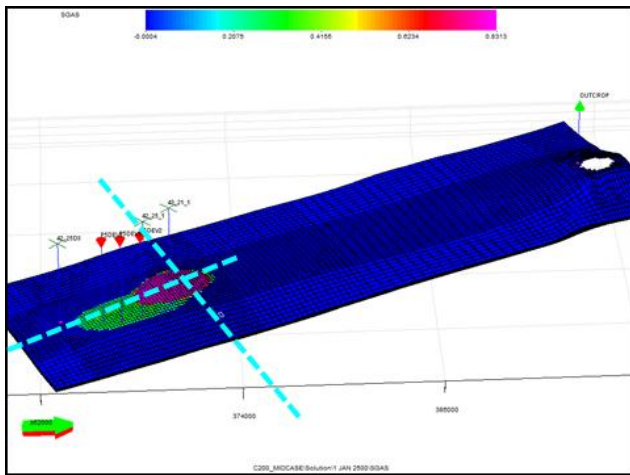
- Cell number (N_x, N_y, N_z) = (500, 1, 200);
- ΔX = 5m;
- ΔY = 3000m; and
- ΔZ = 1m.

The top layer of the model is used to represent the CO₂ plume in the crest of the reservoir structure at a depth of 1299m TVDSS. Using a pore volume multiplier of 20, the top layer has a free CO₂ initially in place

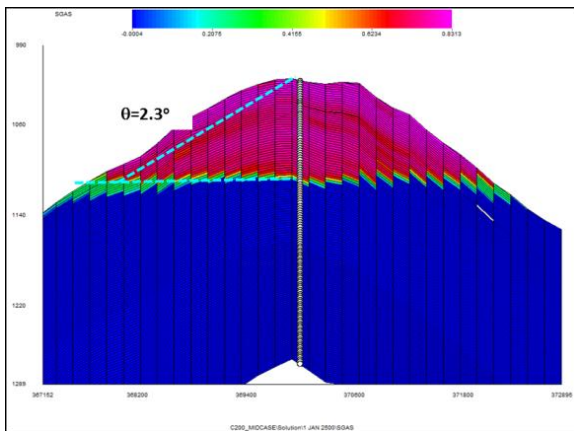
of 2.24 billion sm^3 , which is about a tenth of the CO_2 at the crest of Endurance at the end of injection. The 2D sector model is therefore considered scalable to the CO_2 storage in Endurance.

Porosity and permeability were distributed across the model in the manner described in Section 8.3.2.2. Firstly porosity was defined as a linear function of depth with a value of 0.27 at the top and 0.14 at the base. Then horizontal permeability was defined from Equation 8.4 with an approximate value of 2020mD at the top and 19mD at the base of the model. Additionally, a small random variation in permeability is also applied to initiate the development of the dense brine fingers as described in . Fluid and rock properties pertinent to the simulation are listed in Table 8.17. The PVT inputs (viscosity, solubility, etc.) are generated based on the correlations found in the technical literature.

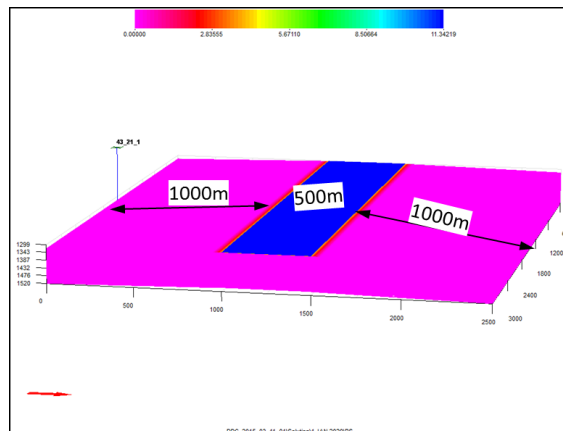
Figure 8.79: Construction of the DDC model



(a) Full Field Model



(b) 2D Slice, X-Direction



(c) Full DDC model

Table 8.17: Critical Parameters of DDC Using Typical Bunter Properties

Attribute	Value	Unit
Temperature	56	°C
Reservoir pressure	141	bar
Salinity	250, 0000	Mg/kg
Viscosity	9.0×10^{-4}	Pa.s (kg/s/m) 0.9 cP
Diffusion coefficient	2.0×10^{-9}	m ² /s
K _v /K _H	0.15	

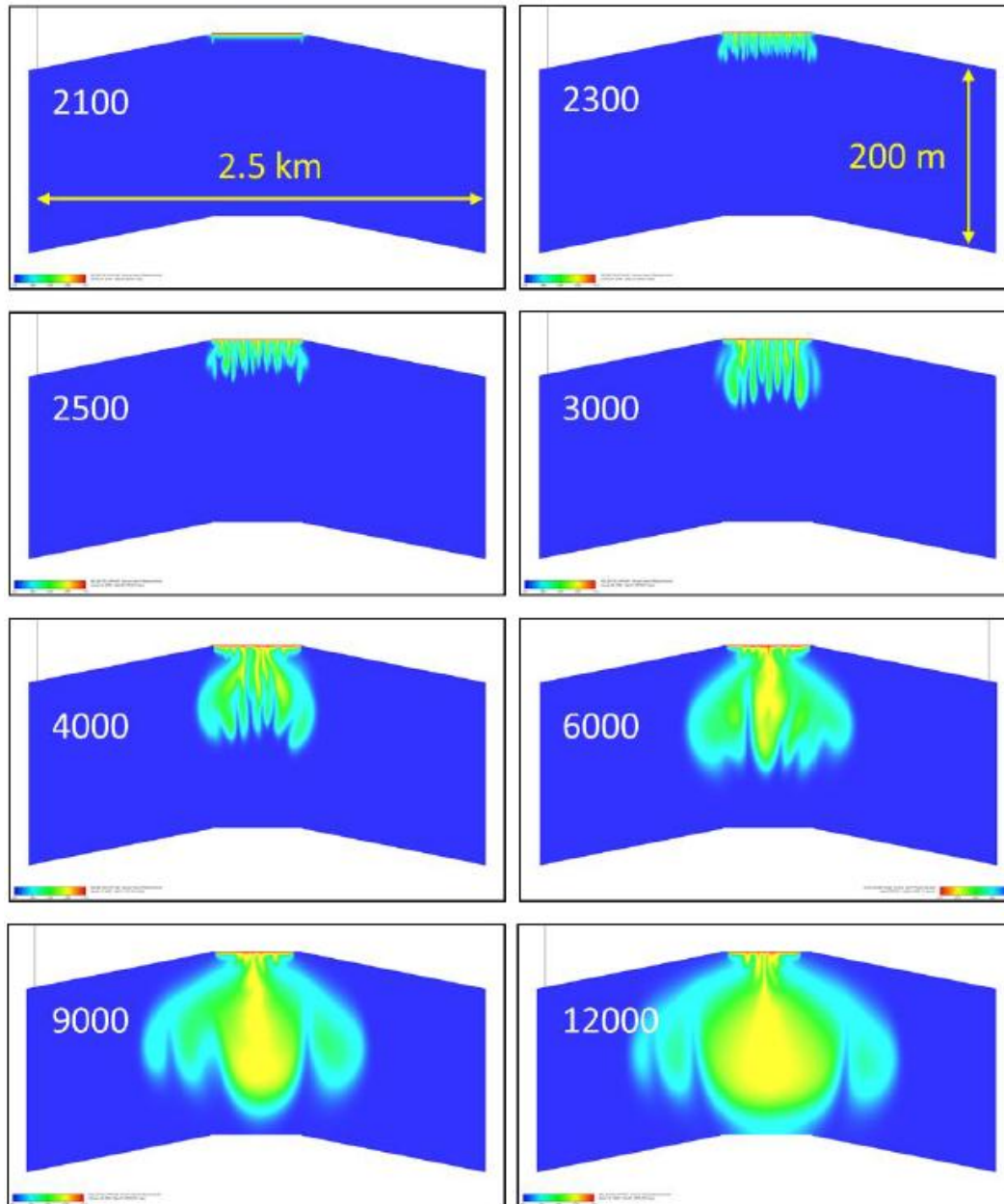
8.4.2 DDC Simulation Results

The CO₂-in-Brine concentration (in m³ of CO₂ per m³ of brine, both at standard conditions) is shown in Figure 8.80. The eight cross-sections are shown at 01/January/YYYY where YYYY is the year shown.

The onset of convective fingers is discernable 100 years post injection. The process starts out with multiple fingers which then broaden and coalesce as CO₂-laden brine propagate downward whilst the lighter brine flows upward, a phenomenon that has been widely reported by several researchers.

The plume of saturated brine does not reach the base of the model until around the year 12000, i.e. about 10,000 years after the cessation of injection, at which time about 25% of the initial CO₂ in place had dissolved.

Figure 8.80: CO₂-in-Brine Distribution at Stated Years



8.5 Possible Influence and Effects on Regional Hydrocarbon Developments

Hydrocarbon developments in the SNS that are likely to be influenced by CO₂ injection into Endurance are fields producing (or that previously have produced) gas from the BSF. Table 8.18 shows the production data from the eight gas fields within the potential regional area of influence around Endurance and Figure 6.3 shows their locations. As gas is produced from a gas reservoir and the reservoir depressurizes, water encroaches from the underlying aquifer into the reservoir to provide pressure support. Any process that increases the pressure of the underlying aquifer such as CO₂ injection will increase this pressure support. Although the gas fields listed in Table 8.18 produce wholly or partly from the BSF, only a subset (Esmond,

Caister-Bunter, Forbes & Gordon) show evidence of hydraulic connectivity to a shared aquifer with Endurance and close enough to receive any significant transient pressure support from CO₂ injection into Endurance.

The Hewett field is the dominant producer but only 35% of its production comes from the BSF (the rest is from Hewett Sandstone and Zechstein Carbonates). Moreover, water influx into the Hewett BSF interval has been shown to be limited due to local faulting in this area and this applies also to the Little Dotty reservoir. Both Hewett and Dotty are therefore probably not in hydraulic communication with Endurance.

Figure 3.4 shows that Orwell is located just south of the Cleaver Bank Zone where the Bunter Sandstone is partially eroded; thus limiting any potential pressure communication with Endurance. Data on the dynamic behaviour of the Hunter field is not available and would probably be of little value in properly assessing its hydraulic connectivity to Endurance given the insignificant production from this field relative to other fields within the regional area of influence.

To summarise, the influence of CO₂ injection into the Endurance Storage Site upon regional hydrocarbon developments is likely to be non-existent or immeasurably small. The gas fields that share a common aquifer with Endurance have either ceased producing or have too weak hydraulic connectivity to the sector of the Bunter aquifer within the potential regional area of influence to receive any measureable pressure communication with Endurance.

Table 8.18: Cumulative Production from Bunter Gas Fields

Field	Cumulative Gas Production to 2013	
	Msm ³	Date Production Ceased
Caister-Bunter	3,202	-
Esmond	8866	Mar 1995
Forbes	1473	Feb 1993
Gordon	3994	Feb 1995
Hewett ¹	122,378	Still Flowing
Hunter	41	-
Little Dotty ²		
Orwell	8618	Jan 2000

Hewett Field has reservoirs in Upper Bunter (BSF), Lower Bunter or Hewett Sandstone and Zechstein Carbonates. Little Dotty production is via Hewett 48/29-A platform.

8.6 Conclusions

The Bunter sandstone formation is extensive in the UK SNS with an area in excess of 20,000 km², an average thickness of 250m and an average porosity of 19% implying a PV of 1000x10⁹m³ or more. How much of this volume is connected to Endurance is unknown, but the post-production pressure history of the Esmond Gas field and pressure measurements taken in Endurance between 1990 and 2013 provide some evidence to suggest they are connected.

The seabed outcrop of the Bunter sandstone formation to the East of Endurance is seen to be more of an opportunity than a threat. Geological arguments favour the outcrop is both in hydrodynamic communication with Endurance and open to flow to the seabed; thus forming a natural pressure relief well.

Thermodynamic considerations would suggest the brine salinity in the upper portion of the outcrop is more like that of seawater than that of Endurance, so any expulsion of fluid should have minimal effect on the seabed. In the worst case of minimal extra aquifer volume, the maximum flow rate from the outcrop will be approximately $3500\text{m}^3/\text{d}$ which is comparable to what might be expected from a single high-rate high water-cut well in a mature North Sea Oil Field.

A simple material balance model suggests the pressure increase in Endurance from injecting the first load of 53.6MT of CO_2 over a twenty year period in excess of 194bar; probably enough to fracture the reservoir and cap rock. However, it is believed Endurance is connected to a much larger volume which could be in excess of $1000 \times 10^9 \text{m}^3$. Even if this were the case, because of the distances involved, not all this volume can be expected to react in the timescales of the injection and it is suggested that no additional benefit is derived from a volume in excess of $100 \times 10^9 \text{m}^3$, which is 20 times that of Endurance itself. The pressure increase expected at the crest of the structure from injecting first load is between 25bar and 65bar with a most likely value of 40bar.

The speed at which the CO_2 will flow from the perforations of the injectors, assumed to be in the Lower Bunter, in the North-West of Endurance to the crest depends on: horizontal and vertical permeabilities, maximum gas (CO_2) relative permeability, drainage critical gas saturation, and the presence or not of horizontal baffles or barriers.

It is expected that the time from injector to crest is two to five years with a most likely value of 3.5 years. The only parameter listed which might conceivably slow the progress of the CO_2 plume is the presence of horizontal baffles or barriers. No direct evidence for such features is seen on seismic over Endurance or present in any of the well logs in the structure although these were seen in the Caister gas field in the Bunter sandstone formation.

Current understanding suggests that 4D seismic monitoring will be able to track the CO_2 plume.

The relative permeability measurements undertaken on core taken from Endurance have produced what may appear to many as being anomalous results in that the maximum gas relative permeability (at irreducible water saturation) $K_{rg}(S_{wi}) > 1$. However, this result is far from anomalous and could have been predicted.

The injection of the Phase 1 maximum mass of 53.6MT is expected to pool at the crest of the structure and no scenario can be envisaged where the CO_2 can get beyond the spill of the Endurance structure. In fact there is no known mechanism by which the CO_2 can get out of the upper peak and into the eastern lower peak of Endurance.

Cooling of the reservoir by the cold CO_2 is thought to be highly localised to the near wellbore region although the work done here has not been able to consider conductive cooling of the cap rock as the CO_2 flows down through the well. The geomechanical modelling done in parallel to this study suggests the biggest risk to the failure of the seal is more likely due to cooling than pressurising-up from the Phase 1 loading.

The Bunter sandstone formation in Endurance is considered to be fair to good to very good in terms of reservoir quality; hence there should be more than enough permeability in the Lower Bunter to allow well perforations to be set deep thereby maximising the opportunity for residual trapping although the relative

permeability data indicate the amount of residual trapping might be quite low. It had been thought this strategy would also keep the cold injectant away from the cap rock where it could lead to thermal fracturing.

9 Production Chemistry

9.1 Summary

Steady state flow assurance studies as reported in report K34 Flow Assurance demonstrate that CO₂-water hydrates will not be a concern under steady state conditions given the proposed maintenance of the water fraction at sub-hydrate forming levels (50ppmv). K34 also comments on the CO₂ composition specification. Results from the modelling of transient processes, including initial start-up, restart, turndown, ramp up etc., show that single-phase conditions will be maintained in both the pipeline and the wells. However, results from geochemical modelling and experiments studies suggest a propensity towards halite precipitation near the well bore. The management of this near-well halite precipitation will therefore constitute the main process requiring chemical intervention during White Rose CO₂ injection operations.

Injection of CO₂ into a saline aquifer is known to cause the evaporation of resident brine in the vicinity of the injection well leading to salt precipitation. The precipitate may reduce formation effective porosity, permeability, and consequently impact the injectivity.

Halite precipitation studies suggest that permeability (and in turn injectivity) impairment as a result of halite precipitation is likely to be negligible as long as CO₂ injection is kept continuous and no well shut-in occur. Maintaining a continuous CO₂ injection creates a hydraulically connected CO₂-saturated 'dry-out zone' around the injection well that exerts a back pressure which prevents the displaced salt-laden brine from flowing back towards the well to evaporate and deposit salt in the pore space. If a well is shut for planned routine maintenance or unplanned repairs then the CO₂ back pressure around the well is removed causing brine to flood the dry out zone and eventually the wellbore. On restart of CO₂ injection, near-well brine will evaporate into the CO₂ stream and leave behind a higher solid saturation and therefore a lower formation permeability than before shut-in, reducing well injectivity. This injectivity impairment is commonly remedied by water washing, where less saturated brine is injected ahead of the CO₂ stream to dissolve the near-well precipitated salt and also dilutes the formation brine around the well.

Current operations design philosophy envisages one water wash treatment every six months per well. Of vital importance during water-wash is the need to optimise not just the rates and volumes, but also the composition of the injected water to ensure compatibility with formation water and prevent adverse reactions with well construction equipment.

Water wash will inadvertently lead to the creation of a CO₂/water mixture, creating enabling conditions for formation of hydrate (and possibly corrosion of production/injection tubing). MEG is selected for primary inhibition and remediation of hydrates since it is less volatile and therefore has a lower tendency to cause formation 'dry-out' than Methanol. MEG also carries less handling risk than Methanol. Methanol is considered as a remote contingent should MEG be unsuccessful.

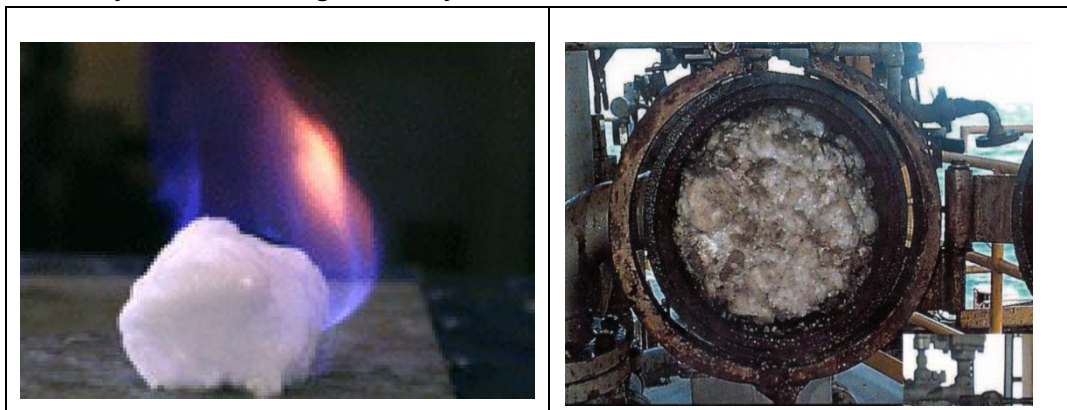
No potential scaling issues are anticipated. The use of 25% chromium duplex stainless steel in the production/injection tubing is selected to mitigate corrosion issues. Asphaltenes and wax are not considered risks for CO₂ injection wells.

9.2 Hydrate Inhibition Requirements

The flow assurance studies provide key input data for qualifying well conditions and assessing potential hydrate issues under flowing and shut in conditions.

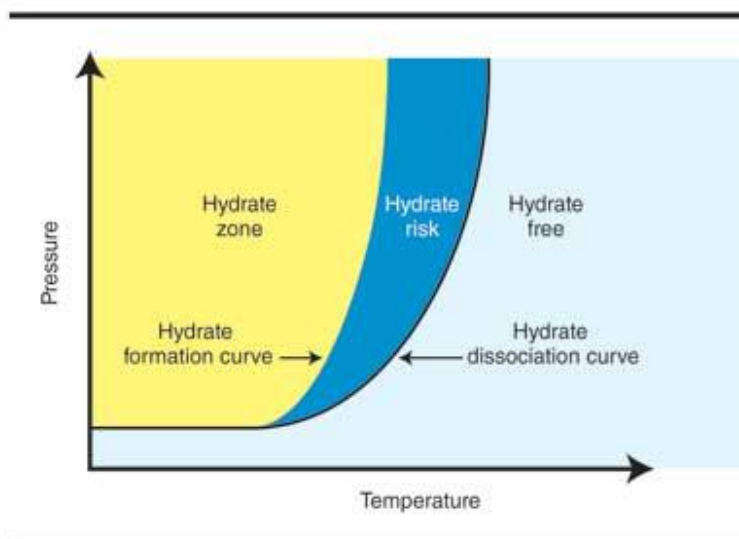
Natural gas hydrates (or clathrates) are crystalline compounds formed by water with natural gases and associated liquids. The hydrates are solid ice like crystals composed of cages of water molecules surrounding 'guest' gas molecules such as methane, ethane, propane, and carbon dioxide (Figure 9.1). Hydrates can block any type of flowline, production tubing, and pipeline. However unlike ice, hydrates can form at much higher temperatures than 32°F / 0°C.

Figure 9.1: Hydrate - US Geological Survey



The pressure-temperature regions (See Figure 9.2 below) in which hydrates form, stabilise and dissociate depends on the composition of the injected or produced stream.

Figure 9.2: Hydrate Formation Curve



The larger part of gas hydrates (90% by weight) consists of water whereas the remaining 10% corresponds to the weight of gas which is trapped in the hydrate lattice.

Gas hydrate formation and dissociation is chemically fully reversible which means that gas and water from which gas hydrates are composed evolve chemically unaltered if these hydrates are melted.

Because hydrates consist of water and gas, hydrates grow predominantly at locations where both the water and gas are in abundant supply. This is why hydrate growth is most pronounced at the interface between liquid water and gas or between liquid water and liquid saturated in an appropriate hydrate forming gas.

Free water in gas is a serious problem because it tends to freeze in the field equipment in the form of hydrates making meters and valves inoperative and plugging chokes or pipelines.

The above formation process is accelerated when there are high gas velocities, pressure pulsations or other agitation, such as at elbows, which cause mixing of hydrate components.

The higher the gas pressure, the higher the temperature at which hydrates will form.

The higher the specific gravity of the well steam, the higher the temperature is for hydrate formation.

At equal pressures ethane, propane, H₂S, and CO₂ form hydrates at higher temperatures than methane. In a gas well hydrate formation is therefore promoted the greater the fraction of these impurities relative to methane in the gas, whereas nitrogen and pentane plus have no noticeable effect. In a CO₂ injection stream there is a similar need to consider the impact of impurities in the gas stream to accurately understand hydrate behaviour (Ref. 26, 27, 28, 29, 30, 31 and 32).

9.2.1 General Hydrate Management

9.2.1.1 General Operational Prevention

The first step towards hydrate prevention involves removing free water, maintaining high temperatures, and maintaining or reducing pressures in the well so as to ensure the well is only operated within the hydrate free region of the P-T hydrate formation curve. Beyond this approach the use of chemical inhibitors can be considered.

9.2.1.2 Removal of Free Water / Use of Nitrogen

The prevention or removal of free water can be seen achieved at the top of the well through stringent control of CO₂ injection stream quality (<50 ppmv water content), and surface pipework flushing with nitrogen. Deeper in the well however the presence of water is more likely through formation water influx when CO₂ injection is shut in, or a standing residual water wash column is present. In these scenarios then N₂ injection can be considered to prevent the formation of an interface between CO₂ and water. This would be used to remove CO₂ before a water wash treatment, and then again to remove residual standing water after a water wash treatment, before CO₂ injection was resumed.

9.2.1.3 Temperature

The long seabed pipeline length and low starting temperature mean that pipeline insulation can only marginally influence arrival temperature. Heating is impractical from a cost and technical perspective.

Whilst fluid could be heated at surface during a shut in the isolated well contents would revert to ambient conditions. In the deeper parts of the well this would mean a rise in temperature. In the shallower parts of the well exposed to the air gap under winter conditions then a cooling process will occur. Thus a further downhole heating system would also be required adding further cost, complexity and reliability issues. Insulation in the shallow part of the well without heating would only maintain the already low temperature of the injected stream at best rather than elevate temperature as might be required to make a meaningful difference. Insulation deeper in the well would simply prevent beneficial geothermal heat energy being provided from the formations adjacent to the well.

9.2.1.4 Pressure

Maintaining or reducing the well pressure is an option that can in theory be readily used to reduce hydrate risk at shut in. If a deep-set safety valve is present in the completion then the pressure above the valve can be bled off before the column above cools and enters the hydrate forming region. However if the prior operation has been steady state CO₂ injection with no free water present (<50 ppmv) and that this is true for the lowest shut in temperature then no hydrate risk should be present from a shut in of such a dry gas. If water content is higher than planned however then the reduction in pressure, and vaporisation of liquid CO₂ as a gas cap may need further consideration in terms resultant local pressure temperature impact and attendant hydrate risk.

Whilst reducing pressure in the well during a shut in may help to prevent a low temperature high pressure scenario initially it must be recognised that in order to resume injection that pressure must once again be re-applied and the low temperature high pressure scenario although successfully deferred still needs to be addressed.

9.2.1.5 Chemical Inhibition

Chemical inhibitors act to prevent hydrates forming. They are injected either into the flow stream or spotted in concentrated pill form in areas of highest concern due to an anticipated potential of high pressure, low temperature, and free water. Examples of such areas of highest concern are across valves (TRSV, Xmas Tree, Manifolds valves, or chokes), and within small bore surface pipework. These chemical inhibitors are one of two types; Thermodynamic Inhibitors (THIs) (methanol, glycol, isopropanol,) and Low Dose Hydrate Inhibitors (Kinetic Inhibitors, Hydrate Dispersant Inhibitors). Methanol and glycol are the two commonest chemical inhibition and remedial solutions.

9.2.1.6 Methanol

Methanol (MeOH) can be used to both prevent and remove hydrates. Historically in oil and gas wells methanol has been 'the favoured choice to remove hydrates given glycol is not very effective at melting hydrates' (Ref. 15). Methanol dissolves in any free water accumulation to prevent hydrates. It can be pumped neat. However it is sometimes prepared as a 10weight% to 40weight% aqueous solution as a means to improve stability and reduce evaporation, given its flammable nature and neat flashpoint of 51°F. Use of methanol requires appropriate specialist pipework, pumps with compatible seals, bunding, and assessment and management of fire / explosion risks.

Neat methanol has an SG of 0.79 and as such is positively buoyant with respect water.

9.2.1.7 Glycols

MEG historically in oil and gas wells has been the most commonly used product for the 'inhibition rather than removal of hydrates' (Ref. 33). It is less volatile than methanol with a higher molecular weight. It is generally mixed in an aqueous solution of 20% to 80% by volume.

Glycol has an SG of 1.11.

Experience has demonstrated that care needs to be exercised when applying pressure to deepwater control or service lines to ensure that the control line fluid has not separated into discrete water and glycol phases. A mitigation applied is periodic flushing / cycling of static control line fluids to prevent this.

Methanol vs Glycol Hydrate remediation: Thermodynamic Hydrate Inhibitors (THIs), which include methanol and MEG, all work on the same thermodynamic concept: temperature depression. The decrease in hydrate formation temperature depends on the mole percent of chemical inhibitor in the produced water. So, when talking about "effectiveness," no THI is more effective than the other. All THIs follow the same principle and they all will deliver the same end result.

Methanol is sometimes considered more effective because it has a lower molecular weight and density than MEG. This means that, theoretically, less volume of methanol is needed for a given well than MEG to get the same temperature depression based on an assumed similar temperature depression response per molar concentration. This may however not be strictly true if different molar concentrations are required to produce the same response and if different hydrate forming species (CH₄, CO₂ etc.) respond differently. Table 9.1 lists properties of typical hydrate inhibitors.

Further, in reality a number of operational factors may also play a role in determining a preference in a given situation. One explanation may be to recognise that different hydrate problem scenarios require different solutions based the following;

- fluid density and type in the well above the hydrate blockage;
- fluid density and type in the well below the hydrate blockage;
- size / length of the hydrate blockage – approachable contact area versus volume;
- treatment deployment options;
- lubricated into the well from above the hydrate;
- directly by chemical injection line immediately above hydrate;
- directly by chemical injection line immediately below the hydrate;
- directly by chemical injection line immediately at the hydrate; and
- Coil tubing well intervention deployed.

Methanol aqueous solutions have a considerably lower freezing point than MEG aqueous solutions and thus a lower minimum application temperature as illustrated in Figure 9.3. It can also be seen that MEG concentrations greater than 60% to 70% weight in water are counterproductive in terms of further freezing point reductions. Excess methanol concentrations are not an issue however in freezing points terms given the minimum temperature conditions possible in CO₂.

As an illustration, a MEG pill deployed from above would be more effective based on negative buoyancy in sinking through freshwater column than a methanol pill that would float above. Conversely, a MEG pill introduced from below a hydrate plug would sink away from the problem. Other considerations include:

- methanol has high solvability and is considerable less viscous than glycol thus in some instances it may be able to effectively access / penetrate more rapidly an extended length of hydrate plug or mass;
- methanol is easily vaporised and distributed into gas streams;
- methanol may be preferable for plugs in horizontal flowline / pipeline environments where buoyancy is not an issue, or where access is direct;
- methanol suffers high gas and condensate losses due to higher vapour pressure; and
- MEG carry less HSE risks than methanol because it is less volatile and does not burn clear like methanol. The HSE risks of methanol are however manageable if the right equipment and procedures are in place.

Table 9.1: Hydrate Inhibitor Properties

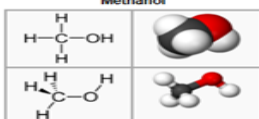
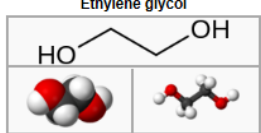

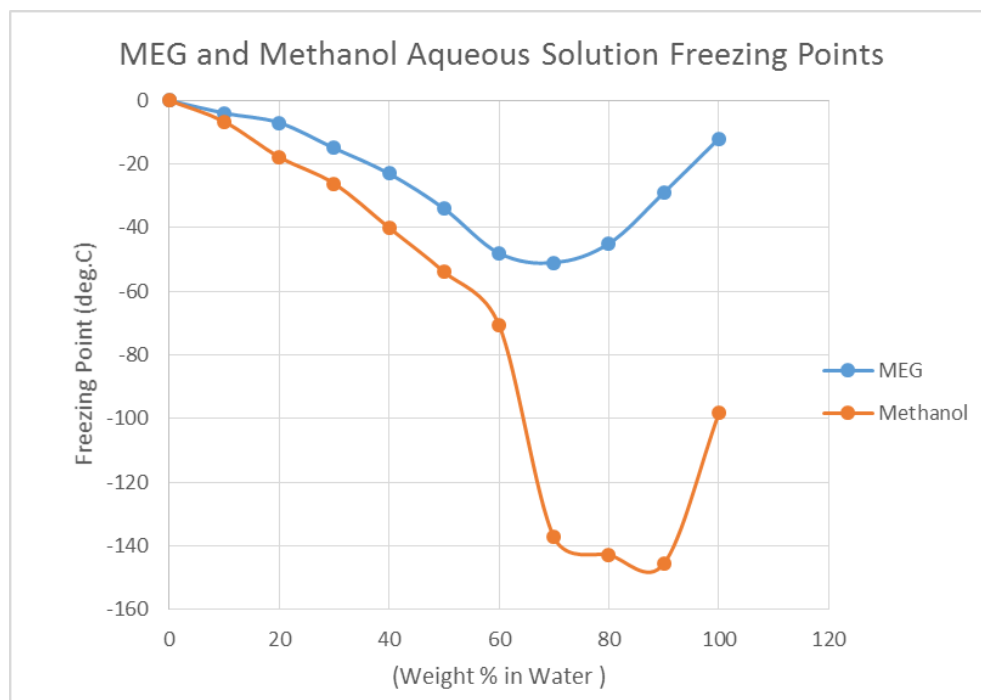
Inhibitor	Methanol (MeOH)	Monoethylene glycol (MEG)	Tri-ethylene glycol (TEG)
Density at 20°C (kg/L)	0.787	1.11	1.12
Viscosity at 20°C (cP)	0.5	18	36
Freezing Point (°C)	-98	-13	-5
Moles per kg at 20°C	31.21 g moles	16.11 g moles	6.65 g moles
Moles per Litre at 20°C	24.56 g moles	17.88 g moles	7.45 g moles
Molecular Weight	32.04 g/mol	62.07g/mol	150.17 g/mol
Molecular Formula / Structure	CH ₄ O Methanol 	C ₂ H ₆ O ₂ Ethylene glycol 	C ₆ H ₁₄ O ₄ Triethylene glycol 

Figure 9.3: MEG and Methanol Aqueous Solution Freezing Points



Salts: the greater the salinity of the free water phase the better inhibited is the fluid with respect to hydrate formation. Hence hydrate formation becomes progressively less likely in turn at the interface with the following phases; condensed water, seawater, completion brine / formation water.

9.2.1.8 Kinetic Inhibitors

The kinetic inhibitors are low dose hydrate inhibitors. Compared with methanol or glycol over the longer term they can potentially offer significant gains in terms of cost, logistics, and safer product handling.

One form is known as Thermodynamic Hydrate Inhibitors (THIs), which delay hydrate nucleation and or crystal growth, to extend the operating range within the hydrate forming window. They are water soluble and can be used in conjunction with methanol and glycol aqueous solutions to reduce treatment volumes at increasing water cuts.

Another form of kinetic inhibitors is dispersant low dose hydrate inhibitors. These are known as Hydrate Growth Inhibitors (HGIs) and although they do not prevent hydrates from forming they act to prevent hydrate agglomerating or bonding together. For other forms of HGIs, rather than disperse, they emulsify to prevent agglomeration.

The general industry-view of low dosage hydrate inhibitors is that there no consistent procedure for correctly selecting and optimising these products. This is because they are known to perform in only narrow windows with respect to liquid/gas ratios, and may partition under static conditions.

Hence the introduction of these products is only considered for long term steady state scenarios where incremental introduction and gradual removal of primary glycol / methanol inhibitors can be managed. As

a result use of kinetic hydrate inhibitors are not considered suited for transient hydrate risk conditions of the proposed CO₂ injection wells.

9.2.2 Hydrate Modelling

9.2.2.1 Well Parameters

The three proposed injection wells have similar wellpaths and reservoir depths (PS W1, PS W2, PS W3). They feature a 55 degree tangent section that provides a radius of separation of 1500m at target depth. The well design comprises 9-5/8 inch production casing, with a cemented and perforated 7 inch liner. The target perforation interval is across 200ft TVD of liner with bottom shot 30m above the base of the reservoir section.

9.2.2.2 Static Shut in Well temperature and pressure Profiles

A series of static gradient ambient temperature profiles have been generated. They are based on the expected bottom hole pressure for a series of potential fluid columns in the well (freshwater, seawater, formation water, CO₂, and nitrogen).

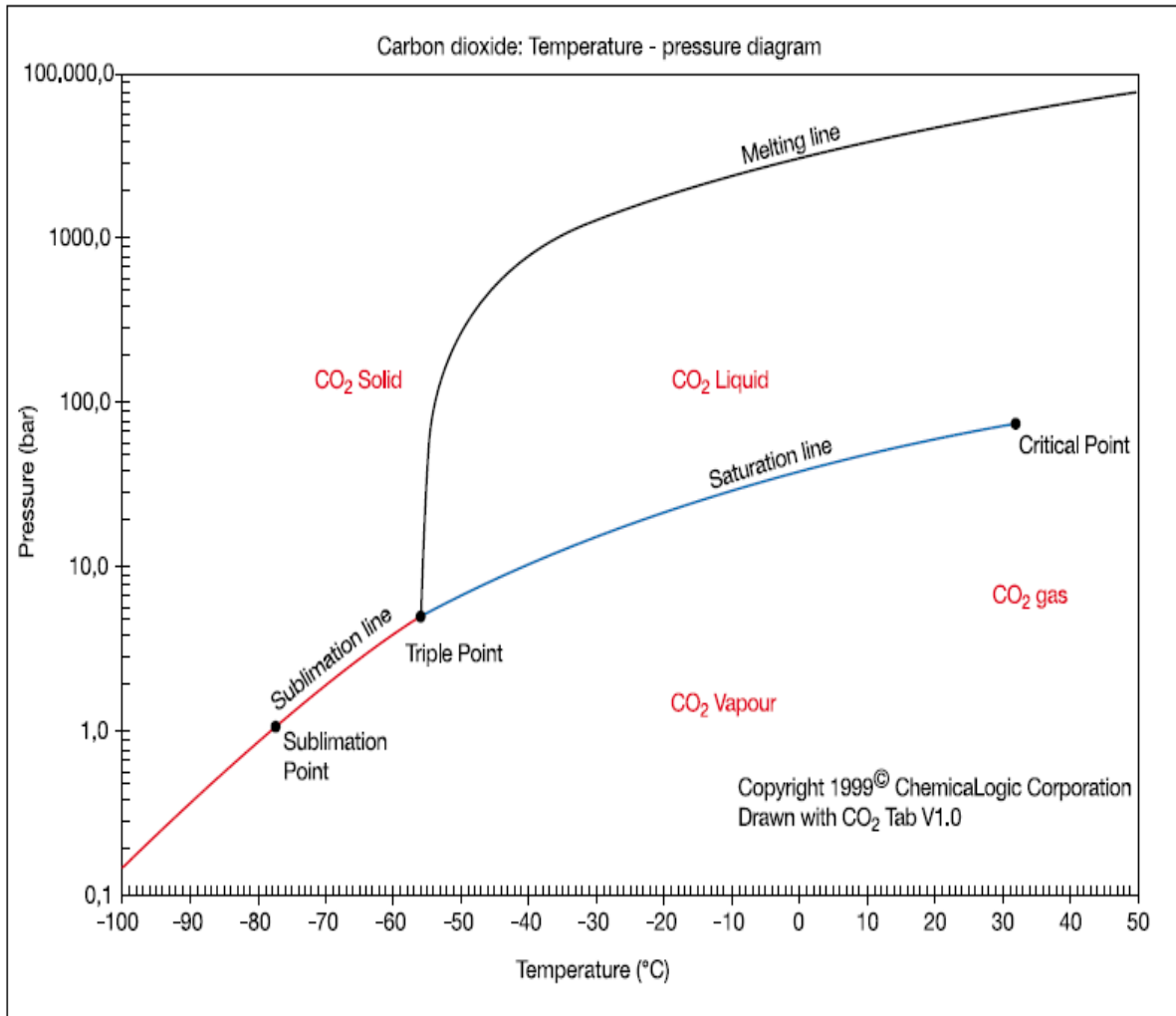
Table 9.2: Shut in Tubing Head Pressures

Fluid/Gas	Depth (ft tvdss)	Depth (ft TVD rkb) RTE 114ft	Reservoir Temp. (°F)	Reservoir Pressure (psi)	Gradient (psi/ft)	Fluid / Gas Density (ppg)	Surface Shut in Tubing Head Pressure (psi)
Formation Brine	4608	4722	140 (60°C.)	2200 (151bar)	0.541	10.41 ppg	Sub-hydrostatic (full column 356psi overbalance or 658ft below rig floor at balance)
Seawater	4608	4722	140 (60°C.)	2200 (151bar)	0.444	8.54 ppg	100 (7bar)
Nitrogen	4608	4722	140 (60°C.)	2200 (151bar)	0.067	1.28 ppg	1800 (124bar)
CO ₂	4608	4722	140 (60°C.)	2200 (151bar)	0.314	6.04 ppg	715 (50bar)

At initial conditions a formation brine column is supported to a height 658ft below drill floor / platform facility. Seawater, CO₂ and nitrogen columns develop closed in tubing pressures pressure of 7bar, 50bar and 124bar respectively (Table 9.2).

The static CO₂ column is a mixture of a liquid column with a gas cap as illustrated in the phase diagram (Figure 9.4) and with the Prosper Petex modelled gradient profile in Figure 9.5. At reservoir depth under the conditions of 151bar, and 60°C the CO₂ is liquid. At surface under shut in conditions of 50bar and circa 6°C to 16°C (summer-winter) the CO₂ is in a gaseous state (Table 9.3).

Figure 9.4: CO₂ Phase Diagram

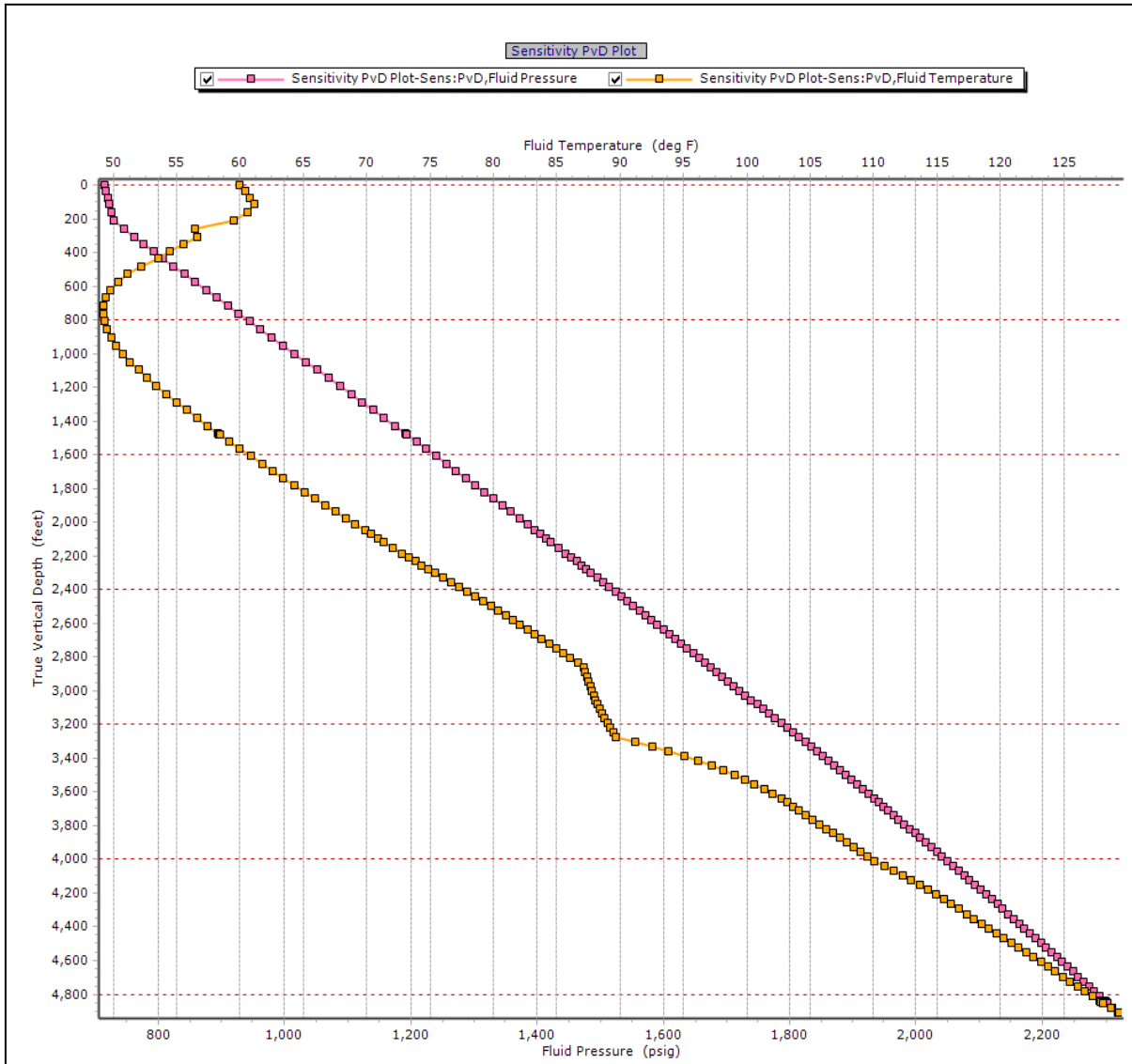


Reservoir pressure will increase over the 25 year injection lifecycle period to between 200bar and an upper 230bar limit based on fracture gradient risk. This will result in an entirely liquid CO₂ column being supported in due course.

Table 9.3: Pressure Temperature vs Depth Model Input

Properties	Parameter	Units
Surface Temperature	60	°F
Seabed Temperature	40	°F
Reservoir Temperature	135	°F
WHP	715	psig
BHP [~]	2313	psig
Reservoir Pressure	2313	psig

Figure 9.5: Prosper Petex Pressure Temperature vs Depth Plot



9.2.2.3 Hydrates in the Context of white rose ccs project

In comparison to the operation of oil and gas wells the experience of operating CO₂ CCS injection wells is limited.

In recent years there has been an industry wide effort associated with improving characterisation of flow assurance hydrate behaviour with respect to carbon dioxide and CCS projects (Ref. 27, Ref. 28). National Grid is involved directly in these efforts through an ongoing joint Industry Project at Heriot-Watt University (Ref. 30, Ref. 31 and Ref. 32).

Some of the work carried out to date is now reviewed with consideration to their applications to optimising well design and well performance for the White Rose project.

Whilst any study should consider a comprehensive range of operating scenarios the expected areas of highest concern are shut in conditions, cold production / injection, and well intervention activities.

9.2.2.4 Hydrate Formation Curves

Multiflash Infochem Software Version 4.2.16, November 2013 (Ref. 34 and 35) has been used to develop a series of CO₂ hydrate formation curves based on the expected injected CO₂ stream composition, and that of the various potential water phase compositions to verify the nature of hydrate exposure risks.

The following scenarios have been considered for occurrence of water in the well:

- water introduced within the CO₂ stream (in vapour form or condensed) < 50 pmv;
- seawater used for periodic water wash operations using that has a salinity based on a 'Total Dissolved Solids' (TDS) content of 35,000mg/L; and
- saline formation water which may enter the well during shut in periods. The column of fluid that will be supported will increase with time in line with rising reservoir pressure due to CO₂ injection operations. (Salinity TDS circa 304,000mg/L).

9.2.2.5 Input Data

See Table 9.4 for hydrate modelling temperature and pressure input data; KKD Report K34 provides Pure CO₂ and Mixture Phase Envelopes.

Table 9.4: Hydrate Modelling Input Data

Properties	Parameter	Units
Surface Temperature	60 / 15.5	°F /°C
Min Arrival Temperature	37.4 / 3	°F /°C
Reservoir Temperature	135 / 57.2	°F /°C
Max Arrival Pressure	2900 / 200	psi / bar
Bottom Hole Pressure Worse Case	2900 / 200 r	psi / bar
Reservoir Pressure	2313 / 159	psi / bar

9.2.2.6 CO₂ 99% Composition #1 Fresh Water Case

In this first case a hydrate curve has been generated based on the presence of freshwater and a CO₂ stream composition #1 (Table 9.5) as detailed below, based on the potential range of CO₂ injected stream properties.

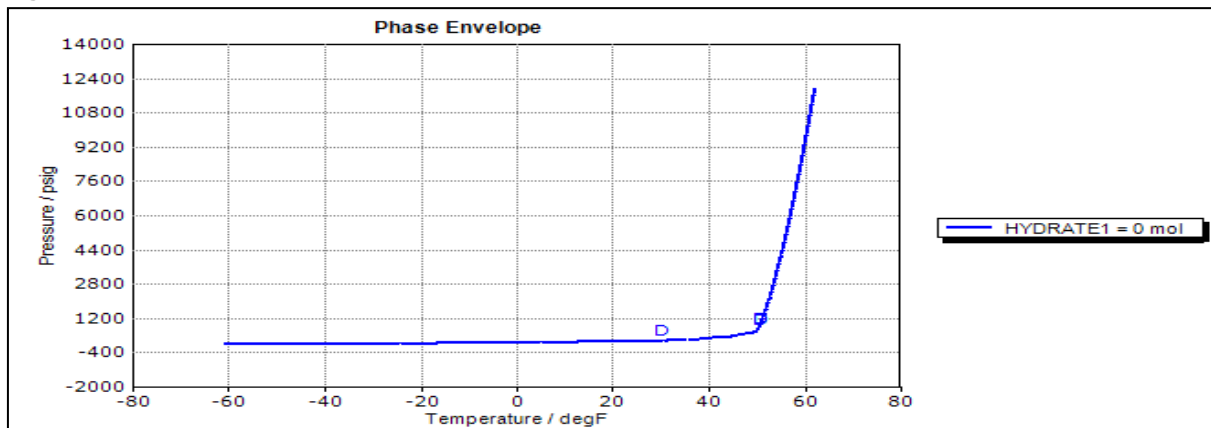
Table 9.5: CO₂ Mixture Composition #1

Components	% Mole
CO ₂	99.049
N ₂	0.722
H ₂ S	0.002
CO	0.200
NO	0.005
NO ₂	0.005

Components	% Mole
SO ₂	0.010
O ₂	0.001

The results for a pressure and temperature (PT) flash calculation at 37.4°F (3°C) and 2639 psig, and 2900psig (182/200barg) chosen to reflect potential surface conditions indicate that hydrates will occur. At a temperature of 37.4°F, the calculated dissociation pressure is 240psig. At a pressure of 2900psig, the calculated dissociation temperature is 53.6°F.

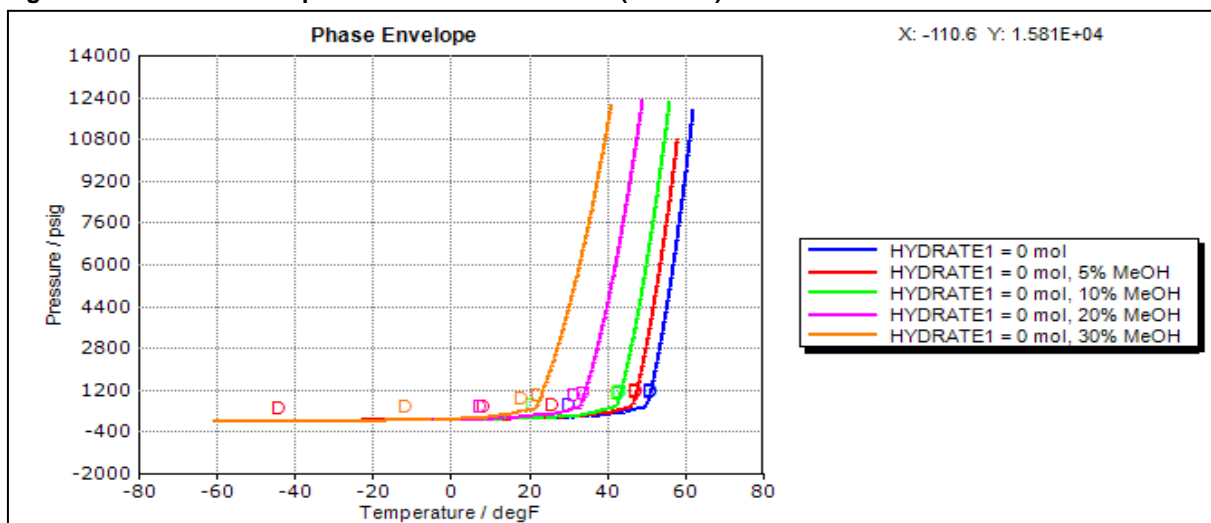
Figure 9.6: Phase envelope Comp#1, freshwater, no inhibitor



Hydrate Phase Envelope: further hydrate curves were then developed based on the same composition #1, and freshwater but with various weight in water % (i.e. % mass) concentrations of methanol and glycol chemical inhibitors.

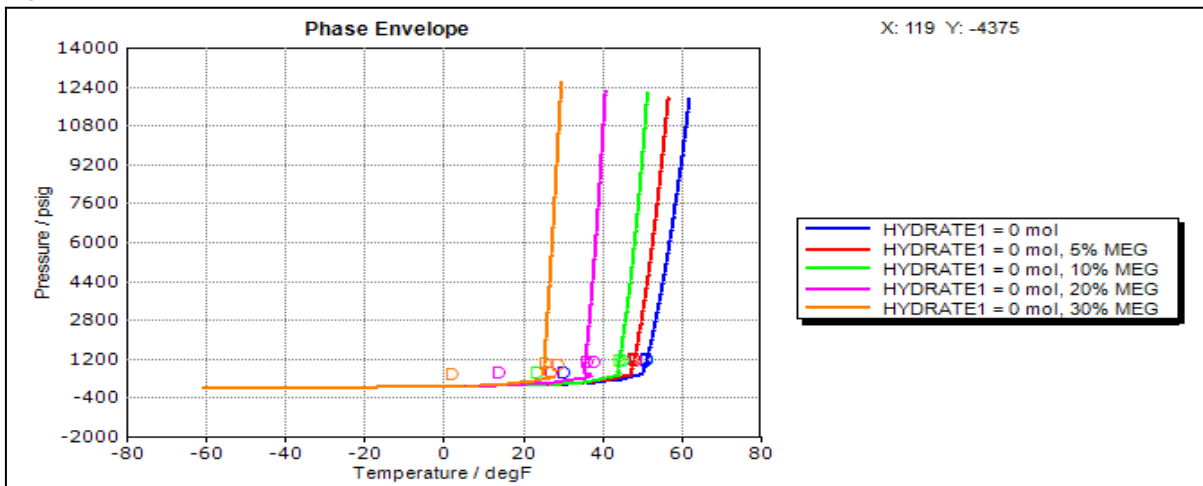
Methanol Inhibitors

Figure 9.7: Phase envelope with Methanol inhibitors (% Mass)



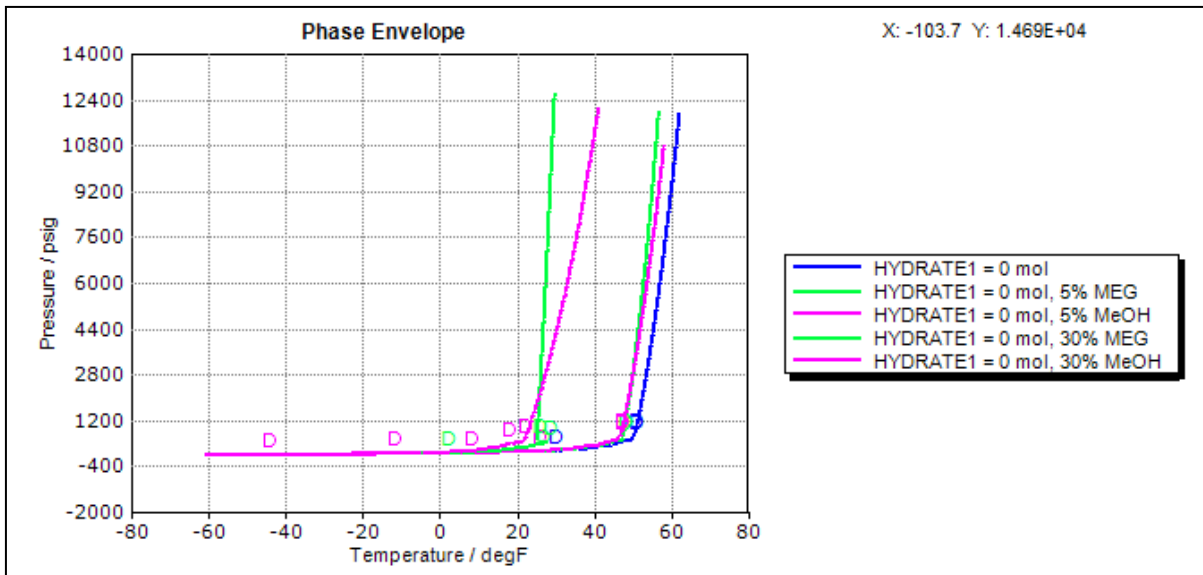
MEG Inhibitors

Figure 9.8: Phase envelope with MEG inhibitors (% Mass)



Methanol vs MEG Inhibitors Comparison

Figure 9.9: Phase envelope Comparison Methanol vs MEG (%Mass)



9.2.2.7 CO₂ 99% Mixture Composition #1 Formation Water Case

In this second case a hydrate curve has been generated based on the presence of formation water and a CO₂ stream composition #1 (Table 9.6) as detailed below, based on the potential range of CO₂ injected stream properties.

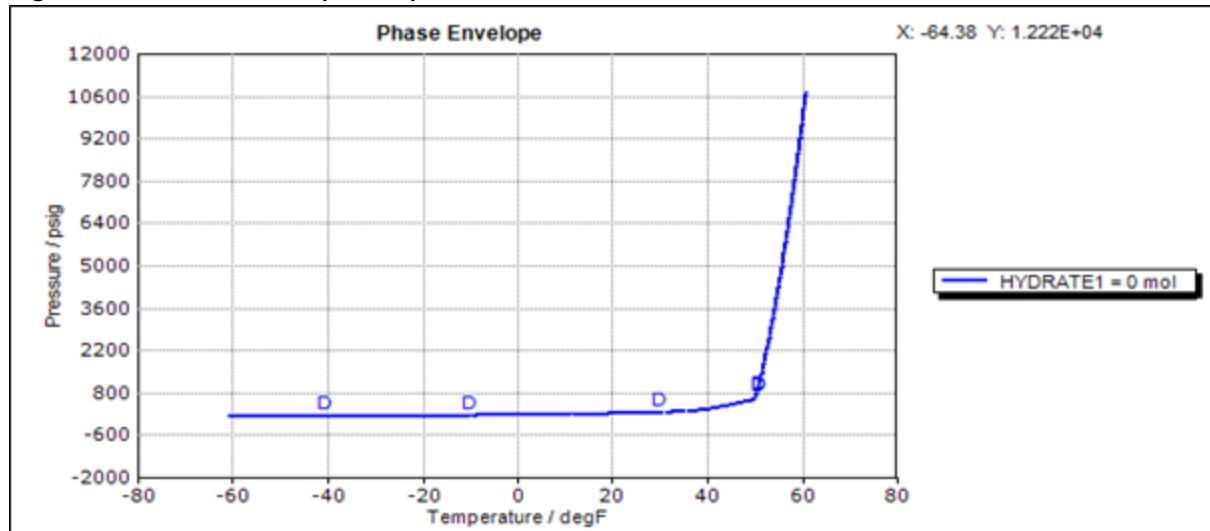
Table 9.6: CO₂ Mixture Composition #1

Components	% Mole
CO ₂	99.049
N ₂	0.722
H ₂ S	0.002
CO	0.200
NO	0.005
NO ₂	0.005
SO ₂	0.010
O ₂	0.001

The results for a pressure and temperature (PT) flash calculation at 135°F (57.2°C) and 2900psig, and 3100psig (200/214barg) chosen to reflect potential downhole conditions indicate that hydrates will not occur under these conditions. At a pressure of 3100psig the calculated dissociation temperature is 53.6°F.

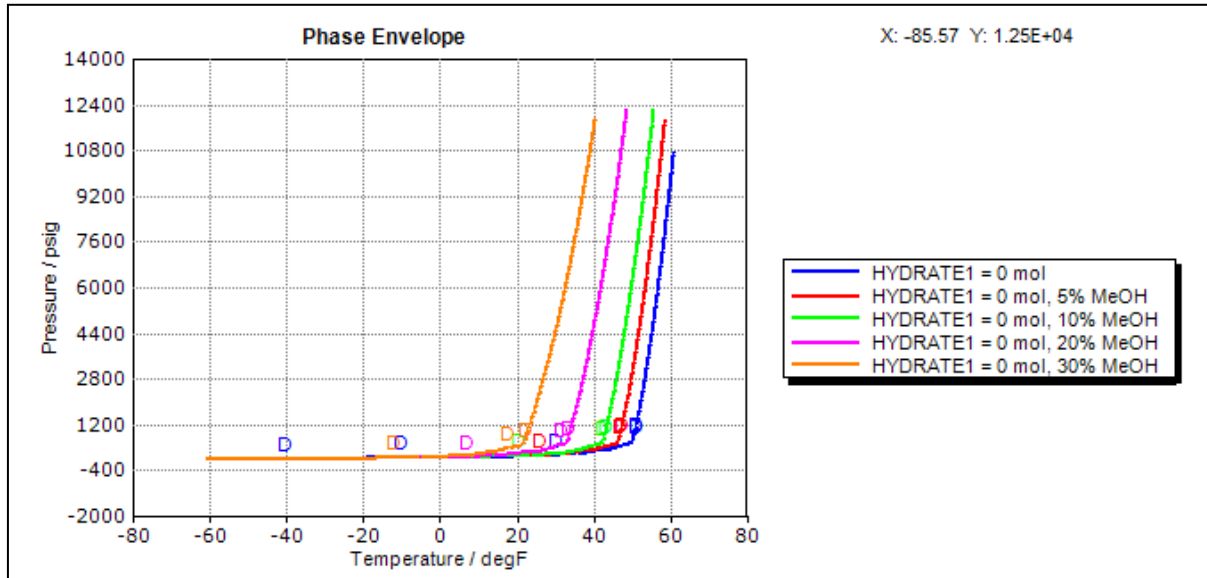
Phase Envelope: further hydrate curves were then developed based on the same composition #1, and formation water, but with various weight in water % (or % mass) concentrations of methanol and glycol chemical inhibitors.

Figure 9.10: : Phase envelope Comp#1, formation water, no inhibitor



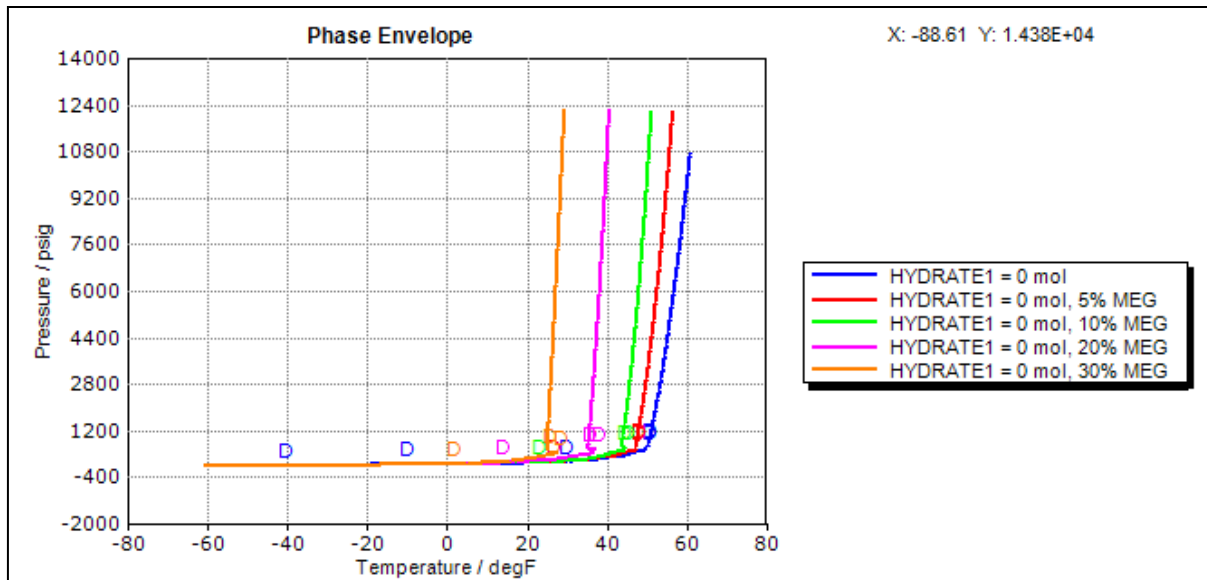
Methanol Inhibitors

Figure 9.11: Phase envelope with Methanol inhibitors (% Mass)



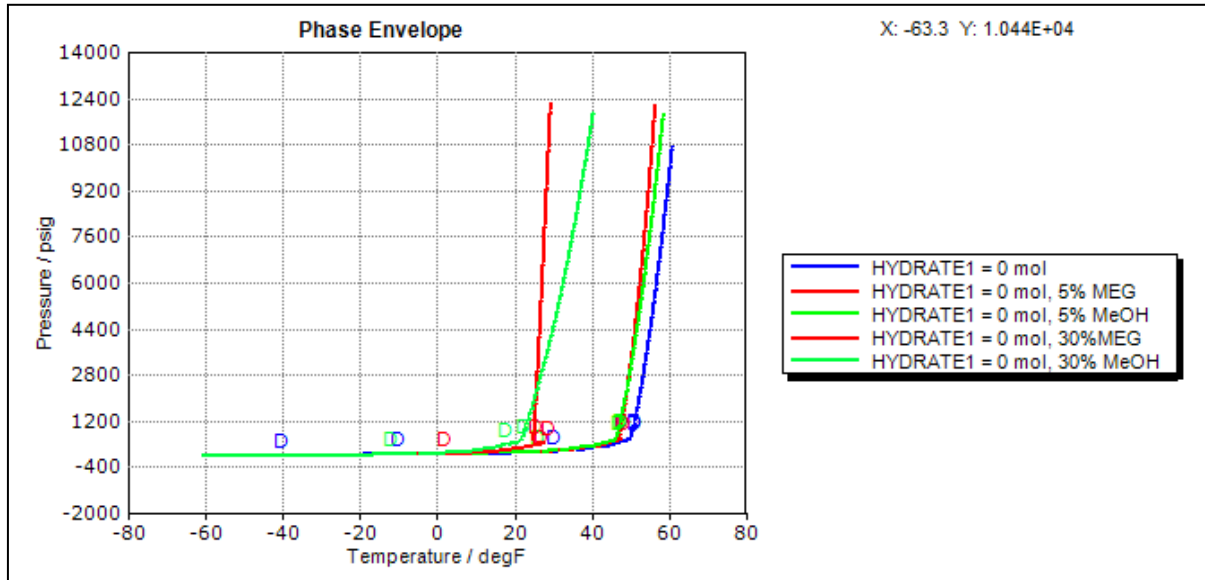
MEG Inhibitors

Figure 9.12: Phase envelope with MEG inhibitors (% Mass)



Methanol vs MEG Inhibitors Comparison

Figure 9.13: Phase envelope Comparison Methanol vs MEG (% Mass)



9.2.2.8 CO₂ 99% Mixture Composition #1 Seawater Case

In this third case a hydrate curve has been generated based on the presence of seawater and a CO₂ stream composition #1 (Table 9.7) as detailed below, based on the potential range of CO₂ injected stream properties.

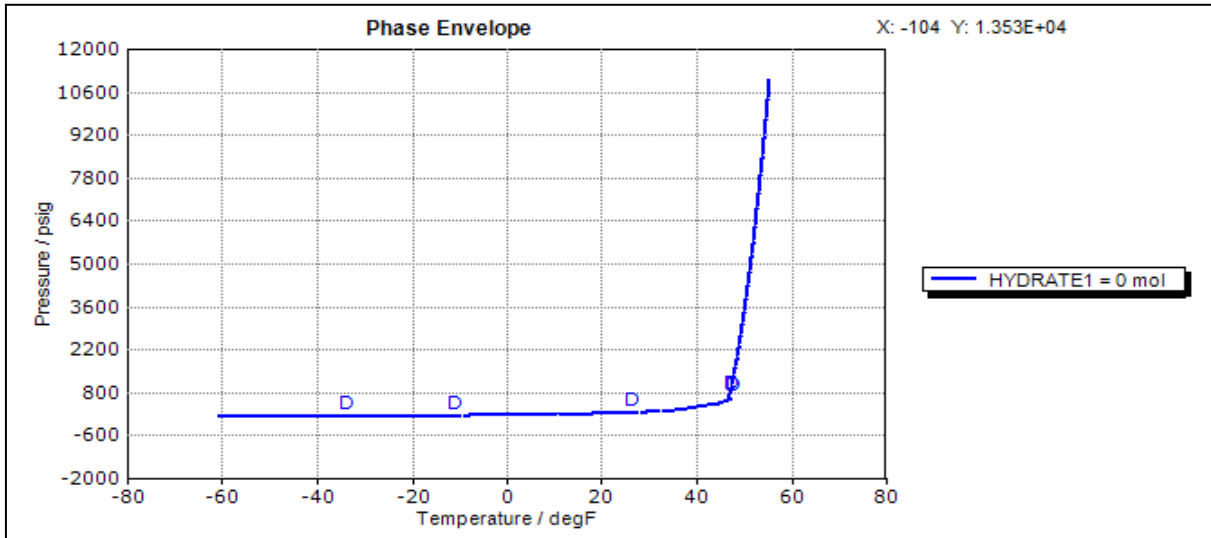
Table 9.7: CO₂ Mixture Composition #1

Components	% Mole
CO ₂	99.049
N ₂	0.722
H ₂ S	0.002
CO	0.200
NO	0.005
NO ₂	0.005
SO ₂	0.010
O ₂	0.001

The results for a pressure and temperature (PT) flash calculation at 37.4 deg F (3°C) and 2900 psig, (200barg) chosen to reflect potential surface conditions indicate that hydrates will occur under these conditions. At a temperature of 37.4 °F the calculated dissociation pressure is 283.2 psig. At a pressure of 2900 psig the calculated dissociation temperature is 49.5 °F.

Phase Envelope

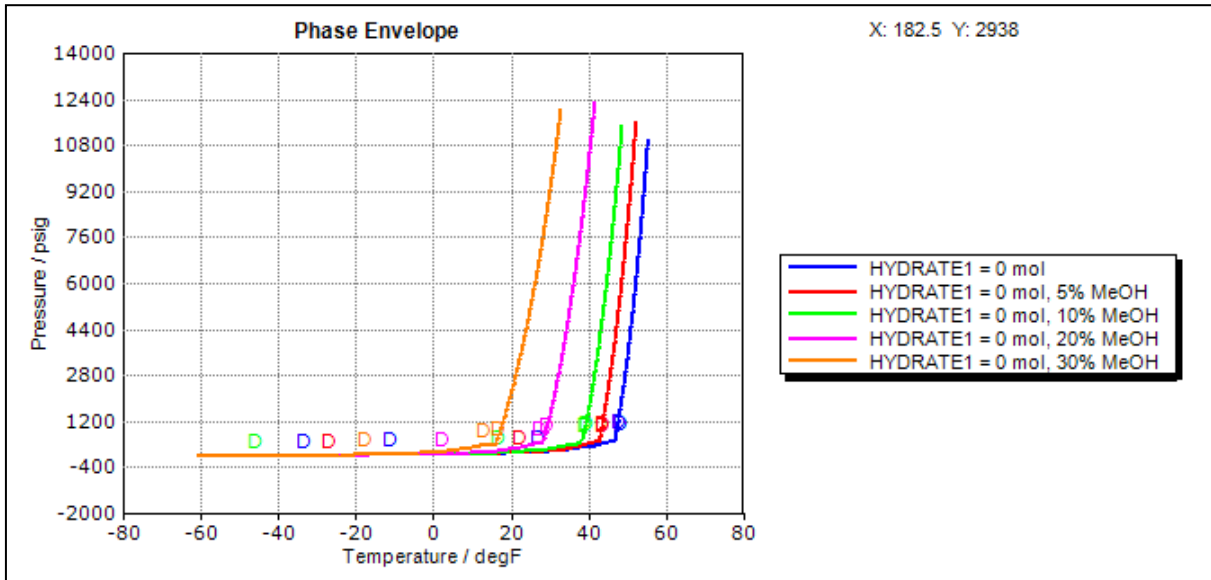
Figure 9.14: Phase envelope, Comp#1, seawater, no inhibitor



Further hydrate curves were then developed based on the same composition #1, and formation water but with various weight in water % (or % mass) concentrations of methanol and glycol chemical inhibitors.

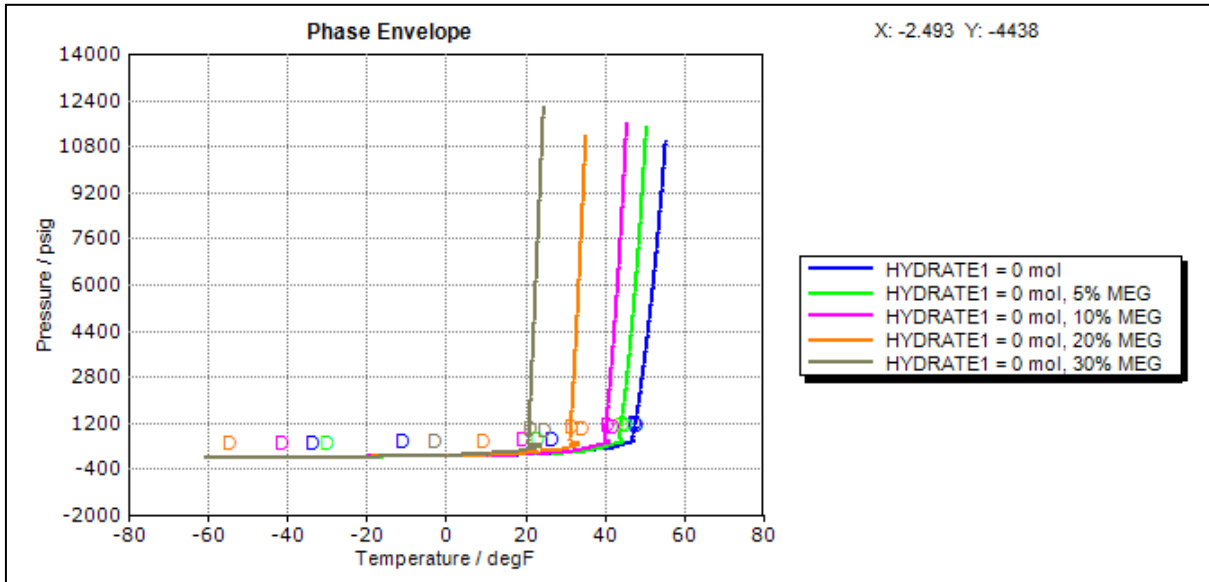
Methanol Inhibitors

Figure 9.15: Phase envelope with Methanol inhibitors (% Mass)



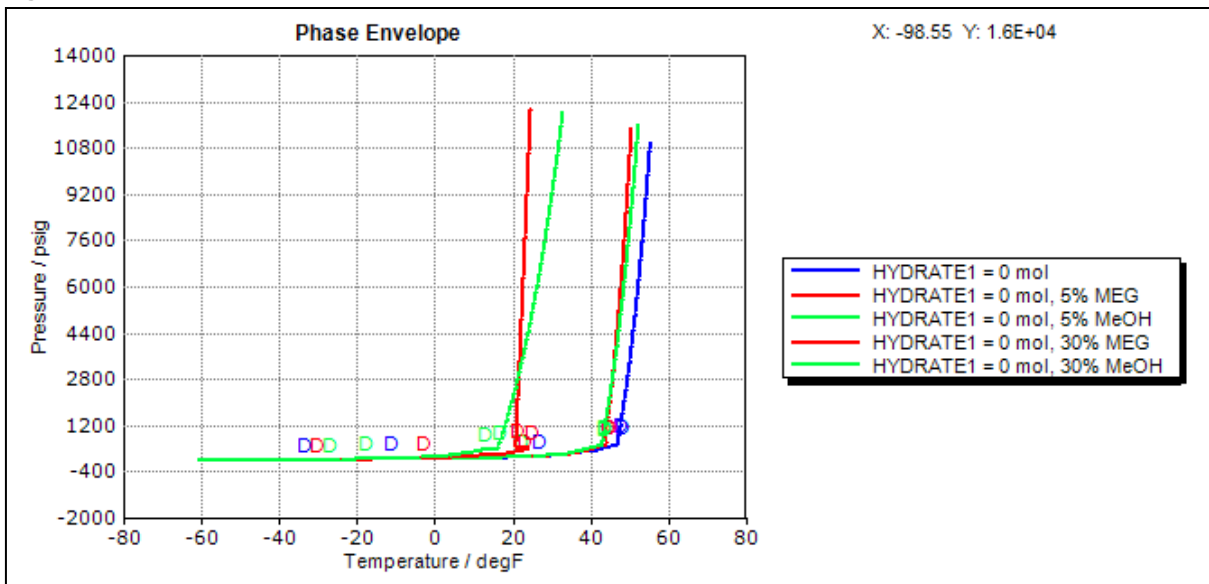
MEG Inhibitors

Figure 9.16: Phase envelope with MEG inhibitors (% Mass)



Methanol vs MEG Inhibitors

Figure 9.17: Phase envelope Comparison Methanol vs MEG (% Mass)



9.2.2.9 CO₂ 96% Mixture Composition #2 Fresh Water Case

In this fourth case a hydrate curve has been generated based on the presence of freshwater and a CO₂ stream composition #2 (Table 9.8) as detailed below, based on the potential range of CO₂ injected stream properties.

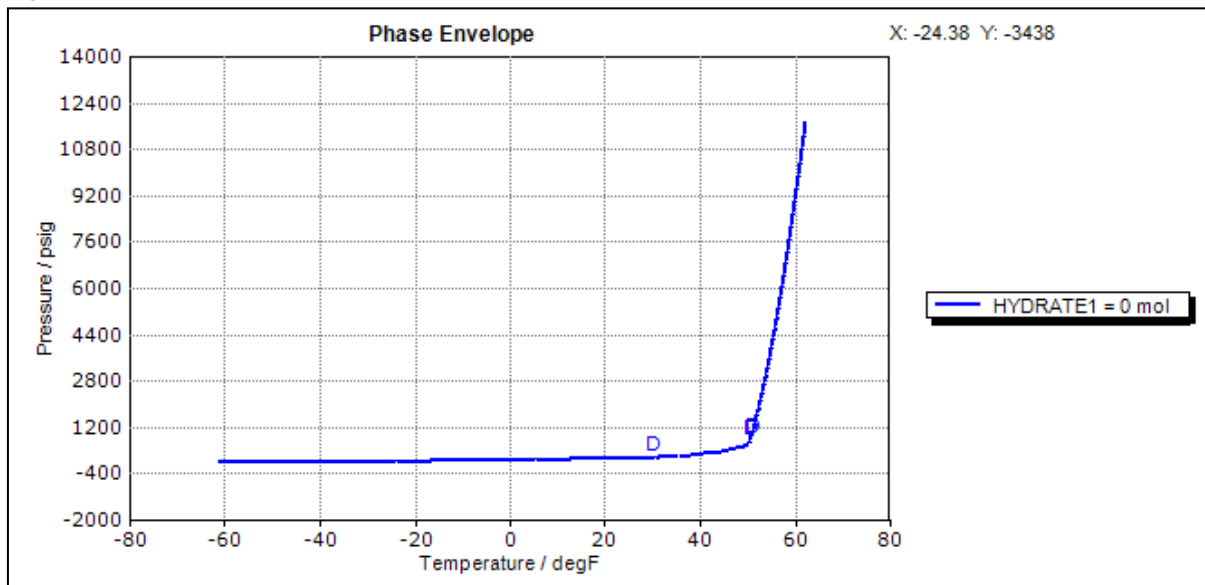
Table 9.8: CO₂ Mixture Composition #2

Components	% Mole
CO ₂	96.000
N ₂	1.444
H ₂ S	0.002
CO	0.400
NO	0.010
NO ₂	0.010
SO ₂	0.020
O ₂	0.002

The results for a pressure and temperature (PT) flash calculation at 37.4°F (3°C) and 2639psi and 2900psig, (182barg/200barg) chosen to reflect potential surface conditions indicate that hydrates will occur under these conditions. At a temperature of 37.4°F the calculated dissociation pressure is 242.6psig. At a pressure of 2900psig the calculated dissociation temperature is 53.7°F.

Phase Envelope

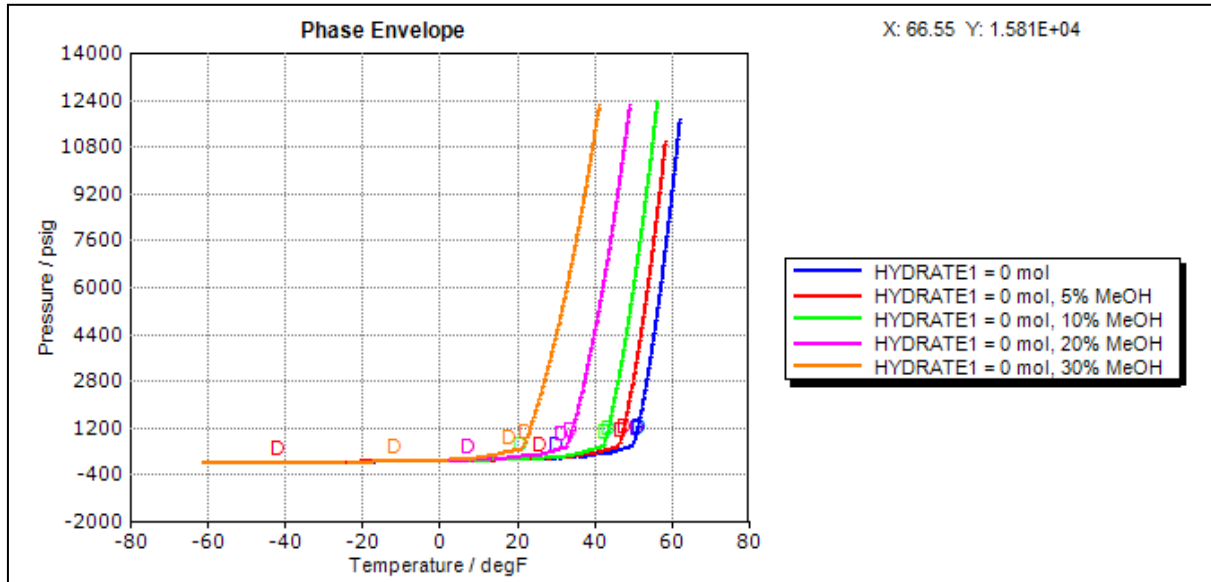
Figure 9.18: Phase envelope, Comp#2, freshwater, no inhibitor



Further hydrate curves were then developed based on the same composition #2, and fresh water but with various weight in water % (or % mass) concentrations of methanol and glycol chemical inhibitors.

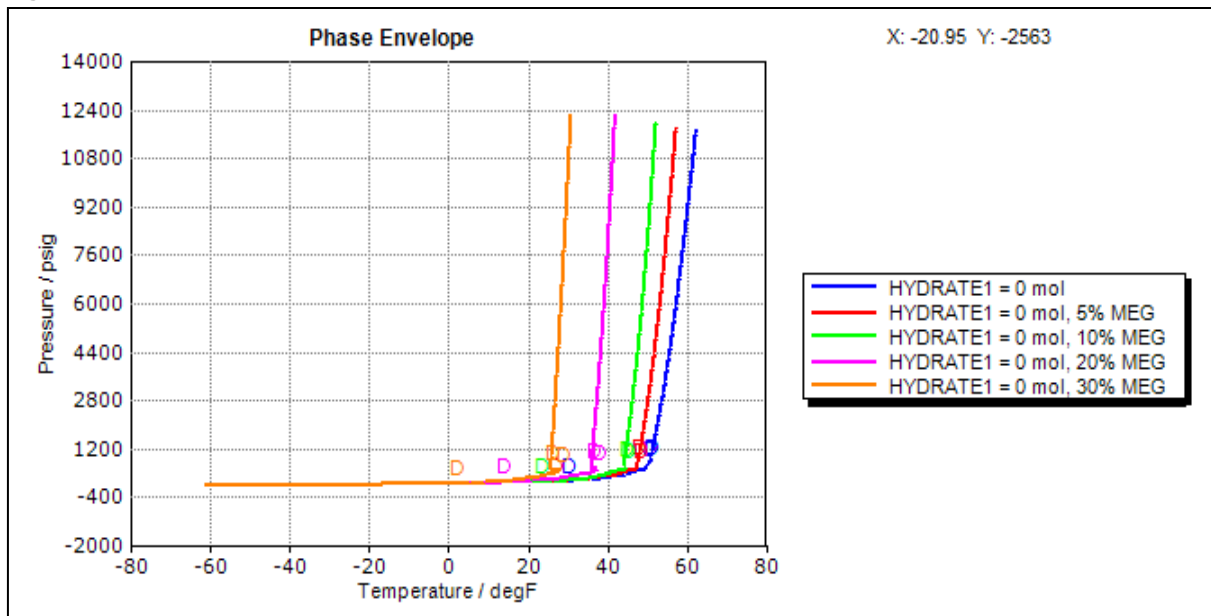
Methanol Inhibitor

Figure 9.19: Phase envelope with Methanol inhibitors (% Mass)



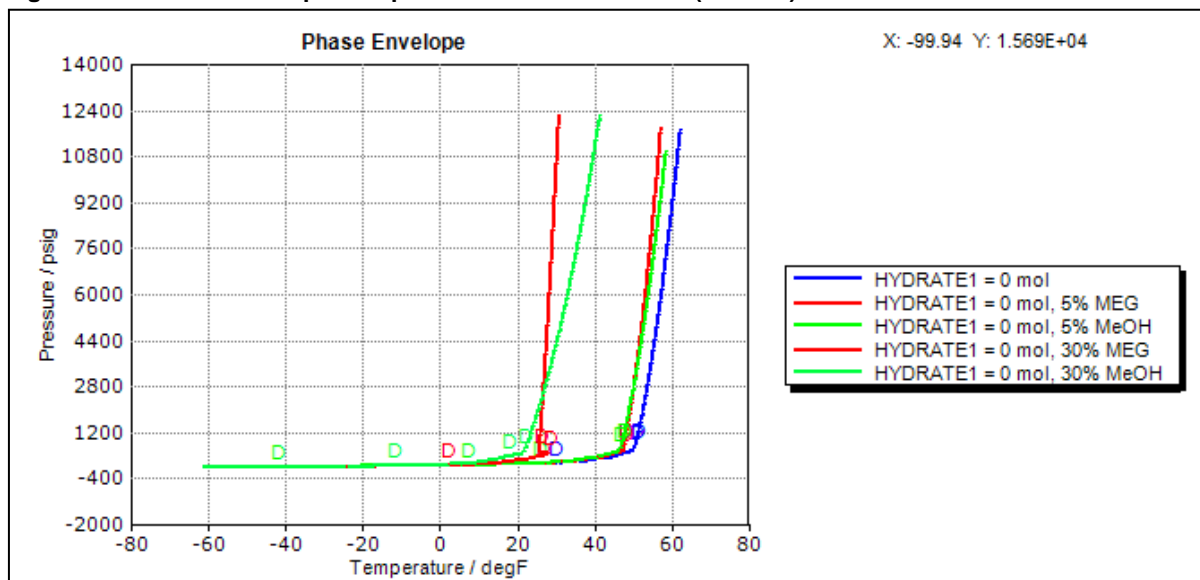
MEG Inhibitor

Figure 9.20: Phase envelope with MEG inhibitors (% Mass)



Methanol vs MEG Inhibitor

Figure 9.21: Phase envelope Comparison Methanol Vs MEG (% Mass)



9.2.2.10 Summary of Hydrate Modelling

The modelling above has demonstrated that a hydrate risk is present in the upper segment of the well under shut in conditions for all combinations of CO₂ stream composition and freshwater, seawater, and formation brine if present.

Use of chemical inhibitors methanol or MEG have been demonstrated to be effective at shifting the hydrate envelope to the left and thus reducing the hydrate threshold temperature for the various 96-99% CO₂ stream composition cases considered.

A minimum concentration in the water phase of 50% by mass of either methanol or MEG is required in theory to achieve an adequate reduction in the hydrate threshold temperature for the expected minimum wellbore temperature (-4°F / -20°C) conditions.

In practical terms a 70% MEG concentration by volume is recommended to counter any dilution and in reflection that concentrations greater than 70% are counterproductive in terms of increasing the freezing point of the MEG / water mixture.

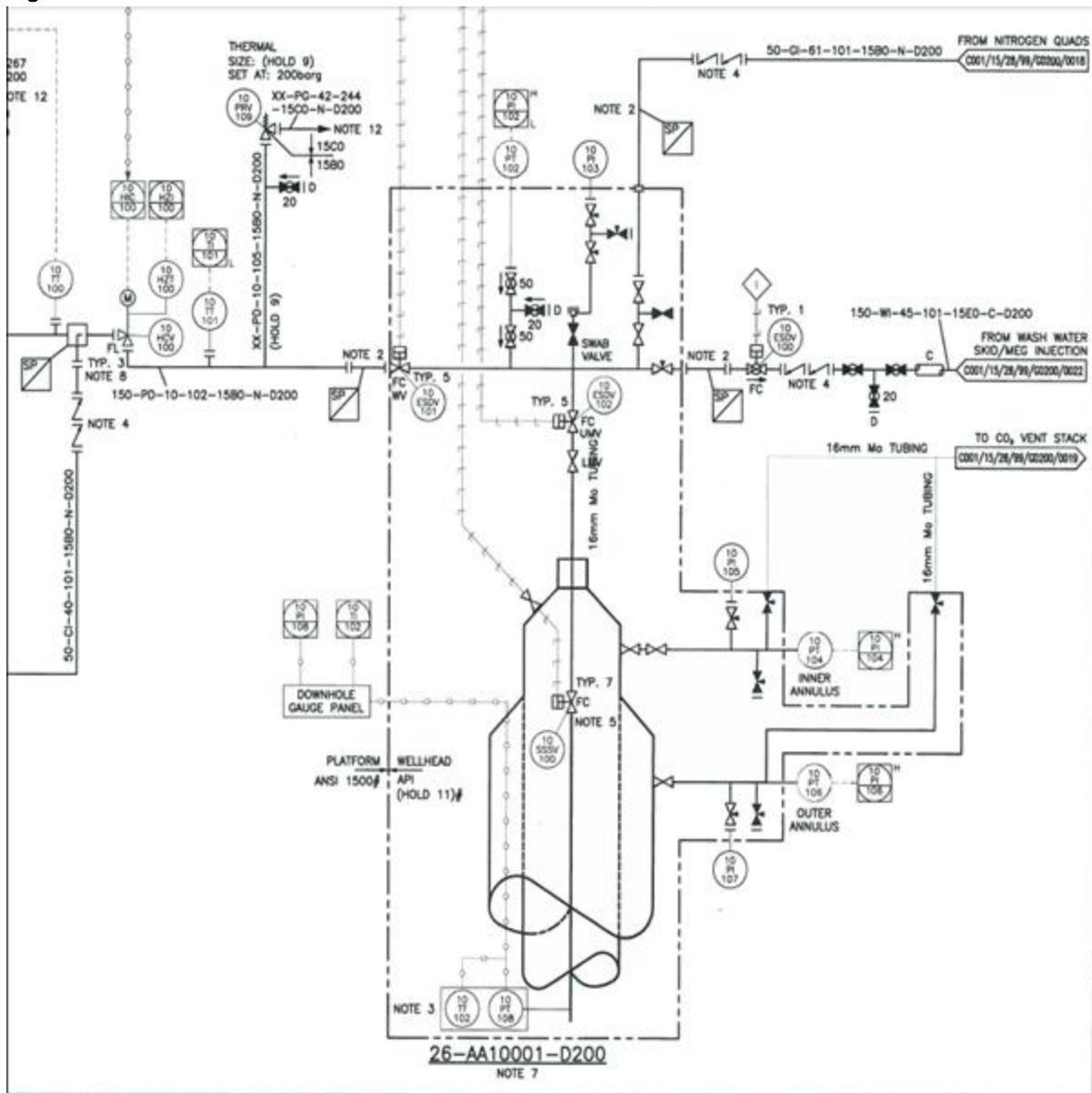
If considered for use a then 70% MEG concentration by volume is recommended to counter any dilution and in reflection that concentrations greater than 70% add no gain in terms of relevant applicable further reductions in the freezing point of the methanol / water mixture which is already well below required minimum performance temperatures for well CO₂ injection operations.

9.2.3 Recommended Hydrate Prevention Practice

9.2.3.1 Well Configuration

A Platform P&ID schematic extract is shown in Figure 9.22 to further illustrate the proposed well to platform interface arrangements.

Figure 9.22: Xmas Tree Platform Interface



9.2.3.2 Shut in / Start Up

A brine column is assumed present in the well at start up, and this will initially be completion brine. At subsequent shut-ins the well will contain formation water that has fluxed into the wellbore or seawater

residual from water wash intervention activities. In order to minimise hydrate risk the surface pipework would be purged of brine, water, and oxygen using the nitrogen purge system. Inhibited displacement spacers or pills should be spotted between any CO₂ / water phases, supplemented by nitrogen purging as nitrogen capacity allows. MEG treatment pill, volume of nominally 10bbls to 25 bbls (1.6 m³ to 4m³), is proposed.

Start-up procedures should consider staged approach to equalisation across valves and choke to allow equilibration to ambient temperature to minimise hydrate risk.

The optimum MEG / water compositional ratio of any pills should be optimised as a follow up to the flow assurance and hydrate characterisation and inhibition studies. For operational planning purposes a 70/30 MEG / water by volume ratio has been considered. Hydrate modelling suggest an situ 50% MEG volume fraction as adequate. However, a 70/30 ratio affords some margin for dilution should any free water be present in the well.

For hydrate remediation purposes MEG is considered for primary inhibition and remediation. Methanol is considered as a remote contingent for direct xmas tree cavity injection via chemical injection line should MEG be unsuccessful. This reflect the concern that methanol poses a formation risk due to halite precipitation.

9.2.4 Operating / Treatment System Requirements

9.2.4.1 Monoethylene Glycol (MEG)

For reasons outline in Section 9.2.1.7, MEG is preferred over methanol for hydrate inhibition and remediation for the White Rose project.

The current proposed platform documents detail the provision of MEG for treatment of the well. The MEG is supplied in bulk tanks (circa 13 bbls (2m³)). These would be landed stored on the weather deck and adjacent to the platform chemical injection system which comprises a pump and metering system.

The expected treatment concentration required in the water phase for effective inhibition for budgetary / planning purposes is 70% by volume. Details are discussed in Section 9.3.

9.2.4.2 Low Dose Hydrate Inhibitors

Low dose hydrate inhibitor products in general industry use can help to reduce logistical demands and costs over the longer term provided they are suitably qualified through appropriate study and applied to carefully defined stable conditions for which performance confidence is high.

However there does not appear to be a clear wells application in this CCS scenario given the base case understanding that the steady state conditions in this scenario carry negligible hydrate risk with water fraction maintained in the CO₂ injection stream at less than 50 ppmv.

9.2.4.3 Saline Brine

In theory with respect hydrates then use of a saline brine instead of seawater could be considered to improve the inherent level of hydrate inhibition of the water wash fluid however this would be counter to the driver of the aim to effectively removing the near wellbore salt.

9.2.4.4 Nitrogen

The provision of nitrogen has been considered in order of increasing capacity as discussed below.

Bottle Nitrogen

Low volume solution suited for surface line purging to ambient pressure to flush remove oxygen and water from pipework.

This is the currently proposed platform system.

Liquid Nitrogen tanks

Adequate to provide an N₂ purge capability of the entire well tubing volume (180 bbls / 28 m³) by injecting any washwater / formation water column into the reservoir. This would require circa 1-1/2 tanks.

Further consideration is required with respect manpower, service interval, SIMOPs use as discussed in separate ongoing workover intervention submission document WFP10.

Atmospheric Nitrogen System.

Adequate to provide repeated N₂ purge capability of the entire well tubing volume (180 bbls / 28 m³) by injecting any washwater / formation water column into the reservoir.

The purity of nitrogen produced using an atmospheric system is lower than a tank or bottle system and oxygen scavenger may be required.

9.3 Water Wash Specification

Geochemical modelling and experiments of CO₂-brine interactions during White Rose CO₂ injection suggest that near-well halite precipitation in the pore spaces – caused by removal of all the water in the near wellbore region, so-called drying-out – is likely. Due to the relative buoyancy of CO₂ to the formation brine, fresh formation brine flows into the near wellbore region when injection ceases. This provides the source for additional drying-out and subsequent halite precipitation, leading to a reduction in porosity which can reduce the permeability and therefore the injectivity. This in turn leads to a build-up in pressure and the risk of hydraulic fracturing which can compromise reservoir and cap-rock integrity. A water wash system is proposed to remedy this problem this problem can be remedied by using a water wash system. The section reviews the requirement for a water wash system which may impact completion metallurgy and completion design. The design of the water wash system will consider volumes required and the pressure and rate requirements in order to define the hydraulic horse power of the service pump.

9.3.1 Water Wash Parameters

The necessary water wash frequency was established through a variety of scenario analysis as approximately once every six months, making the base case as once or twice a year per well. For the White Rose project, a modular water wash package is considered fit for purpose, taking into account available platform interfaces and a short to medium term requirement. The required rates, injectivity, horsepower and filtration requirements are outlined below.

Based on the results of subsurface modelling and core analysis, the following water wash rate, duration and frequency used for the treatment design are:

Table 9.9: Water Wash Parameters

Water Wash Data	Application Rate
Water wash rate	175gpm (954m ³ /day)
Water wash duration	7 days per well
Water wash frequency	1 – 2 per year

In order to confirm the required rates are achievable without exceeding the fracture gradient, water wash injectivity rates were modelled using PROSPER. For inflow performance a single layer Darcy model with Wong-Clifford was chosen and sensitivities run based on the following parameters:

- permeability: 50md, 100md, 260md, 500md & 800md (Figure 9.23);
- reservoir thickness: 1014ft TVD (from P5W3 formation tops);
- perforated Interval: 100ft, 200ft ,300ft ,400ft & 500ft (assumed) (Figure 9.25);
- reservoir pressure: 2313 psi at top perforation at 7013ftMDBRT/4851ftTVD*; and
- wellhead pressures: 250 psig, 300 psig, 500 psig, 750 psig, 1000 psig.

*Reservoir pressure has been extrapolated to capture the sensitivity for top of perforation at 7013ftMDBRT/4851ft TVD. It has been extrapolated from the main reservoir pressure of 2048psi (141.2bara)@4383TVDSS.

Figure 9.23: PROSPER Injectivity rates modelling results, permeability sensitivity

Liquid Injection Rate, Stb/d:

		WHP, psig				
		250	300	500	750	1000
Permeability, K mD	800	1057	1731	4427	7798	11171
	500	1952	3197	8177	13953	18788
	260	4076	6676	15314	23432	29794
	100	6051	9912	19232	27980	35163
	50	7535	12342	21463	30189	37640

Bottom Hole Pressure (BHP), psig:

		WHP, psig				
		250	300	500	750	1000
Permeability, K mD	800	2385	2431	2615	2845	3076
	500	2379	2422	2592	2789	2954
	260	2366	2400	2514	2620	2704
	100	2354	2380	2444	2504	2553
	50	2345	2365	2404	2441	2473

Nb: Skin = 2
Perf Interval = 200 ft

Figure 9.24: PROSPER Injectivity rates modelling results, skin sensitivity

Liquid Injection Rate, Stb/d:

		WHP, psig				
		250	300	500	750	1000
Skin	20	4076	6676	15314	23432	29794
	15	3887	6366	14863	22742	29131
	10	3610	5911	14170	21683	28095
	5	3369	5518	13541	20719	27132
	2	3160	5174	12966	19839	26234

Bottom Hole Pressure (BHP), psig:

		WHP, psig				
		250	300	500	750	1000
Skin	20	2366	2400	2514	2620	2704
	15	2367	2402	2522	2633	2723
	10	2369	2405	2534	2652	2752
	5	2370	2407	2545	2669	2779
	2	2372	2410	2556	2684	2804

Nb: Permeability = 260 mD
Perf Interval = 200 ft

Figure 9.25: PROSPER Injectivity rates modelling results, perforated interval sensitivity

		WHP, psig				
		250	300	500	750	1000
Perforated Interval, ft	100	2681	4391	11233	17687	23817
	200	3887	6366	14863	22742	29131
	300	4729	7745	16758	25345	31851
	400	5350	8762	17987	26679	33528
	500	5833	9554	18859	27596	34680

Liquid Injection Rate, Stb/d:

		WHP, psig				
		250	300	500	750	1000
Perforated Interval, ft	100	2375	2414	2573	2723	2865
	200	2367	2402	2522	2633	2723
	300	2362	2394	2488	2578	2646
	400	2358	2387	2466	2540	2599
	500	2355	2382	2451	2515	2566

Bottom Hole Pressure (BHP), psig:

Nb: Skin = 5
Permeability = 260 mD

The results show that given a base case of 2048 psi reservoir pressure, 1014ftTVD reservoir thickness, 200ft of perforated interval, skin of 5 and 260mD permeability, a water injection rate of 6366 Stb/day (1012m³/day) can be achieved with a surface pump pressure of 300psig and keeping within the fracture gradient.

Table 9.10: Achievable pump pressures with proposed pumping equipment

HPP	Rate Required	Pump pressure (psi)
51	175gpm (954m ³ /day)	500
102	175gpm (954m ³ /day)	1000
153	175gpm (954m ³ /day)	1500
204	175gpm (954m ³ /day)	2000
250	175gpm (954m ³ /day)	2448

Solids filtration for the CO₂ (circa 10µm) is to be provided to ensure the quality of the injected CO₂ is such that particulate matter does not pose a risk of pore throat plugging which in turn would lead to a near wellbore injection skin. The main CO₂ stream solids risk identified is understood to be from residual solid particulates that may be present in the pipeline as a manufacturing artefact. The water wash modular package will also need to include a solids filtration system that also ensures the quality of the injected fluid in such that particulate matter does not pose a risk of pore throat plugging which in turn would lead to a near wellbore injection skin.

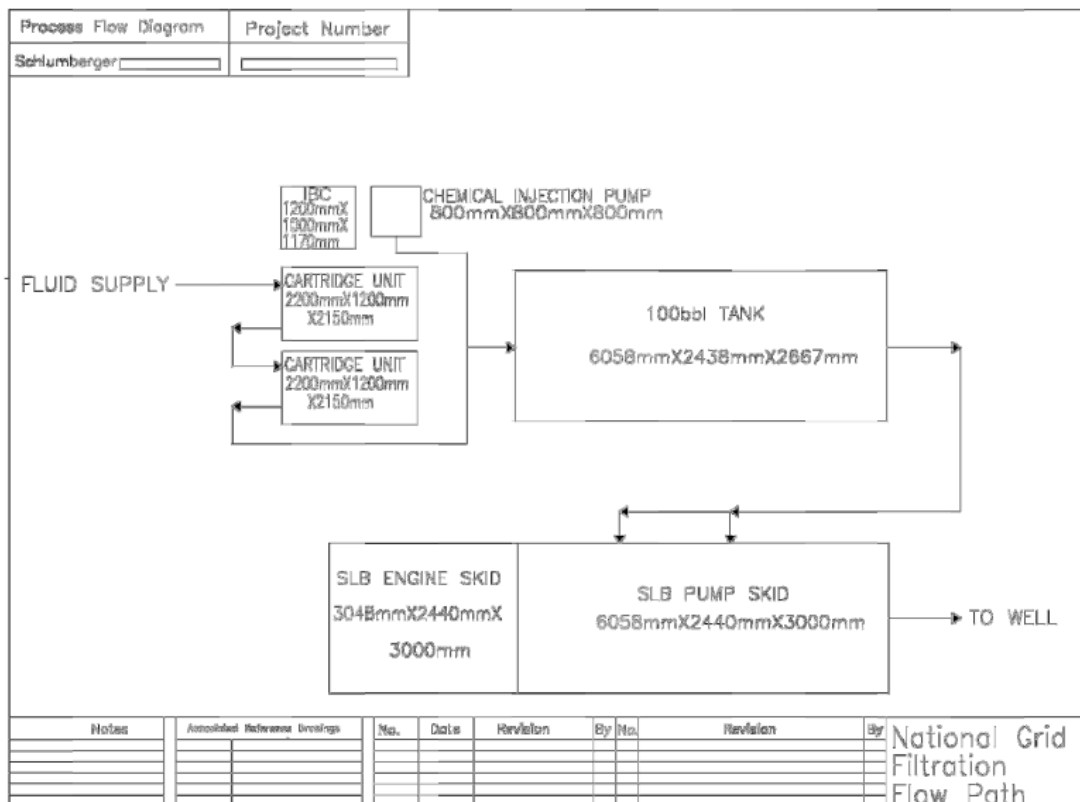
9.3.2 Water Wash Solution

The following describe the processes and equipment used to achieve the rate and filtration requirements based on the parameters set out above and also discusses additional factors which may affect the water wash treatment.

9.3.2.1 Equipment Specification

With the requirements set out above and the platform specifications taken into account, MI Swaco were asked to provide equipment details for a modular water wash skid solution capable of the required rates. The proposed skid consists of a pumping unit, chemical injection pump and two filtration cartridge units (Figure 9.26).

Figure 9.26: Layout of Temporary wash skid (Ref: 25)



9.3.2.2 Redundancy

Due to a requirement for 24hr operations, running for seven days per well, the chosen system has 100% redundancy to ensure that operations can take place without disruption.

9.3.2.3 Filtrations and Sea Water Source

As sea water typically poses no problems with respect to filtering, two twin vessel cartridge filter units are proposed. The first unit would be dressed with 10µm nominal filters to provide the initial filtration phase

and to protect the second unit. The second unit would be dressed with 2µm absolute filter elements providing the polish to ensure that the filtered fluid meets the cleanliness specification for pumping downhole. The flexibility of these units means that final micron ratings for the filtration can easily be adjusted pending final core analysis results.

The quality of the sea water source should be considered as part of the sea water lift system. The possibility of algal blooms in the sea water should be considered as part of the water wash skid filtration design and operation. Algal blooms can be formed when the mixing of sediments and nutrients from the bottom reach the zone where light penetrates, typically <20 m. Under these conditions, growth of plankton populations is stimulated and blooms can form in Spring, Summer and Autumn, (Ref. 24). The plankton that make up the blooms are typically classified by size. Femtoplankton are smaller than 0.2 microns and mainly comprises marine viruses. Larger are the picoplankton (0.2-2 microns), nanoplankton (2-20 microns), microplankton (20-200 microns), mesoplankton (0.2-2 microns) and macroplankton (2-20 microns). The spring bloom plankton is dominated by algal diatoms, most of which may be classed as microplankton (2-200 microns) and small flagellates, classed as nanoplankton (2-20 microns). Provision for managing this can be done in the form of the filters described above and biocide. The proposed 2 filters with 99.98% removal efficiency should prove an effective barrier against algal blooms entering the system. A planned chemical injection package also allows for the injection of a biocide to mitigate algal bloom development.

9.3.2.4 Chemical Inhibitors

A chemical injection precision pump package is required in the set up to allow biocide, oxygen scavenger, scale inhibitor and hydrate inhibitor to be injected in to the fluid stream at the correct dosage. Although the preferred injection points have been outlined in the table below, provision for chemical injection has been made on the upper mezzanine deck. Further detailed design will have to be undertaken to assess the suitability of these points. Chemical injection pumps can be provided as part of the modular water wash package if required. OR-11 (Oxygen scavenger provided by MI Swaco, similar products are also provided by other companies) is expected to be injected @ 100 ppm between the filter skid and the stock tank, with MB-5919 (Biocide provided by MI Swaco, similar products are also provided by other companies) injected at 500ppm between the stock tank and the HP pump. Scale inhibitor SI- 414N (provided by MI Swaco, similar products are also provided by other companies) is expected to be injected, prior to or upstream of the Oxygen scavenger (OR-11). These recommendations would require further laboratory testing to confirm their effectiveness and to be further optimised.

Water wash operations carry the greatest risk for corrosive environmental conditions to be developed in the wellbore, either before, during or after treatment through the combination of the presence of H₂O, CO₂ and O₂. It is therefore important that the metallurgy selected for the completion include the use of martensitic steels or 22% chromium and 25% chromium duplex stainless steel.

Based on the requirement of 175gpm (954m³/day) of water for 7 days, the following volumes of chemicals have been estimated as required:

Table 9.11: Estimation of chemical dosage and quantities required per water wash treatment

Chemical	Dosage	Quantity Required per water wash treatment (4200bbls)	Recommended Injection Point	Quantity of IBC (Intermediate bulk container) needed per water wash treatment
OR-11 Oxygen Scavenger	100ppm	1000 Litres	Between the filter skid and stock tank	1
MB 5919	500ppm	3500 Litres	Between the stock tank and HP pump	4 -5
Scale Inhibitor SI-414N	50 -100 ppm	Up to 1000 litres	Upstream of OR-11 injection in the sea water	1
Hydrate Inhibition	To be specified in WFS 4 Hydrate Inhibition Requirements	To be specified in WFS 4 Hydrate Inhibition Requirements	To be specified in WFS 4 Hydrate Inhibition Requirements	To be specified in WFS 4 Hydrate Inhibition Requirements

Modelling was undertaken by MISWACO to determine whether scale inhibitor would be required for pre-treatment of the well prior to the water washes. The scaling potential of mixtures of the brines was evaluated using ScaleSoftPitzer software. This allows identification of whether there is a scaling risk in a given scenario and if so then what type. The results are also used to select test conditions for any subsequent scale inhibitor performance testing, to ensure that scaling conditions in the test are representative. The calculation uses the known concentrations of ions in the seawater and formation water, plus the temperature and pressure. The software then compares the solubility limits of various potential scale types compared with the concentration of the appropriate pair of scaling ions in the combined brine in each case. The scale types that were assessed include barium, strontium and calcium sulphate, calcium carbonate and sodium chloride.

The results show that Barite (BaSO_4) is determined to be mildly oversaturated with a maximum tendency to scale when the formation water is mixed at a (60:40) ratio with the injected sea water. The maximum saturation ratio at ~3 is relatively low and it was determined that the mass of barite scale that could potential form is very low, in the order of 1-2mg/L. Celestite (SrSO_4) saturation ratio was calculated to be <1 and consequently the formation of downhole scale was not perceived as a risk. Calcium carbonate scale formation is highly unlikely as the saturation ratio is <0.01. The calcium sulphate scales gypsum and hemihydrate are also below saturation (<1) and risk of scale is negligible. Calcium sulphate scale anhydrite form had very mild oversaturation with a maximum saturation ratio just over 1 at mixing ratios between 10% and 50% sea water.

Although the scale prediction modelling indicated that a low scaling potential (and low mass of scale) for Barite, it is recommended that the initial sea water injection pre-treatments include scale inhibitor as a component of the application package. Recommended dosages can be found in the table above.

The platform will provide suitable support in terms of skid and storage for the supply of glycol to the wells for the purpose of hydrate inhibition. Details of hydrate inhibition requirements will be discussed in details in in WFS 4 Hydrate Inhibition requirements.

9.4 Conclusions

Results from modelling of transient processes, including initial start up, restart, turndown, ramp up, etc, show that single-phase conditions will be maintained in both the pipeline and the well during White Rose CO₂ injection. The system pressure re-establishes steady state operation after 2-3 hours following ramp-up or turndown of the flowrate (temperatures can take significantly longer due to the thermal inertia of the soil surrounding the onshore pipeline).

Once steady state conditions have been established, CO₂-water hydrates are not a concern given the proposed maintenance of the water fraction at sub-hydrate forming levels (50 ppmv).

The use of water wash to remove halite precipitation in the near well reservoir region presents the greatest risk of hydrate formation and well corrosion. The use of MEG is preferred as the primary chemical inhibition treatment.

Prewash MEG flush with a flowrate of 7,071 kg/h results in the pressure upstream of the wellhead remaining below the MAOP of 182 barg.

With a reservoir pressure of 150 barg, performing water wash in winter could result in wellhead pressures of around 146 barg, increasing up to 177 barg if water temperature does not rise as modelled while flowing down the tubing. The MAOP at the wellhead could be exceeded if the operation is not changed when the reservoir pressure increases later in field life. Injecting the same total volume of wash water over 9 days instead of 7 should prevent this from happening under the most conservative scenario considered.

The operating pressure at the wellhead during postwash MEG flush is not expected to exceed the MAOP in any case. The highest pressure would occur if MEG flush is started immediately after water wash, reaching 179 barg in the worst case.

Start-up following the water wash operation is not predicted to result in hydrate formation due to the MEG flushing prior to start-up, despite temperatures down to -19°C being predicted. Low temperatures can also be further mitigated by making use of the facility to inject nitrogen into the well prior to start-up to reduce J-T cooling.

No potential scaling issues are anticipated whilst the use of 25% chromium duplex stainless steel in the production tubing is selected to mitigate corrosion issues. Asphaltenes and wax are not considered risks for CO₂ injection wells.

10 Overview Field Development

10.1 Storage Permit Application

Carbon Sentinel Limited a subsidiary of National Grid Carbon, seeks consent to develop the Endurance Structure as a Carbon Capture and Storage Complex and commence the injection of CO₂ in to it.

The application is made in line with the UK legislation: The Storage of Carbon Dioxide (Licensing etc.) Regulations 2010 and the Storage of Carbon Dioxide (Termination of Licences) Regulations 2011) and EU CCS Directive on Geological Storage of Carbon Dioxide (Directive 2009/31/EC).

In November 2012, CSL was awarded the UK's first CO₂ Appraisal and Storage Licence (CS001) and in February 2013 the Crown Estate awarded an Agreement for Lease to CSL for the Endurance Storage Site.

The work undertaken by National Grid Carbon for the appraisal and characterisation of the site and for the design of the infrastructure was co-funded by both the European Economic Programme for Recovery (EEPR) grant agreement, Energy Technologies Institute (ETI) and DECC's UK CCS Commercialisation Programme.

10.2 Key Technological Aspects

For the offshore sections of the White Rose CCS Project, there are a number of key technological aspects and decisions that have led to this plan for the implementation of the project.

Extensive research, analysis and studies of the available geological, geophysical and well data culminated in the drilling of the 42/25d-3 appraisal well in 2013. The objectives and the design of the evaluation programme for this appraisal well was to gather additional information to assist in characterising the Endurance Storage Complex. Subsequent to the drilling of the well, there was a comprehensive programme of testing and analysis and particularly the work on the core continued for over 20 months. The results and data from this post-appraisal work programme have been included in the suite of geological, reservoir and geomechanical models that have been used to characterise and predict the behaviour of the Endurance Storage Complex.

Both in the characterisation of the Storage Site and in the plan for the development of the Storage Complex, technology and techniques proven in the hydrocarbon exploration and production industry have predominantly been used. Where the specialist requirements for the permanent storage of CO₂ exceed the capabilities or experience of the oil and gas industry, know-how, research and peer review from the CO₂ storage and enhanced oil recovery industries has been incorporated to inform the project design and implementation.

As the White Rose CCS Project plans to use in 20 years less than 2% of the estimated static storage capacity of the Endurance structure, if the behaviour of the Storage Site conforms to expectations after injection has commenced, an application for the expansion of the project may be considered. Pressure response measurements will be used to revise the reservoir models immediately after commencement of CO₂ injection. Approximately four years of continual model updates following injection start-up may be CO₂ required to fine tune the dynamic modelling of the Storage Site and provide additional information to feed into any expansion plan. However, some of the White Rose infrastructure, particularly the pipeline and transport assets have been designed to have spare capacity for a possible future upscaling of the storage volume and to provide a hub for transmission of CO₂ to other nearby storage sites.

Since National Grid's work on CCS commenced over six years ago, the evolution of the project has considered many options and has made some fundamental decisions that have led to the current proposal for the transport and storage infrastructure for CO₂ capture and storage. Having considered both depleted gas fields and saline aquifer structures in the southern part of the North Sea, saline aquifers were prioritised for the first CO₂ store for the Humber area for a number of reasons including:

- availability: most of the gas fields will still be producing at the time the CO₂ store is planned to be developed;
- capacity: the storage capacity of the aquifer structures is generally larger than the volume of the gas fields; and
- storage integrity: it is anticipated that wells drilled for hydrocarbon exploration and development present the greatest risk for the long term security of the CO₂ Storage Complex and as there are significantly fewer wells drilled through the saline aquifer structures, long term Storage Complex security will be superior and containment risks will be minimised.

10.2.1 Use of Dense Phase CO₂ Pipeline:

CO₂ can be transported either in gaseous phase or in dense phase. For longer pipelines in excess of a few kilometres, despite the higher pressure requirements, the advantages of dense phase CO₂ transportation far outweigh the disadvantages:

- higher flow capacity per unit cost; increased capacity outweighs additional cost of increased pressure requirement;
- lower pressure drop per unit mass of CO₂;
- ease of operation and benefits of the use of pumps rather than compressors;
- the use of dense phase also precludes the necessity for the provision of injection compressors on the offshore platform since booster pumps can be located onshore; and
- the dense phase pipeline is to be constructed from carbon steel (rather than high cost chrome/nickel alloy steel) and CO₂ purity is tightly controlled and dehydrated to less than 50 ppm to preclude any corrosion or hydrogen embrittlement issues.

10.2.2 Oversizing of the pipeline for future expansion:

The transportation assets from the Camblesforth Multi-junction to the Endurance platform location have been sized to be able to transport a maximum of 17MTPA of CO₂ compared to the White Rose requirement of up to 2.68MTPA. Should the pressure response of the storage site be satisfactory, it is envisaged that future emitters will connect into the Camblesforth Multi-junction to benefit from the security and cost benefits of shared CO₂ transportation. These additional loads may then be stored in the Endurance Storage Site (if approved via a new Storage Permit application) or alternatively passed to other future storage sites that might be developed nearby.

10.2.3 Use of injection platform instead of a subsea installation:

The decision to use an offshore platform rather than sub-sea facilities was based on operability concerns associated with a 'first-of-a-kind' project. Although the characterisation of the Storage Site and Storage Complex is comprehensive, there is limited experience of CO₂ injection in offshore saline reservoirs and a platform allows for a substantially more flexible operating mode and provides enhanced capability for

monitoring and measurement of key parameters. The reasons for choosing offshore platform over a purely subsea installation include:

- dry trees with their benefit of accessibility;
- workover capabilities from the platform without the need for a well intervention vessel for electric line or slickline interventions or water wash for salt precipitation in the near wellbore region;
- active control of injection pressures and flowrates between wells;
- accurate individual well metering for the allocation of CO₂ volumes between wells;
- filtration of the CO₂ stream before injection;
- data handling for MMV Plan equipment – high data transmission requirements are needed for the seabed micro-seismic array and the downhole pressure and temperature sensors;
- provision for expansion, including water production risers, spare well slots, CO₂ export risers.

10.2.4 CO₂ storage volume

The static CO₂ storage capacity estimate for Endurance using the mid-case NPV (net pore volume) of 4.6 Bm³, a mid-case irreducible (minimum) water saturation of 0.15 and a CO₂ density of 700kg/m³ at in situ condition is equal to 2700MT. This means that the total maximum White Rose CO₂ of 53.6MT will take up only 2% of this capacity. Considered as an isolated volume a 194bar increase in Endurance pressure is predicted as a result of White Rose CO₂ injection, which is probably sufficient to fracture the cap rock. However, it is highly probable that Endurance is not an hydraulically isolated unit but rather both contiguous with the Bunter sandstone that outcrops at the sea bed south east of the structure and also connected to a Greater Bunter aquifer estimated to be at least a hundred times its size. Depending on the size of the connected Greater Bunter aquifer and whether the outcrop is closed or open, the pressure increase at the crest of the structure from injecting White Rose CO₂ is between 38.0bar and 65.0bar with a most likely value of 40bar.

The dynamic capacity depends on the maximum allowable excess pressure (above hydrostatic) to which the Storage Site will be subjected. The excess pressure is a function of the injection rate as well as the connectivity and extent of the aquifer that is attached to the Endurance Structure. Although modelling indicates that pressure relief via water production is not necessary for White Rose volumes, the various relevant factors cannot be definitively determined until injection has commenced and the pressure response of the system has been measured. The evidence that the Esmond gas field, some 60 km to the north, is in pressure communication with the Endurance Storage Site provides a positive indication of the connectivity to the Greater Bunter although quantification is still required.

10.2.5 Storage mechanisms for CO₂

There are four commonly recognised storage or trapping mechanisms for the CO₂ that is injected into underground reservoirs. For each individual reservoir the proportion of the total CO₂ subject to each mechanism is dependent on the type and structural configuration of the rock, the composition of the formation brines, the fill ratio of the Storage Site and the timing. To a lesser extent, the proportions of the CO₂ trapped by each mechanism at each time-step are dependent on the ambient pressure and temperature. Geochemical modelling combined with reservoir simulation results provide the best determination of the magnitude of the proportion attributable to each mechanism during the evolution of the store. The four trapping mechanisms are list below.

1. Structural/Hydrodynamic Trapping – This is the most dominant of the trapping mechanisms at early time. The super-critical CO₂ is more buoyant than the formation brine and will therefore flow up through the sandstone until it meets the caprock and then will continue laterally until it reaches the crest of the structure.
2. Residual Trapping – As the CO₂ percolates through the reservoir from the injection wells it forms a plume that migrates vertically under the influence of buoyancy forces, displacing formation brine. Upward migration of CO₂ continues after injection ceases and as the brine returns to the pore volume previously occupied by the plume, an amount of CO₂ equivalent to the critical gas saturation remains trapped within the rock matrix. The volumes trapped by this mechanism depends on the location of the injection wells compared to the crest of the structure, the depth and extent of the CO₂-brine contact and the depth and profile of the injection perforations
3. Solubility Trapping – This process is caused by the CO₂ being dissolved in the formation brine. It is driven by the diffusion of CO₂ in to the formation brine and therefore occurs in the area of the plume and immediately under the CO₂-brine contact. This process continues for thousands of years. Also, as the brine with CO₂ dissolved in it is denser than the brine itself it consequently initiates convection and downward movement of the CO₂-rich brine. In the very long-term all the structural/hydrodynamically trapped CO₂ will diffuse into the brine.
4. Mineral Trapping – A range of geochemical reactions occur between the CO₂ and the CO₂-rich brine both with the reservoir rock and to a much lesser extent with the caprock. These reactions have been modelled by geochemical simulation.

10.2.6 Geological modelling of the Storage Site and Storage Complex:

For the response and performance of the Storage Site and Storage Complex under operating conditions, extensive use of simulation and modelling is required in order to reliably predict the outcomes of the complicated and inter-related effects. The modelling uses separate platforms for the different sections and each subsequent platform uses the output of preceding stages. The order of precedence of the models used for the Endurance Storage Site and Storage Complex is as listed below.

1. Static geological modelling of the Storage Site and Storage Complex – This model uses as its inputs the seismic interpretation of the structure, the under and overburden. It uses the logs from local and regional wells in order to specify the stratigraphy. For the Storage Site, it uses the log and core analyses to specify the facies for each subdivision and to interpolate and extrapolate the primary rock properties across the structure. The key outputs from this stage of modelling are the structural framework model and the permeability and porosity fields within the reservoir intervals.
2. Reservoir Simulation is the dynamic modelling of the reservoir. Taking the static modelling results and adding permeabilities, relative permeabilities, fluid characteristics and wells, the movement of CO₂ from the injection wells to its final static location are predicted. Additional data comes from the analysis of core and well testing and is significantly upscaled from the limited local results right across the reservoir structure. For these tasks, the information gained from the appraisal well namely; routine and special core analysis results, advanced vertical interference tests and conventional production and injection test interpretation results have been most important. The outputs of the reservoir simulation provided both the expected CO₂ plume migration plus the pressures and temperatures across the structure – key inputs to the geomechanical modelling.
3. Geochemical Modelling – the geochemical modelling assesses the reactions of the Mineral Trapping mechanism over a 10,000 year time-frame. The most significant outputs to be carried over to the geomechanical modelling below are any predicted changes to the mechanical properties of the

reservoir and the cap rock and consequently any long-term changes to the trapping and seal integrity of the Storage Complex.

4. Geomechanical Modelling – This model takes in the full RSFM from the static geological modelling and then populates it with mechanical properties across the structure to predict movement and stress changes based on the pressure and temperature responses from the dynamic simulation of CO₂ injection. The modelling process is more fully described in Section 7.2 and uses confining blocks to establish boundary constraints both laterally and below the underburden. Specific inputs are derived from logs and from mechanical properties testing of core samples. Also included in the model are the North-West striking overburden faults interpreted from seismic data.

10.2.7 Multiple injection wells for maximum system availability

In order to maximise the injected volumes of the CO₂ generated by the White Rose OPP, high system reliability is required from the transport and storage assets. For this reason, three wells will be drilled so that during any interventions that may be required on the wells, the system can continue to operate with one well in a shut-in condition whilst the other two are available to inject at the full production rate of the power plant.

10.3 Additional Components of the Field Development Plan

10.3.1 Measurement, Monitoring and Verification Plan

Proposes equipment and methodologies to assess the conformance of the Storage Complex compared to its predicted response and to monitor its confinement of the stored CO₂. It provides routine and regulatory reporting of storage volumes and regularly updates and revises performance predictions. It is divided over the phases of the project when different requirements for the verification of conformance and confinement are in effect.

10.3.2 Corrective Measures Plan

Describes the measures and actions taken to correct significant irregularities or to close leakages in order to prevent, mitigate or stop the release of CO₂ from the Storage Complex. A significant irregularity detected implies the risk of a leakage or a risk to the environment or to human health. The corrective measures plan acts, in order of priority:

- to prevent risks to human health;
- to prevent risks to the environment; and
- to prevent leakage from the storage complex.

10.3.3 Storage Site and Storage Complex Risk Assessment

Independent scientific and mathematical consultants, Quintessa have conducted a quantitative risk assessment of the Storage Complex.

Determines the risks associated with the underground aspects of CO₂ storage throughout the lifecycle of the White Rose CCS Project and identifies any risks that might call into question the long-term safety, integrity or the effectiveness of the Storage Complex and any risk to human health and the environment.

The results of the risk assessment provide a high level of confidence that long-term containment of the CO₂ planned to be stored will be achieved and the system will evolve to long-term stability. Risks to human health or environmental receptors associated with loss of containment (in the unlikely event that it occurs), the displacement of brine via the outcrop and deformation at the seabed are either low or very low.

10.3.4 Project Environmental Statement

Documents the results of the EIA process, highlighting environmental sensitivities, identifying potential hazards, assessing/predicting risks to the environment and identifying practical mitigation and monitoring measures. The Environmental Impact Assessment process was initiated at an early stage in project planning and relevant information was collected relating to the natural environment and other users of the sea at or within a distance from the proposed pipeline route and surface facilities where interactions were foreseeable. It also considers, as far as possible at this time, the decommissioning of the offshore infrastructure.

11 References

1. Glennie, K. W. and Boergner, P. L. E.. Sole Pit Inversion Tectonics. In Illing, L.V., and Hobson, D.G., eds., *Petroleum Geology of the Continental Shelf of North-west Europe: Special Publication*, Institute of Petroleum, London, p. 110-120.1981
2. Brook, M., Shaw, K., Vincent, C., and Holloway, S., "Gestco case study 2a-1: Storage Potential of the Bunter Sandstone in the UK sector of the southern North Sea and the adjacent area of Eastern England", British Geological Survey commissioned report CR/03/154N, Keyworth, Nottingham, 2003.
3. Wiese, B., Nimitz, M., Klatt, M. and Kühn, M., "Sensitivities of injection rates for single well CO₂ injection into saline aquifers", *Chemie der Erde – Geochemistry*, 70, Suppl. 3, pp. 165-172, (2010)
4. Noy, D.J., Holloway, S., Chadwick, R.A., Williams, J.D.O., Hannis, S.A. and Lahann, R.W., "Modelling large-scale carbon dioxide injection into the Bunter Sandstone in the UK Southern North Sea", *International Journal of Greenhouse Gas Control*, 9, pp. 220-233, (2012).
5. Hassanzadeh, H., Pooladi-Darvish, M., Elsharkawy, A.M., Keith, D.W., and Leonenko, Y., "Predicting PVT data for CO₂-brine mixtures for black-oil simulation of CO₂ geological storage", *International J. Greenhouse Gas Controls*, 2, (2008), pp. 65-77
6. Pruess, K. and Zhang, K., "Numerical Modelling Studies of the Dissolution-Diffusion-Convection Process During CO₂ Storage in Saline Aquifers", Lawrence Berkeley National Laboratory, Nov 2008
7. NORTH SEA GEOLOGY, Technical report produced for Strategic Environmental Assessment – SEA2, TR_008, BGS, Edited by Peter Balson, Andrew Butcher, Richard Holmes, Howard Johnson, Melinda Lewis, Roger Musson Drafting: Paul Henni, Sheila Jones, Paul Leppage, Jim Rayner, Graham Tuggey. Aug 2001
8. Johnson, H, Warrington, G., and Stoker, S. J.: Lithostratigraphic nomenclature of the UK North Sea, 6. Permian and Triassic of the Southern North Sea, BGS, 1994.
9. Heinemann, N., Wilkinson, M., Pickup, G.E., Haszeldine, R.S. and Cutler, N.A., "CO₂ storage in the offshore UK Bunter Sandstone Formation", *International Journal of Greenhouse Gas Control*, 6, pp. 210-219, (2012).
10. <http://www.bgs.ac.uk/science/co2/home.html>
11. Cooke-Yarborough, P., and Smith, E., "The Hewett Fields: Blocks 48/28a, 48/29, 48/30, 52/4a, 52/5a, UK North Sea: Hewett, Deborah, Big Dotty, Little Dotty, Della, Dawn & Delilah Fields", Edited by Gluyas, J.G., and Hichens, H.M., Geological Society, London, *Memoirs*, 2003, v. 20, p. 731-739
12. Bennion, D.B., and Bachu, S.: "Supercritical CO₂ and H₂S – Brine Drainage and Imbibition Relative Permeability Relationships for Intergranular Sandstones and Carbonate Formations", SPE Paper Number 99326, 2006.
13. Appelo, C. A. J. & Postma, D.: *Geochemistry, Groundwater and Pollution*, ninth ed. Balkema, Rotterdam, 2013
14. Verma, A. and Pruess, K., Thermohydrologic conditions and silica redistribution near high-level nuclear wastes emplaced in saturated geological formations. *J. Geophys. Res.* Vol. 93(B2), 1159-1173, 1988
15. Xu, T. and Pruess, K., Numerical simulation of injectivity effects of mineral scaling and clay swelling in a fractured geothermal reservoir, Report LBNL-56175, Berkeley, CA, Lawrence Berkeley National Lab., 2004
16. Pruess, K., and Muller, N., Formation dry-out from CO₂ injection into saline aquifers: 1. Effects of solids precipitation and their mitigation, *Water resources research*, Col. 45, W03402, 2009
17. Peysson, Yannick, Laurent André, and Mohamed Azaroual. "Well Injectivity during CO₂ Storage Operations in Deep Saline aquifers—Part 1: Experimental Investigation of Drying Effects, Salt

- Precipitation and Capillary Forces.” International Journal of Greenhouse Gas Control 22 (March 2014): 291–300. doi:10.1016/j.ijggc.2013.10.031.
18. Grude, S., J. Dvorkin, A. Clark, T. Vanorio, and M. Landrø. “Pressure Effects Caused by CO₂ Injection in the Snøhvit Field.” First Break 31, no. 12 (Dec 2013).
 19. Nermanrud C., Eiken O., Hensen O.R., Statoil, Bolas H.M.N., Simmenes T.H., Teige G.M.G., Hansen H., Johansen, S.: Importance of Pressure Management in CO₂ Storage, OTC23961, Offshore Technology Conference held in Houston, Texas, USA, 6-9 May 2013.
 20. Bolourinejad B., and Herber R : Experimental and Modeling Study of Salt Precipitation During Injection of CO₂ Contaminated with H₂S into Depleted Gas Fields in the Northeast of Netherlands, SPE 164932, 2014.
 21. Rowe, A.M. Jr., and Chou, J.S., “Pressure-Volume-Temperature-Concentration Relation of Aqueous NaCl Solutions”, J. Chem. Eng. Data, 15, p. 61, 1970.
 22. A Guide to potential impacts of leakage from CO₂ storage. Pearce J, Blackford J, Beaubien S, Foekema E, Gemen, V, Gwosdz S, Jones D, Kirk K, Lions J, Metcalfe R, Moni C, Smith K, Steven M, West J and Ziogou F. British Geological Survey. R Research into Impacts and Safety in CO₂ Storage (ISCS), 2014. Available from www.riscs-co2.eu 70 pages.
 23. Jolley, S. J., Fisher, Q. J., Ainsworth, R. B., Vrolijk, P. J. & Delisle, S. (eds) Reservoir Compartmentalization. Geological Society, London, Special Publications, 347, 1–8. DOI: 10.1144/SP347.1 0305-8719/10/\$15.00 # The Geological Society of London 2010.
 24. Bennion, D.B., and Bachu, S.: “Supercritical CO₂ and H₂S – Brine Drainage and Imbibition Relative Permeability Relationships for Intergranular Sandstones and Carbonate Formations”, SPE Paper Number 99326, 2006
 25. “Multi-Speed Performance Curve”, Sulzer GSG 100-300 (C)(Bd) Curve Number 4611.04.421-01,, September 2014
 26. Natural Gas Hydrates, John Carroll, Gulf Publishing, 2003.
 27. Prevention of Hydrate Formation in the CO₂ Injection Wells to the Saline Aquifer, Sung-Oh Yang, and Stephen Hamilton, MSi Kenny (UK) Ltd, and Rohan DeSilver, National Grid Carbon (UK) Ltd, Paper submitted to SPE 16/08/12.
 28. Impact of Common Impurities on CO₂ Capture, Transport, and Storage, 2011-2014 Programme, September 2013, Institute of Petroleum Engineering, Heriot-Watt University.
 29. Tohidi, B., Østergaard, K. K., Danesh, A., Todd, A. C. and Burgass, R. W. “ Structure-H gas hydrates in petroleum reservoir fluids” Department of Petroleum Engineering, Heriot-Watt University, Edinburgh EH14 4AS, Scotland, 2009
 30. Chapoy, A., Nazeri, M., Kapateh, M., Burgass, R., Coquelet, C., Tohidi, B., Effect of Impurities on thermophysical properties and phase behaviour of a CO₂ rich system in CCS, Hydrate Flow Assurance & Phase Equilibria Research, Department of Petroleum Engineering, Heriot-Watt University, Edinburgh EH14 4AS, Scotland, International Journal of Greenhouse Gas Control 19 (2013) 92-100, 2013.
 31. Chapoy, A., Coquelet, C., Haifan, L., Tohidi, B., Vapour-Liquid equilibrium data for the hydrogen sulphide (H₂S) + carbon dioxide (CO₂) system at temperatures from 258 to 313K, Hydrate Flow Assurance & Phase Equilibria Research, Department of Petroleum Engineering, Heriot-Watt University, Edinburgh EH14 4AS, Scotland, Fluid Phase Equilibria 356 (2013) 223-228, 2013.
 32. Burgass, R., Chapoy, A., Duchet-Surchaux, P., Tohidi, B., Experimental water content measurements of carbon dioxide with hydrates at (223.14 to 263.15)K and (1.0 to 10.0) Mpa. Centre for Gas Hydrate Research, Department of Petroleum Engineering, Heriot-Watt University, Edinburgh EH14 4AS, Scotland, J.Chem Thermodynamics 69 (2014) 1-5, 2014.
 33. ABC Guide to Gas Hydrate Awareness, Shell UK Ltd, 2002.
 34. Infochem Multiflash Modelling Software, Version 4.2.16, November 2013

35. Edmonds, B., Moorwood and R. A. S., Szczepanski R. "Hydrate Update", Infochem Computer Services Ltd South Bank Technopark, 90 London Road, London SE 1 6 L Nare 1998.
36. Substrate-controlled succession of marine bacterioplankton populations induced by a phytoplankton bloom, 2012. H. Teeling et al.
37. McCoy, S.T. 2008. The Economics of Carbon Dioxide Transport by Pipeline and Storage in Saline Aquifers and Oil Reservoirs. PhD Thesis, Carnegie Mellon University.
38. CO₂ Near Well Bore Displacement (Halite) Study, Weatherford Laboratories (UK), Winfrith Newburgh Jul 2015.

12 Glossary

Term	Explanation
ϕ	Friction Angle (degrees)
%	Percentage
4D	Four Dimensional (3D and Time)
a, m, n	Coefficients used to Calculate water saturation from Archie Equation
AOI	Area of Interest
API	American Petroleum Institute (generally with reference to material and equipment specifications)
Ar	Argon
Atm	Atmosphere
ATT	Acoustic travel time
AUV	Autonomous underwater vehicle (free swimming submersible)
bar	metric unit of pressure, but not part of the International System of Units (SI). One bar is exactly equal to 100 000Pa and is slightly less than the average atmospheric pressure on Earth at sea level
bara	Absolute Pressure
barg	(Gauge Pressure) Pressure reading relative to current atmospheric pressure
BCU	Base Cretaceous Unconformity
BFV / FFV	Bound fluid volume / free fluid volume from NMR tool
BGS	British Geological Survey
BHP	Bottom Hole Pressure
BHT	Bottom Hole Temperature
BOP	Blow-out preventers for well control
Br	Bromide
BSF	Bunter Sandstone Formation
°C	Degrees Celsius
CCF	Completion Connection Factor
CCS	Carbon Capture and Storage (carbon sequestration)
CH ₄	Methane
Cl	Chloride
C _L	Land constant
CO ₂	Carbon Dioxide
CPI	Computer Processed Interpretation
CPL	Capture Power Limited
CPU	Central Processing Unit
CRA	Corrosion Resistant Alloy
CsCl	Caesium chloride
CT	Computed Tomography
CWC	Concrete Weight Coating (for offshore pipelines)
D	Darcy
DCO	Developments Consents Order
DECC	UK Government's Department of Energy and Climate Change
DINO VAM	Vallourec proprietary casing connection type
DST	drill stem test (a procedure for isolating and testing the pressure, permeability and productive capacity of a geological formation during the drilling of a well)
DT	Delta T - interval transit time from sonic tool

Term	Explanation
DTcl	Delta T value in 100% clay
DTfl	Delta T value in 100% fluid
DTma	Delta T value in 100% matrix
Dual Packer Mini	The Dual Packer Mini-Frac Test is a pressure test using a formation tester such as a MDT to fracture the formation between two inflatable packers that isolate a small area of the formation in a well bore. The data is collected for geomechanical properties.
DVHM	Diffuse Vertical Hardground Model
E100	Blackoil ECLIPSE 100 simulator
E300	Compositional ECLIPSE 300 simulator
ECS	Electron capture Spectroscopy Tool
ELAN	A computer product, which employs statistical methods, error minimizing or probabilities and uses constraint equations. to solve a set of over-determined equations for the "best" answer, to achieve an over-determined case,.
Electro Facies	Facies that have been generated on either raw or processed wireline logs data. Such facies are often based on reservoir quality and may not be related to sedimentological facies that have been logged from core.
EOR	Enhanced Oil Recovery
EPS	End Point Scaling
ESP	Electrical Submersible Pump
EU	European Union
Facies	A body of rock with specified characteristics that could relate to the process of sedimentation or reservoir quality, or both.
FEED	Front End Engineering Design
FEP	Features, Events and Processes. A Feature that represents a component of a storage system or an Event or Process relevant to its evolution. The term includes 'external' FEPs or EFEPs that are part of the global system but external to the storage system; the EFEPs may however act upon the system to alter its evolution (e.g. seismic effects). Together, the FEPs of the system describe conceptual models that may be related to scenarios for system evolution
FIT	Formation Integrity Test
FMI	Fullbore Micro-Resistivity Image Tool
Forewind	Offshore wind farm operator
Frac Test	
FVF	Formation Volume Factor
GASSCO	Langed pipeline operator
GEM-GHG™	A reservoir simulation by Computer Modelling Group Limited specifically designed for simulating CO ₂ sequestration processes.
GM	Geomechanical models
GR	Gamma Ray log
GRnorm	Normalised gamma ray log
GRV	Gross Rock Volume
GWC	Gas Water Contact
H ₂	Hydrogen
H ₂ O	Water
H ₂ S	Hydrogen sulphide
Hardground	In the context of this application the term hardground refers to sandstone that has been cemented by pore filling cements. The reservoir quality of the hardground sandstone is very poor and it

Term	Explanation
	generates an acoustically faster response on sonic logs and can be recognised on seismic data.
Heterolithic	A compound facies type that comprises a range of poorer reservoir quality facies that are commonly seen together. They usually include fine-grained sandstones, silts and shales.
HMI	Human machine interface
HVDC	High voltage direct current (for offshore subsea electric power lines)
II	Injectivity Index
IID	Internal inspection device (intelligent pig)
Isochore	Depth thickness (vertical in this context)
Isochron	TWT thickness (vertical in this context)
ISSM	gamma-ray In-Situ Saturation Monitoring
K_H	Horizontal permeability
KP	Kilometre point (for the offshore pipeline)
K_{rg}^M	The maximum gas (CO ₂) relative permeability
K_V	Vertical permeability
Langeded	UK – Norway gas pipeline interconnector
LAT	Lowest astronomical tide level
Layers	The intervals that subdivide a zone
LER	Local equipment room (platform)
Lithostratigraphy	The description, definition and naming of rock units
LL7	early laterolog resistivity tool
LOT	Leak-off test
LTOBM	Low toxicity oil based mud (for well drilling)
LWD	Logging while drilling equipment
mD	milli Darcy
MD	Measured Depth
MDBRT	measured depth below rotary table (well depth reference)
MDT	The Modular formation Dynamic Tester (MDT) is a Schlumberger wireline tool used for measuring formation pressure and collecting reservoir fluid samples.
MEG	Monoethylene glycol (for hydrate inhibition)
MICP	Mercury Injection Capillary Pressure
Mis-tie	In seismic interpretation, mis-tie refers to the absolute error, in terms of two way travel time, between an interpreted seismic horizon and its associated geological pick at a well location containing a velocity function allowing depth to time transforms.
MMscf	Million standard cubic feet
MMV plan	Measurement, Monitoring and Verification plan
MPa	Mega Pascal
MT	Million tonnes
Mt	Million tonnes (conventional numerically identical definition is megatonne)
MTPA	Million tonnes per annum
Mudline	seabed (at water depth)
MW	Mega Watts
MWD	measurement while drilling equipment
N ₂	Nitrogen

Term	Explanation
NACE	National Association of Corrosion Engineers
NaCl	Sodium chloride (salt)
NCP	Net Confining Pressure
NDE	Non-destructive testing (typically ultrasound, eddy current and radiography)
NGCL	National Grid Carbon Limited
NMR /CMR	Nuclear Magnetic Resonance Tool (generic name / Schlumberger brand)
NO _x	Generic term for the mono-nitrogen oxides, and nitric oxide (NO) and nitrogen dioxide (NO ₂)
NPV	Net Pore Volume
NTG	Net To Gross ratio
NUI	Normally unmanned installation (offshore platform)
O ₂	Oxygen
OBC	Ocean Bottom Cable
OD	Outside diameter (pipelines and casing)
ohmm	units of resistivity measurement
Ooid	Small (up to 2mm in diameter), spheroidal, layered sedimentary grains, usually composed of calcium carbonate and usually formed in shallow tropical seas.
OPP	Oxyfuel power plant
Overburden	Stratigraphic interval above the top of the reservoir.
P _c	Capillary Pressure
PD8010 Parts 1 & 2	British Standard for steel pipelines onshore and subsea
pH	A numeric scale used to specify the acidity or alkalinity of an aqueous solution (the negative log of the activity of the hydrogen ion). Solutions with a pH less than 7 are said to be acidic and solutions with a pH greater than 7 are basic or alkaline. Pure water has a pH of 7.
Phase	The angle or lag/lead of a sine wave with respect to a reference or time zero.
PHI_CMV	Total porosity from CMR tool
PHIE/PHIT	Total Log Porosity / Effective Porosity
PHREEQC	A computer program written in the C programming language that is designed to perform a wide variety of low-temperature aqueous geochemical calculations.
PI	Productivity Index
Polarity	If a seismic amplitude arises from a geological layer that produces an increase in acoustic impedance across it, the polarity is a function of how that seismic amplitude is displayed. By convention, positive polarity is displayed as a peak for an increase in acoustic impedance. If the signal arises from a reflection that indicates a decrease in acoustic impedance, the polarity is termed negative and is displayed as a trough.
ppg	pounds per gallon (for mud density)
ppmv	parts per million by volume
PREN	Pitting resistance equivalent number (in respect of alloy quality)
PRP	Phase reversal polygon is a boundary clearly seen on seismic that separates clean Bunter sandstones (within) from sands strongly affected by halite cementation (outwith). A possible explanation for this boundary is the thermo-haline convection theory (Ref) that may result in salt dissolution within a limited rock volume. See also SPR.
PTA	Pressure Transient Analysis
PV	Pore Volume
PVT	Pressure, volume and temperature and refers to the physical properties shown by hydrocarbon fluids

Term	Explanation
Rc	Uniaxial Compressive Strength
RCA	Routine Core Analysis
Resistivity	A measure of the resisting power of a specified material to the flow of an electric current
RFT	Repeat Formation Tester (wireline tool used for measuring formation pressure and collecting reservoir fluid samples)
RHOB	Bulk formation density
RHOcl	Density value in 100% clay
RHOfl	Density value in 100% fluid
RHOma	Density value in 100% matrix
ROV	Remotely operated vehicle (submersible)
RSFM	Regional Structural Framework Model
Rw / Rt / Rdeep	Water Resistivity / True Resistivity of formation / deep resistivity
SCAL	Special Core Analysis
SD	Standard deviation
SFW	Synthetic Formation Water (also synthetic formation brine)
SG	specific gravity
S _{gc}	The critical gas saturation
S _{gt}	The trapped gas (on imbibition) saturation
S-Lay	Offshore pipeline installation method
SM25CRW	Super duplex stainless steel material to specification API 5CT / ISO 11960
SmartWind	Offshore wind farm operator
SNS	Southern North Sea
SPR	Seismic Phase Reversal (see also PRP)
SST	Single Stage Triaxial
S _{wi}	The irreducible water saturation
T&S System	Transport and storage assets of the White Rose Project
Tartan Grid	A model grid that has a fine scale cell lateral dimensions in a rectangular core area, which become progressively coarser on the margins of that area. Visualised in plan view the grid has a tartan like appearance.
TDS	Total Dissolved Solids
THP	Tubing Head Pressure
TOL	Top of liner (7" production liner)
TVD	true vertical depth
TVDSS	Total vertical depth subsea (referenced to the depth below the Mean Sea Level for wells)
TWC	Thick Walled Cylinder
TWT	Two way traveltime
UK	United Kingdom
Underburden	Stratigraphic interval below the base of the reservoir.
UXO	Unexploded ordinance
V0k	A linear with depth function that takes the form of the equation of a straight line as in $V_i = V_0 + k(z)$. This equation states that the instantaneous velocity (V_i) increases linearly with depth (z) where V_0 is a constant related to the velocity at the start of a particular layer in the velocity model and k is an acceleration term that describes the compaction of the rock interval depth.
VAM TOP (HT)	Vallourec proprietary casing connection type (high temperature rated)

Term	Explanation
Variogram	A variogram is a function that defines how data varies spatially with distance. Variograms can be isotropic, showing the same relationship in all directions, or anisotropic, where the relationship varies in the X, Y and Z directions, respectively.
Vclay, VCL	volume of clay from logs
VIT	A vertical interference test or VIT is method of monitoring a pressure pulse created by drawdown from formation tester such as a MDT across a small interval of formation (2-11m) in a well.
VIT	Vertical Interference Test
VLP	Vertical Lift Performance
WD	Water depth
WHT	Wireline Head Thermometer
WIIP	Water Initially in Place
WWII	The Second World War (1939-1945)
Xline	(cross-line) a seismic line within a 3D survey orthogonal to the direction in which the data was acquired
Zone	The thickness interval between stratigraphically defined horizons